INFLUENCE OF THERMO-MECHANICAL PROCESSING ON FRACTURE BEHAVIOR OF Zr-2.5Nb ALLOY

by

HARSHIT KUMAR KHANDELWAL
ENGG01201104009

Bhabha Atomic Research Centre, Mumbai

A thesis submitted to the

Board of Studies in Engineering Sciences

In partial fulfillment of requirements for

the Degree of

DOCTOR OF PHILOSOPHY

of

HOMI BHABHA NATIONAL INSTITUTE

February, 2016

Homi Bhabha National Institute[1]

Recommendations of the Viva Voce Committee

As members of the Viva Voce Committee, we certify that we have read the dissertation prepared by Harshit Kumar Khandelwal entitled “Influence of Thermo-Mechanical Processing on Fracture Behavior of Zr-2.5Nb alloy” and recommend that it may be accepted as fulfilling the thesis requirement for the award of Degree of Doctor of Philosophy.

Chairman - Dr. D. Srivastava **Date:** 3.2.2016

Guide / Convener - Dr. R. N. Singh **Date:** 03/02/2016

Co-guide - Dr. J. B. Singh **Date:** 03/02/2016

Examiner - Prof. B. P. Kashyap **Date:** Feb. 03, 2016

Member 1 - Dr. K. B. Khan **Date:** 3-2-16

Member 2 - Dr. A. K. Arya **Date:** 03/02/2016

Final approval and acceptance of this thesis is contingent upon the candidate’s submission of the final copies of the thesis to HBNI.

I/We hereby certify that I/we have read this thesis prepared under my/our direction and recommend that it may be accepted as fulfilling the thesis requirement.

Date: 3rd February, 2016

Place: Mumbai

Co-guide **Guide**

---

[1] This page is to be included only for final submission after successful completion of viva voce.

STATEMENT BY AUTHOR

This dissertation has been submitted in partial fulfillment of requirements for an advanced degree at Homi Bhabha National Institute (HBNI) and is deposited in the Library to be made available to borrowers under rules of the HBNI.

Brief quotations from this dissertation are allowable without special permission, provided that accurate acknowledgement of source is made. Requests for permission for extended quotation from or reproduction of this manuscript in whole or in part may be granted by the Competent Authority of HBNI when in his or her judgment the proposed use of the material is in the interests of scholarship. In all other instances, however, permission must be obtained from the author.

(Harshit Kumar Khandelwal)

DECLARATION

I, hereby declare that the investigation presented in the thesis has been carried out by me. The work is original and has not been submitted earlier as a whole or in part for a degree / diploma at this or any other Institution / University.

(Harshit Kumar Khandelwal)

LIST OF PUBLICATIONS ARISING FROM THE THESIS

Journal

1. "Influence of soaking temperature and time on microstructure and mechanical properties of water quenched Zr-2.5Nb alloy", H. K. Khandelwal, R. N. Singh, A. K. Bind, Saurav Sunil, B. N. Rath, J. B. Singh, S. Kumar and J. K Chakravartty, *Material Performance and Characterization*, **2014**, *Vol. 3 (1)*, 216-238.
2. "Comparative study of Basic test and Resistance curve methods for fracture toughness evaluation of heat treated Zr-2.5Nb alloy", H. K. Khandelwal, R. N. Singh, A. K. Bind, Saurav Sunil, and J. K Chakravartty, *Material Performance and Characterization, Special issue on 'Fracture Toughness'*, **2014**, *Vol. 3 (3)*, 21-44.

3. "Tensile properties and Fracture toughness of Zr-2.5Nb alloy pressure tubes of IPHWR220", H. K. Khandelwal, R. N. Singh, A. K. Bind, S. Sunil, J. K. Chakravartty, A. Ghosh, P. Dhandharia, D. Bachawat, R. Shekhar, S. Jaikumar, *Nuclear Engineering and Design*, **2015,** *Vol. 293*, 138-149.

4. "Fracture Toughness Evaluation of Solution Heat Treated Zr-2.5Nb Alloys as per ASTM and ISO Standards", H. K. Khandelwal, R. N. Singh, J. K. Chakravartty, *Journal of Testing and Evaluation*, **2016**, *Vol. 44 (4)*, DOI: 10.1520/JTE20140329.

Conference

1. "Influence of Solution Heat-Treatment parameters on tensile and fracture behavior of Zr-2.5Nb alloy" H. K. Khandelwal, A. K. Bind, S. Sunil, B. N. Rath, R. N. Singh, J. B. Singh, S. Kumar, J. K. Chakravartty, Transactions, *SMiRT-22***,** San Francisco, California, USA - August 18-23, 2013.

2. "Influence of solution heat-treatment and water quenching on fracture toughness of Zr-2.5Nb alloy" H. K. Khandelwal, R. N. Singh, A. K. Bind, Saurav Sunil, B. N. Rath, J. B. Singh, S. Kumar and J. K Chakravartty, *The Indian Institute of Metals NMD-ATM*, 12th to 15th November, 2013.

(Harshit Kumar Khandelwal)

DEDICATIONS

This thesis is dedicated to

The God,

my parents

(Mr. S. K. Khandelwal and Mrs. Shashi Khandelwal)

and

my brother

(Arpit Khandelwal)

ACKNOWLEDGEMENTS

Words are often less to revel one's deep regards. I take the opportunity to express my profound sense of gratitude and respect to all those who directly or indirectly helped me during this work.

I take the opportunity to express my heartfelt adulation and gratitude to my supervisors, **Dr. R. N. Singh, Head, Fracture Mechanics Section** and **Dr. J. B. Singh, Head, Structural Metallurgy Section, BARC, Mumbai** for their unreserved guidance, constructive suggestions and thought provoking discussions in nurturing the work. It has been a benediction for me to spend many opportune moments under the guidance of the perfectionist at the acme of professionalism. I offer regards to **Dr. J. K. Chakravartty, Director, Materials Group and Head, Mechanical Metallurgy Division, BARC, Mumbai** for allowing me to perform the practical work in Mechanical Metallurgy Division.

I sincerely acknowledge the help of **Shri S. Vijayakumar, Former Associate Director, Engineering Directorate, NPCIL, Mumbai** in arranging the full length Zr-2.5Nb pressure tube for conducting present study. I am thankful to **Mr. N. K. Prasad, TPD, BARC, Mumbai** for allowing me to utilize his workshop facilities during material procurement stage. I am thankful to **Mr. M. M. Hussain** and **Mr. A. K. Singh**, **AFD**, **BARC, Mumbai** for allowing me to use the rolling mill. I am thankful to **Dr. Madangopal K., Dr. A. K. Sahu and Mr. P. V. Gaikwad, GAMD, BARC, Mumbai** for facilitating SEM to carry out the fractographic studies, **Dr. D. Srivastava** and **Mr. Suman Niyogi, MSD, BARC, Mumbai** for facilitating the TEM examinations, **Dr. R. Mythili** and **Dr. Saroja SaiBaba, Microscopy & Thermo-Physical Property Division, IGCAR, Kalpakkam** for facilitating the EDS examinations of Carbon extraction replicas, **Dr. Satyam Suwas, Associate Professor, IISc, Bangalore** for facilitating the texture measurements and **Dr. A. Laik** and **Dr. G. K. Dey, Associate Director, Materials Group and Head, Materials Science Division, BARC, Mumbai** for facilitating the EPMA measurement, **Dr. K. V. Mani Krishna** and **Mr. Nachiket A Keskar**, **MSD, BARC, Mumbai** for facilitating EBSD examination and **Mrs. Komal Chandra**, **RACD, BARC, Mumbai** for facilitating the hydrogen analysis. I am also thankful to **Dr. Joy Mittra, BARC, Mumbai** for allowing me to use the grinding machine.

I am also thankful to **Mr. A. K. Balasubramanian, NPCIL** for his support in arranging accommodation for my visit to **NCCCM**, **Hyderabad**. I acknowledge **Mr. A.K. Bind, MMD, BARC, Mumbai** in helping me to understand DCPD testing and tests analysis. Suggestions for the improvement in aesthetics of synopsis from **Dr. R. Tewari**, **MSD, BARC, Mumbai** is also acknowledged.

I would also like to express my deep gratitude to **Mr. K. C. Mazumdar** and **Mr. P. S. Shembe, MMD, BARC, Mumbai** for their valuable technical assistance. Assistance from the technical staff of RSSD, BARC, Mumbai: **Mr. Sachin Bobade**, **Mr. Anil Salakram** and **Mr. C. Andrews**; MSD, BARC, Mumbai: **Mr. R. V. Hatwar, Mr. R. D. Hankare** and **Mr. R. R. Rajagopalan;** MPD, BARC, Mumbai: **Sumanta Behera;** and G&AMD, BARC, Mumbai: **Mr. M. T. Arjune** and **Mr. K. M. V. C. Nair** as well as the technicians of Fitting Shop of Electronics Division is deeply acknowledged. Support from **Mr. Ashok Chaudhary**, **TPD, BARC Mumbai** in allowing to use workshop facility and technical assistance from the staff of TPD workshop: **Mr. S. R. Patankar**, **Mr. Dasharath Hatle**, **Mr. Vishal Pagade**, **Mr. V. S. Moundekar**, **Mr. Ravi Kamble**, **Mr. Sanjay R. Patil**, and **Mr. S. C. Vordekar** is also acknowledged.

I take pride of myself being son of ideal parents for their everlasting desire, extensive sacrifice, affectionate blessings and tremendous help, without which it would not have been possible for me to complete my studies.

Above all, I express my indebtedness to the “ALMIGHTY” God, for all his blessings and kindness, without which this work would not have been performed.

(Harshit Kumar Khandelwal)

CONTENTS

CHAPTER 4: INFLUENCE OF SOLUTION HEAT TREATMENT PARAMETERS ON FRACTURE BEHAVIOR OF Zr-2.5Nb ALLOY ………. 89-160

SYNOPSIS

Zr-2.5Nb alloy pressure tubes constitute the most important in-core component of Pressurized Heavy Water Reactors (PHWRs), by serving as the containment for hot heavy water coolant circulating in reactor’s primary heat transport system. For reactor's safe operation, structural integrity of pressure tubes has to be ensured during service. Fracture behavior is the most important structural integrity aspect of pressure tubes during their normal operation as well as under accidental conditions. Fracture is the measure of resistance to crack propagation. In addition, it also provides the limit of stable crack propagation before catastrophic failure. This crack length is called 'Critical Crack Length' (*CCL*), which governs the necessary safety margin for satisfying Leak Before Break (LBB) condition of pressure tubes. Fracture toughness of an operating pressure tube is the function of its initial microstructure, which is in-turn the function of fabrication route employed for tube manufacturing and its associated Thermo-Mechanical Processing (TMP) parameters.

Pressure tubes currently installed in different PHWRs throughout the world have variability among their as-fabricated microstructures, because of being manufactured employing different fabrication routes viz., 'Cold Worked and Stress Relieved' (CWSR), 'Cold Worked and Annealed' (CWA), 'Water Quenched and Aged' (WQA) and 'Gas Quenched and Aged' (GCA). Out of these, pressure tubes fabricated using WQA route have reportedly shown superior resistance to in-reactor dimensional changes, which ensures their higher operating lives. This has led to renewed interest in the development of WQA route for the manufacturing of pressure tubes of CANDU, Indian PHWRs (IPHWRs) and 'Advanced Heavy Water Reactor' (AHWR).

The WQA routes currently being employed by different countries have variation in their TMP parameters of the three major final stages of fabrication viz., solution heat treatment (SHT), cold working and vacuum aging, and also in their alloy chemistries. These TMP parameters including soaking temperature and duration of SHT, degree of subsequent cold working and soaking temperature of subsequent aging treatment could be important for governing the final microstructure and therefore fracture behavior of the fabricated tube material. Therefore, to utilize WQA route in future applications, it is extremely important to optimize these TMP parameters, so as to ensure the best fracture behavior and hence structural integrity of as-fabricated tube material. Furthermore, these optimized TMP parameters will also be extremely useful for the pressure tube fabrication of modern reactors such as; AHWR, which is being designed for 100 year of operating life, so as to ensure fewer pressure tube replacements and thereby reducing the cost of power production.

The objective of this work was to study the influence of aforementioned TMP parameters associated with SHT, subsequent cold working and vacuum aging stages of WQA route on fracture behavior of Zr-2.5Nb alloy. Selections of TMP parameters for this study were done by taking into consideration the parameters used for the manufacturing of such heat treated tubes by various manufacturers. Table 1 lists the TMP parameters and associated degrees of variability considered in present study.

Table 1: TMP parameters associated with SHT, subsequent cold working and vacuum aging stages of WQA route, employed in the present study.

S. No	**Fabrication Stage**	**TMP Parameters**	**Degree of Variability**	**No. of Conditions**
1	Solution heat treatment	Soaking temperature	850, 870 & 890°C	3 x 2 = 6
		Soaking duration	15 & 30 min	
2	Cold working	Degree of cold work	10 & 20 %	6 x 2 = 12
3	Vacuum aging	Soaking temperature	500 & 540°C	12 x 2 = 24
		Soaking duration	24 h	

This study was performed in three stages corresponding to the final stages of WQA fabrication route. These are:

Stage I: Study of the influence of solution heat treatment parameters; soaking temperature and duration on fracture behavior of Zr-2.5Nb alloy,

Stage II: Study of the influence of degree of cold working on fracture behavior of Zr-2.5Nb alloy, under various solution heat treated conditions, and

Stage III: Study of the influence of aging temperature on fracture behavior of Zr-2.5Nb alloy under various cold worked & solution heat treated conditions.

The fracture behavior was studied at RT (25°C) and reactor operating temperature (300°C), in terms of fracture resistance *J-R* curves, crack initiation (J_Q) and propagation toughness ($J_{F(max)}$, *dJ/da* & *CCL*) parameters, determined as per ASTM and ISO standards. In addition, tensile properties, micro-hardness, microstructure, crystallographic texture, Nb partioning, phase analysis and fractography studies were also performed to understand the fracture behavior.

This thesis is organized in seven chapters. Chapter 1 'Introduction', describes the background, motivation and objective of the study. Chapter 2 'Literature Review' presents the summarized literature concerning Zr-2.5Nb alloy pressure tubes, their structural integrity concerns, fabrication, relevance of fracture behavior and various fracture toughness evaluation approaches. Chapter 3 'Experimental Procedures' describes details of various test procedures employed for the study. Chapters 4, 5 and 6 respectively present the results and discussion of stage I, II and III studies. Chapter 7, Conclusion summarizes the outcomes of three studies and suggests the optimized TMP parameters of WQA route for ensuring best fracture behavior of as-fabricated tube material. At the end, suggestions for conducting future studies are highlighted. Some of the key results of Chapters 4, 5 and 6 are described in brief as follows.

Chapter 4: Influence of SHT Parameters on Fracture Behavior of Zr-2.5Nb alloy

Chapter first describes the influence of SHT temperature (850-890°C) and soaking duration (15-30 min) on microstructural features, examined using optical microscopy. Solution heat treated materials comprised two phase (primary α & α’) microstructures having substantial reduction in primary α precipitates from ~ 36 to 6% with increasing SHT temperature from 850 to 890°C (Figure 1 (a)). The image analysis of microstructure showed that primary α grain size has weak dependence on SHT parameters; however, increase in SHT temperature and soaking duration causes substantial grain coarsening of α’ (Figure 1 (a)). Crystallographic texture examinations performed using X-ray diffraction showed small variation of Kearns parameters along axial, transverse and radial directions, and therefore suggested random texture of these materials (Figure 1 (b)). Also, SHT, specially performed from a higher soaking temperature with longer soaking duration ensured superior degree of randomness in texture. Electro Probe Micro Analyzer (EPMA) examinations were performed to study the partitioning of major ‘β stabilizer’ alloying element (Nb) between α-Zr and β-Zr phases at SHT temperature. The examinations showed superior Nb partitioning during SHT performed at higher soaking temperature with longer soaking duration.

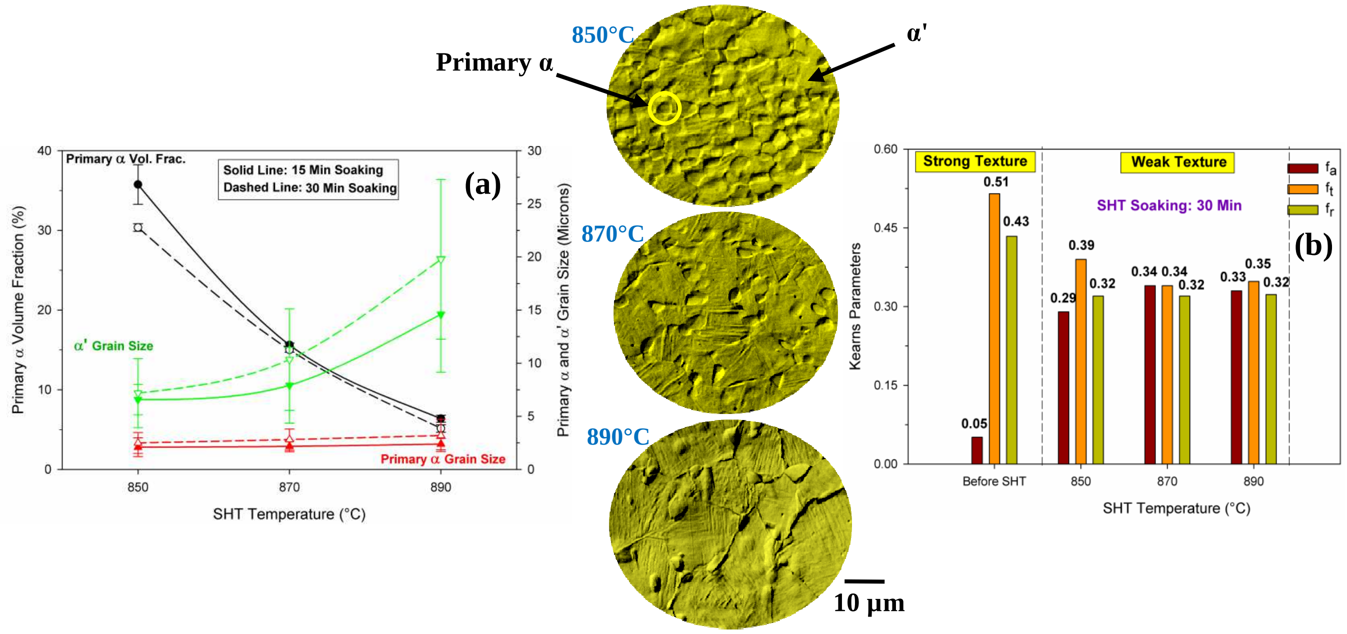

Figure 1: (a) Variation of primary α volume fraction and primary α & α’ grain size as a function of SHT temperature, and (b) Influence of SHT on Kearns texture parameters of Zr-2.5Nb alloy.

Variation of SHT temperatures within 850-890°C and soaking duration within 15-30 min domains did not significantly influence the tensile behavior of solution heat treated Zr-2.5Nb alloy. Within these ranges, tensile strengths exhibited marginal reduction with increase in SHT temperature and duration, Figure 2 (a). During SHT, soaking duration governed the sensitiveness of tensile properties on SHT temperatures; longer soaking resulted in lower dependence of tensile properties on SHT temperature, Figure 2 (b).

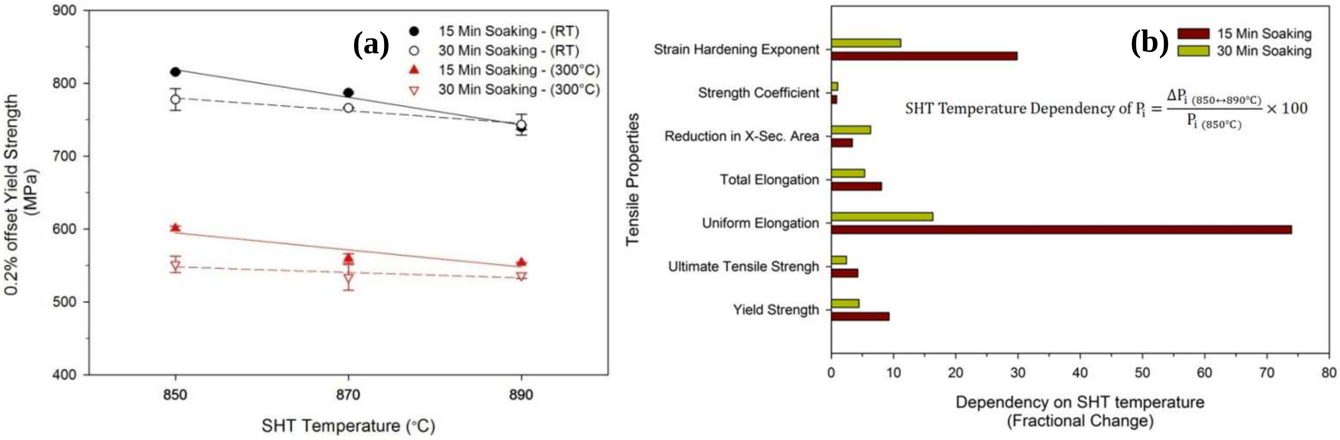

Figure 2: (a) Influence of SHT parameters on tensile strengths of Zr-2.5Nb alloy and (b) Influence of soaking duration on SHT temperature dependency of various tensile properties.

Fracture toughness was evaluated using Compact Tension, C(T) specimens with Direct Current Potential Drop (DCPD) technique used for monitoring the crack extension. The fracture toughness of solution heat treated Zr-2.5Nb alloy was practically unaffected by SHT temperatures within 850-890°C range. However, increase in SHT soaking duration from 15 to 30 min at a given SHT temperature caused marginal improvement in fracture toughness, especially at lower SHT temperatures (Figure 3).

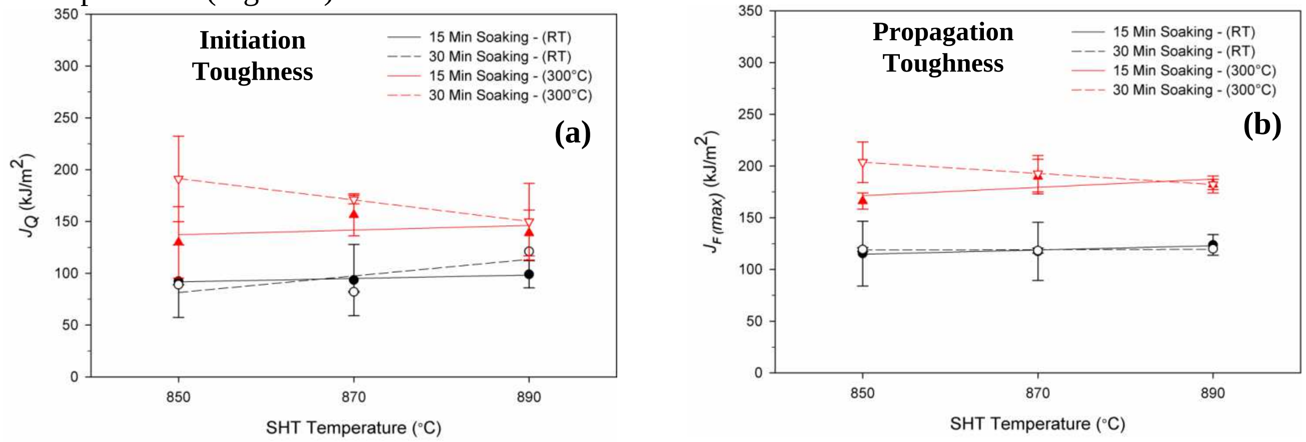

Figure 3: Influence of SHT parameters on (a) initiation (J_Q) and (b) propagation fracture toughness ($J_{F(max)}$) parameters of Zr-2.5Nb alloy at RT and 300°C.

The observed reduction in tensile strength and insignificant variation in fracture toughness parameters within 850-890°C range suggested the combined influence of decrease in primary α volume fraction, increase in grain size (especially of α' phase), and decrease in Nb super-saturation of α'. Furthermore, marginal reduction in tensile strength and improvement in fracture toughness with increasing SHT soaking duration suggested the combined influence of grain coarsening along with higher degree of Nb and O partitioning between α-Zr and β-Zr phases at SHT temperatures.

Fracture toughness examinations were followed by their correlation through the fractographic features, studied using Scanning Electron Microscopy (SEM). For this, fractographic examinations were performed at different fractured locations of the broken specimen viz., fatigue pre-cracked, stretched zone and stable tearing regions. The fatigue pre-cracked surfaces, which visually exhibited typical shiny and flat appearance, comprised several plateau like features oriented along the direction of crack propagation, and therefore representing the fatigue crack propagation paths. Under ambient condition, SHT parameters had weak influence on the streched zone widths (SZWs), by exhibiting variation between 45-67 μm (Figure 4). Nevertheless, at 300°C, materials soaked for 30 min duration, in contrast to 15 min during SHT, exhibited relatively wider stretched zones. This, therefore also indicated the higher initation toughness of longer soaked materials.

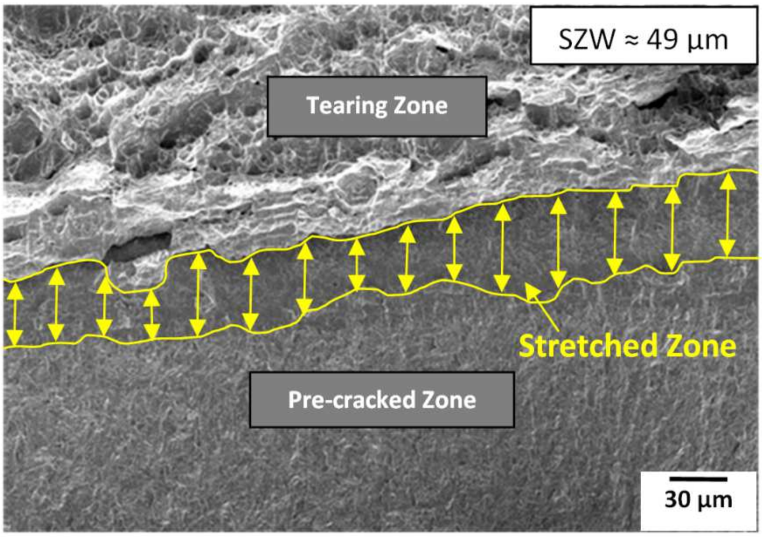

Figure 4: Stretched zone formation ahead the pre-crack tip in one of solution heat treated Zr-2.5Nb alloy during fracture under ambient condition.

The fracture surfaces of six solution heat treated materials showed typical dimple structure characteristic of a ductile failure, having a mixture of marginally parabolic (elongated) and equiaxed shaped dimples (Figure 5). The dimples had in-homogeneity in their sizes, which therefore suggested the non-uniform distribution of their nucleation sites.

Under ambient fracture condition, dimples were relatively smaller in size, having size distribution from < ~ 1 µm to as big as ~ 6 µm, Figure 5 (a). In contrast, fracture at 300°C resulted in the formation of relatively bigger and deeper dimples, having size in-homogeneity ranging from ~ 2 µm to as big as ~ 30 µm, Figure 5 (b). In addition, dimples formed at 300°C, in contrast to those formed under ambient condition contained typical deformation markings on their walls (Figure 5 (b)), which therefore also indicated higher plasticity and toughness of solution heat treated materials at elevated temperature.

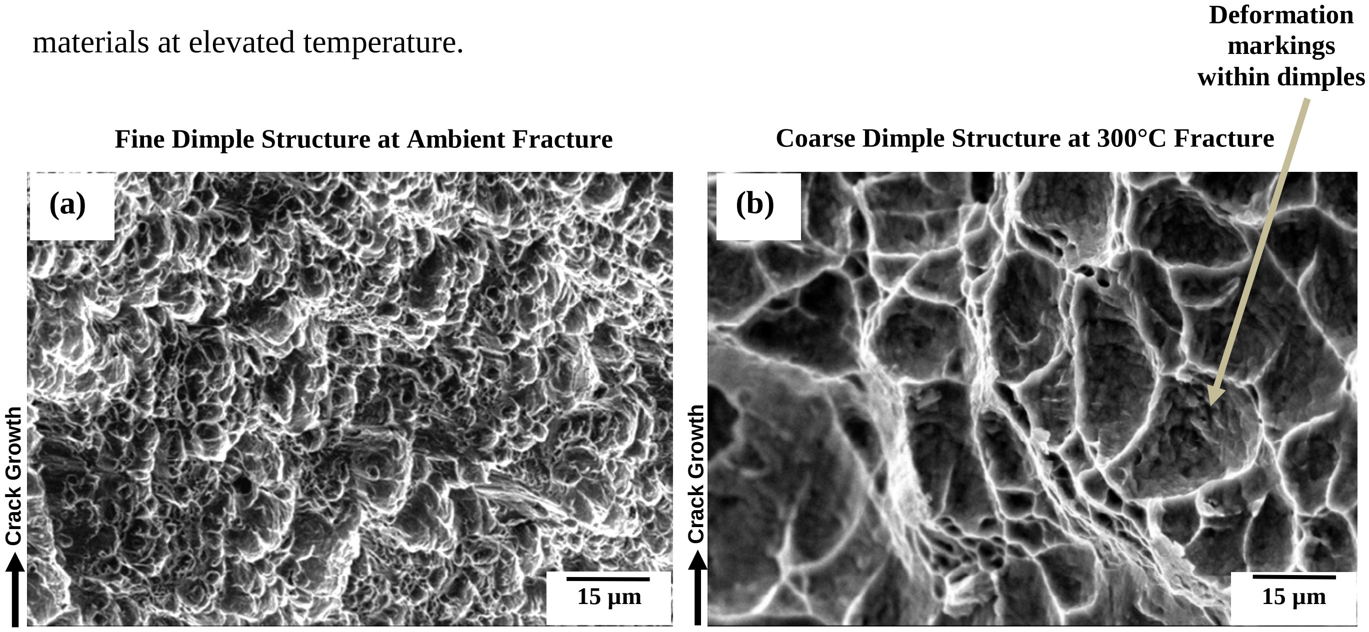

Figure 5: Fractographs showing typical dimple structure characteristics of ductile fractures at (a) ambient and (b) 300°C.

Chapter 5: Influence of Degree of Cold Work on Fracture Behavior of Solution Heat Treated Zr-2.5Nb alloy

This chapter describes influence of 0-20% degree of cold working (rolling) on fracture behavior of Zr-2.5Nb alloy, under different solution heat treated conditions. Chapter begins by presenting changes in microstructural features, describing elongated grain morphologies along rolling direction, Figure 6 (a). Crystallographic texture examinations of these cold worked materials showed that cold rolling treatment causes basal pole alignment along radial (i.e., compressive strain) direction with corresponding reduction along axial (i.e., rolling) direction, Figure 6 (b).

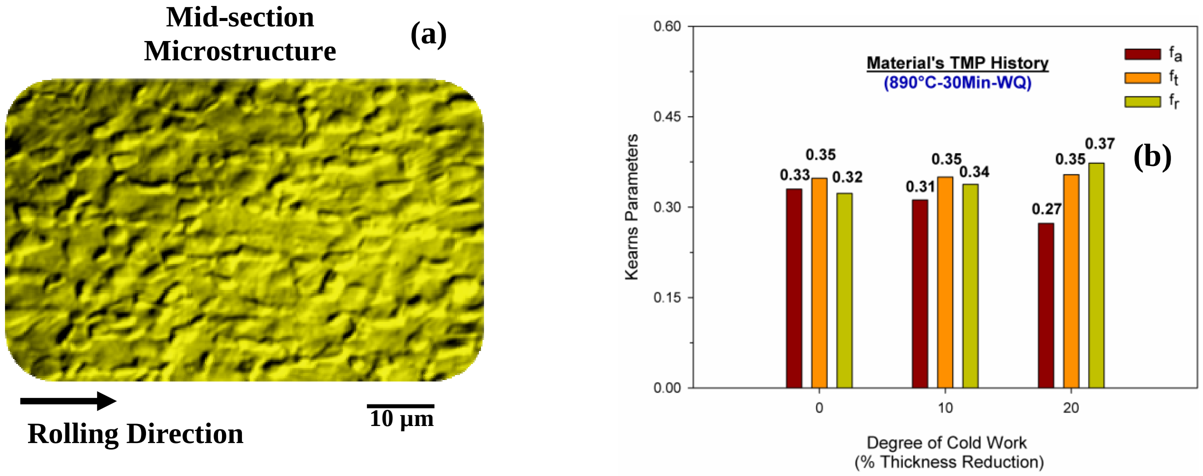

Figure 6: (a) Elongated mid-section microstructure of solution heat treated Zr-2.5Nb alloy after cold rolling, and (b) Influence of cold working on Kearns texture parameters of solution heat treated Zr-2.5Nb alloy.

Cold working treatment had notable influence on tensile properties, under ambient condition, Figure 7 (a). However, at 300°C, it showed weak influence on ductility and strain hardening characteristics, Figure 7 (b). Initial 10% cold working caused major changes in the tensile properties. However, with subsequent additional 10% cold working, further changes in tensile properties were marginal. Parameters such as soaking duration used during SHT, degree of imparted cold working and selected test temperature governed the sensitiveness of tensile properties with SHT temperature. With increase in any of these factors, tensile properties became less dependent on SHT temperature.

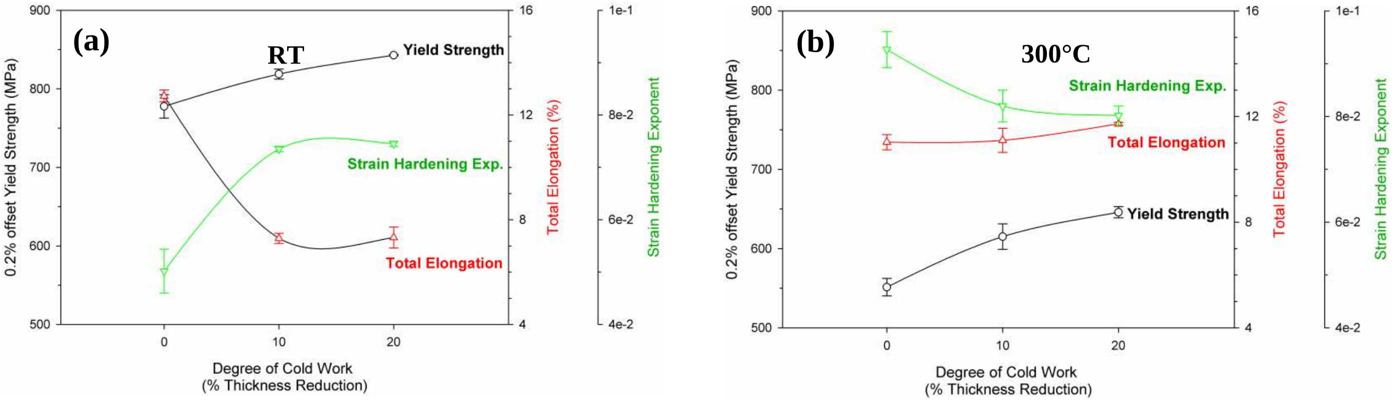

Figure 7: Influence of cold working on tensile properties of solution heat treated Zr-2.5Nb alloy at (a) RT and (b) 300°C.

Cold working, in general decreased the fracture toughness of solution heat treated materials, though up to 20% cold work such changes were not significant (Figure 8 (a)). Also, different cold worked materials, irrespective of having variable prior SHT histories, had comparable fracture toughness.

SEM fractography examinations were performed to study fracture surface features. The fracture surfaces of cold worked materials, similar to SHT materials showed typical dimple structure characteristic of a ductile failure. However, contrary to SHT materials, cold worked materials exhibited relatively shallow dimples, especially on the narrow central flat fractured region and the clusters of fine dimples, which therefore indicated reduction in fracture toughness because of cold working, Figure 8 (b). Morphology wise, dimples of cold worked materials were almost similar to those of the solution heat treated materials, exhibiting a mixture of parabolic and equiaxed shape.

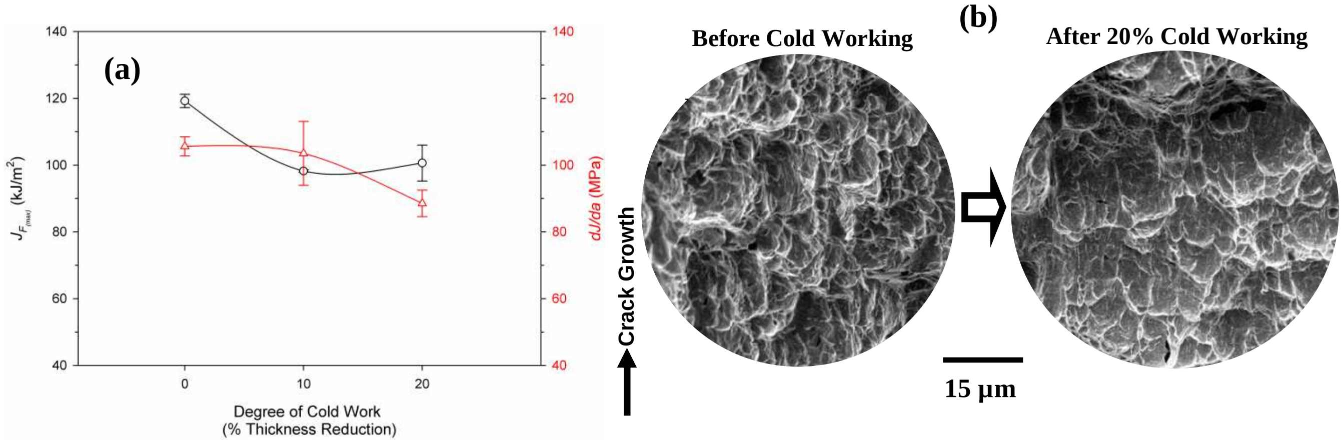

Figure 8: (a) Influence of cold working on fracture toughness of solution heat treated Zr-2.5Nb alloy and (b) SEM fractographs, illustrating change in dimple features because of cold working.

Quantification of fracture surface areas performed using image analysis technique suggested increase in central flat fracture area with increase in degree of cold working. This therefore suggested that cold working upto 20% causes shifting of state of stress ahead of the crack tip towards plain strain condition.

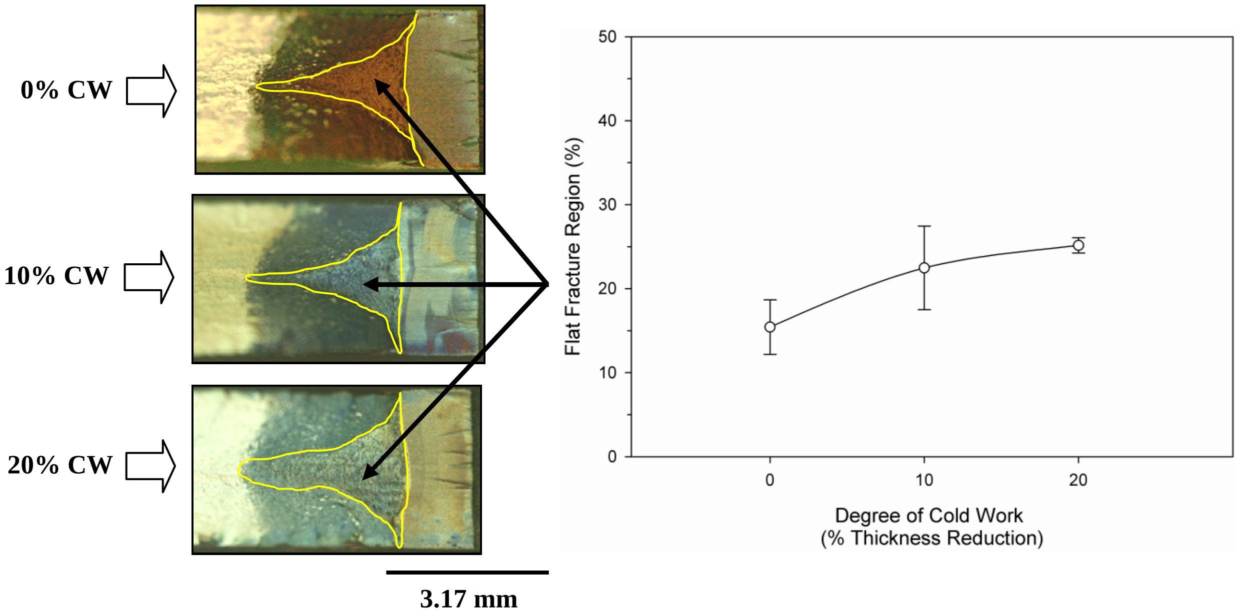

Figure 9: Influence of cold working on central flat fractured region (enclosed by yellow boundaries) in solution heat treated Zr-2.5Nb alloy. In these figures (Left), regions enclosed by yellow boundaries represent the flat fractured regions.

Chapter 6: Influence of Aging Temperature on Fracture Behavior of Cold Worked-Solution Heat Treated Zr-2.5Nb alloy

This chapter describes third stage study, under which influence of aging temperatures (500-540°C) on fracture behavior of Zr-2.5Nb alloy under different cold worked-solution heat treated conditions was studied. Aging at 500 and 540°C for 24 h results in the dissociation of metastable α’ phase into α-Zr and β-Zr/β-Nb phases. Under such prescribed aging condition, very fine precipitation of β phase was expected, whose size is in nanometer range, which is therefore too small to view in an optical microscope. To investigate such fine β precipitate, Transmission Electron Microscope (TEM) examinations were performed. Examinations showed array like β network at the lath boundaries of α' (Figure 10). Selection of aging temperature determined the nucleation and growth rate of β precipitates, as aging at 540°C in contrast to 500°C resulted in relatively higher density and coarser size of β precipitates. Aging at 500°C resulted in the precipitation of 23.9 nm average size, with variation ranging from 11.4 to 36.1 nm. However, aging at 540°C resulted in relatively coarser precipitation having an average size of 33.8 nm, with variation ranging from 10.3 to 67.9 nm. Morphology wise, majority of β precipitates were oval in shape, though few were having circular shape.

To examine precipitate chemistry, β particles were extracted from the matrix through carbon replicas and subsequently examined using Energy Dispersive Spectroscopy (EDS). The examinations showed significant difference in Nb concentrations within selected aging temperature window; aging at 500°C caused Nb enriched β-Nb precipitation (avg. concentration: 92%), while aging at 540°C caused the Nb lean β-Zr precipitation (avg. concentration: 8%), Figure 10.

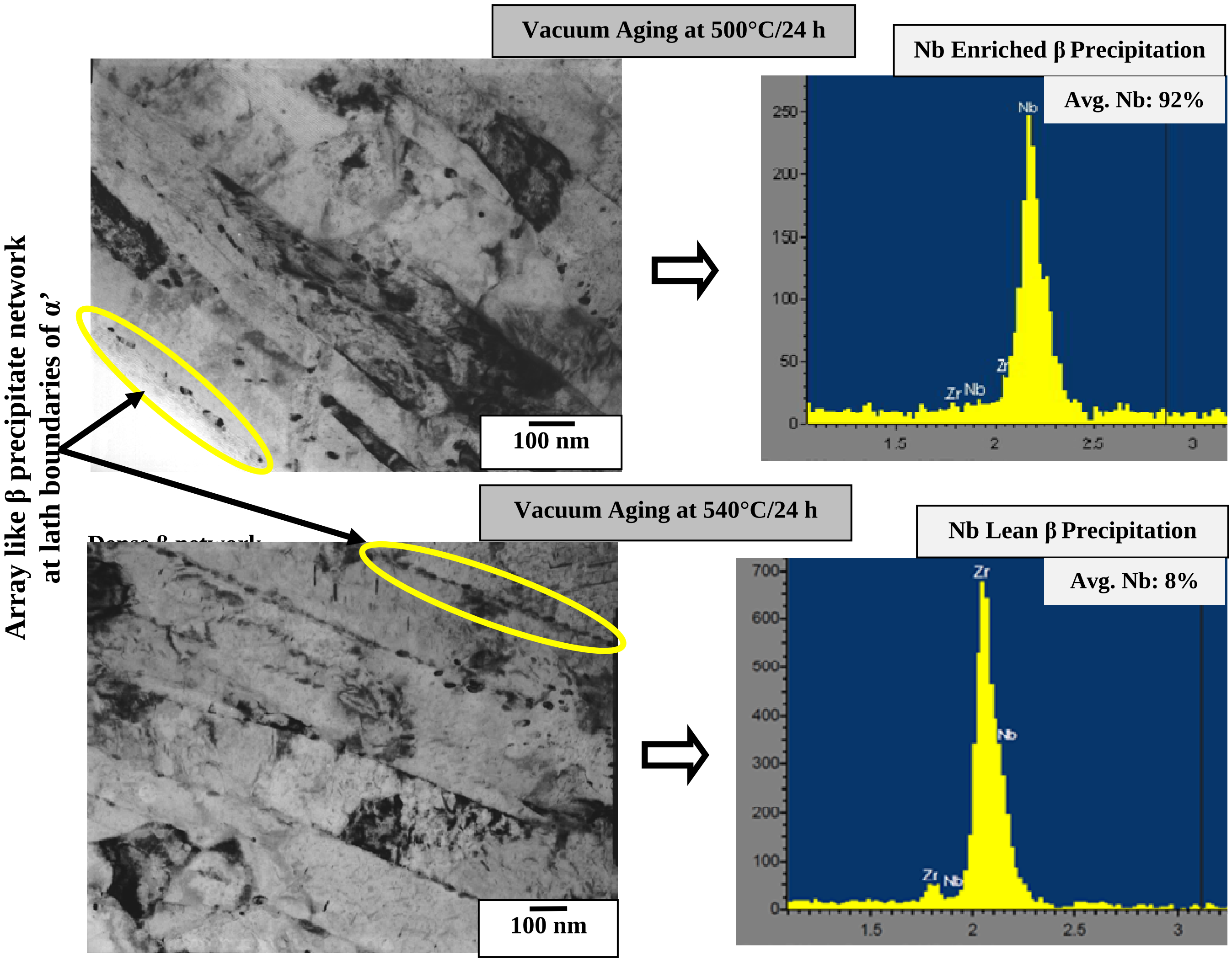

Figure 10: Influence of aging temperature on β precipitation (Left) and its chemistry (EDS spectra, in right) in a WQA Zr-2.5Nb alloy.

The crystallographic texture examinations suggested that under WQA condition, Zr-2.5Nb alloy exhibited relatively weaker basal pole texture as compared to under CWSR condition (Figure 11).

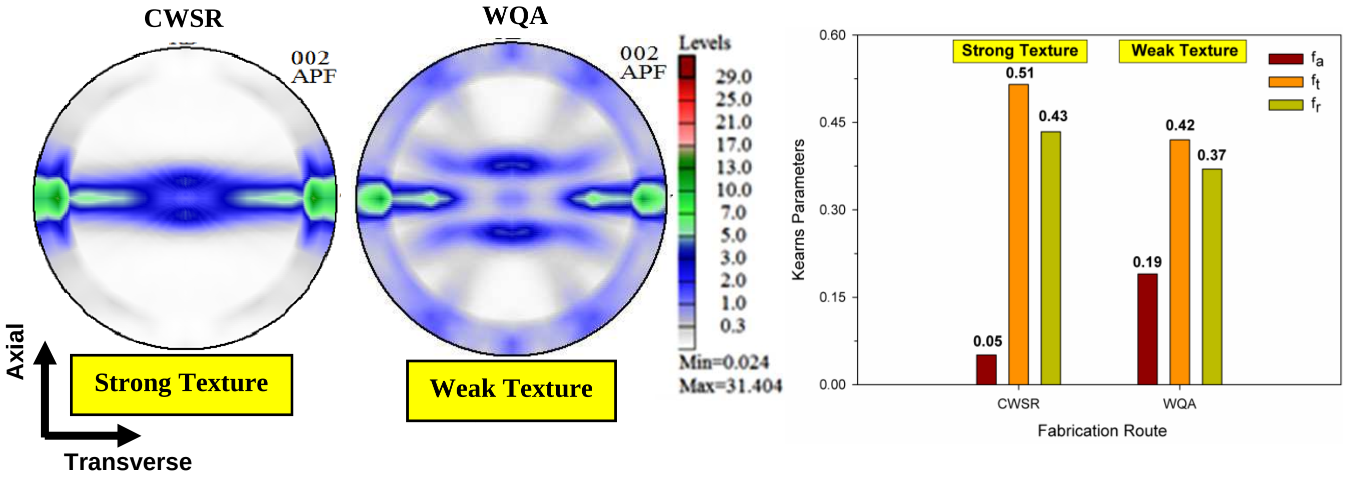

Figure 11: Comparison of basal pole texture of Zr-2.5Nb alloy under CWSR and WQA conditions; (Left) pole figures and (Right) Kearns texture parameters.

Tensile property examinations of WQA materials showed appreciable reduction of strength, and strain hardening characteristics, however, considerable improvement in ductility after aging, Figure 12. Also, variable TMP histories of WQA materials did not have significant influence on tensile properties.

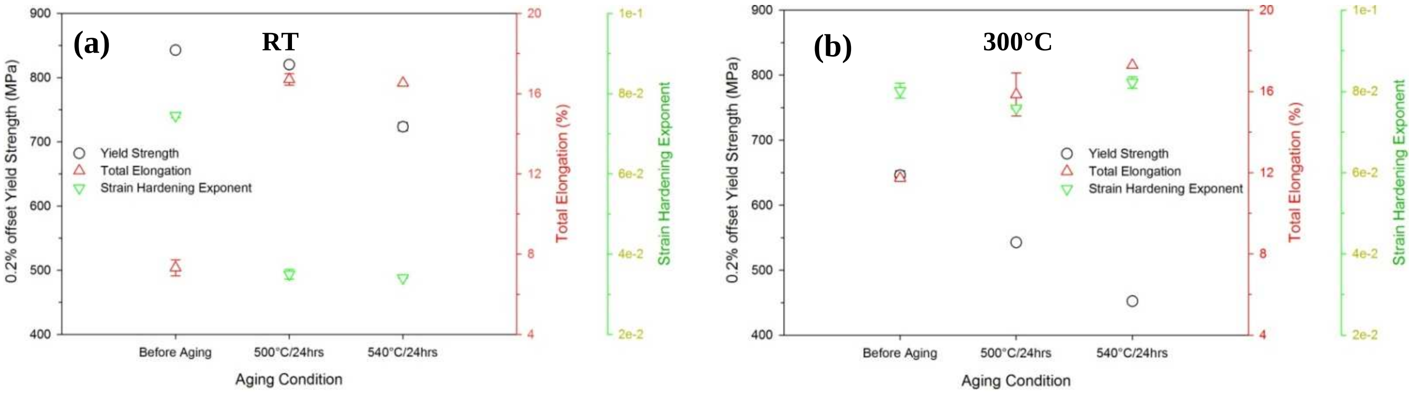

Figure 12: Influence of aging treatment on tensile properties of cold worked-solution heat treated Zr-2.5Nb alloy at (a) RT and (b) 300°C.

Under WQA condition, Zr-2.5Nb alloy possessed higher strength than under CWSR condition, especially at RT, Figure 13. This suggested the contribution of martensitic microstructure having finer substructure than CWSR tube material. In terms of ductility, WQA material was practically comparable with quadruple melted, QM-CWSR Indian pressure tube material. WQA material, showed appreciably lower strain hardening characteristics as compared to CWSR materials, which therefore suggested the influence of relatively much finer grain structure of CWSR materials.

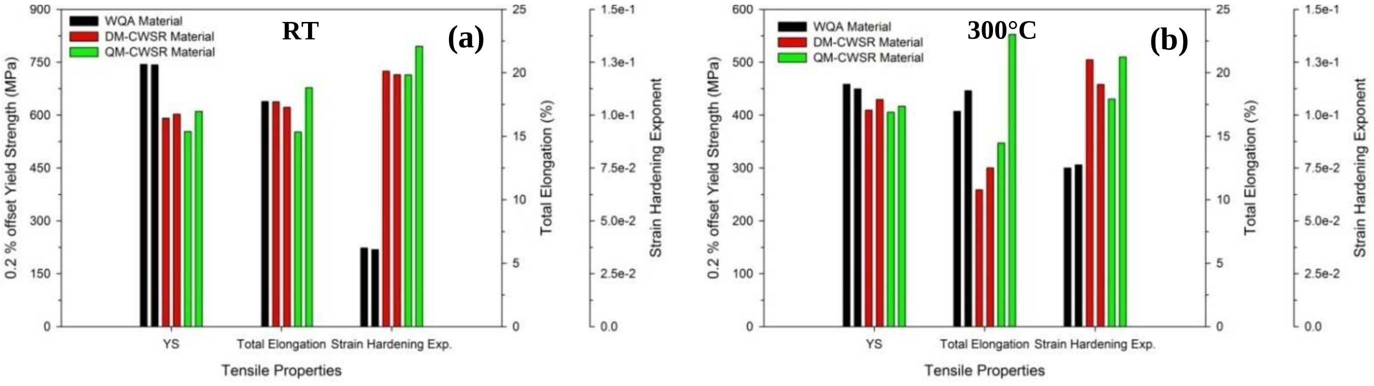

Figure 13: Comparison of tensile properties of Zr-2.5Nb alloy under WQA (850°C/15Min/WQ+20%CW+540°C/24h) and Indian CWSR (double melted, DM and quadruple melted, QM) conditions at (a) RT and (b) 300°C.

Fracture toughness examinations of WQA materials showed that under ambient condition, aging treatment reduced the fracture toughness of cold worked-solution heat treated Zr-2.5Nb alloy, Figure 14 (a). However, at 300°C, the aged materials as compared to cold worked materials had relatively higher fracture toughness, Figure 14 (b). Such different influences of aging treatment on fracture toughness parameters at RT and 300°C were subsequently justified through the fractographic examinations of the broken specimens and role of strain hardening exponent (as discussed subsequently).

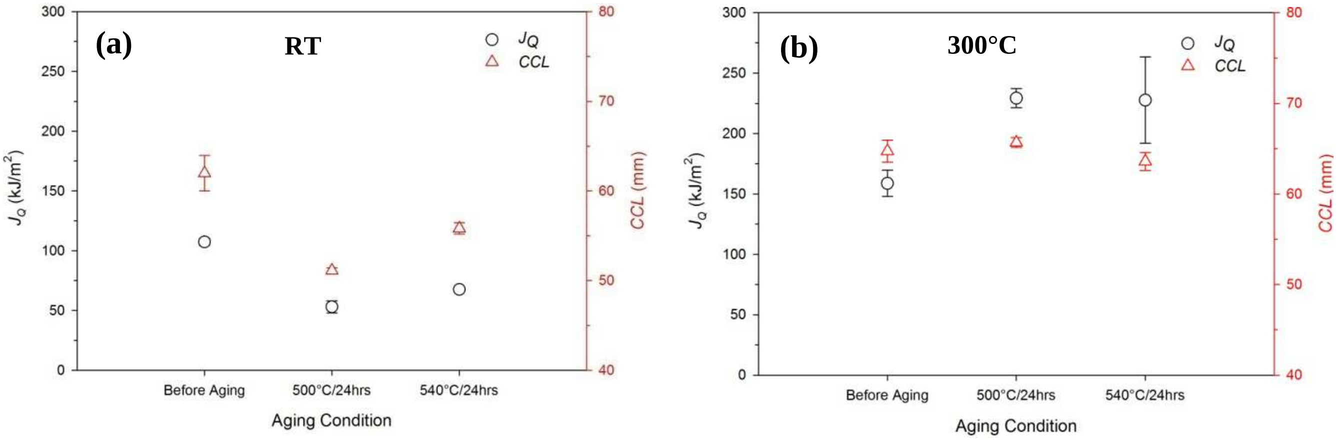

Figure 14: Influence of aging treatments on fracture toughness parameters of cold worked-solution heat treated Zr-2.5Nb alloy at (a) RT and (b) 300°C.

Fractography examinations of WQA materials showed several axial splits under ambient fractured condition, which were oriented along crack growth direction (Figure 15 (b)). Presence of such low energy (brittle) fractured sites resulted in lower fracture toughness of WQA Zr-2.5Nb alloy under ambient condition. In contrast, fracture surfaces of WQA materials tested at 300°C did not show the formation of such low energy sites, which therefore contributed to enhanced toughness after aging treatment. Another important observation was that the WQA materials, under ambient condition, exhibited larger central flat fracture, which was associated with superior 'tunnelling' characteristic (Figure 15 (a)), despite having lower fracture toughness. As described earlier that aging treatments caused significant reduction in strain hardening exponents under ambient condition. The lower strain hardening of WQA materials could also aid in facilitating localized deformation, resulting in reduction of fracture toughness, Figure 15 (c).

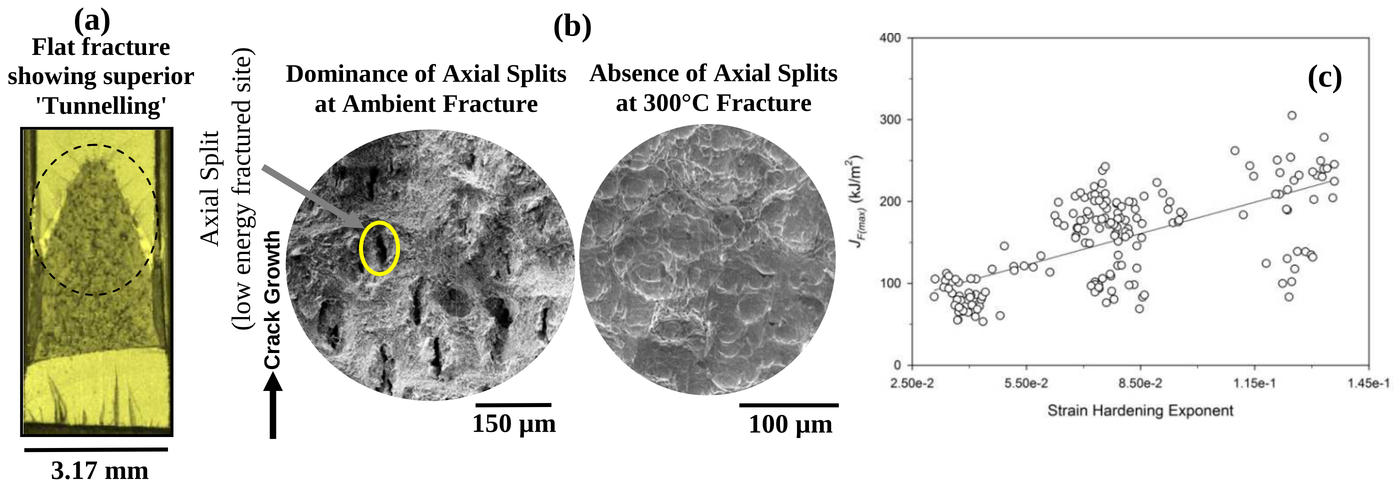

Figure 15: (a) WQA material exhibited superior flat and ‘tunnelled’ fracture under ambient condition, (b) Fractographs showing the presence of axial splits at ambient and their absence at 300°C fractured conditions, and (c) Plot showing the influence of material’s strain hardening exponents on fracture toughness.

Stretched zones ahead of pre-cracked region in WQA materials showed good agreement with the observed influence of aging treatments on initiation toughness. Aged-cold worked materials exhibited considerable reduction in SZW under ambient condition and improvement at 300°C, as compared to cold worked materials, Figure 16 (a). SZW could be an indirect measure of initiation toughness. Considering this, a correlation was made between SZW and initiation toughness for

WQA material. Study suggested that the initiation toughness based on SZW, $J_{i\ (SZW)}$ parameter is considerably lower than J_Q parameter, derived from the standard 0.2 mm offset Blunting Line approach, Figure 16 (b).

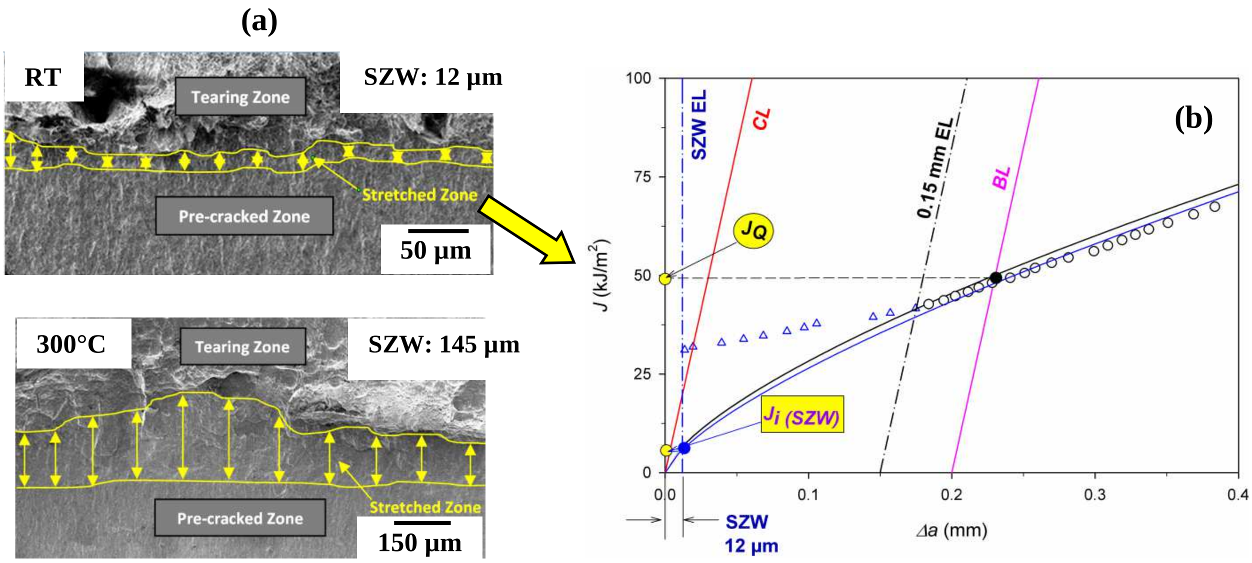

Figure 16: (a) Stretched zone formation in WQA Zr-2.5Nb alloy, and (b) Correlation of SZW with initiation toughness ($J_{i\ (SZW)}$) and its comparison with the standard initiation toughness parameter (J_Q).

SHT temperature within 850-890°C domain had marginal influence on the *CCL* parameters of WQA Zr-2.5Nb alloy. Nevertheless, SHT performed at relatively lower temperature, ensured better stable crack propagation resistance of WQA Zr-2.5Nb alloy, by exhibiting higher fracture resistance slope (*dJ/da*), Figure 17 (a). Such improvement in propagation resistance because of the use of lower SHT temperature suggested that after aging, microstructural features viz., higher primary α volume fraction, lower α’ grain size along with higher degree of Nb super-saturation in α' are beneficial for fracture behavior of WQA Zr-2.5Nb alloy (Figure 18 (a)). Selection of SHT soaking duration within 15-30 min domain had practically similar influence on fracture behavior of WQA Zr-2.5Nb alloy.

This study suggested that prior degree of cold work plays an important role in governing the fracture behavior of WQA Zr-2.5Nb alloy, especially at elevated temperature. Though, similar to SHT parameters, degree of cold working also had weak influence on *CCL* parameters of WQA Zr-2.5Nb alloy (Figure 17 (b)), thereby suggesting nearly insensitive limit of catastrophic failure. Nevertheless, higher cold working appeared to be desirable for ensuring superior stable crack propagation resistance. This therefore suggested the influence of higher cold working on greater extent of recovery during aging and higher number of β nucleation sites during aging, caused by increased dislocation density, resulting in finer distribution of β phase, leading to improvement in the fracture behavior of WQA Zr-2.5Nb alloy. The tensile property examinations, which showed lower strengths of 20% prior cold worked WQA materials, suggested such influence of the higher degree of cold working on greater extent of recovery as well as higher β precipitate density during subsequent aging treatment.

This study also suggested that increase in aging temperature by ~ 10% (i.e., 500-540°C) caused considerable variation in β precipitate volume fraction, its size and distribution and composition, resulting in improvement in fracture toughness. Here again, aging temperature marginally influenced the *CCL* parameters, however considerably influenced the stable crack propagation resistance of WQA Zr-2.5Nb alloy, especially under ambient condition (Figure 17 (c)). This suggested the role of higher β precipitate volume fraction, coarser precipitate size, Nb lean precipitate, along with higher degree of recovery in improving the propagation resistance of WQA Zr-2.5Nb alloy (Figure 18 (b)).

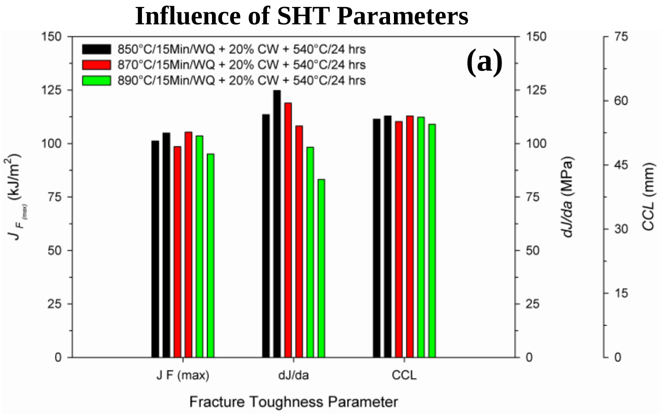

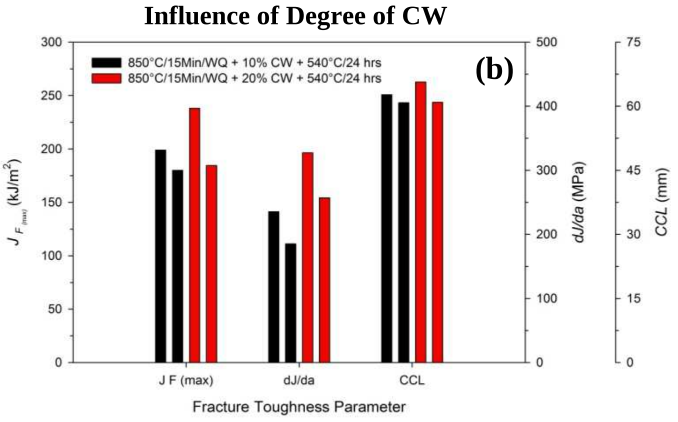

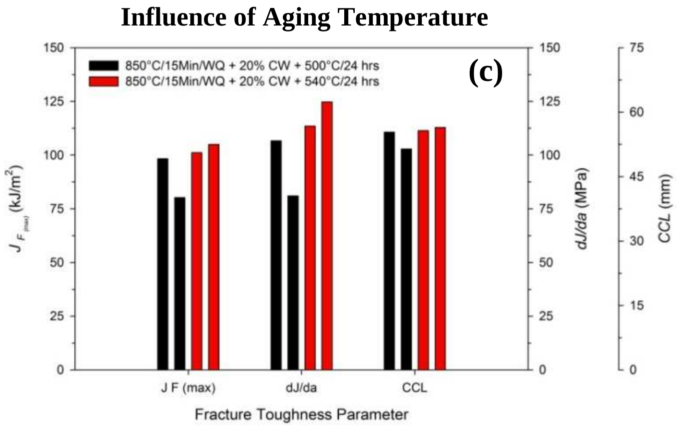

Figure 17: Influence of TMP parameters (a) SHT temperature, (b) degree of cold working and (c) aging temperature on fracture toughness parameters of WQA Zr-2.5Nb alloy. Here, plots (a) & (c) show the influences under ambient condition, and plot (b) shows the influence at 300°C.

In summary, *CCL* parameter of WQA Zr-2.5Nb alloy was weakly sensitive to even large variation in its TMP parameters. However, combination of TMP parameters viz., SHT at 850°C for 15-30 min, followed by 20% cold working and subsequent aging at 540°C for 24 h provided best stable crack propagation resistance of WQA Zr-2.5Nb alloy.

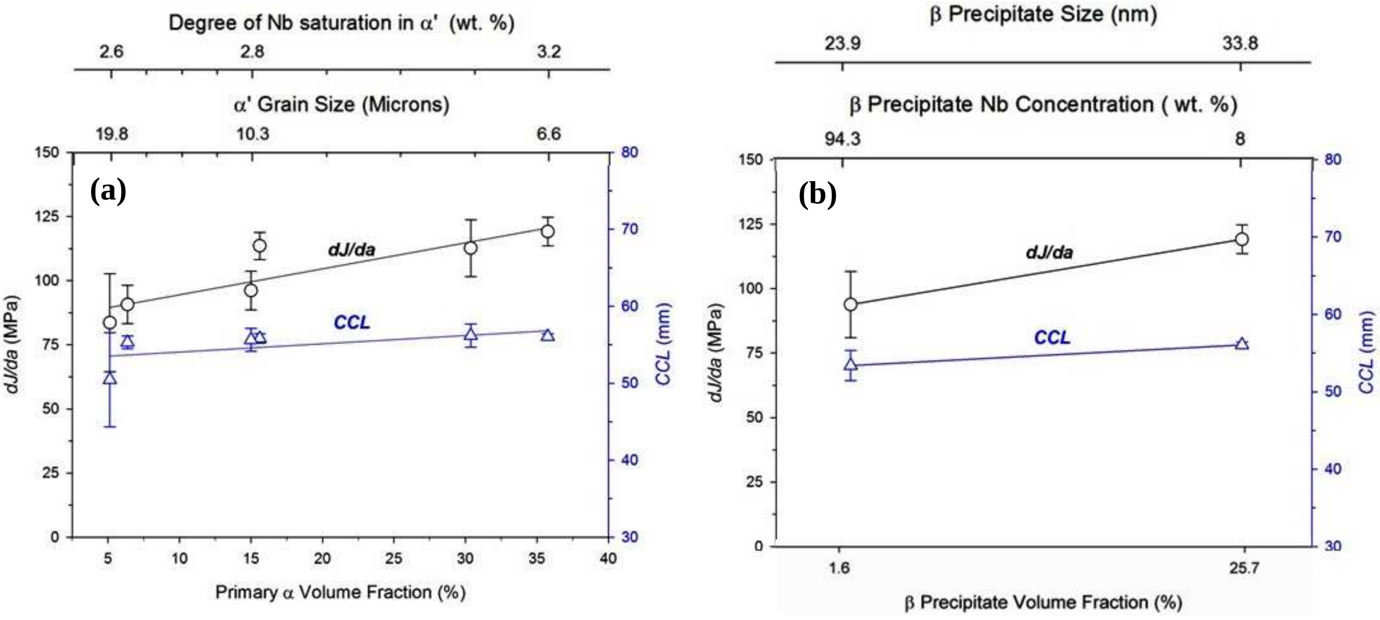

Figure 18: Influence of microstructural features on propagation toughness and *CCL* of WQA Zr-2.5Nb alloy.

This work also demonstrates a comprehensive study to assess the influence of different analysis approaches on fracture toughness parameters of Zr-2.5Nb alloy under solution heat treated, subsequently cold worked and vacuum aged conditions. For this, different evaluation methodologies suggested by ASTM E1820-11 standard such as; single specimen ('Resistance Curve', RC) and multi specimen ('Basic Test', BT) methods were used for evaluating the fracture toughness parameters. Also, differences in analysis procedures recommended by ASTM E1820-11 standard and ISO 12135:2002 (as amended in year 2008) standard were highlighted and their influence on fracture toughness parameters were studied. The RC method, in contrast to BT method ensured conservative estimation of fracture toughness, as at a particular crack length it predicted relatively less J parameter (Figure 19 (a)). Deviation in J parameters derived from these two methods had dependence on crack length, such that it increased with a/W ratio. The initiation toughness, J_Q and propagation toughness, $J_{F(max)}$ were practically insensitive to these approaches, however, resistance curve slope (dJ/da) had substantial dependence. To reduce the deviations and also to ensure its independence with crack length, an optimised range of 3-4 for the second crack growth correction parameter 'α' in BT method was suggested.

Under a given combination of geometry and loading condition (i.e., specimen dimensions, load and LLD values), both ASTM and ISO approaches provided practically identical J parameters, Figure 19 (a). This, therefore emphasized that the 'Ductile Crack Growth' (DCG) correction methodologies considered by these standards has similar influence on J parameters. However, the post processing of J-R curve recommended by these standards primarily caused deviations in J_Q and dJ/da parameters. However, $J_{F(max)}$ parameter showed insensitiveness to these analysis approaches. Deviation in ASTM and ISO derived toughness parameters was the function of material's flow stress, such that high strength materials showed least deviation (Figure 19 (b)).

One of the important conclusions of this study was that *CCL*, an important toughness parameter used for assessing the adherence to LBB criteria is practically insensitive to different analysis approaches (Figure 19 (c)). This therefore, suggested that the assessment of safety margins for necessary LBB condition of WQA pressure tubes is independent to fracture analysis approaches.

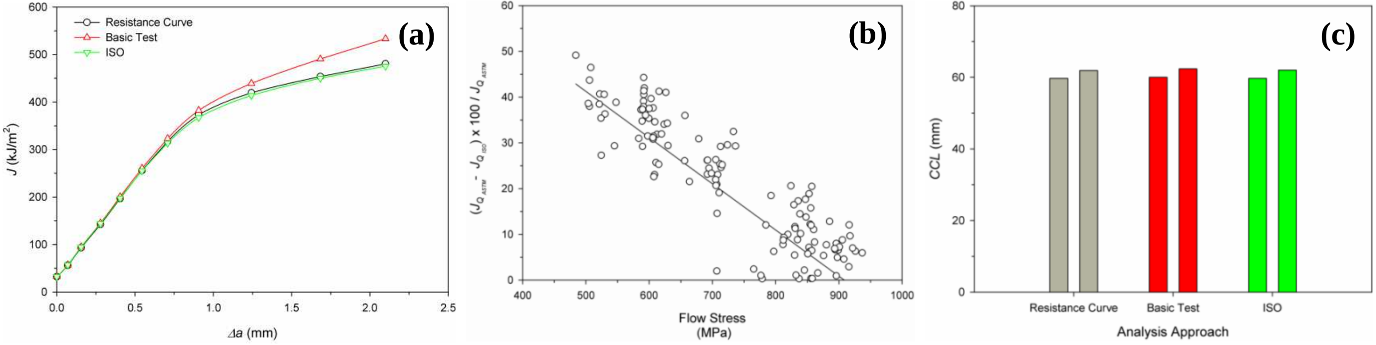

Figure 19: (a) Influence of analysis approaches on fracture resistance *J-R* curves of WQA material (b) Influence of flow stress on deviation in ASTM and ISO derived Initiation toughness, and (c) Plot showing independence of *CCL* parameters to different analysis approaches.

One of the major highlights of this work is that WQA material exhibits fracture toughness analogous (though marginally higher) than double melted DM-CWSR material at ambient (Figure 20 (a) & (b)) and comparable to quadruple melted QM-CWSR material at 300°C (Figure 20 (c) & (d)), despite having relatively coarser grain size and weaker texture. This is expected to ensure lower in-reactor dimensional changes due to reduced irradiation growth and irradiation induced creep and hence improving the useful lives of pressure tubes.

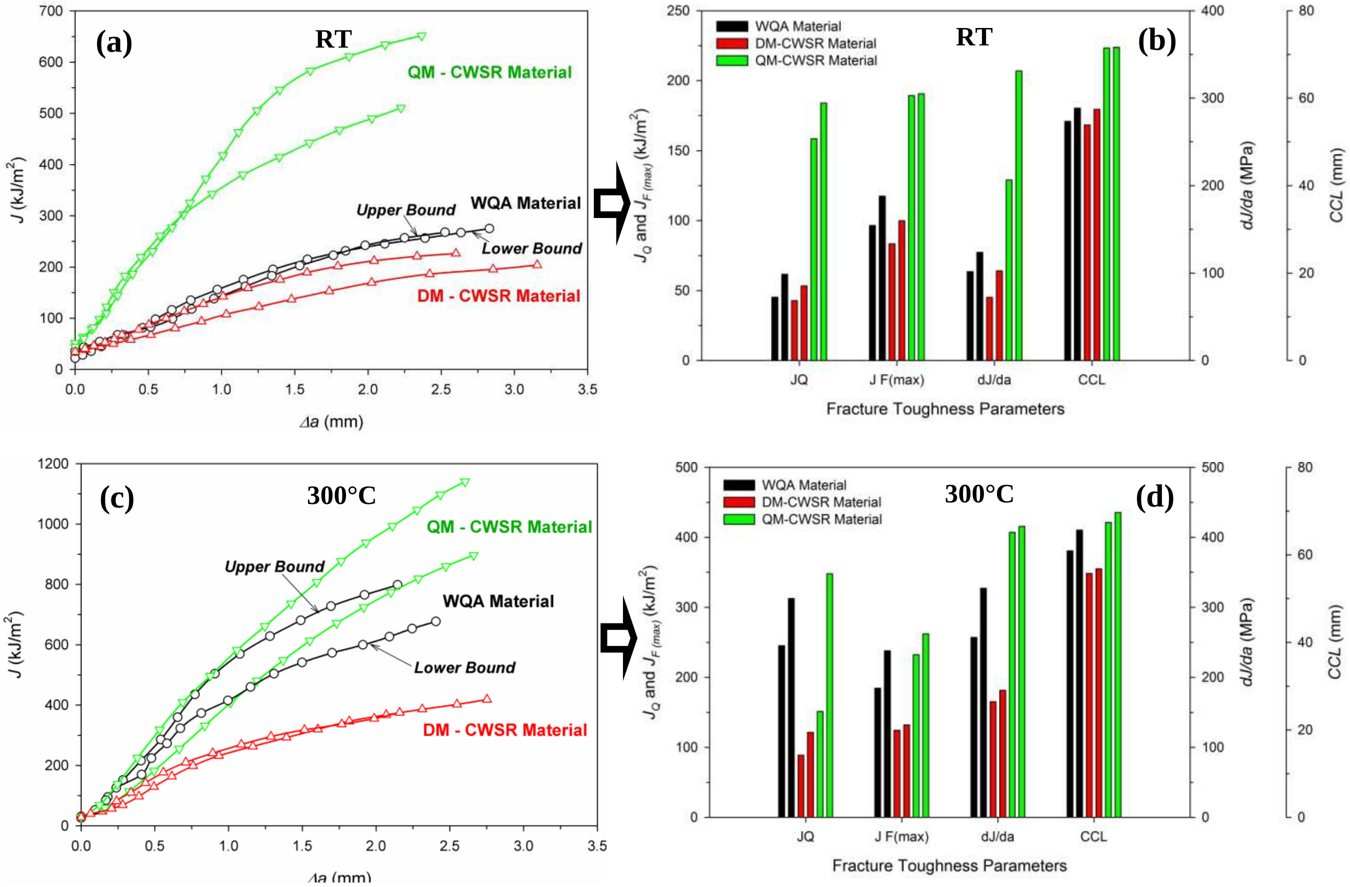

Figure 20: Comparison of fracture behavior of Zr-2.5Nb alloy under WQA (850°C/15Min/WQ+20%CW+540°C/24h) and Indian CWSR (double melted, DM and quadruple melted, QM) conditions at (a) & (b) RT and (c) & (d) 300°C.

LIST OF FIGURES

LIST OF TABLES

NOMENCLATURE

$a_{(i)}$	Instantaneous crack length corresponding to the i^{th} data point
$a_{(i-1)}$	Instantaneous crack length corresponding to the $(i\text{-}1)^{\text{th}}$ data point
a_o	Initial crack length
a/W	Normalized crack length (ratio of crack length to specimen width)
A_{pl}	Area under load vs. plastic displacement curve (determined using crack growth corrected unloading slope)
$A_{pl\ (i)}$	Area under i^{th} load vs. i^{th} plastic displacement curve (determined using crack growth corrected unloading slope)
$A_{pl\ (i-1)}$	Area under $(i\text{-}1)^{\text{th}}$ load vs. $(i\text{-}1)^{\text{th}}$ plastic displacement curve (determined using crack growth corrected unloading slope)
$b_{(i-1)}$	Remaining ligament (also known as 'uncracked ligament') corresponding to the $(i\text{-}1)^{\text{th}}$ data point
b_o	Initial remaining ligament
B	Specimen thickness
B_e	Specimen's effective thickness
B_N	Specimen thickness after side grooving
$CLL_{(i)}$	Instantaneous compliance of the specimen corresponding to crack length a_i
d	Internal diameter of pressure tube
dJ/da	Slope of valid region of J-R curve, obtained after linear fit
$dJ/da_{\ ASTM}$	dJ/da parameter derived following ASTM E1820-11 standard
$dJ/da_{\ ISO}$	dJ/da parameter derived following ISO 12135:2002 standard
$D_{Transverse}$	Primary α grain dimension along transverse direction
$D_{\alpha'}$	Grain size of α' (i.e., prior β) phase
$D_{\beta\ Precipitate}$	Grain size of the β precipitate
E	Material's elastic modulus
$\mathrm{H_{eq}}$	Equivalent Hydrogen
$\mathrm{H_{850°C}}$	Vickers hardness of solution heat treated material, soaked at 850°C
$\mathrm{H_{890°C}}$	Vickers hardness of solution heat treated material, soaked at 890°C
J	J-integral
$J_{(i)}$	J parameter corresponding to the i^{th} data point

$J_{\left(\frac{ai}{W}\right)_{BT}}$	*J* parameter at i^{th} normalized crack length (a_i/W) derived using BT method
$J_{\left(\frac{ai}{W}\right)_{RC}}$	*J* parameter at i^{th} normalized crack length (a_i/W) derived using RC method
$J_{\left(\frac{ai}{W}\right)_{ASTM}}$	*J* parameter at i^{th} normalized crack length (a_i/W) derived using ASTM approach
$J_{\left(\frac{ai}{W}\right)_{ISO}}$	*J* parameter at i^{th} normalized crack length (a_i/W) derived using ISO approach
$J_{i\ (SZW)}$	Initiation fracture toughness parameter derived using Stretched Zone Width
J_Q	Initiation fracture toughness (*J* parameter at the intersection of power law fit *J-R* curve with 0.2 mm offset blunting line)
$J_{Q\ ASTM}$	Initiation fracture toughness determined as per ASTM E1820-11 standard
$J_{Q\ ISO}$	Initiation fracture toughness determined as per ISO 12135:2002 standard
$J_{0.5}$	*J* parameter at the intersection of the power law curve with the 0.5 mm offset line
$J_{1.5}$	*J* parameter at the intersection of the power law curve with the 1.5 mm offset line
J_{el}	Elastic component of *J*-integral
$J_{el\ (i)}$	Elastic component of *J*-integral corresponding to the i^{th} data point determined considering instantaneous crack length (a_i)
J_{pl}	Plastic component of *J*-integral
$J_{pl\ (i)}$	Plastic component of *J*-integral corresponding to the i^{th} data point
$J_{pl\ (i-1)}$	Plastic component of *J*-integral corresponding to the $(i-1)^{th}$ data point
J_{max}	Maximum *J* integral capacity of the specimen
$J_{max\ ASTM}$	ASTM E1820-11 standard derived specimen's maximum *J* integral capacity
$J_{max\ ISO}$	ISO 12125:2002 standard derived specimen's maximum *J* integral capacity
$J_{F(max)}$	*J* integral corresponding to the maximum load
$J_{F(max)\ ASTM}$	*J* parameter corresponding to maximum load, derived from ASTM

	E1820-11 standard
$J_{F(max)\ ISO}$	J parameter corresponding to maximum load, derived from ISO 12125:2002 standard
K	Strength Coefficient
K_o	Stress intensity factor based on initial crack length, a_o
$K_{(i)}$	Stress intensity factor corresponding to the i^{th} data point
K_{MAX}	Maximum Stress Intensity Factor
L_f	Final gage length of tensile specimen after fracture
M	The Folias factor
n	Strain Hardening Exponent
Nb_{α}	Nb concentration (in wt. %) of α-Zr phase
Nb_{β}	Nb concentration (in wt. %) of β-Zr phase
$Nb_{\alpha'}$	Nb concentration (in wt. %) of α’ phase
$Nb_{\beta\ Precipitate}$	Nb concentration (in wt. %) of β precipitate
P_{MAX}	Maximum Load
$P_{(i-1)}$	Load corresponding to the $(i\text{-}1)^{th}$ data point
$P_{i\ (850°C)}$	i^{th} tensile property of the solution heat treated material soaked at 850°C
$P_{i\ (890°C)}$	i^{th} tensile property of the solution heat treated material soaked at 890°C
r	Inner radius of pressure tube
v	Load line displacement after removing machine’s effect
v_{pl}	Plastic part of specimen’s load line displacement
$v_{pl\ (i)}$	Plastic part of specimen’s load line displacement corresponding to the i^{th} data point
$v_{pl\ (i-1)}$	Plastic part of specimen’s load line displacement corresponding to the $(i\text{-}1)^{th}$ data point
V	Volume of Primary α grain
V_{α}	Volume fraction of α-Zr phase
$V_{Primary\ \alpha}$	Volume fraction of primary α phase
$V_{\beta\ Precipitate}$	Volume fraction of the β precipitate
YS_{SHT}	0.2 % offset yield strength of solution heat treated material
YS_{CW}	0.2 % offset yield strength of cold worked-solution heat treated material
σ_h	Hoop stress in pressure tube
σ_Y	Material’s flow stress (taken as mean of yield and ultimate tensile

	strength)
σ_{YS}	Material's yield strength (0.2 % offset)
σ_{UTS}	Material's ultimate tensile strength
σ_{YS}^{T}	0.2% offset yield strength of the material at fracture test temperature
σ_{YS}^{f}	0.2% offset Yield strength of the material at fatigue pre-cracking temperature
τ_{flow}	Shear stress required to move a dislocation within material
τ_0	shear stress when material has no dislocation
ρ	Dislocation density
ρ_{CW}	Dislocation density in cold worked-solution heat treated material
P_{SHT}	Dislocation density in solution heat treated material
$\gamma_{(i-1)}$	Gamma factor corresponding to the (i-1)th data point
ε_{p}	True Plastic strain
$\Delta H_{SHT \rightarrow CW}$	Net change in the hardness of solution heat treated material because of subsequent cold working
$\Delta H_{Lattice\ imperfections}$	Increase in the hardness of material because of lattice imperfection generation
$\Delta H_{Primary\ \alpha\ accumulation}$	Reduction in the hardness of material because of primary α accumulation
$\Delta Nb_{\alpha'\ (850-890^{\circ}C)}$	Change in degree of Nb super saturation in α' within SHT temperatures from 850-890°C
$\Delta V_{Primary\ \alpha\ (850-890^{\circ}C)}$	Change in primary α volume fraction within SHT temperatures from 850-890°C
GPa	Giga Pascal
m	Meter
mm	Millimeter
MPa	Mega Pascal
N	Newton (unit of force)
kg-f	kilogram-force
kJ	kilo-joules
µm	micrometer
°C	degree centigrade

ABBRIVIATIONS

AA	Actual Area
AC Plane	Axial-Circumferential Plane
ACF	Area Correction Factor
APF	Additional Pole Figure
AR Plane	Axial-Radial Plane
ASTM	American Society for Testing and Materials
BL	Blunting Line
BT	Basic Test Method
CDF	Crack Driving Force
CL	Construction Line
C(T)	Compact Tension
CANDU	CANada Deuterium Uranium
CCL	Critical Crack Length
CPS	Counts per Seconds
CW	Cold Work
CWA	Cold Worked and Annealed
CWSR	Cold Work and Stress Relieved
DC(T)	Disc shape Compact Tension
DCG	Ductile Crack Growth
DCPD	Direct Current Potential Drop
DMF	Dislocation Multiplication Factor
DHC	Delayed Hydride Cracking
DIC	Differential Interference Contrast
DM	Double Melting
EBSD	Electron Back Scatter Diffraction
EDS	Energy Dispersive Spectroscopy
EPMA	Electro Probe Micro Analyzer
EL	Exclusion Line
GCA	Gas Cooled and Aged
HCP	Hexagonal Closed Packed
HF	Hydro-Fluoric acid

IPHWR	Indian Pressurized Heavy Water Reactor
ISO	International Organization for Standardization
KANUPP	KArachi NUclear Power Plant
LBB	Leak Before Break
LLD	Load Line Displacement
MIT	Massachusetts Institute of Technology
MWe	Mega Watt Electrical
NPCIL	Nuclear Power Corporation of India Limited
PA	Projected Area
PD	Potential Drop
PHWR	Pressurized Heavy Water Reactor
LWR	Light Water Reactor
BWR	Boiling Water Reactor
PWR	Pressurized Water Reactor
QM	Quadruple Melting
RA	Reduction in cross-sectional Area
RBMK	Reaktor Bolshoy Moshchnosti Kanalniy (*in Russian Language*)
RC	Resistance Curve
RC Plane	Radial-Circumferential Plane
RT	Room Temperature (~25°C)
SC	Strength Coefficient
SD	Standard Deviation
SE(B)	Side Edge Bend
SEM	Scanning Electron Microscopy
SHT	Solution Heat Treatment
SZW	Stretched Zone Width
TE	Total Elongation
TEM	Transmission Electron Microscopy
TMP	Thermo-Mechanical Processing
TMT	Thermo-Mechanical Treatment
TSS	Terminal Solid Solubility
UC	Unloading Compliance
UE	Uniform Elongation

UTS	Ultimate Tensile Strength
WDS	Wavelength Dispersive Spectroscopy
WQ	Water Quenching
WQA	Water Quenched and Aged
YS	Yield Strength

CHAPTER 1

INTRODUCTION

This chapter introduces the structural integrity challenges of Zr-2.5Nb alloy pressure tubes and highlights the importance of fracture behavior in ensuring their safe operation. Various fabrication routes of pressure tube manufacturing, employed throughout the world are summarized and important fabrication steps of the ‘Water Quenched and Aged’ (WQA) route, which has bearing on the mechanical properties, are highlighted. The Thermo-Mechanical Processing (TMP) parameters of the final fabrication stages of WQA route viz., Solution Heat Treatment (SHT), cold working and vacuum aging stages, are presented, which motivated the present work. The objective of work to study influence of TMP parameters of WQA route on fracture behavior of Zr-2.5Nb alloy is justified. The TMP parameters chosen for this study and their basis of selection are discussed briefly, subsequently. In the end, an overview of the contents of individual thesis chapters is presented.

1.1 Background

Zr-2.5Nb alloy pressure tubes constitute the most important in-core component of Pressurized Heavy Water Reactors (PHWRs), and serves as the containment for hot heavy water coolant flowing through reactor's Primary Heat Transport (PHT) system. For reactor's safe operation, structural integrity of pressure tubes has to be ensured during service. The life of an operating pressure tube is primarily governed by its fracture behavior, along with its resistance against typical in-reactor dimensional changes such as diametral expansion, axial elongation and sagging (Figure 1.1). The fracture behavior of an operating pressure tube is a measure of its resistance to crack propagation in typical reactor environment. In addition, it also determines the limit of stable crack propagation before catastrophic failure. This limiting crack length is called 'Critical Crack Length' (*CCL*), which governs the necessary safety margin for satisfying the 'Leak Before Break'

(LBB) criteria of pressure tube design. As the name suggests, LBB represents the situation, under which pressure tube leaks before the catastrophic failure. In other words, under LBB situation, the crack within pressure tube first propagates in stable manner, resulting in the leakage of primary coolant from the tube and subsequently becomes unstable, resulting in the tube rupture. LBB situation is essential for pressure tube's safety, because it provides required response time for an operator to take necessary remedial measures. A higher fracture toughness and therefore a higher *CCL* provides greater safety margin to the pressure tube for such LBB situation and hence is always desirable. Therefore, for ensuring longer operating life, the pressure tubes must possess adequate fracture toughness, by having sufficient resistance to crack propagation, along with a greater *CCL* limit.

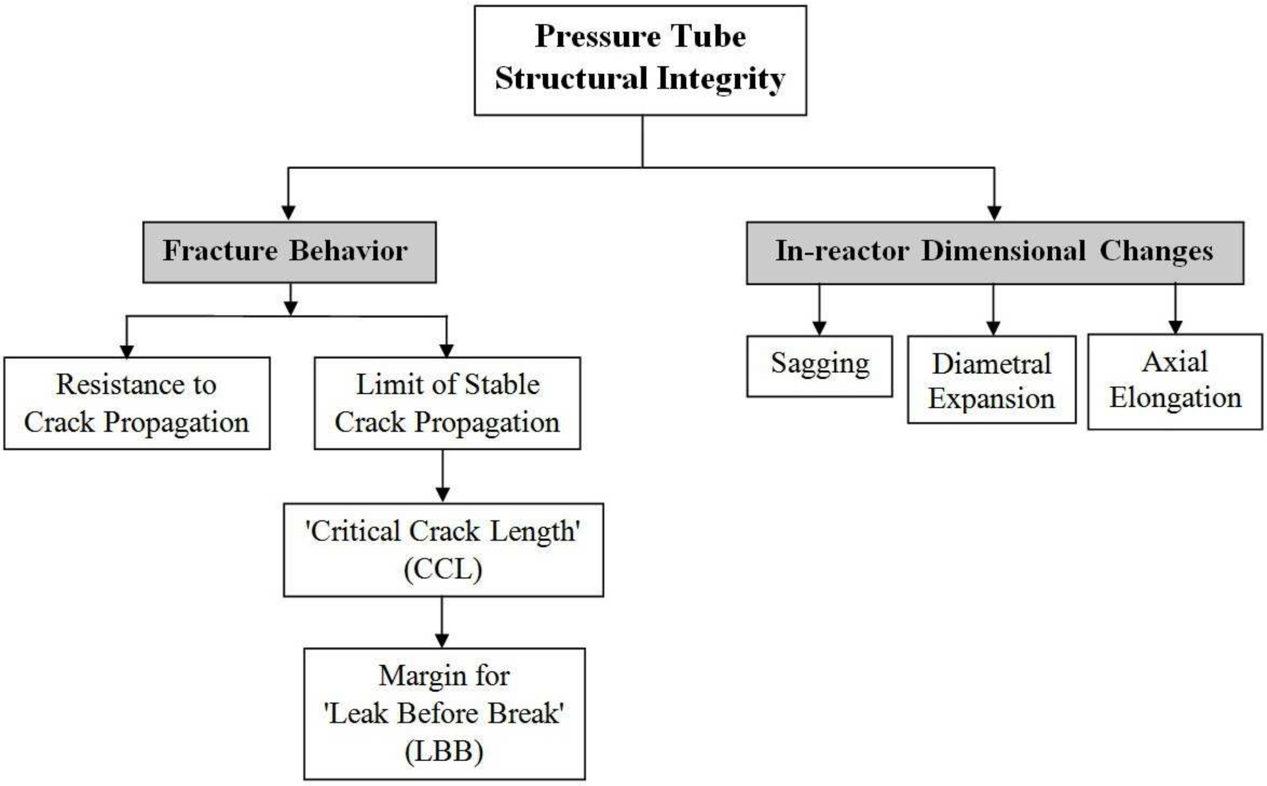

Figure 1.1: Flow chart illustrating the important life limiting factors for the pressure tubes of a nuclear reactor.

Fracture behavior of pressure tube is the function of its initial microstructure, which in-turn is the function of fabrication route employed for tube manufacturing and its associated Thermo-Mechanical Processing (TMP) parameters. The Zr-2.5Nb alloy pressure tubes currently being used in different PHWRs throughout the world have different initial microstructures, because of having differences among the fabrication routes employed for their manufacturing. These fabrication routes include 'Cold Worked and Stress Relieved' (CWSR) route employed for the Indian and CANDU PHWRs; 'Cold Worked and Annealed' (CWA) route employed for all the Russian PHWRs (‘Reaktor Bolshoy Moshchnosti Kanalniy’, RBMK) of 1000 MWe capacity; 'Water Quenched and Aged' (WQA) route employed for the Japanese PHWR ('Fugen'), Pakistani PHWR (KANUPP, Karachi Nuclear Power Plant) and Russian PHWRs (RBMK, Ignalina-1) of 1500 MWe capacity; and 'Gas Quenched and Aged' (GCA) route employed for the RBMK 1500 MWe, Ignalina-2 reactors [1-4].

1.2 Motivation for Study

Among the different fabrication routes being employed for pressure tube's manufacturing, WQA route has become an important area of interest in recent scenario. This is primarily because the tubes fabricated using this route as compared to other routes, have reportedly shown superior resistance against the in-reactor dimensional changes [5]. Utilization of WQA route for pressure tubes of modern reactors such as, 'Advanced Heavy Water Reactor', AHWR (which is designed for 100 years lifetime), such lower in-reactor dimensional changes will ensure fewer pressure tube replacements and thereby reduce the cost of power production.

In WQA fabrication route, Solution Heat Treatment (SHT), subsequent cold working and vacuum aging treatment constitute the final fabrication stages (as illustrated in Figure 1.2). The TMP parameters associated with these stages such as soaking temperature and duration during SHT, degree of cold working and soaking temperature of vacuum aging treatment could have an important role in governing the final microstructure and hence fracture behavior of the fabricated pressure tube material. Furthermore, the WQA routes, currently being employed throughout the world (for pressure tubes of Russian’s RBMK (Ignalina-1), Japanese Fugen, Canadian’s Gentilly-1 and Pakistani’s KANUUP reactors), have variations in their TMP parameters of the three aforementioned final stages and also, in their alloy chemistries, as shown in Table 1.1. The selection of suitable TMP parameters for achieving best in-reactor performance is, therefore, extremely important for utilizing the WQA route for pressure tube fabrication of modern reactors such as; AHWR. However, fabrication of pressure tubes of length about 6 m by WQA route poses technological challenges. The fracture behavior of WQA tubes need to be understood for its thermo-mechanical processing and safety assessment. The open literature, however does not provide sufficient information regarding the influence of these TMP parameters on the fracture behavior of WQA Zr-2.5Nb alloy, so as to achieve an optimum TMP history from fracture behavior view point.

Table 1.1: Pressure tube material chemistries and TMP parameters of WQA fabrication routes employed for pressure tube fabrication for different heavy water cooled nuclear reactors throughout the world [2,4,6-11].

Reactors	**Alloy Chemistry (O content, ppm)**	**Thermo-mechanical Processing Parameters**		
		SHT Temperature (°C)	**Degree of Cold Work (% Thickness Reduction)**	**Vacuum Aging Parameters**
RBMK (water quenched & aged)	400-700	850-870	20-25	515°C/24 h
RBMK (He/Ar quenched & aged	400-700	850-870	20-25	530-540°C/24 h
Fugen	900-1300	887	5-15	500°C/24 h
Gentilly -1	900-1300	880	12	500°C/24 h
KANUPP	900-1300	880	12	500°C/24 h

Present work was therefore, motivated to study the influence of TMP parameters associated with SHT, subsequent cold working and vacuum aging stages of WQA fabrication route on the fracture behavior of Zr-2.5Nb alloy.

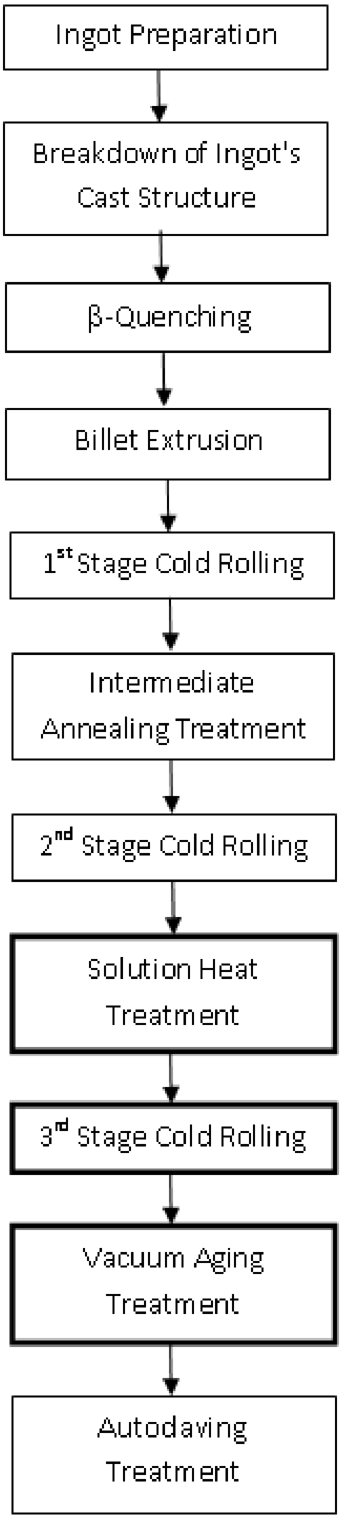

Figure 1.2: WQA fabrication route of Zr-2.5Nb pressure tubes, highlighting the three important TMP stages viz., SHT, cold working and vacuum aging which govern the final microstructure and therefore fracture behavior of the as-fabricated pressure tube material [2].

1.3 Objective of Study

The objective of present work was to study the influence of TMP parameters associated with SHT, subsequent cold working, and vacuum aging stages of WQA fabrication route on the fracture behavior of Zr-2.5Nb alloy. Selections of TMP parameters for this study were done by taking into consideration the parameters used for the manufacturing of such heat treated tubes by various manufacturers (as shown in Table 1.1). For this, during SHT stage, influence of soaking temperature and duration; during cold working stage, influence of degree of cold working; and during vacuum aging stage, influence of aging temperature were planned to study. SHT temperatures were kept lower than the β-transus, so as to avoid significant grain coarsening because of the single phase, β-Zr microstructure, which enhances the irradiation growth. Soaking durations during SHT were limited to 30 min, in order to avoid significant embrittlement of α-Zr phase, caused by the oxygen partitioning from β-Zr to α-Zr at SHT temperature [12]. A maximum 20% degree of subsequent cold working was considered, so as to avoid excessive damage accumulation in the solution heat treated materials during cold working. Aging temperatures of 500 and 540°C were selected to study the influence of β-Nb and β-Zr precipitates on the fracture behavior of WQA Zr-2.5Nb alloy [9]. Table 1.2 shows the TMP parameters of SHT, cold working and vacuum aging stages used in the present study. The three SHT temperatures along with two soaking durations, two degrees of subsequent cold working and two aging temperatures formed a total 24 number of variable TMP conditions (as shown in Table 1.3), under which fracture behavior of Zr-2.5Nb alloy was planned to be studied. This study was performed in three stages viz., (I) SHT, (II) cold working and (III) vacuum aging, so as to study the evolution of fracture behavior of WQA Zr-2.5Nb alloy with TMP stages.

Table 1.2: TMP parameters associated with SHT, cold working and vacuum aging stages of WQA route employed in the present study.

S. No	TMP Stage	TMP Parameters	Degree of Variability	No. of Conditions
1	Solution heat treatment	Soaking Temperature	850, 870 & 890°C	3 x 2 = 6
		Soaking duration	15 & 30 min	
2	Cold working	Degree of cold work	10 & 20 %	6 x 2 = 12
3	Vacuum Aging	Soaking Temperature	500 & 540°C	12 x 2 = 24
		Soaking duration	24 h	

Table 1.3: Test matrix showing 24 variable TMP conditions, under which fracture behavior of Zr-2.5Nb alloy was planned to be studied.

	Thermo-mechanical Processing Parameters		
S. No.	Solution Heat Treatment	Cold Working Ratio	Vacuum Aging Treatment
1	850°C, 15Min	10%	500°C, 24 h
2	850°C, 15Min	20%	500°C, 24 h
3	850°C, 15Min	10%	540°C, 24 h
4	850°C, 15Min	20%	540°C, 24 h
5	870°C, 15Min	10%	500°C, 24 h
6	870°C, 15Min	20%	500°C, 24 h
7	870°C, 15Min	10%	540°C, 24 h
8	870°C, 15Min	20%	540°C, 24 h
9	890°C, 15Min	10%	500°C, 24 h
10	890°C, 15Min	20%	500°C, 24 h
11	890°C, 15Min	10%	540°C, 24 h
12	890°C, 15Min	20%	540°C, 24 h
13	850°C, 30Min	10%	500°C, 24 h
14	850°C, 30Min	20%	500°C, 24 h
15	850°C, 30Min	10%	540°C, 24 h
16	850°C, 30Min	20%	540°C, 24 h
17	870°C, 30Min	10%	500°C, 24 h
18	870°C, 30Min	20%	500°C, 24 h
19	870°C, 30Min	10%	540°C, 24 h
20	870°C, 30Min	20%	540°C, 24 h
21	890°C, 30Min	10%	500°C, 24 h
22	890°C, 30Min	20%	500°C, 24 h
23	890°C, 30Min	10%	540°C, 24 h
24	890°C, 30Min	20%	540°C, 24 h

The fracture behavior was planned to be studied at RT (~25°C) and 300°C, by obtaining samples from each stage of the thermo-mechanical processing, i.e., after SHT, after cold working of the SHT material and after vacuum aging of the cold worked-SHT material. Both fracture initiation and fracture propagation parameters were planned to be determined, according to the ASTM E1820-11 standard. A comparative study to assess the influence of different analysis procedures on the fracture toughness parameters was also performed. For this, fracture toughness parameters were examined using 'Basic Test' and 'Resistance Curve' methodologies. The same set of test data were also analysed as per ISO 12135 standard analysis procedure, to show the influence of test standard on derived toughness parameters. In this work, fracture toughness examinations were also accompanied by tensile properties, microstructure, phase analysis (volume fraction, morphology and composition), crystallographic texture, and SEM fractography studies to understand the fracture behavior. Finally, an attempt was made to rationalize the fracture behavior with microstructural and fractographical observations.

1.4 Structure of Thesis

This thesis contains seven chapters entitled Introduction (1), Literature review (2), Experimental procedures (3), Influence of solution heat treatment parameters on fracture behavior of Zr-2.5Nb alloy (4), Influence of degree of cold working on fracture behavior of solution heat treated Zr-2.5Nb alloy (5), Influence of aging temperature on fracture behavior of cold worked-solution heat treated Zr-2.5Nb alloy (6), Conclusions (7) and Scope for future work. Brief contents of these chapters are presented as under.

Thesis begins with introduction chapter, which commences with introducing reader about the structural integrity challenges of Zr-2.5Nb alloy pressure tubes and highlights the importance of fracture behavior for their safe operation. Various fabrication routes practiced by different countries for the manufacture pressure tubes are introduced. Subsequently, the WQA fabrication route and variability associated with its final stages; SHT, cold working and vacuum aging followed by different countries throughout the world are briefly discussed, which motivated the present study. Subsequently, the objective to study the influence of TMP parameters associated with aforementioned stages on fracture behavior of Zr-2.5Nb alloy is described.

Second chapter presents the summarized view of literature concerning to Zr-2.5Nb alloy and its structural integrity issues. This is followed by a discussion on various life limiting factors of the Zr-2.5Nb alloy pressure tubes, under which in-reactor challenges such as dimensional changes and degradation of mechanical properties including fracture behavior are described. Subsequently, manufacturing of pressure tubes through different fabrication routes are discussed, under which fabrication routes viz., CWSR, CWA, WQA and GCA are individually described. In this respect, major emphasis is given to WQA route and the importance of its associated TMP stages; SHT, cold working and vacuum aging is highlighted. Finally, based on review, limitation of literature is pointed out, which motivated the present study.

Chapter three describes various experimental procedures followed during the course of work. The chapter first introduces the as-received Zr-2.5Nb pressure tube material, over which different thermo-mechanical treatments were given. Subsequently, the methodology of determining β-transus temperature of this material and the precautions undertaken are described, which subsequently formed basis for selecting the SHT temperatures for present work. Procedures of the three thermo-mechanical treatments; SHT, cold working and vacuum aging are subsequently individually described. The procedures of microstructural examinations such as metallography using optical microscopy and Transmission Electron Microscopy (TEM), crystallographic texture using X-ray diffraction, Nb partitioning within primary α and α' phases using Electro Probe Micro Analyzer (EPMA) and Nb assessment of the fine β precipitates formed in aged materials from carbon extraction replica are described individually. Subsequently, procedures of mechanical testing performed including tensile testing, micro-hardness and fracture toughness examinations along with the fractographic examinations conducted through Scanning Electron Microscopy (SEM) are described individually.

Chapter four describes the influence of SHT parameters viz., soaking temperature within 850-890°C domain and duration within 15-30 min domain on fracture behavior of Zr-2.5Nb alloy. Influence on the microstructural features comprising, determination of primary α volume fractions and primary α and α' grain sizes using optical microscopy, basal pole texture using X-ray diffraction and Nb partitioning using EPMA examinations is presented initially, which is followed by the comprehensive study on the mechanical properties such as micro-hardness, tensile properties and fracture toughness. The influence of different evaluation methodologies of fracture toughness parameters is presented, which include the role of single specimen (Resistance Curve) and multi-specimen (Basic Test) methods. Influence of differences in the analysis procedures, suggested by the ASTM and ISO standards on fracture toughness parameters, is also presented. Subsequently, a comprehensive study of the fractographic features at different locations studied using SEM and their correlation with the observations is presented.

Chapter five describes the influence of degrees of cold working, 10 and 20 % on fracture behavior of Zr-2.5Nb alloy, solution heat treated from different soaking temperatures (850-890°C) for different soaking durations (15 and 30 min) followed by water quenching. The chapter begins with describing the influence on the microstructural features including microstructure gradient in the vicinity of free surface through optical microscopy, and the evolution of basal pole texture through X-ray diffraction examinations. Subsequently, influence of degree of cold working on the mechanical properties; micro-hardness, tensile properties and fracture toughness of solution heat treated Zr-2.5Nb alloy is presented. A study of the fracture surface of broken C(T) specimens is illustrated, which comprises the quantitative assessment of fracture surface areas through image analysis approach and fractographic investigations at different locations using SEM.

Chapter six describes the influence of aging temperatures, 500 and 540°C on fracture behavior of Zr-2.5Nb alloy, having variable cold working and solution heat treatment histories. The chapter begins with illustrating the influence on microstructure features, showing the fine precipitations of β-Nb and β-Zr phases during the aging at respective 500 and 540°C for 24 h duration. Subsequently, influence of aging treatment on the basal pole texture of cold worked-solution heat treated Zr-2.5Nb alloy is described. Followed by this, influence on the mechanical properties covering micro-hardness, tensile properties and fracture toughness parameters is discussed. Subsequently, a comprehensive study to examine the influence of different analysis methodologies recommended by ASTM and ISO standards on the fracture toughness parameters is presented. A comparison of the fracture behavior of Zr-2.5Nb alloy under WQA and CWSR conditions is presented. A study of the fracture surfaces of broken C(T) specimens through an image analysis approach is discussed to illustrate the change in proportionate flat region of the fracture surfaces. Subsequently, a study of the fractographic features at different locations through SEM examinations is presented. Finally, an optimum TMP history of WQA Zr-2.5Nb alloy is suggested to assure its structural integrity in terms of fracture behavior.

Finally, chapter seven summarizes the influence of TMP parameters associated with SHT, cold working and vacuum aging stages of WQA route on fracture behavior of Zr-2.5Nb alloy and brings out the optimum TMP parameters for the fracture toughness view point of WQA Zr-2.5Nb alloy. Additionally, the chapter also concludes the influence of different analysis procedures on fracture toughness parameters of Zr-2.5Nb alloy under the three TMP conditions.

Chapter seven is followed by the suggestions for the scope of future work, arising from the present study. The scope includes study of the creep behavior of WQA Zr-2.5Nb alloy, influence of hydrogen concentration on the mechanical properties of WQA Zr-2.5Nb alloy, 'Delayed Hydride Cracking' (DHC) velocity examination of WQA Zr-2.5Nb alloy, Examination of the corrosion resistance of WQA Zr-2.5Nb alloy, to investigate the susceptibility of this material for heavy water and zirconium metal corrosion reaction, and the influence of irradiation on mechanical properties of WQA Zr-2.5Nb alloy.

CHAPTER 2

LITERATURE REVIEW

This chapter summarizes the literature on Zr-2.5Nb alloy, its utility as pressure tube structural material, pressure tubes structural integrity challenges, their manufacturing, fracture behavior and various fracture behavior evaluation methodologies. Chapter commences with an overview of Zr-2.5Nb alloy and basis of its selection for pressure tube application. This is followed by a detailed discussion of various life limiting factors of Zr-2.5Nb alloy pressure tubes, under which in-reactor challenges such as dimensional changes and degradation of mechanical properties including fracture behavior are individually described. Subsequently, the phase diagram of Zr-Nb system is described. Followed by this, a detailed description of various fabrication routes employed for pressure tube manufacturing; CWSR, CWA, WQA and GCA is presented. In this respect, major emphasis is given to WQA route and the importance of its final TMP stages viz., SHT, cold working and vacuum aging is illustrated. Subsequently, the essence of fracture behavior for structural integrity of pressure tubes and its evaluation procedures are discussed. Finally, based on review, limitation of literature is pointed out, which motivated the present study.

2.1 Zr-2.5Nb Alloy for Pressure Tube Applications

Zirconium serves as the base element for various structural materials of a commercial nuclear reactor, primarily because of having lower neutron absorption cross-section and superior corrosion resistance in aqueous medium [13-18]. Its principal application areas include cladding tubes (commonly known as, 'fuel tubes') of light (LWRs) and heavy water reactors (HWRs) and pressure tubes, calandria tubes and garter springs of HWRs. Till date, a number of zirconium based alloys have been developed, which can be broadly classified into two categories, ‘Zr-Sn’ alloys and ‘Zr-Nb’ alloys. The ‘Zr-Sn’ alloys comprise Zircaloy-1, Zircaloy-2, Zircaloy-3 and Zircaloy-4; while the ‘Zr-Nb’ family comprises Zr-1Nb, Zr-2.5Nb and Zr-2.5%Nb-0.5%Cu alloys. Out of these zirconium alloys, only few including Zircaloy-2, Zircaloy-4, Zr-2.5Nb, Zr-1Nb and Zr-2.5%Nb-0.5%Cu have found their place for nuclear applications, as shown in Table 2.1.

Table 2.1: Applications of different zirconium alloys as nuclear structural materials [13,19].

Zr-Alloys	**Alloying Elements**							**Application**	
	Sn	**Fe**	**Cr**	**Ni**	**Nb**	**Cu**	**Zr & other alloying additions and impurities**	**HWR**	**LWR**
Zircaloy-2	1.5	0.12	0.10	0.05	-	-	Balance	Fuel cladding, Pressure tubes, Calandria tube	Fuel cladding
Zircaloy-4	1.5	0.22	0.10	-	-	-	Balance	Fuel cladding, Pressure tubes, Calandria tube	Fuel cladding
Zr-2.5Nb	-	-	-	-	2.5	-	Balance	Pressure tubes	-
Zr-1%Nb	-	-	-	-	1	-	Balance	-	Fuel cladding in some Russian reactors
Zr-2.5%Nb-0.5%Cu	-	-	-	-	2.5	0.5	Balance	Garter Springs	-

The Zr-Nb alloys were primarily developed by Russians, who investigated these alloys with up to 5 wt% Nb and found Zr with 1 wt% Nb suitable for fuel tube applications and Zr with 2.5 wt% Nb suitable for pressure tube applications [19]. The 2.5 wt% Nb alloy of zirconium (commonly known as, 'Zr-2.5Nb' alloy) had several advantages over Zircaloy-2, which was used earlier for the pressure tube applications. The major advantage of Zr-2.5Nb alloy was its superior creep resistance, and other advantages include its higher strength [19,20] and lower absorption of hydrogen/deuterium [20] generated from the corrosion reaction of heavy water coolant with zirconium metal. The Zr-2.5Nb alloy, having ~20% higher strength as compared to Zircaloy-2 [19,20] is advantageous, since the pressure tubes made by the former alloy are relatively thin. The fuel channel data of Indian Pressurized Heavy Water Reactors (IPHWRs) [20] shows that the pressure tubes of Zircaloy-2 used in earlier 220 MWe IPHWRs had nominal wall thickness of 4.03 mm, however, the modified pressure tubes made of Zr-2.5Nb alloy had nominal wall thickness of 3.5 mm.

Furthermore, during reactor operation, the Zr-2.5Nb alloy pressure tubes as compared to conventional Zircaloy-2 pressure tubes showed lower hydrogen/deuterium pickup rate. Moreover, with continuous reactor operation, this pickup rate increased with much lower rate as compared to that of Zircaloy-2 [20]. Since, during reactor operation, corrosion of zirconium metal with light/heavy water results in the generation of nascent hydrogen/deuterium, which on subsequent absorption in zirconium based alloys, causes hydrogen and hydride induced embrittlement [21]. Therefore, it has always been a prerequisite to minimize such hydrogen/deuterium pickup for ensuring the structural integrity of reactor components. Because of showing lower absorption of hydrogen/deuterium, the Zr-2.5Nb alloy, in contrast to Zircaloy-2 proved to be less susceptible to hydrogen/hydride induced structural integrity problems.

Because of the aforementioned advantages, Zr-2.5Nb alloy replaced Zircaloy-2 and is currently being extensively used as the pressure tube material in HWRs. The design lives of such Zr-2.5Nb pressure tubes are far higher (30 years) than that of the conventional pressure tubes of Zircaloy-2 (15 years) [20].

2.2 Structural Integrity Challenges for Zr-2.5Nb Pressure Tubes

Pressure tubes constitute the most important components of a nuclear reactor. The schematic view of the pressure tubes inside a nuclear reactor is shown in Figure 2.1 (a). During reactor operation, pressure tubes face complex environments including irradiation produced during the nuclear fission reaction and absorption of deuterium generated from the corrosion reaction of heavy water coolant with zirconium metal. These environments cause degradation in the mechanical properties of pressure tubes, resulting in the structural integrity challenges for the tubes [22]. In addition, the operating pressure tubes exhibit continuous dimensional changes, which also impose limitation for their operation till the designed life.

The life limiting factors of an operating pressure tube can therefore be broadly classified into following two categories and are being discussed subsequently.

1. In-reactor dimensional changes
2. Mechanical behavior degradation

2.2.1 In-reactor Dimensional Changes

During reactor operation, pressure tubes undergo continuous dimensional changes comprising sagging, axial elongation and diametral expansion. These in-reactor dimensional changes of the tubes are primarily the consequences of the three mechanisms viz., thermal creep, irradiation growth and irradiation creep. Following sections describe these mechanisms and their outcomes, in terms of individual dimensional changes of the pressure tubes.

I. Thermal Creep

The thermal creep (sometimes simply known as ‘creep’) is a time dependent deformation of a material in the presence of a constant elastic loading under isothermal condition. Creep is the function of temperature and applied magnitude of stress. Under ambient condition, in general the creep rate of a material is too small to measure, however it increases with temperature. Additionally, creep rate also increases with the magnitude of applied stress. The creep of a material at higher temperature/at higher stress, associated with a higher rate of deformation, is commonly known as ‘accelerated creep’.

During operation of PHWR220, pressure tubes carry heavy water as the primary coolant, at ~10 MPa pressure and ~300°C temperature. Because of pressurised heavy water, pressure tubes face hoop and longitudinal stresses, which cause creep of the tube and lead in the continuous diametral expansion and elongation of the tube during reactor operation.

II. Irradiation Enhanced Dimensional Changes

During reactor operation, pressure tubes are exposed to neutron irradiation with an approximate flux of 3.7×10^{13} n/cm^2/s and fluence of 3×10^{22} n/cm^2 up to 30 years of design life [20]. This irradiation enhances the creep rate of pressure tubes through the two modes; ‘irradiation growth’ and ‘irradiation creep’, and plays an important role in governing their operating lives. ‘Irradiation growth’ represents the constant volume dimensional changes in pressure tube material caused by irradiation in the absence of any applied stress [23]. This type of dimensional changes is primarily caused by the selective absorption of vacancies and interstitials along some of the crystallographic planes within the material. The second important mode by which irradiation enhances dimensions of the pressure tube is through ‘Irradiation creep’, which represents the constant volume and stress dependent dimensional changes under irradiation condition [23]. The total dimensional change of an operating pressure tube is, therefore, the combined outcome of the changes associated with thermal creep, irradiation growth and irradiation creep mechanisms.

The early pressure tubes installed in the first seven IPHWRs and CANDU (‘CANada Deuterium Uranium’) reactors were unable to survive up to their 15 years designed lives [20]. This was chiefly because, at that time irradiation enhanced dimensional changes of the pressure tube were unknown and the predictions of dimensional changes were exclusively based on the experimental data obtained from the out of reactor creep testing, which resulted in having insufficient design allowances for 15 years of their operation. Later on, empirical relationships based on the periodical observations of tube's dimensional changes [20] were developed to enhance the accuracy of prediction.

In-reactor dimensional changes of an operating pressure tube can be classified into the following three categories:

i. Sagging

During reactor operation, the pressure tubes sag between the spacers, i.e., garter springs which are fitted over them to prevent their contact with the surrounding concentric cooler calandria tubes [20]. In order to reduce sagging between the spacers, numbers of spacers have been increased from two (as in the earlier tubes) to four; in addition, the conventional loose fit garter springs have too been replaced by the tight fitted garter springs to prevent change of its position during reactor operation. In addition to sagging between spacers, the whole fuel channels have also reportedly sagged during operation, resulting in the corresponding sagging of the pressure tubes contained within it, leading in the further enhancement of their sagged curvatures (as illustrated in Figures 2.1 and 2.2). Such fuel channel sagging is the consequence of the creep cause by the dead weights of fuel bundles & coolant contained within it and also, self weight of channel itself.

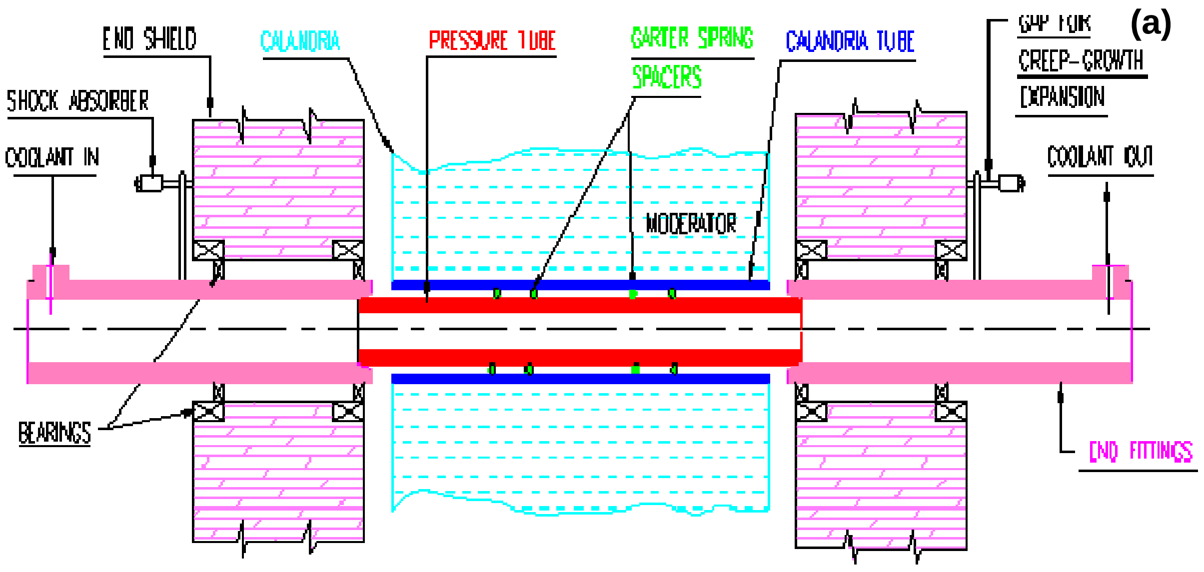

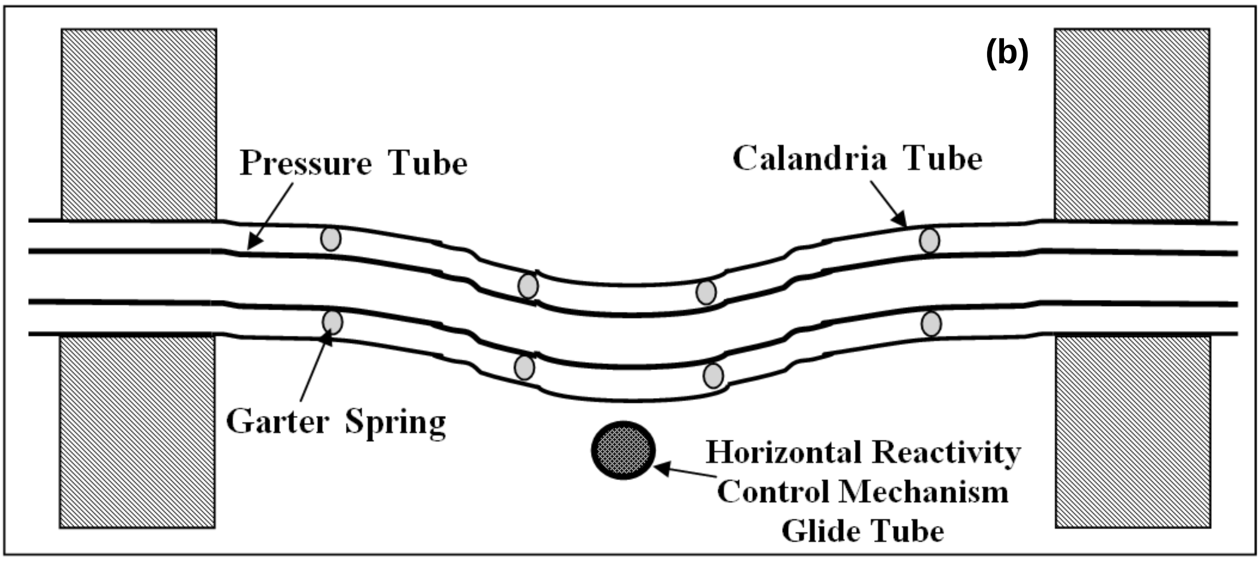

Figure 2.1: (a) Schematic illustration of the location of pressure tubes inside a nuclear reactor, and (b) Schematic illustration of a sagged fuel channel during reactor operation and position of the reactivity control mechanism beneath it to prevent its excessive sagging [20].

Such tube sagging has not been observed to impede the passage of fuel bundles and, therefore, is also not a barrier for thirty years of tube's designed life. As a precaution, a reactivity control mechanism is provided below each of the fuel channels to prevent the extensive sagging (Figure 2.1 [20]). Also, periodic monitoring of the gap between the fuel channel and the reactivity control mechanism is usually performed, especially in the last half period of the designed life.

ii. Axial Elongation

As discussed earlier, during reactor operation, the pressure tubes carry heavy water as the primary coolant at ~10 MPa pressure and ~300°C temperature. The axial stresses developed within the pressure tubes because of pressurized heavy water cause their elongation (Figure 2.2), through thermal creep (as described in Section-2.2.1-I). Additionally, because of the irradiation, creep rate gets accelerated through irradiation growth and irradiation creep mechanisms (as described in Section 2.2.1-II). Therefore, the total elongation of a particular pressure tube is a combined outcome of the thermal creep, irradiation growth and irradiation creep mechanisms [20]. Pressure tube elongation is one of the life limiting factors during reactor operation, since it reduces the space at both of tube's ends leading in the interference of the feeder pipes and other associated structural components attached at tube's ends.

The elongation of a pressure tube, in general increases linearly with the operation time [24]. Richinson et. al. [24] and Causey et. al. [25] showed that the elongation rates of different pressure tubes of a CANDU reactor has considerable scatter, with the maximum elongation rate close to 5 mm/year. This rate is much higher than the anticipated tube elongation rate during the design of the earlier CANDU and Indian pressure tubes, because of which the early pressure tubes were not able to survive up to thirty years of their designed life. Considering this, all of the current CANDU pressure tubes have at least 75 mm bearing space at both of their ends [24].

iii. Diametral Expansion

During reactor operation, the hoop stress developed within pressure tubes because of the pressurised heavy water passing through it, primarily results in their diametral expansion, Figure 2.2 (a). Such diametral expansion may cause the contact between the hot pressure tube and the surrounding cooler calandria tube. This, therefore, could lead to the formation of cold zone at the contact location, which hence results in the high thermal gradient near the contact location. Such high thermal gradient may cause the migration of deuterium/hydrogen towards the contact location, which after exceeding the solubility limit may cause the formation of 'hydride blister' at the contact location [26,27]. The hydride blister being brittle in nature, in the presence of sufficient tensile stress field could crack and, therefore, may result in the unstable failure of the pressure tube. In addition to hydride blister formation, another important reason for limiting the pressure tube's diametral expansion is the thermal hydraulics consideration of avoiding fuel bundle bypass by the pressurized coolant and structural integrity consideration to prevent pinching of calandria tubes by garter springs. Therefore, diametral expansion of pressure tubes is one of the important life limiting factors for their safe operation. Figure 2.2 (b) shows the operating performance (diametral strains) of the pressure tubes fabricated using various routes as a function of the fluence level. As can be seen from this figure [2,11] that the tubes manufactured following the heat treated fabrication routes, especially TMT-2 and the route followed for the Fugen pressure tubes showed lower diametral strains, and therefore better operating performance.

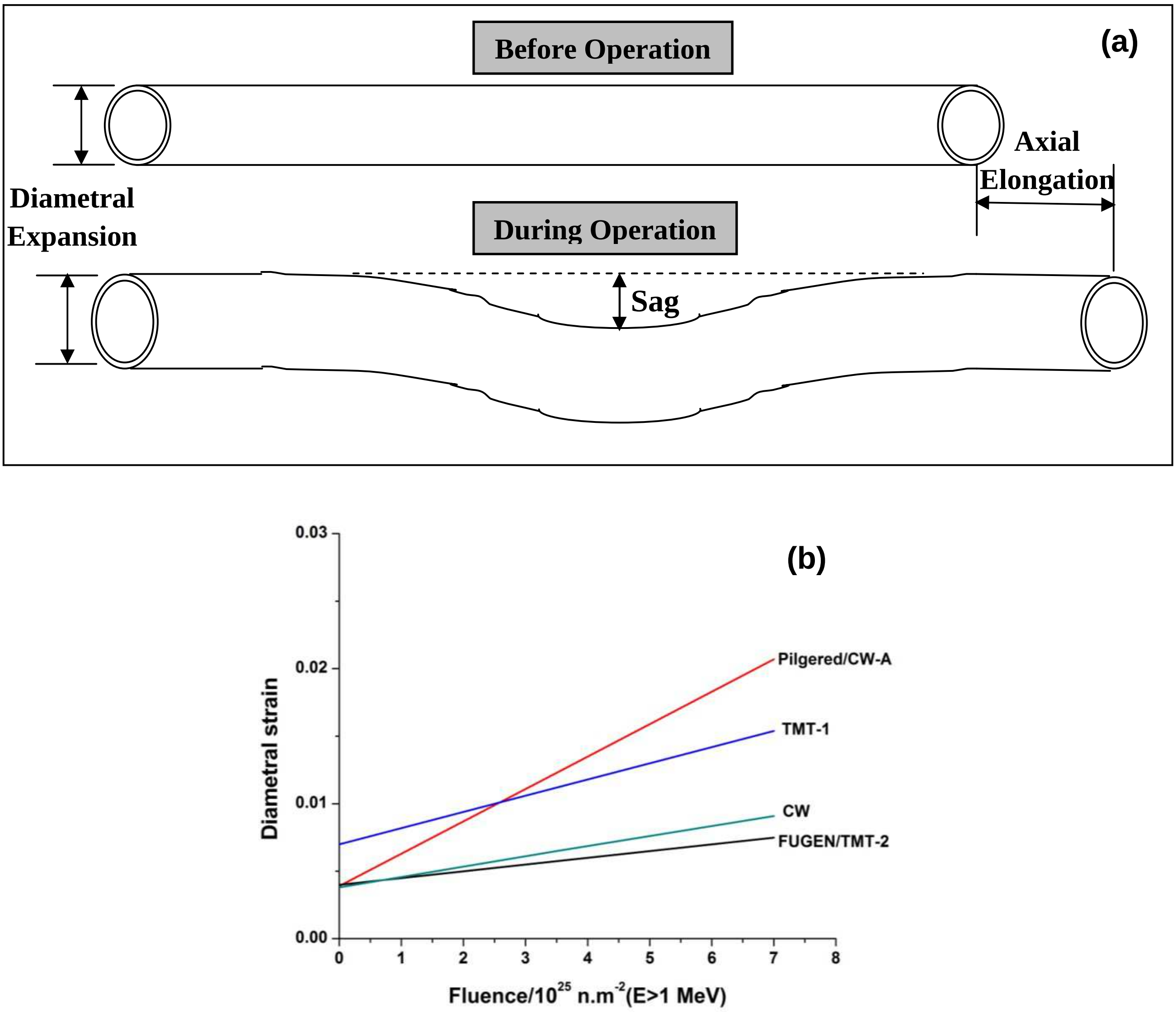

Figure 2.2: (a) Schematic illustration of the three in-reactor deformation modes of an operating pressure tube viz., sagging, axial elongation and diametral expansion [18], and (b) Operating performance (diametral strains) of the pressure tubes fabricated using different routes [2,11].

Ells et al. [28] showed that for CANDU pressure tubes, the design allowance for diametral expansion is 5% of the initial pressure tube diameter. The CANDU pressure tubes showed their diametral expansion rates close to 0.1 mm/year [24]. In the recent pressure tubes, garter spring spacers of reduced diameter are being used, which provide sufficient space for the diametral expansion without squeezing the garter spring between the pressure tube and the surrounding calandria tube [20].

2.2.2 Mechanical Properties Degradation

During reactor operation, the pressure tubes face complex environments including irradiation and absorption of hydrogen/deuterium produced from the corrosion of zirconium metal with the heavy water. These typical reactor environments degrade the mechanical properties of the pressure tubes, and being discussed in detail in the following sections.

I. Degradation from Hydrogen/Deuterium Ingress

As mentioned earlier that the pressure tubes in a nuclear reactor serve as containment channels for heavy water coolant at ~10 MPa pressure and 300°C temperature. Under such operating condition, heavy water reacts with zirconium metal, which leads to the generation of nascent deuterium. A portion of this deuterium is absorbed by the pressure tube, which after exceeding the Terminal Solid Solubility (TSS) results in the formation of deuteride (commonly known by its isotopic name, ‘hydride’) in the shape of plates. The absorption of deutrium both in the form of solid solution and also hydride, induces embrittlement in pressure tube, resulting in the drastic reduction of its fracture toughness. The former form of embrittlement is called 'hydrogen embrittlement', while later form of embrittlement is called 'hydride embrittlement' [21]. Therefore, deutrium absorption induced from the reaction of heavy water coolant with zirconium metal imposes the structural integrity challenge for the pressure tubes.

The hydride embritlement can be classified into two major categories viz., gross embrittlement and localized embrittlement, depending on the influenced region of emrbittlement. Hydride is a brittle phase, and therefore its presence beyond a critical volume fraction causes overall reduction in the fracture toughness of pressure tube material. This type of hydride embrittlement is commonly known as 'gross hydride embrittlement'. The second class of hydride embrittlement is the 'localized hydride emrbittlement', which is caused by the hydrogen migration under thermal and/or hydrostatic stress gradient. Once the local hydrogen solid solubility is exceeded brittle hydride precipitates out. The brittle hydride undergoes failure in an unstable manner under the presence of a critical tensile stress field. Such crack propagation does not occur continuously, rather in steps, which individually are delayed by certain time lag. Such delay for the crack propagation is because of the time required for stress gradient induced deuterium migration towards crack tip and the time required for the subsequent formation of critical size hydride. Such phenomenon involving the discontinuous crack propagation, originated from the brittle failure of hydride, is commonly known as ‘Delayed Hydride Cracking’ (DHC) [21,29-38]. DHC is a form of 'localized hydride emrbittlement'. DHC process is principally characterised in terms of the velocity of crack propagation, symbolized as 'V_{DHC}' [35]. For pressure tube's structural integrity point of view, a low V_{DHC} is always desirable. V_{DHC} of pressure tube material is a function of the crack driving force represented by the stress intensity factor at the crack tip (symbolized as 'K_I'). Below a threshold value of the stress intensity factor (K_{IH}), V_{DHC} becomes negligible, which therefore suppresses the DHC process.

Zr-2.5Nb alloy pressure tubes exhibited comparable corrosion rates as that of the conventional Zircaloy-2 pressure tubes [20]. However, Zr-2.5Nb alloy pressure tubes showed lower hydrogen pick up rate during reactor operation [20]. Furthermore, the DHC velocity of Zr-2.5Nb alloy is higher as compared to that of Zircaloy-2 pressure tubes, because of the higher strength of former material [19,20,36].

Improvements in the fabrication procedures of Zr-2.5Nb alloy pressure tubes have reduced the possibilities of hydrogen/hydride embrittlement. One of such improvements was in the ingot preparation stage, wherein the number of alloy melting steps was increased from two to four. Such increase in the number of alloy melting steps caused reduction in the impurity element concentration such as hydrogen, chlorine, phosphorous, etc. within the ingot, which consequently improved the fracture toughness of as-fabricated pressure tube material. In contrast to conventional double melted Zr-2.5Nb pressure tubes (containing 5-15 wt. ppm hydrogen), the quadruple melted pressure tubes contain hydrogen concentration of <5 ppm [39,40]. Furthermore, the concentrations of other impurity elements such as; phosphorous (<10 ppm) and chlorine (<0.5 ppm) are also lower in the quadruple melted material. Such reduced concentrations of impurity elements in quadruple melted pressure tubes have shown considerable improvement in their fracture toughness [41].

II. Irradiation Induced Degradation

During reactor operation, pressure tubes are exposed to neutron irradiation with an approximate flux of 3.7×10^{13} n/cm^2/s and fluence of 3×10^{22} n/cm^2 up to 30 years of design life [20]. Irradiation induces damage in the microstructure of pressure tube material and causes degradation of its mechanical behavior. The major impacts of irradiation on pressure tube material include increase in its strength and reduction in its ductility & fracture toughness. Increase in strength, caused by irradiation, affects the DHC characteristic of pressure tube material; such that with continuing operation, pressure tubes become more and more susceptible to DHC failure, due to corresponding increase in V_{DHC}. Such strength-V_{DHC} correlation follows a thumb rule, as per which a two fold rise in yield strength results for ~30 fold increase in V_{DHC} [36].

The operating performances of earlier Pickering and Bruce units showed that the mechanical behavior degrades only upto certain level of irradiation fluence and subsequently remain practically unaffected [40,41]. The variation of Ultimate Tensile Strength (UTS) and fracture toughness (*CCL* parameter) with irradiation (as shown in Figure 2.3) respectively suggested the influence upto ~ 1.5×10^{25} and 2.5×10^{25} n/m^2 fluence levels [40] under which UTS increased by 33% and *CCL* decreased by ~ 50%.

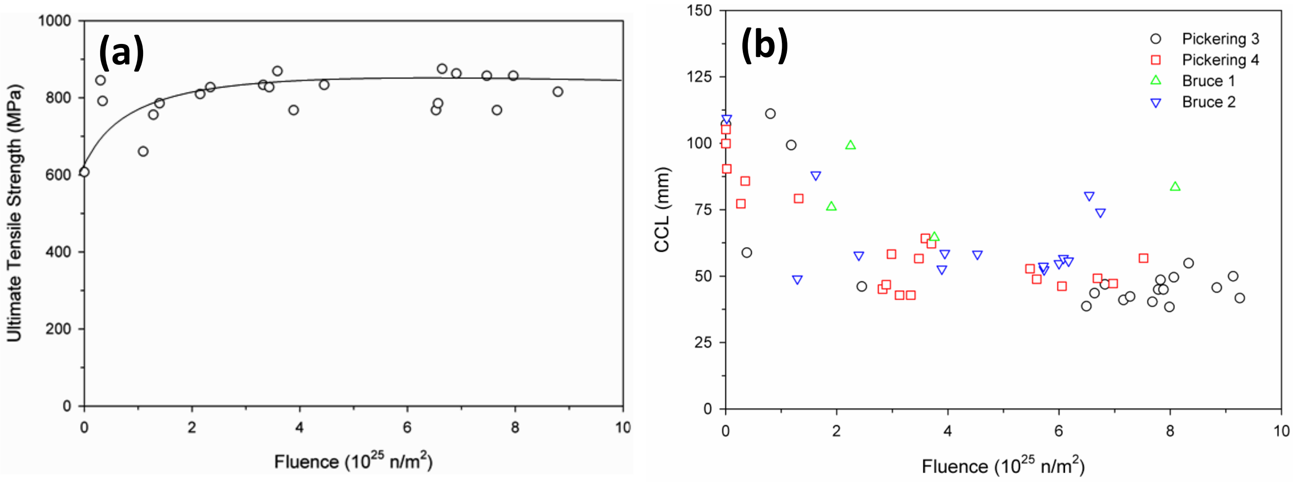

Figure 2.3: Influence of irradiation fluence on (a) Ultimate Tensile Strength, UTS and (b) fracture toughness (*CCL* parameter) of Zr-2.5Nb pressure tubes of Pickering and Bruce units [41].

In terms of LBB criteria (as discussed in Section 1.1, Chapter 1), trend of *CCL* parameter suggests that initially, the pressure tube has large safety margin between LBB and rupture failures, however with continuing operation, such margin reduces and subsequently saturates, resulting in eventually the higher probability of tube rupture.

Though, the degradation in mechanical properties of operating pressure tubes has not been a critical life limiting factor for 30 years of their designed life [41], it is desirable to improve the mechanical behavior, so as to further reduce the possibility of tube rupture.

2.3 Zr-Nb Phase Diagram

The phase diagram of binary Zr-Nb system is shown in Figure 2.4. Zr-Nb system comprises three equilibrium phases viz., α-Zr, β-Zr and β-Nb. The α-Zr phase is a substitutional solid solution of Nb in Hexagonal Closed Packed (HCP) Zr, with extremely limited equilibrium Nb concentration (maximum 0.7 wt. % at 620°C). The β-Zr phase is a substitutional solid solution of Nb in Body Centred Cubic (BCC) Zr, having a maximum equilibrium Nb concentration of 19 wt. % at 620°C. The β-Nb phase is a substitutional solid solution of Nb in BCC Zr, having very high equilibrium Nb concentration varying from 92.2 to 100 wt. %. The alloy having upto 0.7 wt. % Nb comprises single α-Zr phase region upto a β-transus temperature of 866°C and above it shows β-Zr phase. With reference to present work, i.e., alloy containing 2.5 wt. % Nb shows first transformation at 620°C, from the two phase (α-Zr + β-Nb) regime to (α-Zr + β-Zr) regime. In this transformation, the β-Nb phase dissociates into α-Zr and β-Zr.

In Zr-2.5Nb alloy, 844°C represents the second transformation temperature (commonly known as ‘β-transus temperature’), at which the two phase (α-Zr + β-Zr) regime transforms to single β-Zr phase regime. Here, it is important to note that the β-transus temperature of the alloy is a function of the impurity elemental concentrations within it. The β-transus temperature of Zr-2.5Nb alloy is a strong function of its oxygen concentration, and follows a thumb rule, as per which within an oxygen concentration of 1000 ppm, every increase by 100 ppm results for 7°C increase in β-transus temperature. However, opposite to oxygen, iron reduces the β-transus temperature. Alloy having 19 wt.% Nb shows the mono-eutectoid transformation of (α-Zr + β-Nb) to single phase β-Nb region at 620°C.

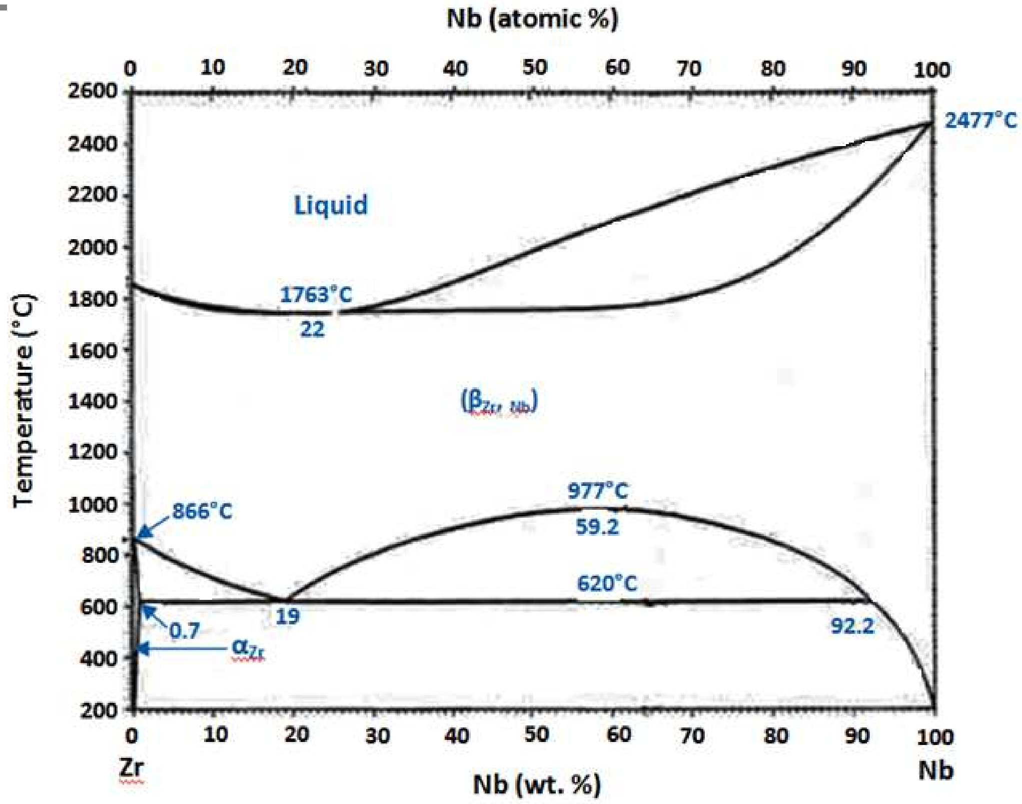

Figure 2.4: Phase diagram of binary Zr-Nb system [42].

2.4 Fabrication of Pressure Tubes

As introduced in Section 1.1, Chapter 1 that presently the Zr-2.5Nb pressure tubes are being fabricated following different routes throughout the world. These fabrication routes include 'Cold Worked and Stress Relieved' (CWSR) route employed for Indian and CANDU PHWRs; 'Cold Worked and Annealed' route employed for all Russian PHWRs (‘Reaktor Bolshoy Moshchnosti Kanalniy’, Russian PHWRs) of 1000 MWe capacity; 'Water Quenched and Aged' route employed for the Japanese PHWR ('Fugen'), Pakistani PHWR (KANUPP, Karachi Nuclear Power Plant) and Russian PHWRs (RBMK, Ignalina-1) of 1500 MWe capacity; and 'Gas Quenched and Aged' route for the RBMK 1500 MWe, Ignalina-2 reactor [1-4]. These fabrication routes are being discussed in detail as follows.

2.4.1 Cold Worked and Stress Relieved Route

The 'Cold Worked and Stress Relieved' route was originally developed for fabricating the Zircaloy-2 pressure tubes of Hanford reactor at Washington. In year 1962, for the first time, Canadians used similar Zircaloy-2 pressure tubes fabricated using the CWSR route for their first CANDU reactor, Nuclear Power Demonstration (NPD) of 22 MWe capacity. Later on, CWSR route was used for fabricating Zircaloy-2 pressure tubes of the subsequent CANDU reactors viz., Douglas Point (200 MWe) and 500 MWe Pickering A (1 & 2). Subsequently, Canadians replaced Zircaloy-2 with Zr-2.5Nb alloy for pressure tubes. This replacement was done because of the several advantages of Zr-2.5Nb alloy over Zircaloy-2 such as superior creep resistance, higher strength and lower absorption of hydrogen/deuterium during reactor operation (as discussed earlier in Section 2.1). In year 1971, for the first time, Canadians used Zr-2.5Nb alloy pressure tubes fabricated using the CWSR route in Pickering A (3 & 4). Later on, Zr-2.5Nb tubes under CWSR condition were used in almost all the subsequent CANDU reactors and are still in operation.

The CWSR route comprises several fabrication stages including ingot preparation through multiple vacuum arc melting cycles, hot working in β-phase field for breaking down the cast structure, log machining & preparation of hollow billets, beta quenching of billets, hot extrusion of billets in two phase (α-Zr+β-Zr) field, cold working and the final autoclaving treatment. Figure 2.5 shows the comparison of Indian CWSR route [3] (currently being followed at Nuclear Fuel Complex (NFC), Hyderabad [35]) and Canadian CWSR route (commonly known as 'Conventional route') [43], highlighting differences in modes of hot working for breaking of the ingot's cast structure, reduction ratios followed during extrusion, modes and degree of imparted cold work. Different stages of CWSR fabrication routes of Indian and Canadian pressure tubes are being discussed below in detail.

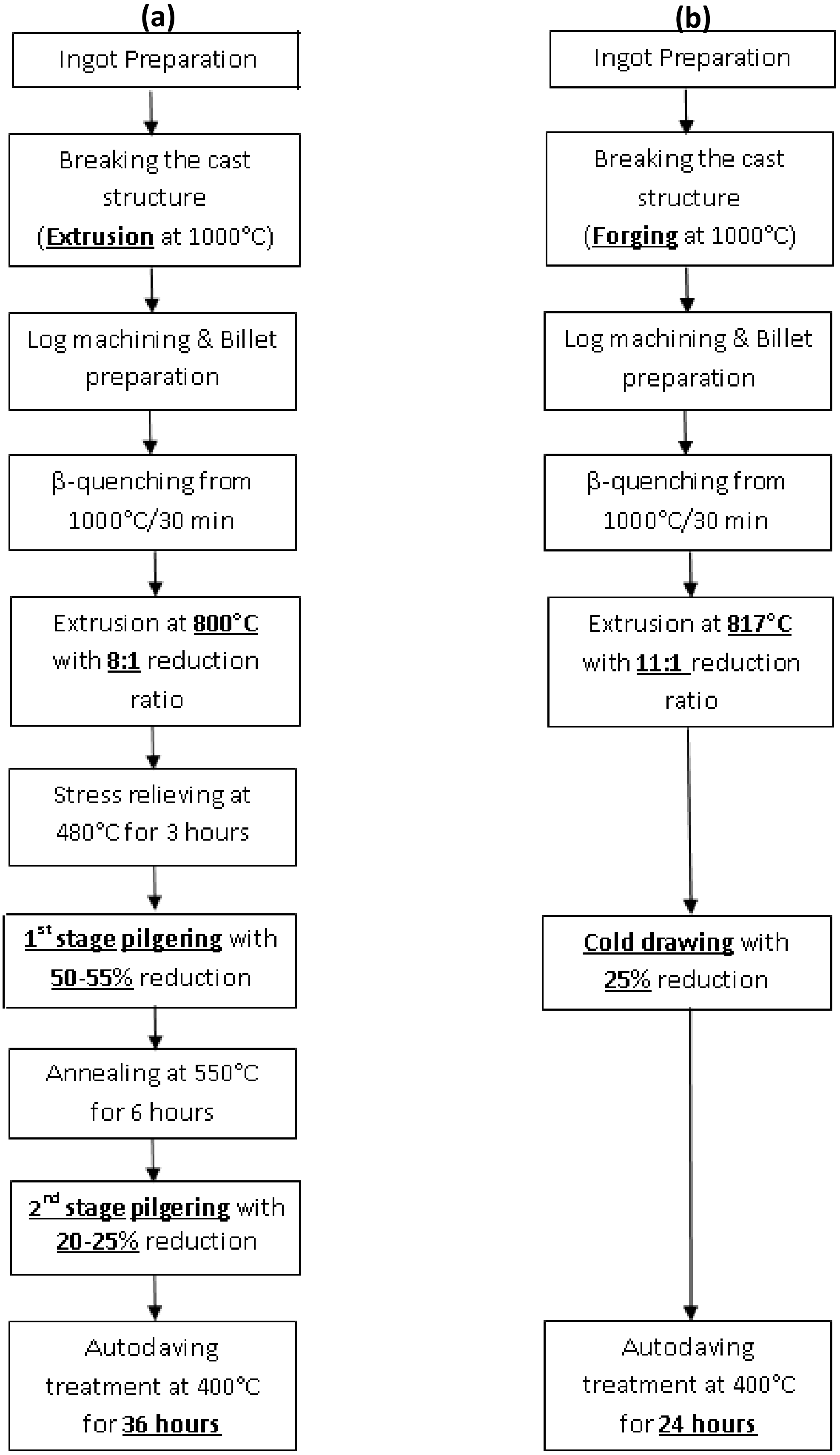

Figure 2.5: CWSR fabrication routes, presently being employed for the pressure tubes manufacturing of IPHWR220 and CANDU reactors [3].

I. Ingot Preparation

Ingot preparation is the first stage of tube fabrication, which comprises melting of Zr-2.5Nb alloy in a consumable electric arc furnace followed by casting in cylindrical shape [20]. As discussed earlier (in Section 2.2.2-I), multi stage alloy melting is being practiced to minimize the impurity concentrations in the ingot and therefore, in the fabricated pressure tube. In addition to adjustment in the number of melting cycles, modification in selection of the raw materials has also ensured the lower carbon content, which contributed to improve the fracture toughness of the fabricated material. The major impurity elements, which are influenced by the multiple stage of melting are chlorine, phosphorous and hydrogen. Presence of these impurity elements in the pressure tube has reportedly [44,45] proven their adverse influence on its fracture toughness through the formation of low energy facets and fissures. Earlier, the ingot used to be prepared following a double melting step, under which it was melted twice with an intermediate cooling stage followed by casting. This double melting step, as compared to single melting reduced the concentration of impurity elements to 5.5-8 ppm chlorine and 5-15 ppm hydrogen [45]. In view of further reducing the concentration of these impurity elements, so as to improve the fracture toughness of as-fabricated pressure tube material, the two stage melting was later on replaced by four stage (quadruple) melting, in addition to the use of selected raw materials. In contrast to conventional double melting step, the quadruple melting step confirmed the lower impurity concentration within pressure tube, having less than 0.5 ppm chlorine and less than 5 ppm hydrogen [45]. Such improvements caused around two fold enhancement in the fracture toughness of as-fabricated pressure tube material [45]. This is why, the quadruple melting step is being extensively followed during the ingot preparation.

II. Break Down of Cast Structure

The cast structure of ingot, in general, exhibits heterogeneity in terms of grain morphology, its size and chemical composition. In the vicinity of ingot surface, because of experiencing the highest cooling rate, grains are usually finer in size and reasonably equiaxed in shape. However, at the inner section of ingot, because of experiencing relatively lower cooling rate, grains are relatively bigger in size with major dimension parallel to the heat flow direction leading in their columnar morphologies. The inhomogeneous chemical composition of ingot can be understood as the consequence of the difference in solid solubilities of solid and liquid phases because of the corresponding dissimilarities in the cooling rates. These microstructural heterogeneities lead to the non-uniform mechanical properties of ingot.

The main reason for breaking the cast structure is to make the ingot amenable to working during subsequent fabrication steps. In addition, cast structure breakdown also creates uniform microstructure for ensuring the uniform mechanical properties [20]. The breakdown mode, its degree and associated strain rate influence the amount of structure breakdown.

In the CWSR fabrication routes of Indian 220MWe tubes and Canadian tubes, the cast structures are being broken while preheating the ingots in a single phase, β-Zr regime at 1000°C. These two routes, however, have differences in the modes of breaking the cast structure. In the Indian route, cast structure is being broken through extrusion, while in the Canadian route, press (rotary) forging is being used for breaking the cast structure. Additionally, the recently fabricated prototype pressure tubes to be used in future IPHWRs; KAPS (Units 3 & 4) and RAPS (Units 7 & 8) of 700MWe capacities were manufactured by employing rotary forging, similar to the Canadian route [46].

III. Log Machining and Billet Preparation

After cast break down, the logs are cut into sections and subsequently machined in the form of hollow billets. Finally, the surface oxide layer formed on the billet surface is removed to reduce the oxygen concentration and also to ensure better surface finish.

IV. Beta Quenching

To randomise the crystallographic texture, billets are heat treated at 1000°C for 30 min followed by water quenching in both the Indian and Canadian CWSR routes [3]. This quenching treatment, is performed in single phase, β-Zr regime, and is commonly known as 'β-quenching'. β-quenching results in the martensitic transformation of β-Zr phase, therefore eliminates the previous thermo-mechanical treatment history by creating a single phase microstructure. In addition to texture randomization, β-quenching also ensures much superior chemical homogeneity and grain structure refinement for achieving better mechanical strength.

Srivastava et al. [3] showed that such β-quenching produces martensite, which comprises both coarser and finer plate sub-structures, as shown in Figure 2.6. The β-Zr phase first transforms to the acicular martensite having coarser plates and subsequently the autocatalytic nucleation results in the generation of the finer plates between the primary coarser plates [3].

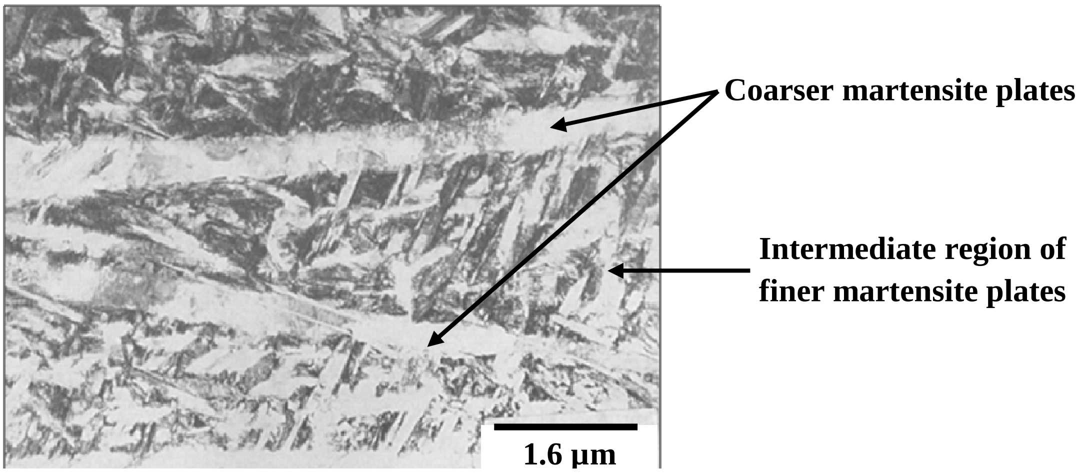

Figure 2.6: Microstructure of β-quenched Zr-2.5Nb billet comprising primary (coarse) martensite plates after initial stage of transformation during beta quenching treatment and later generation, finer martensite plates obtained at final stage of beta quenching [3].

V. Hot Extrusion

After beta quenching, billets are hot extruded in two phase, α-Zr+β-Zr regime. The Indian and Canadian CWSR fabrication routes follow analogous extrusion temperatures, 800°C (Indian) and 817°C (Canadian), however with considerably different extrusion ratios. In the Indian route, billets are extruded at ~8:1 ratio, while in the Canadian route, billets are extruded at relatively higher ratio (11:1). Furthermore, Indian and Canadian extruded billets also have differences in the cooling mediums, such as water spraying employed for Indian billets as compared to air cooling employed of CANDU billets [3,47]. Cheadle [47] showed that the Canadian's way of extrusion has been recently modified, wherein the preheating furnace (gas medium) was replaced to electric to minimise the hydrogen pickup.

Hot extrusion stage plays an important role in governing the microstructural features of the tube such as stacking arrangements of phases, grain size & morphology, and crystallographic texture. Therefore, hot extrusion stage has a strong influence on the final microstructure of as-fabricated pressure tubes.

Extrusion deforms α-Zr grains and arranges them in the form of long and thin stringers, having much thinner stacking of β-Zr grains in between α-Zr stringers, as shown in Figure 2.7 (a). Cooling from extrusion temperature results in the formation of two categories of α-Zr phases viz., oxygen enriched α-Zr and oxygen depleted α-Zr [12,47,48]. Here, it is important to note that oxygen constitutes as an alloying element of Zr-2.5Nb pressure tube material to provide the necessary strengthening effect and is specified within 900-1300 ppm levels. In Zr-Nb system, oxygen acts as α-Zr stabilizer element [48], and therefore has the tendency to migrate from β-Zr to α-Zr at extrusion temperature. This migration consequently results in oxygen enrichment of α-Zr phase. Since α-Zr is one of the equilibrium phases at room temperature, the oxygen enriched α-Zr phase upon cooling from extrusion temperature remains as it is and commonly known as 'Primary α’. In contrast, during cooling, oxygen lean β-Zr phase transforms to α-Zr (containing less oxygen) and niobium enriched β phase [47]. Furthermore, the β grains in Indian extruded material reportedly [3] contain very fine ω phase precipitates, as shown in Figure 2.7 (b). However, because of the heterogeneity of Nb concentrations in β grains, the density of ω phase is reportedly [3] different within different β grains.

Srivastava et al. [3] showed that the Indian hot extruded microstructure comprises 72-80% volume of α-Zr and remaining β phase with respective Nb concentrations of 0.2 and 8-12 wt. %. In contrast, Cheadle [47] showed that the Canadian hot extruded microstructure comprises ~70% α-Zr and remaining β phase with respective Nb concentrations of 0.6 and 20 wt.%. The observed relatively lower Nb concentration within β phase of the Indian extruded material can be understood as the consequence of restricted Nb partitioning because of the post extrusion cooling at relatively higher rate caused by water spraying.

Holt and Ibrahim [49] suggested that the irradiation growth, one of pressure tube’s dimensional changing mechanisms, dominates along the elongation direction of α-Zr phase. Therefore, it is always desired to have a minimum α-Zr grain elongation so as to resist the operating tube’s dimensional changes because of irradiation growth. As mentioned earlier that Indian pressure tubes, in contrast to CANDU pressure tubes employ, a relatively lower extrusion ratio, which therefore results in relatively lower aspect ratio of α-Zr grains, and thus reduces the possibility of irradiation growth induced dimensional changes. A comparison of the grain dimensions of hot extruded Indian and Canadian tubes are shown in Table 2.2 [3,50].

In addition, extrusion performed at 800°C could result in dynamic re-crystallization of the material, which consequently aids in replacing the elongated grains by nearly strain-free equiaxed grains. Because of this, the extruded microstructure comprises α-Zr stringers made up of a series of almost equiaxed grains. However, such microstructure has also reportedly [3] comprised some minor traces of the incomplete recrystallized regions.

Table 2.2: Grain morphologies of α-Zr and β phases under hot extruded condition fabricated from the Indian [3] and Canadian CWSR routes [43,50].

Parameters	**CWSR Route**		
	Indian Route [3]		**Canadian Route** [43,50]
	α-Zr Phase	**β Phase**	**α-Zr Phase**
Length (μm)	10 to 15	5 to 8	15-25
Width (μm)	0.8 to 1.4	0.1 to 0.2	1.5-2.5
Thickness (μm)	0.2 to 0.4	< 0.02	0.3-0.5
Aspect Ratio (Length/ Width)	6 to 10	50 to 80	15 to 20

Cheadle et. al [51] suggested that in general, extrusion treatment reorients the α-Zr grains, such that basal poles alignment dominates towards the circumferential direction. Furthermore, with increasing extrusion ratio, the intensity of basal pole along circumferential direction further increases. That is why, the Canadian extruded tubes because of using higher extrusion ratio (11:1) have relatively intense basal pole density along circumferential direction as compared to Indian tubes, which are extruded at 8:1 ratio [3]. Such crystallographic texture results in anisotropy in the mechanical behavior of extruded material. A higher basal poles alignment along circumferential direction makes the extruded material stronger along circumferential direction [52].

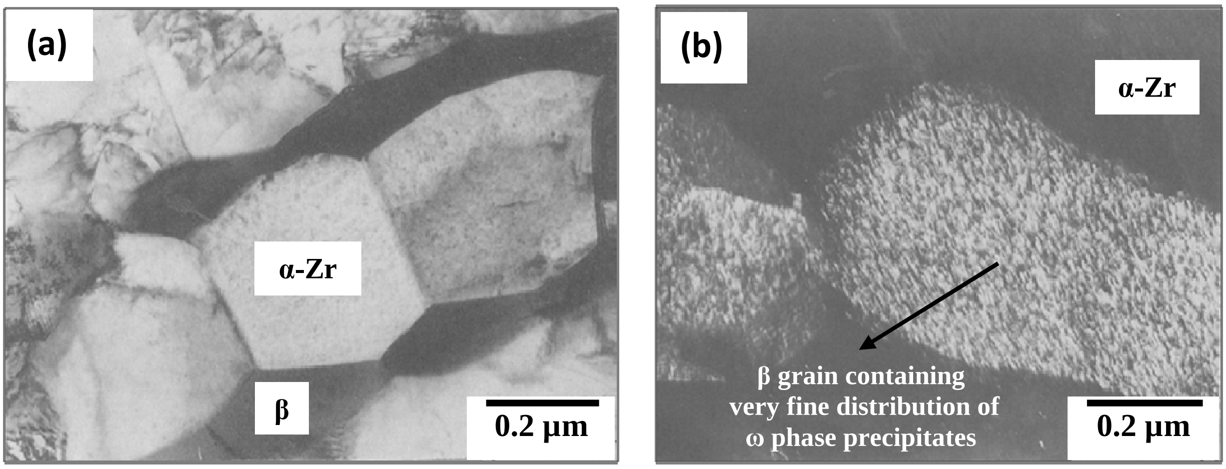

Figure 2.7: (a) Transmission electron micrograph of the Indian hot extruded Zr-2.5Nb alloy in longitudinal (Axial-Circumferential) plane, and (b) Transmission electron (dark field) micrograph of corresponding material, showing fine distribution of ω phase precipitates inside β phase [3].

VI. Cold Working

The hot extruded tubes are provided final dimensions and required dislocation density through subsequent cold working treatment. The Indian and Canadian CWSR routes differ in the modes and degrees of cold working. In Indian fabrication route, extruded tubes are cold worked through pilgering operation performed in two stages. This pilgering operation ensures simultaneous reductions of tube’s wall thickness and diameter. During first stage pilgering, a 50-55% reduction in wall thickness is achieved, while in second stage pilgering, relatively lower (20-25%) thickness reduction is provided. These pilgering stages are accompanied by an intermediate annealing treatment to facilitate the second stage pilgering operation. In contrast, in Canadian fabrication route, the extruded tubes are cold worked in only one stage having 25% thickness reduction through drawing operation.

The cold working operation causes further elongation of α-Zr and β phase stringers, however, marginal increase in α-Zr grain aspect ratio. The first stage pilgering operation introduces a very high dislocation density within α-Zr stringers [3].

In general, pilgering operation is known to change the crystallographic texture of material by causing grain rotations. However, extent of such grain rotations is the function of presence of the secondary phase particles on grain boundaries. The presence of secondary phase causes the deformation strain to localize within it, which restricts the deformation within it and therefore, preventing the rotation of nearby grain. The crystallographic texture of Indian extruded tubes is reportedly [3,53] insignificantly altered by the first stage pilgering operation. The microstructure of first stage pilgered Indian tube reportedly [53] shows minor discontinuity in β-Zr phase along α-Zr boundaries, which causes insignificant alteration of the crystallographic texture.

Here, it is important to note that the dislocation density in as-fabricated pressure tube plays an important role in controlling its in-reactor creep rate, in addition to its strength. Increase in dislocation density not only increases the tensile strength of pressure tube material, however, also enhances its in-reactor creep rate during operation by increasing the extent of irradiation growth. Adamson [54] and Leger & Fleck [55] have shown such effect of decrease in dislocation density on decreasing the irradiation growth of Zircaloy-2 and Zr-2.5Nb alloy. Therefore, an optimum dislocation density in fabricated tube is essential for achieving an optimum combination of its tensile strength and lower in-reactor creep rate. Ibrahim & Chedale [56] and Ibrahim [57] showed that dislocation density of about 2.5×10^{14} per m^2 in the fabricated Zr-2.5Nb pressure tube is optimum for achieving such optimum combination of tensile strength and in-reactor creep, and can be achieved by introducing 20-25% cold work in the final stage of tube fabrication.

Therefore, to reduce dislocation density and also to facilitate second stage pilgering, the first stage heavily pilgered materials are subsequently vacuum annealed at 550°C for 6 h. Selections of annealing temperature (550°C) and soaking duration (6 h) are based on retaining the lamellar structures of α-Zr and β phases and retaining the dislocation density of extruded material. Srivastava et al. [3] showed that the lamellar structures of both α-Zr and β-Zr phases are necessary for achieving optimum tensile properties of Zr-2.5Nb pressure tubes at service temperature of ~300°C and such structure can be retained if annealing temperature is kept lower than 575°C. Furthermore, soaking of 6 h at 550°C causes nearly complete re-crystallization of α-Zr phase, which therefore restores the dislocation density of extruded material [3].

Such, annealing treatment causes the dissolution of fine ω precipitates (formed during extrusion stage) and results in the precipitation of α-Zr within β phase, and therefore, make the β stringers much thinner, Figure 2.8. This α-Zr precipitation is associated with the Nb enrichment of β phase up to 20%. Srivastava et al. [3] and Kumar et al. [53] showed that because of the change in chemical free energy associated with such Nb enrichment and reduction in the interfacial energy, β stringers fragment and grains become nearly equiaxed. Therefore, after annealing, β stringers become more discontinuous in the form of fine particles at the interface of α stringers.

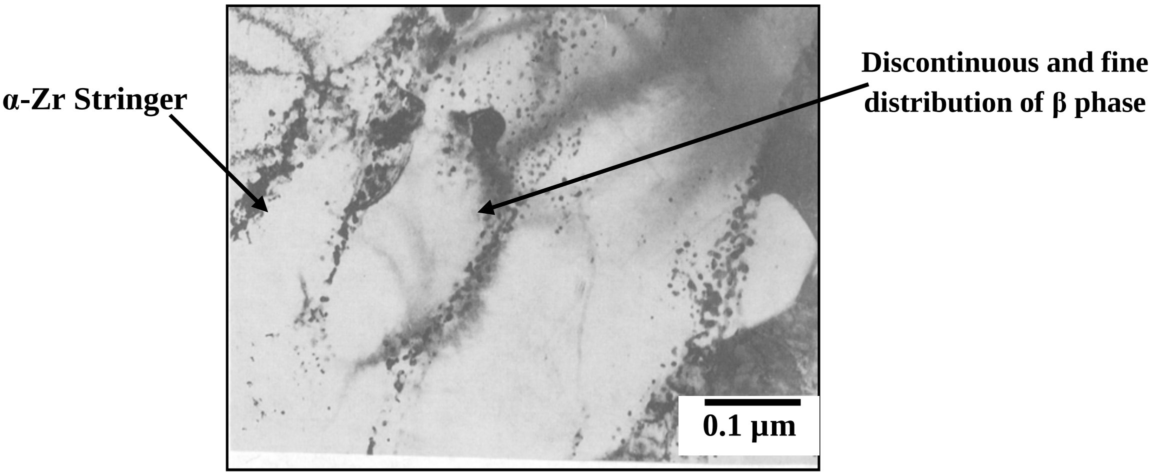

Figure 2.8: Partially recrystallised microstructure of the first stage pilgered Zr-2.5Nb alloy, annealed at 550°C for 3 hours [3].

After annealing, tubes are subjected to second (final) stage pilgering treatment with 20-25% wall thickness reduction, to provide the final dimensions to pressure tubes. This final stage pilgering operation marginally alters the elongated morphologies of α-Zr and β phases [3]. However, it generates more discontinuity in the β phase on α-Zr interfaces. Figure 2.9 shows the second stage pilgered microstructure of the Indian pressure tube, showing such excessive discontinuities in β-Zr phase at α-Zr interfaces [3]. Because of such highly discontinuous β at α-Zr interfaces, second stage cold working results in more α-Zr grain rotations, which thereby causes change in the crystallographic texture [53].

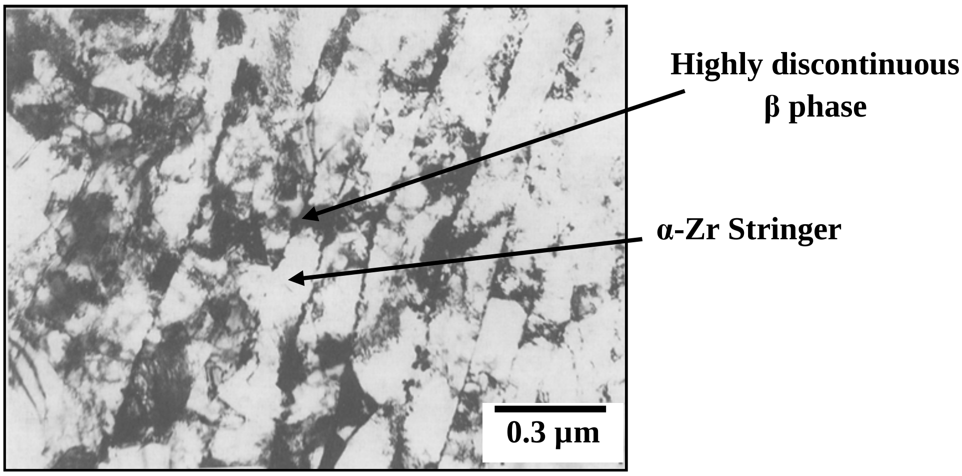

Figure 2.9: Second stage pilgered microstructure [3] of Indian pressure tube, showing the discontinous and very thin β phase (black) in between α-Zr stringers (white). At some locations, β phase can be seen to penetrate the α-Zr stringers.

VII. Autoclaving Treatment

After cold working, the tubes are finally autoclaved in steam environment. The main objective of such autoclaving treatment is to form a hard, impervious and continuous zirconium oxide (ZrO_{2-x}) layer over pressure tube surface, which provides better in-reactor corrosion resistance from the hot heavy water coolant during reactor operation. In addition, the autoclaved layer also provides superior wear resistance to the pressure tube. Autoclaving also acts as stress-relieving treatment, however has insignificant role in altering the previous pilgered microstructure [3]. In both the Indian and Canadian CWSR routes, autoclaving treatments are performed at 400°C; however for different soaking durations viz., 36 h (earlier 72 h [3]) for the Indian tubes and 24 h (earlier 72 h [47]) for the Canadian tubes.

In summary, the pressure tubes of Indian and CANDU reactors fabricated using dissimilar CWSR routes, as shown in Figure 2.5 comprise very fine dual phase microstructure of α-Zr and β phase (~20% Nb). These phases are arranged in lamellar patterns, in which relatively much finer β phase is sandwiched between the elongated α-Zr phase stringers, Figure 2.10 (a). Both the Indian and Canadian pressure tubes have close dislocation densities; 1-5×10^{14} lines per m^2 (Indian tube [3]) and 5-7×10^{14} lines per m^2 (Canadian tube [43]). The crystallographic textures of both the Indian and Canadian tubes are such that maximum basal poles are aligned towards circumferential direction. However, contrary to Indian tubes, the Canadian tubes, because of being fabricated with relatively higher extrusion ratio contains slightly more pronounced basal poles along circumferential direction.

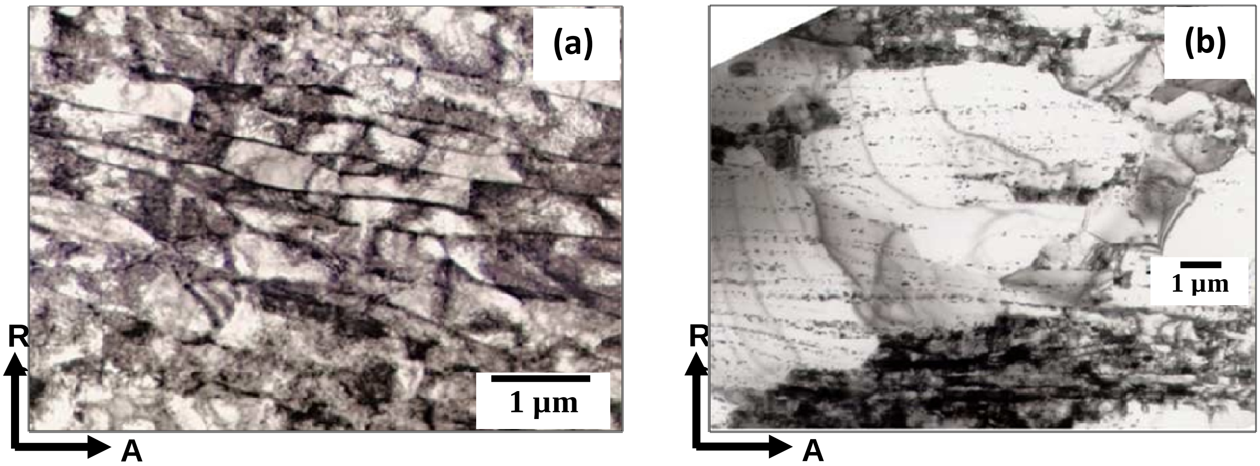

Figure 2.10: (a) Transmission electron micrograph of Zr-2.5Nb pressure tube of CANDU reactor fabricated using CWSR route [2]. (b) Transmission electron micrograph of Zr-2.5Nb pressure tube fabricated using CWA route [2]. Symbols R and A respectively represent the radial and axial directions of the pressure tube.

Table 2.3 summarizes the mechanical properties of as-fabricated Indian and Canadian Zr-2.5Nb pressure tubes, manufactured by respective CWSR routes. Under ambient condition, Indian pressure tubes exhibit superior tensile strength and ducility as compared to the Canadian pressure tubes. However, at reactor operating temperature, 300°C both these tubes have nearly comparable tensile properties. In contrast, under ambient condition, the Canadian CWSR material is tougher than Indian CWSR material. However, at 300°C both of the materials exhibit comparable toughness. Table 2.4 sumarizes the operating performances of Canadian pressure tubes fabricated using CWSR route.

Table 2.3: Mechanical properties of as-fabricated Zr-2.5Nb pressure tubes, manufactured from the Indian and Canadian CWSR routes. In this table, the data shown within parenthesis represents the mean values.

Mechanical Properties	**RT**		**300°C**	
	Indian CWSR PT	**CANDU CWSR PT**	**Indian CWSR PT**	**CANDU CWSR PT**
0.2% offset YS (MPa)	606, 565, 588 (586)	545 [43]	420, 409, 415 (414)	412 [45]
UTS (MPa)	834, 807, 844 (828)	747 [43]	569, 548, 580 (566)	550 [45]
Total Elongation (%)	17, 16, 16 (16)	13 [43]	17, 17, 21 (18)	19 [45]
Fracture Toughness (dJ/da) in MPa	204, 227, 268 (239)	350, 419 (384) [43,45]	370, 390, 396 (385)	330, 400 (365) [43,45]

Table 2.4: Operating performance of Canadian Zr-2.5Nb pressure tubes fabricated through CWSR route.

Challange	**Temperature (°C)**	**Parameter**	**Magnitude**
Effect of neutron irradiation (Neutron Fluence (>1MeV)):: 1.6×10^{24} neutrons per m^2)	25	0.2% offset Yield Strength (MPa)	-
		UTS (MPa)	-
		Total Elongation (%)	-
	300	0.2% offset Yield Strength (MPa)	702 [43]
		UTS (MPa)	756 [43]
		Total Elongation (%)	7 [43]
In reactor dimensional change (Neutron Fluence (>1MeV)): 5.3×10^{24} per m^2)	257	Longitudnal growth rate (per hour)	$1.74^{\pm0.18}\times10^{-4}$ [43]
		Transverse growth rate (per hour)	$2.89^{\pm0.15}\times10^{-4}$ [43]
Corrosion Behavior (from ASTM G 2 tests)		Weight gain (mg/dm^2)	20-27 [43]
Hydride Embrittlement	-	DHC velocity	-
		Hydride orientationangle (circumferencial to radial direction) under 280 MPa hoop stress at 302°C for 2 h soaking followed by furnace cooling	50-60° [43]

2.4.2 Cold Worked and Annealed Route

The 'Cold Worked and Annealed' (CWA) fabrication route, as shown in Figure 2.11, is currently being followed for the pressure tubes of all the RBMK 1000 MWe reactors. The initial fabrication stages of this route such as ingot prepration, breaking down of cast structure, log & billet prepration, beta quenching and hot extrusion are mostly similar to those of the CWSR fabrication routes of the Indian and Canadian pressure tubes (shown in Figure 2.5). However, these initial stages do have marginal differences with the aforementioned CWSR route such as breaking down of cast structure at relatively lower temperature (950°C), as compared to 1000°C and extrusion at relatively lower temperature (700-750°C), in contrast to at ~800°C followed in the CWSR routes. The major differences between CWA and CWSR fabrication routes arise after extrusion stage.

The extrusion stage is followed by a three stage cold working, subsequent annealing, followed by an autoclaving treatment. The first stage cold working comprises 55.5% reduction of wall thickness. This is followed by annealing treatment, performed at 580°C for 3 h, to facilitate the two succeeding cold working stages. The annealed tubes are subsequently sequencially cold worked with 39.4 and 23% wall thickness reductions to achieve final dimensions. These cold worked tubes are then further annealed at 540°C for 5 h to reduce the dislocation density.

These annealed tubes are finally autoclaved at relatively lower temperature (290°C) for relatively higher soaking duration (120 h) as compared to the CWSR routes, to form a stable oxide layer on their surfaces, so as to reduce the corrosion from the hot heavy water coolant and therefore to reduce the deutrium ingress into pressure tubes during operation.

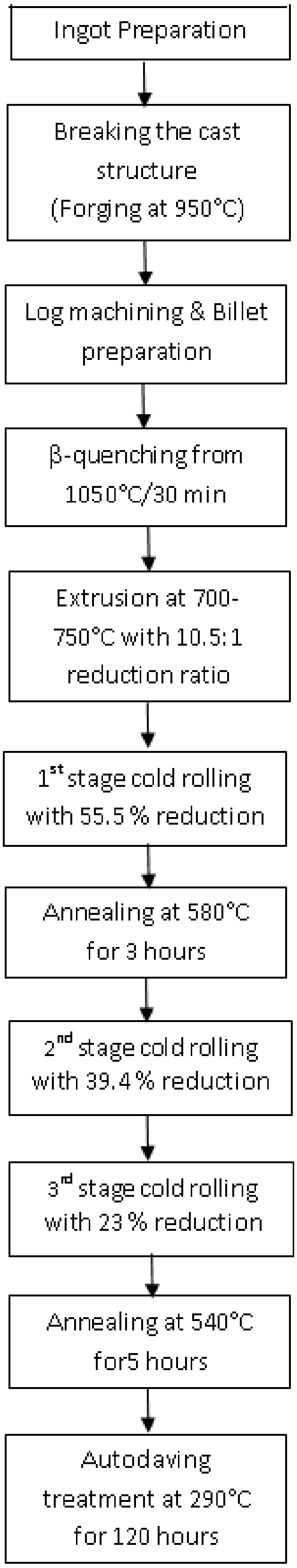

Figure 2.11: CWA route being followed by the Russians for fabrication of pressure tubes of all the RBMK 1000 MWe reactors [2].

This fabrication route is named as 'cold worked & annealed route', because in this route, the cold working is followed by an annealing treatment, prior to autoclaving. This is in contrast to the earlier discussed 'cold worked & stress relieved routes, wherein the cold working step is directly followed by autoclaving.

Coleman et al. [2] showed that the microstructure of pressure tubes fabricated using CWA route comprises a mixture of elongated (non re-crystalized) and equiaxed (re-crystalized) α-Zr grains (having diameter of ~5 µm) along with the discontinuous β-Nb precipitates within grains and along grain boundaries (Figure 2.10 (b)). The texture of CWA pressure tubes are also reportedly [2] different from the CWSR pressure tubes, such that maximum basal poles align in between the circumferencial and radial directions, and remaining along longitudnal direction. Furthermore, tubes fabricated by this route contains about three times lower dislocation density as compared to the Canadian CWSR tubes [2], which therefore reveals the effect of annealing treatment after cold working in CWA route.

2.4.3 Water Quenched & Aged Route

The third important pressure tube fabrication route is ‘Water Quenched & Aged’ (WQA) route. Fabrication stages of WQA route, as shown in Figure 2.12 (a) comprise common initial stages similar to the CWSR route such as ingot preparation, breaking down of cast structure, log & billet preparation, beta quenching and extrusion. These common initial stages are followed by the three important TMP stages, which distinguish WQA route from CWSR route. These stages are, SHT in two phase (α-Zr+β-Zr) field, followed by cold working and subsequent vacuum aging treatment. Takayam [5] showed that the pressure tubes under such heat treated condition, in contrast to CWSR condition exhibit superior performance by exhibiting lower in-reactor dimensional changes (~0.7% diametral creep in ~8.7 full power years of operation), apart from having adequate resistance against rest of the in-reactor challenges. WQA route has, therefore, become an important area of research with reference to pressure tube fabrication in recent scenario.

At present, pressure tubes fabricated using the WQA route are under operation in different PHWRs throughout the world such as; Japanese ‘Fugen’, Canadian ‘Gentilly-1’, Russian RBMK (1500 MWe) and Pakistani ‘KANUPP’, however with different Zr-2.5Nb alloy chemistries [2,4,6-11]. Furthermore, TMP parameters such as soaking temperature during SHT stage, degree of imparted cold work and soaking temperature during aging stage in the WQA routes of these pressure tubes too have differences, as described in Table 1.1, Chapter 1. These TMP stages govern the final microstructure and therefore, mechanical properties of pressure tubes fabricated using WQA route. Following section individually describes these three TMP stages of WQA route.

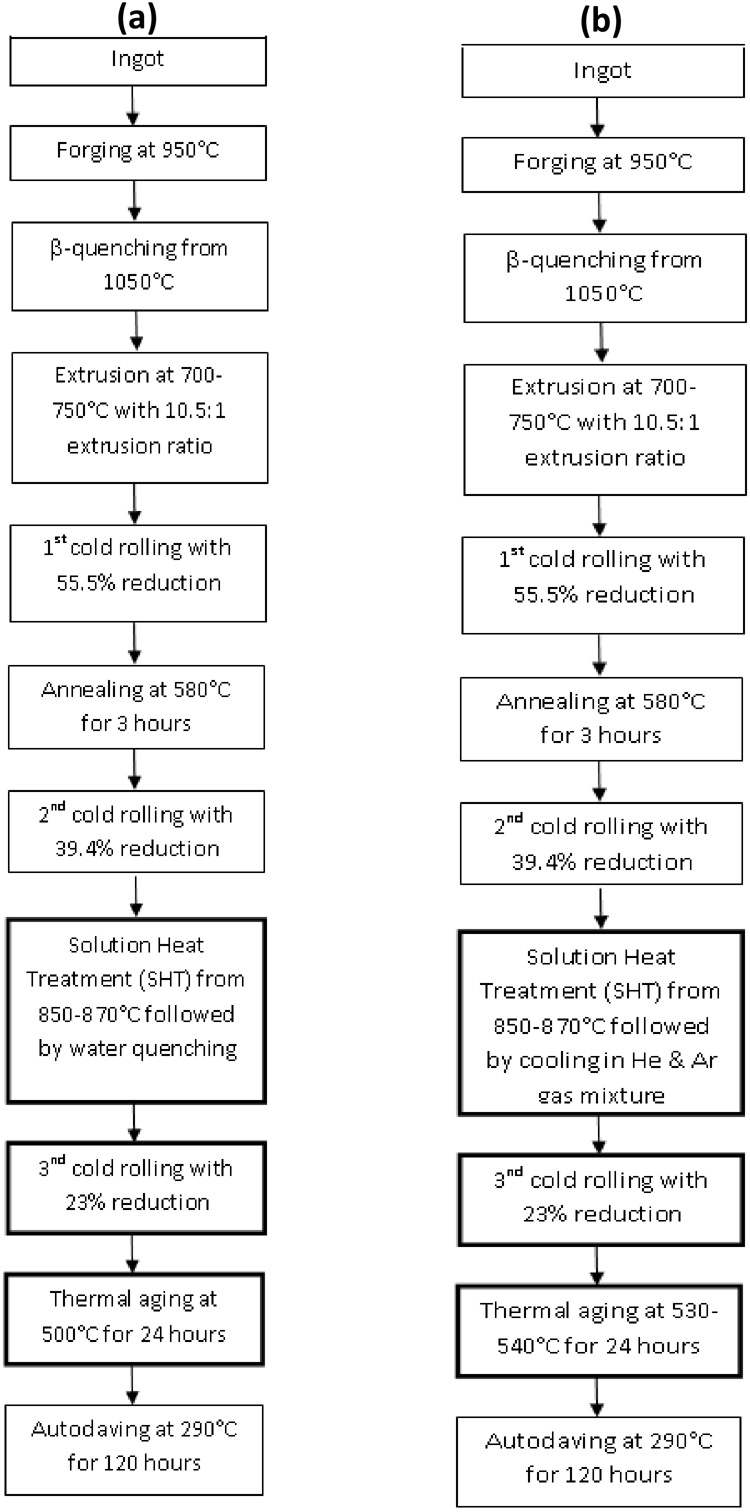

Figure 2.12: Fabrication flow sheets of (a) WQA and (b) GCA Zr-2.5Nb pressure tubes of RBMK 1500 reactors at Ignalina 1 and 2 respectively. These fabrication routes are commonly known as 'TMT-1' and 'TMT-2' respectively [2]. The highlighted TMP stages viz., SHT, cold working and aging treatment control the final microstructure and hence, the mechanical properties of fabricated pressure tubes.

I. Solution Heat Treatment (SHT)

The solution heat treatment comprises soaking of Zr-2.5Nb tubes in two phase (α-Zr+β-Nb) field at a temperature close to but less than the β-transus temperature, followed by water quenching. As discussed earlier in Section 2.3, β-transus temperature represents the temperature, above which alloy contains single equilibrium phase, β-Zr. The SHT temperature is usually kept lower than β-transus temperature, because above β-transus, existence of single phase, β-Zr in the alloy may cause significant grain coarsening, which reportedly [58,59] enhances the possibility of irradiation induced embrittlement. Quenching from SHT temperature results in diffusionless martensititc transformation of β-Zr, however the α-Zr phase remains as it is, thereby producing the two phase microstructure comprising primary α and martensite (commonly known as α') phases. Both of these phases have Hexagonal Close Packed (HCP) crystal structures. Hunt and Niessen [60] showed that the transformation of β-Zr during cooling is a function of both soaking temperature and cooling rate. As the soaking temperature decreases, a lower cooling rate is required for martensitic transformation. Additionally, as the cooling rate increases, driving force for martensitic transformation increases too.

Selections of SHT temperature and soaking duration govern the microstructural features such as phases, their volume fractions, grain sizes and chemical compositions, which could consequently influence the mechanical properties of water quenched Zr-2.5Nb alloy.

As mentioned earlier (in Section 2.4.1-V) that being α-Zr stabilizer, oxygen in Zr-Nb system has the tendency to migrate from β-Zr to α-Zr at SHT temperature [61]. Since at SHT temperature, the volume fraction of α-Zr is much lower than that of β-Zr, such oxygen partitioning may cause excessive oxygen enrichment of α-Zr phase, if a higher soaking duration is used. Additionally, oxygen in Zr-Nb system also acts as a strengthening element, which may induce embrittlement. Therefore, a longer soaking duration at SHT temperature may cause the excessive embrittlement of α-Zr phase, which might result in its failure during subsequent cold working stage. Hence, the SHT soaking duration is usually kept ≤ 30 min to avoid such excessive α-Zr embrittlement.

Opposite to oxygen, niobium acts as a β phase stabilizer element and has the tendency to migrate from α-Zr to β-Zr at SHT temperature. The kinetics for such Nb partitioning, similar to oxygen is governed by the magnitudes of soaking temperature and duration used during SHT. Higher the soaking temperature and duration, faster will be the kinetics and therefore larger will be the degree of partitioning.

Literature [2,4,6-11] shows that the pressure tubes fabricated using WQA route, currently being used in different PHWRs throughout the world have dissimilar alloy chemistries, especially among their oxygen concentrations and also in the employed SHT temperatures, as shown in Table 1.1, Chapter 1. The WQA pressure tubes of Russian's RBMK reactor contain 400-700 ppm oxygen and use SHT temperature in 850-870°C regime. In contrast, Japanese pressure tubes of 'Fugen' reactor, which contain relatively higher oxygen (900-1300 ppm) use 887°C as SHT temperature. Furthermore, pressure tubes of Canadian 'Gentilly-1' and Pakistani 'KANUPP' reactors contain similar 900-1300 ppm oxygen and use 880°C as SHT temperature.

II. Cold Working

During SHT, water quenching produces martensite, which is super saturated with Nb. Literature [62] shows that because of excessive niobium concentration, the solution heat treated Zr-2.5Nb alloy possesses low resistance to corrosion, which is one of design criteria for the pressure tubes. Therefore, in order to bring down such excessive niobium concentration, so as to improve the corrosion resistance of the solution heat treated material, vacuum aging operation is performed.

However, for extracting such excessive niobium during aging treatment, dislocation density plays an important role. Being higher energy sites, dislocations act as the nucleation sites for the fine precipitation of equilibrium β-Zr/β-Nb phase within metastable α’ phase during aging treatment. Therefore, to generate such necessary dislocation network, so as to extract Nb from α' phase, the SHT stage is followed by a cold working stage. In addition to dislocation network, the cold working treatment also ensures final dimensions to the pressure tubes.

The degree of cold work imparted in this stage is however, restricted because of the higher dislocation density, which reportedly enhances the in-reactor deformation rates of pressure tubes [54,55]. Furthermore, a higher degree of imparted cold work on the solution heat treated materials may also induce excessive embrittlement, and hence is undesirable. Therefore, selection of the optimum degree of cold work is an important concern during fabrication of such heat treated pressure tubes. The heat treated pressure tubes currently installed in different PHWRs throughout the world were fabricated employing different amount of cold working, as shown in Table 1.1, Chapter 1. For example, the pressure tubes of RBMK reactor were imparted 20-25% cold work, those of Fugen reactor follow relatively lower cold work (5-15%) and those of Gentilly-1 and KANUUP reactors ~12% cold work.

III. Vacuum Aging Treatment

The cold worked-solution heat treated pressure tubes are subsequently thermally aged in vacuum for the equilibrium precipitation of fine β phase, within the metastable α’ phase. The dislocation network generated during previous cold working stage aid the precipitation of β phase by enhancing nucleation sites.

Analogous to the earlier discussed variations in SHT temperature and degree of cold working, the aging temperatures employed for the fabrication of WQA pressure tubes are also different, as shown in Table 1.1, Chapter 1. For example, the heat treated tubes of RBMK reactor are aged at

515°C for 24 h duration, while those of Fugen, Gentilly-1 and KANUUP reactors are aged at 500°C for same 24 h duration.

After aging, similar to the earlier discussed CWSR fabrication route, the pressure tubes are finally autoclaved in steam environment to form hard & stable surface oxide layer, so as to provide better corrosion resistance from the hot heavy water coolant and therefore, to reduce the deuterium ingress into pressure tubes during reactor operation. The autoclaving treatment does not change microstructure (Figure 2.13 (a)) to a noticeable extent.

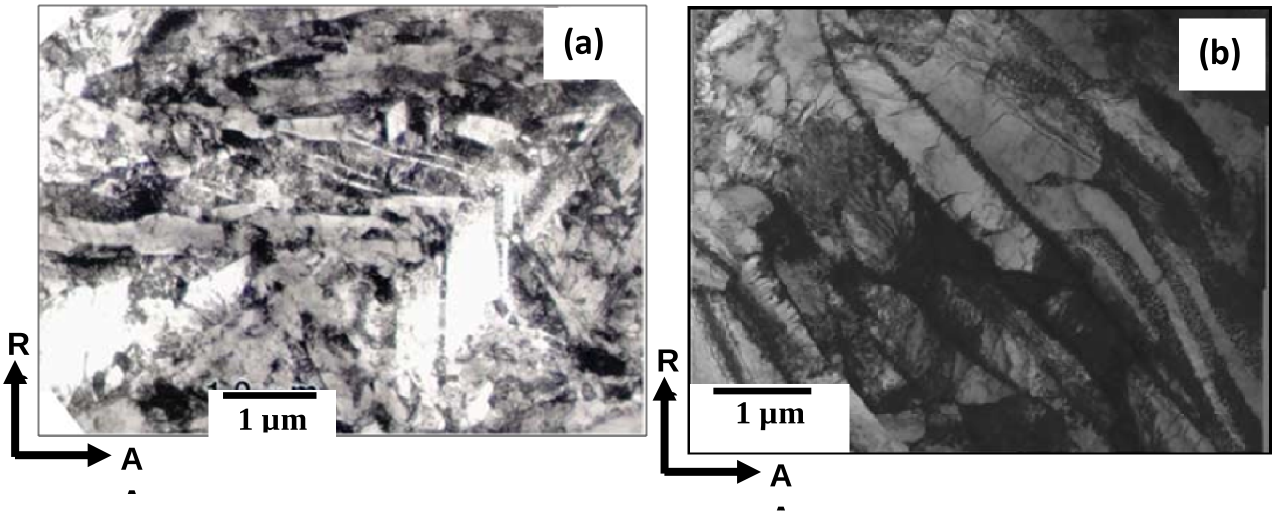

Figure 2.13: (a) Transmission electron micrograph of Zr-2.5Nb pressure tube fabricated using WQA route [2]. (b) Transmission electron micrograph of Zr-2.5Nb pressure tube fabricated using GCA route [2]. Symbols R and A respectively represent the radial and axial directions of the pressure tube.

2.4.4 Gas Cooled & Aged Route

The fourth fabrication route, which is being employed for the manufacture of pressure tubes of RBMK 1500 MWe reactors is ‘Gas Cooled & Aged’ (GCA) route. This fabrication route, as shown in Figure 2.12 (b), is mostly similar to the WQA route, except for using gas cooling (cooling in the mixture of He and Ar gasses) in place of water quenching. Also, the GCA route followed for RBMK reactor uses slightly higher aging temperature, 530-540°C, in contrast to 515 and 500°C, as followed in the WQA routes of RBMK-1000 MWe and Fugen, Gentilly-1 & KANUPP pressure tubes.

Coleman et al. [2] showed that the microstructure of GCA pressure tubes comprises widmanstratten α, α-Zr along with the β-Nb precipitates, Figure 2.13 (b). This is in contrast to the microstructure of WQA pressure tube of RBMK 1000 MWe reactors, which comprises martensitic α', primary (untransformed) α-Zr along with β-Nb precipitates. The crystallographic texture of GCA pressure tubes is reportedly [2] comparable to that of the CWSR pressure tubes. Also, the dislocation density of these GCA pressure tubes is reportedly [41] similar to that of the CWA pressure tubes.

2.5 Importance of Fracture Behavior for Pressure Tube Integrity

The structural integrity of pressure tubes has always been a prime concern for their safe operation. Fracture behavior of pressure tube material determines its resistance to crack propagation and therefore, is central to assessing the major structural integrity concerns. In addition, fracture behavior also governs the extent of stable propagation of a crack, before the achievement of unstable propagation situation. The limit for such stable crack propagation is called 'Critical Crack Length', *CCL*. For pressure tube's safe operation, *CCL* governs the safety margin for the necessary LBB situation and time available for the operator to take necessary remedial actions under coolant leaking situations. As one of the design parameters, *CCL* of a pressure tube (a function of propagation toughness, $J_{F(max)}$ parameter) must be greater than 4 to 7 times of its wall thickness, so as to prevent its catastrophic failure by ensuring LBB type of failure. A higher *CCL* provides greater safety margin to pressure tube for such LBB situations and therefore is always desirable. Therefore, for ensuring the higher operating life, pressure tube material must possess sufficient resistance against fracture (crack initiation and propagation), along with a greater *CCL* limit.

Figure 2.14 summarizes the importance of fracture behavior for structural integrity of pressure tubes.

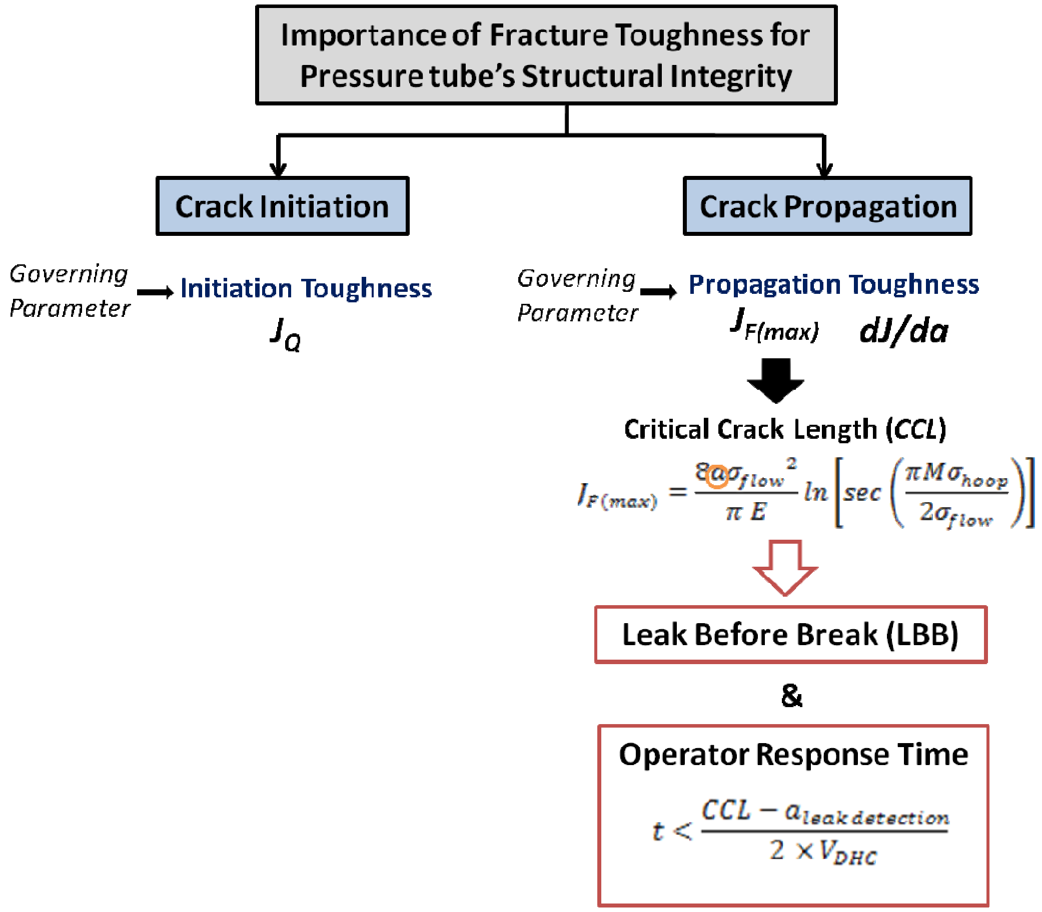

Figure 2.14: Flow chart illustrating the importance of fracture toughness for assessment of pressure tube's structural integrity.

2.6 Fracture Toughness Evaluation and Analysis Procedures

J-integral [63] is the most widely used fracture toughness parameter, which represents the complementary strain energy ahead of crack tip per unit area of crack extension. In contrast to stress intensity factor (*K* parameter) [64,65], which is valid for the brittle materials having insignificant plasticity, *J*-integral has been identified as the parameter which can be used even for the elasto-plastic materials, which are associated with high crack tip plasticity [66-68]. Additionally, because of *J*-integral, it has now become possible to characterize the fracture toughness in terms of crack tip strain energy field using the specimens having lower thickness, rather than using thicker specimens (as applicable for K_{IC} testing under plain strain condition [69]).

A number of approaches [70-77] have been proposed in the literature to quantify the J parameter for several cracked geometries. These approaches are based on different ductile crack growth (DCG) correction procedures.

ASTM E1820–11 [78], which is the one of the most widely used standards for the evaluation of fracture toughness, recommends the use of two DCG methods proposed by Ernst et al. [73] and Wallin & Laukkanen [70] for the evaluation of J parameter. The former method requires single specimen for the construction of fracture resistance (J-R) curve, and evaluation of the fracture toughness parameters. This method is referred in the standard as ‘Resistance Curve Method (RC)’. On the other hand, the methodology proposed by Wallin & Laukkanen is a multi specimen approach for determining the fracture toughness. This approach is referred in the standard as ‘Basic Test Method (BT)’. These two DCG methods are being described in the subsequent sections.

2.6.1 Resistance Curve Method

The RC method is based on the DCG correction procedure, proposed by Ernest et al. [73] in year 1981 at Westinghouse R&D centre for the evaluation of J parameter and therefore constructing the J-R curve using the single specimen. Because of the requirement of only one specimen rather than the use of multiple specimens for constructing the fracture resistance curve (as in case of BT method), the RC method is currently widely in practice.

In the RC method, apart from measuring the load and LLD, simultaneous crack extension measurement in the specimen during the test is essential. Although, there are a number of ways to quantify the crack extension during the test, the three methods are most common in practice, Unloading compliance (UC) [78,79], Potential drop (PD) [79-89] and the Normalization method [78,90-93]. In the UC method, the assessment of crack growth is made using the slope of load-unloading LLD curve. However, in PD approach, change in material's electrical resistance as a function of crack growth is measured. In the normalization procedure, the *J-R* curve is constructed using the load-LLD data and the specimen's crack lengths before and after the test. The procedure of determining the *J* parameter using RC method is being presented below.

The *J* parameter corresponding to i^{th} data point can be considered as the summation of its elastic and plastic components, as shown in Equation 2.1.

$$J_{(i)} = J_{el\,(i)} + J_{pl\,(i)} \tag{2.1}$$

The elastic component of *J* parameter corresponding to i^{th} data point (i.e., $J_{el\,(i)}$) is given by,

$$J_{el\,(i)} = \left[\frac{(1-\nu^2)K_{(i)}{}^2}{E}\right] \tag{2.2}$$

where, the stress intensity factor ($K_{(i)}$) is a function of the applied load, specimen's geometry and dimensions such as; width (W), thickness (B) and instantaneous crack length ($a_{(i)}$) and is expressed as,

$$K_{(i)} = \left[\frac{P}{\sqrt{(BB_N W)}}\right] f\left(\frac{a_i}{W}\right) \tag{2.3}$$

The function $f\left(\frac{a_i}{W}\right)$ depends on the specimen's geometry.

The DCG correction procedure for determination of plastic component of *J* parameter is represented as,

$$J_{pl\,(i)} = \left[J_{pl\,(i-1)} + \left(\frac{\eta_{pl\,(i-1)}}{b_{(i-1)}}\right)\frac{A_{pl\,(i)}-A_{pl\,(i-1)}}{B_N}\right]\left[1-\gamma_{(i-1)}\left(\frac{a_{(i)}-a_{(i-1)}}{b_{(i-1)}}\right)\right] \tag{2.4}$$

where, the incremental plastic area, represented by the term $A_{pl\,(i)} - A_{pl\,(i-1)}$ is given by Equation 2.5. The functions $\eta_{pl\,(i-1)}$ and $\gamma_{(i-1)}$, which are the functions of the specimen's dimensions i.e., remaining un-cracked ligament at (*i-1*)th data point($b_{(i-1)}$) and *W*, are represented by Equations 2.6 and 2.7 respectively.

$$A_{pl\,(i)} = A_{pl\,(i-1)} + \frac{[P_{(i)} - P_{(i-1)}][v_{pl\,(i)} - v_{pl\,(i-1)}]}{2} \tag{2.5}$$

$$\eta_{pl\,(i-1)} = 2 + \frac{0.522\, b_{(i-1)}}{W} \tag{2.6}$$

$$\gamma_{(i-1)} = 1 + 0.76\, b_{(i-1)}/W \tag{2.7}$$

The plastic components of LLD (after removing machine's effect) i.e., $v_{pl\ (i)}$ *and* $v_{pl\ (i-1)}$, can be determined by subtracting the respective elastic components *(i.e.,* $v/C_{LL(i)}$ *and* $v/C_{LL(i-1)}$*)* from the total LLD, *v* (after removing machine's effect).

Here, the term $C_{LL(i)}$, represents the instantaneous compliance of the specimen, corresponding to the crack length a_i, and for C(T) geometry is given as,

$$C_{LL(i)} = \frac{1}{EB_e}\left(\frac{W+a_i}{W-a_i}\right)^2 \left[2.1630 + 12.219\left(\frac{a_i}{W}\right) - 20.065\left(\frac{a_i}{W}\right)^2 - 0.9925\left(\frac{a_i}{W}\right)^3 + 20.609\left(\frac{a_i}{W}\right)^4 - 9.9314\left(\frac{a_i}{W}\right)^5\right] \tag{2.8}$$

where, the term B_e is the effective specimen thickness, represented using Equation 2.9.

$$B_e = B - \frac{(B-B_N)^2}{B} \tag{2.9}$$

The *J*-integral values thereby determined are finally used to construct the fracture resistance (*J-R*) curves, based on which, the fracture toughness parameters such as initiation toughness (J_Q) and propagation toughness (such as; *dJ/da*) can be determined using the standard procedure [78]. As per the recommendations of ASTM E1820–11 standard [78], in order to determine the fracture toughness parameters from *J-R* curve, the data points that are bound by limiting *J*-integral parameter, J_{limit} (expressed by Equation 2.10), and 0.15 mm & 1.5 mm exclusion lines (ELs) should be called as the region of qualified data points and subsequently selected for a two parameter power law fit (Equation 2.11). The 0.15 and 1.5 mm ELs are drawn parallel to the construction line (expressed using Equation 2.12), with the offset of 0.15 and 1.5 mm respectively. In addition to this, at least one data point must lie between 0.15 mm EL and 0.5 mm offset line and 0.5 mm offset line & 1.5 mm EL. The magnitude of *J* at the intersection of the power law fit curve with the 0.2 mm offset line (commonly known as 'Blunting Line' (BL)) represents the initiation toughness (J_Q). Figure 4.15 shows the schematic representation of the analysis procedure recommended by ASTM E1820-11 standard for the determination of fracture toughness parameters.

$$J_{limit} = \frac{b_o \sigma_Y}{7.5} \tag{2.10}$$

$$J = x(\Delta a)^y \tag{2.11}$$

$$J = 2\sigma_Y \Delta a \tag{2.12}$$

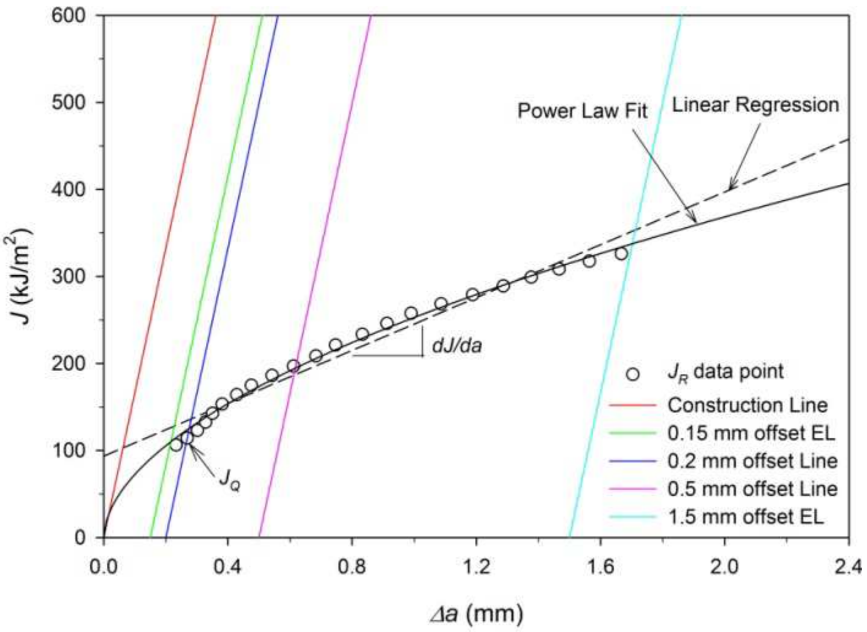

Figure 2.15: Schematic representation of the analysis procedure recommended by ASTM E1820-11 standard for the evaluation of fracture toughness parameters viz., initiation toughness (J_Q) and propagation toughness (*dJ/da*).

2.6.2 Basic Test Method

Basic test (BT) method is another DCG procedure recommended by ASTM E1820-11 standard for the evaluation of *J* parameter. This method is based on the DCG correction procedure proposed by Wallin & Laukkanen in year 2004 at Technical Research Centre of Finland (VTT) to quantify the *J* parameter and hence constructing the *J-R* curve using multiple specimens [70]. In order to construct *J-R* curve, a number of specimens, which are exactly similar in geometry and size are required to be individually tested for different crack growth levels. Test raw data obtained from each specimen, finally results for the creation of one data point on the *J-R* curve. The amount of crack growth occurring during the test in the individual specimen is monitored by physically marking of the crack advancement. Heat tinting and fatigue post cracking are the two most commonly used methods to physically mark this crack growth region. In the former method, the tested specimen is heated and soaked to form oxide layer on the fracture surface, which correspondingly results for differentiable color contrast between fractured and non fractured regions. However, in the later method, crack growth during the test is determined by allowing further crack growth using fatigue cycling to artificially create physically differentiable fractured and fatigue post cracked regions. After physically marking the crack growth region, specimens are required to be torn apart into two halves, subsequently the marked region is optically measured and the crack growth is determined using the standard ‘nine point average’ method [78].

BT method involves two major stages for determination of *J* parameter, which is subsequently used to construct the *J-R* curve. These stages are being discussed as follows:

Stage I (J determination without considering crack growth)

In the first stage of BT method, *J* parameters from the individual specimens are evaluated on the basis of the initial crack length, a_o (assuming that there was no crack growth taking place during the test). Subsequently, in the second stage, such *J* values are corrected for their respective actual crack growth levels using a DCG correction procedure [70]. The *J* parameter based on initial crack length (i.e., J_o) can be considered as the summation of its elastic and plastic components;

$$J_O = J_{elo} + J_{plo} \tag{2.13}$$

where, the elastic component of *J* [64] is given by Equation 2.14.

$$J_{elo} = \left[\frac{(1-\upsilon^2)K_o{}^2}{E}\right] \tag{2.14}$$

The term K_o, represents the stress intensity factor based on the initial crack length and is given by Equation 2.15.

$$K_o = \left[\frac{P}{\sqrt{(BB_NW)}}\right] f\left(\frac{a_0}{W}\right) \tag{2.15}$$

The term $f(a_o/W)$ in Equation 2.15 is a function of specimen geometry and size, such as initial crack length (a_o), specimen width (W) and specimen thickness (B).

The plastic component of *J*-integral [70,94,95] on the basis of initial crack length (J_{plo}) is given as,

$$J_{Plo} = \frac{\eta_{pl}A_P}{B_Nb_0} \tag{2.16}$$

where, the term A_P represents the area under load vs. plastic load line displacement curve and is evaluated by assuming the unloading slope equivalent to that of initial loading slope i.e., without considering the crack growth (as shown in Figure 2.16). B_N, which represents the effective thickness of the specimen after side grooving, can be considered equivalent to the specimen thickness (B), if no side grooving is provided in the specimen.

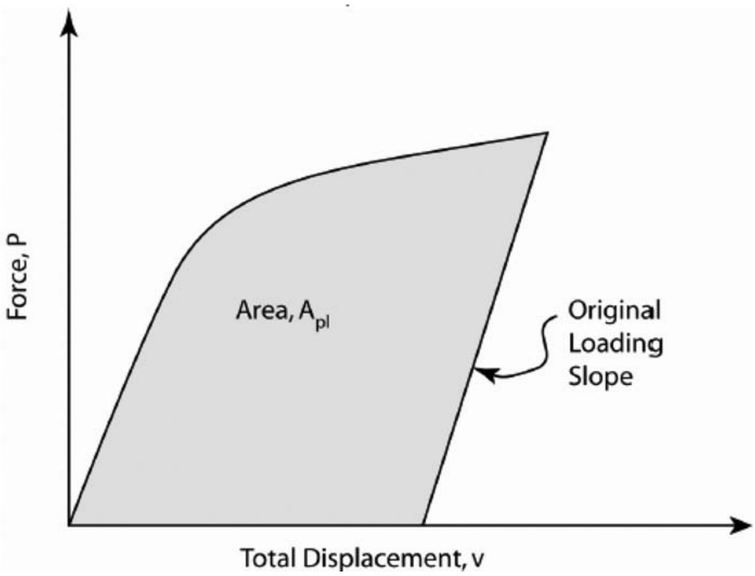

Figure 2.16: Plastic area under load vs. load line displacement plot used for the calculation of the plastic component of *J*-integral, J_{pl} in BT method [78].

The term η_{pl} represents the plastic eta factor, and is a function of specimen's geometry and its dimensions. This can be determined for the C(T) specimen geometry using Equation 2.17 [96].

$$\eta_{pl} = 2 + 0.522 \left[\frac{b_0}{W}\right] \tag{2.17}$$

Stage II (Crack Growth Correction)

The *J* parameters derived from the individual specimens, which were determined in the first stage on the basis of initial crack length, are required to be corrected for their respective actual crack growth levels in the second stage. Initially, these *J* parameters are corrected for the crack growth as [70],

$$J = J_{elo} + \frac{J_{plo}}{1+\left(\frac{\alpha-0.5}{\alpha+0.5}\right)\frac{\Delta a}{b_o}} \tag{2.18}$$

where, parameter α, which is a function of the specimen geometry is taken as 1 for single edge bend, SE(B) specimen and 0.9 for C(T) & disc shape compact tension DC(T) specimens.

The *J* parameters, thereby determined, are required to be fitted using power law equation (Equation 2.19). For this regression analysis, only the data points, which satisfy $\Delta a/b_o \geq 0.05$

condition are considered. The power coefficient, obtained from this regression analysis, is subsequently used in the final crack growth correction (as shown by Equation 2.20) [70].

$$J = J_{1mm} \Delta a^{m} \tag{2.19}$$

$$J = J_{elo} + \frac{J_{plo}}{1+\left(\frac{\alpha-m}{\alpha+m}\right)\frac{\Delta a}{b_o}} \tag{2.20}$$

The *J* parameters, therefore determined using the aforementioned BT methodology are finally used to construct the fracture resistance *J-R* curves, based on which, the fracture toughness parameters such as, initiation toughness (J_Q) and the propagation toughness ($J_{F(max)}$ and dJ/da) can be determined following the standard procedure recommended by the ASTM E1820–11standard as discussed earlier [78].

2.6.3 Fracture Toughness Evaluation as per ISO Standard

International Organization for Standardization (ISO) 12135:2002 [97,98] is another widely used standard procedure for the evaluation of fracture toughness of metallic materials. The ASTM E1820-11 and ISO 12135:2002 standard procedures are not only based on different ductile crack growth (DCG) correction methodologies to quantify the *J* integral parameter, but also differ in the way of analysis of the fracture resistance, *J-R* curve for the evaluation of fracture toughness parameters. For the sake of continuity, brief description of DCG method and *J-R* curve analysis procedure recommended by the ISO 12135:2002 standard is discussed as under.

In contrast to the ASTM E1820-11standard, the ISO 12135:2002 standard [97,98] recommends the use of another DCG correction procedure to quantify the *J* parameter. As per this standard, the expression of *J* parameter for C(T) specimens is given by Equation 2.21.

$$J = \left[\frac{(1-\nu^{2})K_o{}^{2}}{E}\right] + \left[\left(\frac{\eta_{pl}A_{pl}}{B_N(W-a_o)}\right)\left(1-\frac{(0.75\,\eta_{pl}-1)\Delta a}{W-a_o}\right)\right] \tag{2.21}$$

The first term in Equation 2.21 represents the elastic component of J integral based on the initial crack length, a_o (assuming that there was no crack extension taking place during the test). However, the second term represents the crack growth corrected plastic component of J integral. In Equation 4.21, the stress intensity factor based on initial crack length (i.e., K_o) can be determined in the manner similar to as discussed earlier for ASTM procedure (using Equation 2.3), keeping the initial crack length, a_o in place of instantaneous crack length, a_i.

In order to determine the fracture toughness parameters as per ISO 12135:2002 standard, the J-R curve is constructed and subsequently analyzed using a different procedure from that discussed earlier for the ASTM standard. In contrast to the ASTM E1820-11 standard, the valid data points of J-R curve as per ISO standard are bound by the 0.1 mm and Δa_{max} ELs (drawn on the basis of the construction line, defined by Equation 2.22). The term Δa_{max} represents the maximum crack growth capacity of the specimen and is expressed as Equation 2.23. In addition to this, at least six data points must form the J-R curve, and minimum one data point must reside within each of the four equal crack sectors between 0.1 mm and Δa_{max} regime. Subsequently, these valid data points are fitted using a three parameter power law (Equation 2.24) rather than using a two parameter power law, Equation 2.13 as discussed earlier for ASTM standard. Similar to the ASTM standard, the initiation toughness (J_Q) as per the ISO standard is defined by the magnitude of J-integral at the intersection of power law fit curve with 0.2 mm BL. Figure 2.17 shows the schematic representation of the analysis procedures, recommended by ASTM E1820-11 and ISO 12135:2002 standards for the determination of fracture toughness parameters.

$$J = 3.75\sigma_{UTS}\Delta a \tag{2.22}$$

$$\Delta a_{max} = 0.1b_o \tag{2.23}$$

$$J = A + x(\Delta a)^y \tag{2.24}$$

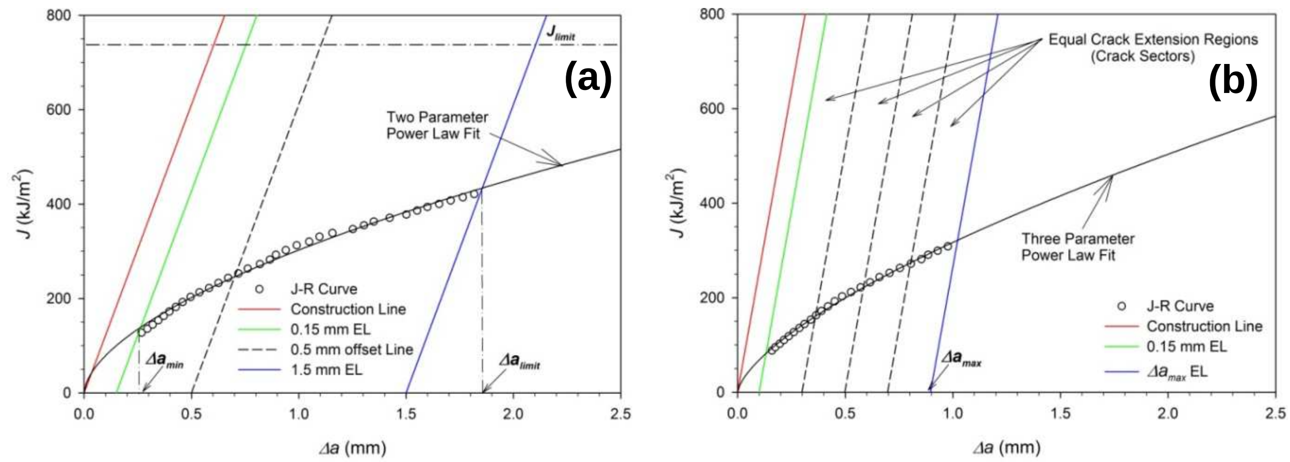

Figure 2.17: Schematic representation of the analysis procedures of fracture resistance *J-R* curves recommended by (a) ASTM and (b) ISO standards for the evaluation of fracture toughness parameters.

2.7 Limitation of Literature

As discussed, with reference to pressure tube fabrication, the WQA route has become an important area of research in recent senario. Literature have shown that WQA routes being followed throughout the world have differences among their TMP parameters associated with SHT, subsequent cold working and vacuum aging stages (as illustrated in Table 1.1, Chapter-1). These TMP stages play an important role in governing the microstructure and fracture behavior of as-fabricated pressure tube material. Therefore, for utilization of WQA fabrication route for future applications, an optimum selection of TMP parameters associated with these TMP stages is important, so as to ensure favorable fracture behavior of as-fabricated material. Furthermore, this selection is also important for utilizing WQA route for pressure tubes of the modern reactors such as, AHWR. The opern literature, however, does not provide sufficient information regarding the influence of these TMP parameters on fracture behavior of Zr-2.5Nb alloy, so as to ensure an optimum fracture behavior of as-fabricated WQA material.

Therefore, present work is focused to study the influence of TMP parameters such as SHT temperature & soaking duration, degree of subsequent cold working and aging temperature on

WQA Zr-2.5Nb alloy. The TMP parameters for this study were chosen by working out a comprehensive matrix of the TMP parameters used for the fabrication of heat-treated pressure tubes.

CHAPTER 3

EXPERIMENTAL PROCEDURES

This chapter describes various experimental procedures, followed during the course of work. The chapter begins with introducing as-received Zr-2.5Nb pressure tube material, to which different thermo-mechanical treatments were imparted. Subsequently, methodology of assessing β-transus temperature of this material and precautions undertaken are described, which subsequently formed basis for selecting the SHT temperatures for this study. Procedures of material procurement under the three TMP stages viz., SHT, cold working and vacuum aging are subsequently described. The details of microstructural examinations such as metallography using optical microscopy and TEM examinations, crystallographic texture using X-ray diffraction, Nb partitioning between primary α and α' phases through EPMA and Nb measurement within fine β precipitates formed in aged materials through carbon extraction replica are individually described in detail. Subsequently, procedures of mechanical testing including tensile testing, micro-hardness and fracture toughness evaluations along with the fractographic examinations using SEM are individually described.

3.1 Preliminary

A full length CWSR Zr-2.5Nb alloy quadruple melted pressure tube of 540 MWe IPHWR having length of ~ 6 m, wall thickness of ~ 4.3 mm and internal diameter of 103 mm, was received from 'Nuclear Power Corporation of India Ltd.' (NPCIL) for this study. The chemical composition of this pressure tube material is listed in Table 3.1. The tube material contains on an average 2.61 wt. % niobium as the major alloying element, and 1036 ppm oxygen as minor alloying element. The tube was manufactured from quadruple melted ingot, as a result the concentrations of impurity elements such as; hydrogen (3 ppm), chlorine (<0.5 ppm) and phosphorous (<10 ppm) were considerably lower within this material.

Table 3.1: Chemical composition of as-received Zr-2.5Nb pressure tube, used for present study.

Chemical Element	Symbol	Amount	Chemical Element	Symbol	Amount
Niobium	Nb	2.57-2.65 wt.%	Copper	Cu	< 30 ppm
Oxygen	O	990-1082 ppm	Boron	B	< 0.5 ppm
Hafnium	Hf	< 50 ppm	Cadmium	Cd	< 0.5 ppm
Hydrogen	H	2-4 ppm	Lead	Pb	< 25 ppm
Chlorine	Cl	< 0.5 ppm	Magnesium	Mg	< 20 ppm
Nitrogen	N	34-39 ppm	Phosphorous	P	< 10 ppm
Iron	Fe	680-725 ppm	Titanium	Ti	< 35 ppm
Carbon	C	73-593 ppm	Tungsten	W	< 25 ppm
Aluminium	Al	51-75 ppm	Uranium	U	< 1 ppm
Nickel	Ni	< 70 ppm	Vanadium	V	< 10 ppm
Tin	Sn	25-28 ppm	Chromium	Cr	120-125 ppm
Manganese	Mn	6-7 ppm	Molybdenum	Mo	< 25 ppm
Silicon	Si	< 87 ppm	Zirconium	Zr	Remaining

3.2 Establishment of β-transus Temperature

In Zr-Nb system, the term 'β-transus' is used to specify the temperature of transformation of dual phase (α-Zr+β-Zr) to single phase β-Zr. The β-transus temperature, therefore represents temperature at and above which, material contains only β-Zr phase. For binary Zr-2.5Nb alloy, the β-transus temperature is 844°C (see the phase diagram in Figure 2.4 [42]). For the heat treated fabrication routes of Zr-2.5Nb pressure tubes (both WQA and GCA routes), the β-transus temperature is an important parameter, especially during the SHT stage, wherein the soaking temperature is recommended to be close to but less than the β-transus temperature [58,59]. This is because, above β-transus temperature, existence of only β-Zr phase enhances the possibility of significant grain coarsening, which can have an adverse effect on ductility of the resulting material and also enhances the possibility of irradiation growth [58,59].

As discussed in Section 2.3 (Chapter 2), the β-transus temperature is a strong function of oxygen concentration present in the alloy. Oxygen in Zr-Nb system acts as α-Zr stabilizer element, which therefore, increases the β-transus temperature of alloy. This oxygen concentration- β-transus temperature dependence follows a thumb rule, as per which, within an oxygen concentration of 1000 wt. ppm, every increase by 100 wt. ppm results in corresponding 7°C rise in the β-transus temperature [58]. In contrary to oxygen, iron being a β-Zr stabilizer element, reduces the β-transus temperature of the alloy. Other impurity elements could also have influence on the β-transus temperature of the alloy. Therefore, it was required to determine the actual β-transus temperature of as-received pressure tube material, to decide the soaking temperatures of SHT stage for the present study.

3.2.1 Methodology

β-transus temperature of the as-received pressure tube material was experimentally determined by water quenching the small coupons of this material from the hypothetical temperature, 910°C and observing the resulting primary α phase volume fraction. For this, a 12.5 mm wide ring was cut from the middle section of as-received pressure tube, Figure 3.1 (a). Six numbers of small samples were subsequently cut from this ring and later on cleaned ultrasonically using acetone in order to remove any lubricant or foreign particle present on its surface, Figure 3.1 (b). In order to avoid oxidation during the heat treatment, these samples were sealed inside the quartz capsules filled with helium gas at a pressure of 75 torr, Figure 3.1 (c).

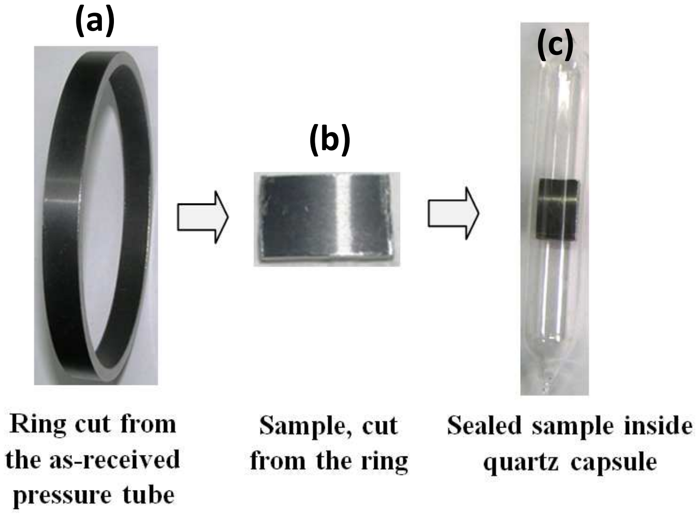

Figure 3.1: Sample preparation stages for the β-transus temperature assessment of as-received pressure tube material.

After sealing, sample was soaked at 910°C for 15 min duration in a resistance heating furnace followed by water quenching. The sample temperature was controlled using a standard K-type thermocouple (Chromel-Alumel) tied on the sealed sample using Nichrome wire. The thermocouple tip was kept close to the sample, so as to obtain accurate sample temperature. Before heat treatment, furnace was allowed to attain 910°C, after which the sample was loaded. The sample was then allowed to attain the desired temperature, after which the soaking time was counted. During water quenching, quartz capsule was broken immediately after immersing the capsule in water. During heat treatment, calibrated multimeter and K-type thermocouples were used for sample temperature measurement. For measuring sample temperature, milivolt reading at the cold junction of K-type thermocouple was measured using multimeter and corresponding temperature was determined from the milivolt-temperature chart of K-type thermocouple. In order to add cold junction compensation correction, temperature at the cold junction was added to this temperature, so as to obtain the actual sample temperature.

Metallographic examination of the heat treated material was performed using optical microscopy. For this, the heat treated sample was mounted in a steel ring using cold setting resin. After solidification, sample was removed from the ring and subsequently sequentially manually polished using abrasive silicon carbide papers of grit sizes 150, 320, 600 and 800. The polished sample was subsequently swab etched using a solution of 10% hydrofluoric acid (HF), 45% nitric acid (HNO_3) and 45% water (H_2O). After etching, sample microstructure was examined using ‘ZEISS’ (model-"Axiovert 40 MAT") optical microscope. The area (volume) fractions of the resulting phases were determined through image analysis performed using the commercial ‘Image J’ software.

Optical micrograph of the heat treated sample, as shown in Figure 3.2, showed minor traces of primary α (~ 1%) phase along with the martensitic α’ phase. Such a low volume fraction of primary α phase suggested that the β-transus temperature of as-received pressure tube material is very close to 910°C. Therefore, this experiment nearly validates the hypothetical β-transus temperature as predicted by the thumb rule.

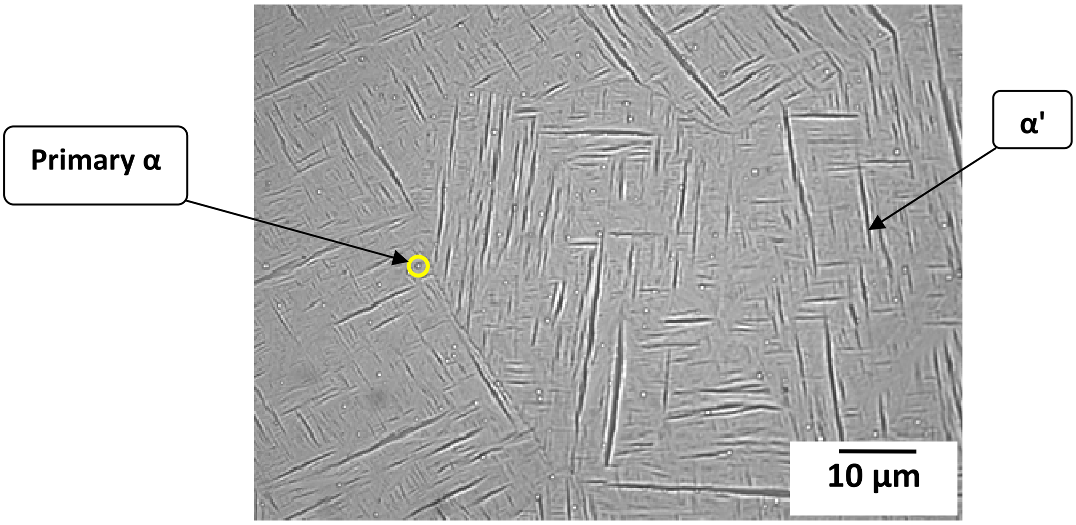

Figure 3.2: Optical micrograph of as-received pressure tube material after water quenching from 910°C for 15 min soaking duration. The micrograph shows minor traces of primary α phase along with the matrix of martensitic α' phase.

3.3 Trial Heat Treatments and Selection of TMP Parameters

As discussed in Chapter 1 (Section 1.2), the WQA pressure tubes presently being used in different PHWRs throughout the world have variability in their TMP parameters and also in their alloy chemistries. The SHT temperatures used for WQA tubes range between 850-890°C, degree of cold working is limited to 23% and aging temperatures are in 500-540°C range. The selections of TMP parameters for this study were therefore done by taking into consideration the parameters used for the manufacturing of heat treated tubes by various manufacturers.

The β-transus temperature of as-received pressure tube material (close to 910°C), as established both experimentally and theoretically [99], formed the basis for selecting actual SHT temperatures, for the present study. Three SHT temperatures viz., 850°C, 870°C and 890°C were subsequently selected for performing the trial heat treatments on the as-received pressure tube material. The objective of these trial heat treatments was to finalize the three soaking temperatures to be used during the actual SHT. For this, a 10 cm long spool was cut from the as-received pressure tube using ‘ITL KASTO’ (model no.- IT 300PH) band saw. This spool was subsequently axially slit at 120° angle to form three curved plates. These curved plates were then flattened using warm rolling at 400°C in a two high rolling mill. For flattening, the warm rolling operation was selected, since it results in lesser surface unevenness on the rolled material as compared to the cold rolling operation. Additionally, the warm rolling operation, in contrast to cold rolling, also requires relatively lower deformation force.

The three flattened plates were later on individually solution heat treated by soaking at $855^{\pm2}$, $870^{\pm2}$ and $892^{\pm2}$°C for 15 min duration in a neutral salt bath furnace followed by water quenching. Before individual heat treatments, the furnace was allowed to attain the desired temperature. Temperature control of the furnace was within ±2°C from the desired value. After attaining the desired temperature, furnace was switched off and the individual plates, tied by the K-type thermocouples were inserted inside the hot salt bath, so as to avoid any electrical shock. Thereafter, the furnace was re-switched on. The time interval for which the furnace was switched off was <10 seconds. Individual plate was then allowed to attain the desired temperature, after which soaking time was counted. After soaking, plates were immediately dipped in water for quenching. The measurement of temperature using K-type thermocouples was done in similar manner, as discussed in the previous Section 3.2.2.

After heat treatment, metallographic examinations of the solution heat treated plates was performed using optical microscopy. For this, small coupons were cut from the individual plates and prepared following mounting, polishing and etching in similar manner as discussed in Section-3.2.2. Microstructures of these three heat treated materials were subsequently examined in ‘ZEISS’ (model-"Axiovert 40 MAT") optical microscope. Figure 3.3 shows the optical microstructures of the three solution heat treated materials comprising primary α and α’ phases, having decreasing primary α volume fraction with increasing soaking temperatures. Corresponding to respective $855^{\pm2}$, $870^{\pm2}$ and $892^{\pm2}$°C soaking temperatures (average values), the measured primary α volume fractions were 38, 20.2 and 6%. Considering such variation in primary α volume fractions, three SHT temperatures viz., 850, 870 and 890°C were selected for performing the actual SHTs for this study.

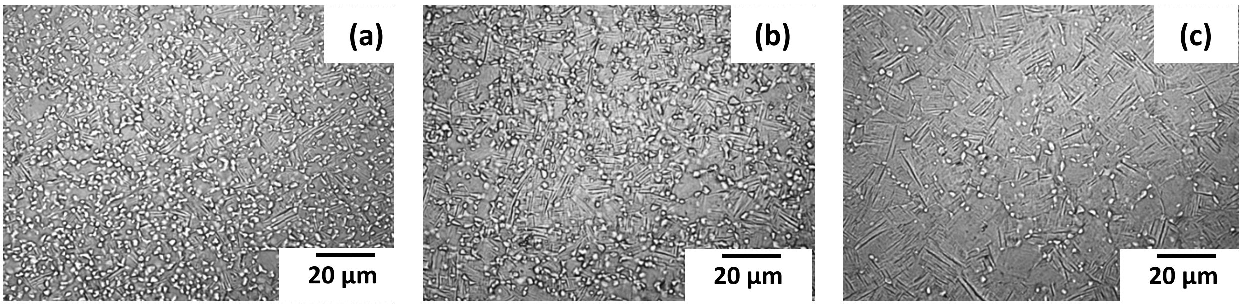

Figure 3.3: Optical microstructures of Zr-2.5Nb alloy under three preliminary trial solution heat treated conditions. Figures (a), (b) and (c) show the microstructures of materials soaked at $855^{\pm2}$, $870^{\pm2}$ and $892^{\pm2°}$C (average values), respectively for 15 min duration followed by water quenching.

As discussed in Chapter 2 (Section 2.4.1-IV) that oxygen being α-Zr phase stabilizer element, has tendency to migrate from β-Zr phase to α-Zr phase at the SHT temperatures. Oxygen in Zr-Nb system, also acts as a strengthening element, which simultaneously induces embrittlement. At the SHT temperature, since volume fraction of β-Zr phase is far higher than that of α-Zr phase, such oxygen segregation could result in significant embrittlement of α-Zr phase, depending on the soaking duration used. As the soaking duration at a particular SHT temperature increases, the amount of oxygen partitioned increases too, thereby resulting in the greater embrittlement of α-Zr phase [12]. Therefore, considering this, a maximum soaking for 30 min duration apart from 15 min was planned to be used during SHTs, for this study.

In order to study the influence of degree of cold working on solution heat treated materials, two degrees of cold working viz., 10 and 20% were planned to be imparted on the solution heat treated materials. The cold working was limited to 20%, since a further higher cold work (> 20%) could result in cracking of the solution heat treated material.

To study the influence of aging temperature on the cold worked-solution heat treated Zr-2.5Nb alloy, aging was planned to be performed at two soaking temperatures, 500 and 540°C for 24 h under vacuum followed by furnace cooling, so as to examine the influence of β-Zr and β-Nb precipitations [9].

3.4 Test Matrix Formulation

The three SHT temperatures (850, 870 and 890°C), with two soaking durations (15 and 30 min), followed by two degrees of cold working (10 and 20%), and subsequent aging at two soaking temperatures (500 and 540°C) for 24 h duration yielded 24 number of variable TMP conditions (as discussed in Chapter 1). Under each of these 24 TMP conditions, fracture behavior was planned to be examined at ambient and 300°C after each sub-stage (i.e., SHT/CW/Aging), to study the evolution of fracture behavior in these sub-stages. Table 3.2 shows the material designations followed in this work to represent 24 conditions along with individual sub-stages, for examining fracture behavior of Zr-2.5Nb alloy.

Table 3.2: Material designations used in the present study

Thermo-mechanical Processing Parameters				
S. No.	**Solution Heat Treatment**	**Cold Working Ratio**	**Vacuum Aging Treatment**	**Condition Code**
1	**850°C, 15Min**	**10%**	**500°C, 24 h**	
1.1	850°C, 15Min	-	-	A1
1.2	850°C, 15Min	10%	-	A1B1
1.3	850°C, 15Min	10%	500°C, 24 h	A1B1C1
2	**850°C, 15Min**	**20%**	**500°C, 24 h**	
2.2	850°C, 15Min	20%	-	A1B2
2.3	850°C, 15Min	20%	500°C, 24 h	A1B2C1
3	**850°C, 15Min**	**10%**	**540°C, 24 h**	
3.3	850°C, 15Min	10%	540°C, 24 h	A1B1C2
4	**850°C, 15Min**	**20%**	**540°C, 24 h**	
4.3	850°C, 15Min	20%	540°C, 24 h	A1B2C2
5	**870°C, 15Min**	**10%**	**500°C, 24 h**	
5.1	870°C, 15Min	-	-	A2
5.2	870°C, 15Min	10%	-	A2B1
5.3	870°C, 15Min	10%	500°C, 24 h	A2B1C1
6	**870°C, 15Min**	**20%**	**500°C, 24 h**	
6.2	870°C, 15Min	20%	-	A2B2
6.3	870°C, 15Min	20%	500°C, 24 h	A2B2C1
7	**870°C, 15Min**	**10%**	**540°C, 24 h**	
7.3	870°C, 15Min	10%	540°C, 24 h	A2B1C2
8	**870°C, 15Min**	**20%**	**540°C, 24 h**	
8.3	870°C, 15Min	20%	540°C, 24 h	A2B2C2
9	**890°C, 15Min**	**10%**	**500°C, 24 h**	
9.1	890°C, 15Min	-	-	A3
9.2	890°C, 15Min	10%	-	A3B1
9.3	890°C, 15Min	10%	500°C, 24 h	A3B1C1
10	**890°C, 15Min**	**20%**	**500°C, 24 h**	
10.2	890°C, 15Min	20%	-	A3B2
10.3	890°C, 15Min	20%	500°C, 24 h	A3B2C1
11	**890°C, 15Min**	**10%**	**540°C, 24 h**	
11.3	890°C, 15Min	10%	540°C, 24 h	A3B1C2
12	**890°C, 15Min**	**20%**	**540°C, 24 h**	
12.3	890°C, 15Min	20%	540°C, 24 h	A3B2C1

Thermo-mechanical Processing Parameters				
S. No.	**Solution Heat Treatment**	**Cold Working Ratio**	**Vacuum Aging Treatment**	**Condition Code**
13	**850°C, 30Min**	**10%**	**500°C, 24 h**	
13.1	850°C, 30Min	-	-	A4
13.2	850°C, 30Min	10%	-	A4B1
13.3	850°C, 30Min	10%	500°C, 24 h	A4B1C1
14	**850°C, 30Min**	**20%**	**500°C, 24 h**	
14.2	850°C, 30Min	20%	-	A4B2
14.3	850°C, 30Min	20%	500°C, 24 h	A4B2C1
15	**850°C, 30Min**	**10%**	**540°C, 24 h**	
15.3	850°C, 30Min	10%	540°C, 24 h	A4B1C2
16	**850°C, 30Min**	**20%**	**540°C, 24 h**	
16.3	850°C, 30Min	20%	540°C, 24 h	A4B2C2
17	**870°C, 30Min**	**10%**	**500°C, 24 h**	
17.1	870°C, 30Min	-	-	A5
17.2	870°C, 30Min	10%	-	A5B1
17.3	870°C, 30Min	10%	500°C, 24 h	A5B1C1
18	**870°C, 30Min**	**20%**	**500°C, 24 h**	
18.2	870°C, 30Min	20%	-	A5B2
18.3	870°C, 30Min	20%	500°C, 24 h	A5B2C1
19	**870°C, 30Min**	**10%**	**540°C, 24 h**	
19.3	870°C, 30Min	10%	540°C, 24 h	A5B1C2
20	**870°C, 30Min**	**20%**	**540°C, 24 h**	
20.3	870°C, 30Min	20%	540°C, 24 h	A5B2C2
21	**890°C, 30Min**	**10%**	**500°C, 24 h**	
21.1	890°C, 30Min	-	-	A6
21.2	890°C, 30Min	10%	-	A6B1
21.3	890°C, 30Min	10%	500°C, 24 h	A6B1C1
22	**890°C, 30Min**	**20%**	**500°C, 24 h**	
22.2	890°C, 30Min	20%	-	A6B2
22.3	890°C, 30Min	20%	500°C, 24 h	A6B2C1
23	**890°C, 30Min**	**10%**	**540°C, 24 h**	
23.3	890°C, 30Min	10%	540°C, 24 h	A6B1C2
24	**890°C, 30Min**	**20%**	**540°C, 24 h**	
24.3	890°C, 30Min	20%	540°C, 24 h	A6B2C1

3.5 Material Preparation and Thermo-mechanical Treatments

In order to study the fracture behavior of Zr-2.5Nb alloy under different thermo-mechanical conditions, a total sixteen number of spools (twelve having 18 cm length and four having 40 cm length) were cut from the as-received pressure tube using ‘ITL KASTO’ (model no.-IT300PH) band saw. The individual tube spools were subsequently axially slit at 120° angle into three curved plates. These axially slit sections were later on flattened using warm rolling at 400°C.

3.5.1 Solution Heat Treatment

After flattening, Zr-2.5Nb alloy plates were individually solution heat treated in two phase regime (α-Zr + β-Zr) at $850^{\pm2}$, $870^{\pm2}$ and $890^{\pm2}$°C (average values) for two soaking durations, 15 and 30 min in the salt bath furnace followed by water quenching. Table 3.3 shows the heat treatment matrix of Zr-2.5Nb alloy plates. The heat treatment procedure and precautions undertaken were similar to as followed during the trial heat treatments (discussed in Section 3.3). After soaking in salt bath, plates were immediately dipped in water for quenching.

Table 3.3: Details of Zr-2.5Nb alloy plates subjected to solution heat treatment in this work.

SHT Temperature (°C)	**Soaking Time (Min)**	**Number of plates**
850	15	7
	30	7
870	15	7
	30	7
890	15	7
	30	7
Total number of plates solution heat treated		**42**

3.5.2 Cold Rolling

Out of 42 number of solution heat treated plates, 36 plates were subsequently cold rolled with either of 10 or 20% thickness reduction ratios in a ‘KARL DOELITZSCH’ two high rolling mill. The details of cold rolled-solution heat treated Zr-2.5Nb alloy plates are listed in Table 3.4. Rolling direction was along the plate length (i.e., along the length of as-received pressure tube), as shown in Figure 3.4. Rolling operation was performed in multiple passes with ~2% thickness reduction in each pass, so as to minimize the possibility of plate failure during rolling. Rolling resulted in the average plate elongation by ~ 22 and 34% corresponding to respective 10 and 20% thickness reductions, with minor average alteration in their widths (by < 2%). For a given degree of cold work, three plates were cold rolled, one for the cold work stage characterization, and rest two for the characterization after subsequent aging treatments at 500 and 540°C.

Table 3.4: Test matrix showing different cold work-solution heat treatment conditions, considered in the present study.

S. No	**Condition**	**SHT Parameters**		**Degree of cold work (% thickness reduction)**	**Number of plates rolled**
		Soaking temperature (°C)	**Soaking duration (Min)**		
1	850°C-15Min-WQ+10%CW	850	15	10	3
2	870°C-15Min-WQ+10%CW	870	15	10	3
3	890°C-15Min-WQ+10%CW	890	15	10	3
4	850°C-30Min-WQ+10%CW	850	30	10	3
5	870°C-30Min-WQ+10%CW	870	30	10	3
6	890°C-30Min-WQ+10%CW	890	30	10	3
7	850°C-15Min-WQ+20%CW	850	15	20	3
8	870°C-15Min-WQ+20%CW	870	15	20	3
9	890°C-15Min-WQ+20%CW	890	15	20	3
10	850°C-30Min-WQ+20%CW	850	30	20	3
11	870°C-30Min-WQ+20%CW	870	30	20	3
12	890°C-30Min-WQ+20%CW	890	30	20	3
Total number of solution heat treated plates, which were cold rolled					**36**

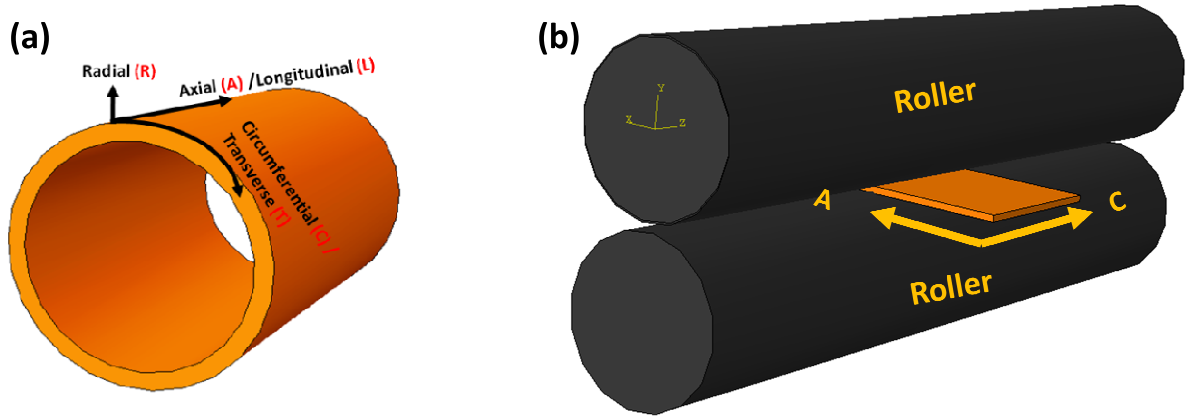

Figure 3.4: Schematic showing (a) three orthogonal directions of the pressure tube spool, and (b) orientation of plate during rolling in a two high rolling mill.

3.5.3 Vacuum Aging Treatment

To examine the influence of aging temperature on Zr-2.5Nb alloy under different cold worked-solution heat treated conditions, out of every three cold rolled plates having similar SHT and CW histories (as listed in Table 3.4), two plates were thermally aged under vacuum (one at 500°C and another at 540°C for 24 h followed by furnace cooling). Therefore, a total 24 numbers of plates were thermally aged for this study. Before aging, these 24 plates were sealed in the batches of 12 plates in two galvanized steel boxes. On each box, one copper tube was brazed at the centre to remove the residual air within it, by connecting tube to the vacuum pump. Subsequently, these boxes were evacuated using vacuum pump. After attaining a vacuum of < 2 torr within the boxes, individual copper tubes were cold shut by hammering it. Three thermocouples, positioned at the left, right and middle regions of the boxes, were spot welded over it to monitor the temperature during aging.

Before individual aging treatments, furnace was allowed to attain the desired temperature. Temperature control of the furnace was within ±3°C from the set value. After attaining the set furnace temperature, furnace was switched off and the individual boxes were placed inside the furnace so as to avoid any electrical shock. Thereafter, the furnace was re-switched on. The time interval for which the furnace was switched off was <15 seconds. The box was then allowed to attain the desired temperature, after which soaking time was counted. Later on, after 24 h of soaking, the boxes were allowed to be furnace cooled. For measuring temperature using K-type thermocouples, similar procedure was followed as discussed in Section 3.3.

3.6 Characterization

3.6.1 Microstructural Characterization

I. Microstructure Examinations

Metallographic examinations of Zr-2.5Nb alloy under solution heat treated, cold worked and aged conditions were performed using optical microscopy. For this, coupons of dimension ~10 mm × 10 mm were cut from the individual solution heat treated, cold worked and aged plates. These samples were subsequently mounted in the steel rings using cold setting resin. During mounting, a specific color code was assigned for each TMP condition. After solidification, mounted samples were removed from the rings and later on, sequentially manually polished using abrasive silicon carbide papers of grit sizes 150, 320, 600 and 800. The polished samples were subsequently swab etched using the solution of 10% HF, 45% HNO_3 and 45% H_2O. After etching, microstructures of the samples were examined in ‘OLYMPUS’ (Model No-GX 51) optical microscope. The area (volume) fractions of phases were determined through the image analysis performed using commercial ‘Image J’ software.

II. Crystallographic Texture Examinations

SHTs result in two phase microstructures, comprising varying volume fractions of primary α and α’ phases. Both of these phases have HCP crystal structures. The basal pole textures of solution heat treated, subsequently cold worked and vacuum aged materials were examined using X-ray diffraction technique following Kearns method [100]. For this, samples under such heat treated conditions with varying thermo-mechanical processing (TMP) parameters such as solution heat treatment (SHT) temperature, degree of cold working and aging were prepared and scanned in a X-ray diffractometer, with ψ angle varying from 0 to 75° and ϕ angle varying from 0 to 360° with 5° increments. The basal pole figures were extrapolated for ψ angle regime of 75 to 90° based on five pole figures viz., <100>, <002>, <101>, <102> and <110>. Finally, the Kearns parameters representing texture anisotropy along the three mutually perpendicular directions viz., axial (f_a), transverse (f_t) and radial (f_r) were determined using the commercial 'LaboTex' software. These Kearns parameters provide an effective volume fraction of basal poles distributed in transverse, radial and axial directions. The effective volume fraction of orientation parameter (f) of a particular crystal plane in a particular tube direction is given as, [100].

$$f = \frac{\int_0^{\pi/2} I_\varphi \sin\varphi \cos^2\varphi \, d\varphi}{\int_0^{\pi/2} I_\varphi \sin\varphi \, d\varphi} \tag{3.1}$$

where I_φ is the average X-ray intensity (in units of times random) at an angle of tilt, φ of the diffraction plane of a crystal oriented with respect to a reference sample direction.

For the texture analysis, samples (10 mm × 10 mm) were sequentially manually polished using abrasive silicon carbide papers of grit sizes 150, 320, 600, 800, 1200 and 2400. These manually polished samples were subsequently chemically polished using a solution of 70% HNO_3 and 30% HF, diluted by 100% water, so as to remove any cold worked surface layer formed during manual polishing operation. The polished samples were subsequently cleaned using the soap solution followed by an ultrasonic cleaning in acetone.

III. EPMA Examinations

As mentioned in Chapter 2 (Section 2.4.3-I) that niobium in Zr-Nb system acts a β stabilizer element and has the tendency to migrate from α-Zr to β-Zr phase at SHT temperature. A qualitative study for Nb concentrations in the two phases viz., primary α and α’ was performed to examine the extent of Nb partitioned between α-Zr and β-Zr phases at SHT temperature. For this purpose, Nb concentrations in these two phases under two extreme SHT conditions (850°C-15Min-WQ and 890°C-30Min-WQ) were estimated using Wavelength Dispersive Spectroscopy (WDS) through an Electro Probe Micro Analyzer (EPMA). These two SHT conditions were chosen, in order to estimate the extent of Nb partitioning that occurred between α-Zr and β-Zr phases for the two extreme conditions among the six SHTs. For this, samples having dimension of 10 mm × 10 mm were sequentially manually polished using abrasive silicon carbide papers of grit sizes 150, 320, 600 and 800. To locate the phases in scanning electron microscope during EPMA examination, the polished samples were lightly swab etched using solution comprising 10% HF, 45% HNO_3 and 45% H_2O. Later on, these samples were cleaned using soap solution followed by an ultrasonic cleaning in acetone. For the EPMA examination, a voltage of 20 kV and a current of 20 mA was used.

IV. TEM Examinations

Aging treatments at 500 and 540°C for 24 h result in the fine precipitation of β phase, which is few tens of nanometer in size, and therefore too small to be visible under optical microscope. To investigate the formation of such fine β precipitates and to study their size, morphology and location, thin foils of WQA materials were prepared and examined through TEM. For this, foils of ~100 µm thickness were prepared and subsequently electro-polished using a solution of 80% methanol (CH_3OH) and 20% perchloric acid ($HClO_4$) (commonly known as '80-20' solution) in 'Struers' (Model: Tenupol-5) jet thinner. The electro-polishing operation was performed at -48°C under 20 volt supply. The electro-polished samples contained a small hole, near which the material was too thin to be electron transparent. The electro-polished samples were cleaned using methanol, and subsequently examined under a 'PHILIPS' (model no: 'CM 200') transmission electron microscope.

To examine the β precipitate chemistry, in terms of Nb concentration, Energy Dispersive Spectroscopy (EDS) examination of these thin foils is essentially not the accurate approach. This is primarily because of the effect of matrix that could be added while analyzing the precipitates, which consequently result in getting biased Nb concentrations of β precipitates. Therefore, for precipitate chemistry examinations, 'carbon extraction replica' technique was used, under which the fine β precipitates were extracted from the material through carbon replicas and subsequently examined through EDS. For this, samples from aged materials were initially deeply etched, so as to weaken the precipitate embedded in the matrix. These deeply etched samples were subsequently coated with thin carbon film using 'BAL-TEC' (model no: 'MED 020') carbon evaporation coater. Before coating, individual sample was placed in a coating chamber and a vacuum of the order of 10^{-5} mbar was attained. Sample was carbon coated through spark action by supplying a current of 90 amps for 65 sec duration. To easily extract the carbon film, small square markings were made on the coating. The coated sample was subsequently dipped in a dilute solution of 6% nitric acid and 2% hydrofluoric acid in 92% water. The film segments instantaneously extracted from the sample within a short duration of 10-20 seconds and floated in the solution. Subsequently, individual extracted carbon film segments were collected through the copper grids, subsequently cleaned in methanol and later on examined for Nb concentration through an energy dispersive spectroscope attached with the transmission electron microscope.

3.6.2 Mechanical Behavior Examinations

Influence of different TMP parameters such as SHT temperature & soaking duration, degree of cold working and aging temperature on Zr-2.5Nb alloy was studied in terms of tensile properties, micro-hardness and fracture toughness parameters. Following sub-sections describe the details of specimen fabrication and individual examinations stages.

I. Specimen Fabrication

During reactor operation, pressure tubes face almost two fold stress along circumferential direction as compared to longitudinal direction. Therefore, for pressure tube's structural integrity point of view, axial crack propagation resistance is more critical than transverse crack propagation resistance. During pressure tube fabrication, extrusion direction is along the axial direction of the tube. The solution heat treated materials, because of having nearly equiaxed grain morphologies, should exhibit specimen orientation independent crack growth resistance. However, after cold working, crack growth resistance of the solution heat treated materials could become the function of specimen orientation. Considering this, for the present work, the ‘Compact Tension’, C(T) specimens used for fracture toughness evaluation and the tensile specimens were oriented such that the loading direction remained perpendicular to axial direction. Figure 3.5 shows schematic illustration of the location of tensile and C(T) specimens in one of Zr-2.5Nb alloy plates. Specimens from the individual plates were machined using wire-cut Electric Discharge Machining (EDM) process. To avoid specimen machining from the end sections of the plates, a safety margin of 10 mm was provided at both the ends of individual plate. Detailed drawings of tensile and C(T) specimens used for the present study are shown in Figures 3.6 and 3.7. After machining, C(T) specimens were ground to achieve 3.17 mm thickness.

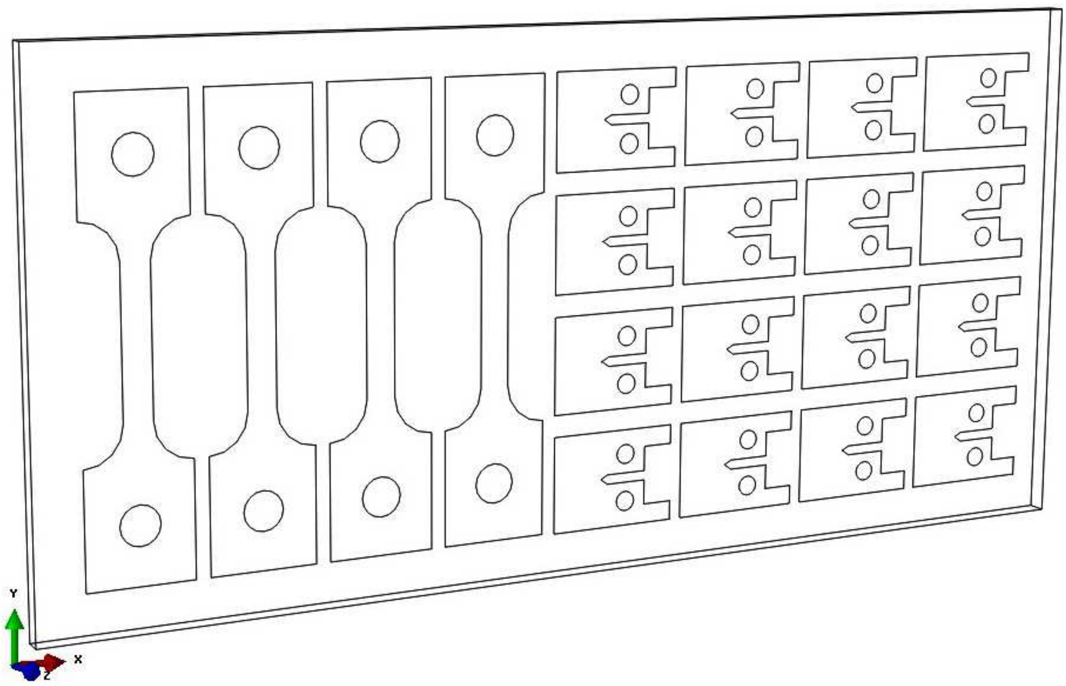

Figure 3.5: Schematic illustration of the location and orientation of tensile and C(T) specimens machined from the individual plates.

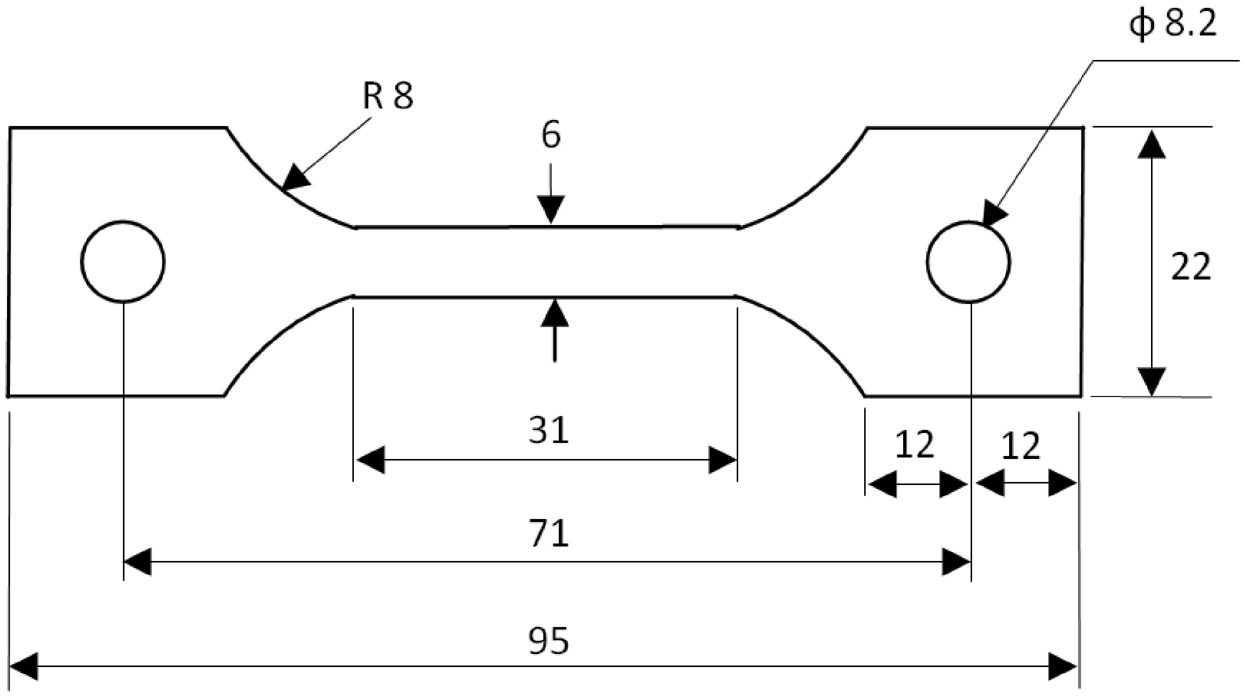

Figure 3.6: Detailed drawing of flat tensile specimen used in the present work for tensile properties evaluation. In this drawing, all dimensions are in mm.

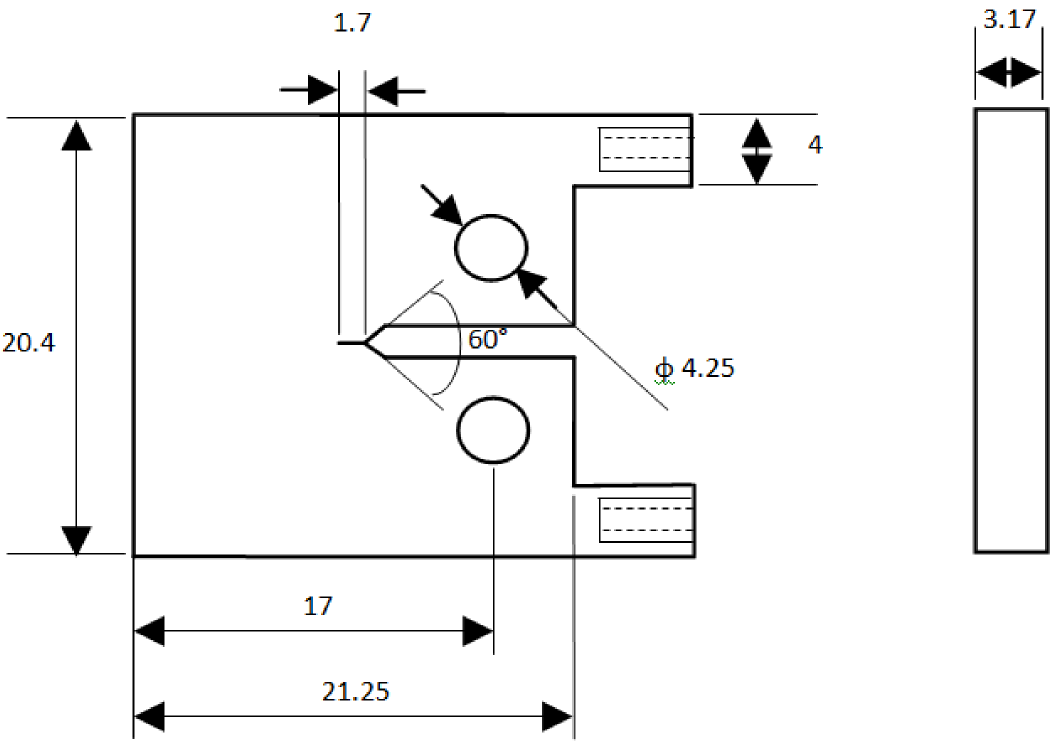

Figure 3.7: Detailed drawing of C(T) specimen used in the present work for fracture toughness evaluation. In this drawing, the dimensions are in mm.

II. Tensile Property Examinations

In order to study the influence of SHT parameters, degree of cold working and aging temperature on tensile properties of Zr-2.5Nb alloy, tensile tests were conducted on an electro-mechanical ‘Zwick/Roell’ universal testing machine (Model No.- ‘KAPPA 100 DS’) at RT (~25°C) and reactor operating temperature, 300°C under a nominal strain rate of 10^{-4} /s. A three zone resistance heating furnace was used for high temperature testing and the specimen temperature was controlled within ±1°C during the test. During the tests, specimen temperature was controlled using three K-type thermocouples, tied on the three locations of the parallel portion of specimen using ‘Nichrome’ wires. A maximum sample heating rate of 15°C per min was used. For high temperature tests, before actual testing individual specimens were soaked for one hour after attaining the desired temperature, in order to attain thermal equilibrium throughout the specimen’s cross-section. Under each TMP condition, one duplicate test was performed at both RT and 300°C.

III. Micro-Hardness Examinations

To study the micro-hardness of Zr-2.5Nb alloy under different TMP conditions, Vickers hardness were examined using ‘ESEWAY’ (Model No- ‘NEXUS-4304’) hardness tester. The tests were conducted using a standard pyramidal shape diamond indenter with 1kg-f load and 10 sec dwell duration. To determine scatter in hardness data, minimum five measurements were taken for individual condition. Samples used for the hardness testing were sequentially manually polished using silicon carbide papers of grit sizes 150, 220, 320, 600, 1200, and 2400. Subsequently, for removing any minor cold worked layer formed on the polished surface, these samples were chemically polished using a solution of 70% HNO_3 and 30% HF, diluted by 100% water. To study the anisotropy in material behavior, hardness was examined on the three mutually perpendicular planes viz., Axial-Circumferential (AC), Axial-Radial (AR) and Radial-Circumferential (RC). Additionally, to investigate the hardness gradient across material thickness, tests were conducted at different depth levels from the free surface.

IV. Fracture Toughness Examinations

For the fracture toughness evaluation of Zr-2.5Nb alloy under different thermo-mechanical processing conditions, C(T) specimens having 17 mm width and 3.17 mm thickness were used. The fracture mechanics theory is based on the assumption of sharp crack tip. Fatigue cycling is one of the methods for creating the sharp crack tip and is recommended by ASTM E1820-11 standard [78]. Therefore, before testing, in order to obtain sharp initial crack tip, these specimens were pre-cracked using fatigue cycling in a high frequency resonance fatigue machine ‘RUMUL’ at ~ 70 Hz frequency upto an initial normalized crack length, a_o/W of 0.5. The fatigue pre-cracking was done in four sequentially decreasing maximum loading steps (650, 550, 450 and 350N) with a load ratio of 0.1.

During fatigue pre-cracking, magnitude of the applied load governs the plastic zone size ahead of crack tip, which consequently affects the sharpness of the crack tip. Loads of low magnitudes are always preferred during this operation in order to achieve minimum crack tip blunting and maximum sharpness. However, it is always a challenging task to pre-crack the specimen at lower loads, since lower loads require long time for crack propagation. Moreover, at such lower loads, it is usually very difficult to in-situ visualize the pre-cracked length within the specimen domain. Therefore, while performing pre-cracking operation, it is very important to select the optimum load in order to minimize the crack tip blunting for ensuring the sharper crack tip and to in-situ visualize the pre-cracking length.

Pre-cracking loads were decided according to the guidelines of ASTM E1820-11 standard [78]. Limiting conditions for the fatigue load to be used in the first pre-cracking step are governed by the following two criteria:

a. Criteria-1: Maximum Stress Intensity Factor (K_{MAX})

As per this criteria, maximum stress intensity factor at the machined notch and subsequently first stage crack tip is limited by [78],

$$\mathrm{K_{MAX}} = \left(\frac{\sigma_{\mathrm{YS}}^{\mathrm{f}}}{\sigma_{\mathrm{YS}}^{\mathrm{T}}}\right)\left(0.063\sigma_{\mathrm{YS}}^{\mathrm{f}}\right)\mathrm{MPa}\sqrt{\mathrm{m}} \tag{3.2}$$

where, $\sigma_{\mathrm{YS}}^{\mathrm{f}}$ and $\sigma_{\mathrm{YS}}^{\mathrm{T}}$ are material's yield strength at respective fatigue pre-cracking and test temperatures. These yield strengths are along the perpendicular direction of crack propagation.

Calculations of the first step fatigue pre-cracking load for the solution heat treated Zr-2.5Nb alloys are shown below. Similar calculations were performed for the corresponding fatigue loads of the subsequently cold worked and aged materials.

The minimum and hence conservative value of aforementioned limiting stress intensity factor should be corresponding to the maximum yield strength of different solution heat treated materials having variable SHT temperature and soaking duration histories. The maximum yield strength of different solution heat treated Zr-2.5Nb alloys considered in this study was 813.42 MPa (Details are provided in Chapter 4).

Therefore, from Equation 3.2, limiting value of the stress intensity factor (K_{MAX}) ahead crack tip during first fatigue pre-cracking step was calculated as,

$$\mathrm{K_{MAX}} = \left(\frac{\sigma_{YS}^{f}}{\sigma_{YS}^{T}}\right)\left(0.063\sigma_{YS}^{f}\right)\ \mathrm{MPa\sqrt{m}}$$

$$= \left(\frac{813.42}{813.42}\right)(0.063 \times 813.42)\ \mathrm{MPa\sqrt{m}}$$

$$\approx 51.25\ \mathrm{MPa\sqrt{m}}$$

For C(T) specimen geometry, the stress intensity factor, K_i is related to force P_i, and crack length a_i as,

$$\mathrm{K_i} = \frac{\mathrm{P_i}}{(\mathrm{BB_N W})^{0.5}} f\left(\frac{\mathrm{a_i}}{\mathrm{W}}\right) \tag{3.3}$$

where, $$f\left(\frac{\mathrm{a_i}}{\mathrm{W}}\right) = \frac{\left\{\left(2+\frac{a_i}{W}\right)\left[0.886+4.64\left(\frac{a_i}{W}\right)-13.32\left(\frac{a_i}{W}\right)^2+14.72\left(\frac{a_i}{W}\right)^3-5.6\left(\frac{a_i}{W}\right)^4\right]\right\}}{\left(1-\frac{a_i}{W}\right)^{\frac{3}{2}}} \tag{3.4}$$

Here, B represents specimen thickness, B_N represents net thickness, (distance between the roots of the side grooves in side grooved specimen) and W represents the specimen width.

For the present C(T) specimen geometry, $B=B_N=3.17$ mm (since the specimens do not have side grooves); W=17 mm; and the original crack size (i.e., physical crack size at the start of pre-cracking) a_o= 6.8 mm.

Therefore, from Equation 3.4,

$$f\left(\frac{\mathrm{a_i}}{\mathrm{W}}\right)=\frac{\left\{\left(2+\frac{\mathrm{a_i}}{W}\right)\left[0.886+4.64\left(\frac{\mathrm{a_i}}{W}\right)-13.32\left(\frac{\mathrm{a_i}}{W}\right)^2+14.72\left(\frac{\mathrm{a_i}}{W}\right)^3-5.6\left(\frac{\mathrm{a_i}}{W}\right)^4\right]\right\}}{\left(1-\frac{\mathrm{a_i}}{W}\right)^{\frac{3}{2}}}$$

$$=\frac{\left\{\left(2+\frac{6.8}{17}\right)\left[0.886+4.64\left(\frac{6.8}{17}\right)-13.32\left(\frac{6.8}{17}\right)^2+14.72\left(\frac{6.8}{17}\right)^3-5.6\left(\frac{6.8}{17}\right)^4\right]\right\}}{\left(1-\frac{6.8}{17}\right)^{\frac{3}{2}}}$$

$$\approx 4.0108$$

Finally, the maximum limiting load (P_{MAX}) for first fatigue pre-cracking step was calculated as,

$$\mathrm{P_{MAX}}=\frac{\mathrm{K_{MAXL}(BB_NW)^{0.5}}}{f\left(\frac{\mathrm{a_i}}{\mathrm{W}}\right)}$$

$$=\frac{(51.25\times\sqrt{1000})\times(3.17\times3.17\times17)^{0.5}}{4.0108}$$

$$= \mathbf{5280.85\ N}$$

b. Criteria-2: P_m

The maximum limiting load (P_m), according to this criterion is represented by Equation 3.5.

$$\mathrm{P_m}=\frac{0.4\mathrm{Bb_o^2}\sigma_\mathrm{Y}}{2\mathrm{W}+\mathrm{a_o}} \tag{3.5}$$

Where, b_o is 'original un-cracked ligament' i.e., distance from the original crack front (machined notch) to the back edge of C(T) specimen (i.e., bo = W-a_o); σ_Y is the flow stress of material, taken as the mean of yield and ultimate tensile strengths.

$$P_m=\frac{0.4\times3.17\times(17-6.8)^2\times850.88}{(2\times17)+6.8}$$

$$= \mathbf{2751.24\ N}$$

Therefore, the selected 650N load, for first fatigue pre-cracking step is highly conservative as compared to the corresponding load recommended by the ASTM E1820-11 [78] standard. The variation of stress intensity factors ahead the crack tip of C(T) specimens in the four fatigue pre-cracking steps are shown in Figure 3.8. From first to fourth stage, the stress intensity factor decreases continuously because of using relatively lower pre-cracking loads. Moreover, because of increasing crack length, under the individual pre-cracking steps, the stress intensity factor increases too. In the first stage, maximum stress intensity factor ranged from ~ 12 to 13 MPa√m, while in the last step, it has variation from 8 to 9 MPa√m.

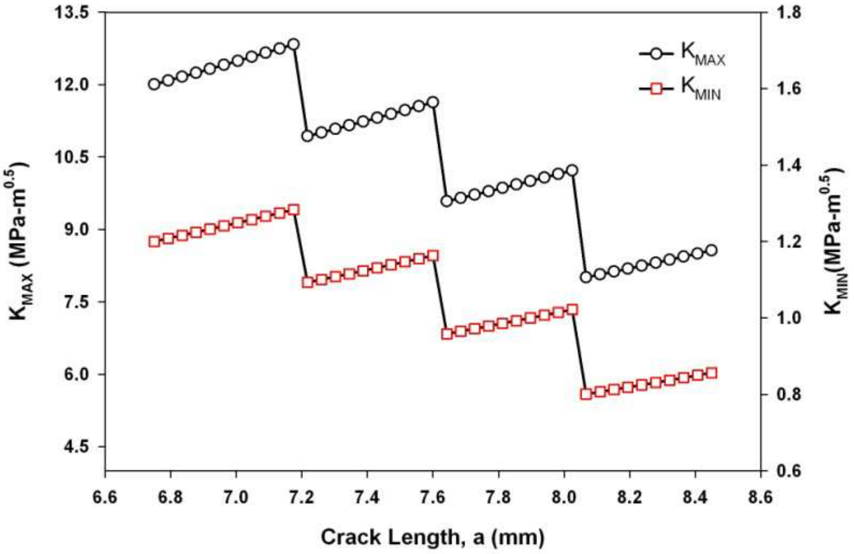

Figure 3.8: Variation of stress intensity factors during the four fatigue pre-cracking steps.

Fracture toughness examinations of these fatigue pre-cracked C(T) specimens were performed in an electro-mechanical ‘Zwick/Roell’ universal tester (model ‘KAPPA 100 DS’) at 0.2 mm/min pulling rate. During testing, ‘Direct Current Potential Drop’ (DCPD) technique was used for monitoring the crack growth [65]. For this purpose, a constant direct current of 6 Amps was supplied to the specimen through 1 mm diameter copper leads [66]. The DCPD voltage was measured using 0.2 mm diameter platinum wires, which were spot welded within 1 mm distance from the notch opening of the specimen. Figure 3.9 shows the details of experimental set-up used for fracture toughness examination. For each TMP condition, one duplicate test was performed at both RT and 300°C.

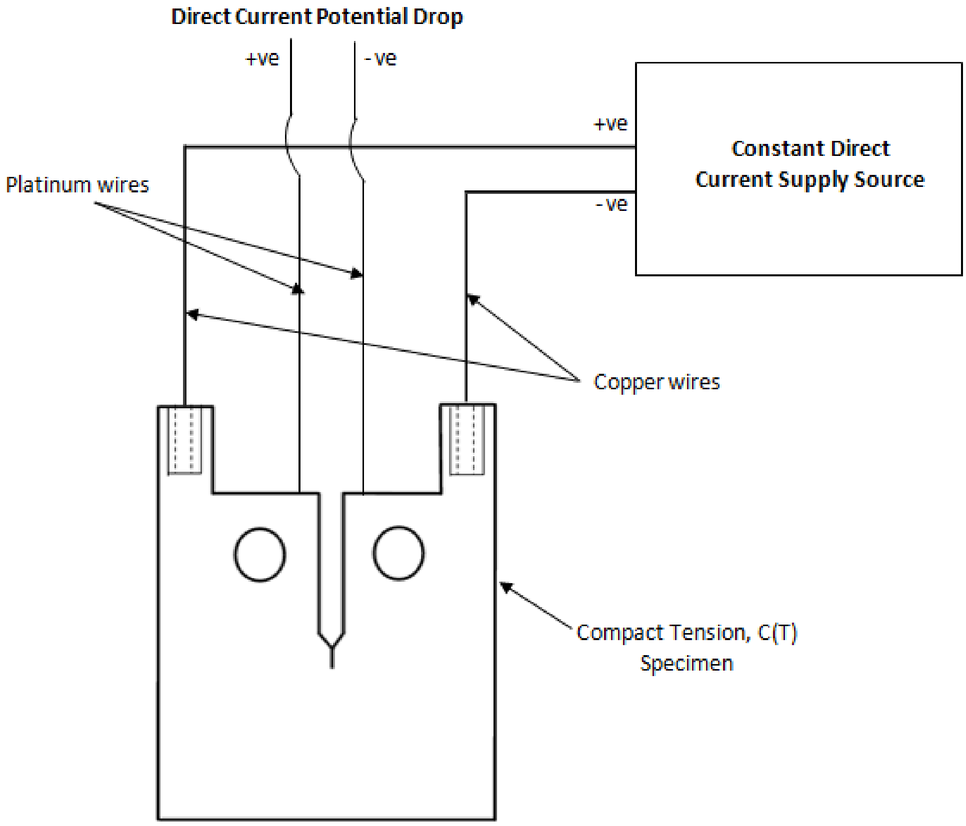

Figure 3.9: Schematic representation of the DCPD unit in a fracture toughness testing.

The fracture toughness was evaluated in terms of *J*-integral parameters. For this, fracture resistance, *J-R* curves were constructed and subsequently analyzed using the ASTM E1820-11 [78] and ISO 12135:2002 [97,98] standards. The fracture toughness was determined in terms of initiation toughness, J_Q and propagation toughness, $J_{F(max)}$ and dJ/da parameters.

V. Fractographic Examinations

Fracture surfaces of the broken C(T) specimens were examined in a 'Nanoeye' mini Scanning Electron Microscope (SEM), in view of investigating the failure mechanisms responsible for fracture. For this, comprehensive fractographic studies at different fractured locations viz., fatigue pre-cracked, stretched zone and slanted & straight fractured regions were performed.

CHAPTER 4

INFLUENCE OF SOLUTION HEAT TREATMENT PARAMETERS ON FRACTURE BEHAVIOR OF Zr-2.5Nb ALLOY

This chapter describes the influence of SHT parameters; soaking temperature within 850-890°C domain and duration within 15-30 min domains on fracture behavior of Zr-2.5Nb alloy. Chapter commences by describing the influence of SHT parameters on the microstructural features comprising phase volume fractions and grain sizes using optical microscopy, basal pole texture using X-ray diffraction and Nb partitioning using EPMA examinations. Followed by this, the influence of SHT parameters on mechanical properties viz. micro-hardness, tensile properties and fracture toughness is presented. Subsequently, a study of the influence of different evaluation procedures on fracture toughness parameters is presented, which include the influence of single specimen (Resistance Curve) and multi-specimen (Basic Test) methods and that of the test standards viz., ASTM E1820 and ISO 12135. Subsequently, a comprehensive study of the fractographic features at different fractured locations studied using SEM and their correlation with the observations is presented. Finally, correlation between the microstructural features with the tensile properties and fracture toughness parameters is discussed.

4.1 Microstructural Observations

4.1.1 Optical Microstructures

Solution heat treatments of Zr-2.5Nb alloy in two phase regime (α-Zr+β-Zr) at 850, 870 and 890°C for two soaking durations (15 and 30 min) followed by water quenching resulted in the two phase microstructures comprising primary α and martensite (commonly known as α’) phases. The α’ phase is the product of diffusion-less transformation of β-Zr phase during water quenching. Figure 4.1 shows the optical microstructures of Zr-2.5Nb alloy solution heat treated from 850-890°C regime for 15 and 30 min soaking durations on the Axial-Circumferential (AC) plane. The primary α phase was practically featureless, however α’ phase exhibited typical martensitic relief after etching, especially under differential interference contrast (DIC) mode of optical microscopy. Image analysis of the micrographs through ‘Image J’ software was performed to determine volume fractions of the two phases. For this, under each of the six SHT conditions, five micrographs, covering a sample area of ~ 0.014 mm^2 were analyzed to determine volume fractions of the two phases. Image analysis revealed that with increase in soaking temperatures from 850 to 890°C, primary α volume fraction decreased, and that of α’ phase increased, as shown in Figure 4.2 (a). With increase in SHT temperature from 850-890°C, volume fraction of primary α phase decreased considerably, from 35.75±2.48% to 6.37±0.44% and from 30.36±0.47% to 5.14±0.46% under respective 15 and 30 min soaking durations.

As shown in Figure 4.2 (b) that SHT temperature had weak influence on the primary α size. Nevertheless, increase in soaking duration from 15 to 30 min at a particular SHT temperature caused marginal grain coarsening of primary α. The prior β (i.e., α’) grain size had considerable dependence on both soaking temperature and duration. Increase in soaking temperature within 850-890°C domain resulted in increase of α’grain size by more than 100% (as can be seen from Figure 4.2 (c)). Also, increase in soaking duration, especially at higher SHT temperature resulted in much coarser size of α’.

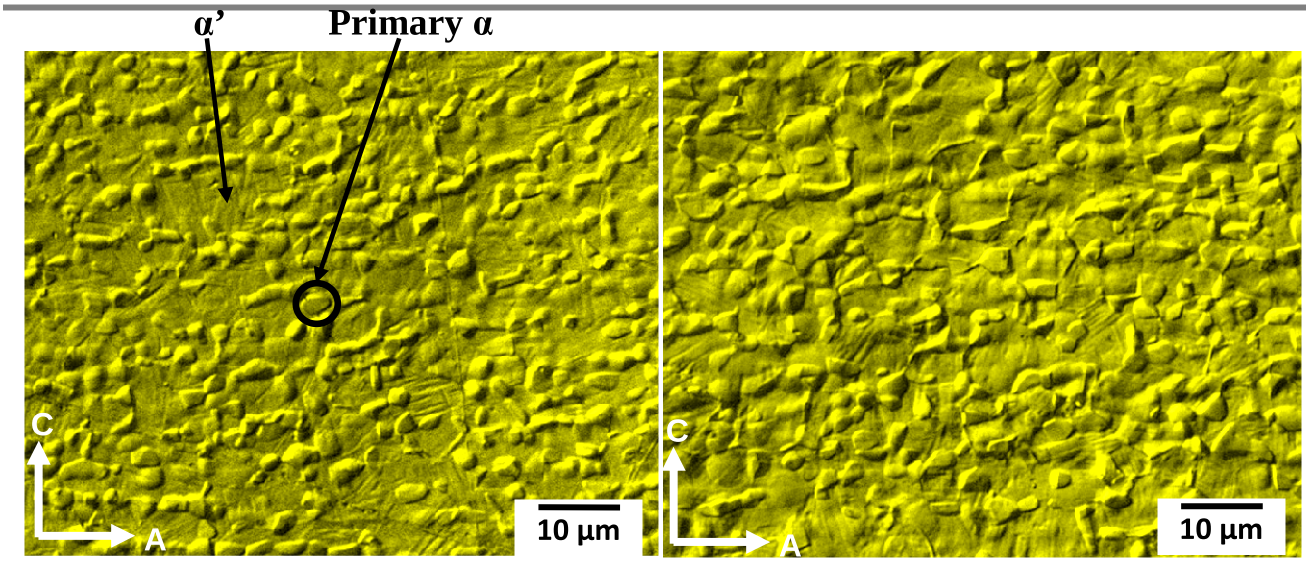

850°C-15Min-WQ **850°C-30Min-WQ**

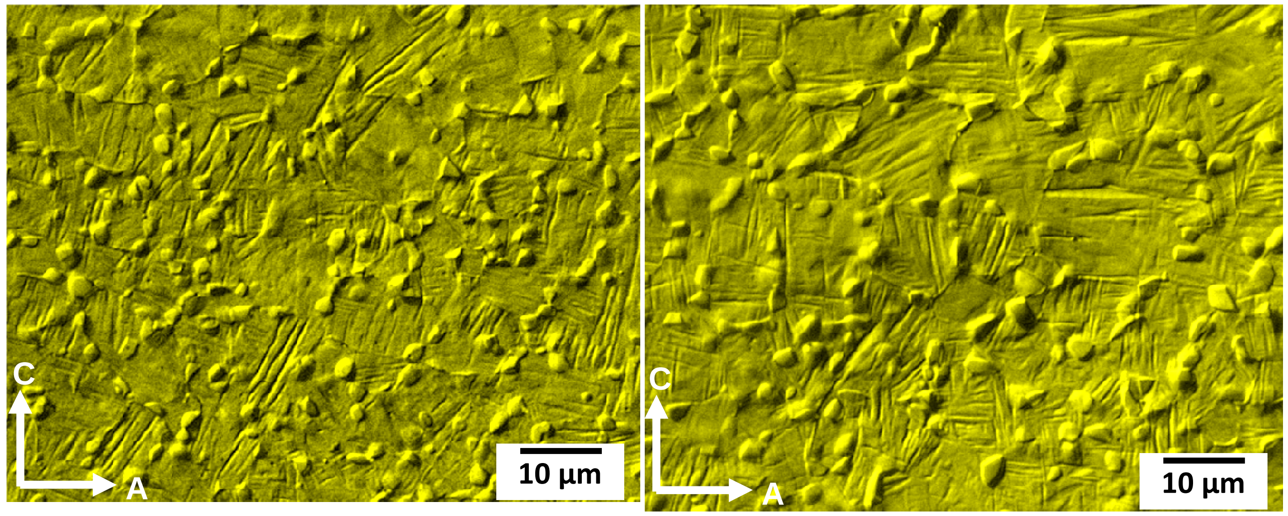

870°C-15Min-WQ **870°C-30Min-WQ**

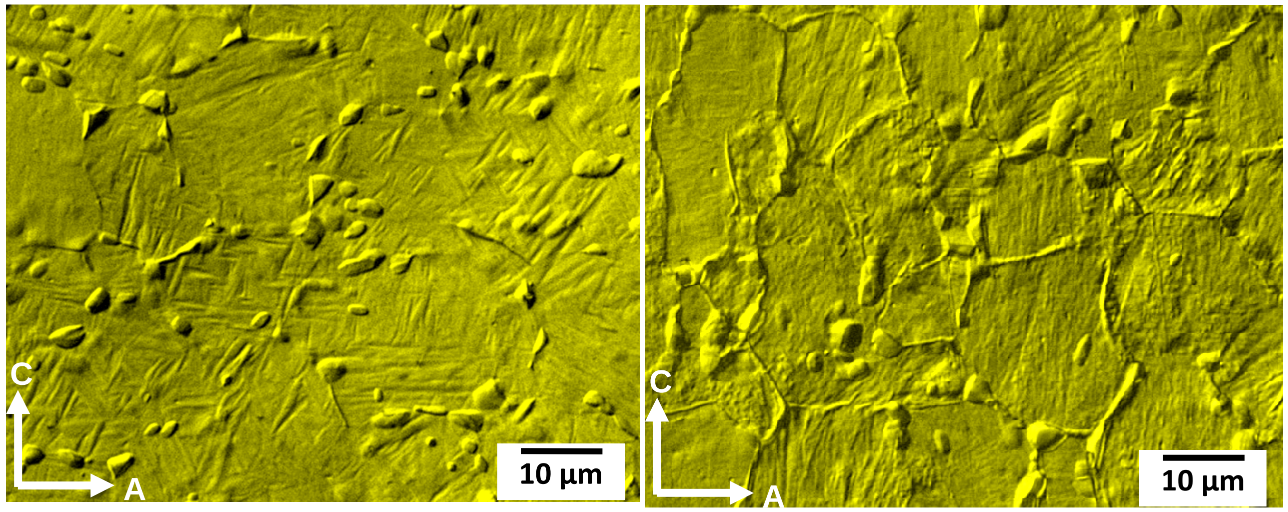

890°C-15Min-WQ **890°C-30Min-WQ**

Figure 4.1: Optical microstructures of Zr-2.5Nb alloy under six solution heat treated conditions. In these micrographs, symbols A and C respectively represent the axial and circumferential directions.

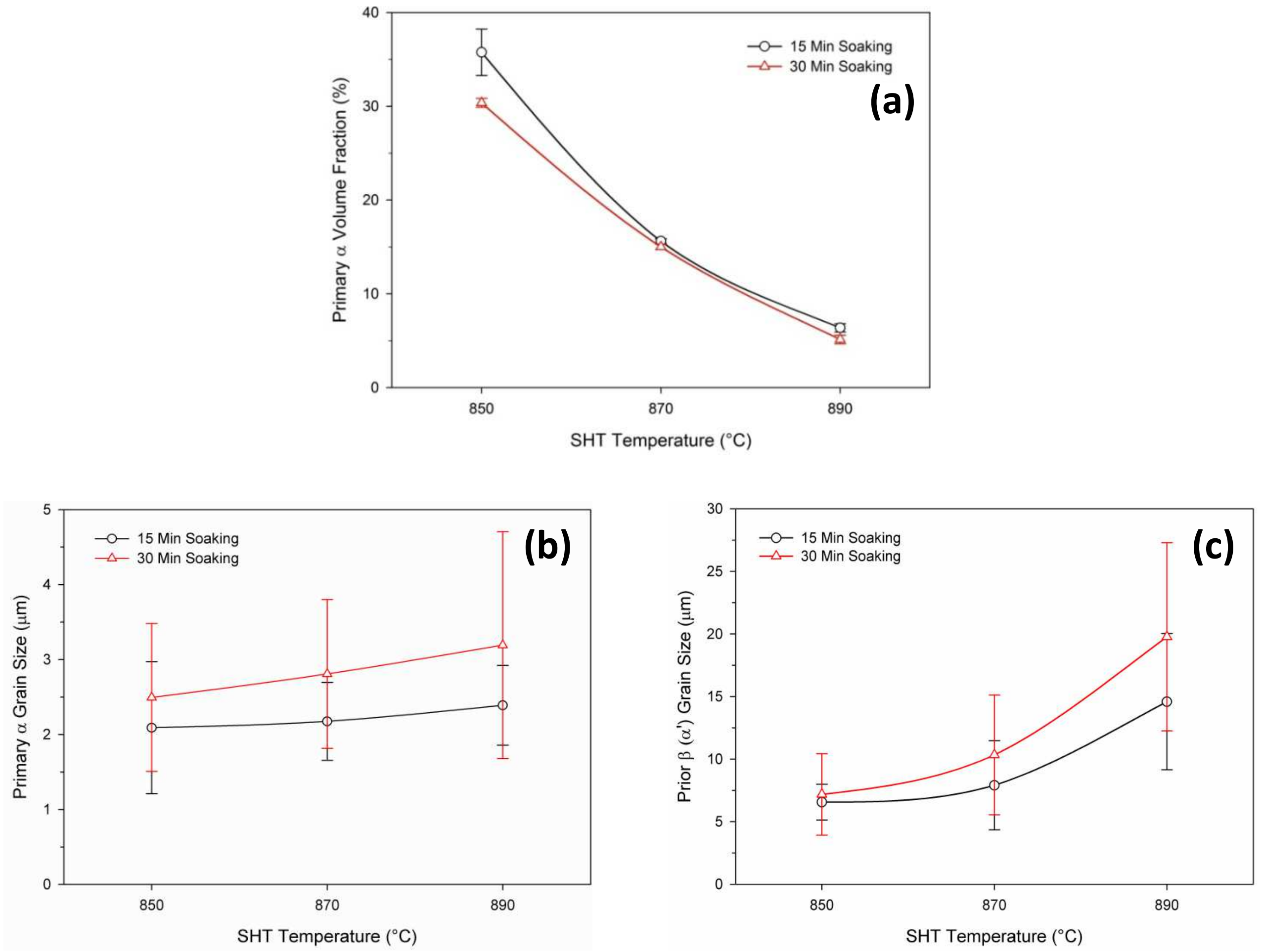

Figure 4.2: Influence of SHT parameters; soaking temperature and duration on (a) primary α phase volume fraction, and (b) primary α & (c) α’ (i.e., prior β) grain sizes.

4.1.2 Crystallographic Texture

Before solution heat treatment, the as-received Zr-2.5Nb alloy (under CWSR condition) exhibited strong texture by having significant variations among the basal pole texture coefficients (Kearns parameters) along axial (0.05), transverse (0.52) and radial (0.43) directions. After solution heat treatment within 850-890°C regime followed by water quenching, the resulting primary α and α’ phases have hexagonal close packed crystal structure. The texture of solution heat treated materials, as shown in Figure 4.3 represents the overall basal pole alignment along three mutually perpendicular axial, transverse and radial directions. After solution heat treatment, texture coefficients along axial, transverse and radial directions became nearly equal, suggesting random texture of the SHT material. Furthermore, with increase in SHT temperature and duration, the degree of randomness along three mutually perpendicular directions increased. The pole figures of Zr-2.5Nb alloy, as shown in Figure 4.4 suggest that the texture after solution heat treatment as compared to parent CWSR condition is much weaker.

The texture of both 15 and 30 min soaked materials also suggested that as the SHT temperature increases, more and more basal poles got aligned towards the axial direction with the corresponding reduction along transverse and radial directions. As a result, after solution heat treatment, the basal pole texture became practically randomised having nearly one third distribution along each of the three orthogonal directions.

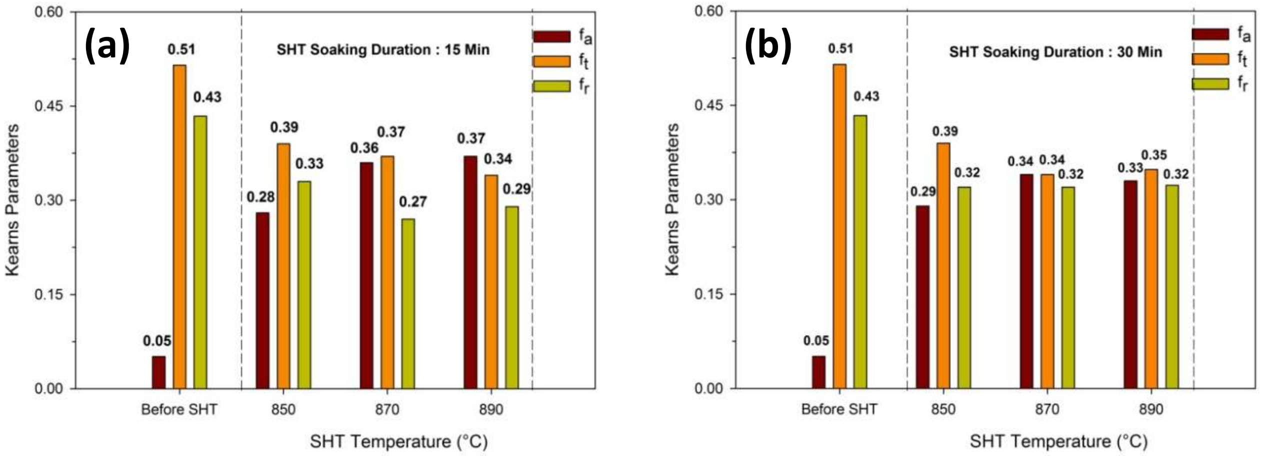

Figure 4.3: Influence of SHT temperature on the basal pole texture (Kearns Parameters) of water quenched Zr-2.5Nb alloy along three mutually perpendicular, axial (f_a), transverse or circumferential (f_t) and radial (f_r) directions. Figure (a) and (b) respectively show the Kearns parameters of the alloy soaked for 15 and 30 min durations.

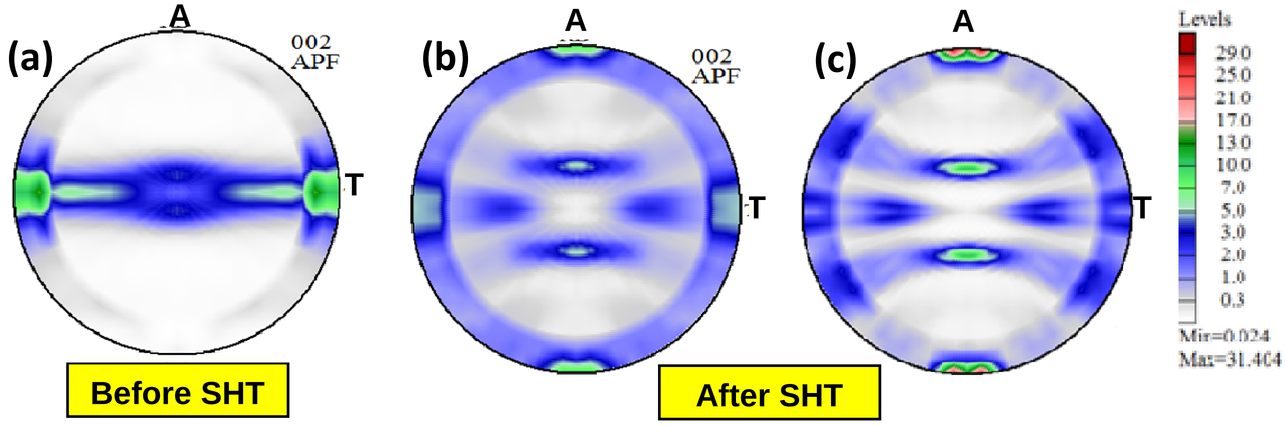

Figure 4.4: Additional basal Pole Figures (APFs) of Zr-2.5Nb alloy before (a) and after solution heat treatment (b) & (c). Figure (b) and (c) respectively show the APFs of alloy heat treated from 850 and 890°C after being soaked for 30 min duration followed by water quenching. Symbols A and T respectively indicate the axial and transverse directions. Sample normal was along radial direction.

4.1.3 Chemical Composition Analysis (Study of Nb Partitioning)

Nb, the major alloying element, acts as a β stabilizer in Zr-Nb alloy. As discussed, water quenching from two phase (α-Zr + β-Zr) regime results in diffusion-less transformations of α-Zr and β-Zr to respective primary α and α’ phases. Increasing soaking temperature and duration during SHT is expected to decrease the Nb chemistries of phases. To study such Nb segregation, the water quenched materials under two extreme SHT conditions viz., 850°C-15Min-WQ and 890°C-30Min-WQ were examined in an Electron Probe Micro-analyzer (EPMA) using Wavelength Dispersive Spectroscopy (WDS) technique.

Figures 4.5 and 4.6 show the rate of photons of a specific wavelength, emitted from the Nb element present in primary α and α’ phases in terms of counts per seconds (CPS) for the two extreme solution heat treated conditions. As can be seen from these figures that the combination of higher soaking temperature and duration resulted in a lower Nb counts from the primary α phase. This therefore, emphasizes that increasing soaking temperature and duration causes decrease in Nb concentration in α-Zr (therefore, primary α) phase. This fact can be understood from the phase diagram also. Figure 4.7 (a) shows the reported [58] phase diagrams of Zr-2.5Nb alloy with three different oxygen concentrations viz., 170, 1400, and 5350 ppm. However, the Zr-2.5Nb alloy, considered in this study contains on an average 1036 ppm of oxygen. To estimate the phase transformation lines for the alloy having 1036 ppm oxygen, a linear interpolation of the phase transformation lines of 170 and 1400 ppm was performed. The interpolated transformation line was subsequently shifted to achieve the β-transus temperature for 2.5 wt. % Nb concentration as 915°C, as earlier (Chapter-3) experimentally established for the present material. As can be seen from this figure (Figure 4.7 (b)) that with increase in temperature from 850-890°C, the Nb concentration of α-Zr phase decreases. Such Nb concentration dependence of α-Zr with temperature is shown in Table 4.1. Also, a longer soaking duration is expected to decrease the Nb concentration in α-Zr phase. This therefore, also correlates the observed lower Nb counts obtained from the primary α phase at higher soaking temperature and duration.

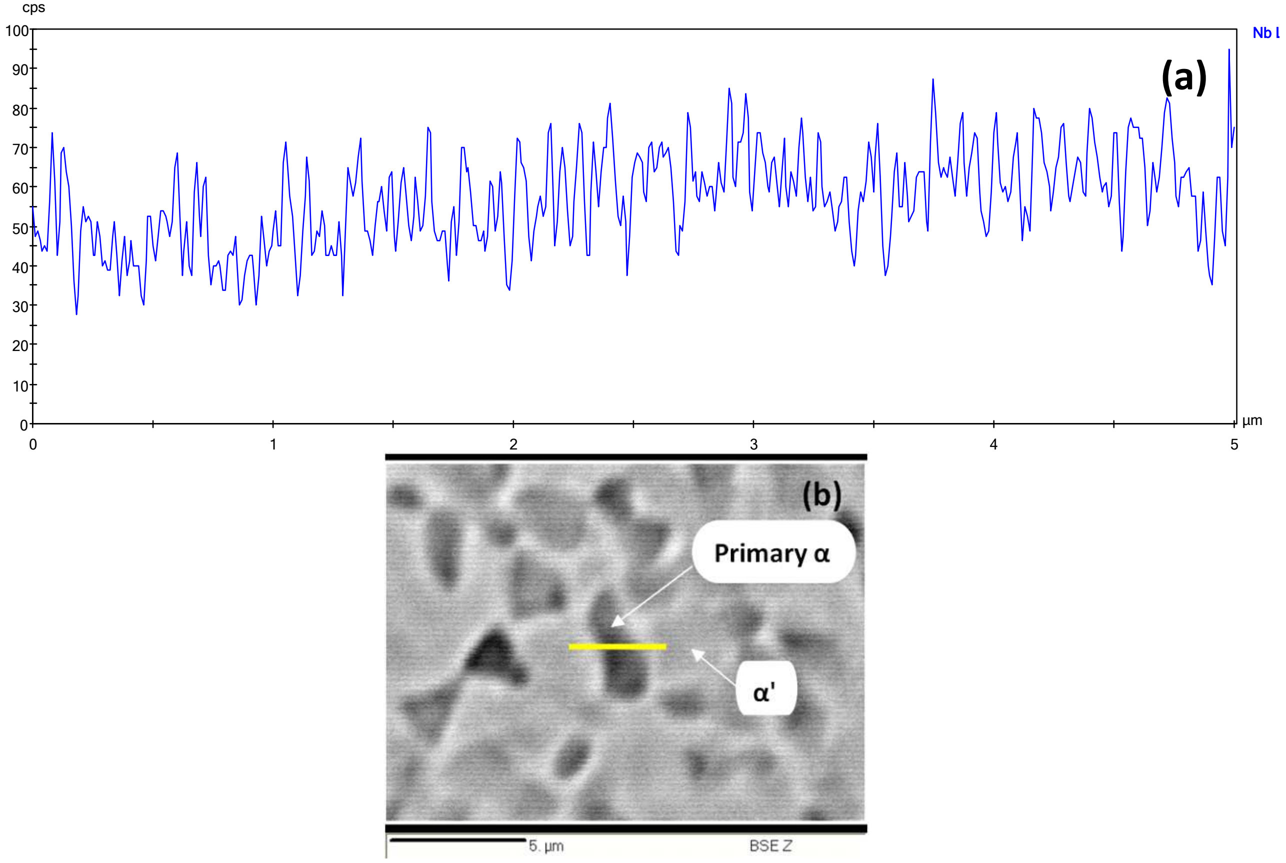

Figure 4.5: (a) EPMA derived Nb CPS spectra from primary α and α’ phases in the solution heat treated Zr-2.5Nb alloy, soaked at 850°C for 15 min duration. Figure (b) shows the yellow line covering the two phase regions, along which WDS scanning was performed.

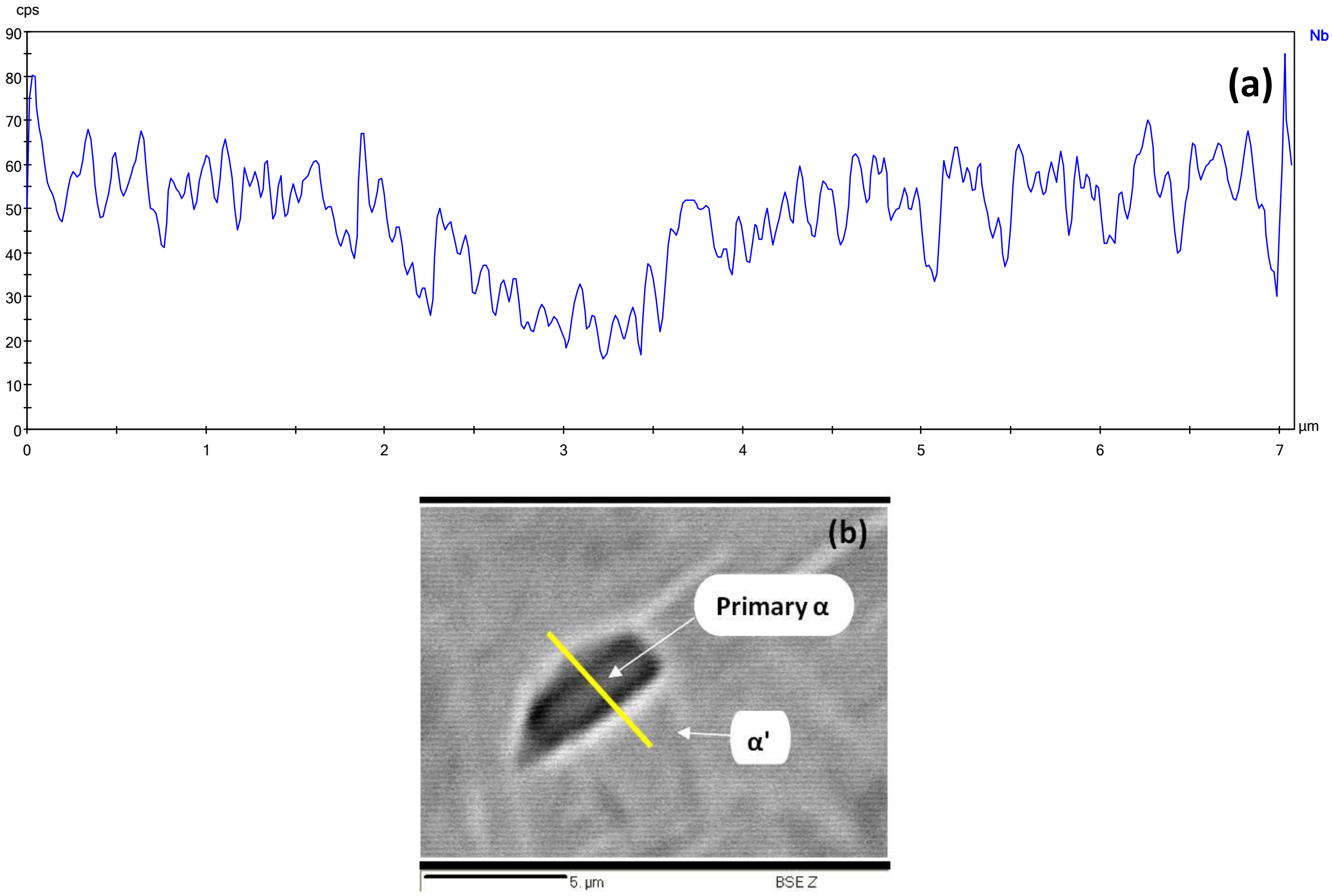

Figure 4.6: (a) EPMA derived Nb CPS spectra from primary α and α’ phases in the solution heat treated Zr-2.5Nb alloy, soaked at 890°C for 30 min duration. Figure (b) shows the yellow line covering the two phase regions, along which WDS scanning was performed.

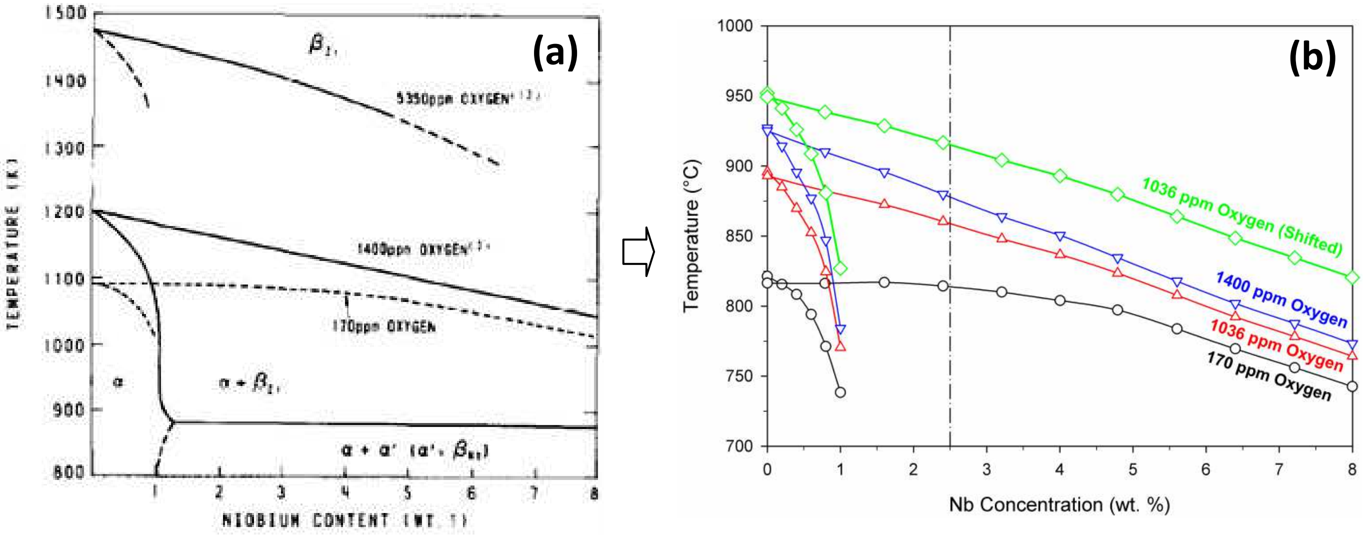

Figure 4.7: (a) Phase diagrams of Zr-Nb alloy having three oxygen concentrations viz., 170, 1400, and 5350 ppm [58] and (b) Phase diagram of Zr-Nb alloy, derived from Figure (a) for 1036 ppm oxygen concentration, which is equivalent to the average oxygen concentration of Zr-2.5Nb alloy used for the present investigation.

Table 4.1: Variation of Nb concentrations in α-Zr phase with SHT temperatures, as quantified from the phase diagram of the alloy having 1036 wt. ppm oxygen (as shown in Figure 4.7 (b)).

S. No.	**Temperature (°C)**	**Nb in α-Zr (wt. %)**
1	850	0.92
2	870	0.84
3	890	0.73

4.2 Mechanical Behavior

4.2.1 Micro-Hardness

In order to examine material's anisotropy, Vickers hardness of Zr-2.5Nb alloy under both the parent (as-received material under CWSR condition) and solution heat treated conditions were investigated on the three mutually perpendicular AC, AR and RC planes. The as-received material exhibited hardness in the range of 2.24 to 2.62 GPa (228.3 to 266.7HV1) and showed anisotropy, under which maximum hardness was observed on the AR plane (ranging from 2.45 to 2.62 GPa, i.e., 249.4 to 266.7HV1) and minimum on the RC plane (ranging from 2.24 to 2.38 GPa, i.e., 228.3 to 242.2HV1), see Figure 4.8 (a). A typical indent profile observed after the indentation during hardness testing is shown in Figure 4.8 (b). Under 1 kg-f load, the indent diagonal lengths on AC, AR and RC planes were respectively 85.9-88.5, 83.4-86.2 and 87.5-91.9 µm.

The solution heat treated materials were found to have sharp hardness gradient in the vicinity of free surface. While approaching towards the depth from free surface, hardness decreased drastically, and subsequently gets practically saturated. Up to a depth of 200-225 µm from the free surface (i.e., below 4-6 % of material's thickness), hardness showed such sharp transition. Such evolution of hardness in the solution heat treated materials as a function of depth from the free surface is shown in Figure 4.9.

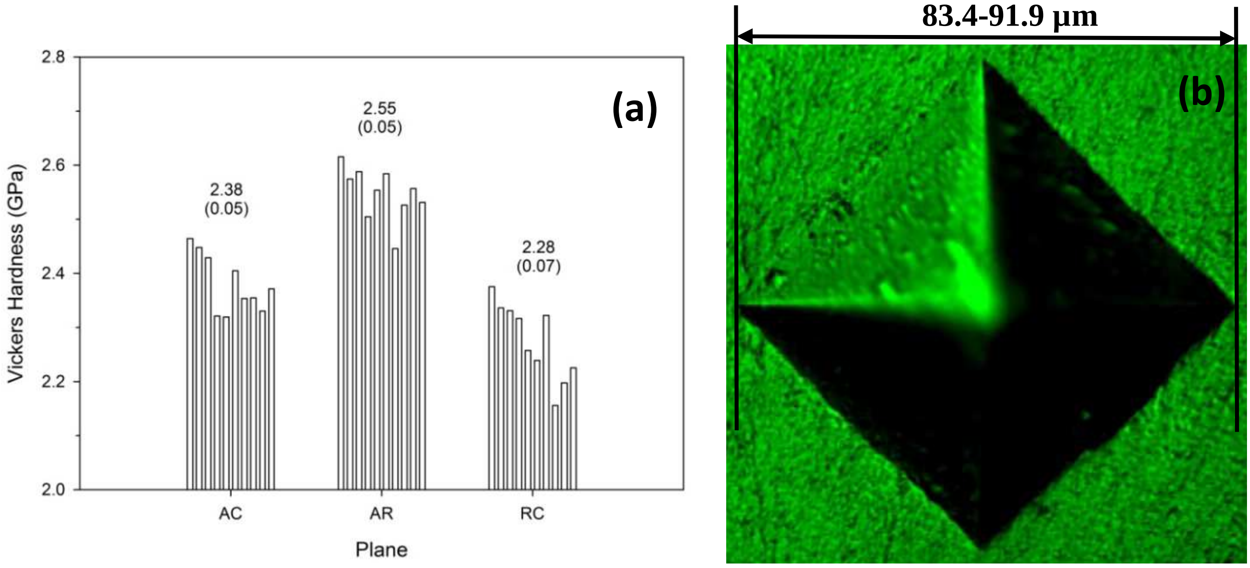

Figure 4.8: (a) Vickers hardness anisotropy in as-received Zr-2.5Nb alloy under CWSR condition. Plot shows the hardness variation on three mutually perpendicular AC, AR, and RC planes of as-received pressure tube material. In this Figure, over each bar group, the average hardness value along with corresponding standard deviation (within parentheses) is shown. (b) Typical indent impression formed on the surface during hardness testing. The indent diagonal lengths for parent CWSR material were between 83.4-91.9 µm under 1kg-f load.

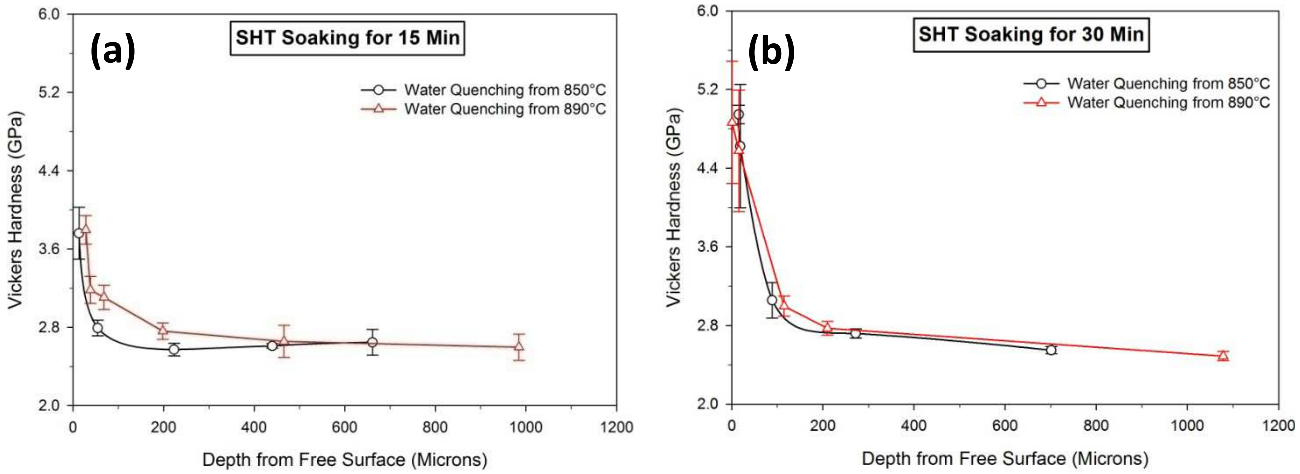

Figure 4.9: Variation of Vickers hardness with depth from the free surface in solution heat treated Zr-2.5Nb alloy on AC plane. Plots (a) & (b) are respectively for the materials soaked for 15 and 30 min durations during solution heat treatment.

The saturated mid section hardness (hardness measured on the middle section of specimen thickness) of the solution heat treated Zr-2.5Nb alloy on AC, AR and RC planes is shown in Figures 4.10 (a)-(c). After solution heat treatment, hardness with respect to parent (CWSR) material increased by 2.4 to 9.2 % depending on the soaking temperature and duration used during the heat treatment. In contrast to as-received (parent) CWSR material, the solution heat treated materials were nearly isotropic and exhibited marginal variation of hardness on three mutually perpendicular planes. During solution heat treatment, with increasing soaking temperature and duration, hardness decreased. Though, within the soaking temperature regime of 850-890°C and soaking duration regime of 15-30 min, such influence was insignificant, as shown in Figures 4.10 (a)-(c). Under 1 kg-f load, the indent diagonal length was lying in the band of 80-85 microns.

Figure 4.10 (d) shows the dependence of hardness on soaking temperature under 15 and 30 min durations on the three mutually perpendicular planes. Here the soaking temperature dependence of hardness at a particular plane was calculated as per Equation 4.1.

$$\text{Hardness dependence on SHT temperature} = \frac{\mathrm{H}_{850°\mathrm{C}} - \mathrm{H}_{890°\mathrm{C}}}{\mathrm{H}_{850°\mathrm{C}}} \times 100 \qquad (4.1)$$

In Equation 4.1, terms $\mathrm{H}_{850°\mathrm{C}}$ and $\mathrm{H}_{890°\mathrm{C}}$ respectively represent the hardness of materials soaked at 850°C and 890°C on a particular plane.

Out of AC, AR and RC planes, hardness on the AC plane, showed highest dependence on soaking temperature (as, within 850-890°C regime, hardness decreased by 5.3 and 2.8 % under respective 15 and 30 min soaking durations). On the AR plane, such dependence was comparatively lower (as, respective reductions were 3.9 and 2.3 %), and on the RC plane, hardness was observed to be least dependent on the soaking temperature (as, respective reductions were 3.3 and 0.8 %). Therefore, higher soaking duration during the solution heat treatment results in the lower soaking temperature dependent hardness.

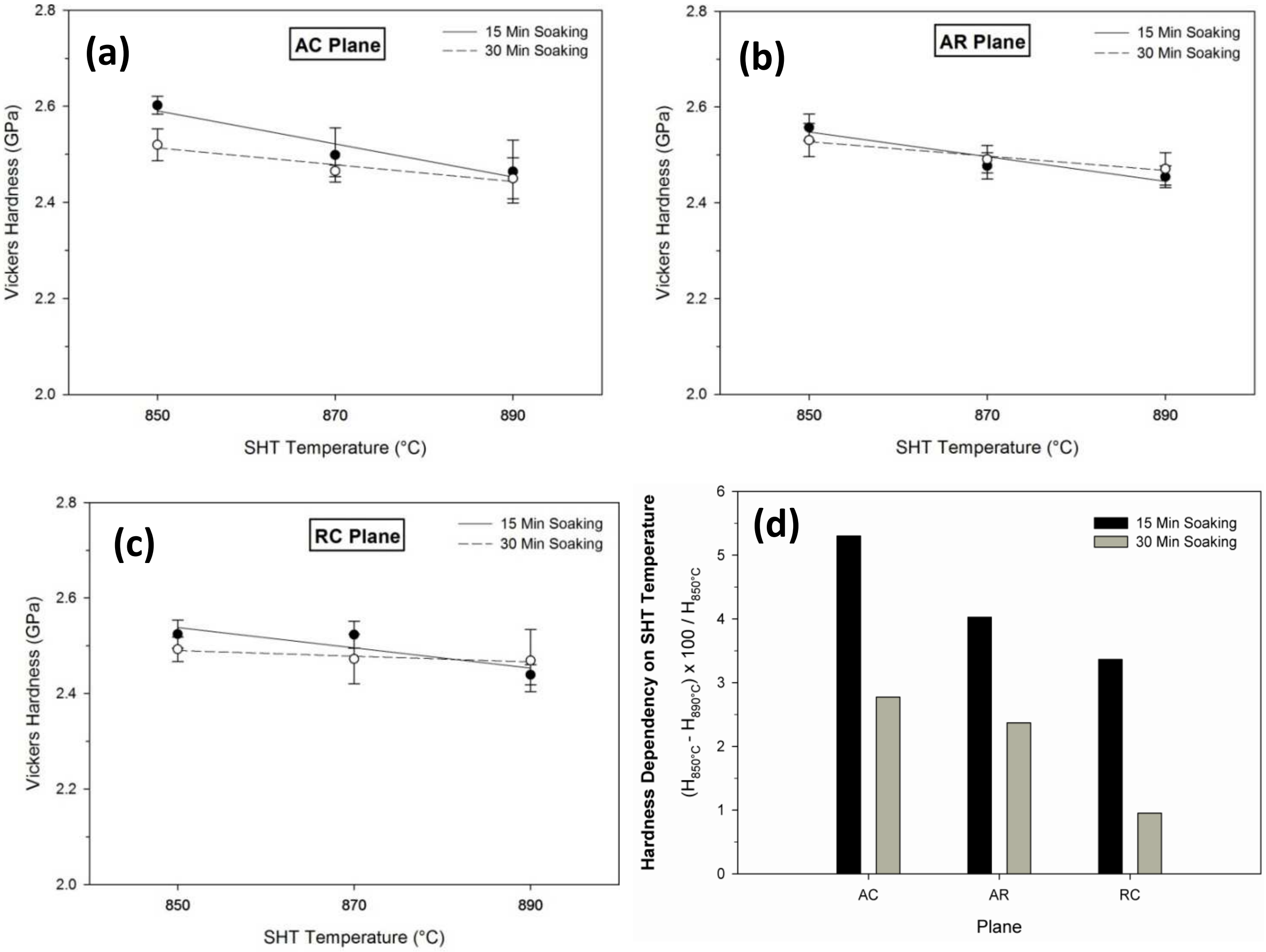

Figure 4.10: Influence of SHT parameters, soaking temperature and duration on the mid section Vickers hardness of Zr-2.5Nb alloy on (a) AC, (b) AR and (c) RC planes. Figure (d) shows the dependency of hardness on soaking temperature within 850-890°C regime on these three planes. Here, each bar represents the percentage reduction in hardness with increase in soaking temperature from 850 to 890°C on a particular plane.

4.2.2 Tensile Properties

I. Tensile Strengths

Influence of solution heat treatment parameters on the tensile behavior of Zr-2.5Nb alloy is shown in Figures 4.11-4.16. The flow curves of Zr-2.5Nb alloy under different solution heat treated conditions are illustrated in Figure 4.11.

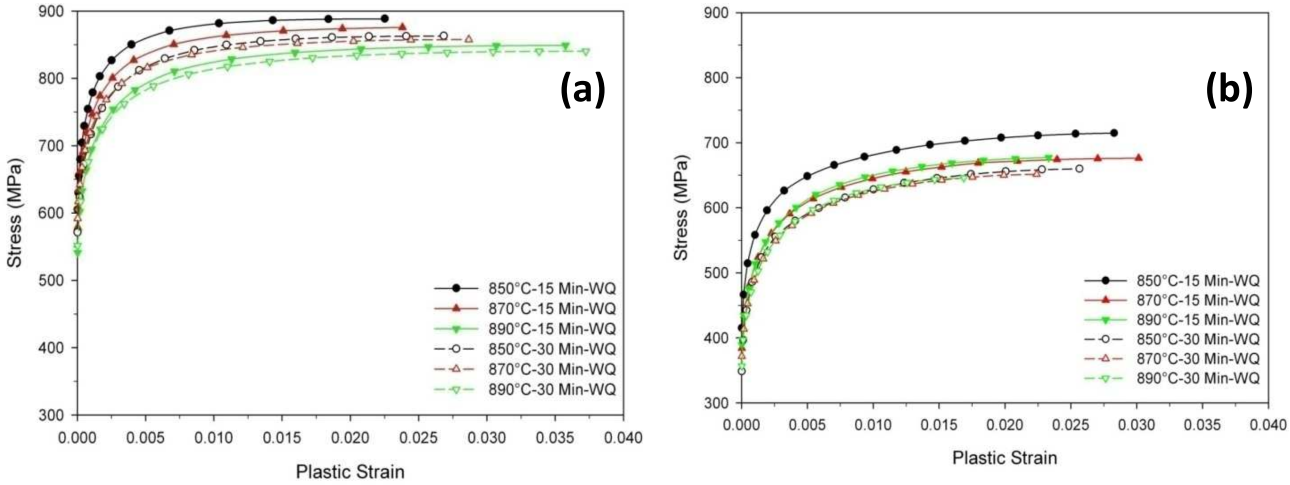

Figure 4.11: Lower bound flow curves of Zr-2.5Nb alloy under different SHT conditions at (a) RT and (b) 300°C.

During solution heat treatment, with increase in soaking temperature from 850-890°C and soaking duration from 15 to 30 min, the tensile strengths of Zr-2.5Nb alloy decreased, though the observed variations were not significant. Figure 4.12 shows the influence of soaking temperature and duration during solution heat treatment on the tensile strengths (0.2 % offset yield strength, YS and ultimate tensile strength, UTS) of Zr-2.5Nb alloy. Under 15 min soaking period, increase in soaking temperature from 850-890°C resulted in ~ 9 and 5 % reductions in the respective YS and UTS parameters. As the soaking duration increased, the tensile strengths decrease and became less sensitive to the soaking temperatures. Under 30 min soaking duration, increase in soaking temperature from 850-890°C resulted in the respective comparatively lower reductions (by < 5 %). The dependence of tensile strengths on soaking period decreased as the soaking temperature increased. For 890°C soaking temperature, the RT tensile strengths were almost similar for the two soaking durations (as the deviation was < 0.5 %), as shown in Figure 4.12 (a) and (b). However, at 300°C, the deviations in the tensile strengths of 15 and 30 min soaked materials were within 3-5 % respectively.

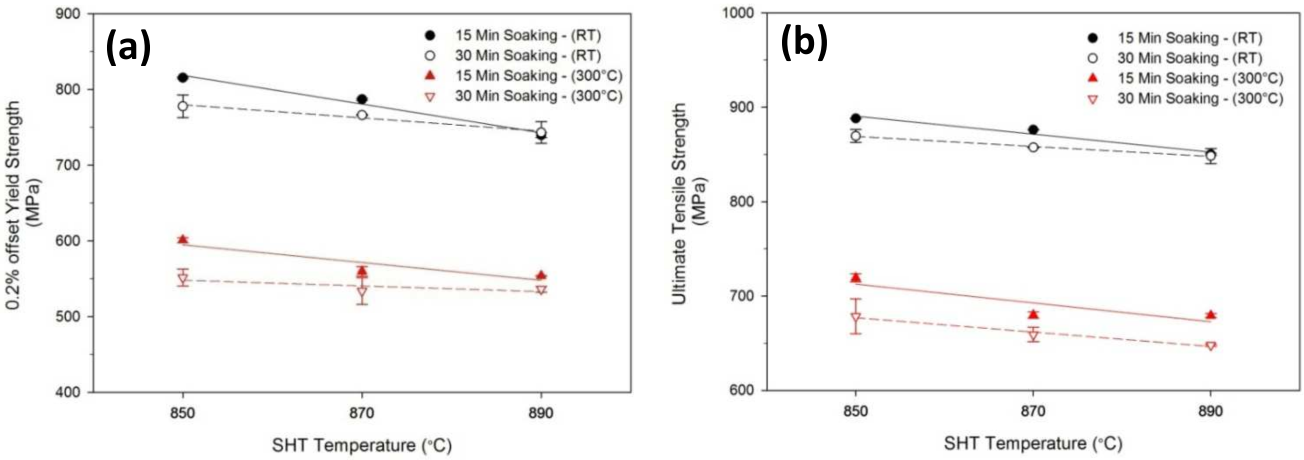

Figure 4.12: Influence of SHT parameters on (a) 0.2% offset yield strength, and (b) ultimate tensile strength of Zr-2.5Nb alloy.

II. Uniform Elongation

The uniform elongation (UE), which represents the extent of homogenous deformation within the specimen during uni-axial testing and measured as the magnitude of plastic strain corresponding to the point of maximum stress, is shown in Figure 4.13 for Zr-2.5Nb alloy under different solution heat treated conditions. The solution heat treated materials examined in this work showed UE in the range of 2-4 %. Under ambient condition, UE increased with increase in soaking temperature from 850-890°C. For 15 min soaked material, UE increased almost linearly with soaking temperature. However, for 30 min soaked material, UE showed comparatively less dependence on soaking temperature (by 16.3 %). At 300°C, opposite to ambient condition, UE decreased with increase in soaking temperature (by less than 30% for both soaking periods).

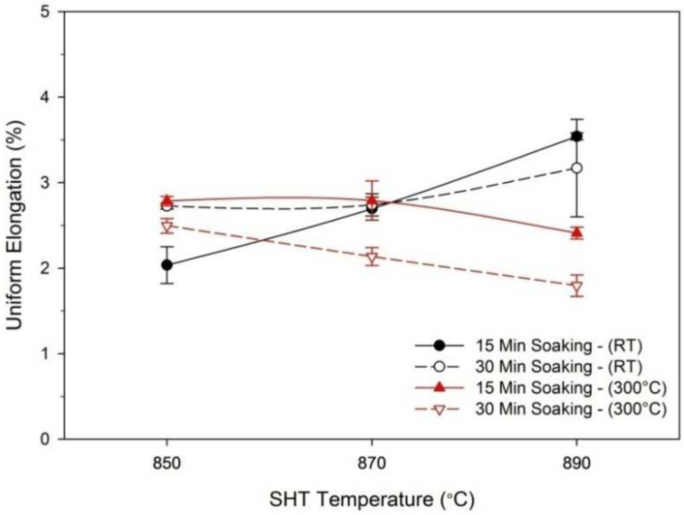

Figure 4.13: Influence of SHT parameters on the uniform elongation of heat-treated Zr-2.5Nb alloy.

III. Ductility

The ductility of Zr-2.5Nb alloy under different solution heat treated conditions were determined in terms of total elongation (TE) and reduction in cross section area at fractured location and is shown in Figure 4.14.

For the measurement of ductility in terms of TE, two parallel lines having a gage length of 25 mm were marked on the parallel section of the specimen, and TE was calculated as per the Equation 4.2.

$$\text{TE (in \% age)} = \frac{L_f - L_i}{L_i} \times 100 \tag{4.2}$$

In Equation 4.2, L_i and L_f represent the initial (before test, i.e., 25 mm) and final (after fracture of the specimen) gage lengths.

In contrast to the other tensile properties, TE parameter exhibited considerable scatter. Under ambient condition, the average trend showed that during solution heat treatment, as the soaking temperature increased from 850-890°C, TE increased marginally, by < 8%. However, at 300°C, the average TE trend was unaffected upto the 870°C soaking temperature, though reduced afterwards, as shown in Figure 4.14 (a). With increase in soaking duration at a given temperature from 15 to 30 min, TE exhibited reduction. Opposite to the general behavior of ductility with temperature, TE of these solution heat treated Zr-2.5Nb alloy decreased with increase in temperature.

The second ductility parameter viz., reduction in cross-sectional area at fractured location was found to be practically insensitive to the soaking temperature, as shown in Figure 4.14 (b). As the soaking duration during solution heat treatment increased, reduction in cross-sectional area increased.

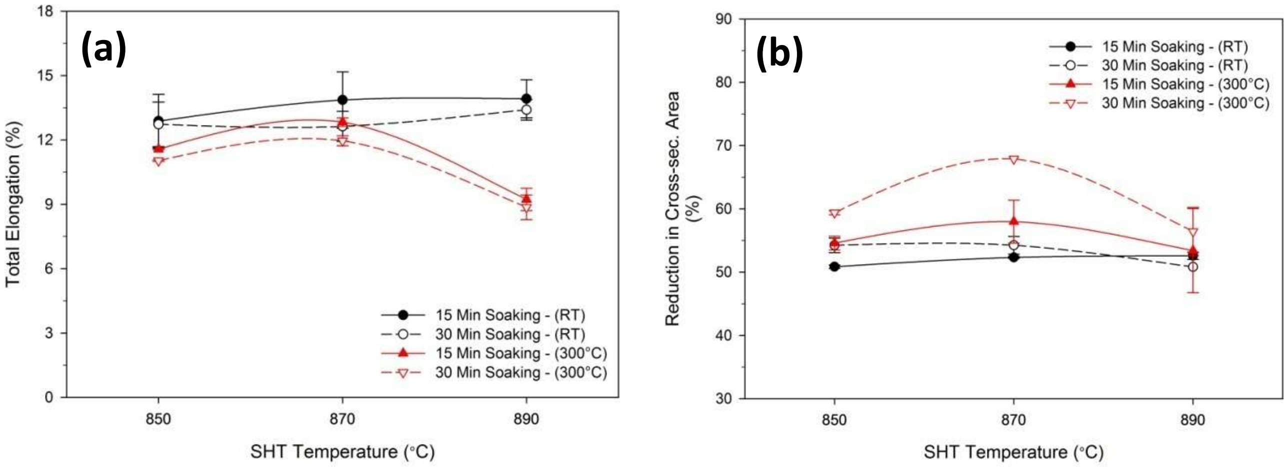

Figure 4.14: Influence of SHT on the ductility of Zr-2.5Nb alloy. Plot (a) shows the variation of total elongation, and plot (b) shows the variation of reduction in fracture cross-sectional area of the Zr-2.5Nb alloy under different solution heat treated conditions.

IV. Strain Hardening Behavior

The strain hardening parameters of the solution heat treated Zr-2.5Nb alloy were determined using the Holloman's empirical power law hardening relationship [102], given as;

$$\sigma = K\varepsilon_p^{\ n} \tag{4.3}$$

where, σ represents the true stress corresponding to the true plastic strain, ε_p; coefficients K & n respectively represent the strength coefficient and strain hardening exponent.

During solution heat treatment, as the soaking temperature increases, strain hardening exponent of the heat treated material increases, as shown in Figure 4.15 (a) though the observed variations were marginal. Under 15 min soaking condition, within 850-890°C temperature domain such increase was ~30 and 20% respectively at RT and 300°C. Higher soaking duration at a particular temperature resulted in higher and comparatively less soaking temperature sensitive hardening exponent of the resulting material. The material soaked for 30 min, as compared to 15 min showed practically soaking temperature insensitive exponent. As the soaking temperature increased, the difference in hardening exponents of 15 and 30 min soaked materials decreased and at 890°C soaking temperature, such deviation became negligible.

The strength coefficient was practically insensitive to the soaking temperature and duration used during the solution heat treatment, as shown in Figure 4.15 (b). In contrast to RT, at (300°C), the coefficients exhibited ~10% reduction.

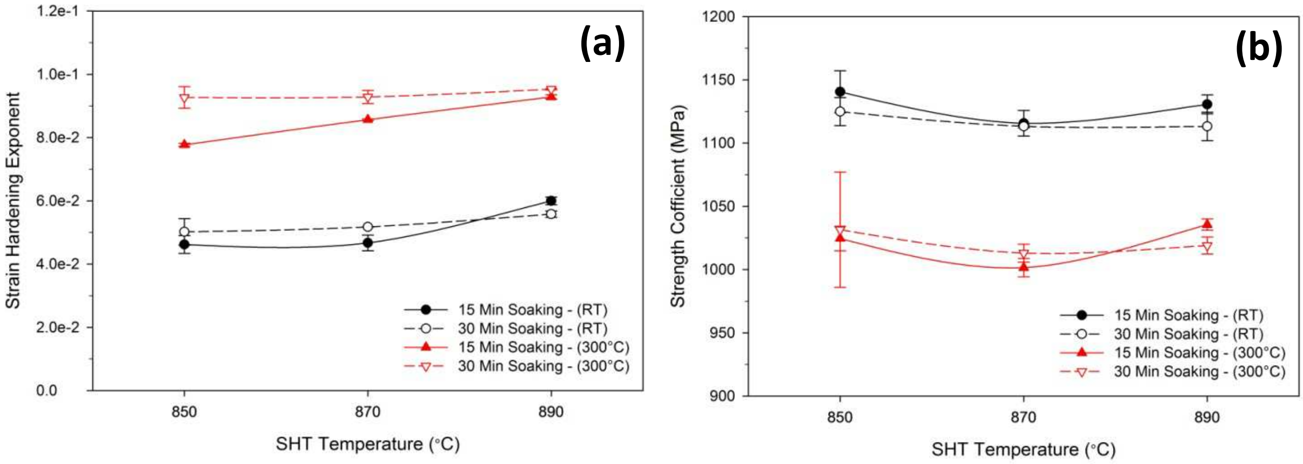

Figure 4.15: Influence of SHT parameters on the Hollomon's strain hardening parameters of Zr-2.5Nb alloy. Plots show the variation of (a) strain hardening exponent, and (b) strength coefficient of Zr-2.5Nb alloy under different solution heat treated conditions.

Therefore, in summary, during SHT, variation of soaking temperature within 850-890°C regime and soaking duration within 15-30 min domain insignificantly influenced the tensile properties of Zr-2.5Nb alloy. Furthermore, with increase in soaking duration from 15-30 min, the dependency of most of the tensile properties on soaking temperature within 850-890°C domain decreased. Such dependencies of different tensile properties on the soaking temperature can be seen in Figure 4.16. The dependency parameters in Figure 4.16 were calculated as follows;

$$\text{SHT Temperature Dependency of } P_i = \frac{P_{i\,(850°C)} - P_{i\,(890°C)}}{P_{i\,(850°C)}} \times 100 \tag{4.4}$$

In Equation 4.4, P_i represents the ith tensile property of the solution heat treated material and $P_{i\,(850°C)}$ & $P_{i\,(890°C)}$ respectively represent the ith property of solution heat treated material soaked at 850 & 890°C.

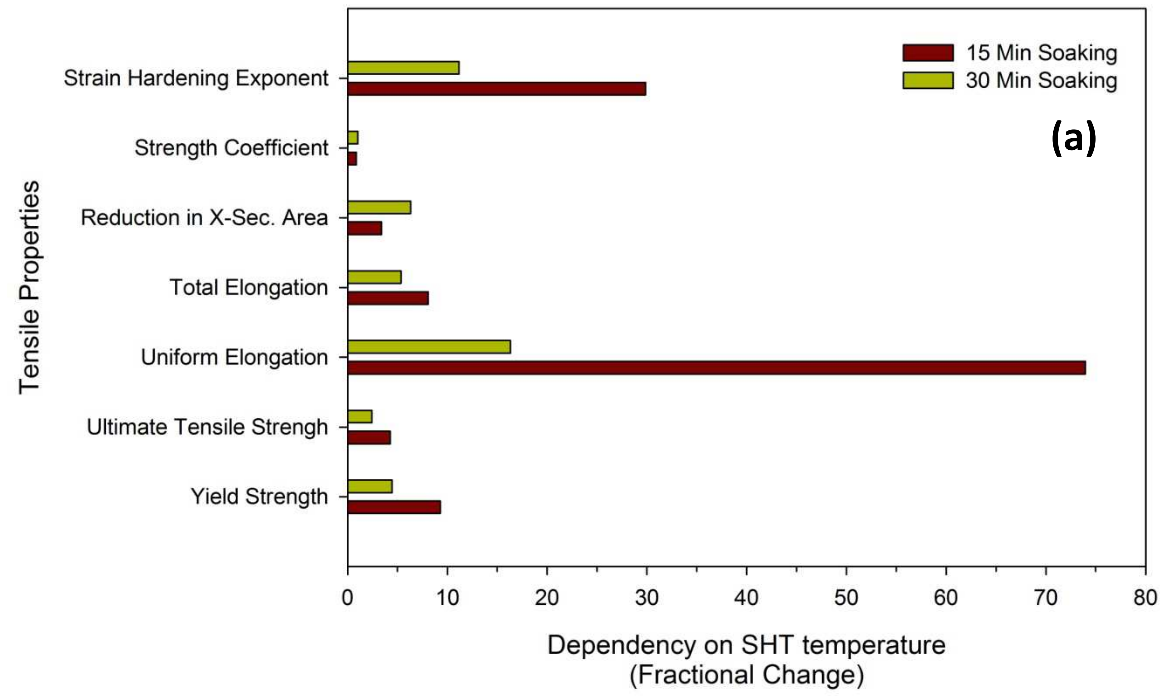

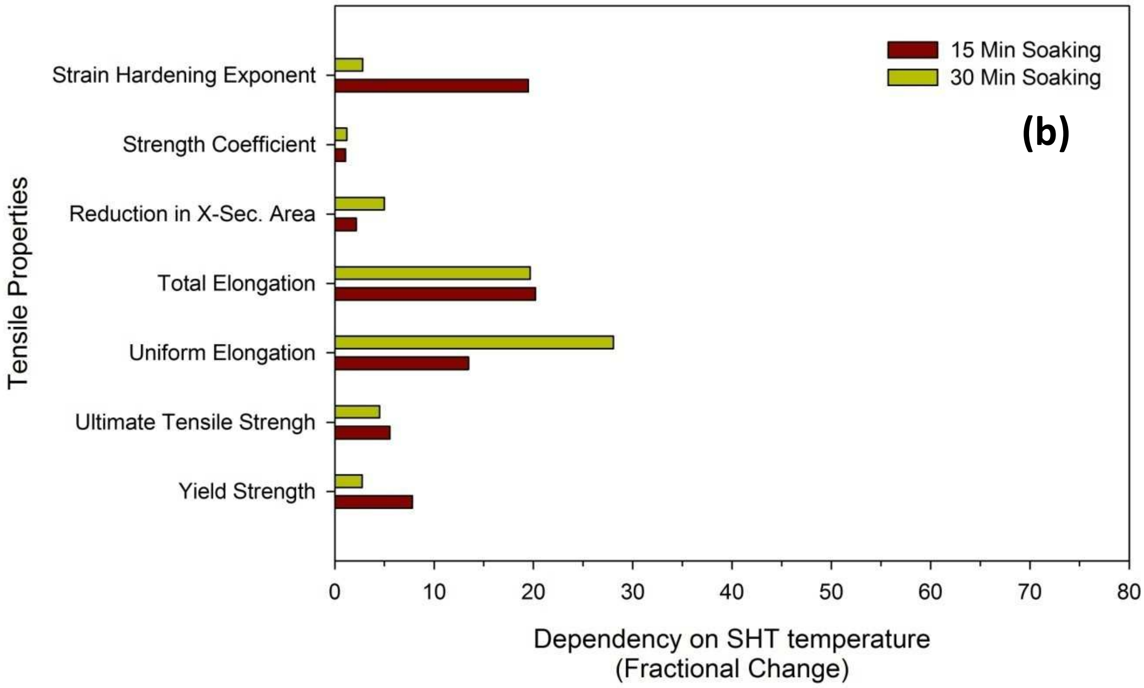

Figure 4.16: Dependency of different tensile properties on the soaking temperature within 850-890°C domain for 15 and 30 min soaked conditions. Plots (a) and (b) respectively show the dependency at RT and 300°C. Here, the dependence of tensile properties within 850-890°C soaking temperature regime was determined using Equation 4.3.

4.2.3 Fracture Toughness Parameters

For the evaluation of fracture toughness parameters of Zr-2.5Nb alloy under different solution heat treated conditions, C(T) specimens having 17 mm width and 3.17 mm thickness were used. During testing, crack growth in the specimen was monitored using the DCPD technique [103]. The details of specimen preparation stages, specimen grinding & fatigue pre-cracking and the fracture testing procedure are described in Section 3.6.2 (IV), Chapter 3.

I. Test Raw Data

Figure 4.17 shows the raw data obtained after the fracture testing of one of the solution heat treated materials. The raw data comprised the time dependent load, load line displacement (LLD) and DCPD signals. The DCPD signal comprised three notable regions: initial LLD independent region (lying within the initial linear region of load-LLD plot), followed by the two successive higher slope regions. In contrast to ambient condition, the DCPD-LLD curve at 300°C, had relatively lower slope, which thereby indicates that the material's crack growth resistance increased with temperature.

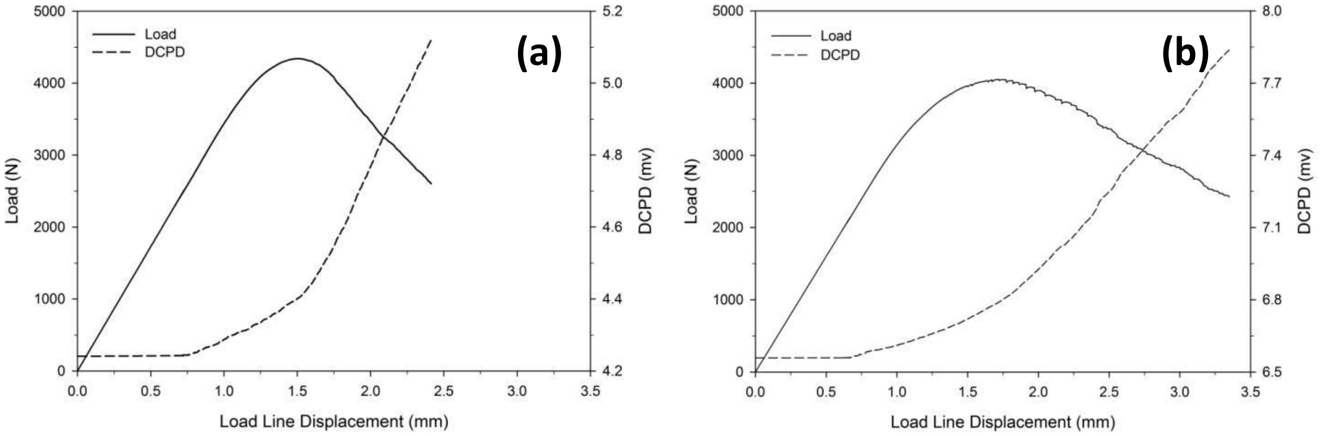

Figure 4.17: Typical raw data of the fracture test (plots of load vs. load line displacement, in solid lines and DCPD vs. load line displacement, in dashed lines) performed at (a) RT and (b) 300°C.

II. *J-R* Curve Analysis

A. Resistance Curve Test Method

The schematic illustration of the *J-R* curve analysis procedure recommended by ASTM E1820-11 standard (using Resistance Curve Test Method) for the evaluation of fracture toughness parameters for one of the solution heat treated materials is shown in Figure 4.18. In contrast to ambient condition (Figure 4.18 (a)), the *J-R* curve (as shown by the hollow circles) exhibited higher slope at 300°C (Figure 4.18 (b)), which indicates increase in crack growth resistance with temperature.

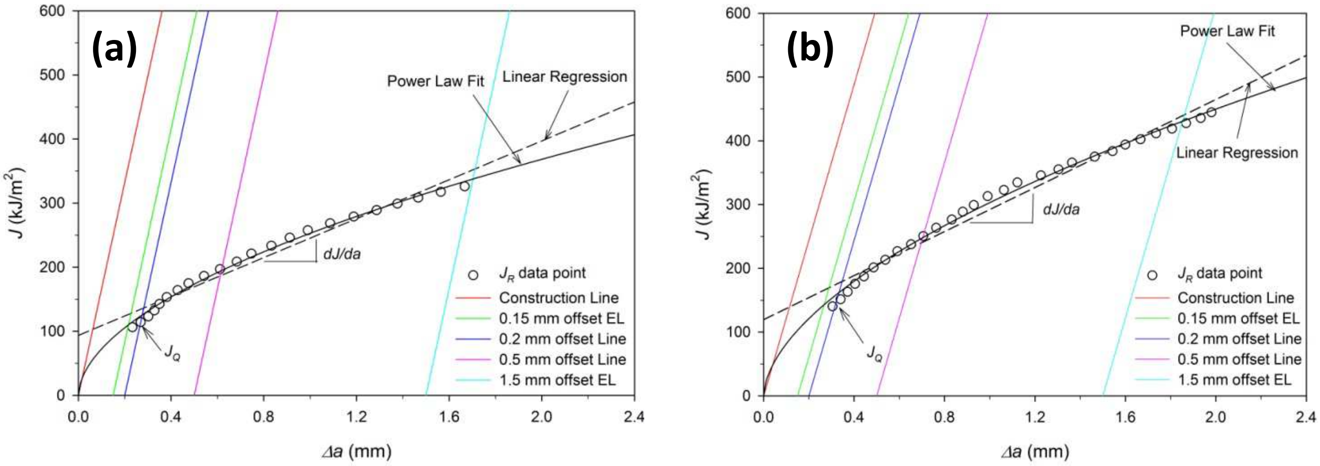

Figure 4.18: Schematic illustration of the *J-R* curve analysis procedure for the evaluation of fracture toughness parameters for one of the solution heat treated Zr-2.5Nb alloy. Plots (a) and (b) represent the *J-R* curve analysis using data obtained from tests performed at RT and 300°C respectively.

i. Fracture Resistance (J-R) Curves

The lower bound fracture resistance behavior of Zr-2.5Nb alloy under six solution heat treated conditions is illustrated in Figure 4.19. Variations of SHT parameters do not cause drastic difference on the lower bound fracture resistance, *J-R* curves of water quenched Zr-2.5Nb alloy. Nevertheless, at RT, for 15 min soaking at SHT temperature, the *J*-values for a given LLD marginally shifts to higher values with increase in SHT temperature. For 30 min soaking, the *J*-values for a given LLD are comparable for 850 and 870 and higher for 890°C condition. Thus, 890°C condition shows higher lower bound *J*-values for both 15 and 30 min soaking, which is good as the higher resistance requirement is more important at RT. Increase in test temperature from RT to 300°C caused substantial improvement in the *J*-values at a given LLD value, which therefore suggests the improved fracture resistance of solution heat treated Zr-2.5Nb alloys at elevated test temperature, Figure 4.19 (b).

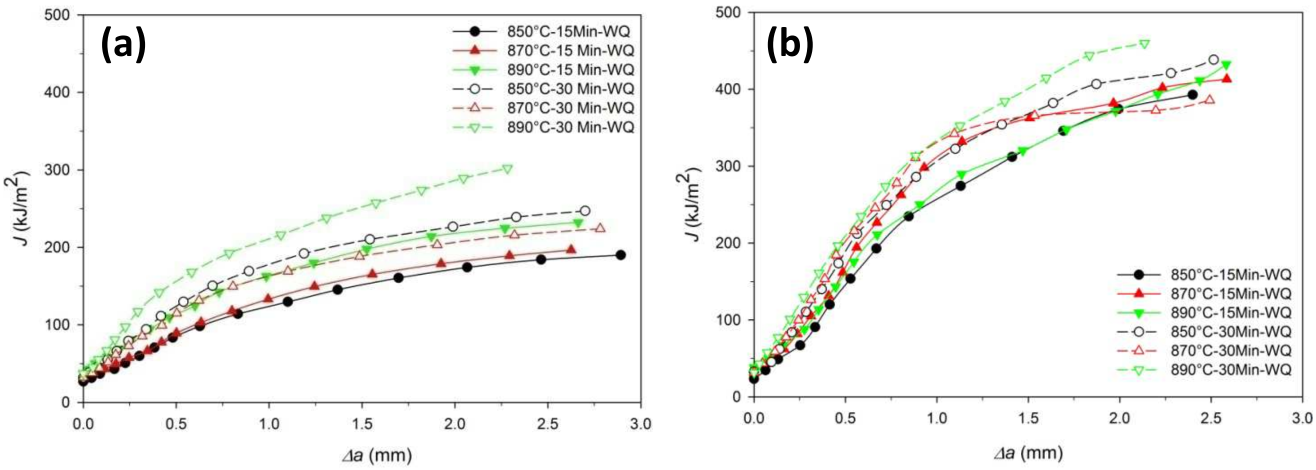

Figure 4.19: Influence of SHT parameters on the fracture resistance, *J-R* curves of Zr-2.5Nb alloy; (a) Plot of lower bound *J-R* curves under different SHT conditions at RT, (b) corresponding plot at 300°C.

ii. *Initiation Toughness, J_Q parameter*

Figure 4.20 shows the influence of SHT parameters on the initiation toughness of Zr-2.5Nb alloy. Under ambient condition, the linear fit suggests that the initiation toughness had weak dependence on the SHT temperature and soaking duration. Increasing temperature from RT to 300°C caused considerable improvement in the initiation toughness. Also, at 300°C, the initiation toughness exhibited considerable scatter. At 300°C, materials soaked for 15 min duration had practically independent initiation toughness with SHT temperatures. Materials soaked for longer duration (30 min) during SHT showed improvement in the initiation toughness (by 15-20%). These materials had dependence of initiation toughness with SHT temperatures, as per the linear trend, increasing SHT temperature from 850-890°C resulted in decrease in toughness.

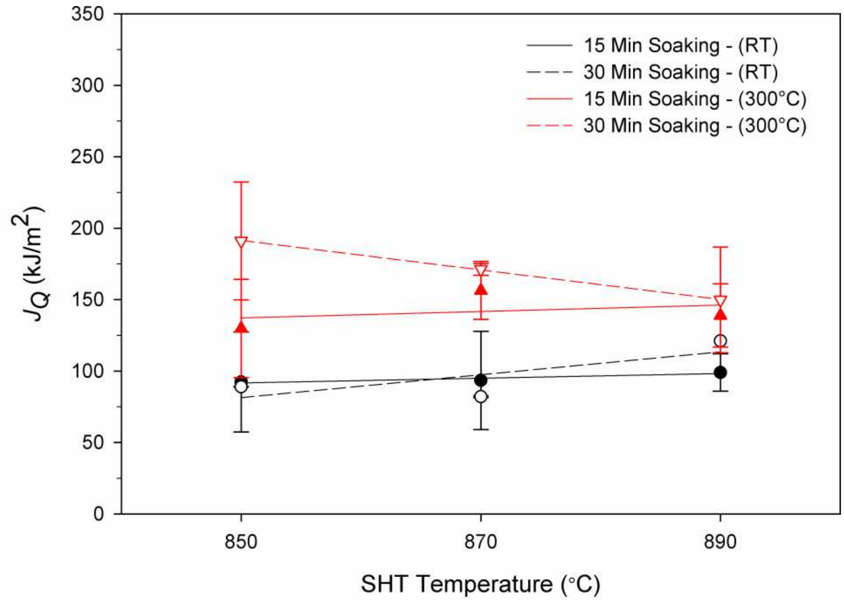

Figure 4.20: Influence of SHT parameters on the initiation fracture toughness, J_Q of Zr-2.5Nb alloy.

iii. Propagation toughness, $J_{F(max)}$ Parameter

As discussed earlier, $J_{F(max)}$ parameter represents the magnitude of J parameter corresponding to the point of maximum load during the test and hence is one of the propagation toughness parameters. Figure 4.21 shows the influence of SHT parameters on the $J_{F(max)}$ parameter of Zr-2.5Nb alloy. The linear fit suggests that under ambient condition, the $J_{F(max)}$ parameter was weakly dependent on the SHT temperature and soaking duration. With increase in temperature from RT to 300°C, the $J_{F(max)}$ parameter showed considerable improvement (by ~50%). At 300°C, materials, especially soaked at lower SHT temperatures, showed improvement in $J_{F(max)}$ parameter with increase in soaking duration.

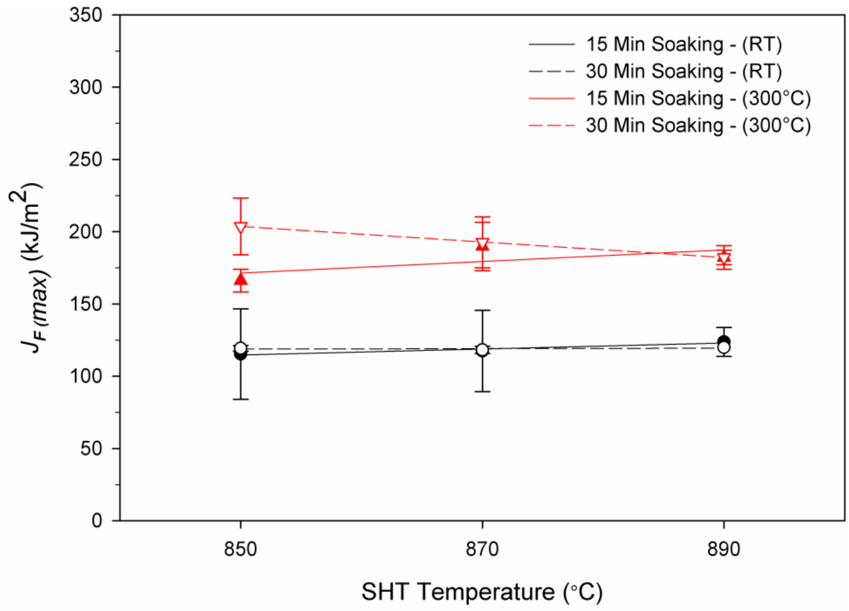

Figure 4.21: Influence of SHT parameters on the propagation toughness, $J_{F(max)}$ parameter of Zr-2.5Nb alloy.

iv. Propagation toughness (dJ/da Parameter)

The *dJ/da* parameter represents the slope of qualified region of the *J-R* curve, and therefore is another propagation toughness parameter. Figure 4.22 shows the influence of SHT parameters on the *dJ/da* parameter of Zr-2.5Nb alloy. Here again, the linear trend suggests that under ambient condition, the *dJ/da* parameter had weak dependence on the SHT temperature and soaking duration. Increasing temperature from RT to 300°C caused considerable improvement in the *dJ/da* parameters. At 300°C, the trend shows slight dependence on SHT temperature; as with increase in SHT temperature, *dJ/da* exhibited slight improvement. Furthermore, at 300°C test temperature, increasing soaking duration from 15-30 min at individual SHT temperature resulted in the consistent improvement in *dJ/da* parameters.

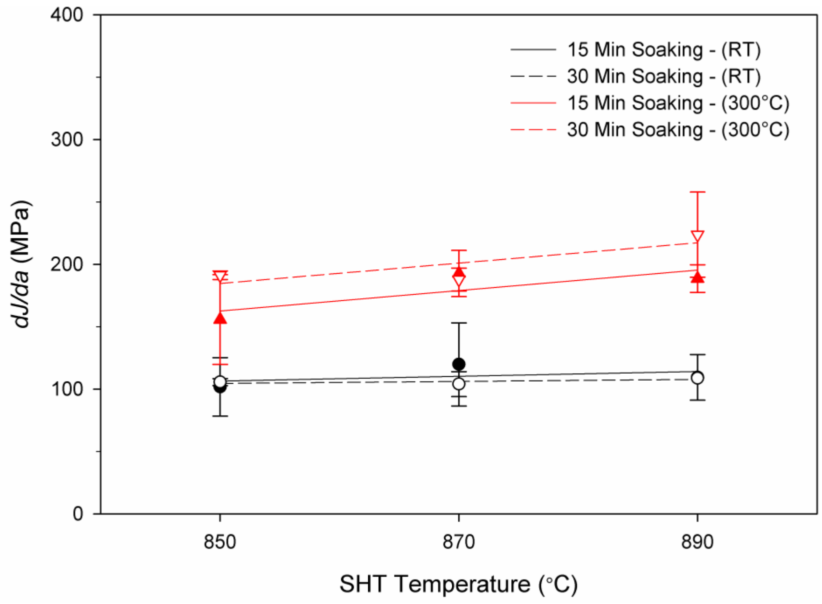

Figure 4.22: Influence of SHT parameters on another propagation toughness, parameter, *dJ/da* of Zr-2.5Nb alloy.

Therefore, in summary, the fracture toughness parameters of Zr-2.5Nb alloy had weak dependence on SHT parameters, especially under ambient condition. However, a longer soaking at a particular SHT temperature during SHT resulted in the improvement in fracture toughness parameters, especially at 300°C.

B. Basic Test Method

One of the major novelty of the current evaluation approach is in the determination of fracture toughness parameters using BT method (the multiple specimen approach) with single specimen data. In order to determine the fracture toughness parameters using BT method, instead of testing multiple equivalent dimension specimens for different crack extension levels and constructing the *J-R* curves based on the physically marked crack growth data, the *J-R* curves were constructed based on the crack extension monitored using the single specimen DCPD technique. Therefore, in the present evaluation approach, the multiple specimens based BT methodology is applied as the single specimen method, based on the crack extension data obtained from DCPD technique.

i. *Fracture Resistance (J-R) curves*

For a given crack extension, the BT method, in contrast to RC method estimates higher *J* parameter, resulting in the corresponding higher *J-R* curves, as shown in Figures 4.23 and 4.24.

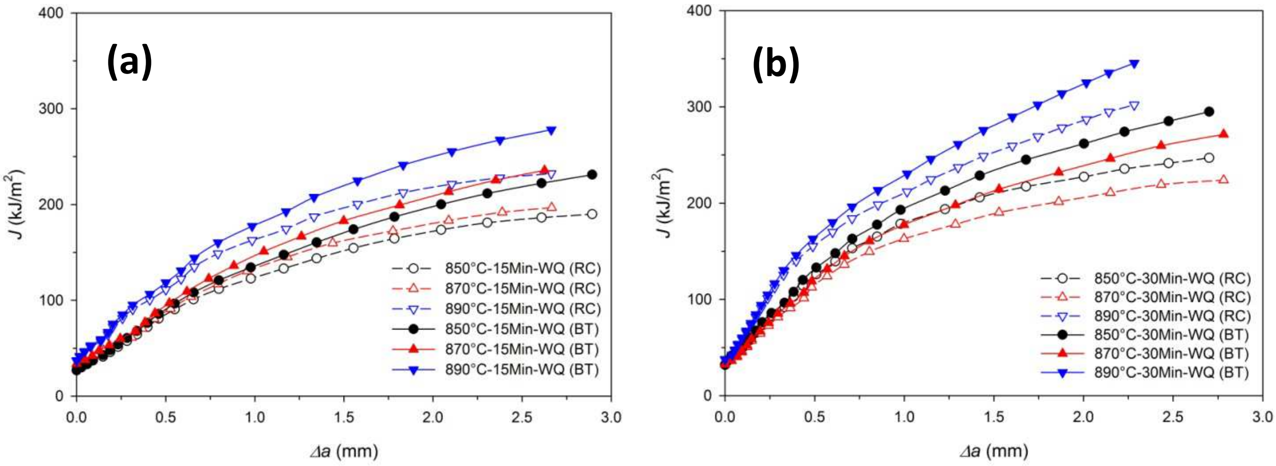

Figure 4.23: Comparison of RT-lower bound *J-R* curves of solution heat treated Zr-2.5Nb alloy, derived using BT and RC methods under (a) 15 min and (b) 30 min SHT soaking conditions.

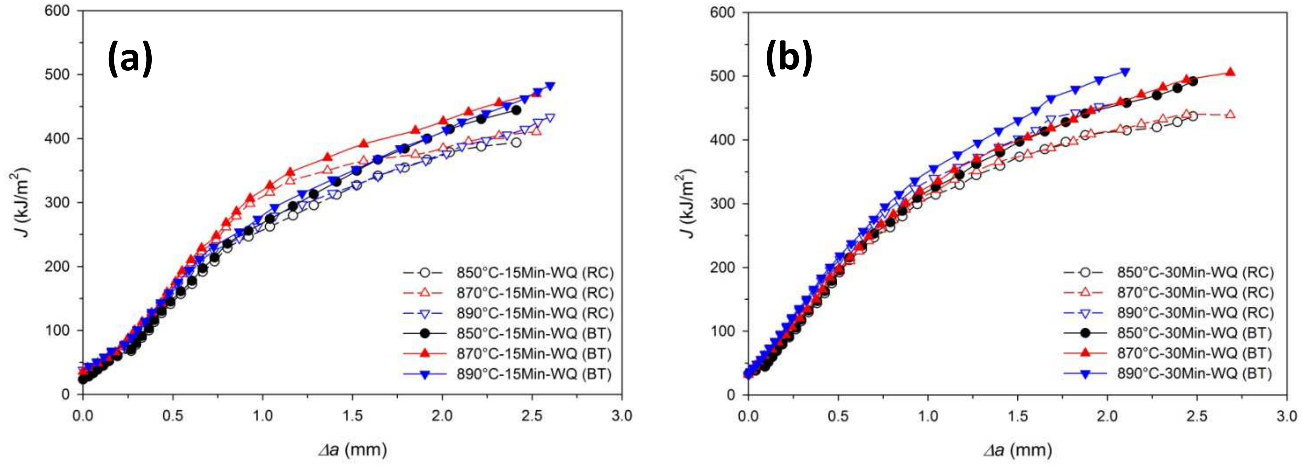

Figure 4.24: Comparison of the lower bound *J-R* curves of solution heat treated Zr-2.5Nb alloy, derived using BT and RC methods at 300°C under (a) 15 and (b) 30 min SHT soaking conditions.

Figure 4.25 shows the deviations in the *J* values as a function of normalized crack lengths. Here, the deviations were calculated as per Equation 4.5.

$$\text{Deviation (in \%)} = \frac{J_{(\frac{ai}{W})_{BT}} - J_{(\frac{ai}{W})_{RC}}}{J_{(\frac{ai}{W})_{RC}}} \times 100 \qquad (4.5)$$

In Equation 4.5, terms $J_{(\frac{ai}{W})_{BT}}$ and $J_{(\frac{ai}{W})_{RC}}$ respectively represent the *J* parameter at i^{th} normalized crack length (a_i/W) derived using BT and RC methods.

The deviations in *J-R* curves derived following these two methods increased with the crack growth, Figure 4.25. For smaller crack extension (*a/W* < ~ 0.54), the deviation in the resistance curves obtained using the two methods were insignificant (< 5%), however with the subsequent crack growth, the deviation increased rapidly. Corresponding to *a/W* of 0.63, the deviation reached to ~20%. With increase in test temperature from RT to 300°C, the deviation in the *J* parameter decreased.

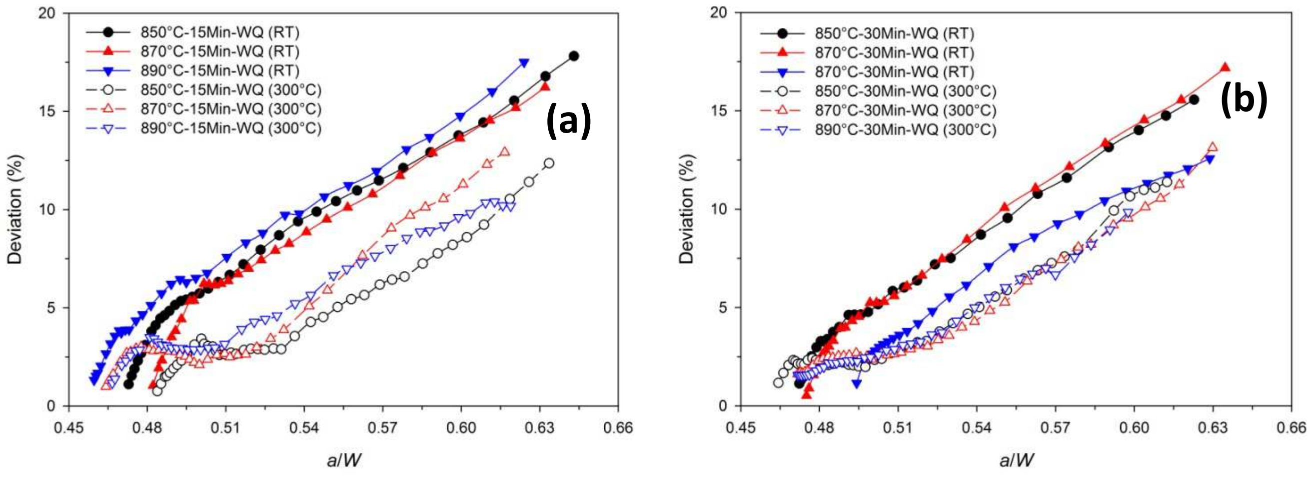

Figure 4.25: Deviations in the *J-R* curves derived using BT and RC methods as a function of crack extension. Plot (a) shows the deviations in the *J-R* curves for 15 min soaked solution heat treated materials and plot (b) shows the corresponding deviation for 30 min soaked materials.

ii. Initiation Toughness

Figure 4.26 shows the comparison of initiation toughness evaluated from the *J-R* curves using BT and RC methods. BT method, in contrast to RC method estimated marginally higher (by < 5%) initiation toughness of the six solution heat treated materials. This deviation was observed to decrease with increase in the test temperature. However, the dependency of initiation toughness on the solution heat treatment parameters; soaking temperature (850-890°C) and soaking duration (15-30 min) remained equivalent to that as shown by the RC method. Similar to RC method, the initiation toughness data derived using the BT method exhibited significant scatter, especially at 300°C.

As summary, the RC method, in contrast to BT method conservatively estimated the initiation toughness under six solution heat treatment conditions. Deviations in initiation toughness data obtained from the two standard approaches were marginal, especially at 300°C test temperature.

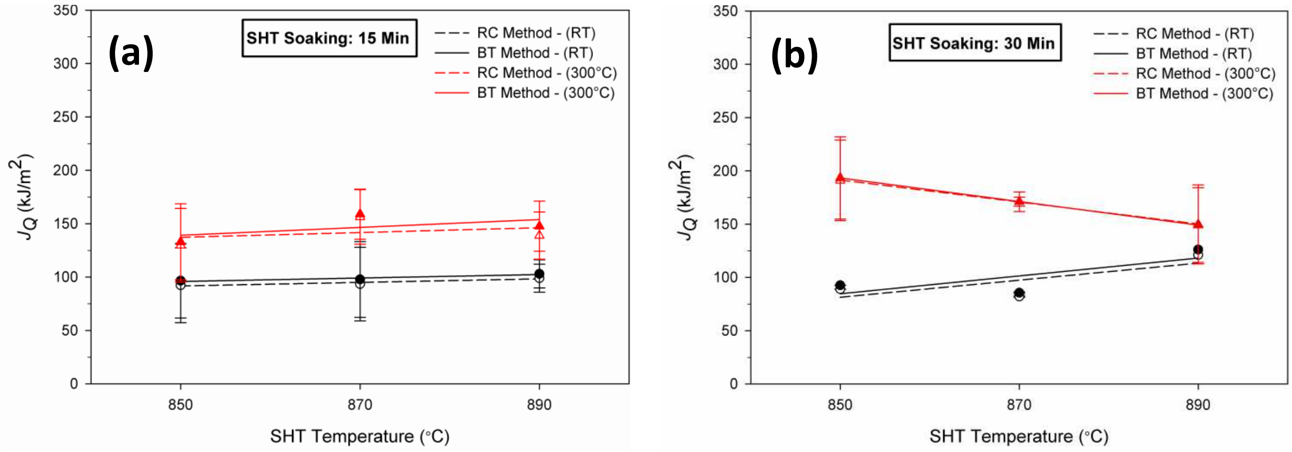

Figure 4.26: Influence of BT and RC methodologies on the initiation toughness, J_Q parameters of (a) 15 and (b) 30 min soaked solution heat treated Zr-2.5Nb alloy.

iii. $J_{F(max)}$ Parameter

Similar to initiation toughness, the $J_{F(max)}$ parameter derived using BT method was found to be marginally higher as compared to the RC method for the six solution heat treatment conditions, shown in Figure 4.27. The corresponding deviations in this parameter were close to 6% under ambient condition and 3% at 300°C. Here again, the BT method showed analogous dependence of $J_{F(max)}$ on SHT parameters, as evaluated by the RC method.

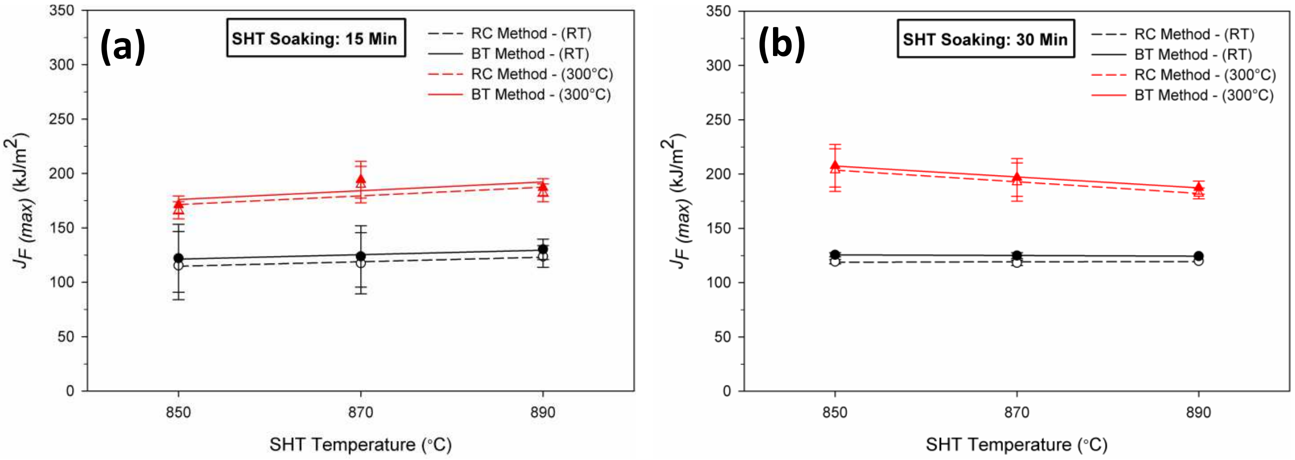

Figure 4.27: Influence of BT and RC methodologies on the propagation toughness $J_{F(max)}$ parameters of (a) 15 and (b) 30 min soaked solution heat treated Zr-2.5Nb alloy.

iv. dJ/da Parameter

In contrast to the earlier discussed initiation toughness (J_Q) and propagation toughness ($J_{F(max)}$) parameters, in which the two DCG approaches have marginal influence on the results, the *dJ/da* parameter showed significant dependency on these evaluation approaches (shown in Figure 4.28). Similar to J_Q and $J_{F(max)}$ parameters, RC method conservatively estimates the *dJ/da* parameter. Under RT and 300°C, the deviation between *dJ/da* parameters obtained from the two methods were respectively ~15 and 8%. The dependency of *dJ/da* on solution heat treatment parameters;

soaking temperature (850-890°C) and soaking duration (15-30 min) remained equivalent to that shown by the RC method.

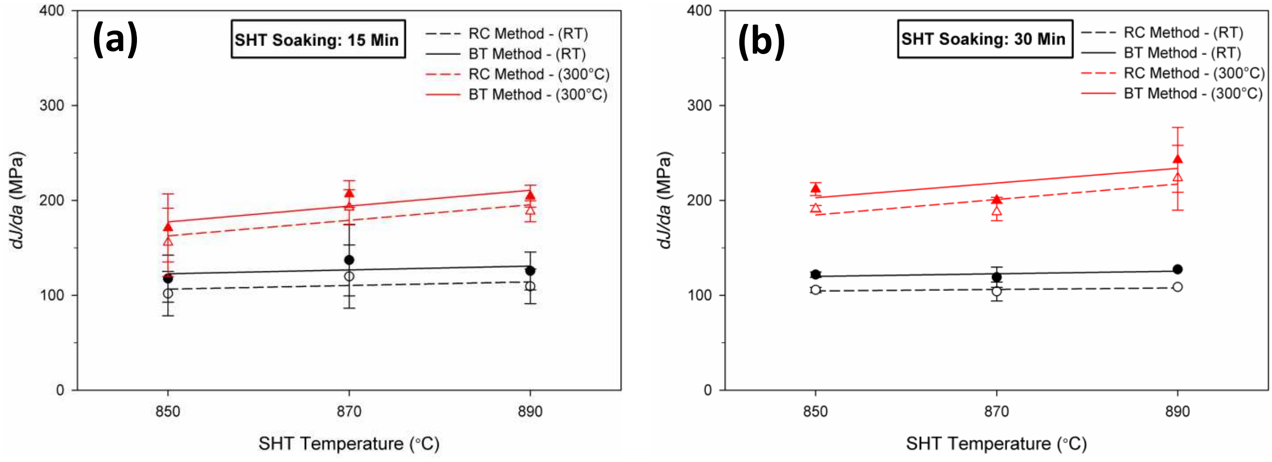

Figure 4.28: Influence of BT and RC methodologies on the propagation toughness *dJ/da* parameters of (a) 15 and (b) 30 min soaked solution heat treated Zr-2.5Nb alloy.

Therefore, in summary, the RC method in contrast to BT method, conservatively estimates the fracture toughness of Zr-2.5Nb alloy under six solution heat treated conditions. Though the recommended evaluation methodologies suggested by the ASTM E1820-11 standard does not have much influence on J_Q and $J_{F(max)}$ parameters, the slope of the resistance curve strongly depends on the method of evaluation.

C. Fracture Toughness Evaluation as per ISO Standard

As discussed in Section 2.5 (c), Chapter 2 that, the major difference between the ASTM and ISO standard procedures lies not only in the expression for *J*, but also in the analysis procedure of the *J-R* curve to determine the fracture toughness parameters. Following sections describe the influence of ASTM and ISO standard procedures on fracture behavior of solution heat treated Zr-2.5Nb alloy.

i. *Fracture Resistance (J-R) Curves*

Comparisons of the ASTM and ISO derived lower bound *J-R* curves of Zr-2.5Nb alloy under six SHT conditions are shown in Figure 4.29 and 4.30 at respective RT and 300°C. The ASTM standard, in contrast to ISO showed conservative estimation of the *J-R* curves. Nevertheless, the deviations between ASTM and ISO derived *J* parameters at a particular crack extension level were marginal, especially at 300°C.

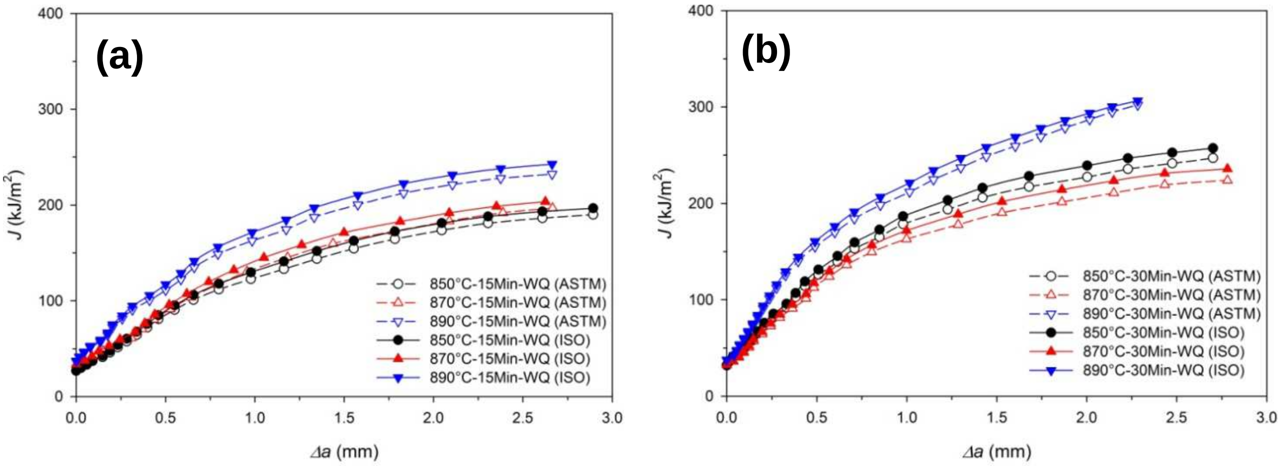

Figure 4.29: Comparison of the ASTM and ISO derived RT-lower bound *J-R* curves of Zr-2.5Nb alloy, solution heat treated for (a) 15 & (b) 30 min soaking durations. As is evident from this figure, for a given crack extension the *J* parameters derived using the ISO method are slightly higher.

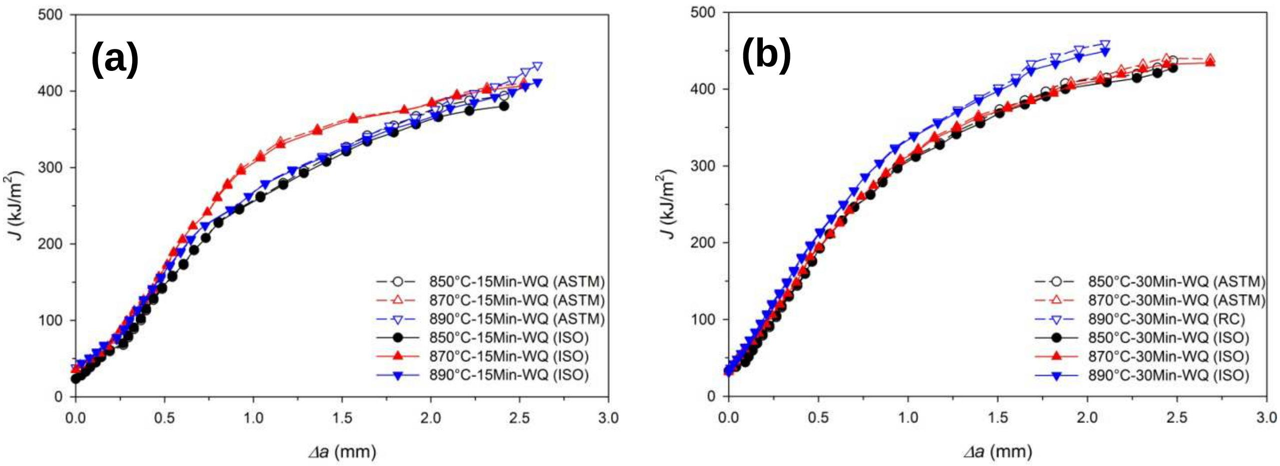

Figure 4.30: Comparison of the ASTM and ISO derived lower bound *J-R* curves at 300°C for Zr-2.5Nb alloy, solution heat treated for (a) 15 & (b) 30 min soaking durations. As is evident from this figure that at a particular crack extension, the *J* parameters are practically independent to the ASTM and ISO standards.

Figure 4.31 shows the deviations in the *J* values as a function of normalized crack lengths. Here, the deviations were computed as per Equation 4.6.

$$\text{Deviation (in \%)} = \frac{J_{(\frac{ai}{W})_{ISO}} - J_{(\frac{ai}{W})_{ASTM}}}{J_{(\frac{ai}{W})_{ASTM}}} \times 100 \qquad (4.6)$$

In Equation 4.6, terms $J_{(\frac{ai}{W})_{ISO}}$ and $J_{(\frac{ai}{W})_{ASTM}}$ respectively represent the *J* parameter at ith normalized crack length (a_i/W) derived using ISO and ASTM procedures.

Under ambient test condition, the deviations in the *J-R* curves initially increased with the crack extension, reached to ~ 6% at *a/W* of ~ 0.55 and later on became almost saturated, see Figure 4.31. In contrast to RT, the magnitudes of deviations in the *J-R* curves derived from the two standards were almost half at 300°C for the six SHT conditions. Similar to RT, at 300°C the magnitude of deviation between the *J* parameter increased marginally within a very small crack extension regime, *a/W* < ~ 0.5. However, with the further crack growth, marginal reduction in the deviations were observed.

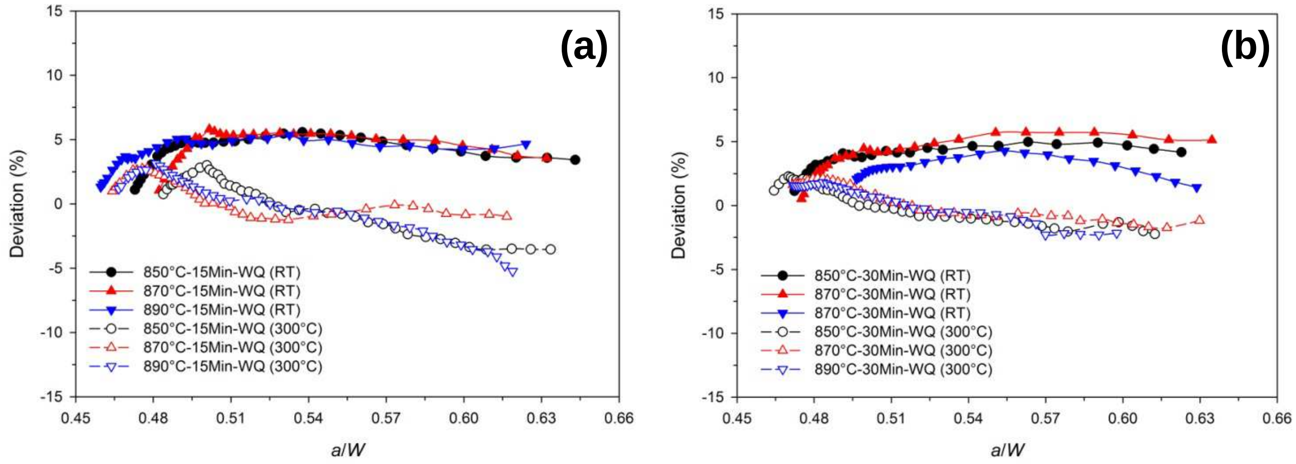

Figure 4.31: Deviation in the *J* parameters derived as per ASTM and ISO standards at different crack extension levels for Zr-2.5Nb alloy solution heat treated for (a) 15 and (b) 30 min soaking durations.

Therefore, the *J-R* curves of the six solution heat treated materials derived as per the ASTM and ISO standards were very close, especially at 300°C.

ii. Initiation Toughness

The initiation toughness of the six solution heat treated materials determined as per ISO standard were found to be less than that determined using the ASTM standard. The difference in the evaluation procedures suggested by the two standards leading to the deviation in the initiation toughness data is shown in Figure 4.32. Under ambient condition, deviation in the J_Q parameters derived using the two standards was < 10%. However, at 300°C, the deviation reached to 30-50% (Figure 4.33). Nevertheless, the trends of initiation toughness determined from the two standards with the solution heat treatment parameters, soaking temperature and duration were analogous. Therefore, though the deviations in the *J-R* curves derived using the two standards were marginal; the J_Q parameters evaluated from these resistance curves had significant difference.

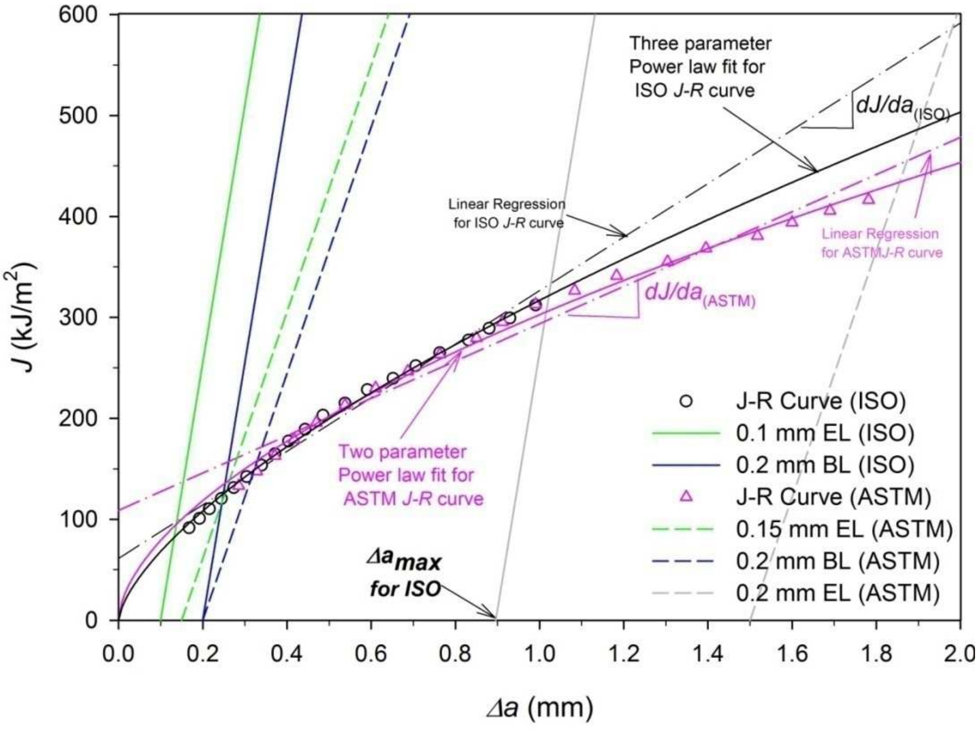

Figure 4.32: Comparison of the evaluation procedures of initiation toughness (J_Q) and propagation toughness (*dJ/da*) parameters suggested by ASTM E1820-11 and ISO 12135:2002 standards.

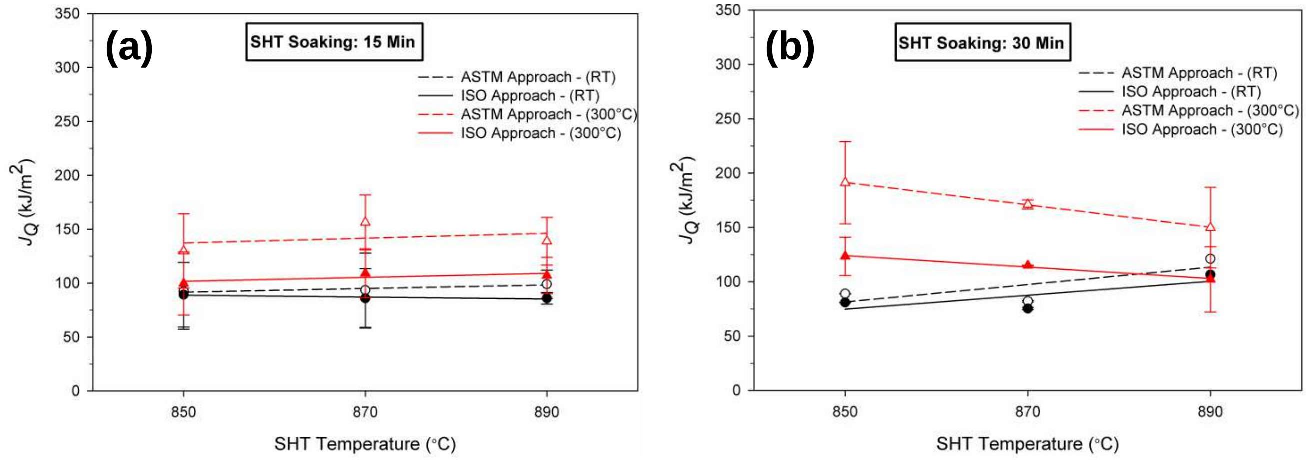

Figure 4.33: Influence of ASTM and ISO evaluation procedures on the initiation fracture toughness parameter (J_Q) of Zr-2.5Nb alloy, solution heat treated from the three soaking temperatures for (a) 15 min and (b) 30 min soaking durations.

Figure 4.34 shows the influence of material’s flow stress on the deviation in ASTM and ISO derived initiation toughness parameters. Here, the normalized difference between ASTM and ISO derived initiation toughness data (i.e., $J_{Q\,ASTM}$ and $J_{Q\,ISO}$ respectively) for the six different solution heat treated conditions determined at both RT and 300°C are simultaneously plotted and compared with respect to corresponding flow stress. The resulting trend suggested that such deviation decreased with increase in material’s flow stress.

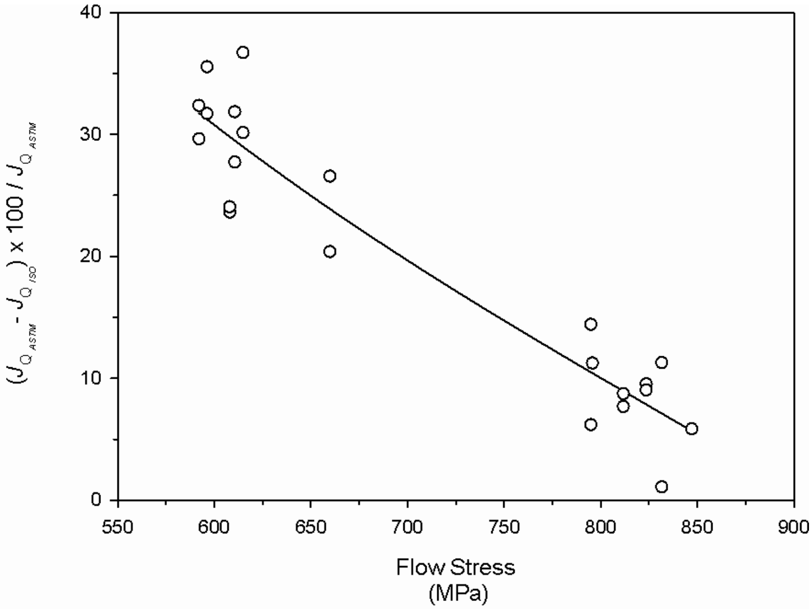

Figure 4.34: Influence of material’s flow stress on the normalized difference between the ASTM and ISO derived initiation toughness parameters.

iii. $J_{F(max)}$ *Parameter*

Unlike initiation toughness, the $J_{F(max)}$ parameters derived using the two standard approaches were almost comparable, especially at 300°C, Figure 4.35. At RT, the ISO derived $J_{F(max)}$ parameters were ~ 5% higher than those derived from the ASTM standard, whereas at 300°C, the deviations became as close as 1%.

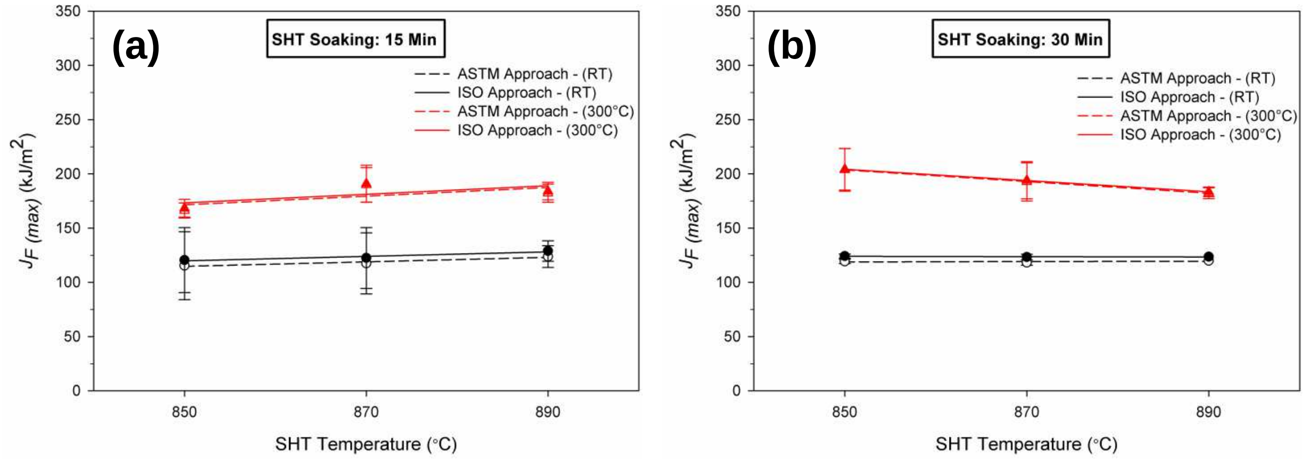

Figure 4.35: Influence of ASTM and ISO evaluation procedures on the $J_{F(max)}$ parameters of Zr-2.5Nb alloy, solution heat treated from the three soaking temperatures for (a) 15 min and (b) 30 min soaking durations.

Therefore, unlike the initiation toughness, the ASTM standard, in contrast to ISO standard conservatively estimates the $J_{F(max)}$ parameter. The marginal deviations observed between the $J_{F(max}$ parameters derived from the two standards are attributed to the insignificant deviations in the *J-R* curves derived as per these standards, as shown in Figures 4.29 and 4.30.

When the entire $J_{F(max)}$ data derived from the two standards at both RT and 300°C were simultaneously compared, the trend (Figure 4.36) suggested that though the deviations were marginal, it increased with the flow stress.

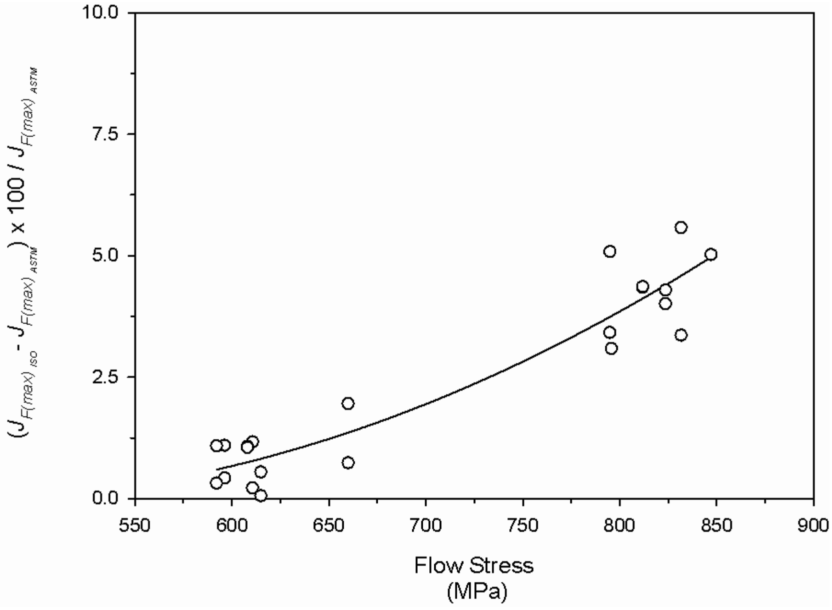

Figure 4.36: Influence of material’s flow stress on the normalized difference between the ASTM and ISO derived $J_{F(max)}$ parameters.

iv. dJ/da Parameter

In contrast to the initiation toughness and $J_{F(max)}$ parameter, the *dJ/da* parameters determined from the two standards exhibited appreciable difference, as shown in Figure 4.37. Similar to $J_{F(max)}$, ASTM standard resulted for the conservative estimation of *dJ/da* parameter. The deviation in the *dJ/da* parameter was observed to be > 50%. Such appreciable difference in the *dJ/da* parameters because of the difference in the analysis procedure of the two standards is illustrated in Figure 4.34.

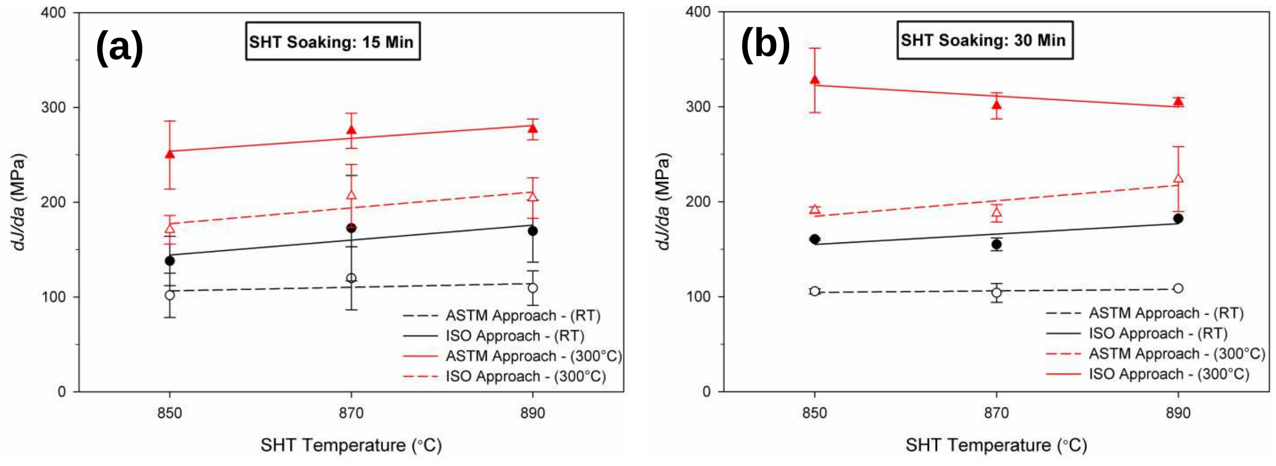

Figure 4.37: Influence of ASTM and ISO evaluation procedures on the *dJ/da* parameters of Zr-2.5Nb alloy, solution heat treated from the three soaking temperatures for (a) 15 min and (b) 30 min soaking durations.

To compare the extent of variations in *dJ/da* parameters derived from ASTM and ISO standards, the normalized difference between *dJ/da* data derived from these standards for the six solution heat treated conditions were simultaneously plotted with respective flow stress values in Figure 4.38. Significant normalized deviations in *dJ/da* parameters obtained by the two methods were practically insensitive to material's flow stress. Nevertheless, as shown earlier in Figure 4.37 that in terms of absolute differences (without normalizing), material tested under ambient condition (having higher strength) showed relatively lower deviations in *dJ/da* parameters.

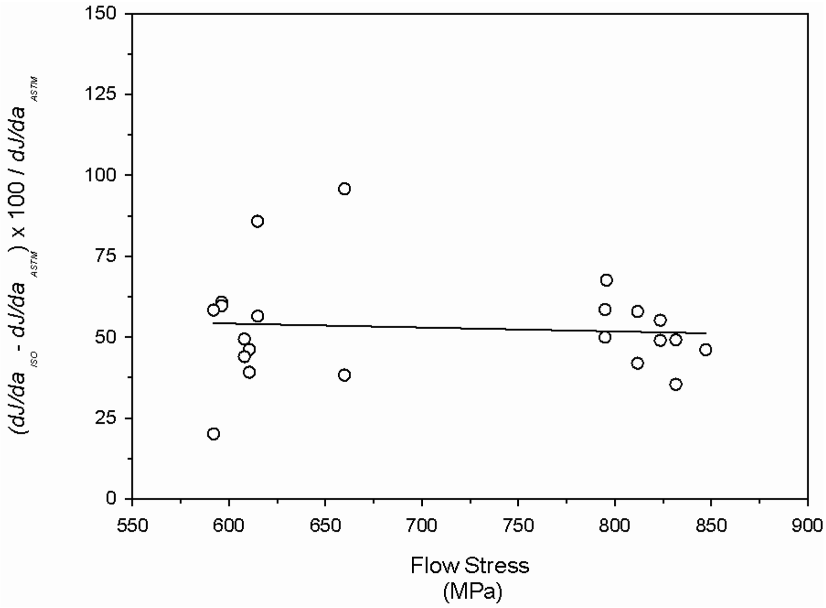

Figure 4.38: Influence of material's flow stress on the normalized difference between the ASTM and ISO derived *dJ/da* parameters.

Therefore, in summary, the *J-R* curves of six heat treated materials derived from the ASTM and ISO standards had marginal deviations. However, fracture toughness parameters (initiation toughness (J_Q) and slope of qualified *J-R* region (*dJ/da*)) derived from these standards had appreciable differences, especially at 300°C.

However, the $J_{F(max)}$ parameter showed practically insensitiveness to these evaluation approaches. Earlier, this parameter has also showed practically insensitiveness to the RC and BT evaluation methodologies. This therefore, emphasizes that the *CCL* parameters of solution heat treated Zr-2.5Nb alloy (which are the function of $J_{F(max}$ parameters, as described in Section 2.5, Chapter 2) will also be practically insensitive to these analysis approaches.

4.3 Study of Fracture Surface

The fracture surfaces of the broken C(T) specimens revealed typical mixed mode failure (mode I & III) comprised of 45^o oriented fracture surfaces, as shown in Figure 4.39. Such 45° oriented surfaces were accompanied by central narrow flat region. The fracture surfaces were broadly classified into the two major categories: uni-planer and bi-planer fracture. In the uni-planer fracture, the specimen failed from one plane, Figures 4.39 (a) & (b), whereas, in case of bi-planer fracture, the specimen failed from the two planes, Figures 4.39 (c) & (d). The fracture surfaces, in case of bi-planer fracture had typical ‘hill & valley’ appearance, as shown in Figure 4.39 (d).

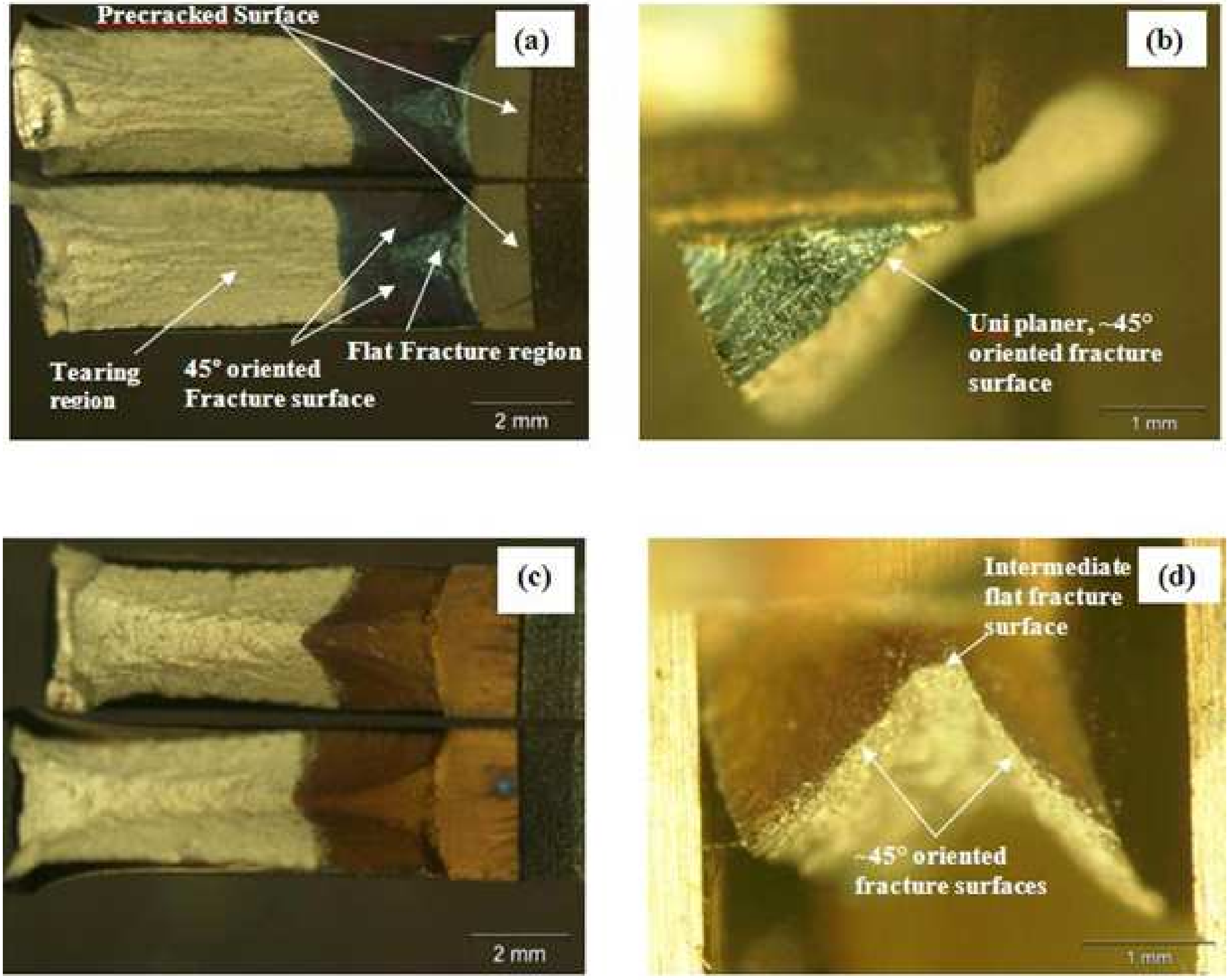

Figure 4.39: Fracture surfaces of solution heat treated Zr-2.5 Nb alloy, illustrating (a) & (b) uni-planner shear failure and (c) & (d) bi-planner shear failure.

Table 4.2 shows the stable crack growth fracture surface areas of the broken C(T) specimens under various solution heat treated conditions. These areas were measured by the image analysis performed using the ‘Image-J’ software. On an average, the total fracture surface areas were ~ 10.8 mm^2 under ambient condition, and marginally lower, ~ 9 mm^2 under 300°C. The intermediate narrow flat region covers ~13-28 % region of the total fractured area. This mixed mode failure suggests that the state of stress ahead of the crack tip was close to plane stress condition, under which, the material in general shows specimen size dependent higher fracture toughness.

Table 4.2: Fracture surface areas of the broken C(T) specimens of Zr-2.5Nb alloy under different solution heat treated conditions.

Soaking Temperature (°C)	**Soaking Duration (Min)**	**Test Temperature (°C)**	**Fracture Surface Area**		
			Total area (mm^2)	***Flat area (mm^2)***	***Fraction flat area (%)***
850	15	25	11.89	1.65	13.91
	15	25	12.57	1.72	13.70
870	15	25	9.05	1.69	18.67
	15	25	11.16	1.36	12.18
890	15	25	9.66	2.28	23.63
	15	25	11.66	1.78	15.29
850	30	25	10.52	2.48	23.57
	30	25	10.82	2.44	22.52
870	30	25	11.03	1.56	14.12
	30	25	11.05	1.57	14.21
890	30	25	10.42	2.59	24.86
850	15	300	9.15	1.73	18.90
	15	300	9.54	1.83	19.16
870	15	300	8.93	1.82	20.42
	15	300	9.08	2.52	27.75
890	15	300	7.93	1.87	23.63
	15	300	8.94	1.82	20.35
850	30	300	8.33	1.88	22.59
	30	300	7.53	2.13	28.22
870	30	300	9.10	1.77	19.47
	30	300	11.94	1.97	16.49
890	30	300	9.23	1.76	19.09
	30	300	8.76	1.94	22.18

In order to ensure the specimen size independent and lower bound fracture toughness, the plane strain state of stress must prevail ahead the crack tip. For such plane strain condition, the specimen’s thickness must exceed a critical value. According to the ASTM E1820-11 standard

[78], in order to attain the plane strain condition, following specimen thickness criteria must satisfy.

$$B > \frac{25 \times J_Q}{\sigma_Y} \tag{4.7}$$

In Equation 4.7, B represents the specimen thickness, J_Q is the initiation fracture toughness, and σ_Y is the material's flow stress along the loading direction in the fracture test.

Table 4.3 lists the critical specimen thickness required to achieve the plane strain condition for Zr-2.5Nb alloy under six solution heat treated conditions. Under ambient condition, in majority of cases, this critical thickness was lower than the used 3.17 mm thickness. However, under 300°C fracture condition, the critical thickness increased appreciably and found to be much higher than the used thickness.

Table 4.3: Critical specimen thickness required to satisfy plane strain condition in C(T) specimens (as suggested by ASTM E 1820-11 standard, Equation 4.7) for Zr-2.5Nb alloy under six solution heat treated conditions.

S. No.	**SHT Condition**	**Minimum specimen thickness required for plane strain condition (mm)**	
		RT	**300°C**
1	850°C-15Min-WQ	1.69	4.92
2	870°C-15Min-WQ	2.81	6.40
3	890°C-15Min-WQ	3.11	5.71
4	850°C-30Min-WQ	2.70	7.77
5	870°C-30Min-WQ	2.53	7.17
6	890°C-30Min-WQ	3.80	5.78

4.3.1. SEM Fractography

I. Pre-cracked Surface

Visually, the fatigue pre-cracked surfaces exhibited typical shiny and flat appearence (as shown in Figure 4.39). The SEM fractography revealed several plateaus presented on the pre-cracked surface, over which the fatigue crack propagated, as shown in Figure 4.40. Most of these plateaus were oriented along the direction of crack propagation. In addition, the fracture surfaces exhibited some micro-cracks, oriented at ~ 45° angle to the crack growth direction.

II. Fracture Surface

The fractographic features of the broken C(T) specimens of Zr-2.5Nb alloy under six solution heat treated conditions are shown in Figures 4.41-4.44. The fracture surfaces showed typical dimple structure characteristic of a ductile failure, signifying the operating fracture mechanism was micro-void coalescence. On the basis of morphology, the observed dimples fell into the two categories; dimples having marginally parabolic (elongated) shape and dimples having equiaxed shape. On the 45° oriented fracture surface, the major axes of the parabolic dimples were along the specimen thickness, especially at 300°C, suggesting the shearing failure on this surface as shown in Figure 4.42. In contrast, on the flat fractured region, the major axes of the parabolic dimples were along the specimen width direction, emphasizing the opening (i.e., tearing) failure on this surface, see Figure 4.44. Most of the parabolic dimples were not completely surrounded by the lips; however, few of them were having oval shape. The existence of these two types of dimples suggests mixed mode failure (mode-I & III) of these materials. The dimples had in-homogeneity in terms of their sizes and therefore suggested the non uniform distribution of their nucleation sites. Under ambient fracture condition, the dimples had sizes ranging from < ~ 1 µm to as big as ~ 6 µm. The fracture at 300°C temperature resulted in the formation of relatively bigger and deeper dimples, having size in-homogeneity ranging from ~ 2 µm to as long as ~ 30 µm. In addition, these dimples, in contrast to those formed at ambient condition contained typical deformation markings on their walls. The bigger & deeper dimple size and the deformation markings on its walls are the characteristic features of the considerable plastic deformation of a material [103,104]. The observed increase in dimple size with test temperature suggests that the number of nucleation sites decreases and the spacing among them increases with test temperature. Because of this, after nucleation, the void has to grow considerably before its coalescence with the nearest growing void. The higher crack growth resistance shown by Zr-2.5Nb alloy under six solution heat treated conditions at 300°C, in contrast to ambient condition, can be seen as the consequence of such reduction in the void nucleation sites and increase in the spacing among them.

III. Stretched Zone Ahead of Pre-cracked Region

During testing, material ahead of pre-cracked tip in C(T) specimen deforms plastically before getting fractured. Therefore, before the crack starts to propagate, material ahead the pre-cracked region undergoes certain stretching, leading in the formation of a distinguished zone ahead pre-cracked region, which is called ‘Stretched Zone’. Figures 4.45 and 4.46 shows the stretched zones ahead of pre-cracked regions in Zr-2.5Nb alloy under six solution heat treated conditions tested at RT and 300°C respectively. Under ambient test condition, SHT parameters did not show any significant influence on the streched zone widths (SZWs) of Zr-2.5Nb alloy. At this condition, average SZWs were ranging between 45-67 µm. Nevertheless, at 300°C fractured condition, the materials soaked for 30 min duration, in contrast to 15 min during SHT, exhibited relatively wider stretched zones.

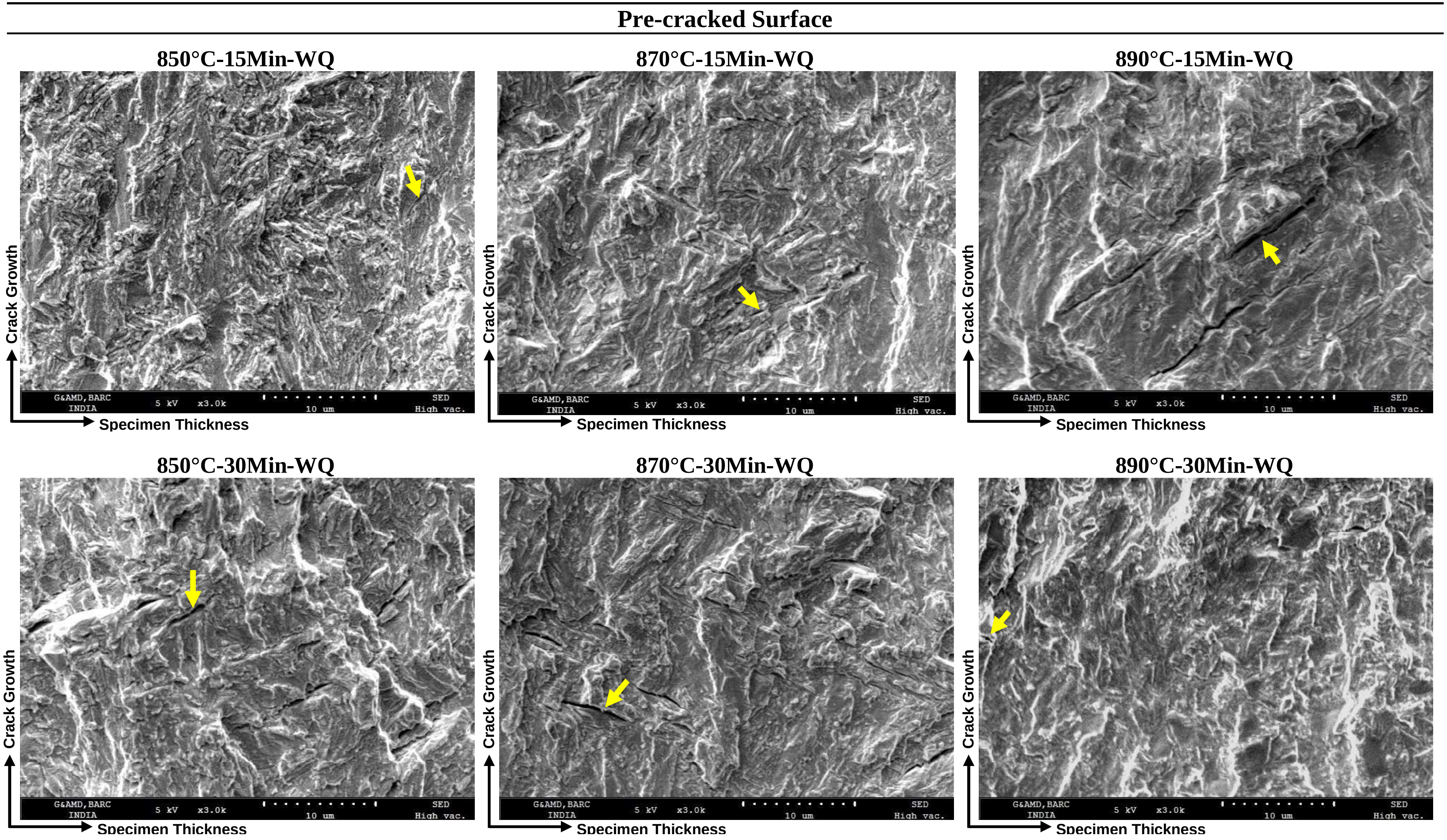

Figure 4.40: SEM fractographs illustrating the fatigue pre-cracked surfaces of the broken C(T) specimens in six solution heat treated conditions (mentioned above the fractographs). The arrow marked on the individual fractograph points towards the micro-crack, oriented at typically ~45° to the crack growth direction.

45° Oriented Fracture Surfaces Demonstrating Fracture at RT

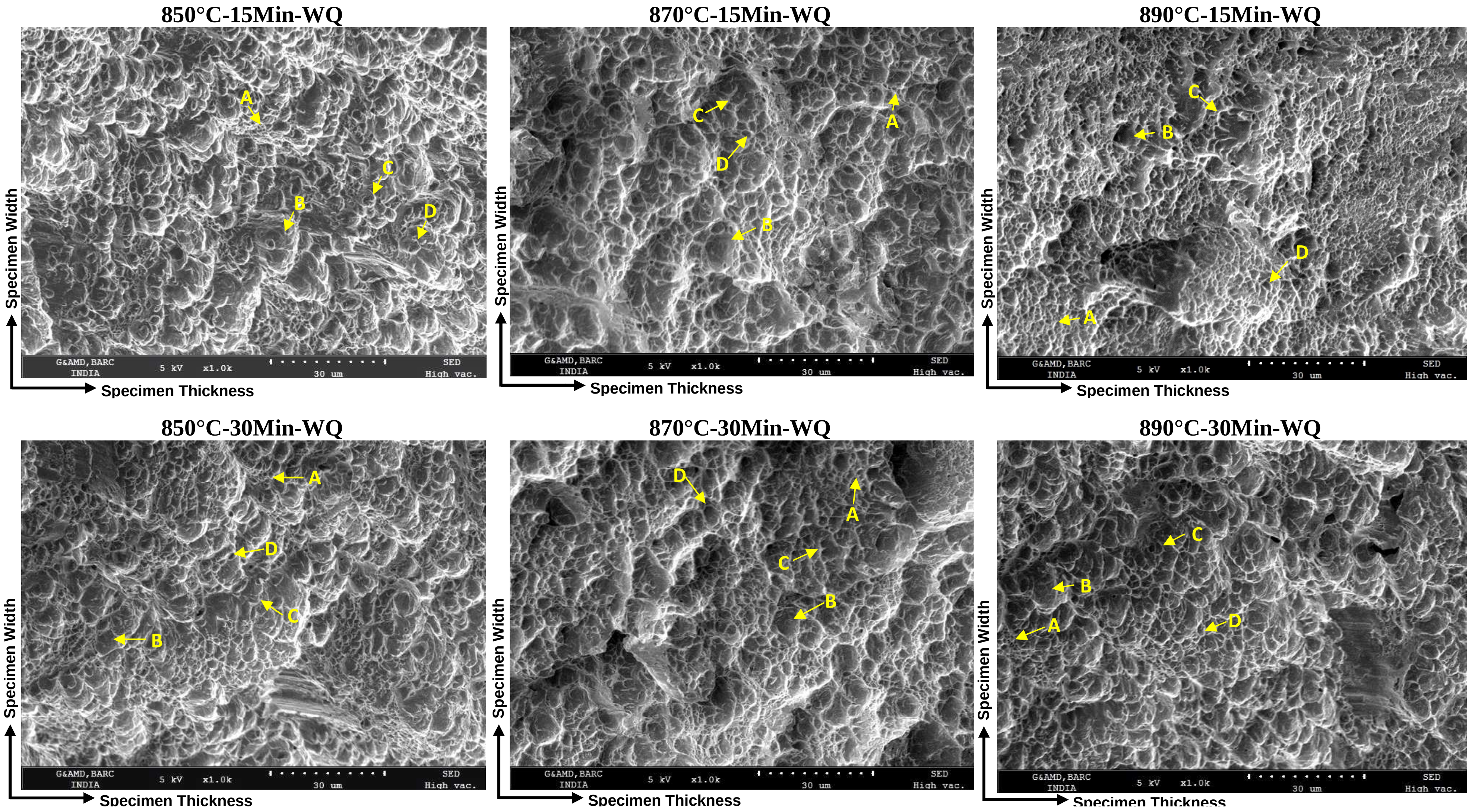

Figure 4.41: SEM fractographs illustrating the inclined fracture surfaces of the broken C(T) specimens in six solution heat treated conditions (mentioned above the fractographs), tested under ambient condition. Distinguished fracture features are indicated by the arrows. Feature A shows the fine size dimple, B shows the big dimple, C shows the dimple, not completely surrounded by its lip and D shows the dimple having oval shape.

45° Oriented Fracture Surfaces Demonstrating Fracture at 300°C

850°C-15Min-WQ **870°C-15Min-WQ** **890°C-15Min-WQ**

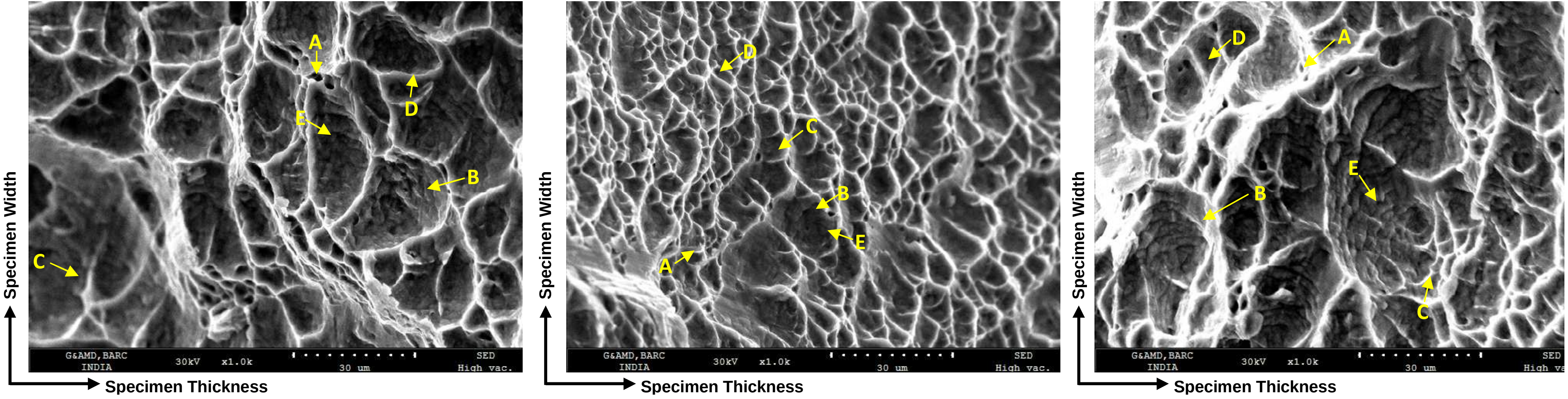

850°C-30Min-WQ **870°C-30Min-WQ** **890°C-30Min-WQ**

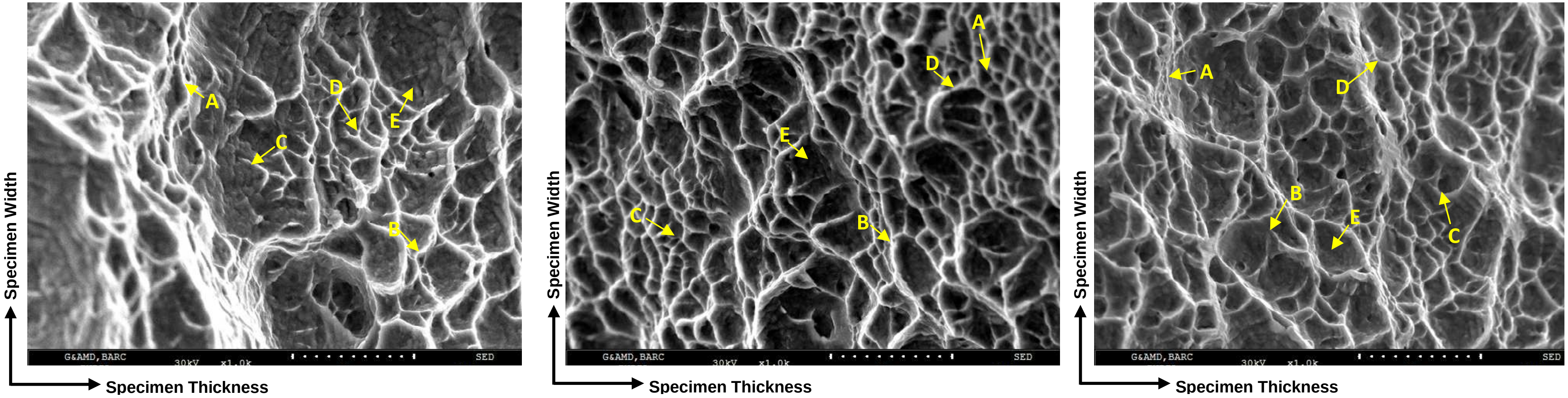

Figure 4.42: SEM fractographs illustrating the inclined fracture surfaces of the broken C(T) specimens in six solution heat treated conditions (mentioned above the fractographs), tested at 300 °C. Distinguished fracture features are indicated by the arrows. Feature A shows the fine size dimple, B shows the big dimple, C shows the dimple, not completely surrounded by its lip, D shows the dimple having oval shape and E shows typical deformation markings within dimples.

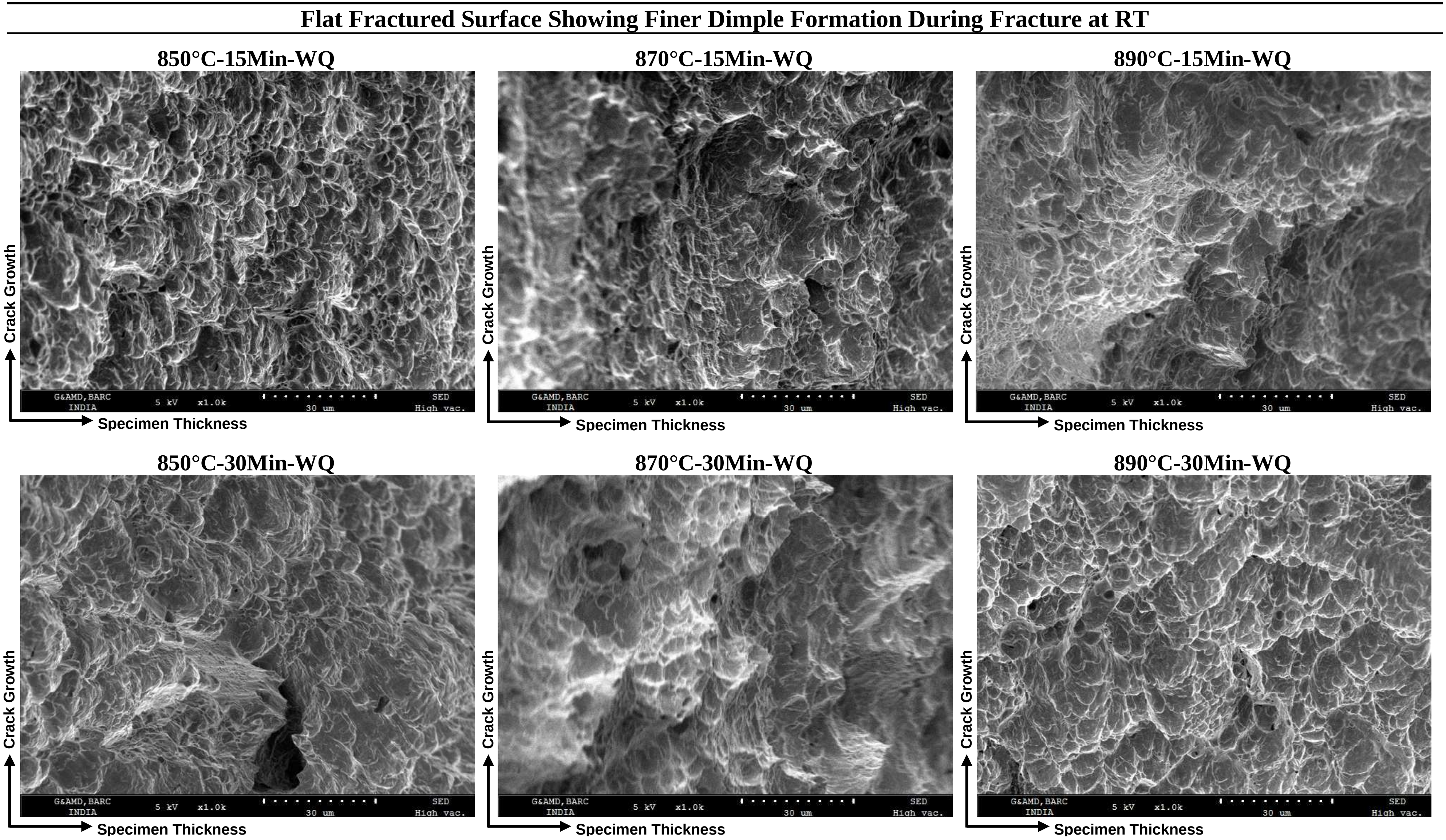

Figure 4.43: SEM fractographs illustrating the flat fractured regions of the broken C(T) specimens in the six solution heat treated conditions, (mentioned above the fractographs), tested under ambient condition.

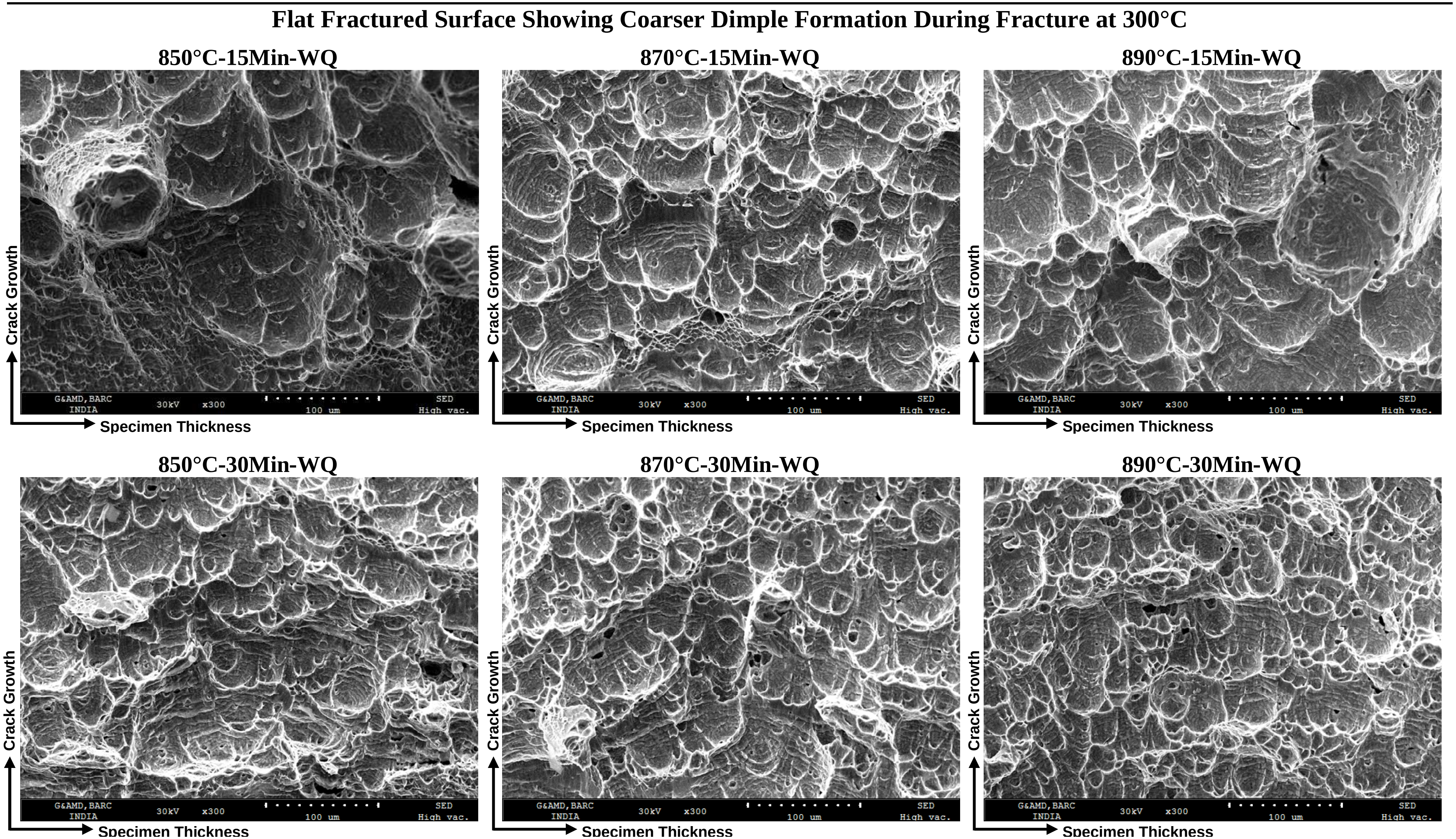

Flat Fractured Surface Showing Coarser Dimple Formation During Fracture at 300°C

850°C-15Min-WQ **870°C-15Min-WQ** **890°C-15Min-WQ**

850°C-30Min-WQ **870°C-30Min-WQ** **890°C-30Min-WQ**

Figure 4.44: SEM fractographs illustrating the flat fractured regions of the broken C(T) specimens in the six solution heat treated conditions, (mentioned above the fractographs), tested at 300°C.

Stretched Zone Formation Ahead of Pre-cracked Region at RT

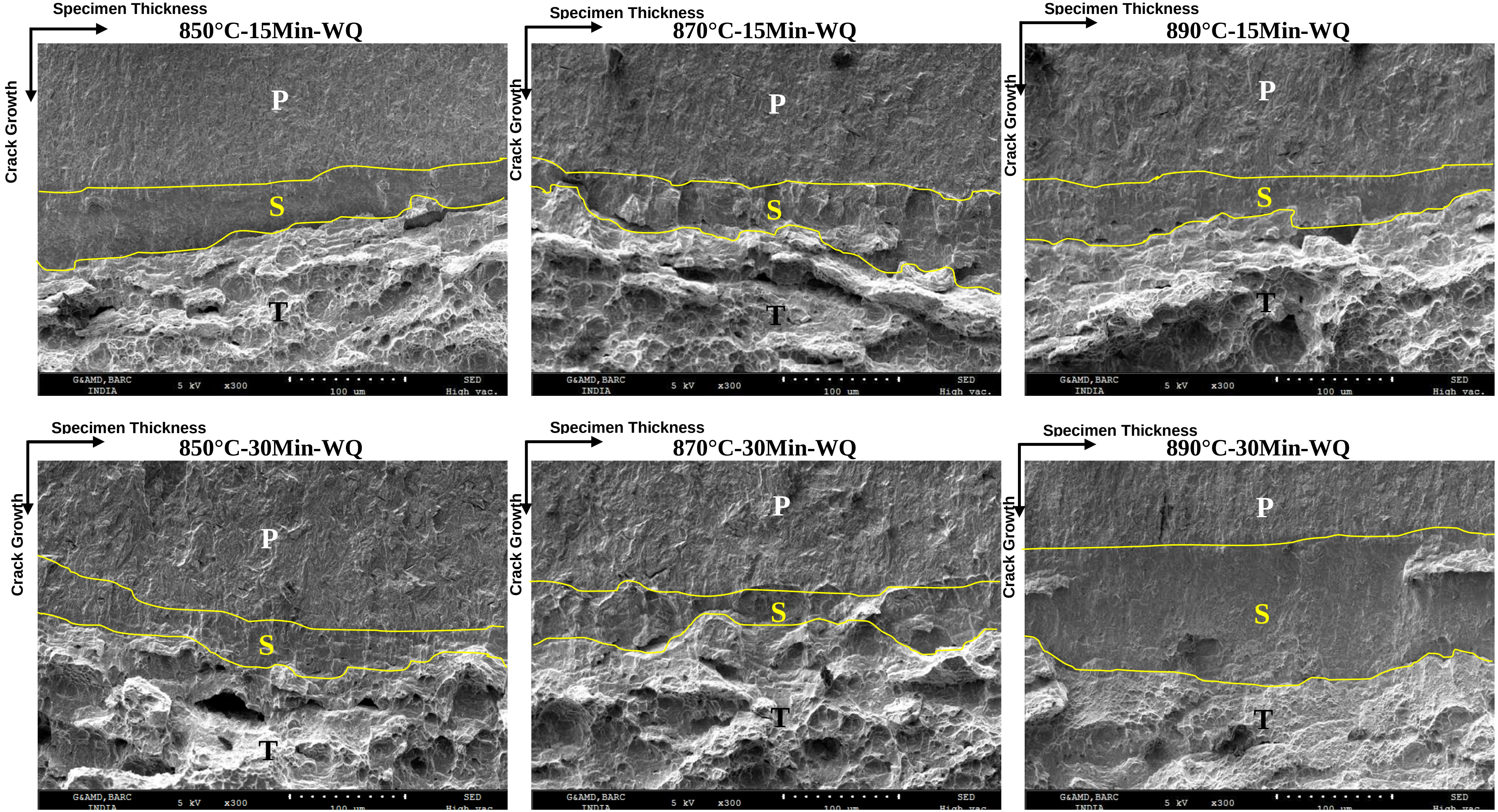
850°C-15Min-WQ

870°C-15Min-WQ

890°C-15Min-WQ

850°C-30Min-WQ

870°C-30Min-WQ

890°C-30Min-WQ

Figure 4.45: SEM fractographs illustrating the stretched zone formations ahead of pre-cracked regions in broken C(T) specimens under six SHT conditions, (mentioned above the fractographs), tested at RT. In the individual fractograph, stretched zone (S) is bounded by the yellow lines, which separate the pre-cracked (P) region from the tearing (T) region.

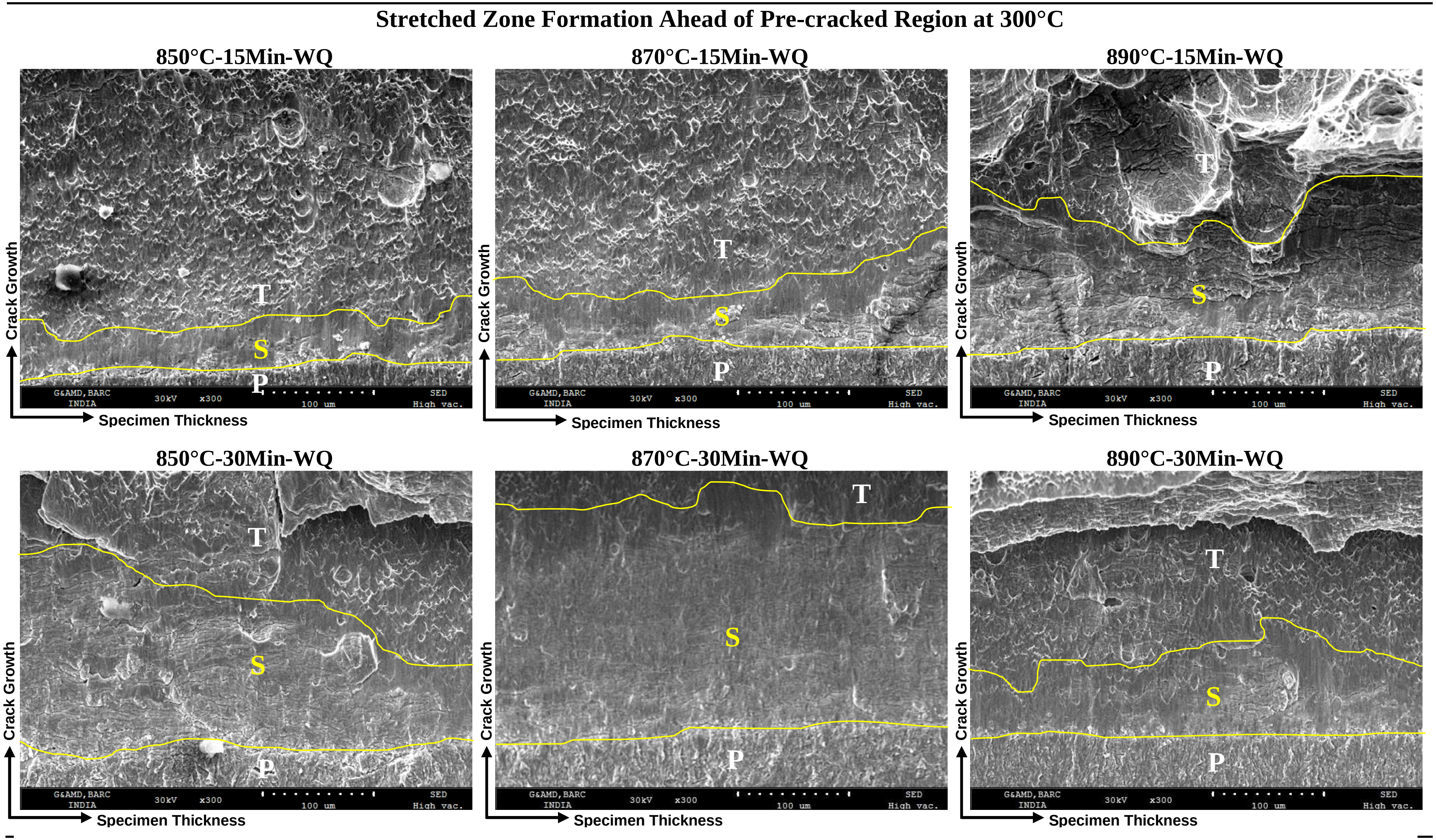

Figure 4.46: SEM fractographs illustrating the stretched zone formations ahead of pre-cracked regions in broken C(T) specimens under six SHT conditions, (mentioned above the fractographs), tested at 300°C. In the individual fractograph, stretched zone (S) is bounded by the yellow lines, which separate the pre-cracked (P) region from the tearing (T) region.

4.4 Discussion

Influence of SHT parameters on the microstructural features and the mechanical properties including tensile properties, micro-hardness and fracture behavior of Zr-2.5Nb alloy were described in this chapter. These effects are being discussed as under:

The present study has shown that increase in SHT temperature within 850-890°C, for up to 30 min soaking duration causes considerable microstructural changes. This includes reduction in primary α volume fraction and increase in grain sizes (especially of prior β, i.e., α'). Another important microstructural change could be the degree of super saturation of the β stabilizer Nb within α' phase. Assuming that after 30 min of soaking, the phase equilibrium has been reached, the Nb concentration of β phase (therefore α' phase) for different SHT conditions can be determined as below:

From the phase diagram, following 'Inverse Liver' rule:

$$V_{\alpha} = \frac{Nb_{\beta} - 2.5}{Nb_{\beta} - Nb_{\alpha}} \tag{4.8}$$

where, the term V_{α} represents volume fractions of α-Zr; terms Nb_{α} & Nb_{β} respectively represent the Nb concentrations (in wt. %) of α-Zr & β-Zr phases.

Therefore, the average Nb concentration of β-Zr (hence, degree of Nb super saturation in α', $Nb_{\alpha'}$) is given by;

$$Nb_{\beta} = \frac{2.5 - (V_{\alpha} \times Nb_{\alpha})}{(1 - V_{\alpha})} = Nb_{\alpha'} \tag{4.9}$$

Here, the term V_{α} (volume fraction of primary α) for the six solution heat treated conditions has been described at the beginning of this chapter (Figure 4.2 (a)). The variation of Nb_{α} with SHT temperature has been illustrated in Table 4.1, as determined from the phase diagram

(Figure 4.7 (b)). Using these values one can compute Nb_{β}, for the six solution heat treated conditions, as described below.

A. **For 850°C/15Min**

$$Nb_{\beta} = \frac{2.5-(0.36\times0.92)}{(1-0.36)} = 3.38 \text{ wt. \%}$$

B. **For 870°C/15Min**

$$Nb_{\beta} = \frac{2.5-(0.16\times0.84)}{(1-0.16)} = 2.81 \text{ wt. \%}$$

C. **For 890°C/15Min**

$$Nb_{\beta} = \frac{2.5-(0.06\times0.73)}{(1-0.06)} = 2.62 \text{ wt. \%}$$

D. **For 850°C/30Min**

$$Nb_{\beta} = \frac{2.5-(0.30\times0.92)}{(1-0.30)} = 3.19 \text{ wt. \%}$$

E. **For 870°C/30Min**

$$Nb_{\beta} = \frac{2.5-(0.15\times0.84)}{(1-0.15)} = 2.79 \text{ wt. \%}$$

F. **For 890°C/30Min**

$$Nb_{\beta} = \frac{2.5-(0.05\times0.73)}{(1-0.05)} = 2.60 \text{ wt. \%}$$

Therefore, in summary, the variations of SHT temperature within 850-890°C and soaking duration within 15-30 min domains results in the variation in primary α volume fraction, grain sizes of primary α and prior β (α’) and degree of Nb super saturation of α’ phase. These microstructural variability associated with the SHT parameters variations are illustrated in Table 4.4.

Table 4.4: Influence of SHT parameters on the microstructural features of Zr-2.5Nb alloy.

S. No.	**SHT Temp. (°C)**	**Soaking Duration (Min)**	**Microstructural Features**						
			Primary α Volume Fraction (%)		**Primary α grain size (μm)**		**Prior β (α’) grain size (μm)**		**Degree of Nb super saturation in α’ (wt. %)**
			Avg.	**SD**	**Avg.**	**SD**	**Avg.**	**SD**	
1	850	15	35.8	3.50	2.1	0.29	6.6	0.81	3.38
2		30	30.4	0.66	2.5	0.39	7.2	1.74	3.19
3	870	15	15.6	0.36	2.2	0.26	7.9	1.44	2.81
4		30	15.0	0.40	2.8	0.40	10.3	2.01	2.79
5	890	15	6.4	0.63	2.4	0.30	14.6	2.94	2.62
6		30	5.1	0.65	3.2	0.82	19.8	3.71	2.60

The present study shows that increase in soaking duration from 15-30 min at a particular SHT temperature decreases the tensile strength of solution heat treated material. With increase in soaking duration at a particular SHT temperature, the major microstructural change was grain coarsening (especially of α’). In addition to this, increase in soaking duration also caused insignificant reduction in primary α volume fraction and therefore in the degree of Nb super saturation in α’ (Table 4.4). Increase in grain size, in principle lowers the strength of a material. This is because, the grain boundaries act as barrier for dislocation motion, and hence for the slip, by which most of the crystalline materials deform plastically. A coarser grain size therefore decreases the amount of grain boundaries and dislocation interaction, and hence the strength of the material. Another reason of the observed decrease in strength with increasing soaking duration could be the reduction in degree of Nb super saturation in α’. Here, it is important to note that Nb, a β stabilizer element, causes solid solution strengthening in Zr-Nb alloys. The reduction in degree of super saturation of Nb in α’ therefore emphasizes for corresponding decrease in the strength of α’ and hence of the heat treated material. In addition, oxygen, an α stabilizer element, also acts as the strengthening element in Zr. At SHT temperature, oxygen has the tendency to segregate from β-Zr to α-Zr. Such oxygen partitioning is a function of the soaking duration at SHT temperature. A higher soaking duration causes a higher degree of oxygen partitioning, and consequently lowers the oxygen concentration in β-Zr (and hence in α') [12]. Therefore, the reduction in oxygen concentration in α' due to longer soaking also emphasizes for the corresponding decrease in the strength of α' and hence of the heat treated material. Therefore, the reduction in tensile strength with increasing SHT soaking duration could be understood as the consequence of increasing grain size and reduction in degree of Nb super saturation of α' along with the higher degree of oxygen depletion in α', caused by increased oxygen partitioning at SHT temperatures.

This study showed that an increase in SHT temperature from 850 to 890°C causes reduction in tensile strengths and micro-hardness. As can be seen from Table 4.4 that such increase in SHT temperature caused considerable reduction in primary α volume fraction, increase in grain size (especially of prior β, i.e., α'), and Nb depletion in β-Zr phase, resulting in a lower degree of Nb super saturation in α'. In addition to this, at higher SHT temperature, a higher degree of oxygen partitioning, therefore, higher degree of oxygen depletion in α' is also expected. This is because of the increased driving force (i.e., kinetics) for oxygen partitioning at higher soaking temperature. Out of these microstructural changes, the grain coarsening, reduced degree of Nb super saturation in α' and increased degree of oxygen deplition in α' are expected to decrease the strength of heat treated material (as explained earlier). In contrast, reduction in primary α volume fraction; in other words, increase in α' volume fraction is expected to increase the strength of material because of increasing fraction of martensitic phase. Therefore, the observed reduction in tensile strength and micro-hardness with increasing SHT temperature could be understood as the combined result of changes in metallurgical parameters viz., decrease in primary α volume fraction, increase in grain size (especially of α’ phase), and decrease in Nb super-saturation of α’ along with higher degree of oxygen depletion in α’.

The influence of microstructural features on tensile properties of solution heat treated Zr-2.5Nb alloy is illustrated in Figure 4.47. As can be understood from this figure that the tensile properties, other than strength; including ductility and strain hardening characteristics have weak dependence on the microstructural features.

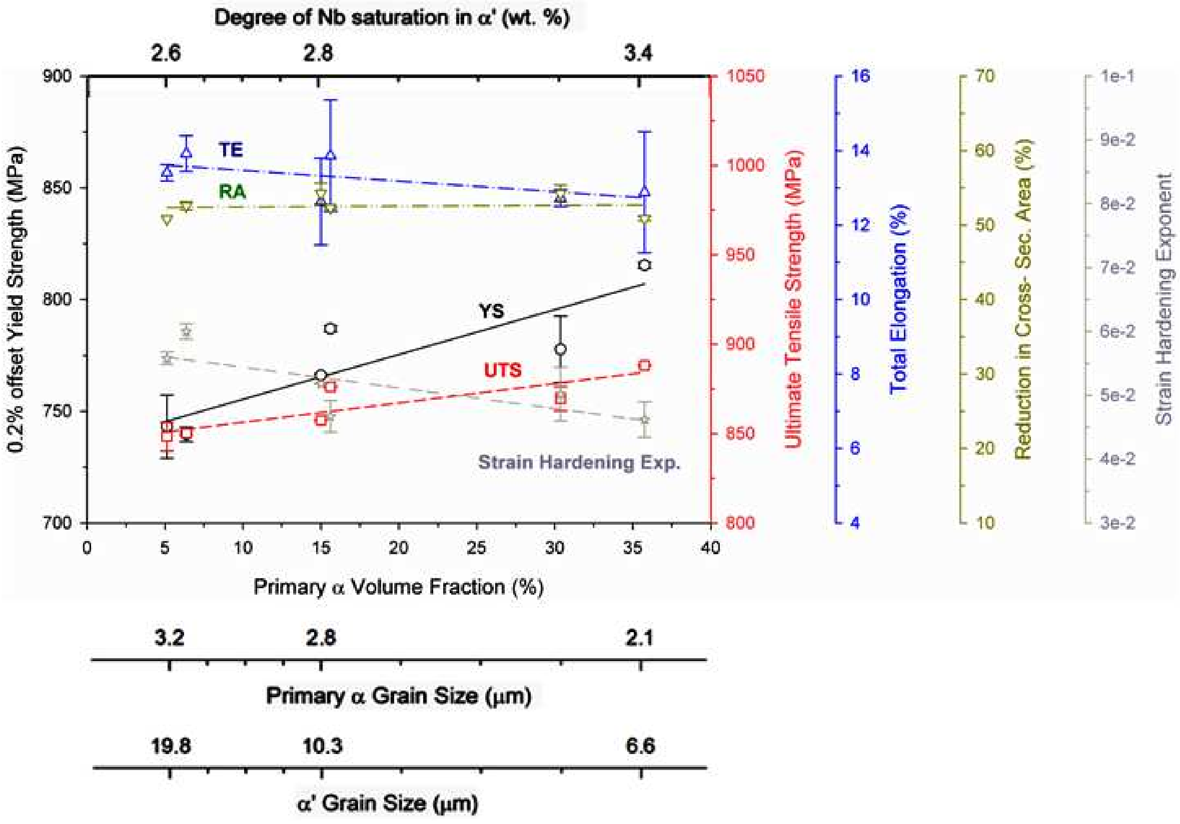

Figure 4.47: Correlation of microstructural features with tensile properties of solution heat treated Zr-2.5Nb alloy.

Another important observation of the present study was that longer soaking results in lower dependence of tensile properties on SHT temperature. With increase in soaking duration, the difference in microstructural parameters viz., primary α volume fraction and degree of Nb super saturation in α’ corresponding to 850 and 890°C decreases. In the other words, longer soaking makes lower dependence of the aforementioned microstructural features on SHT temperature. This phenomenon is illustrated in Figure 4.48 (a). In this figure, the dependence of microstructural features on soaking durations in shown.

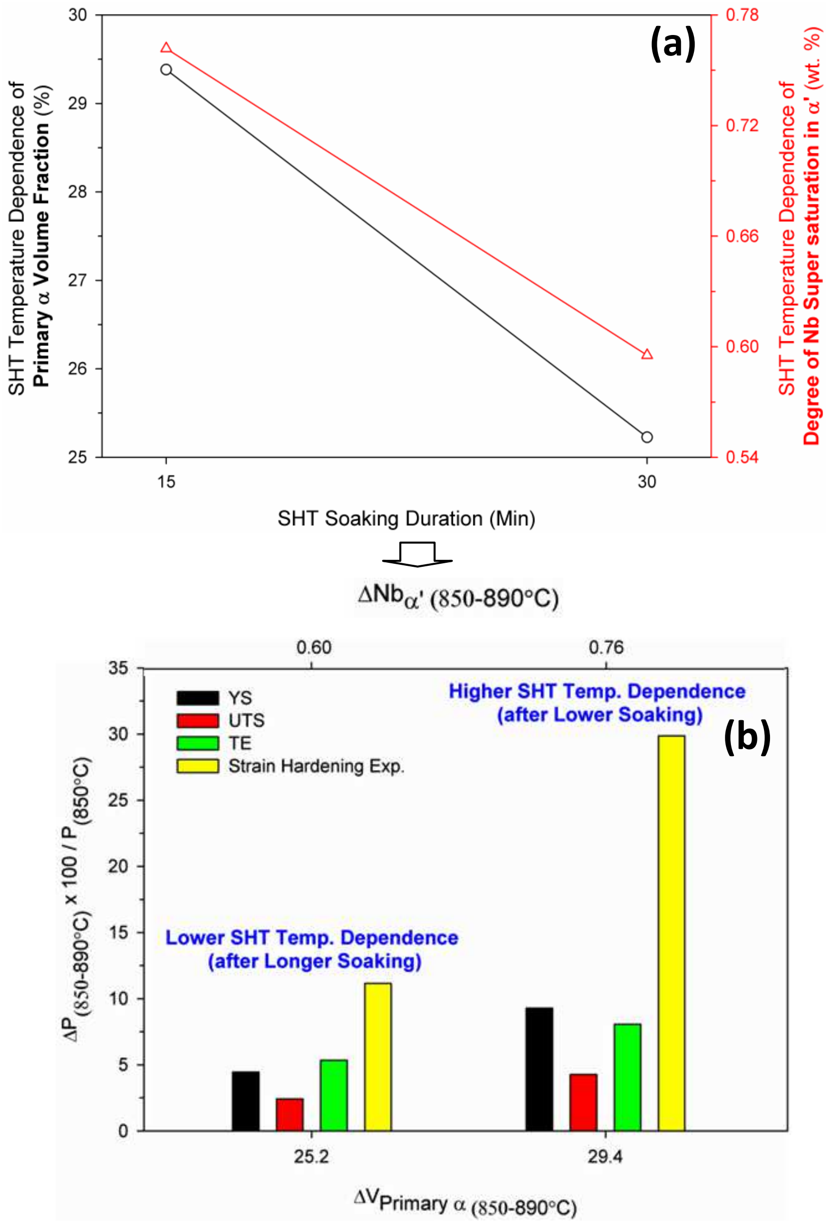

Figure 4.48: (a) Influence of soaking duration on SHT temperature dependence of the microstructural features. (b) Correlation of the soaking temperature dependence of microstructural features with that of tensile properties of solution heat treated Zr-2.5Nb alloy.

Such lower dependence of microstructural features on SHT temperatures could explain the cause of obtaining the lower dependence of tensile properties on SHT temperatures. Figure 4.48 (b) shows the correlation between the change in primary α volume fraction and degree of Nb super saturation within 850-890°C regime with sensitivity of tensile properties on SHT temperatures.

The fracture toughness parameters of solution heat treated Zr-2.5Nb alloy were weakly sensitive to the SHT parameters viz., soaking temperature and duration, especially under ambient condition. Such weak dependence of fracture behavior could therefore be understood as the net outcome of the combined play among corresponding microstructural changes viz., primary α volume fraction, grain size, and degree of Nb super saturation in α’, along with degree of oxygen depletion in α’.

The present study showed that the solution heat treated materials exhibit hardness gradient in the vicinity of the free surface. Within a narrow regime of ~200-225 µm below from the free surface, hardness shows such sharp transition by exhibiting substantial reduction followed by saturation. Such hardness gradient with depth from the free surface in solution heat treated materials could be understood as the consequence of corresponding variations in temperature gradients during water quenching, resulting in corresponding variations in cooling rates as a function of depth from the free surface. Because of having highest temperature gradient, the free surface experiences highest cooling rate. While approaching towards depth from free surface, because of having relatively lower temperature gradient, cooling rate decreases. In the vicinity of free surface, such temperature gradients are much higher than that at the inside region. Therefore, the cooling rates exhibit drastic changes in the vicinity the free surface, as compared to the inside region. Therefore, the hardness variation dominates in the vicinity of the free surface. In the inside region, the cooling rate variations are not to be too high to cause notable changes in the hardness.

This study showed that the fracture surfaces of the broken C(T) specimens comprised sufficiently high fraction of the 45° oriented fracture region with a narrow intermediate flat region. This indicates that the specimens were fractured under nearly plane stress condition. The nature of stress field ahead the crack tip (i.e., plane stress or plane strain) is primarily controlled by the thickness of test specimen during fracture test along with the strength of material. A thicker specimen results in a stress field closer to plane strain condition under which, the material, which tries to deform along thickness direction due to the application of load, faces significantly high constraint. Such constraint is usually provided by the stress component acting along the direction opposite to thickness direction. On the other hand, under plane stress condition, such stress component becomes negligible. Because of this, the material is free to deform along the thickness direction, resulting in the formation of a plastic zone size ahead the crack tip, which is nearly three times to that under plane strain condition [105,106]. The fracture toughness under plane stress condition is higher than that under plane strain condition. Under plane stress condition, such a higher fracture toughness is due to the additional resistance to the material fracture (other than bond energy), which is provided by the formation of plastic zone ahead of crack tip and commonly known as ‘plastic dissipation energy’. The plane strain fracture toughness is independent of the constraint conditions ahead the crack tip and thereby follows 'similitude' principle, which is why it behaves as the material property. However, because of being dependent on the crack tip constraint conditions, the plane stress fracture toughness is essentially not a material property.

The fractographic investigations of the broken C(T) specimens showed microvoid coalescence fracture mechanism and therefore, indicated that the fracture was typically ductile under the six SHT conditions. The higher dimple size, as observed during the fracture at 300°C, correlates the observed higher fracture toughness of these materials at elevated temperature.

4.4.1. Influence of Analysis Procedures on Fracture Toughness Parameters

A. Resistance Curve and Basic Test Methodologies

The magnitude of crack extension (Δa) corresponding to the initiation toughness (J_Q) was in the range of ~0.28 to 0.45 (which is corresponding to *a/W* of ~0.49 to 0.52). At such lower *a/W*, the deviation between *J* parameters derived from the two standard methods are marginal both at 25 and 300°C. Therefore, initiation toughness derived using RC and BT methods showed marginal deviation and, therefore, it was marginally dependent on these two methods.

Similarly, corresponding to maximum load, the magnitude of *a/W* was observed to be closer to that of initiation toughness (i.e., a/W~0.55). Therefore the marginal deviation observed in J_{max} parameters obtained from the two standard methods is attributed to the insignificant deviation in the *J-R* curves at such lower *a/W*.

In contrast to J_Q and J_{max} parameters, appreciable deviation observed in *dJ/da* data of RC and BT methods can be understood as the consequence of the observed higher deviation between the *J* parameter at higher crack extension levels.

As discussed in Chapter 2 (Equations 2.18 and 2.20) that in BT method, α is the only parameter, which can be varied, though it has been assigned the fixed value of 1 for SE(B) specimen and 0.9 for Compact Tension, C(T) & Disc Compact Tension, DC(T) specimens [78]. In order to investigate the reason of increasing deviation in the *J* parameter with crack extension, a parametric study was performed by varying this parameter to examine its effect on the magnitude of deviation between the *J-R* curves obtained from the two methods. It was observed that parameter α govern the respective magnitude of deviation between the *J-R* curves. The effect of parameter α on the deviation between the *J-R* curves obtained from BT and RC methods is shown in Figures 4.49 and 4.50 for RT and 300°C, respectively. As the magnitude of α parameter increases, the slope of *J-R* curve decreases, which correspondingly decreases the deviation between the *J-R* curves obtained from these methods. At 300°C test temperature, the optimum value of parameter α (at which *J-R* curves obtained from the two methods showed marginal deviations) was lying in the range of 2.9 to 3.9 for different solution heat treated conditions (Figure 4.50). In contrast, at RT (Figure 4.49), with increase in parameter α from 0.9 to 10, sharp drop in the deviation was observed. However, beyond this (for α > 10), the magnitude of deviation became insensitive to this parameter such that with increase of α from 10 to 25 and from 25 to even 75, the *J-R* curves of the two methods were not overlapping.

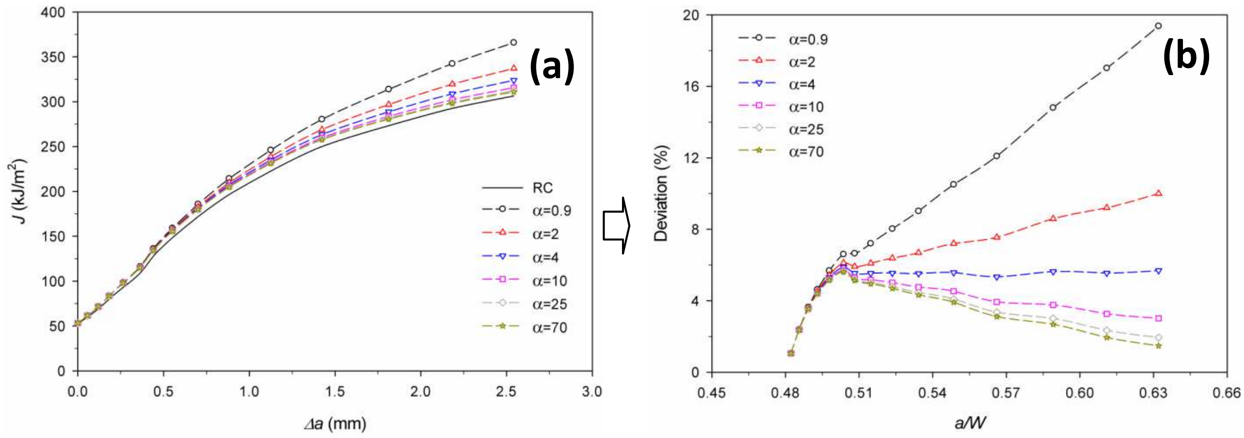

Figure 4.49: Influence of ductile crack growth correction parameter α on (a) RT- *J-R* curves derived from the BT method, and (b) their respective deviations from the *J-R* curve derived from the RC method. The plots are shown for SHT condition viz., 850°C-15Min-WQ. For rest of the five SHT conditions, parameter α had similar influence.

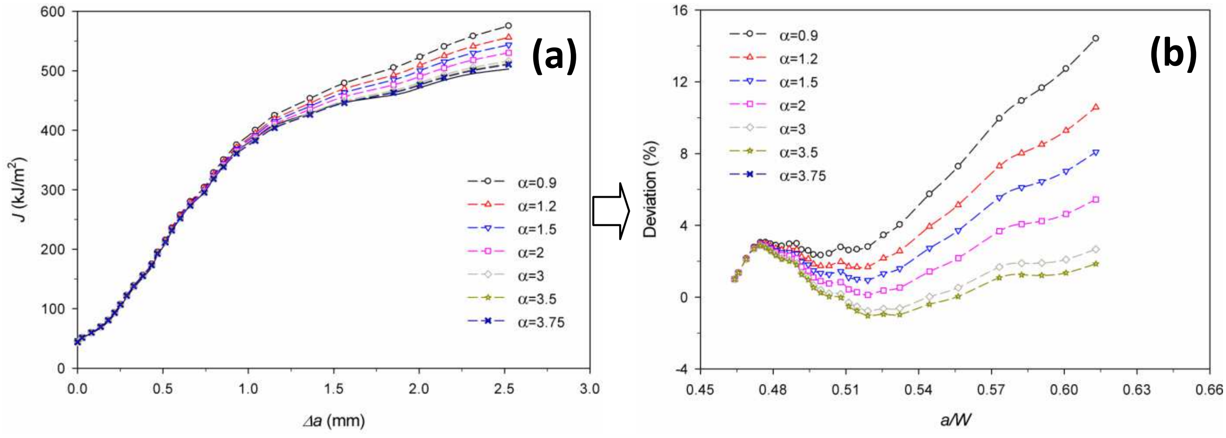

Figure 4.50: Influence of ductile crack growth correction parameter α on (a) *J-R* curves derived from the BT method at 300°C, and (b) their respective deviations from the *J-R* curve derived from the RC method. The plots are shown for SHT condition viz., 850°C-15Min-WQ. For rest of the five SHT conditions, parameter α had similar influence.

Therefore, the optimum value of α, which results for marginal deviations between the *J-R* curves of the RC and BT methods, was observed to be a function of material's flow stress. At high temperature, where the flow stress was ranging from 591 to 659 MPa, optimum value of parameter α was lying in the range of 2.9 to 3.9. However, at RT, where material's flow stress was in the range of 795 to 847 MPa, even 75 was not optimum value for the respective deviations.

Therefore, this study concludes that the assigned 0.9 value for α parameter is attributed to the observed increase in deviation in *J* parameter with crack extension.

B. Influence of Test Standards

The ASTM and ISO standard procedures differ not only in suggesting different expressions for the evaluation of *J* parameter, but also the analysis procedures recommended by these standards for evaluating the fracture toughness parameters are also different. The major differences in the analysis procedures of these standards include differences in the recommended slopes of construction lines, differences in the recommended exclusion lines to bound the valid *J-R* region and differences in the power law equation (i.e., two or three parameter) to fit the valid *J-R* curve. Because of the observed small differences in the *J-R* curves determined from the two standards, $J_{F(max)}$ data derived from these standards showed marginal differences. The observed difference in the initiation toughness data is primarily because of using blunting lines of different slopes. However, the contribution for the deviation in the initiation toughness data because of the difference in power law fitting equations used by the two standards is effectively less. The difference in propagation toughness data (*dJ/da*) is mainly attributed to the use of dissimilar exclusion lines for binding the valid *J-R* region. In the following sections, the influence of difference in the two standard procedures on the evaluated fracture toughness results is being discussed in detail.

Despite the observed negligible difference between the *J-R* curves derived using ASTM [78] and ISO [97,98] standards, particularly at elevated test temperature (i.e., 300°C), for all the heat treated conditions (Figure 4.30), the fracture toughness parameters such as initiation toughness (J_Q) and *dJ/da* showed appreciable difference (> 30%). This suggests that the difference in the *J-R* curve analysis procedures of the two standards dominates over the difference in the expressions of *J* parameter to construct the *J-R* curve.

The slope of construction line and therefore 0.2 mm offset line ('Blunting Line', BL) recommended by the ISO standard was found to be almost twice as compared to the ASTM standard (as shown in Figure 4.51). It can be seen from Figure 4.52 that as the slope of blunting line increases, the magnitude of initiation toughness reduces. Therefore, the initiation toughness derived from ASTM standard, were higher than those derived from ISO standard (Figure 4.33). Furthermore, from Table 4.5, it can be seen that the difference in the magnitude of coefficients (*x* and *y*) of the two power law equations used for fitting the valid *J-R* curves region is effectively less (as the coefficient *A* was closer to zero in majority of the cases). Therefore, difference in the power law equations recommended by the two standards does not contribute much to the observed difference in the initiation toughness parameters; rather, the difference is primarily because of the difference in the blunting line slopes recommended by these standards.

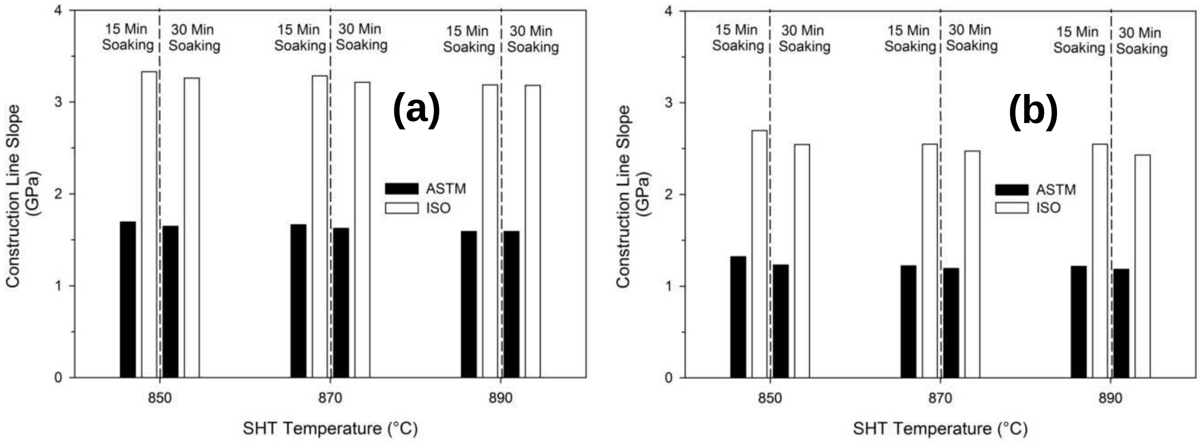

Figure 4.51: Influence of test standards on the construction line slopes of Zr-2.5Nb alloy under different solution heat treated conditions at (a) RT and (b) 300°C.

The blunting lines are supposed to model the initial portion of *J-R* curve. Therefore, the ISO standard, in contrast to ASTM standard, because of recommending higher BL slope, appears better for such initial region. In addition, initiation toughness determined from ISO standard is conservative for safety view point.

Table 4.5: Comparison of the coefficients of *J-R* curve power law fitting equations, suggested by ASTM E1820-11 (two parameter) and ISO 12135:2002 (three parameters) for Zr-2.5Nb alloy under different solution heat treated conditions.

Soaking Temperature (°C)	**Soaking Duration (Min)**	**Test Temperature (°C)**	**Coefficients of ASTM's two parameter equation** **Equation:** $J=x\,(\Delta a)^y$ ***Units:*** ***J*** **in kJ/m^2 and** Δa **in mm**		**Coefficients of ISO's three parameter equation** **Equation:** $J=A+X\,(\Delta a)^Y$ ***Units:*** ***J*** **in kJ/m^2 and** Δa **in mm**		
			x	***y***	***A***	***X***	***Y***
850	15	25	123.1	0.56	1.28E-08	136.4	0.63
870	15	25	252.8	0.54	1.96E-08	274.0	0.61
	15	25	131.4	0.59	2.40E+01	122.7	0.86
890	15	25	162.3	0.50	9.64E+00	166.5	0.60
	15	25	215.2	0.52	1.25E-07	239.8	0.63
850	30	25	174.5	0.52	7.99E-08	192.3	0.60
	30	25	179.3	0.55	2.96E-08	195.9	0.61
870	30	25	176.9	0.59	2.04E+01	175.5	0.79
	30	25	159.0	0.51	1.81E+00	176.6	0.61
890	30	25	210.9	0.46	2.44E-07	230.2	0.55
850	15	300	242.3	0.75	2.21E-08	271.0	0.92
	15	300	253.6	0.44	3.37E-07	283.6	0.59
870	15	300	285.8	0.72	9.65E-10	317.5	0.91
	15	300	303.4	0.58	1.61E-08	317.3	0.67
890	15	300	312.6	0.60	1.25E-07	337.1	0.73
	15	300	254.0	0.67	2.21E-07	277.7	0.80
850	30	300	291.0	0.63	1.61E-08	317.0	0.80
	30	300	358.4	0.56	4.79E-08	389.5	0.78
870	30	300	297.4	0.60	4.15E-09	321.0	0.76
	30	300	312.4	0.65	6.04E-09	339.6	0.81
890	30	300	320.3	0.59	2.08E-07	342.6	0.72
	30	300	297.2	0.89	2.98E-08	302.7	1.00

Compared to RT, at 300°C, significant deviation in initiation toughness parameters derived from the ASTM and ISO standards were observed. This is due to the fact that as the test temperature increases, because of increasing toughness, the slope of *J-R* curve increases too. Because of this, difference between the intersecting points of ASTM and ISO derived *J-R* curves with the respective blunting lines increases. This correspondingly resulted in larger deviations observed in the high temperature initiation toughness parameters obtained by the two standards. Figure 4.52 shows a schematic illustration of such phenomenon, which resulted in higher deviation between the initiation toughness parameters obtained from the two standards at elevated temperature.

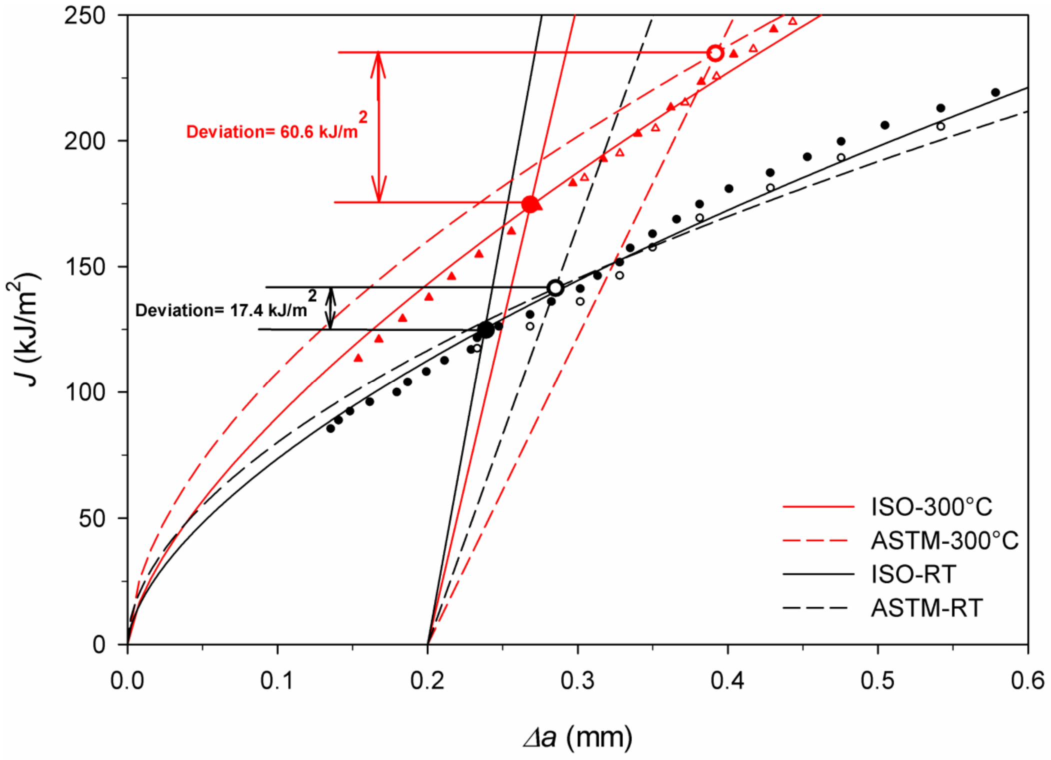

Figure 4.52: Plot showing a magnified view of the intersection of four power law fit *J-R* curves (ISO derived curve at RT & 300°C and ASTM derived curve at RT & 300°C) with respective blunting lines to determine the initiation toughness for 870°C-15Min-WQ SHT condition. In this figure solid and hollow circle symbols respectively represent the valid *J-R* curve data points as per ISO and ASTM standards at RT. Similarly, the solid and hollow triangle symbols represent the respective data points at 300°C. It is evident from this figure that with increasing test temperature, the differences between the initiation toughness parameter derived from the two standards increases. Similar behavior was observed for the other five heat treatment conditions.

From the present study it was observed that the difference between $J_{F(max)}$ data obtained from the two standards was insignificant (maximum ~5%) (as shown in Figure 4.36) for all heat treated conditions. Since the $J_{F(max)}$ parameter represents the magnitude of J corresponding to maximum load during the test, such small differences in the $J_{F(max)}$ parameters can be understood as the consequence of the insignificant deviations between *J-R* curves derived from these standards (as shown earlier in Figure 4.31).

According to the recommendation of ASTM standard [78], 0.15 and 1.5 mm offset crack extension ELs are used to define the qualified region of the *J-R* curve. However, the ISO standard recommends ELs with offset of 0.1 mm crack extension and maximum crack extension capacity of the specimen (i.e., Δa_{max}) to define the qualified *J-R* region (as described in Figure 2.17, Chapter 2). Since the magnitude of Δa_{max} as per the ISO standard is typically about 40 % lower than 1.5 mm (as evident from Figure 4.32), the ISO standard considers smaller range of crack extensions for valid *J-R* curve data points as compared to the ASTM standard. These data points lie at smaller crack extension during which *J* shows a strong dependency on crack extension. Therefore, the slope of valid *J-R* curve region, *dJ/da* derived using the ISO standard was markedly higher as compared to the ASTM standard. This phenomenon is schematically illustrated in Figure 4.53. In contrast to RT, the higher difference observed in this parameter at 300°C temperature is due to the additional effect of increase in the slope of *J-R* curve with test temperature (which can be also considered in terms of increase in material's fracture toughness with test temperature).

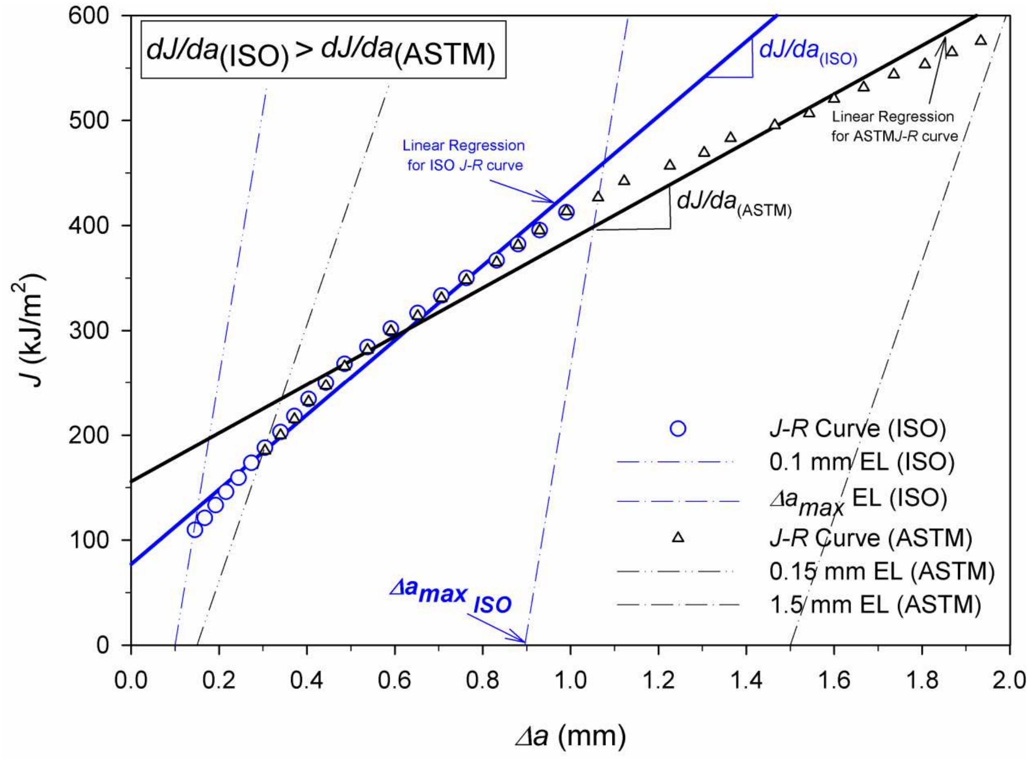

Figure 4.53: Schematic justification for obtaining higher propagation toughness parameter (*dJ/da*) from ISO standard as compared to ASTM standard in a solution heat treated material. Plot shows the difference in the qualified *J-R* regions recommended by ASTM and ISO standards. ISO standard considers smaller range of crack extensions as valid *J-R* curve data points as compared to ASTM standard, which consequently results in higher ISO derived *dJ/da* parameter.

The maximum J integral (J_{max}) and crack extension (Δa_{max}) capacities recommended by the two standards also have differences, as shown in Equations 4.10 & 4.11 and 4.12 & 4.13. ASTM standard in contrast to ISO, recommends almost half J_{max} and 2.5 fold Δa_{max} capacities (as shown in Table 4.6). The materials soaked at higher temperature, and for longer duration during solution heat treatment exhibited relatively lower J_{max} capacity. This is because water quenching from higher soaking temperature and with longer soaking duration results in the corresponding lower strength of Zr-2.5Nb alloy, (as described earlier). Reduction in material's strength caused by increase in test temperature from RT to 300°C resulted in nearly

25% reduction in the J_{max} capacity. In contrast, since Δa_{max} is the only function of specimen's initial un-cracked ligament, the six heat treated materials had same Δa_{max} capacity.

$$J_{max_{ASTM}} = \min\left(\frac{b_o\sigma_Y}{10}, \frac{B\sigma_Y}{10}\right) \tag{4.10}$$

$$J_{max_{ISO}} = \min\left(\frac{a_o(\sigma_{YS}+\sigma_{UTS})}{40}, \frac{B(\sigma_{YS}+\sigma_{UTS})}{40}, \frac{b_o(\sigma_{YS}+\sigma_{UTS})}{40}\right) \tag{4.11}$$

$$\Delta a_{max_{ASTM}} = 0.25b_o \tag{4.12}$$

$$\Delta a_{max_{ISO}} = 0.1b_o \tag{4.13}$$

Table 4.6: Maximum *J*-integral and crack extension capacities recommended by ASTM E1820-11 and ISO 12135:2002 standards for Zr-2.5Nb alloy under six solution heat treated conditions.

Soaking Temperature (°C)	**Soaking Duration (Min)**	**Test Temperature (°C)**	J_{max} **(kJ/m^2)**		Δa_{max} **(mm)**	
			ASTM	**ISO**	**ASTM**	**ISO**
850	15	25	253.3	127.3	2.13	0.85
870	15	25	247.8	123.9		
	15	25	247.0	123.5		
890	15	25	240.1	120.0		
	15	25	240.8	120.4		
850	30	25	244.6	122.3		
	30	25	247.9	123.9		
870	30	25	241.9	121.0		
	30	25	244.3	122.2		
890	30	25	241.1	120.5		
850	15	300	194.0	97.0	2.13	0.85
	15	300	200.0	100.0		
870	15	300	179.5	91.1		
	15	300	183.8	93.2		
890	15	300	184.2	93.4		
	15	300	184.2	93.4		
850	30	300	182.0	91.0		
	30	300	180.8	90.4		
870	30	300	177.7	89.5		
	30	300	179.5	90.4		
890	30	300	175.8	87.9		
	30	300	178.8	89.4		

The difference in *J-R* curves derived from ASTM and ISO standards was found to be smaller at 300°C than RT for all the heat treated materials considered in the present investigation.

Conversely, the difference between fracture toughness parameters such as J_Q and *dJ/da* derived from these resistance curves following the analysis procedure of ASTM and ISO standards were observed to be higher at 300°C than RT (Figure 4.33 and 4.37). Since the fracture toughness parameters (J_Q and *dJ/da*) of these materials at 300°C were considerably higher than at RT, these two competing phenomena suggest that with increasing material's fracture toughness, even if the difference between fracture resistance curves derived as per ASTM and ISO standards decreases, the difference in the *J-R* curve analysis procedures of these standards leads to increase the difference in J_Q and *dJ/da* parameters.

4.5 Summary

Present study showed the influence of solution heat treatment parameters on fracture behavior of Zr-2.5Nb alloy and is summarized as follows:

i. Solution heat treatment of Zr-2.5Nb alloy from 850-890°C temperature regime resulted in two phase (primary α and α’) microstructures. Variation in soaking temperature (850-890°C) and duration (15-30 min) during SHT caused variation in the microstructural features comprising phase volume fractions, grain sizes and composition. With increasing SHT temperature from 850-890°C, primary α volume fraction exhibited considerable reduction (from ~ 36 to 5%). Primary α grain size was weakly dependent on the SHT parameters; however, increase in SHT temperature and soaking duration caused substantial grain coarsening of prior β (i.e., α’). Increasing soaking temperature and duration also decreased the degree of Nb super saturation in α’. In addition, increasing soaking temperature and duration was also expected to increase the degree of oxygen depletion in α’.

ii. SHT, especially performed at higher soaking temperature for longer soaking duration, resulted in the randomization of basal pole texture with nearly one third distribution along the three principal directions viz., axial, circumferential and radial.

iii. Increasing soaking temperature from 850-890°C and duration from 15-30 min caused reduction in the tensile strength of solution heat treated Zr-2.5Nb alloy. Under ambient condition, the fracture toughness parameters of solution heat treated Zr-2.5Nb alloy were practically independent of the SHT parameters. Nevertheless, at 300°C, longer SHT soaking showed improvement in fracture resistance. These observations suggested the combined effect of microstructural changes associated with increasing soaking temperature viz., decrease in primary α volume fraction, increase in grain size (especially of α’ phase), decrease in Nb super-saturation of α’ and increase in degree of oxygen depletion in α’; and those associated with increasing soaking duration viz., grain coarsening along with decrease in degree of Nb super-saturation of α’ and increase in degree of oxygen depletion in α’ on the tensile and fracture behavior.

iv. During SHT, soaking duration governed the sensitiveness of tensile properties on SHT temperatures, such as longer soaking results in the lower dependence of tensile properties on SHT temperature. This study showed that for longer soaking, the microstructural features viz., primary α volume fraction and degree of Nb super saturation in α’ have lower dependence on SHT temperatures. Such lower dependence of microstructural features on SHT temperatures could therefore explain the cause of obtaining lower dependence of tensile properties on SHT temperatures.

v. Zr-2.5Nb alloy under the six solution heat treated conditions, as considered in this study showed typical dimple structure characteristics of a ductile failure, signifying the micro-void coalescence fracture mechanism. Fracture at elevated temperature (300°C), in contrast to RT resulted in the formation of relatively coarser dimples, having typical deformation markings on their surfaces. Under ambient fracture condition, the dimple had size variation from < ~ 1 µm to as big as ~ 6 µm. In contrast, during fracture at 300°C, the dimple had size variation from ~ 2 µm to as high as ~ 30 µm. Such coarser dimple formation during fracture at 300°C, correlated with the observed improvement in crack growth resistance of these solution heat treated materials at elevated temperature.

vi. The fractographic investigations of the broken C(T) specimens of Zr-2.5Nb alloy under different solution heat treated conditions showed the stretched zone formation ahead of the pre-cracked tip. Under ambient condition, the SHT parameters had no drastic influence on the streched zone widths, SZWs; as the average SZWs varried between 45-67 µm. Nevertheless, at 300°C fractured condition, longer soaking resulted in the formation of relatively wider stretched zones. The SZWs therefore showed good agreement with the observed influence of SHT parameters on the fractrue behavior.

vii. In this study, influence of analysis approaches such as ASTM recommended single specimen (RC) method, Multi-specimen (BT) method and ISO methodology on fracture toughness parameters of solution heat treated Zr-2.5Nb alloy is described. The study showed that $J_{F(max)}$ parameter was practically insensitiveness to both RC & BT evaluation methodologies and ASTM and ISO evaluation approaches. This therefore suggests that the *CCL* parameter (function of $J_{F(max)}$ parameter) of solution heat treated Zr-2.5Nb alloy is practically independent to these fracture toughness analysis approaches.

CHAPTER 5

INFLUENCE OF DEGREE OF COLD WORKING ON FRACTURE BEHAVIOR OF SOLUTION HEAT TREATED Zr-2.5Nb ALLOY

This chapter presents the influence of degree of cold working (10 and 20%) on fracture behavior of Zr-2.5Nb alloy, solution heat treated in two phase (α-Zr+β-Zr) regime at 850, 870 and 890°C for 15 or 30 min soaking durations followed by water quenching. The chapter commences with describing the influence of cold working on the microstructural features including microstructure gradient in the vicinity of sample thickness using optical microscopy and the evolution of basal pole texture using X-ray diffraction technique. Subsequently, influence on the mechanical properties such as micro-hardness, tensile properties and fracture toughness are presented. Fracture toughness parameters including initiation and propagation toughness, evaluated as per the ASTM standard are discussed. Subsequently, a study of the fracture surface of broken C(T) specimens is illustrated, which includes the quantitative assessment of fracture surface areas through image analysis approach and fractographic investigations at different surface regions through SEM.

5.1 Microstructural Observations

5.1.1 Optical Microstructures

As described in Chapter 4 that water quenching from two phase (α-Zr+β-Zr) regime at 850-890°C results in diffusionless martensitic transformation of β-Zr phase to α', whereas α-Zr phase remained as it is after quenching (and commonly known as ‘primary α’). The solution heat treated materials therefore, comprise two phase (primary α and α’) microstructures having considerable reduction in primary α volume fraction from ~ 36 to ~ 6% with increasing SHT temperature from 850-890°C for 15-30 min soaking duration.

Figures 5.1 and 5.2 show the evolution of microstructures of Zr-2.5Nb alloy, under different solution heat treated conditions with increasing degree of cold rolling. As can be seen from these figures that the cold rolling treatment resulted in elongated grain microstructures of solution heat treated materials.

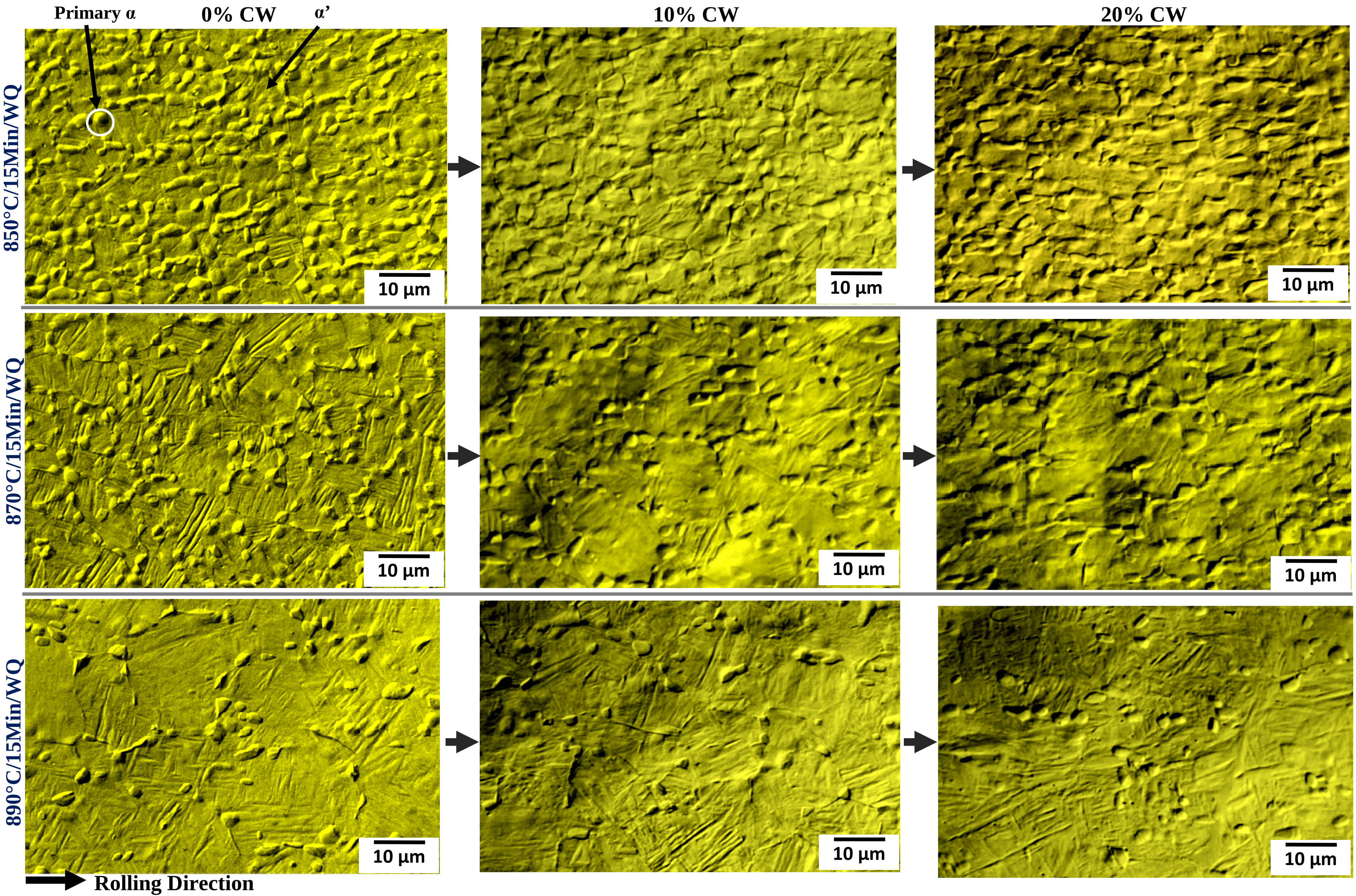

Figure 5.1: Influence of degree of cold working on mid-section optical microstructures of solution heat treated (15 min soaked) Zr-2.5Nb alloy.

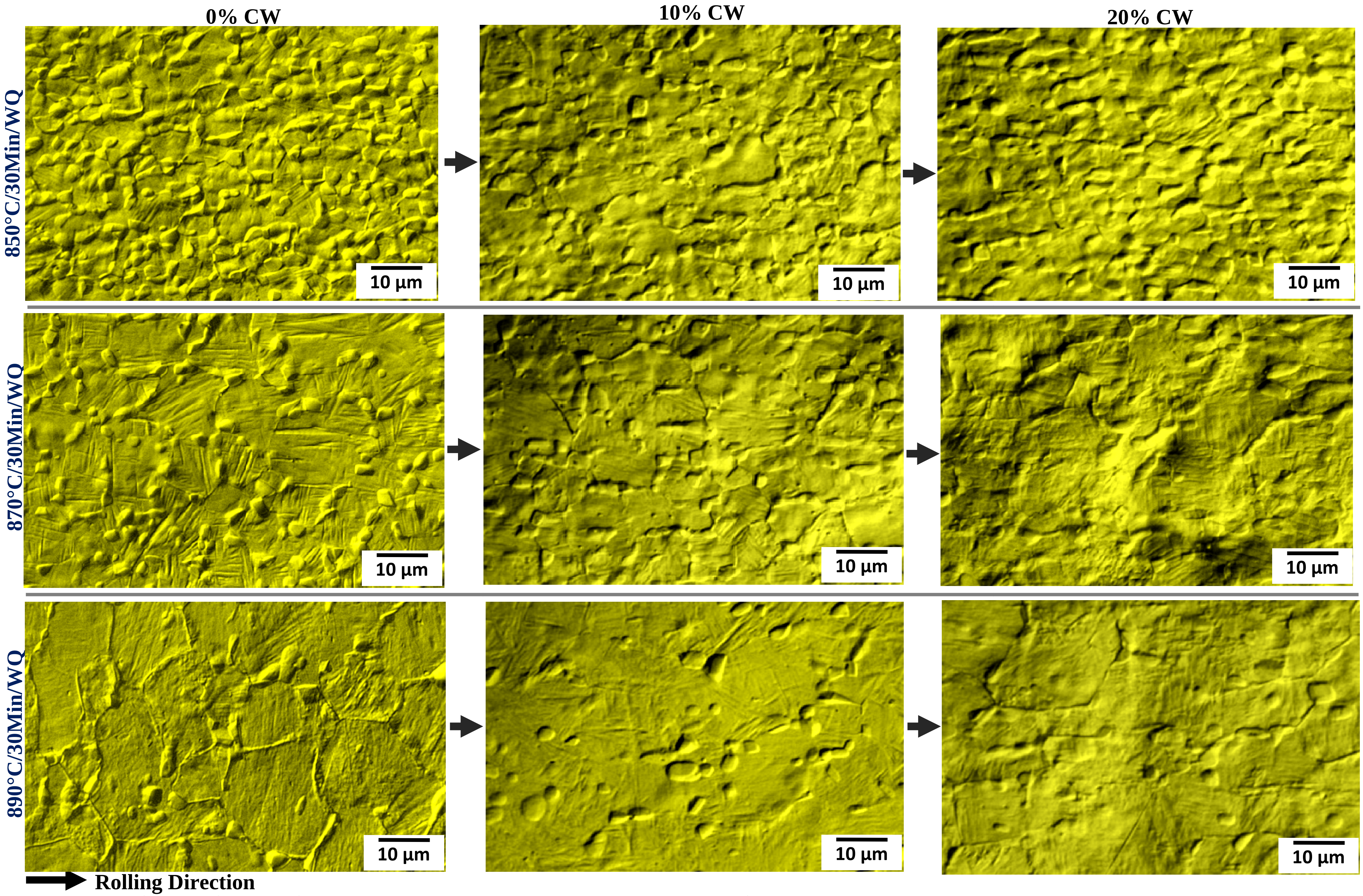

Figure 5.2: Influence of degree of cold working on mid-section optical microstructures of solution heat treated (30 min soaked) Zr-2.5Nb alloy.

5.1.2 Microstructure Gradient in the Vicinity of Free Surface

After cold working, the solution heat treated Zr-2.5Nb alloy exhibited a sharp gradient of primary α volume fraction in the vicility of free surface. Figure 5.3 shows such microstructue gradient in the vicility of free surface in a cold worked material obtained using Electron Back Scatter Diffraction (EBSD) derived band contrast imaging mode. While approaching towards depth from free surface, within a tiny regime, primary α volume fraction decreased substantially and subsequently got saturte. Such sharp transition of primary α volume fraction exsisted within a region of ~268 microns below the free surface (equivalant to 7% of the material thickness), in which the primary α volume fraction decreased from ~78% (at the free surface) to ~6%. Similar feature was observed for all other cold worked materials.

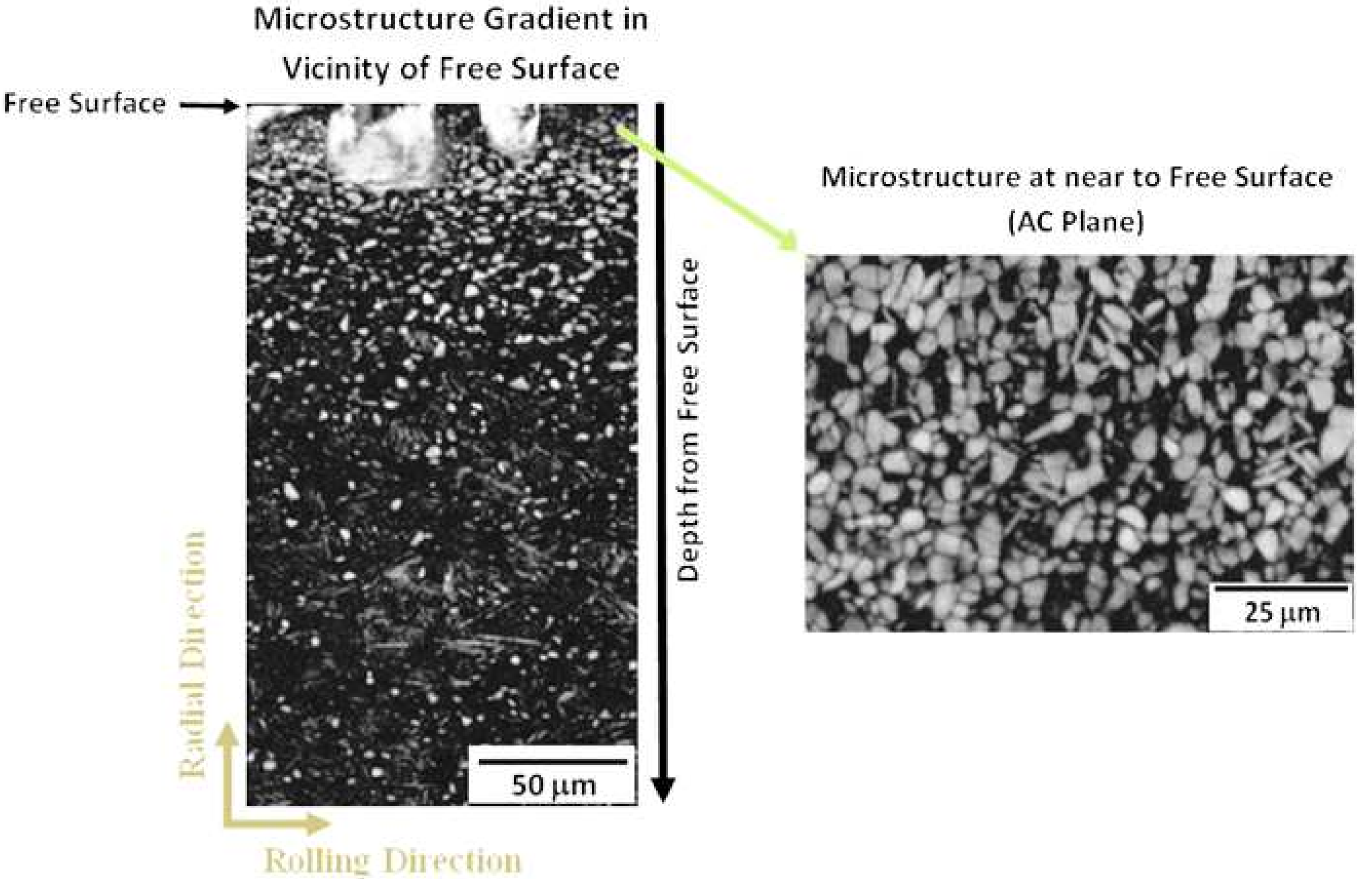

Figure 5.3: EBSD derived band contrast microstructure, showing the primary α gradient in the vicinity of free surface in cold worked-solution heat treated material. This material was solution heat treated at 890°C for 30 min followed by 10% cold working.

5.1.3 Crystallographic Texture

Figure 5.4 shows the influence of degree of cold work on basal pole texture (Kearns parameters) of Zr-2.5Nb alloy under two extreme solution heat treated conditions along plate's axial (rolling), transverse (width) and radial (thickness) directions. As mentioned in Chapter 4 that both primary α and α' phases have hexagonal close packed crystal structure. Texture shown in Figure 5.4 represents the fractions of total basal poles (both of primary α & α' phases) aligned in a particular direction i.e., axial, transverse or radial. Figure 5.5 shows the basal pole figures of Zr-2.5Nb alloy before and after cold working.

With the subsequent cold rolling treatment, basal pole alignment became more prominent along radial (i.e., compressive strain) direction with corresponding reduction along axial (i.e., rolling) direction. Nevertheless, upto 20% cold working, such changes in the basal pole texture of solution heat treated Zr-2.5Nb alloy are not significant. The materials, previously solution heat treated at a higher soaking temperature (890°C), as compared to 850°C still after cold working showed much randomized texture.

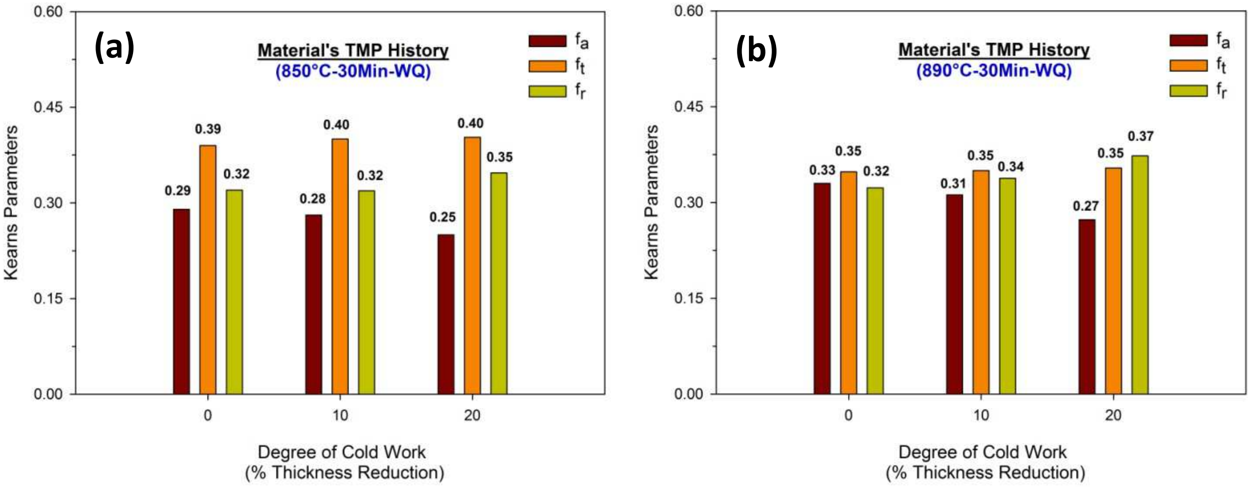

Figure 5.4: Influence of degree of cold working on the basal pole texture (Kearns parameters) of Zr-2.5Nb alloy, solution heat treated from (a) 850ºC temperature for 30 min duration and (b) 890ºC temperature for 30 min duration followed by water quenching.

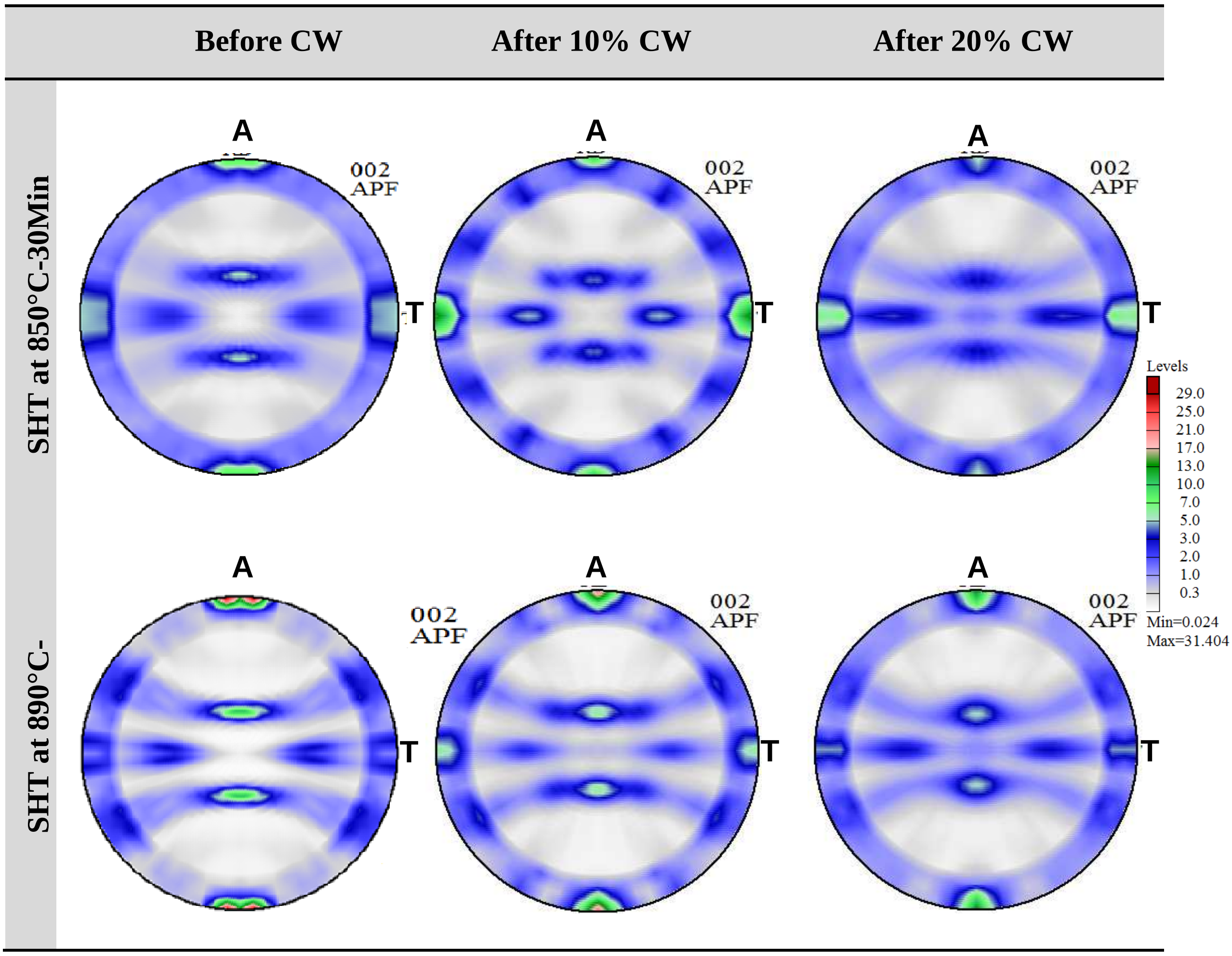

Figure 5.5: Additional basal Pole Figures (APFs) of Zr-2.5Nb alloy under two extreme solution heat treated and cold worked conditions. Symbols A and T respectively indicate the axial and transverse directions. Sample normal was along radial direction.

5.2 Mechanical Behavior

5.2.1 Micro-Hardness

Hardness of solution heat treated material increased with increasing degree of cold working. Figure 5.6 (a) shows such dependence of hardness on degree of cold working for one of solution heat treated Zr-2.5Nb alloy on the three mutually perpendicular AC, AR and RC planes. As can be understood from this figure that similar to solution heat treated condition, after cold working, the materials are still practically isotropic, by exhibiting close variation of hardness on the three mutually perpendicular planes. Similar isotropic behavior were shown by the rest of cold worked-solution heat treated materials.

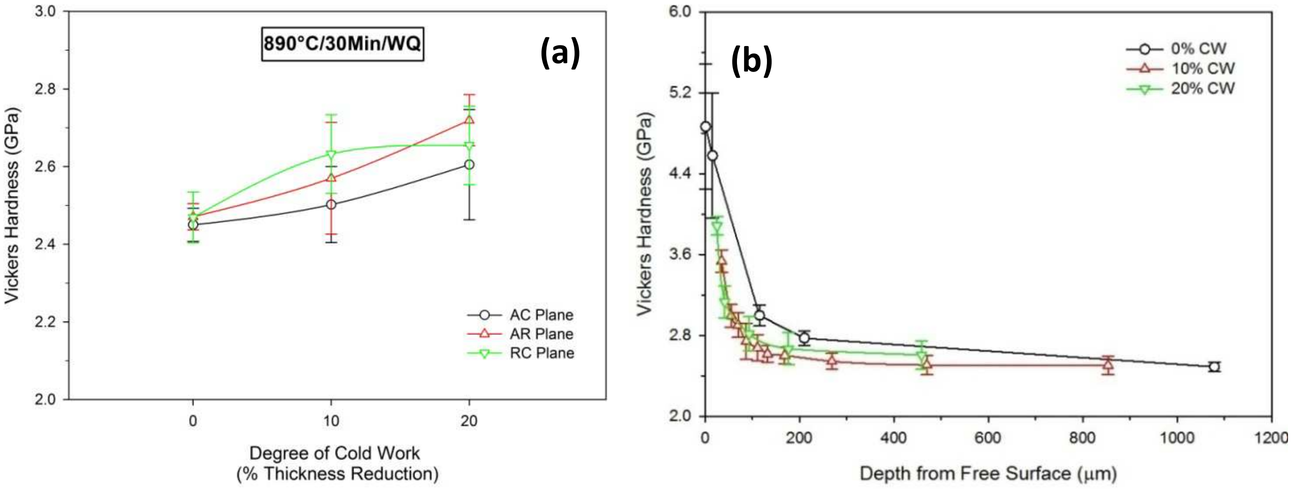

Figure 5.6: (a) Orientation dependence of mid-section Vickers hardness in cold worked-solution heat treated Zr-2.5Nb alloy, and (b) Variation of Vickers hardness as a function of depth from the free surface in this material, before and after cold working.

After cold working, the solution heat treated materials exhibited a sharp hardness gradient in the vicinity of their free surfaces, similar to before cold working. While approaching towards depth from the free surface, within a very small region of ~200 μm, the hardness showed such sharp transition by exhibiting ~35% reduction, followed by saturation with further increase in depth. Figure 5.6 (b) shows the variation of hardness with depth from the free surface in one of solution heat treated materials. An important observation of this study was that within such small transition region, the hardness of cold worked material was marginally lower than that of its parent (i.e., solution heat treated) condition. This phenomenon is later on explained in Discussion section, in terms of the accumulation of primary α in the vicinity of free surface and its possible consequence in reducing the hardness within such small transition region.

5.2.2 Tensile Properties

I. Flow curves

Figure 5.7 shows the influence of degree of cold working on the lower bound flow behavior of Zr-2.5Nb alloy under different solution heat treated conditions. The flow stress showed strong dependence on the initial 10% cold working, by exhibiting a maximum 12% increase at RT. In contrast, the subsequent additional 10% cold working, had relatively less effect (maximum 4%) in further increasing the flow stress.

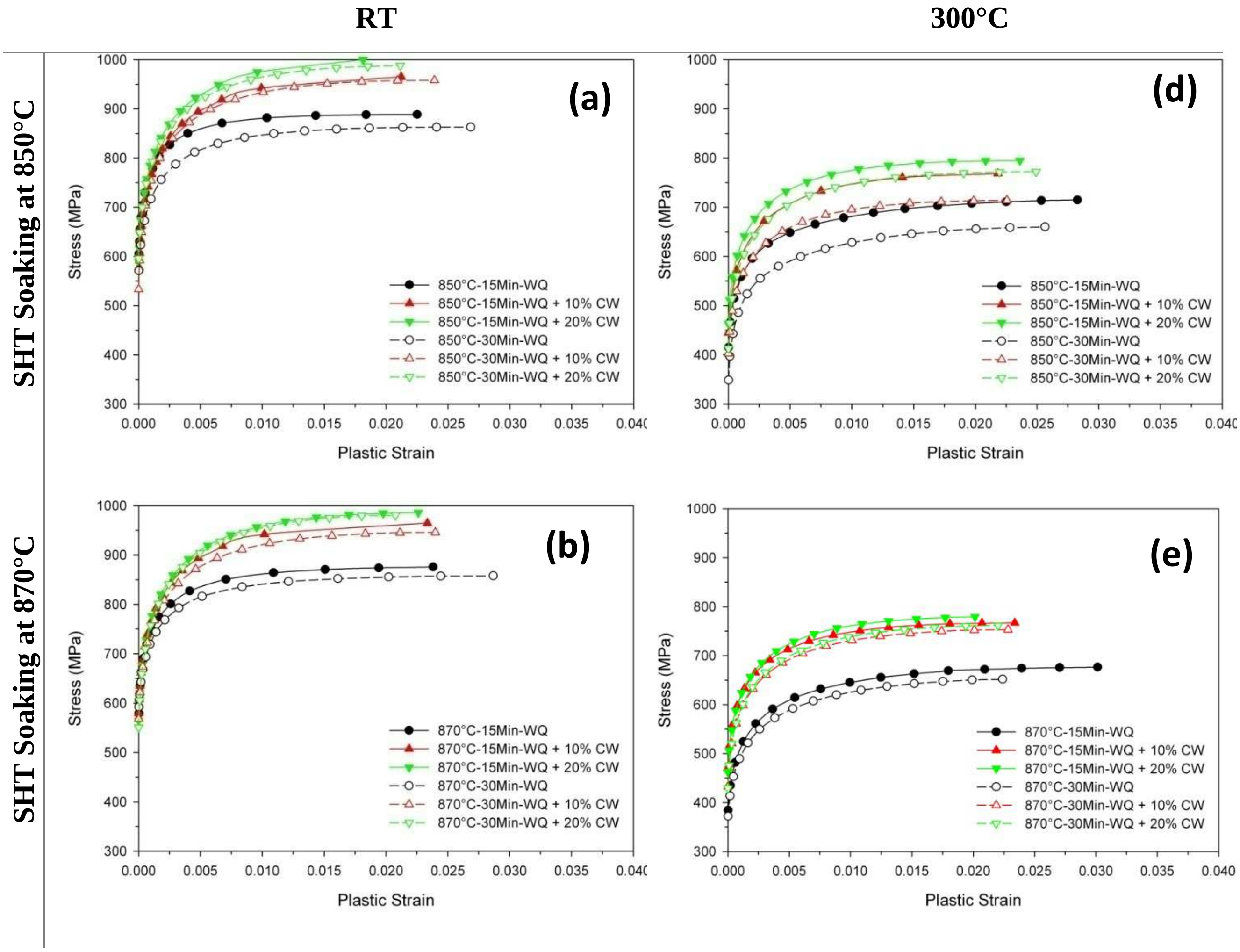

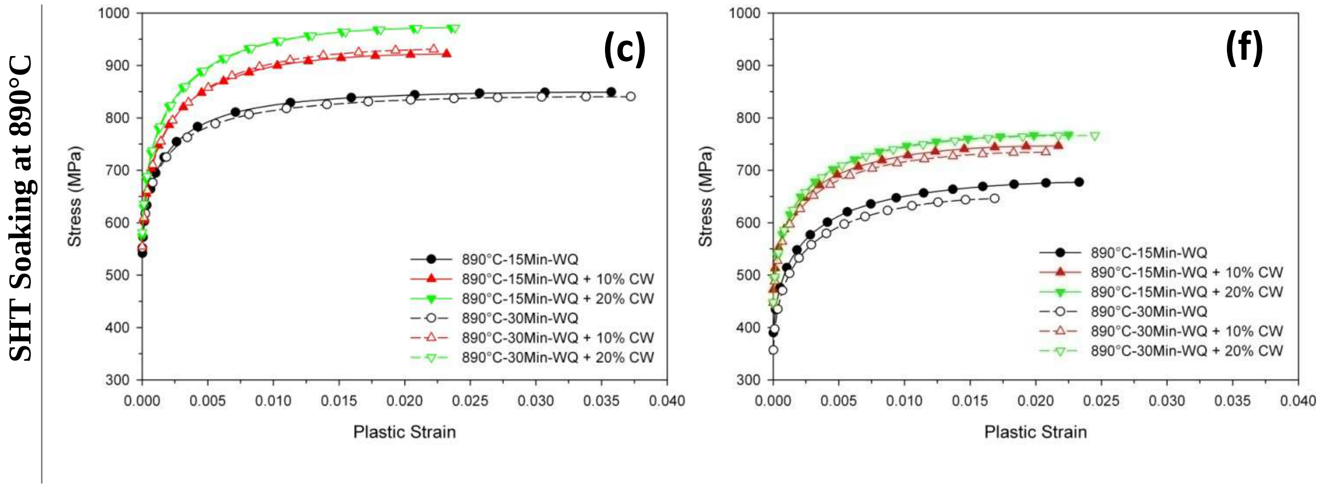

Figure 5.7: The lower bound flow behavior of Zr-2.5Nb alloy under different cold worked-solution heat treated conditions. Figures (a), (c) and (e) respectively represent the RT-flow behavior of the materials previously heat treated from 850, 870 and 890°C temperatures during solution heat treatment stage and Figures (b), (d) and (f) represent the corresponding flow behavior at 300°C.

As discussed in Chapter 4 that increase in SHT temperature and soaking duration though, does not have significant influence on the flow stress; however, decreased the flow stress of solution heat treated material. After cold working, such dependence of flow stress on SHT parameter became further weaker. Increasing temperature from RT to 300°C, resulted in the appreciable reduction (by 20-25%) of flow stress.

II. Tensile Strength

Figures 5.8 and 5.10 respectively show the influence of degree of cold working on tensile strength; 0.2% offset yield strength (YS) and UTS of Zr-2.5Nb alloy, having different solution heat treatment histories. Tensile strengths of the six solution heat treated materials, considered in this study, increased with increase in degree of cold working. Initial 10% cold working, in contrast to the additional 10% cold working had relatively strong influence on the tensile strength. After initial 10% cold working, YS exhibited ~5% and ~15% increase at RT and 300°C respectively. In contrast, with subsequent additional 10% cold working, further increase in YS of these materials were comparatively lower (<5%). Similar dependence of UTS on degree of cold working was observed.

Another important observation was that the materials solution heat treated from higher temperature still exhibited relatively lower tensile strengths, even after cold working. However, such strengths dependence on SHT temperatures is relatively weaker after cold working. In addition to this, the materials soaked for longer duration have relatively weak SHT temperature sensitive tensile strengths, even after cold working.

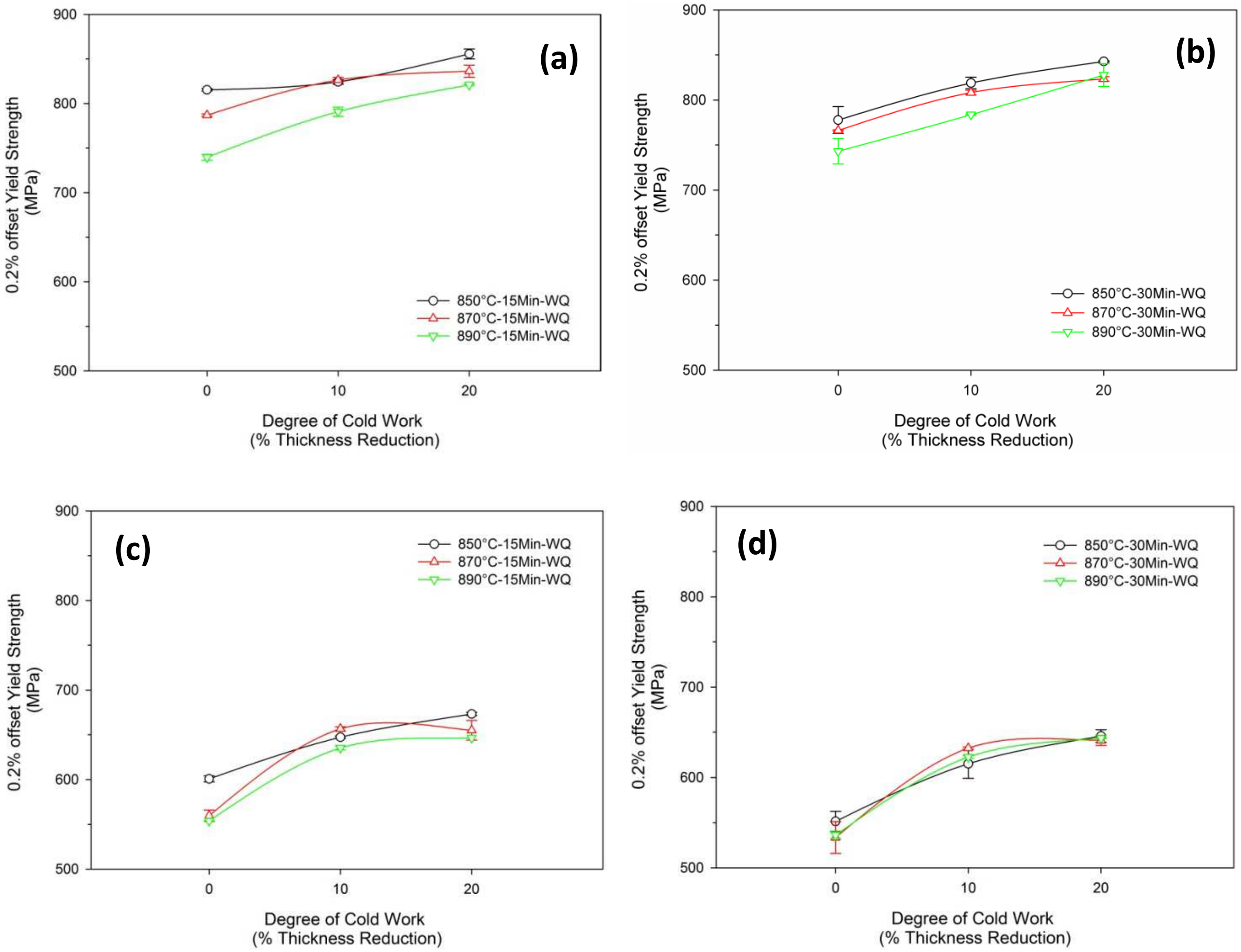

Figure 5.8: Influence of degree of cold work on 0.2% offset yield strength of Zr-2.5Nb alloy under different solution heat treated conditions. Plots (a) & (b) respectively show the RT-YS of the cold worked materials, previously soaked for 15 min duration during solution heat treatment stage. Plots (c) & (d) show the respective YS variations at 300°C.

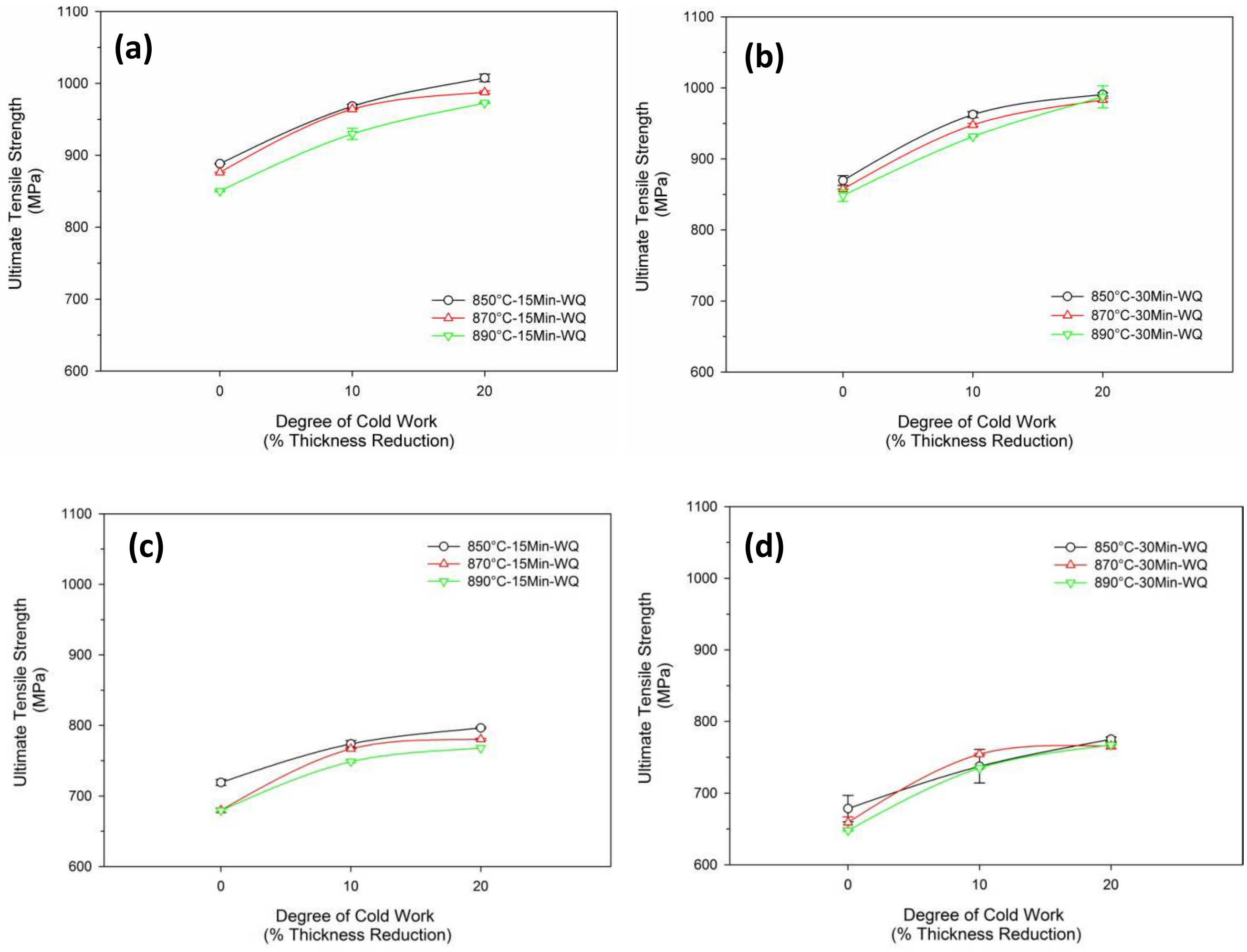

Figure 5.9: Influence of degree of cold work on ultimate tensile strengths of different solution heat treated Zr-2.5Nb alloy. Plots (a) & (b) respectively show the RT-UTS of the cold worked materials, previously soaked for 15 min duration during solution heat treatment stage. Plots (c) & (d) show the respective UTS variations at 300°C.

III. Uniform Elongation

Figure 5.10 shows the influence of degree of cold work on the uniform elongations, UEs (plastic strain corresponding to maximum stress) of Zr-2.5Nb alloy under different solution heat treated conditions. The UEs, in general decreased with increase in degree of cold working, especially under ambient condition, Figure 5.10 (a) & (b). However, at 300°C, UEs showed relatively weak dependence on the cold working treatment, Figure 5.10 (c) & (d). Another important observation was that the UEs of cold worked materials were practically insensitive to the SHT parameters viz., soaking temperature and duration.

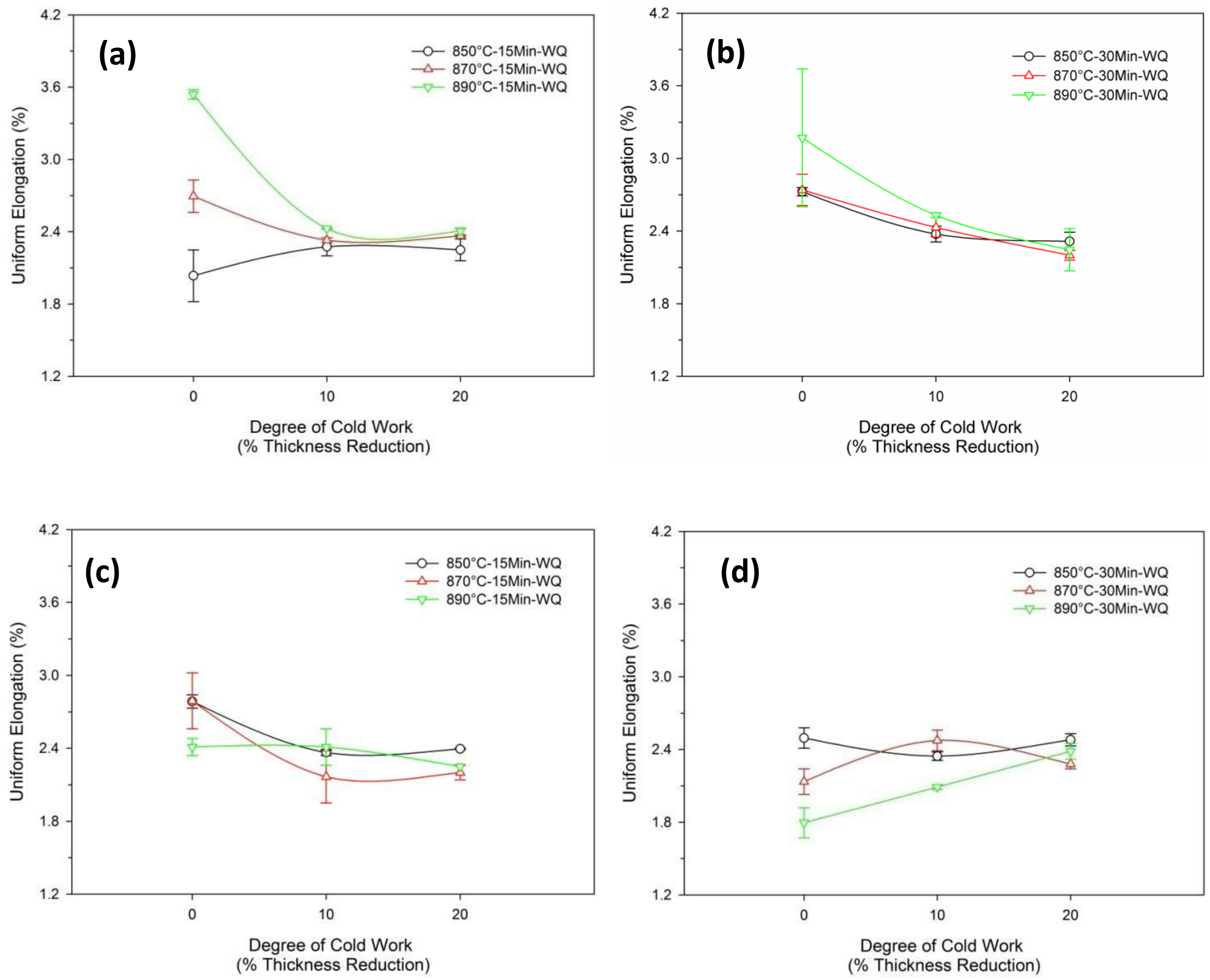

Figure 5.10: Influence of degree of cold work on the uniform elongations, UEs of different solution heat treated Zr-2.5Nb alloy. Plots (a) & (b) respectively show the RT-UEs of the cold worked materials, previously soaked for 15 min duration during solution heat treatment stage. Plots (c) & (d) show the respective UE variations at 300°C.

IV. Ductility

A. Total Elongation

Figure 5.11 shows the influence of degree of cold working on the total elongations, TEs (corresponding to 25 mm gage length) of Zr-2.5Nb alloy under different solution heat treated conditions. Here, TEs were determined by measuring the change in specimen gage length marked on its parallel region after fracture, as per Equation 4.2, Chapter 4.

Under ambient condition, TEs of the six parent heat treated materials were almost similar (ranging 12-14%), and thereby suggest that neither soaking temperature nor duration during the heat treatment significantly influenced the ductility of Zr-2.5Nb alloy. After the introduction of 10% cold work, TEs of the solution heat treated materials decreased appreciably (by almost 40%). With subsequent additional 10% cold work, further changes in TEs, similar to tensile strengths were marginal. Nevertheless, as per the average trend, TEs of the 30 min soaked materials were observed to be marginally lower than that of 15 min soaked materials for both parent heat treated and subsequently cold worked materials.

Opposite to its general trend with temperature, TEs of the solution heat treated materials at 300°C were marginally lower than at RT. Introduction of both 10 and 20% cold workings did not significantly affect the TEs of these materials at 300°C temperature, as shown in Figures 5.11 (c) & (d). However, after cold working, following general trend, TEs of solution heat treated materials at 300°C were higher than at RT.

Therefore, prior used soaking temperature and duration during the solution heat treatment stage did not play significant role in altering the TEs of Zr-2.5Nb alloy after cold working. At reactor operating temperature (300°C), both SHT and cold worked materials have practically similar TEs.

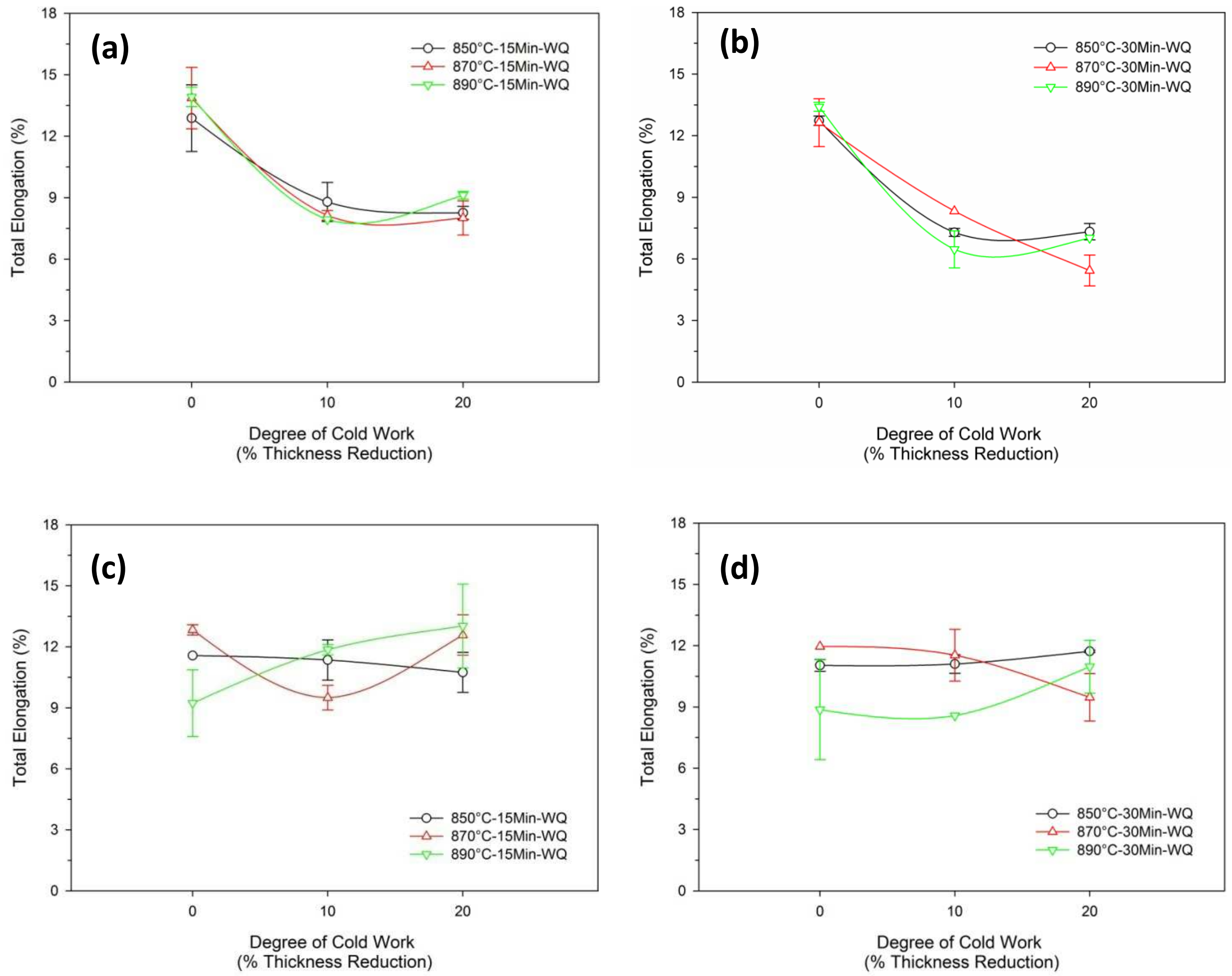

Figure 5.11: Influence of degree of cold work on the ductility (Total elongation, TE corresponding to 25 mm gage length) of different solution heat treated Zr-2.5Nb alloy. Plots (a) & (b) respectively show the RT-TEs of the cold worked materials, previously soaked for 15 and 30 min duration during solution heat treatment stage. Plots (c) & (d) show the respective TE variations at 300°C.

B. Reduction in Fracture Cross-sectional Area

Figure 5.12 shows the influence of degree of cold working on another ductility parameter; reduction in fracture cross-sectional areas of Zr-2.5Nb alloy under different solution heat treated conditions. Introduction of 10% cold work on the solution heat treated materials, resulted in substantial drop in reduction in fracture cross-sectional area under ambient condition; as cold working caused ~50% reduction in fracture cross-sectional area. With the subsequent additional

10% cold work, reduction in fracture cross-sectional area of the heat treated materials was observed to be marginally affected. Irrespective of previously used solution heat treatment temperature and soaking duration, the cold worked-solution heat treated materials exhibited almost similar reductions in fractured area, therefore signifying comparable behavior of these materials.

With increase in temperature from RT to 300°C, reduction in fracture cross-sectional area of the solution heat treated materials exhibited marginal increase (Figure 4.14 (b), Chapter 4), however, after cold working, it increased appreciably (by ~50%). In contrast to RT, reduction in fracture cross-sectional area of the solution heat treated materials at 300°C was observed to be insignificantly influenced by the degree of cold working.

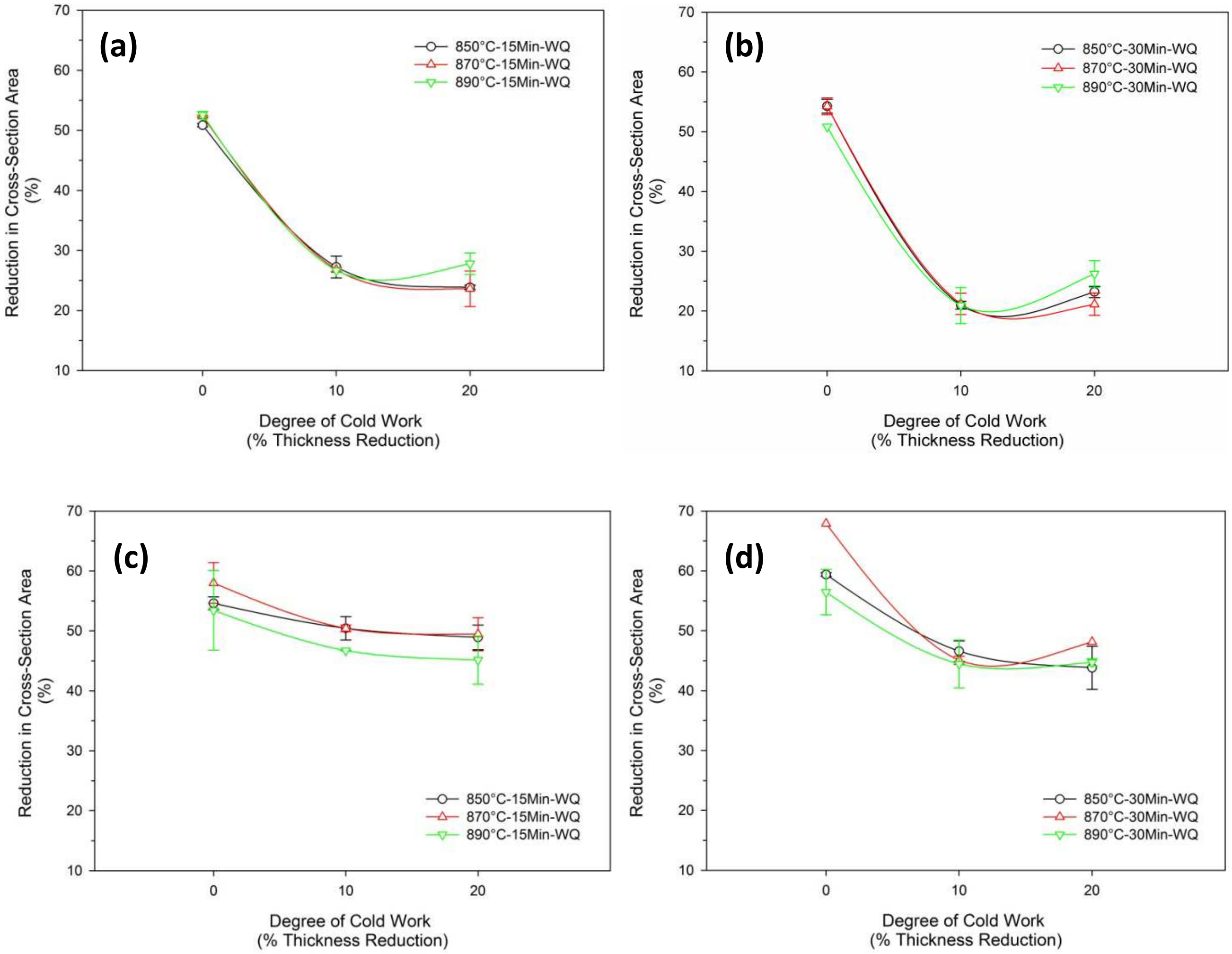

Figure 5.12: Influence of degree of cold work on another ductility parameter, the reduction in fracture cross section areas of different solution heat treated Zr-2.5Nb alloy. Plots (a) & (b) respectively show the RT-cross section reductions of the cold worked materials, previously soaked for 15 and 30 min duration during solution heat treatment stage. Plots (c) & (d) show the respective cross section reductions at 300°C.

V. Strain Hardening Behavior

A. *Strength Coefficient*

Figure 5.13 shows the influence of degree of cold working on strength coefficients of Zr-2.5Nb alloy under different solution heat treated conditions. Here, the strength coefficients were determined using the Hollomon's empirical power law work hardening relationship (Equation 4.3, Chapter 4) [102].

The strength coefficient of solution heat treated materials increased with increase in degree of cold working. Similar to tensile strength, the strength coefficients were also strongly dependent to the initial 10% cold working, and exhibited 20-30% increase at RT and <10% increase at 300°C. In contrast, with the additional 10% cold working, such changes were relatively lower viz., 6-10% at RT and closer to 4% at 300°C. Therefore, under ambient condition, strength coefficients had strong dependence on the degree of cold working.

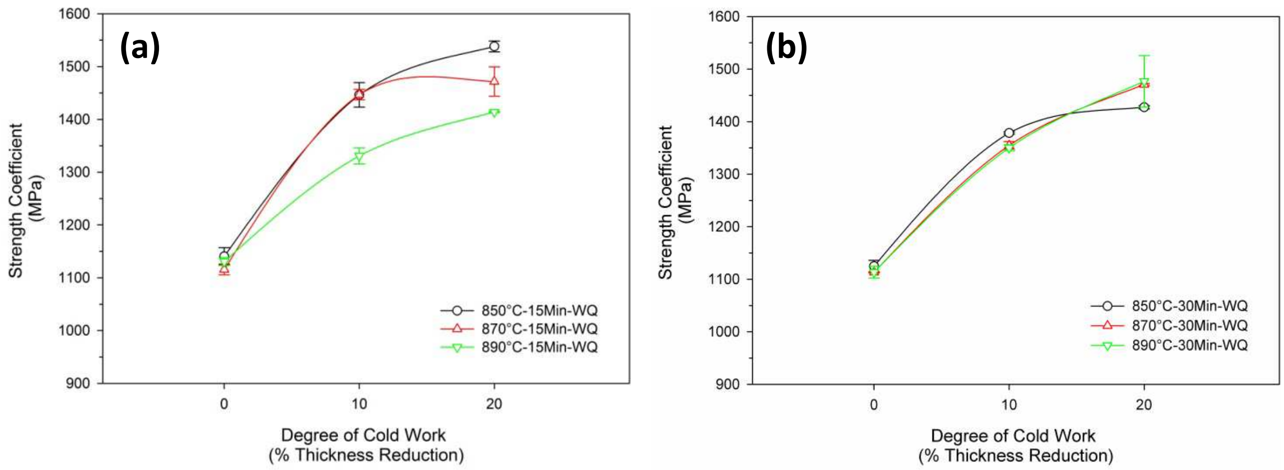

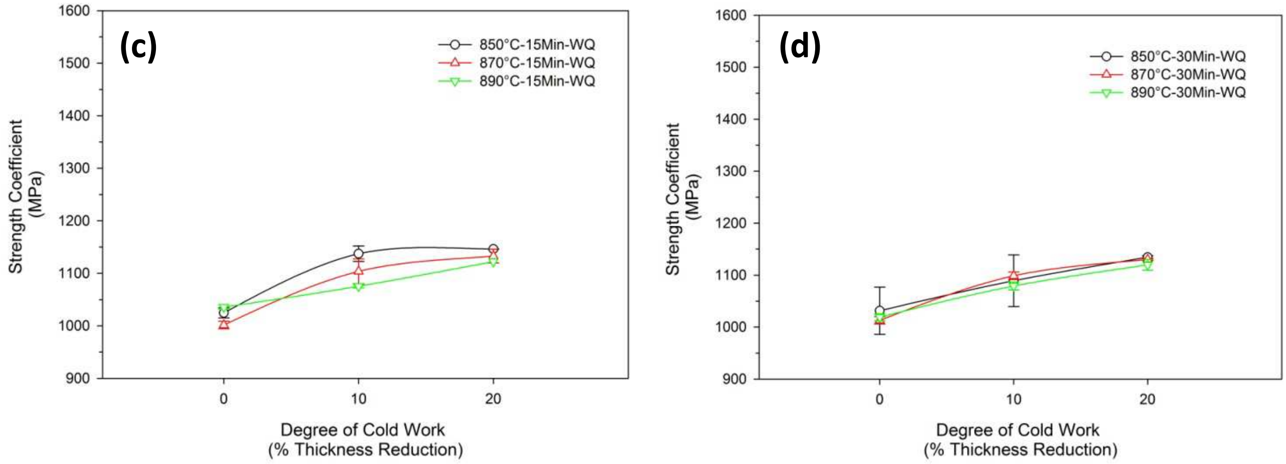

Figure 5.13: Influence of degree of cold working on the strength coefficients of Zr-2.5Nb alloy under different solution heat treated conditions. The strength coefficients were determined as per Hollomon’s work hardening relationship (Equation 4.3, Chapter 4). Plots (a) & (b) respectively show the RT-strength coefficients of the cold worked materials, previously soaked for 15 and 30 min duration during the solution heat treatment stage. Plots (c) & (d) show the respective coefficients at 300°C.

B. *Strain Hardening Exponent*

Figure 5.14 shows the influence of degree of cold working on strain hardening exponents of Zr-2.5Nb alloy under different solution heat treated conditions. Here, the strain hardening exponents were determined using the Hollomon’s empirical power law work hardening relationship (Equation 4.3, Chapter 4) [102].

The strain hardening exponents of solution heat treated materials increased with increase in degree of cold working. Similar to tensile strengths and strength coefficient, the strain hardening exponents were also strongly dependent on the initial 10% cold working, and exhibited 40-75% increase at RT. In contrast, with the additional 10% cold working, further changes were marginal. At 300°C, strain hardening exponents were weakly influenced by the cold working treatment, however a marginal reduction was observed after cold working.

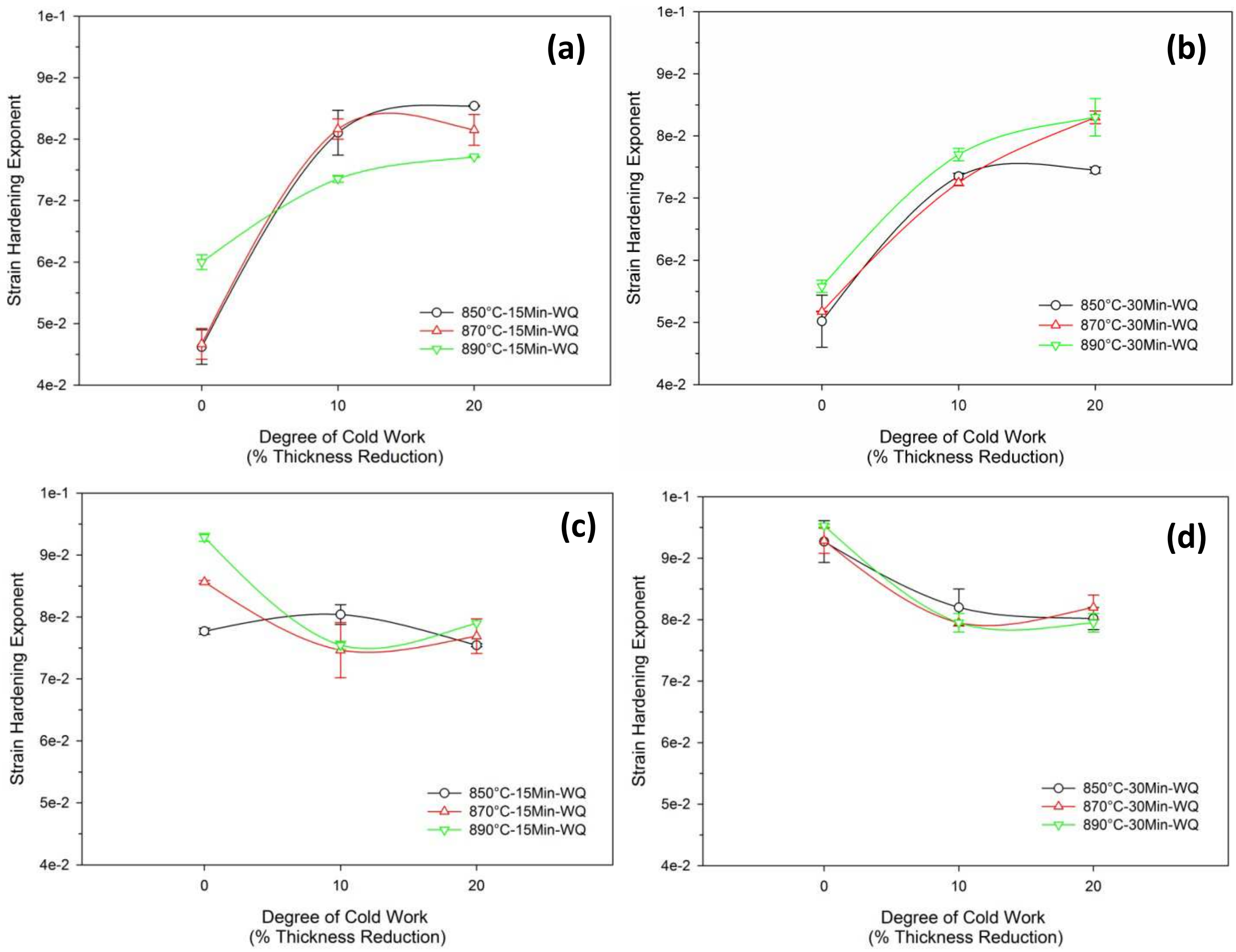

Figure 5.14: Influence of degree of cold working on the strain hardening exponents of Zr-2.5Nb alloy under different solution heat treated conditions. Plots (a) & (b) respectively show the RT-hardening exponents of the cold worked materials, previously soaked for 15 and 30 min duration during the solution heat treatment stage. Plots (c) & (d) show the respective hardening exponents at 300°C.

In summary, the tensile properties of solution heat treated Zr-2.5Nb alloy are strongly sensitive to the initial 10% cold working; however with subsequent additional 10% cold working these properties further exhibited marginal changes. Increase in cold working within 0-20% domain increases the tensile strengths and strain hardening characteristic, however causes substantial reduction in the ductility of solution heat treated materials.

5.2.3 Fracture Behavior

I. Fracture Resistance, *J-R* curves

The fracture resistance, *J-R* curves of different cold worked-solution heat treated Zr-2.5Nb alloy are shown in Figure 5.15. In majority of the cases, after imparting 10% cold work, the *J* parameters of solution heat treated materials decreased, signifying reduction in fracture toughness. However, subsequent additional 10% cold work resulted in marginal improvement of *J* parameters. Under ambient condition, in general, the *J-R* curves of SHT and cold worked materials had no major differences, however at 300°C, such differences became notable.

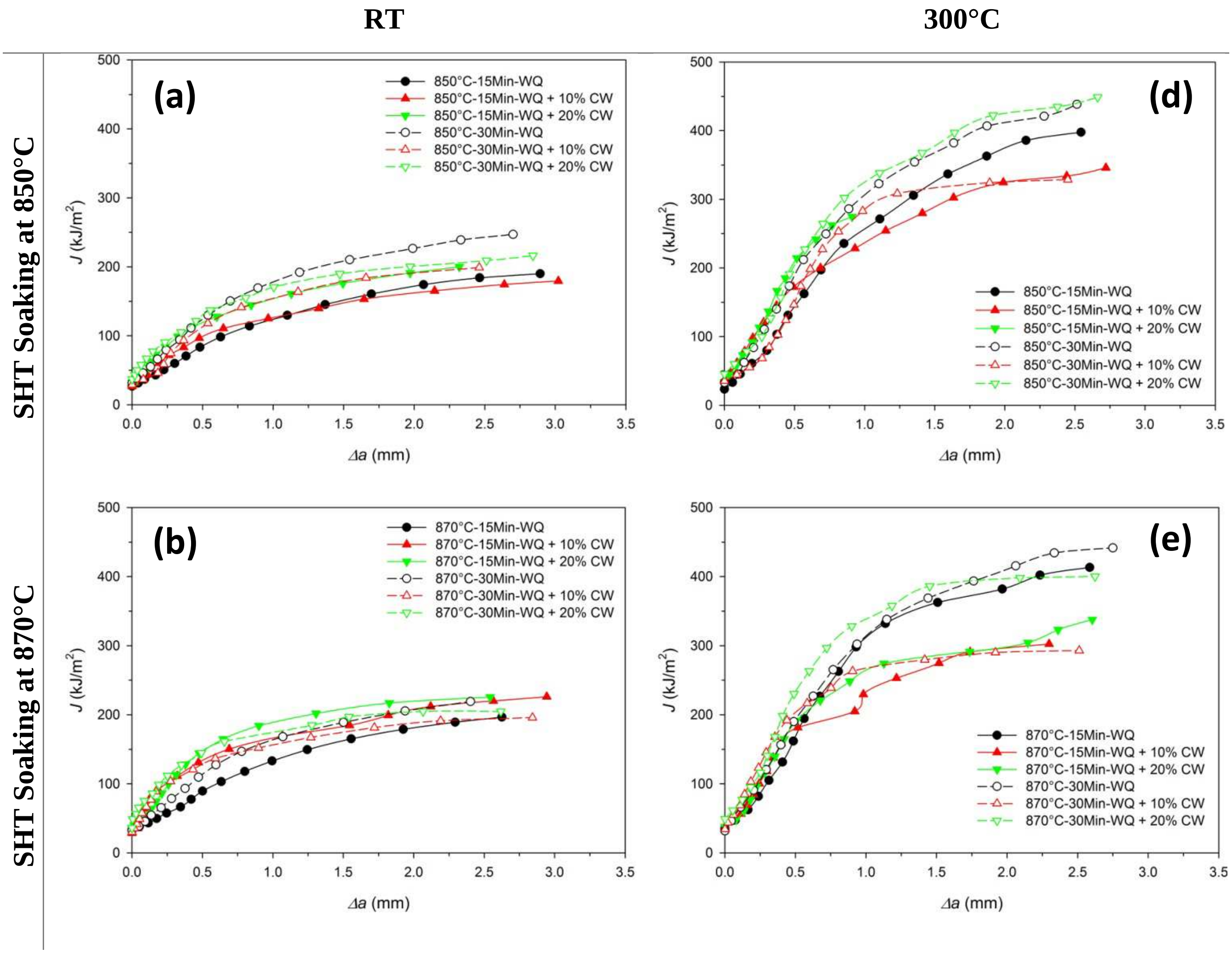

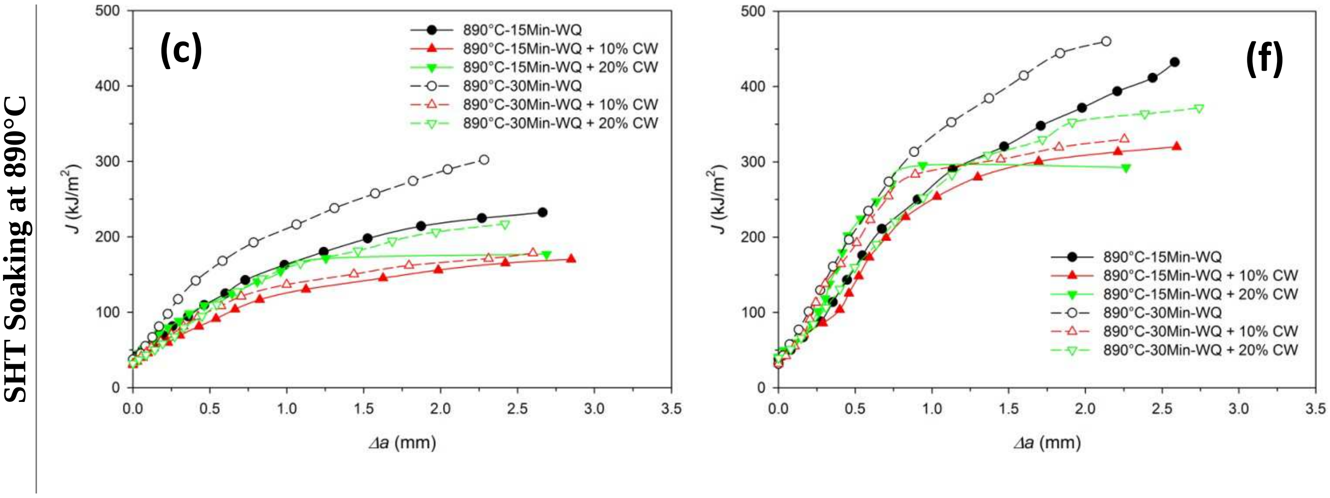

Figure 5.15: The lower bound fracture resistance behavior of different solution heat treated and subsequently cold worked Zr-2.5Nb alloy (a), (b) & (c) at RT and (d), (e) & (f) at 300°C.

II. Fracture Toughness

Influence of degree of cold working on the fracture toughness parameters; $J_{F(max)}$ and *dJ/da* of Zr-2.5Nb alloy under different solution heat treated conditions at ambient temperature is shown in Figure 5.16. Cold working, in general had weak influence on the $J_{F(max)}$ parameters of solution heat treated materials, especially soaked for longer duration (Figure 5.16 (c)). Cold working mainly influenced the slope of resistance curve, i.e., *dJ/da* parameter. Increasing degree of cold working caused reduction in the *dJ/da* parameters of solution heat treated materials (by 20-35%), which therefore suggests the reduction in propagation resistance of these materials (Figure 5.16 (b) & (d)).

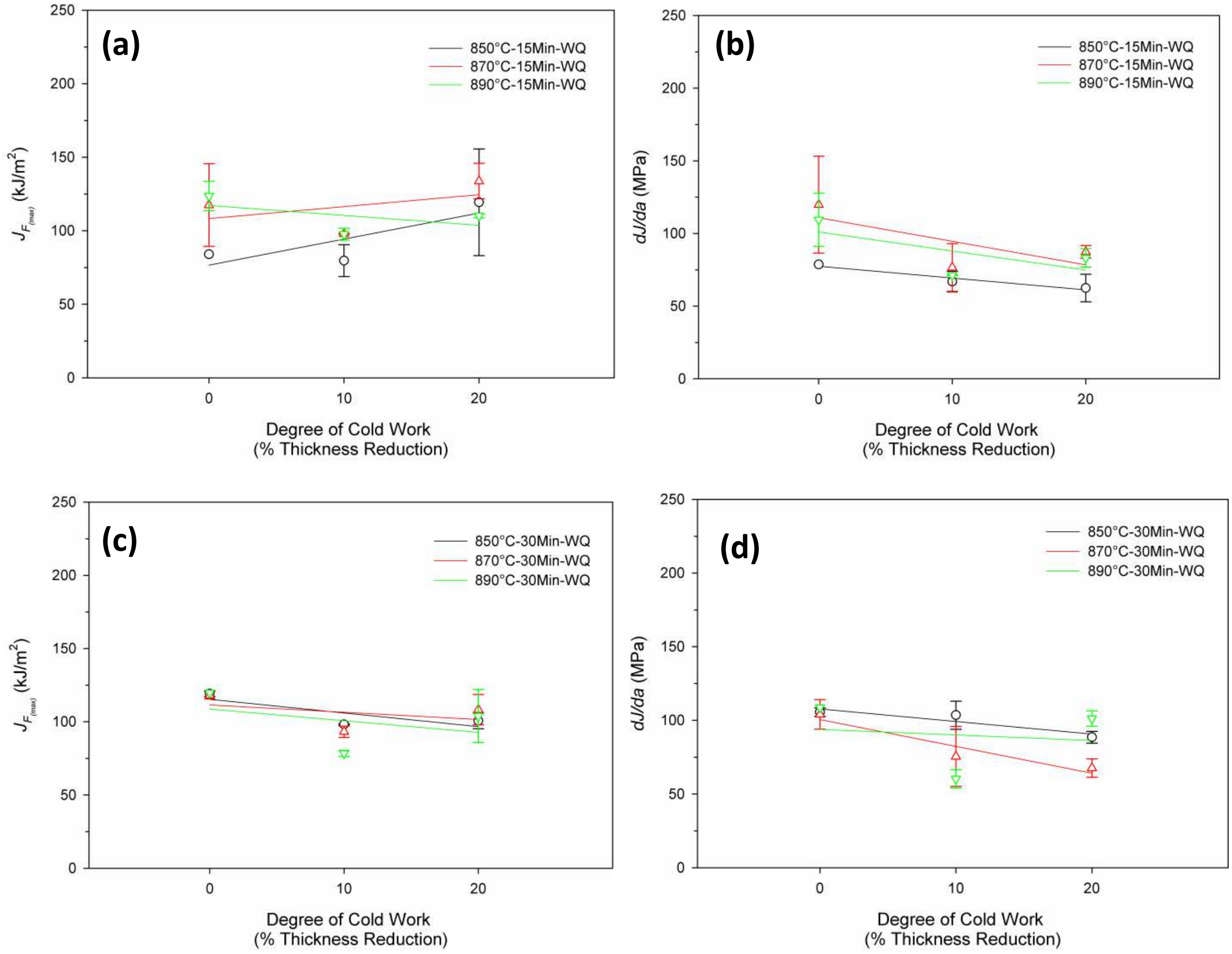

Figure 5.18: Influence of degree of cold working on the fracture toughness parameters of solution heat treated Zr-2.5Nb alloy under ambient condition.

Figure 5.17 shows the influence of degree of cold working on the fracture toughness parameters at 300°C. Increasing temperature from RT to 300°C resulted in appreciable increase of $J_{F(max)}$ (by > 50%) and *dJ/da* parameters (by > 70%). At 300°C, the *dJ/da* parameter exhibited considerable scatter as compared to at RT. Here again, the $J_{F(max)}$ parameters of solution heat treated materials were weakly influenced by the cold working treatment, Figure 5.17 (a) & (c).

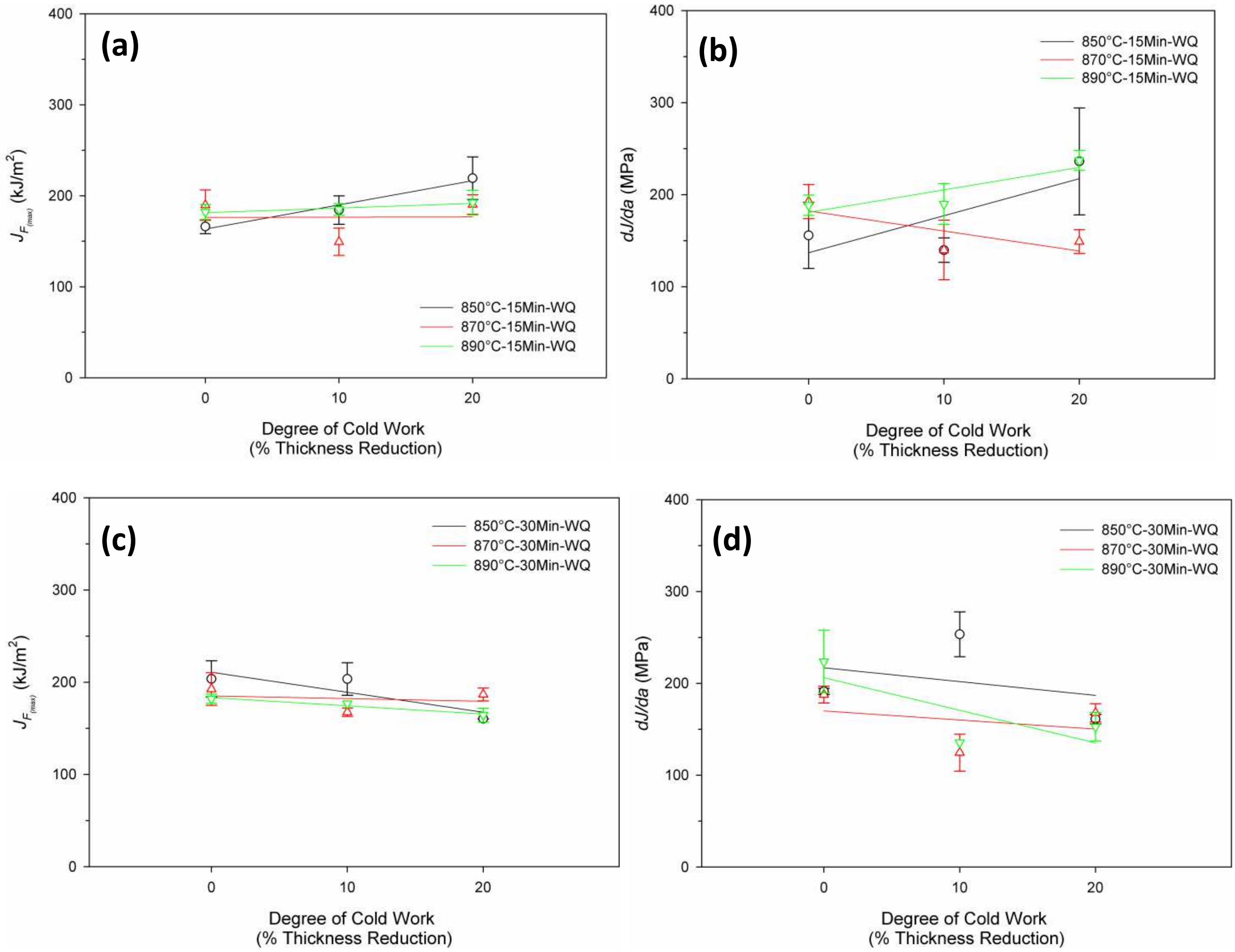

Figure 5.17: Influence of degree of cold working on the fracture toughness parameters of solution heat treated Zr-2.5Nb alloy at 300°C.

5.3 Study of Fracture Surface

The visual fracture surface features of broken C(T) specimen of one of the solution heat treated Zr-2.5Nb alloy under solution heat treated and subsequently 10% and 20% cold working conditions are shown in Figure 5.18. Similar to solution heat treated materials, the fracture surface of cold worked materials showed typical inclined regions (Region-C) with a central narrow flat region (Region-B). However, after cold working, the solution heat treated materials, in general exhibited relatively larger flat region, especially under ambient test condition, suggesting for the shifting of state of stress towards plane strain condition.

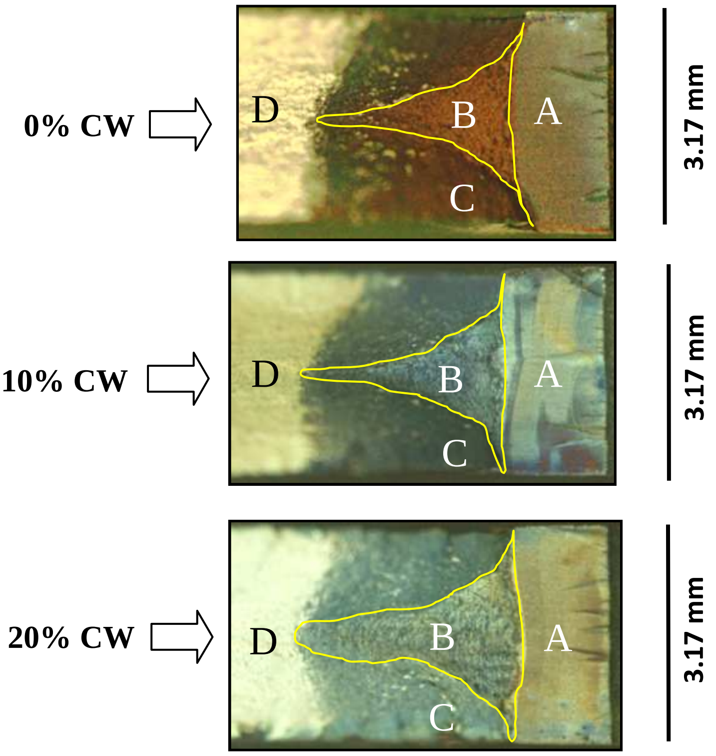

Figure 5.18: Evolution of fracture surfaces of the broken C(T) specimens of Zr-2.5Nb alloy, under SHT, subsequently 10% cold worked and 20% cold worked conditions. Each fracture surface exhibits four distinct regions: Pre-cracked region (A), Flat fracture region (B), Inclined fractured region (C) and Post cracked region (D). From these fractographs, it can be seen that with increase in degree of cold working, the area occupied by flat region (B) on the fracture surface increases.

The fracture surface areas of broken C(T) specimens were measured through image analysis using 'Image-J' software. Figure 5.19 shows the dependence of flat fractured areas on degree of cold working for the six solution heat treated materials. With increase in degree of cold working, the flat fractured region in general, increased especially under ambient fractured condition, Figure 5.19 (a) & (b). Under ambient fractured condition, with reference to SHT materials which showed an average flat region of 1.9 mm^2, subsequently 10 and 20% cold worked materials had respectively larger flat regions of 2.5 and 3 mm^2. In contrast, at 300°C fractured condition, flat fracture regions had relatively weak dependence on the degree of cold working, Figure 5.19 (c) & (d). Under this condition, with reference to parent materials which showed an average flat region of 1.8 mm^2, the subsequently 10 and 20% cold worked materials comprised respective flat regions of 1.9 and 2.4 mm^2.

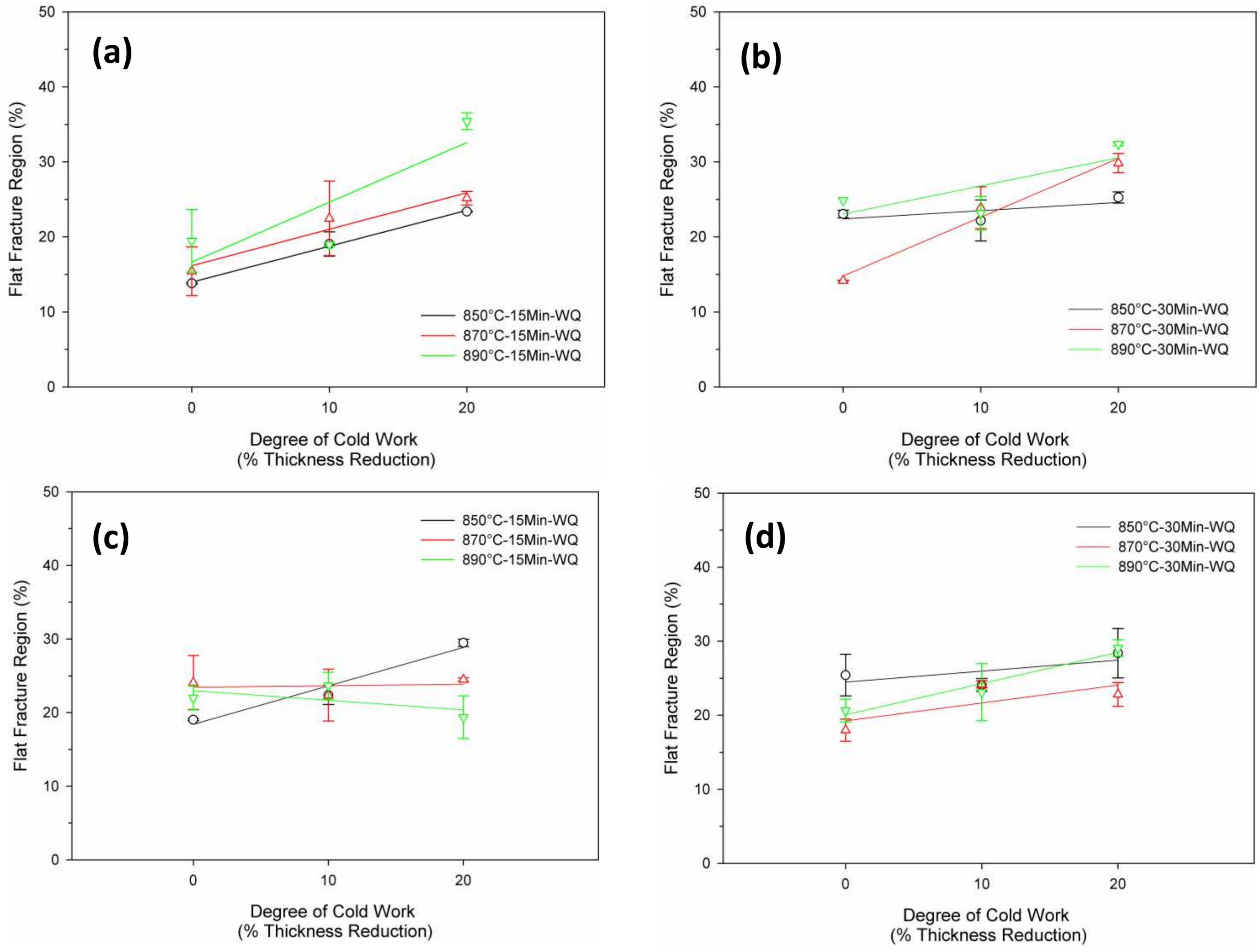

Figure 5.19: Influence of degree of cold working on the proportionate flat fractured areas of the broken C(T) specimens for the six solution heat treated Zr-2.5Nb alloy. Plots (a) & (b) respectively show the flat fractured areas of the RT tested cold worked materials, previously soaked for 15 and 30 min duration during the SHT stage. Plots (c) & (d) show the respective flat fractured areas of the C(T) specimens tested at 300°C.

5.3.1 SEM Fractography

I. Pre-cracked Surface

Fatigue pre-cracked surfaces of both the parent heat treated and subsequently cold worked materials exhibited typical plateaus like features, which were in general, oriented along the crack propagation direction. Figure 5.20 shows such features for the two extreme SHT conditions viz., 850°C-15Min-WQ and 890°C-30Min-WQ, before and after cold working. During fatigue pre-cracking, the cracks seemed to propagate along such plateaus. The pre-cracked surface features of the parent heat treated and cold worked materials were almost similar.

II. Fracture Surface

Figures 5.21-5.24 show the comparison of fractographic features of parent heat treated and subsequently cold worked materials under two extreme SHT conditions viz., 850°C-15Min-WQ and 890°C-30Min-WQ. Similar to solution heat treated materials, fracture surface of subsequently cold worked materials exhibited typical dimple structure characteristic of a ductile failure. The dimples in cold worked materials, similar to SHT materials, had size in-homogeneity, which indicate the non uniform distribution of nucleation sites.

The dimple morphologies of cold worked materials can be categorized into parabolic (elongated) and equiaxed shapes, similar to the parent heat treated materials. Under ambient fracture condition, majority of the dimples on inclined fracture surface were nearly equiaxed in shape, though minor were having slight ovality. In contrast, fracture at 300°C resulted in the formation of mostly parabolic shaped dimples whose major axes was oriented at ~45° angle to specimen thickness direction, as shown in Figure 5.22. Majority of such elongated dimples were not completely surrounded by their lips. Based on dimple morphology, the solution heat treated and subsequently cold worked materials were nearly analogous under ambient fracture condition. However, at

300°C, dimples of the cold work materials exhibited significantly higher degree of ovality as compared to that observed in the solution heat treated materials. Additionally, cold worked materials showed relatively finer dimple structure as compared to parent materials.

Dimples on the intermediate narrow flat fractured region of both the solution heat treated and subsequently cold worked materials, in general exhibited elongated morphology having their major axes along sample width direction, thereby suggesting the crack propagation along sample width direction on this plane, see Figures 5.23 and 5.24. In contrast to SHT materials, cold worked materials exhibited relatively shallower dimples on this narrow flat region.

As can be seen from Figures 5.25 and 5.26 that cold working did not has drastic influence on the SZWs ahead pre-cracked regions of different solution heat treated materials. Furthermore, at 300°C fracture condition, materials previously soaked for 30 min duration in contrast to 15 min during SHT, showed marginally wider stretched zones, even after cold working.

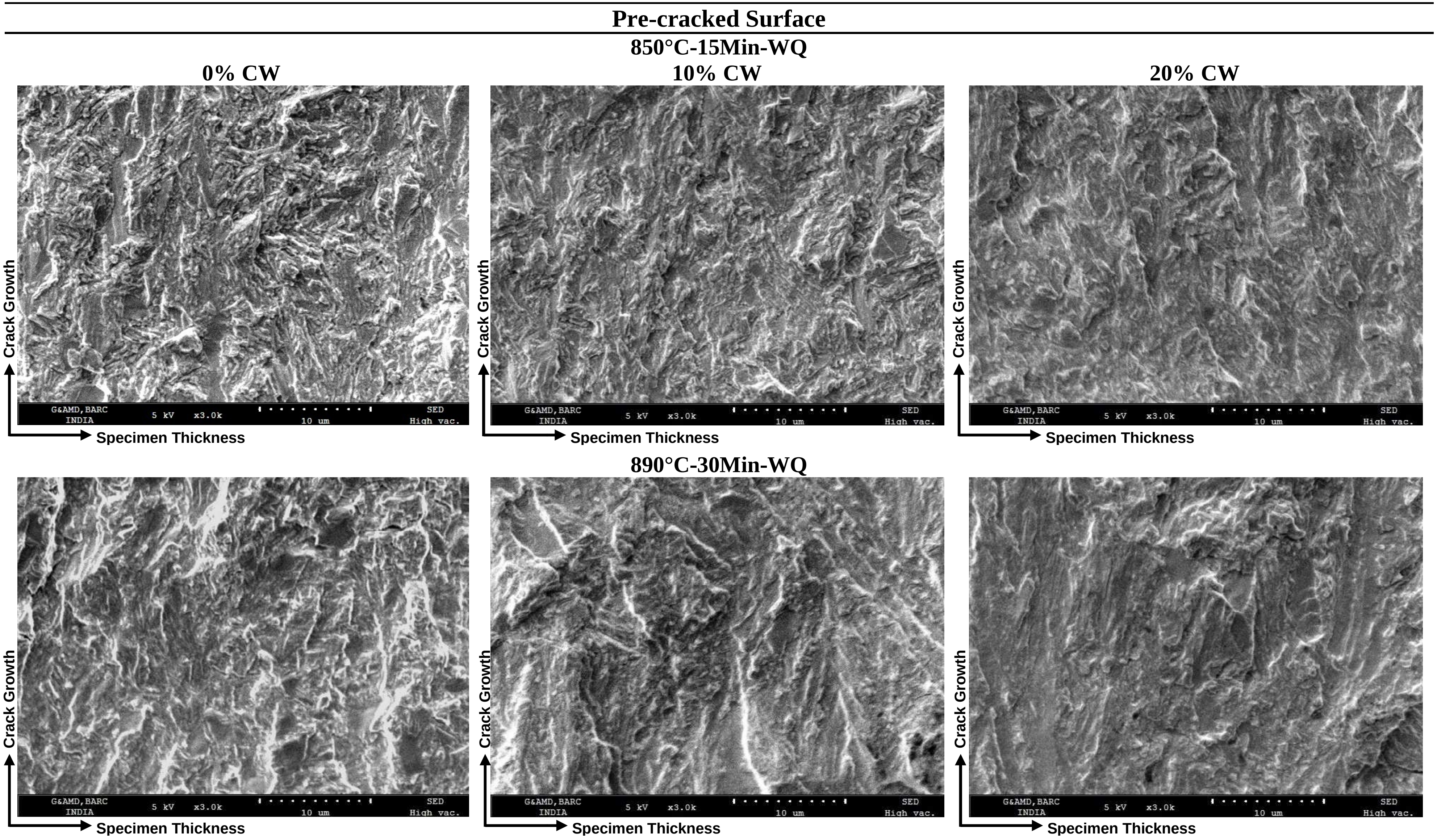

Figure 5.20: SEM fractographs illustrating the fatigue pre-cracked surfaces of the broken Zr-2.5Nb alloy C(T) specimens under solution heat treated, and subsequently cold worked with 10 & 20% thickness reductions.

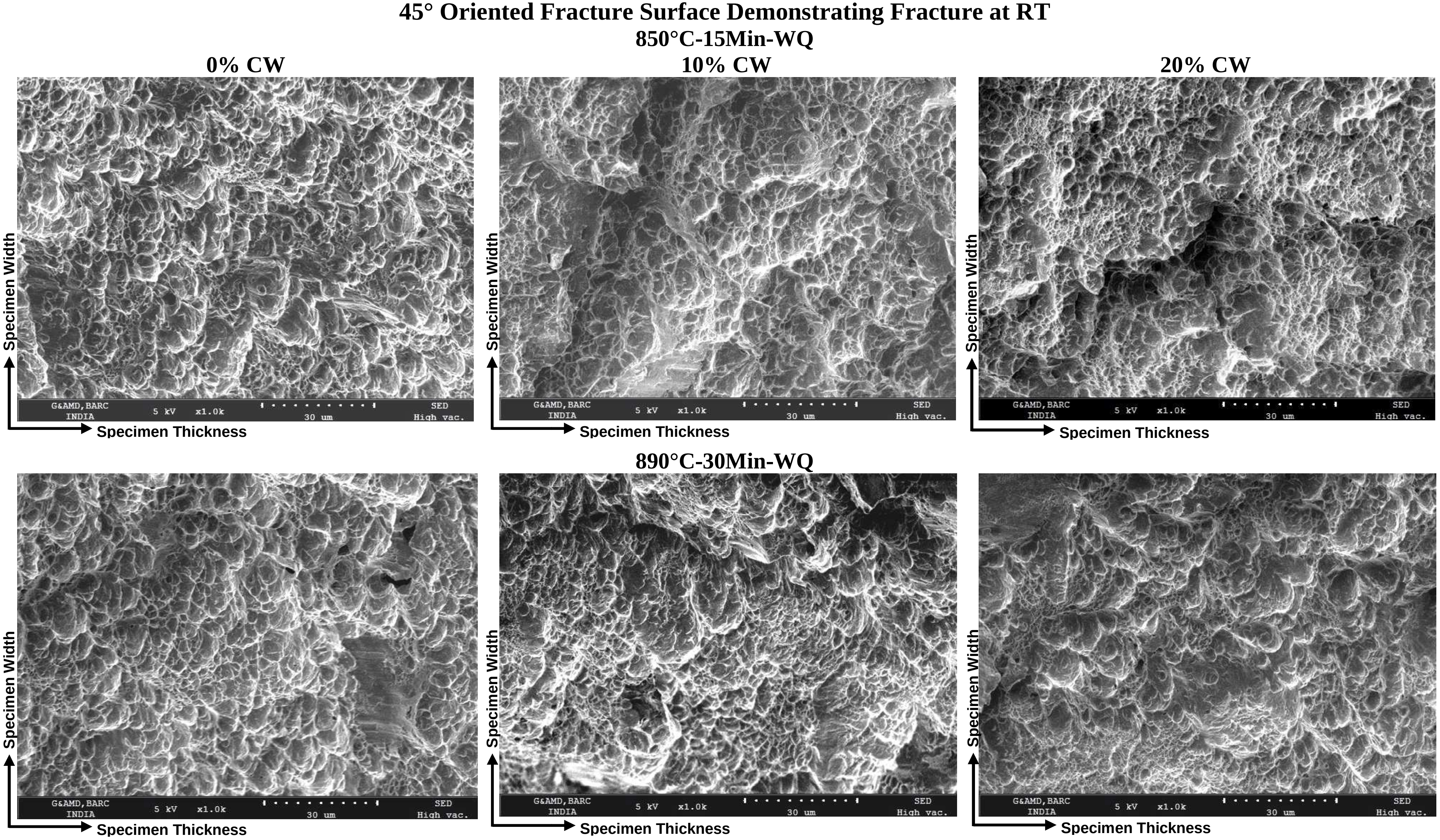

45° Oriented Fracture Surface Demonstrating Fracture at RT

850°C-15Min-WQ

0% CW

10% CW

20% CW

890°C-30Min-WQ

Figure 5.21: SEM fractographic features at the inclined regions of the broken Zr-2.5Nb alloy C(T) specimens under solution heat treated and subsequently cold worked with 10 & 20% thickness reductions, tested at RT.

45° Oriented Fracture Surface Demonstrating Fracture at 300°C

850°C-15Min-WQ

0% CW **10% CW** **20% CW**

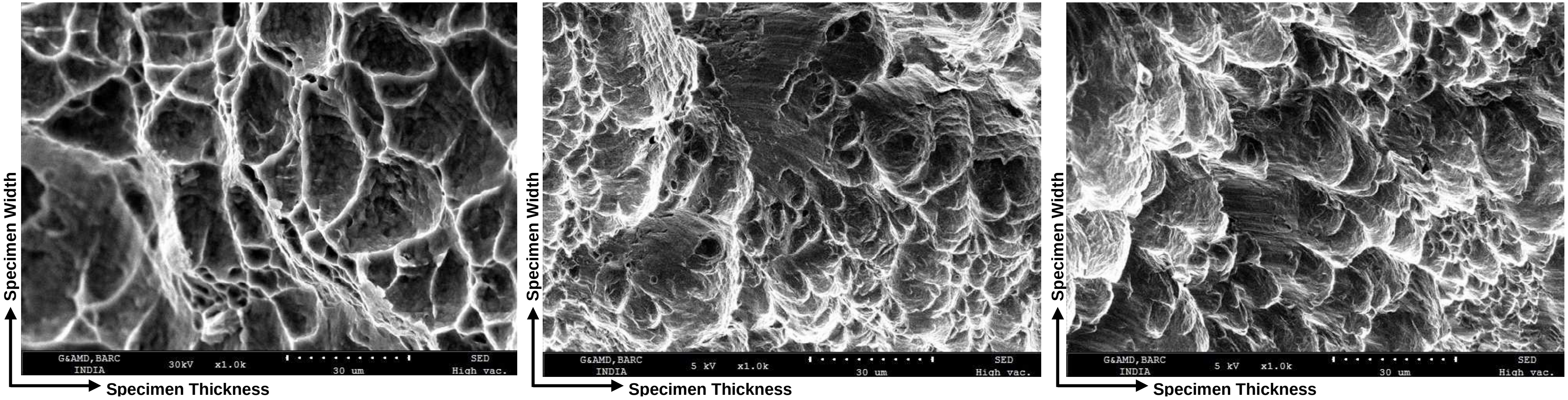

890°C-30Min-WQ

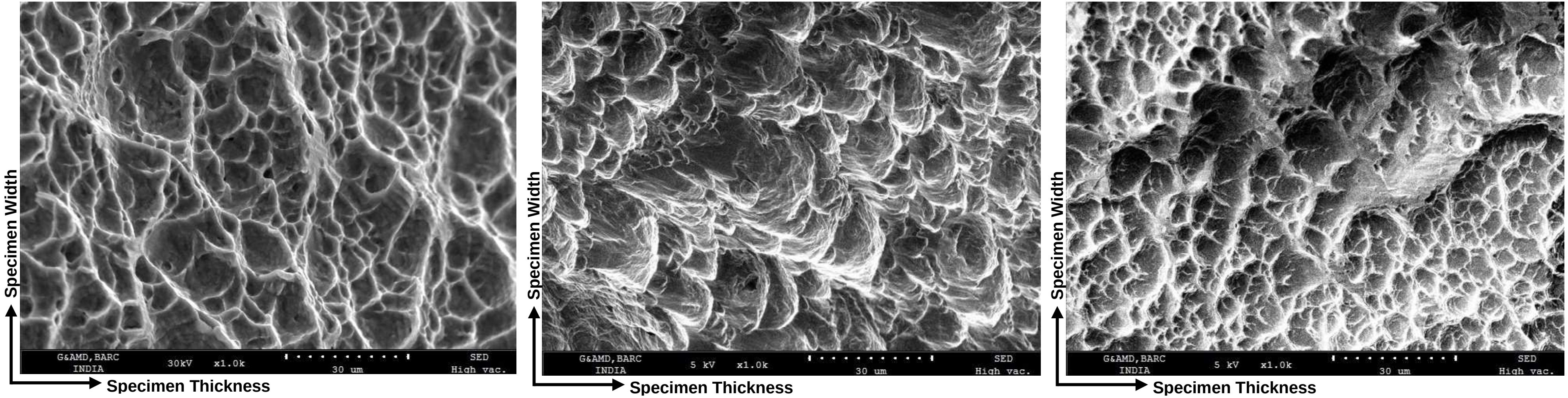

Figure 5.22: SEM fractographic features at the inclined regions of the broken Zr-2.5Nb alloy C(T) specimens under solution heat treated and subsequently cold worked with 10 & 20% thickness reductions, tested at 300°C.

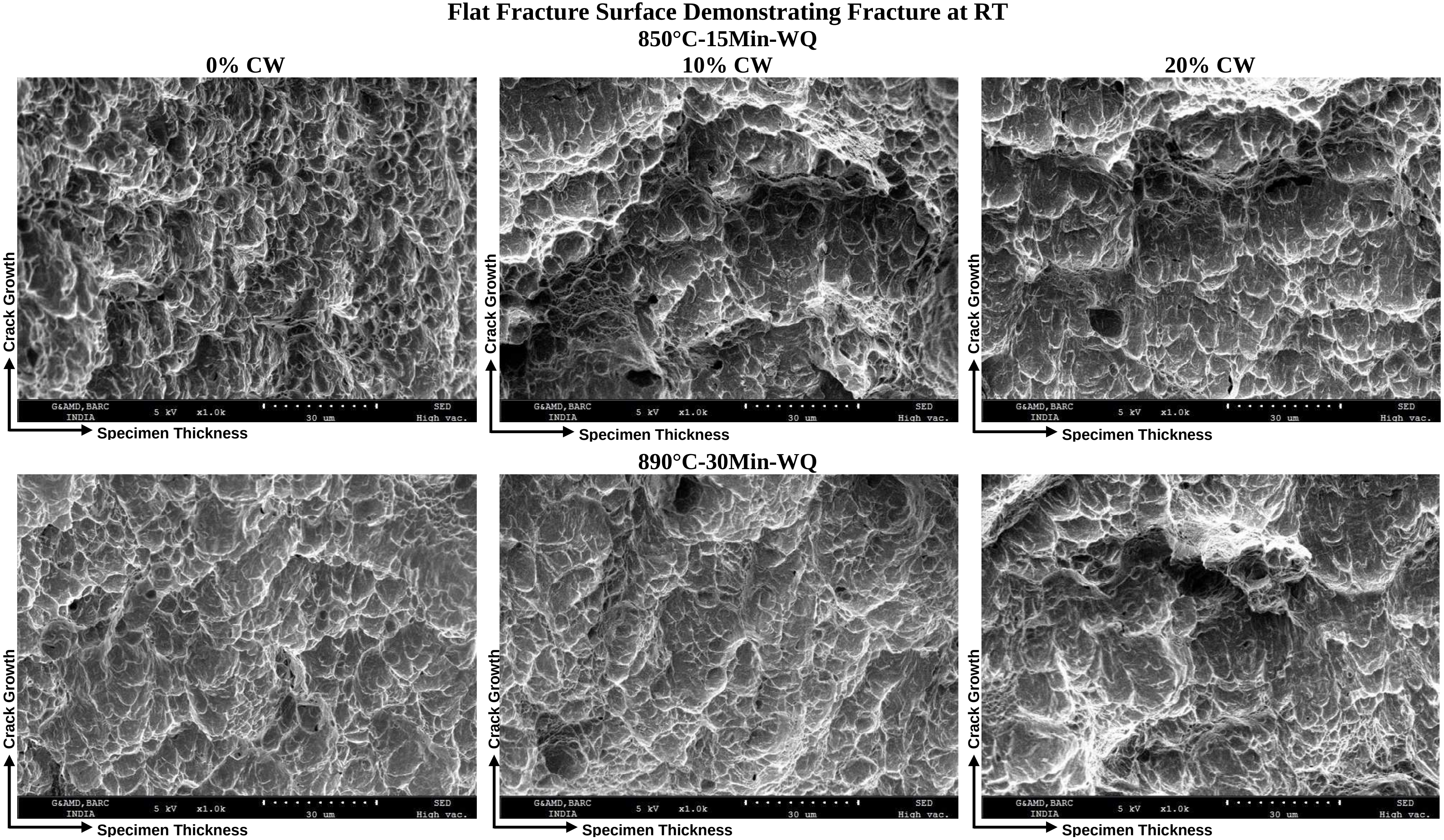
Flat Fracture Surface Demonstrating Fracture at RT

850°C-15Min-WQ

0% CW **10% CW** **20% CW**

890°C-30Min-WQ

Figure 5.23: SEM fractographic features at the flat fractured region of the broken Zr-2.5Nb alloy C(T) specimens under solution heat treated and subsequently cold worked with 10 & 20% thickness reductions, tested at RT.

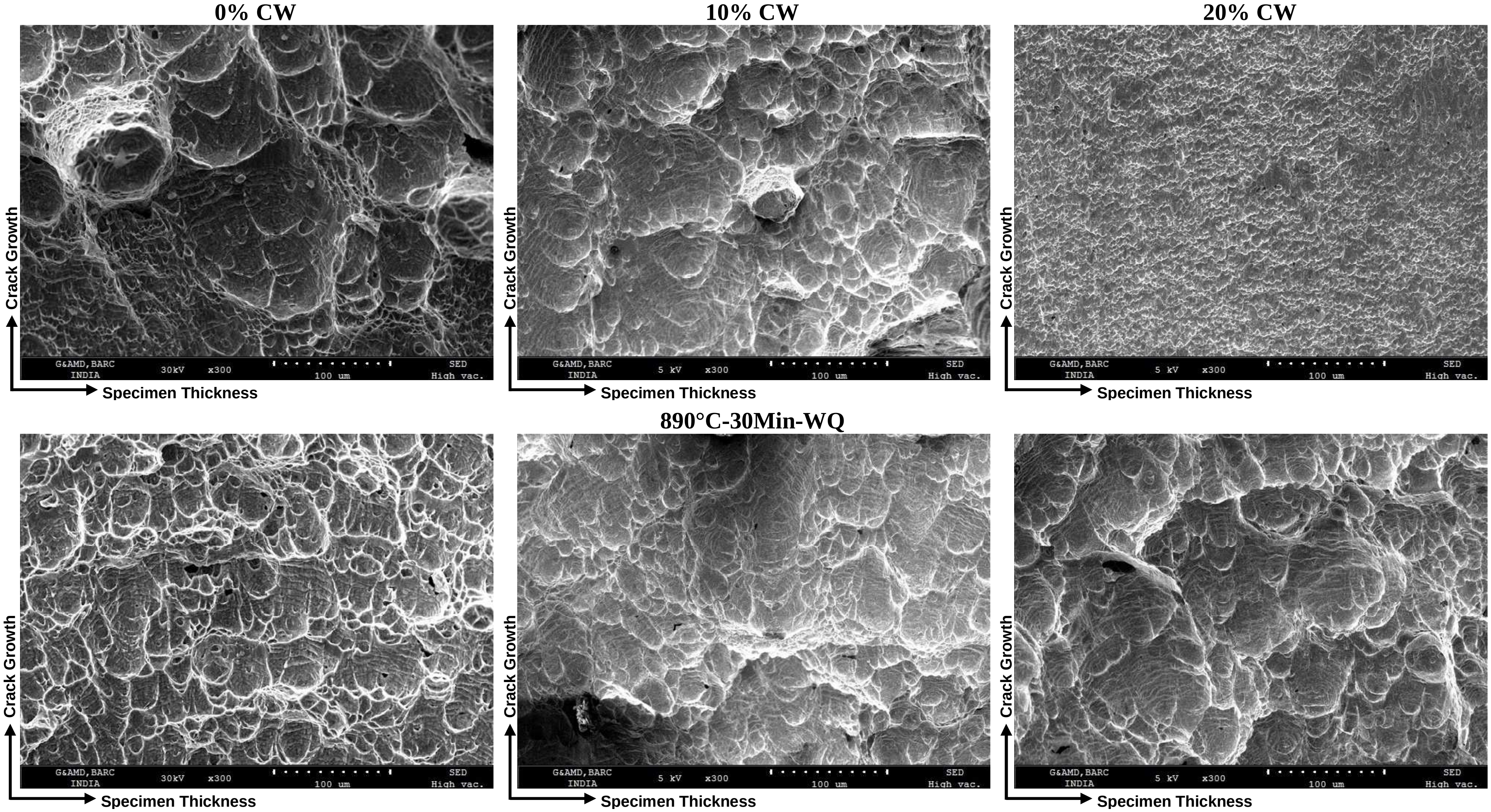

Flat Fracture Surface Demonstrating Fracture at 300°C

850°C-15Min-WQ

0% CW **10% CW** **20% CW**

890°C-30Min-WQ

Figure 5.24: SEM fractographic features at the flat fractured region of the broken Zr-2.5Nb alloy C(T) specimens under solution heat treated and subsequently cold worked with 10 & 20% thickness reductions, tested at 300°C.

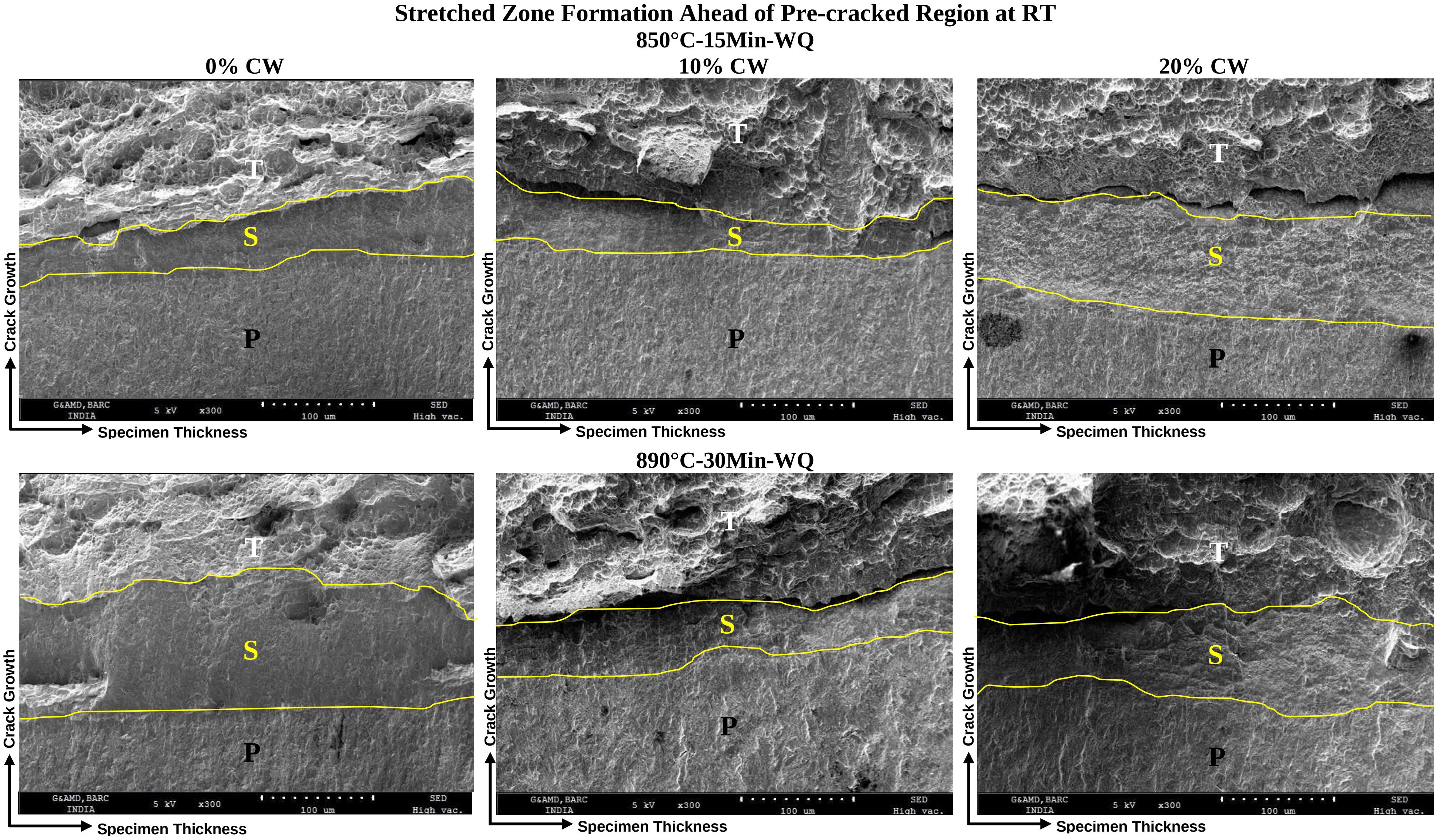

Figure 5.25: SEM fractographs showing the stretched zone formation ahead the pre-cracked regions of the broken C(T) specimens under solution heat treated and subsequently cold worked with 10 & 20% thickness reductions, tested at RT. In individual figures, the stretched zone (S) is bounded by the yellow lines, which separate pre-cracked (P) region from tearing (T) region.

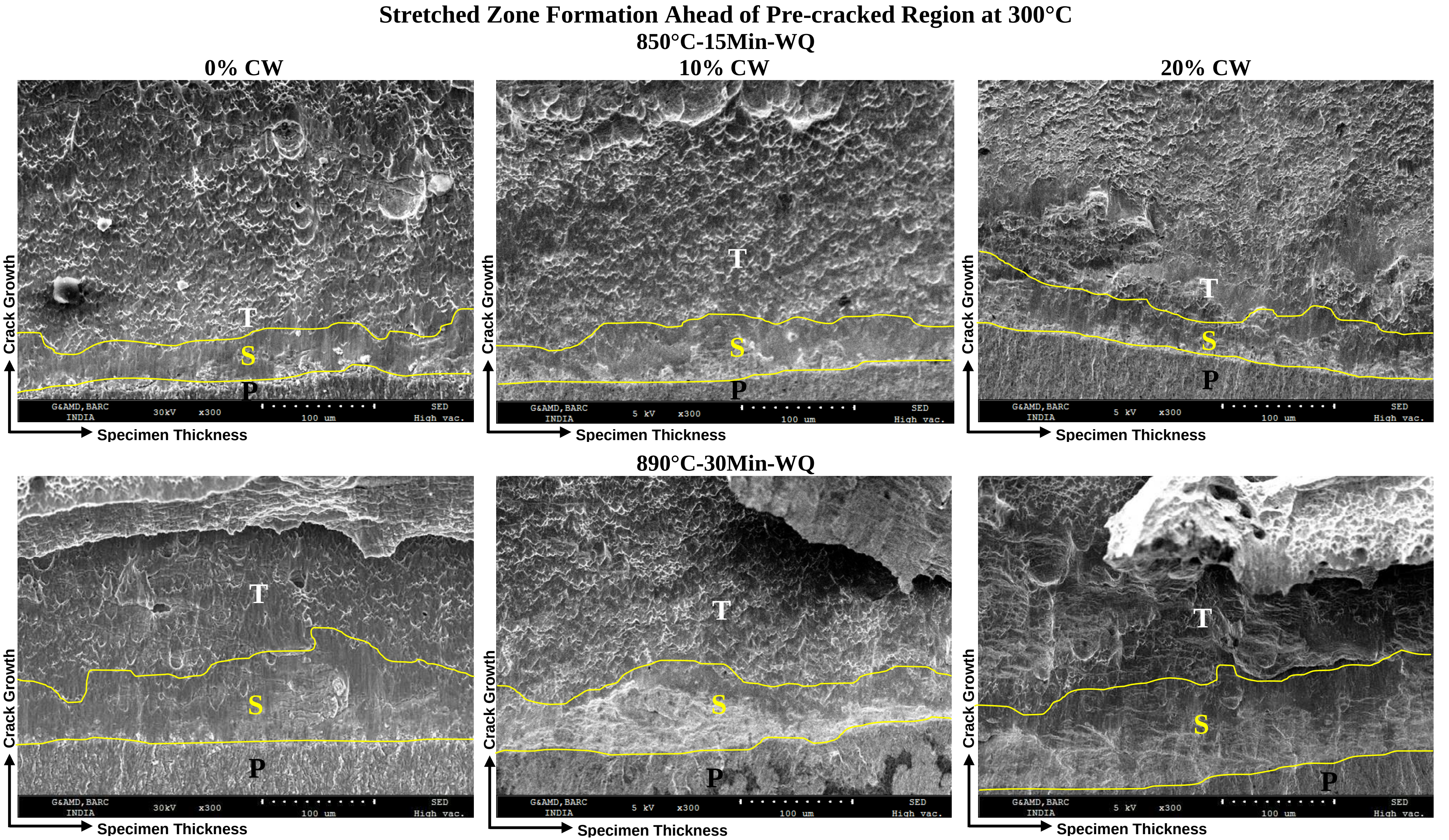

Figure 5.26: SEM fractographs showing the stretched zones formation ahead the pre-cracked regions of the broken C(T) specimens under solution heat treated and subsequently cold worked with 10 & 20% thickness reductions, tested at 300°C. In individual figures, the stretched zone (S) is bounded by the yellow lines, which separate pre-cracked (P) region from tearing (T) region.

5.4 Discussion

With increase in degree of cold rolling, observed increase in the tensile strengths of different cold rolled-solution heat treated materials can be attributed to increase in dislocation density in the material because of plastic deformation. This enhanced dislocation density results in higher number of interactions between the strain field of one dislocation with that of another and thereby leads the enhanced resistance to the dislocation movement and hence for the plastic deformation. This results in the enhanced tensile strength of the plastically deformed material as compared to the parent (un-deformed) material.

Since, the energy expended (i.e., work done) during any deformation process (such as; rolling) is always conserved as per the law of conservation of energy. During elastic deformation, the energy expended in deforming the material is entirely stored in that material itself and is recoverable in nature. However, most of the energy expended during material’s plastic deformation is converted into heat energy and minor part of it is stored within the material itself in the form of crystalline imperfections such as point defects, line defects (i.e., dislocations), stacking faults, etc. This stored energy during plastic deformation is a function of the induced strain (i.e., degree of deformation). Additionally, for lower strain regime, increase in material’s stored energy because of a given strain is higher than the stored energy induced by the same magnitude of additional strain. In the other words, the magnitude of increase in stored energy because of a specified strain increment decreases and moves towards saturation with the additional degree of deformation. Furthermore, with increase in degree of cold work, the dislocation density increases, which increases the strength of material (such dislocation-strength relationship is expressed using Equation 5.2 [107]). However, with additional cold work the annihilation of dislocation takes place, which results in relatively lower increase in dislocation density.

$$\tau_{flow} = \tau_0 + k\sqrt{\rho} \tag{5.2}$$

In Equation 5.2, τ_{flow} represents the shear stress to move a dislocation, τ_0 represents the shear stress when material has no dislocation, k is a coefficient and ρ represents the dislocation density.

This variation in the stored energy due to plastic deformation has been investigated by several researchers for different materials [108,109]. Therefore, with reference to the present results, with increase in degree of cold rolling from 0 to 10%, the magnitude of stored energy (and therefore, crystal imperfections) would have increased to a much higher extent as compared to the subsequent additional 10% cold working. Since, imperfections are barrier to the motion of dislocations and hence, for the slip, higher number of imperfections generated during initial 10% cold work compared to additional 10% cold work resulted in the observed higher changes in the tensile properties due to the first 10% cold working as compared to the additional 10% cold working.

As discussed in Chapter 4 that the tensile properties other than strength, including ductility and strain hardening characteristic have weak dependence on the SHT parameters. Increase in SHT temperature within 850-890°C regime, and soaking duration within 15-30 min regime, caused reduction in tensile strengths of solution heat treated Zr-2.5Nb alloy. This suggested the combined effect of microstructural changes associated with increasing soaking temperature viz., decrease in primary α volume fraction, increase in grain size (especially of α’ phase), decrease in Nb super-saturation of α’ and increase in degree of oxygen depletion in α’; and those associated with increasing soaking duration viz., grain coarsening along with decrease in degree of Nb super-saturation of α’ and increase in degree of oxygen depletion in α’ on tensile properties of solution heat treated Zr-2.5Nb alloy. After cold working and with increase in degree of cold working, such dependence of tensile strength on SHT parameters became relatively weaker. Figure 5.27 shows the correlation of tensile properties with the microstructural features of solution heat treated Zr-2.5Nb alloy, before and after the cold working treatment.

Similar to before cold working, the fracture toughness parameters of cold worked Zr-2.5Nb alloy were practically insensitive to the microstructural features such as primary α volume fraction and degree of Nb super saturation in α', Figure 5.28.

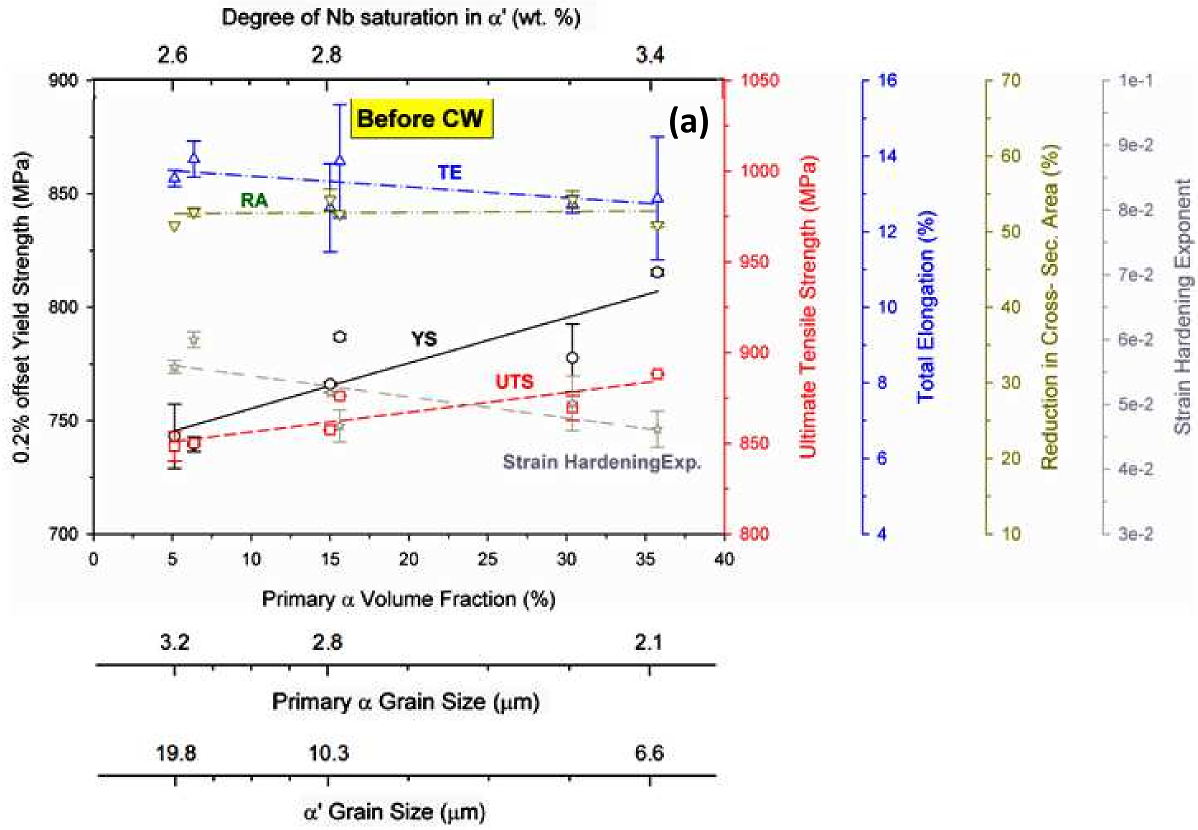

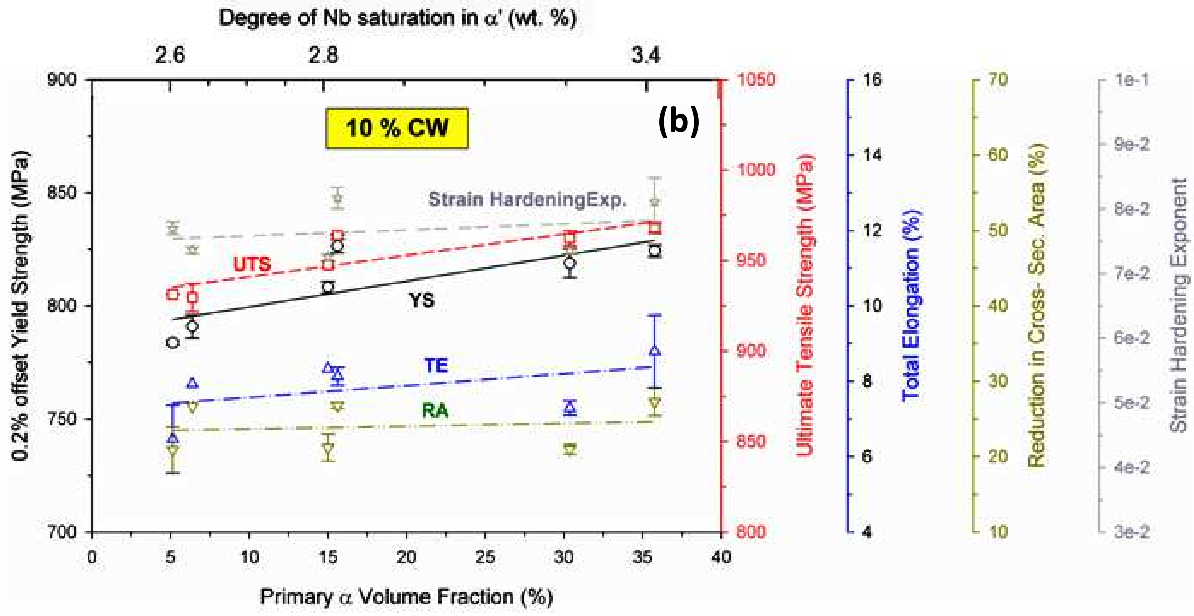

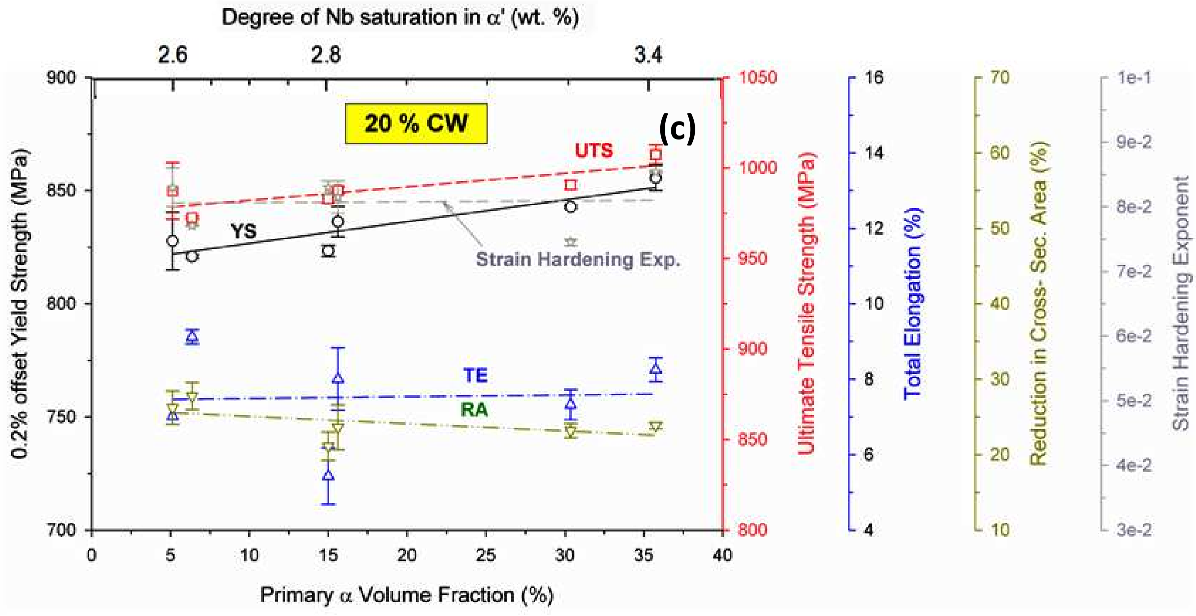

Figure 5.27: Comparison of the microstructural parameters with tensile properties of solution heat treated Zr-2.5Nb alloy (a) before and (b & c) after cold working.

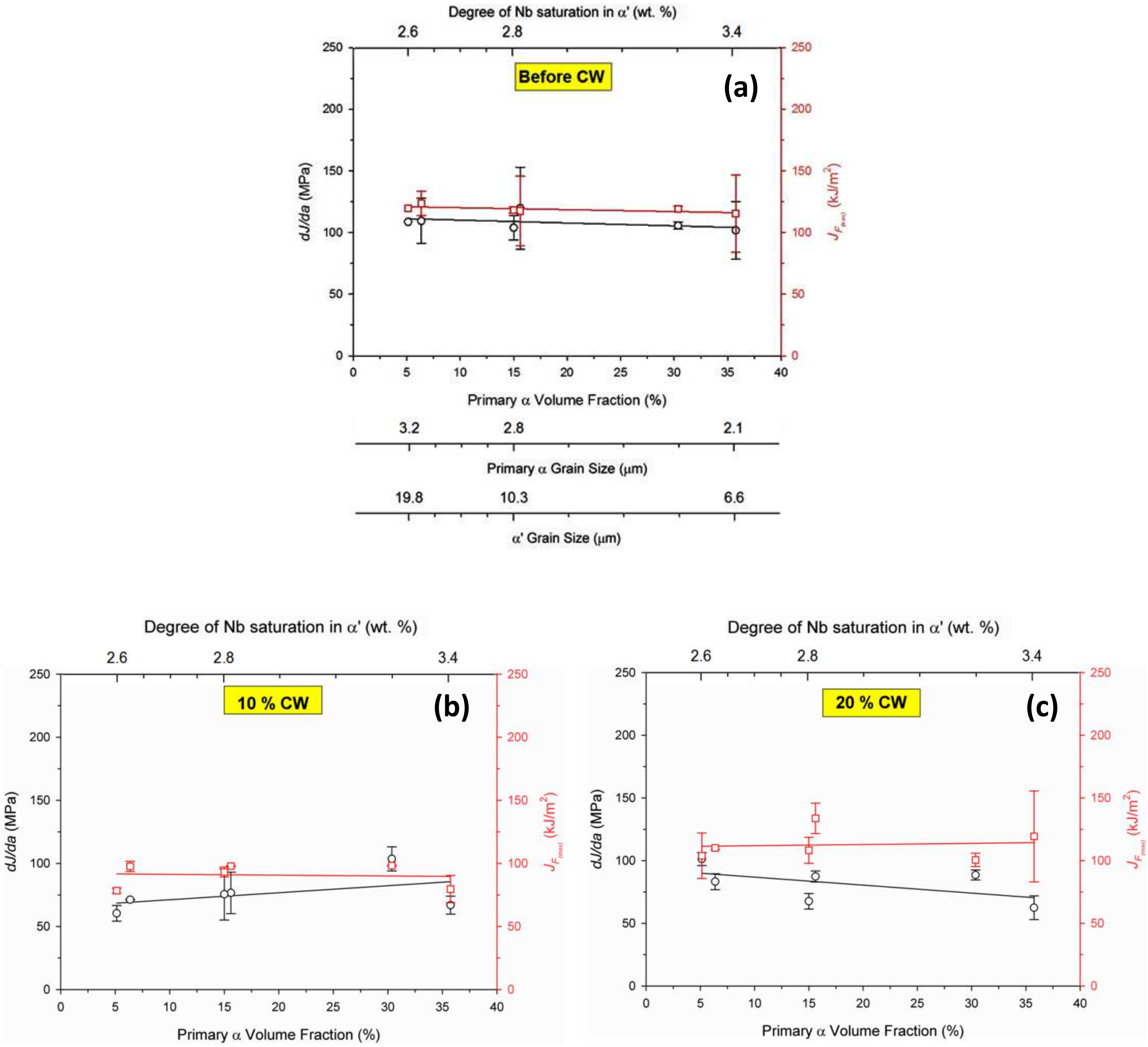

Figure 5.28: Comparison of the microstructural parameters with fracture toughness parameters of solution heat treated Zr-2.5Nb alloy (a) before and (b & c) after cold working.

Introduction of cold working on solution heat treated materials, primarily causes increase in dislocation density. In the present study, a dislocation multiplying parameter 'Dislocation Multiplication Factor' (*DMF*) is proposed to investigate the extent of increase in dislocation density in different solution heat treated materials because of cold working. As shown in Equation 5.3, *DMF* is expressed as the ratio of dislocation density of cold worked material to that of the solution heat treated material. Since, strength is the function of square root of dislocation density (as shown by Equation 5.2 [107]), the *DMF* can also expressed in terms of material's yield strength, i.e., the square of the ratio of yield strength of cold worked material to that of the solution heat treated material.

$$DMF = \frac{\rho_{cw}}{\rho_{\,SHT}} = \left(\frac{YS_{cw}}{YS_{SHT}}\right)^2 \qquad (5.3)$$

In Equation 5.3, terms ρ_{SHT} and ρ_{cw} respectively represent the dislocation densities of materials before and after cold working. Terms YS_{SHT} and YS_{cw} in this equation, respectively represent the yield strengths of materials before and after cold working.

Figure 5.29 (a) shows the dependence of tensile properties on *DMF*. The tensile strengths including yield strength and ultimate tensile strength, along with strain hardening characteristics first increase with increase in *DMF*. With further increase in *DMF*, these properties showed much weaker dependence on *DMF*. In contrast, the ductility of solution heat treated materials first decreased with increase in *DMF*, and became saturated afterwards. This dependence of tensile properties on *DMF* suggested that tensile properties are the strong function of initial 10% cold working, however, subsequent additional 10% cold working weakly influences the tensile properties. Figure 5.29 (b) shows the dependence of fracture toughness parameters on *DMF*. The fracture toughness parameters exhibited marginal reduction with increase in *DMF*.

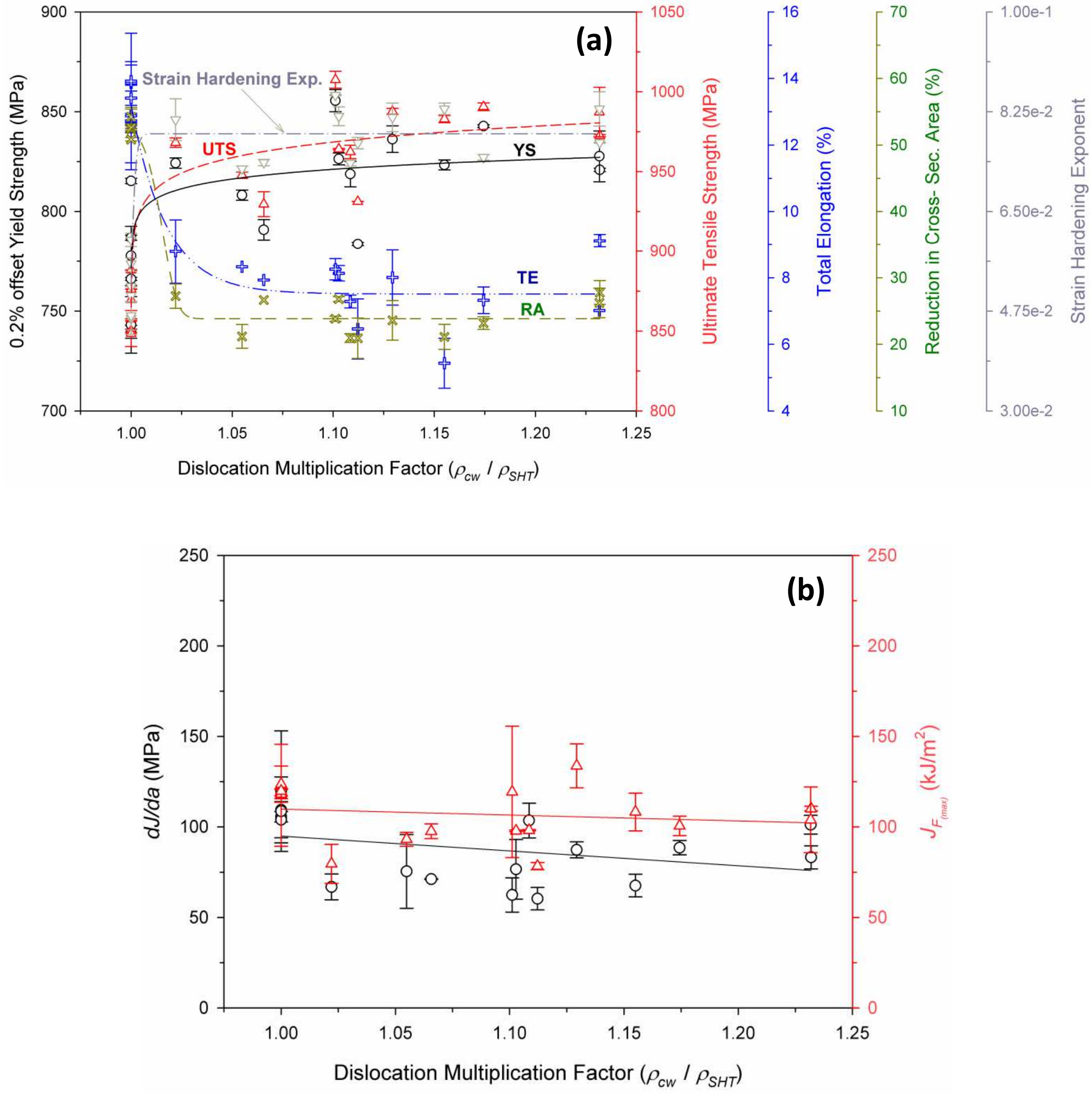

Figure 5.29: Influence of dislocation multiplication factor on (a) tensile properties and (b) fracture toughness parameters of cold worked-solution heat treated Zr-2.5Nb alloy.

Present study shows that the cold worked materials comprise a typical hardness gradient in the vicinity of free surface. This can be understood as the consequence of corresponding variations in degree of cold working with depth. During any cold working operation (such as rolling), the degree of cold work in the vicinity of free surface is highest, and subsequently decreases while approaching towards depth from the free surface. Since the dislocation density is primarily influenced by the cold work (apart from the point imperfections such as vacancies, etc.), the cold worked material exhibited the gradient of such imperfections across thickness, which therefore caused the observed hardness gradient across the thickness.

Present study shows that opposite to general trend, hardness in the vicinity of free surface in solution heat treated materials decreases after cold working. As discussed earlier that the cold working treatment in principle increases the lattice imperfections within material, and therefore is expected to increase its hardness. The present study also showed that the cold worked materials exhibit a typical primary α gradient in the vicinity of their free surfaces. In other words, cold rolling treatment causes accumulation of primary α in the vicinity of free surface. Therefore, the observed reduction in hardness in the vicinity of free surface because of cold working emphasizes the influence of primary α accumulation in decreasing the hardness. In other words, in the vicinity of free surface, the overall change in hardness because of cold working is the net effect of increased hardness due to lattice imperfection generation and decreased hardness because of primary α accumulation, Equation 5.4. This study therefore, also suggests that primary α is relatively softer than α'.

$$\Delta\mathrm{H}_{\mathrm{SHT}\rightarrow\mathrm{CW}} = \Delta\mathrm{H}_{\mathrm{Lattice\ imperfections}} - \Delta\mathrm{H}_{\mathrm{Primary}\ \alpha\ \mathrm{accumulation}} \tag{5.4}$$

In Equation 5.4, term $\Delta\mathrm{H}_{\mathrm{SHT}\rightarrow\mathrm{CW}}$ represents the net change in hardness because of cold working; term $\Delta\mathrm{H}_{\mathrm{Lattice\ imperfections}}$ represents the increase in hardness because of lattice imperfection generation and term $\Delta\mathrm{H}_{\mathrm{Primary}\ \alpha\ \mathrm{accumulation}}$ represents the reduction in hardness because of primary α accumulation.

In order to validate the contributions of lattice imperfection generation in increasing hardness and primary α accumulation in decreasing hardness, the hardness of single phase (β_{Zr}) water quenched and subsequently cold worked Zr-2.5Nb alloy was examined as a function of depth from the free surface. For this, Zr-2.5Nb alloy was water quenched from single phase, β_{Zr}

region at 950°C after being soaked for 15 min duration followed by subsequent 10% cold working through multi-pass rolling. The hardness variation in the vicinity of free surface of this material is shown in Figure 5.30. Within transition region, hardness of this material was appreciably higher than that of the two phase materials, which were examined in the present study. Such increase in hardness of this material can be exclusively considered as the consequence of increase in the lattice imperfections (especially, dislocation densities) because of cold working.

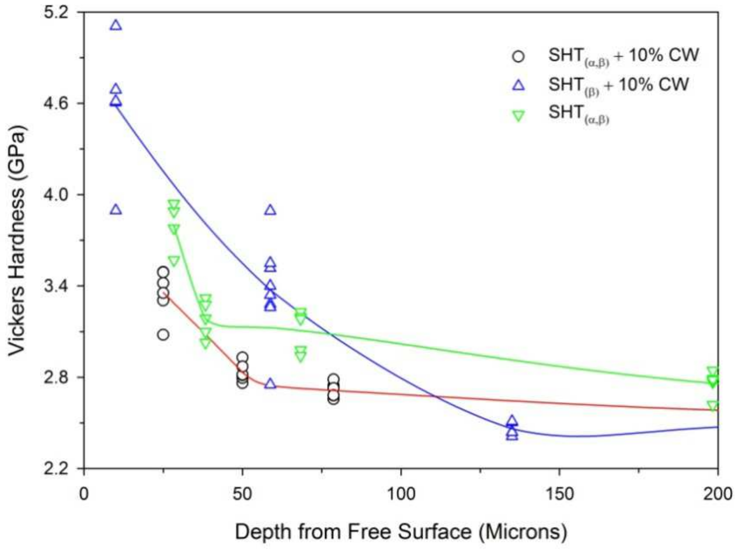

Figure 5.30: Comparison of Vickers hardness of Zr-2.5Nb alloy under solution heat treated (from α+β & β phase fields) and cold working conditions.

The slope of fracture resistance curve, *dJ/da,* of most of the solution heat treated materials, in general decreased with increase in degree of cold work, especially under ambient condition. Such reduction in propagation toughness because of cold working could be correlated through the presence of relatively shallower dimples as observed on the fracture surfaces of cold worked materials (Figure 5.21 and 5.23). Additionally, the 45° oriented fracture surfaces of cold worked materials showed the clusters of very fine dimples at certain locations (as can be seen from Figure 5.21), which also points to the lower fracture toughness of cold worked materials. At 300°C, the fracture surfaces of cold worked-solution heat treated materials exhibited much coarser dimples as compared to those observed at RT. This suggests that at high temperature, density of dimple nucleation sites decreases (in the other words, dimple nucleation sites become relatively farther with each other). This therefore point towards the improvement in fracture toughness of these materials.

Present study showed that after cold working, the solution heat treated materials exhibit relatively larger flat fractured region. Such increase in the flat fractured region, because of cold working treatment can be understood as the consequence of corresponding increase in material’s strength because of cold working. Material's strength is one of the factors that govern state of stress ahead of the crack tip, and in turn influences the mode of fracture. With increase in material's strength, state of stress ahead the crack tip shifts towards plane strain condition [105,106]. Since, flat fracture is an important characteristic feature of the plane strain condition prevailing ahead the crack tip, with increase in material's strength the fracture surface exhibits larger flat region.

5.5 Summary

Present study on the influence of degrees of cold working on fracture behavior of Zr-2.5Nb alloy having variable solution heat treatment histories is summarized as follows:

i. Cold working through rolling resulted in the elongated grain microstructures of solution heat treated materials along rolling direction. Cold rolling treatment caused basal pole alignment along radial (i.e., compressive strain) direction with corresponding reduction along axial (i.e., rolling) direction. Nevertheless, upto 20% cold working, such changes in the basal pole texture of solution heat treated Zr-2.5Nb alloy were not significant.

ii. The tensile properties of solution heat treated Zr-2.5Nb alloy were strongly sensitive to the initial 10% cold working; however with subsequent additional 10% cold working these properties further exhibited lesser changes. Increase in cold working within 0-20% domain increased the tensile strengths and strain hardening characteristic, however caused substantial reduction in the ductility of solution heat treated materials. Increase in dislocation multiplication factor, as caused by increase in degree of cold working, showed good agreement with these observations.

iii. Increase in SHT temperature within 850-890°C, and soaking duration within 15-30 min domain caused considerable reduction in primary α volume fraction and increase in grain size (especially of prior β, i.e., α’) along with a slight decrease in degree of Nb super saturation of α’. These concurrent microstructural changes attributed to decrease the tensile strength of solution heat treated materials. However, after cold working, such microstructural changes had relatively weak influence on the tensile strength. Ductility and strain hardening characteristic were practically insensitive to these microstructural changes.

iv. Cold working mainly influenced the slope of fracture resistance curve, i.e., *dJ/da* parameter. Increasing degree of cold working caused reduction in the *dJ/da* parameters of solution heat treated materials (by 20-35%), suggesting corresponding reduction in the crack propagation resistance of these materials after cold working. Increasing temperature from RT to 300°C, caused considerable improvement in *dJ/da* parameters (by > 70%). However, at 300°C, the *dJ/da* parameter exhibited considerable scatter as compared to that at RT.

v. After cold working, the solution heat treated materials, in general comprised relatively larger flat fractured region, especially under ambient test condition. This suggested the influence of cold working in shifting the state of stress towards plane strain condition.

vi. The fracture surfaces of cold worked materials, similar to SHT materials comprised typical dimple structure characteristic of a ductile failure. However, contrary to SHT materials, the cold worked materials exhibited relatively shallow dimples, especially on the narrow central flat fractured region and the clusters of fine dimples, which correlated the reduction in fracture toughness because of cold working.

vii. The fracture toughness parameters of cold worked-solution heat treated Zr-2.5Nb alloy remained practically insensitive to the microstructural features viz., primary α volume fraction and degree of Nb super saturation in α', similar to before cold working.

viii. Increase in dislocation multiplication factor, as caused by increase in degree of cold working, had good agreement with the reduction in *dJ/da* parameter. In contrast, the $J_{F(max)}$ parameter was practically insensitive to these features, suggesting that the cold working weakly influenced the *J* parameters under small crack growth regime.

CHAPTER 6

INFLUENCE OF AGING TEMPERATURE ON FRACTURE BEHAVIOR OF COLD WORKED-SOLUTION HEAT TREATED Zr-2.5Nb ALLOY

Influence of cold work on solution treated material has been described in the earlier Chapter 5. The alloy in twelve cold worked-solution heat treated conditions was subjected to aging treatment under vacuum at 500 and 540°C for 24 h. The influence of aging treatment on microstructure, hardness, tensile properties and fracture toughness are discussed in this chapter. The microstructural features showing fine precipitations of β_{Nb} and β_{Zr} phases during the aging at 500 and 540°C for 24 h duration is described. Followed by this, influence on the mechanical properties covering micro-hardness, tensile properties and fracture toughness parameters are discussed. A comprehensive comparison of the mechanical behavior of Zr-2.5Nb alloys under WQA and CWSR conditions is presented. Subsequently, a comprehensive study to examine the influence of different analysis methodologies on the fracture toughness parameters is discussed. A study of the fracture surfaces of broken C(T) specimens through an image analysis approach is discussed to illustrate the proportionate flat region of the fracture surfaces. Subsequently, a study of the fractographic features at different locations through SEM examinations is presented. Finally, an optimum TMP history of WQA Zr-2.5Nb alloy is suggested, which ensures the best fracture toughness.

6.1 Microstructural Observations

6.1.1 Optical and TEM Microstructures

The optical microstructures of Zr-2.5Nb alloy after the aging treatments at 500 and 540°C for 24 h durations showed not much difference with those of before aging, i.e., cold worked-solution heat treated conditions. Figure 6.1 shows the optical microstructures of one of the cold worked-solution heat treated materials after aging at 500 and 540°C for 24 h in vacuum followed by furnace cooling, which comprised primary α and tempered α'. In Zr-2.5Nb alloy, aging at 500 and 540°C for 24 h duration, results in the precipitation of β phase, whose size is in nanometre range, which is too small to be seen under an optical microscope. Therefore, to study these fine β precipitates, transmission electron microscopy, TEM examinations of the aged materials were conducted.

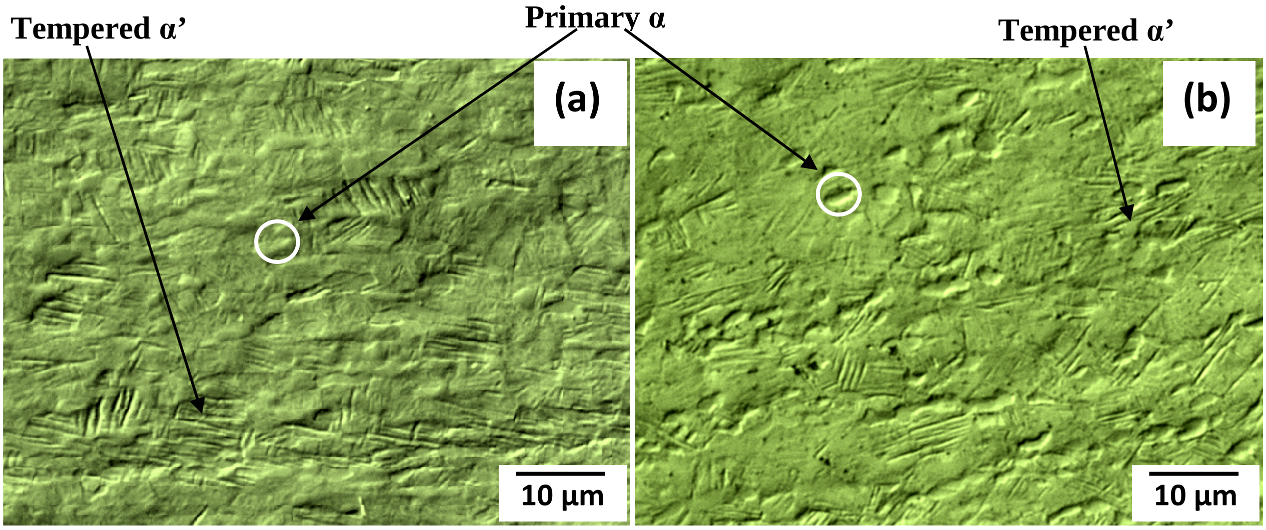

Figure 6.1: Optical microstructures of Zr-2.5Nb alloy, aged at (a) 500 and (b) 540°C for 24 h duration followed by furnace cooling. The material was previously solution heat treated from 850°C for 15 min duration, followed by the 10% cold work.

For this, two aged materials individually soaked at 500 and 540°C temperatures for 24 h having similar previous thermo-mechanical history (i.e., SHT soaked at 850°C for 15 min duration followed by 10% cold working) were examined using TEM. The TEM substructures confirmed the existence of very fine β precipitates, which were formed during the aging treatment, as shown in Figures 6.2 and 6.3. Most of these precipitates were observed on the lath boundaries of martensite (α' phase) in the form of arrays, however, few were located within the martensite laths. During aging, the soaking temperature governed the nucleation and growth rate of β precipitates, as material aged at 540°C in contrast to that aged at 500°C showed relatively higher volume fraction and larger β precipitates. In terms of morphology, most of the β precipitates were oval in shape, though few were having circular shape. For size measurement, 25 nos. of β precipitates were randomly selected and measured using the 'Image-J' software. The material, aged at 500°C had the average precipitate size of 23.9 nm, with variations from 11.4 to 36.1 nm. In contrast, the material, aged at 540°C showed relatively coarser β precipitates having the average size of 33.8 nm, with variations from 10.3 to 67.9 nm.

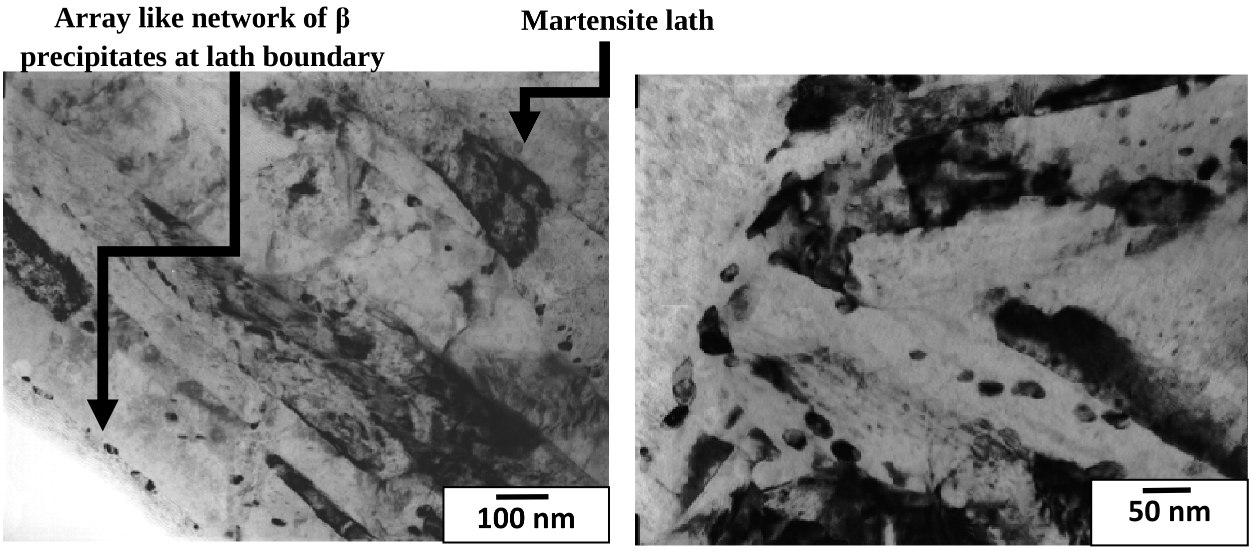

Figure 6.2: TEM substructures of Zr-2.5Nb alloy aged at 500°C for 24 h followed by furnace cooling. This material was previously soaked during SHT at 850°C for 15 min duration followed by 10% cold working.

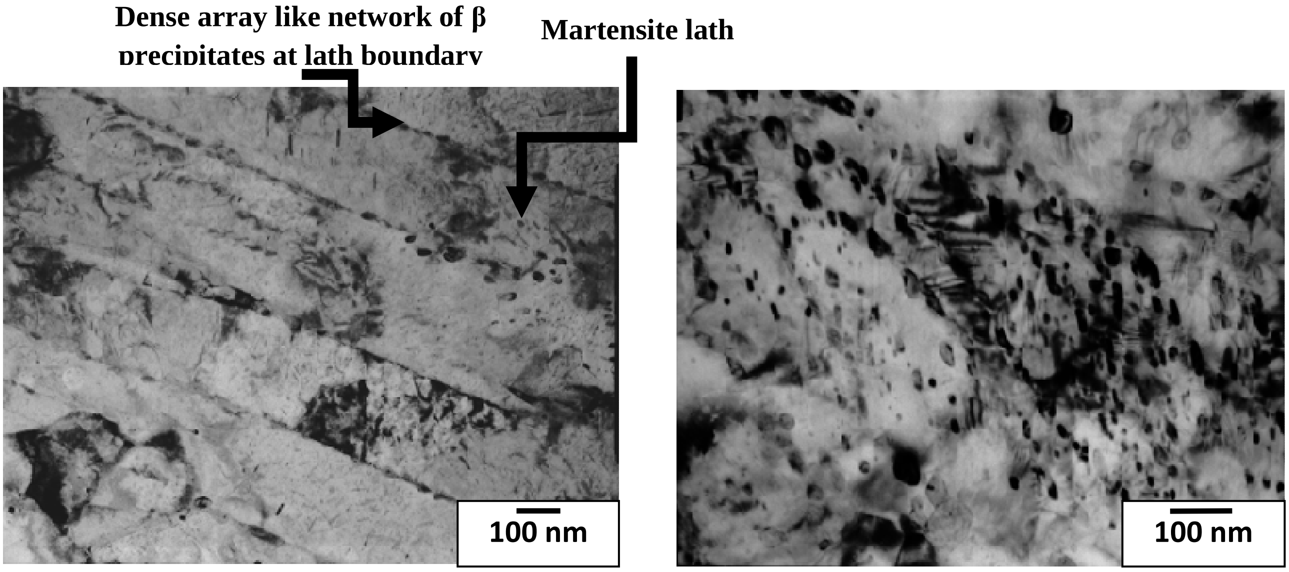

Figure 6.3: TEM substructures of Zr-2.5Nb alloy aged at 540°C for 24 h followed by furnace cooling. This material was previously soaked during SHT at 850°C for 15 min duration followed by 10% cold working.

6.1.2 Nb Concentration Measurement using EDS Analysis

Energy dispersive spectroscopy, EDS analysis was performed to determine the Nb concentration in β precipitates formed during the aging treatments at 500 and 540°C. The EDS analyses were performed on the precipitates, extracted through the Carbon Extraction Replicas. For this, four aged materials having variable thermo-mechanical histories (as shown in Table 6.1) were selected. To quantify the statistics within the Nb concentration data, multiple precipitates were chosen for the EDS analysis. Table 6.1 shows the evaluated Nb concentrations of β precipitates under these four aging conditions. Figure 6.4 shows the β precipitates extracted through carbon replicas and the corresponding Nb spectra. EDS analysis suggested the precipitation of β-Nb and β-Zr phases during the aging treatments at 500 and 540°C respectively for 24 h duration. Also, the degree of cold work (i.e., 10 or 20 %) did not have much influence on the precipitate's Nb concentrations.

Table 6.1: Nb concentrations of the β precipitates after aging treatment in different cold worked-solution heat treated Zr-2.5Nb alloys.

Nb concentration of β precipitates (in weight %)			
TMP Condition 850°C/30Min+10%CW+ 500°C/24h	**TMP Condition** 850°C/30Min+10%CW+ 540°C/24h	**TMP Condition** 850°C/30Min+20%CW+ 500°C/24h	**TMP Condition** 850°C/30Min+20%CW+ 540°C/24h
99.54	4.99	93.64	9.07
75.47	6.56	99.66	10.17
89.03	4.32	92.56	6.02
93.05	5.21	99.00	5.20
97.89	12.5	97.03	6.74
97.24	4.47	94.82	10.03
-	10.09	98.42	2.44
-	8.18	96.73	10.78
-	14.21	-	4.47
-	11.57	-	14.41
-	7.85	-	-
-	7.51	-	-
Average = 92.04	**Average = 8.12**	**Average = 96.48**	**Average = 7.93**

EDS Spectra **Extracted β Precipitates**

TMP Condition: 850°C/30Min+10%CW+500°C/24h

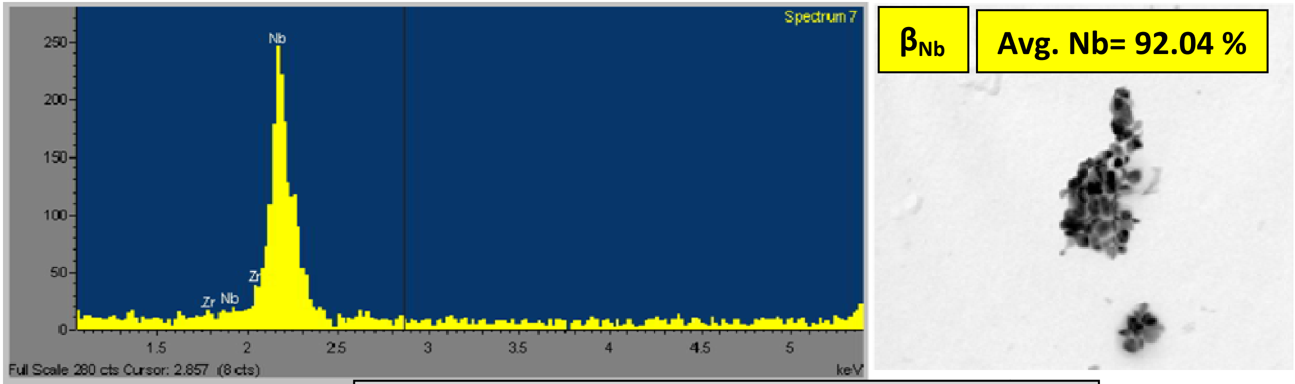

TMP Condition: 850°C/30Min+10%CW+540°C/24h

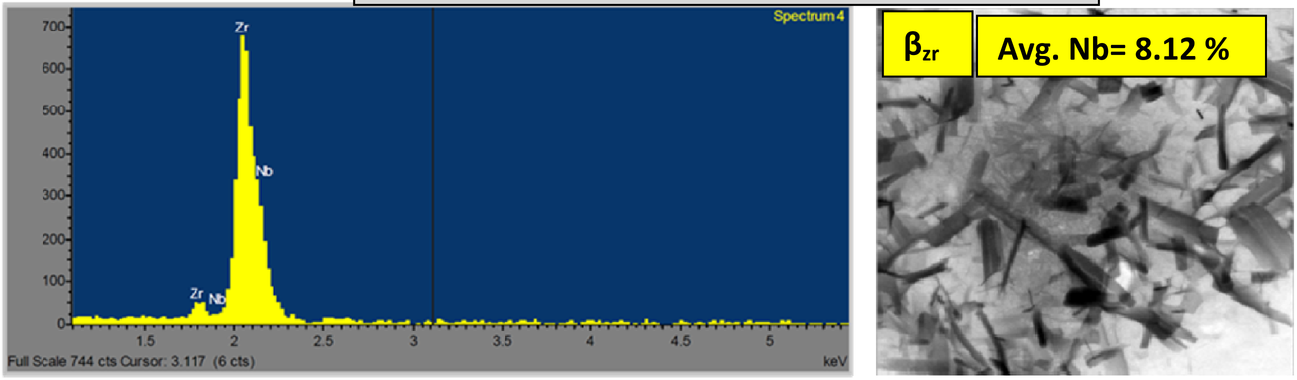

TMP Condition: 850°C/30Min+20%CW+500°C/24h

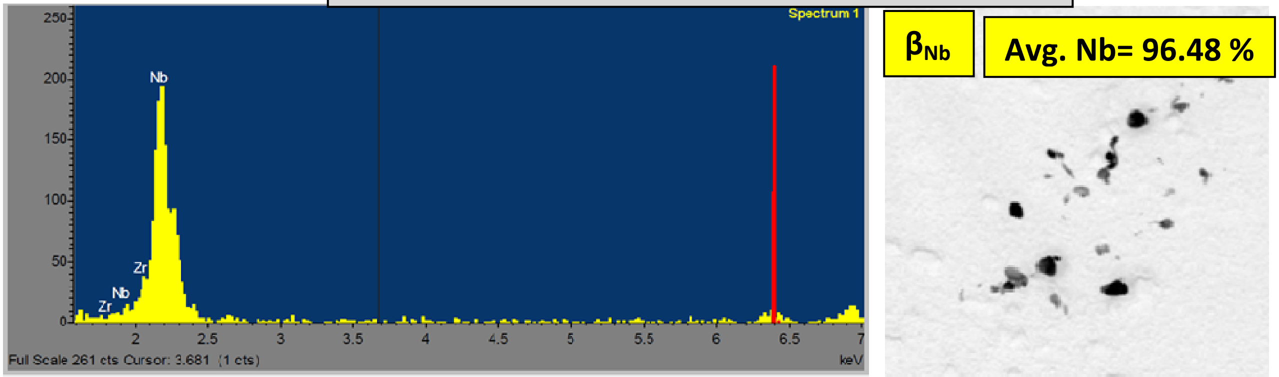

TMP Condition: 850°C/30Min+20%CW+540°C/24h

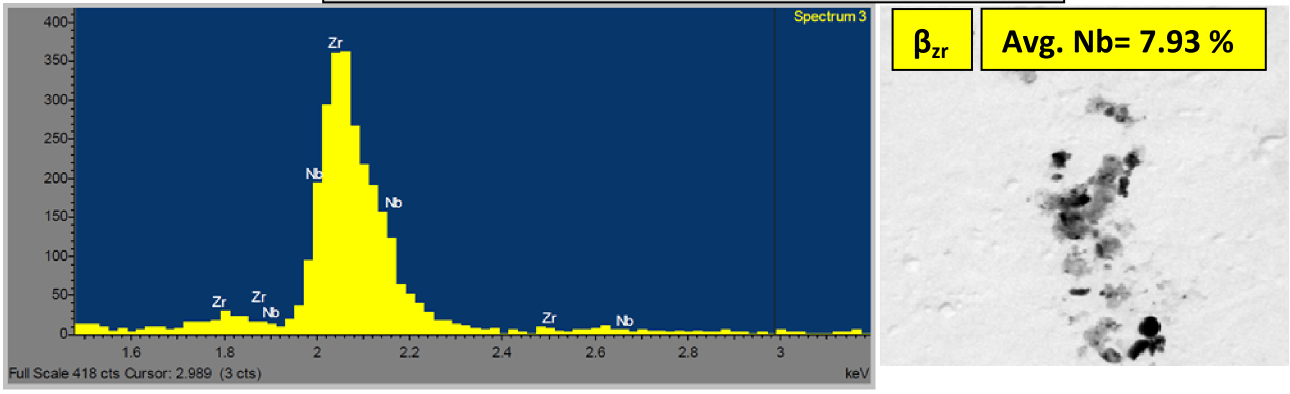

Figure 6.4: EDS spectra (left) for Nb in β precipitates (right), extracted through carbon replicas in aged Zr-2.5Nb alloy.

6.1.3 Crystallographic Texture

The basal pole texture of cold worked-solution heat treated Zr-2.5Nb alloys under different aging conditions in terms of Kearns parameters along three mutually perpendicular directions, axial (f_a), transverse (f_t) and radial (f_r) is shown in Figure 6.5. After aging treatment, texture of these materials became more prominent along transverse and radial directions with corresponding reduction along axial (i.e., previously rolling direction). The texture of aged materials was examined for the extreme SHT temperature conditions viz., 850 and 890°C. As can be seen from Figure 6.5 (a) & (c) and (b) & (d) that the aged materials, previously solution heat treated from a higher SHT temperature exhibit relatively weaker basal pole texture. From Figure 6.5 (a) & (b) and (c) & (d), it appears that similar to before aging, the degree of cold working had no significant influence on the texture of aged materials. Furthermore, the texture of aged materials (especially, those previously solution heat treated from a higher temperature, Figure 6.5 (c) & (d)) suggested that increasing aging temperature from 500 to 540°C also results in increasing degree of randomness in basal pole texture. Therefore, a higher SHT temperature along with higher aging temperature seemed to maintain relatively weaker basal pole texture of the aged materials. The pole figures, as shown in Figure 6.6 suggests that the Zr-2.5Nb alloy under aged conditions have much weaker basal pole texture as compared to that under CWSR condition (as shown in Figure 4.4, Chapter 4).

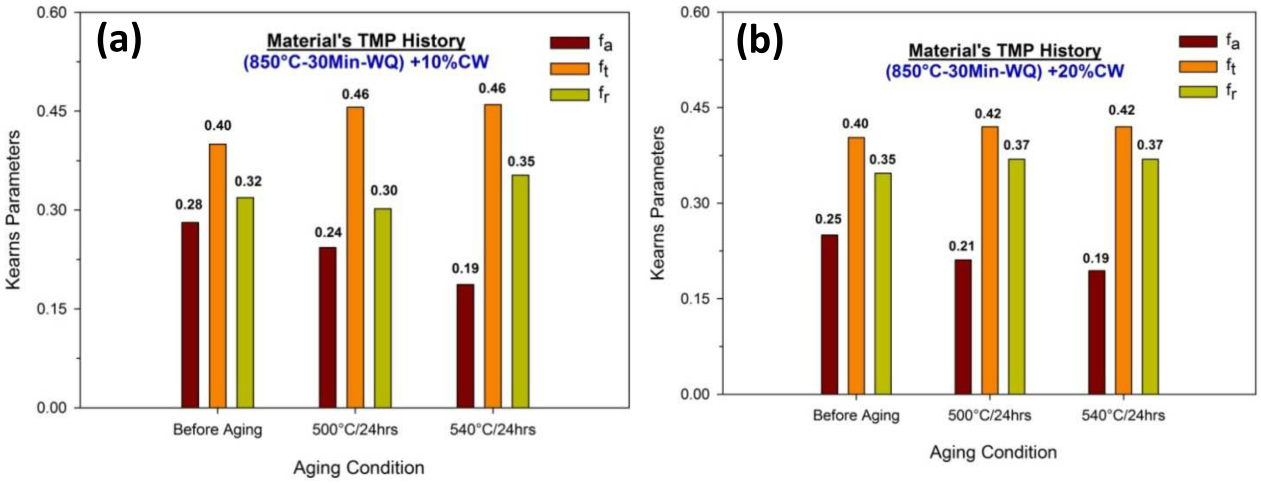

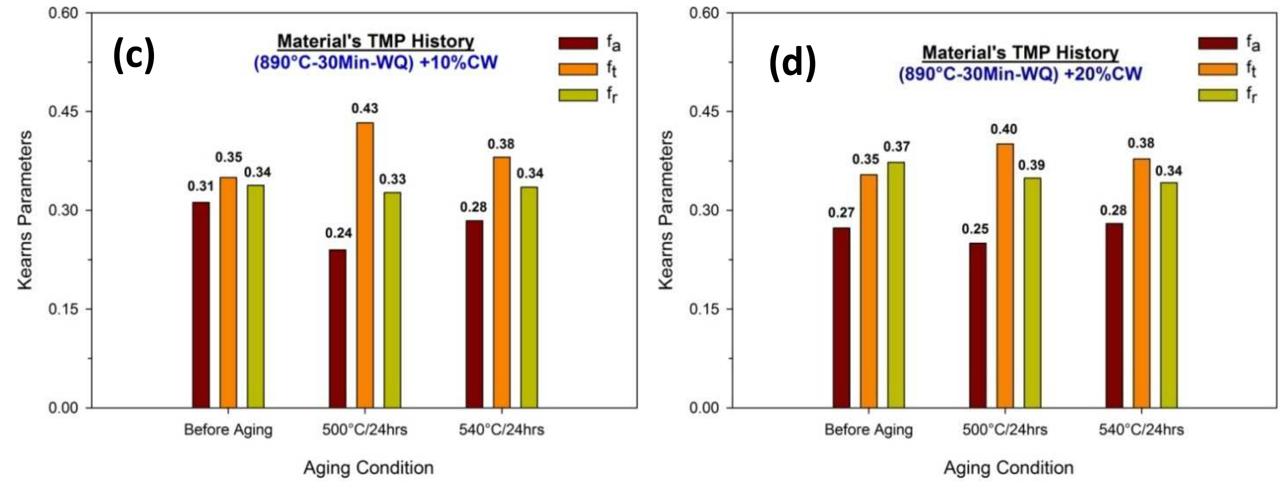

Figure 6.5: Kearns parameters representing basal pole texture of Zr-2.5Nb alloy before and after the aging treatments along three mutually perpendicular directions viz., axial (f_a), transverse (f_t) and radial (f_r).

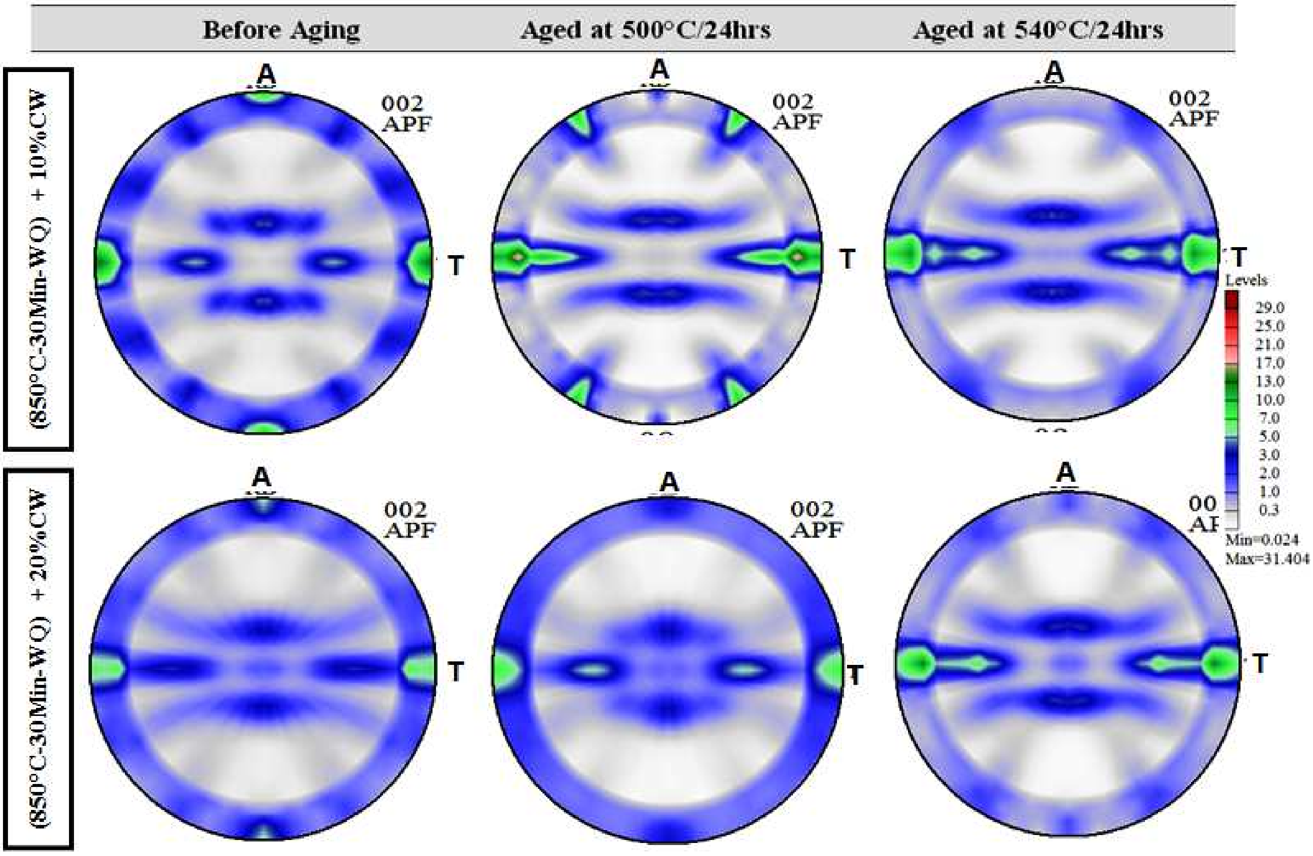

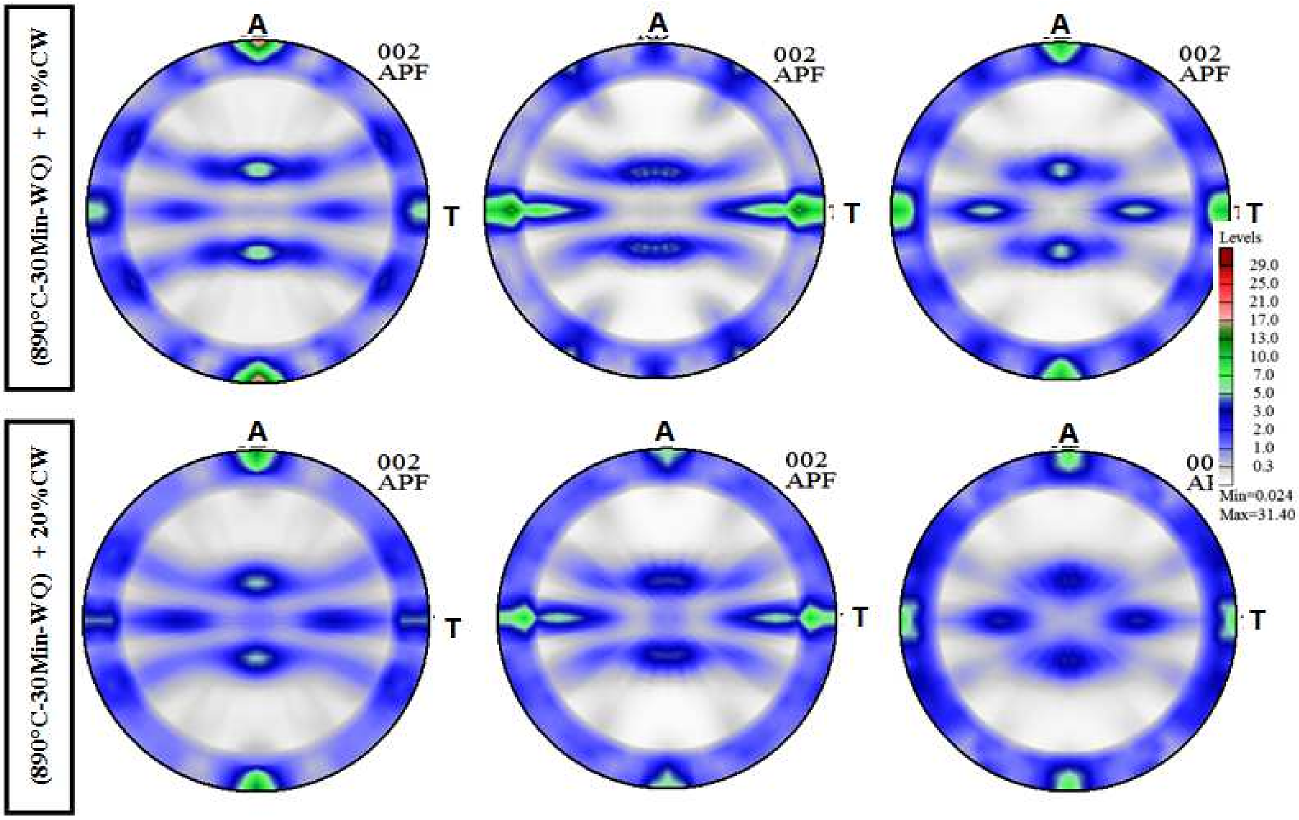

Figure 6.6: Additional basal Pole Figures (APFs) of Zr-2.5Nb alloy before and after the aging treatments at 500 and 540°C for 24 h. Symbols A and T respectively indicate the axial and transverse directions. Sample normal was along radial direction.

6.2 Mechanical Behavior

6.2.1 Micro-Hardness

After aging, cold worked-solution heat treated Zr-2.5Nb alloy, similar to before aging had a sharp hardness gradient in the vicinity of free surface. While approaching towards depth from free surface, hardness decreased, and subsequently got saturated. Aged materials showed such sharp hardness gradient within a narrow region of ~ 200 µm (~ 6% of the material thickness) below the free surface. Figure 6.7 (a) illustrates such hardness profile in a cold worked-solution heat treated Zr-2.5Nb alloy (solution heat treated from 850°C for 15 min+20% CW) before and after aging treatments.. Similar hardness variations were observed in rest of the aged materials.

Aging treatment performed at 500°C for 24 h duration resulted in nearly comparable hardness at each depth levels as exhibited by the cold worked materials. However, aging performed at higher soaking temperature, 540°C for same duration resulted in notable reduction in hardness at respective depth levels from the free surface.

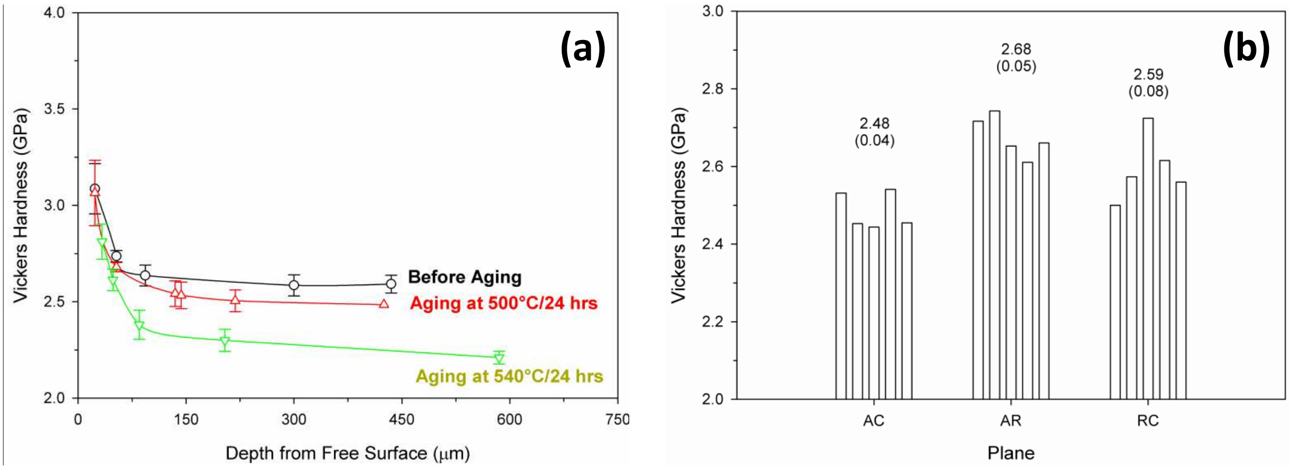

Figure 6.7: (a) Vickers hardness profiles as a function of depth from the free surface in a cold worked-solution heat treated Zr-2.5Nb alloy (solution heat treated from 850°C for 15 min+20% CW) before and after aging treatments. Plot shows the hardness variation on AC plane, (b) Plot showing the orientation dependence of mid-section hardness in this material after aging at 540°C/24 h. In this plot, over each bar group, average hardness value along with corresponding standard deviation (within parentheses) is shown.

To examine the mechanical behavior anisotropy in aged materials, hardness were examined on the three mutually perpendicular planes; AC, AR and RC. Figure 6.7 (b) shows the orientation dependence of hardness in one of aged Zr-2.5Nb alloy (solution heat treated from 850°C for 15 min followed by 20% CW and aging at 540°C/24 h). The aged materials were observed to be practically isotropic, as hardness variations on aforementioned orthogonal planes were very close. Nevertheless, in general, AR plane showed the highest hardness, while AC plane showed the least hardness. Similar isotropy was observed in rest of the aged materials.

6.2.2 Tensile Properties

I. Flow Curves

Figures 6.8-6.11 show the flow curves of various heat treated Zr-2.5Nb alloys having variable thermo-mechanical histories. Aging treatment resulted in decrease in the flow stresses with respect to cold worked Zr-2.5Nb alloy. Aging carried out at the higher temperature, 540°C for 24 h, in contrast to at 500°C for same duration resulted in greater reduction of the flow stresses with respect to cold worked materials. The thermo-mechanical histories of various aged Zr-2.5Nb alloy, such as soaking temperature and duration used during solution heat treatment stage and the degree of cold work had practically no influence on the flow stresses of these materials. However, uniform elongations of the aged materials soaked at 540°C, in contrast to 500°C showed considerable dependence on the prior used SHT temperatures under ambient condition. The 540°C aged materials previously soaked at the lower SHT temperature (850°C), in contrast to 870 and 890°C exhibited considerably higher uniform elongations at RT.

In WQA fabrication route of Zr-2.5Nb alloy pressure tubes for PHWRs (or, for future AHWR) applications (as shown in Figure 1.2, Chapter 1), vacuum aging treatment can be considered as the final mechanical behavior governing treatment, assuming that the subsequent autoclaving treatment has insignificant role in altering the mechanical properties of pressure tubes. Therefore, for comparing heat treated (i.e., WQA) fabrication route of Zr-2.5Nb alloy pressure tubes with the currently followed CWSR route, flow behavior of aged and CWSR (220MWe IPHWRs) materials were determined. For this purpose, CWSR pressure tube materials fabricated using both the earlier used Double Melted, DM and recent Quadruple Melted, QM ingots were used. Sample obtained from one DM and three QM CWSR PTs were used to determine the tensile properties and a comparison of the tensile properties of DM and QM CWSR pressure tubes with those of the aged material is presented.

At RT, DM-CWSR material, in contrast to QM-CWSR material shows slightly higher flow stresses, however, at 300°C both the materials have almost similar flow behavior. Comparison, as illustrated in Figure 6.8-6.11 shows that the aged materials soaked at 500°C exhibited considerably higher flow stresses, however significantly lower uniform elongations as compared to the CWSR materials. In contrast, materials aged at 540°C exhibited nearly comparable flow stresses, though lower uniform elongations as that of the DM and QM CWSR pressure tube materials, especially at RT. Under ambient condition, aged materials, in contrast to CWSR materials had relatively flat flow curves, suggesting the lower strain hardening characteristics of the former materials. In contrast, at reactor operating temperature (300°C), Zr-2.5Nb alloy under both aged and CWSR conditions exhibited relatively less difference in the steepness of flow curves. This flow curve characteristic was quantified in terms of the strain hardening exponents, described subsequently in Section v.

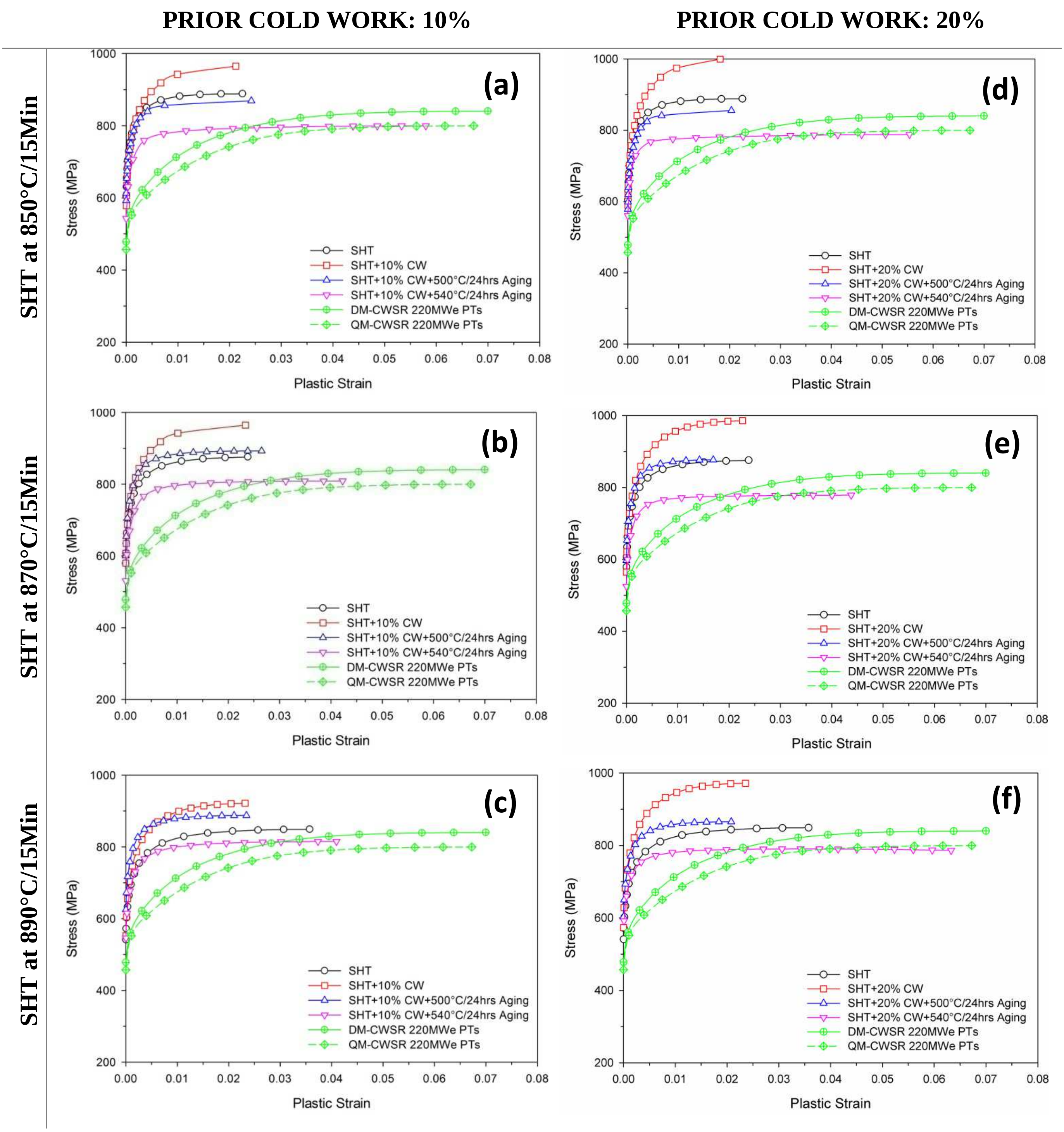

Figure 6.8: Evolution of lower bound flow behavior of Zr-2.5Nb alloy during three TMP stages; SHT, subsequent cold working, and vacuum aging, under ambient condition. Plots show the flow behavior of Zr-2.5Nb alloy previously soaked at 850, 870 and 890°C for 15 min during solution treatment stage. The flow behavior of these heat treated materials were compared with that of Zr-2.5Nb alloys under CWSR conditions in which the pressure tubes of 220MWe IPHWRs are currently being used.

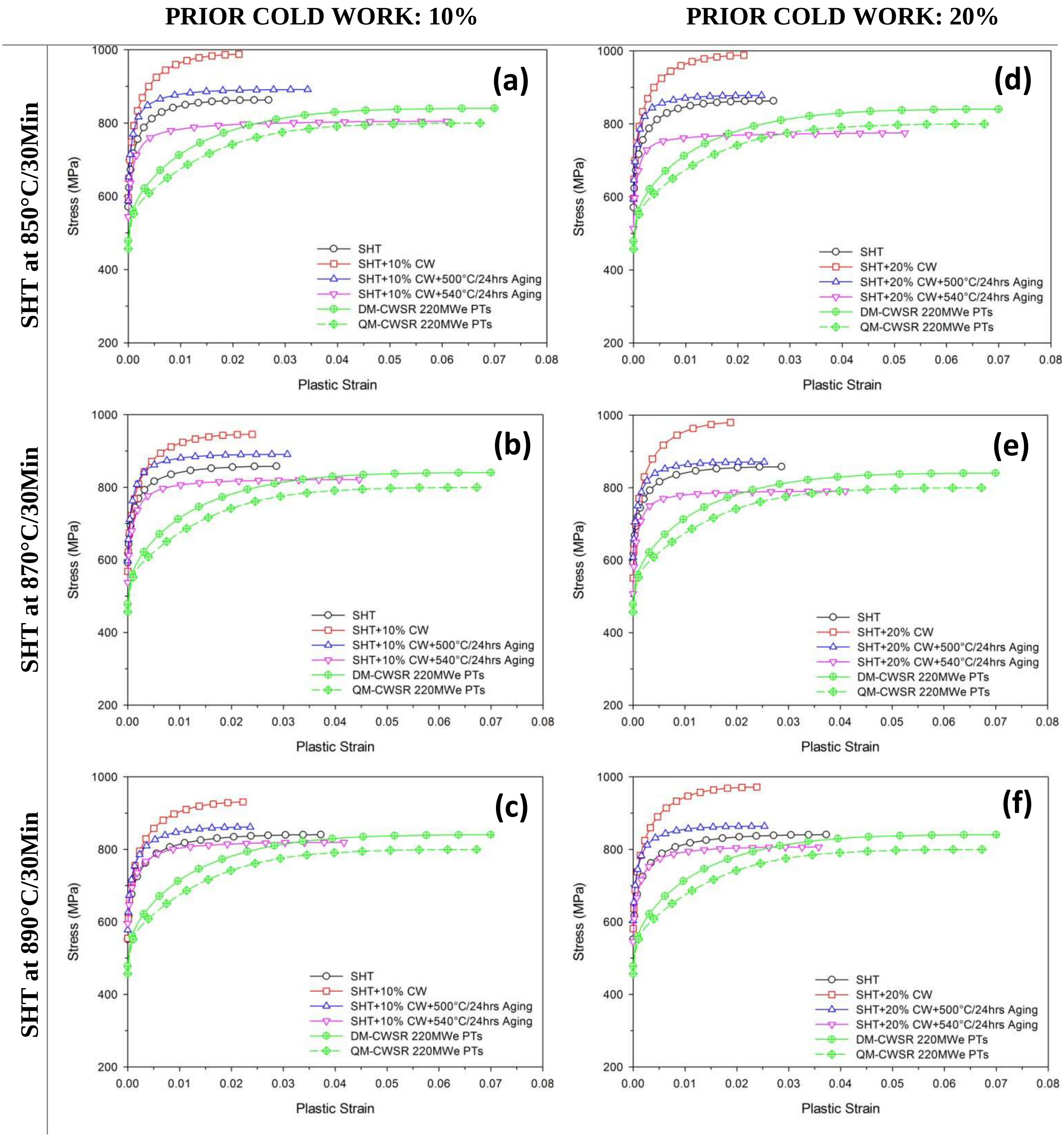

Figure 6.9: Evolution of lower bound flow behavior of Zr-2.5Nb alloy during three TMP stages; SHT, subsequent cold working, and vacuum aging, under ambient condition. Plots show the flow behavior of Zr-2.5Nb alloy previously soaked at 850, 870 and 890°C for 30 min during solution treatment stage. The flow behavior of these heat treated materials were compared with that of Zr-2.5Nb alloys under CWSR conditions in which the pressure tubes of 220MWe IPHWRs are currently being used.

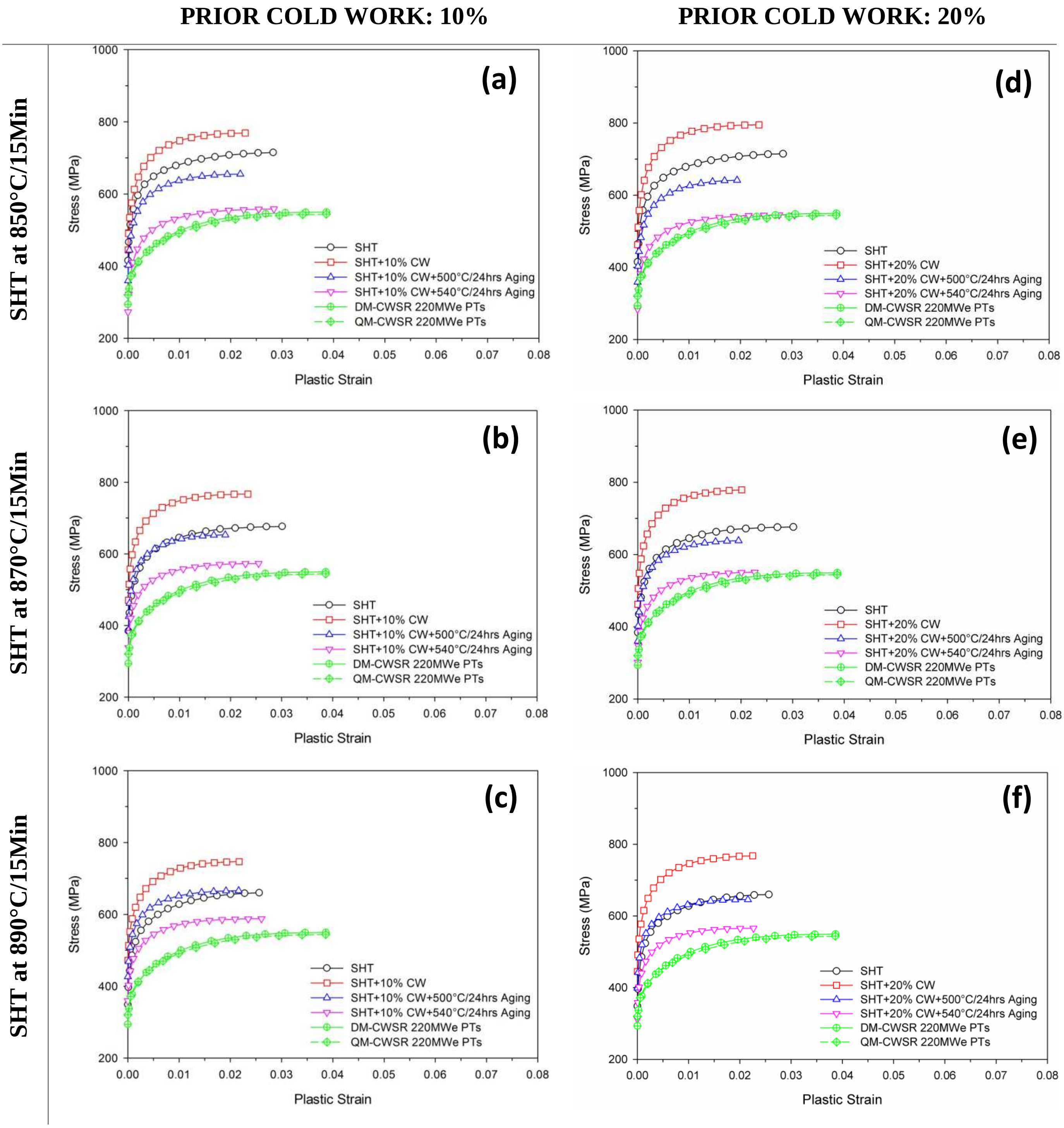

Figure 6.10: Evolution of lower bound flow behavior of Zr-2.5Nb alloy during three TMP stages; SHT, subsequent cold working, and vacuum aging, at 300°C. Plots show the flow behavior of Zr-2.5Nb alloy previously soaked at 850, 870 and 890°C for 15 min during solution treatment stage. The flow behavior of these heat treated materials were compared with that of Zr-2.5Nb alloys under CWSR conditions in which the pressure tubes of 220MWe IPHWRs are currently being used.

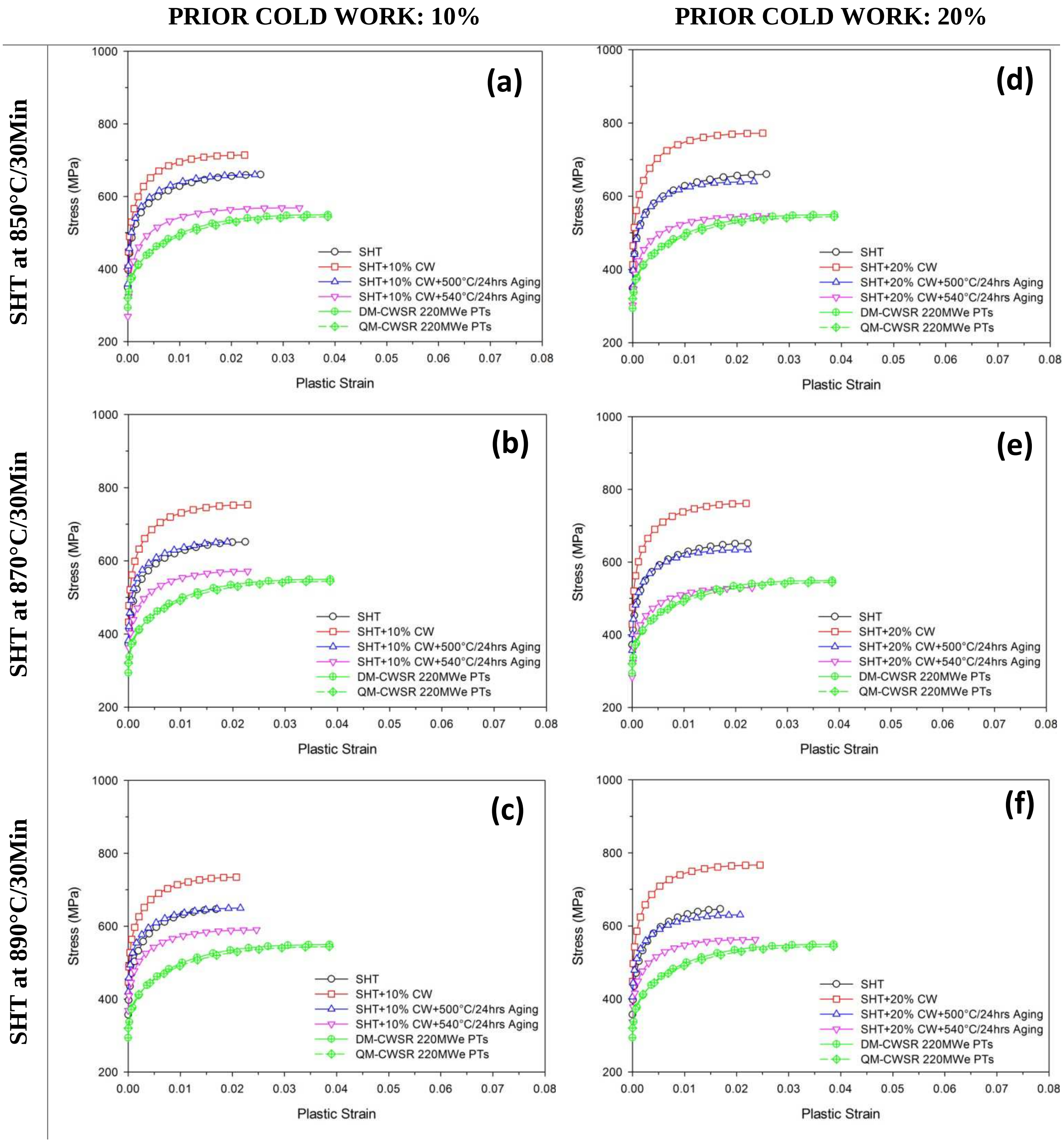

Figure 6.11: Evolution of lower bound flow behavior of Zr-2.5Nb alloy during three TMP stages; SHT, subsequent cold working, and vacuum aging, at 300°C. Plots show the flow behavior of Zr-2.5Nb alloy previously soaked at 850, 870 and 890°C for 30 min during solution treatment stage. The flow behavior of these heat treated materials were compared with that of Zr-2.5Nb alloys under CWSR conditions in which the pressure tubes of 220MWe IPHWRs are currently being used.

II. Tensile Strengths

After aging treatments, tensile strengths of cold worked-solution heat treated Zr-2.5Nb alloy decreased. Aging at 500°C for 24 h, though marginally altered the yield strengths, as the respective reductions were less than 3%. In contrast, aging at relatively higher temperature, 540°C for 24 h resulted in relatively greater, ~ 10% reduction in YSs of these materials, as shown in Figure 6.12. On the other hand, ultimate tensile strengths, UTSs of cold worked materials, in contrast to yield strengths exhibited relatively greater change, maximum by 15 and 22% after the aging treatments at respective 500 and 540°C temperatures, as shown in Figure 6.13. In contrast to RT, at 300°C aging resulted in relatively greater change in the tensile strengths, as the maximum observed reductions were ~ 20 and 30% after the aging at respective 500 and 540°C temperatures.

The soaking temperature used during solution heat treatment stage, influenced the amount of reductions in tensile strength after aging treatment. The cold worked materials, which were previously soaked at higher SHT temperature (890°C), in contrast to 850°C exhibited relatively less change in the tensile strength after aging treatments. The various aged Zr-2.5Nb alloys considered in this study, irrespective of having varying thermo-mechanical histories such as; soaking temperature & duration used during the solution heat treatment stage and imparted degree of cold work exhibited comparable tensile strengths.

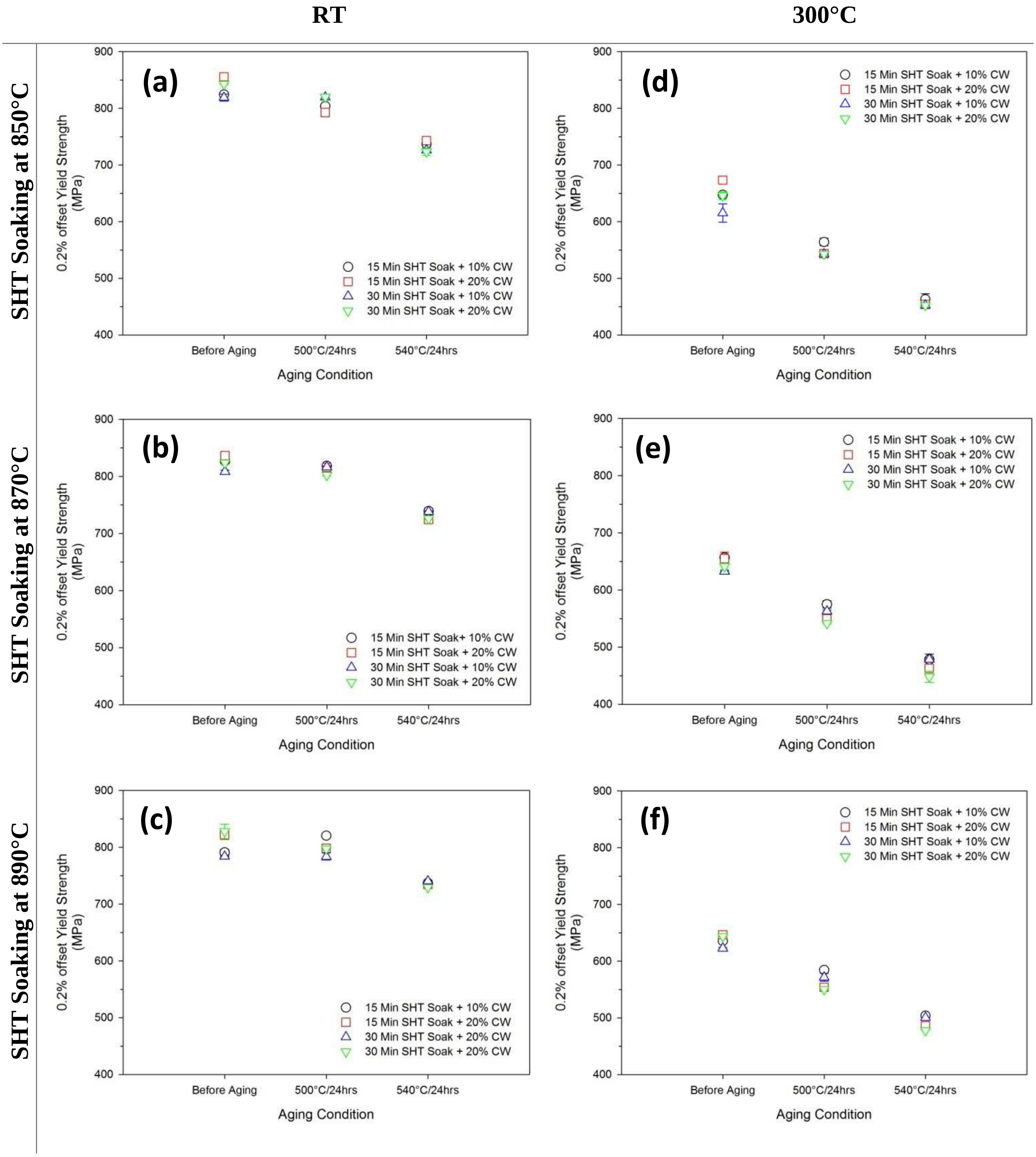

Figure 6.12: Yield strengths of Zr-2.5Nb alloy under different cold worked-solution heat treated conditions before and after the aging treatments at 500 and 540°C for 24 h followed by furnace cooling.

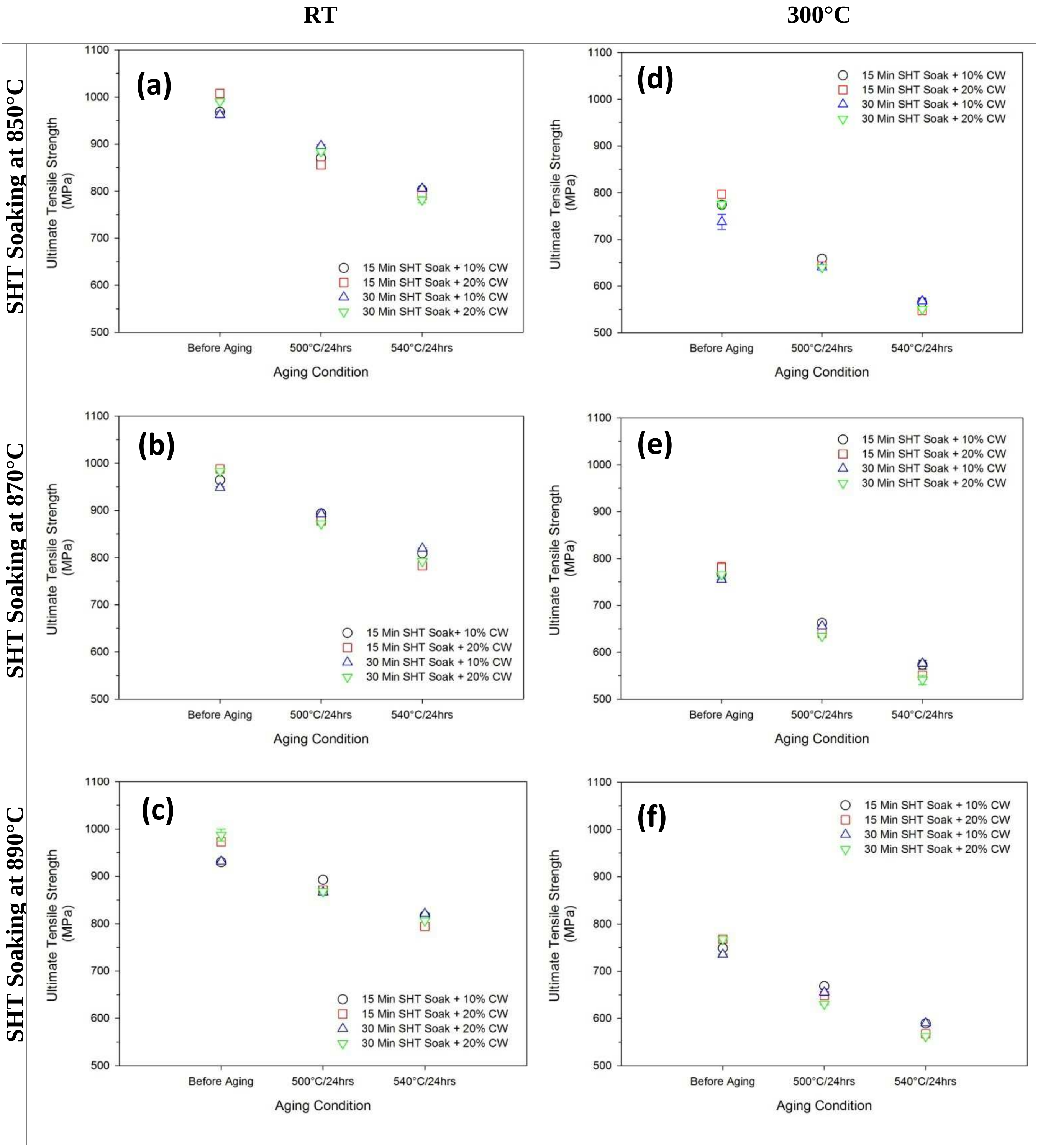

Figure 6.13: Ultimate tensile strengths of Zr-2.5Nb alloy under different cold worked-solution heat treated conditions before and after the aging treatments at 500 and 540°C for 24 h followed by furnace cooling.

To compare the WQA and CWSR fabrication routes of Zr-2.5Nb alloy pressure tubes, tensile strengths of the presently considered aged materials and CWSR materials used for 220MWe IPHWRs were compared. The comparison, Figure 6.14 (a) & (b) shows that under ambient condition, the aged materials soaked at 500 and 540°C for 24 h duration had respectively ~ 37 and 25% higher yield strengths as compared to the QM CWSR materials. In contrast, at 300°C, respective deviations in the yield strengths of these two class of materials were 34 and 14%. UTSs of the aged materials soaked at 500°C were found to be ~5 and 14% higher than that of the CWSR materials at respective RT and 300°C, see Figure 6.14 (c) & (d). However, the aged materials soaked at 540°C had almost comparable UTS as that of CWSR materials.

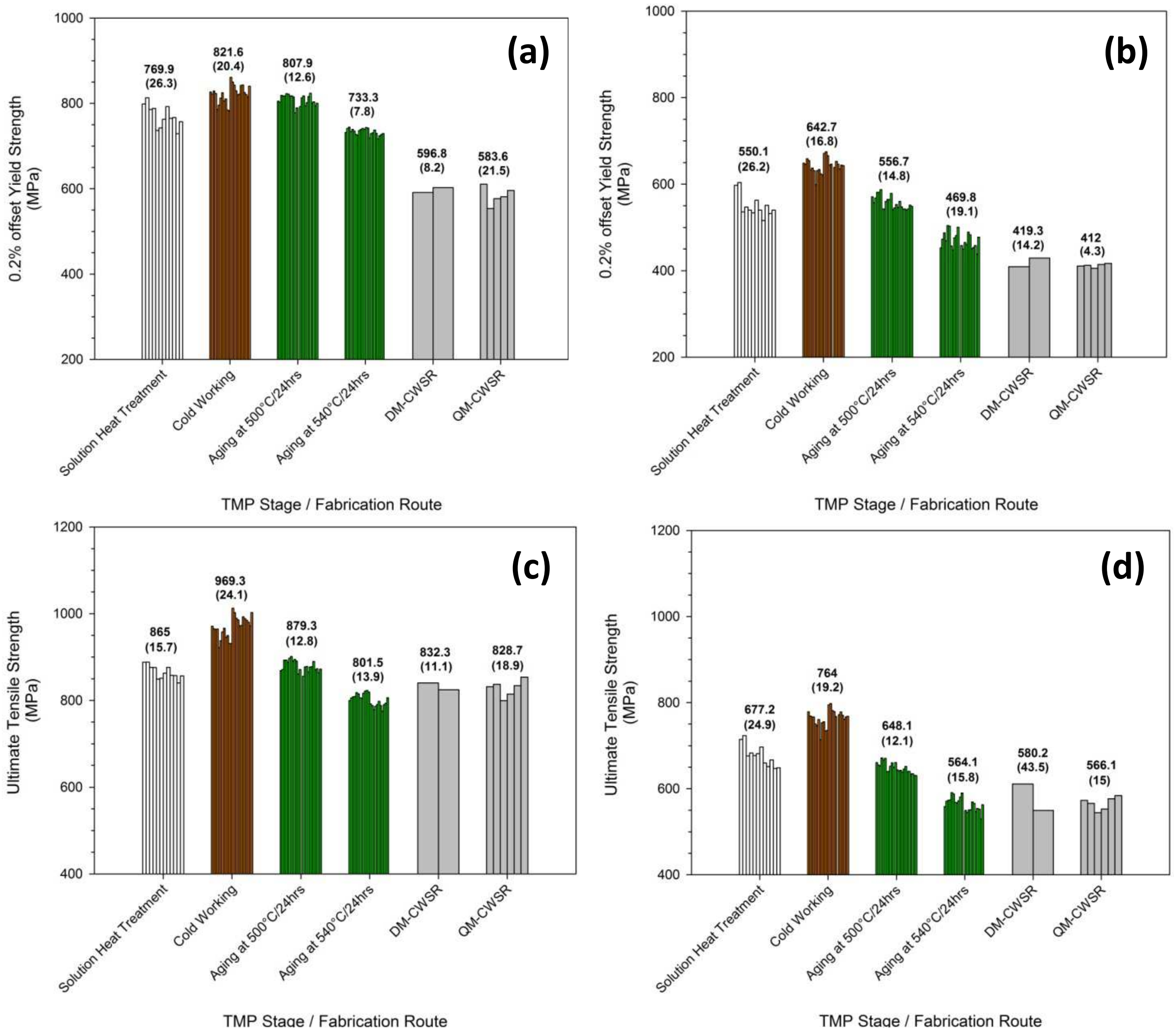

Figure 6.14: Evolution of tensile strengths of Zr-2.5Nb alloy during three TMP stages; SHT, subsequently cold worked & aged and their comparison with CWSR pressure tube material. Plots (a) and (b) respectively show the yield strengths of these two materials at RT and 300°C respectively and plots (c) and (d) respectively show the ultimate tensile strengths of the two materials at RT and 300°C respectively. In these plots, over each bar group, average tensile strength along with the corresponding standard deviation (within parentheses) is shown.

III. Ductility

Aging treatment resulted in significant improvement in ductility of cold worked-solution heat treated Zr-2.5Nb alloy. The ductility was measured in terms of two parameters viz., total elongation (a measure of the induced plastic strain up to fracture) and change (reduction) in fracture cross sectional area. Figures 6.15 and 6.16 show the variation of these two ductility parameters of various cold worked-solution heat treated Zr-2.5Nb alloy before and after the aging treatment. Aging at 500°C for 24 h resulted in increase in both of these ductility parameters by more than two fold for some of the cold worked materials. Aging at the higher soaking temperature, 540°C for 24 h, in general, had nearly similar influence on the ductility of the cold worked materials. Additionally, ductility of the cold worked materials at 300°C, in contrast to RT, changed relatively less after the aging treatment.

Under ambient condition, the thermo-mechanical histories of different cold worked materials considered in this study played a remarkable role in governing their ductility after aging treatment. The aged materials, which were previously soaked at higher SHT temperature showed marginally lower ductility. The aged materials, previously soaked for 30 min, in contrast to 15 min duration in the solution heat treatment stage exhibited relatively less reduction in their fracture cross-section area at RT, thereby suggesting the lower ductility of former materials. Higher degree of imparted cold work resulted in higher ductility of the aged material. In contrast, at 300°C, different aged materials irrespective of their previous varying thermo-mechanical histories had practically similar ductility.

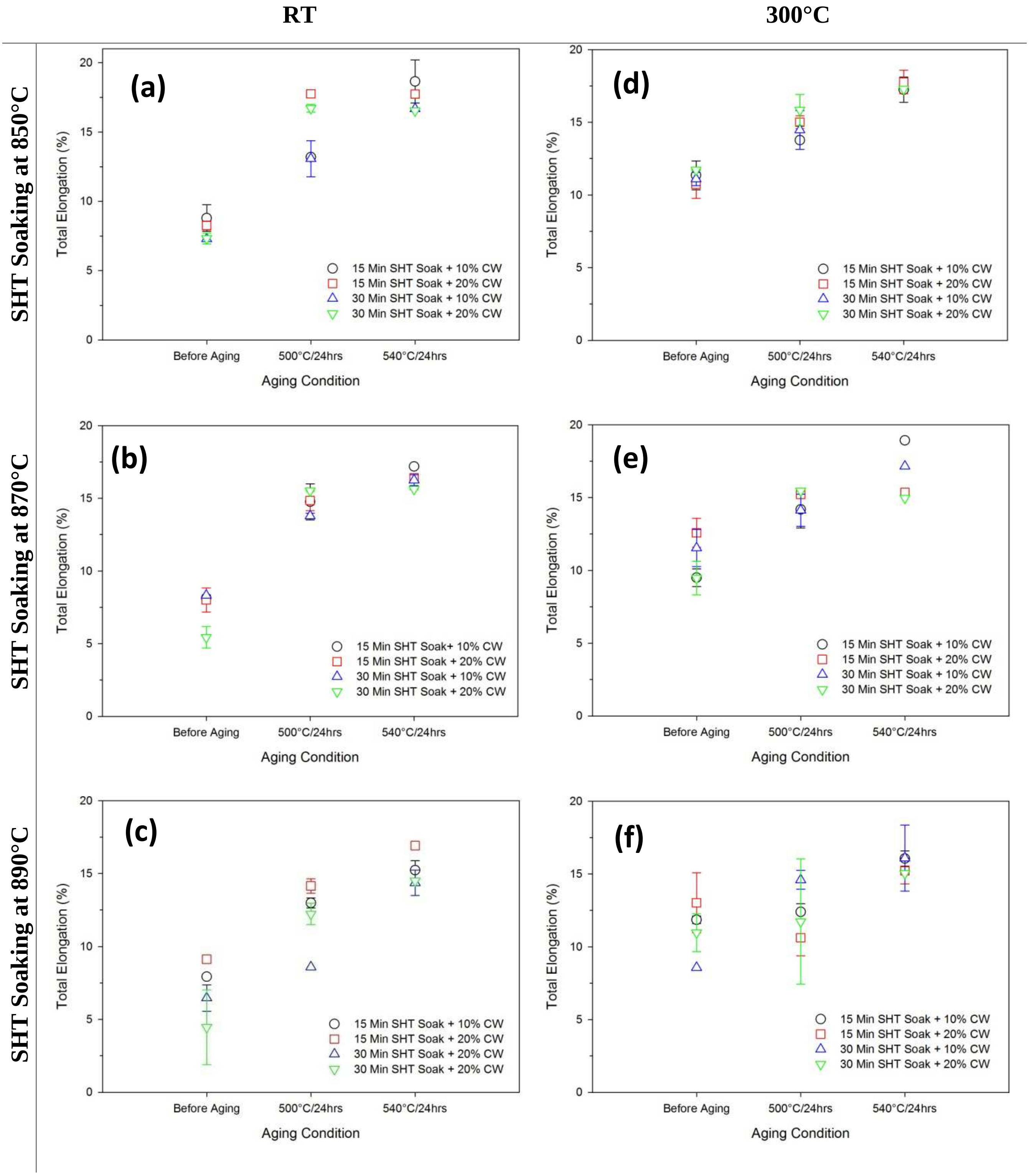

Figure 6.15: Total elongations (a ductility parameter) of Zr-2.5Nb alloy under different cold worked-solution heat treated conditions before and after the aging treatments at 500 and 540°C for 24 h followed by furnace cooling.

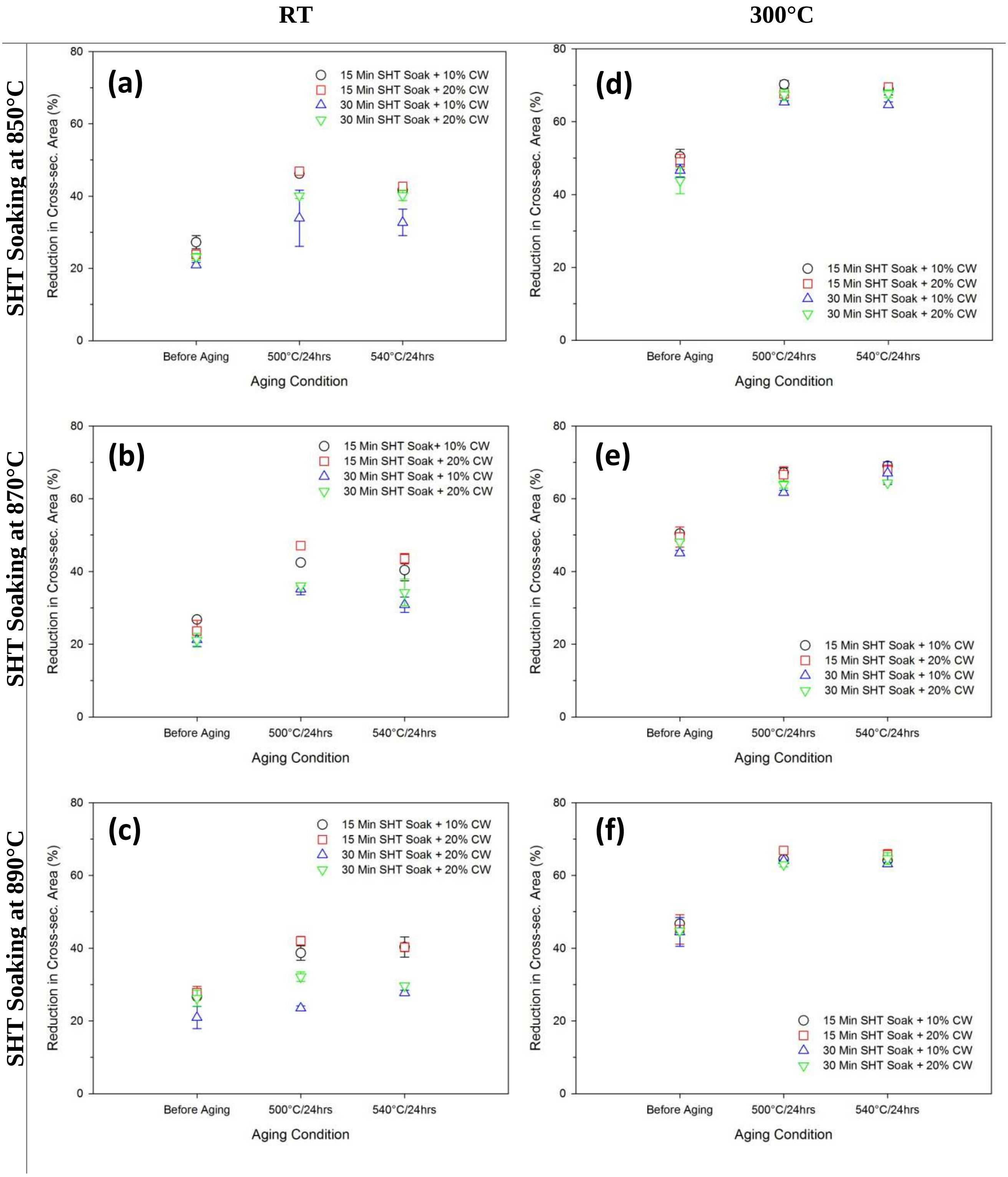

Figure 6.16: Reductions in fracture cross section areas (second ductility parameter) of Zr-2.5Nb alloy under different cold worked-solution heat treated conditions before and after the aging treatments at 500 and 540°C for 24 h followed by furnace cooling.

In contrast to CWSR pressure tube material of 220MWe IPHWR, the materials aged at 500°C showed marginally lower total elongations, however those aged at 540°C possessed nearly comparable elongations (Figure 6.17 (a) & (b)). Under ambient condition, the aged materials showed similar reductions of fracture cross-section areas as shown by CWSR materials. However, at reactor operating temperature of 300°C, the materials aged at either 500 or 540°C temperature exhibited ~18-20% higher reduction in the fracture cross-section area as compared to the CWSR materials, (shown in Figure 6.17 (c) & (d)). Therefore, ductility of Zr-2.5Nb alloys under both heat treated and CWSR conditions were more or less analogous.

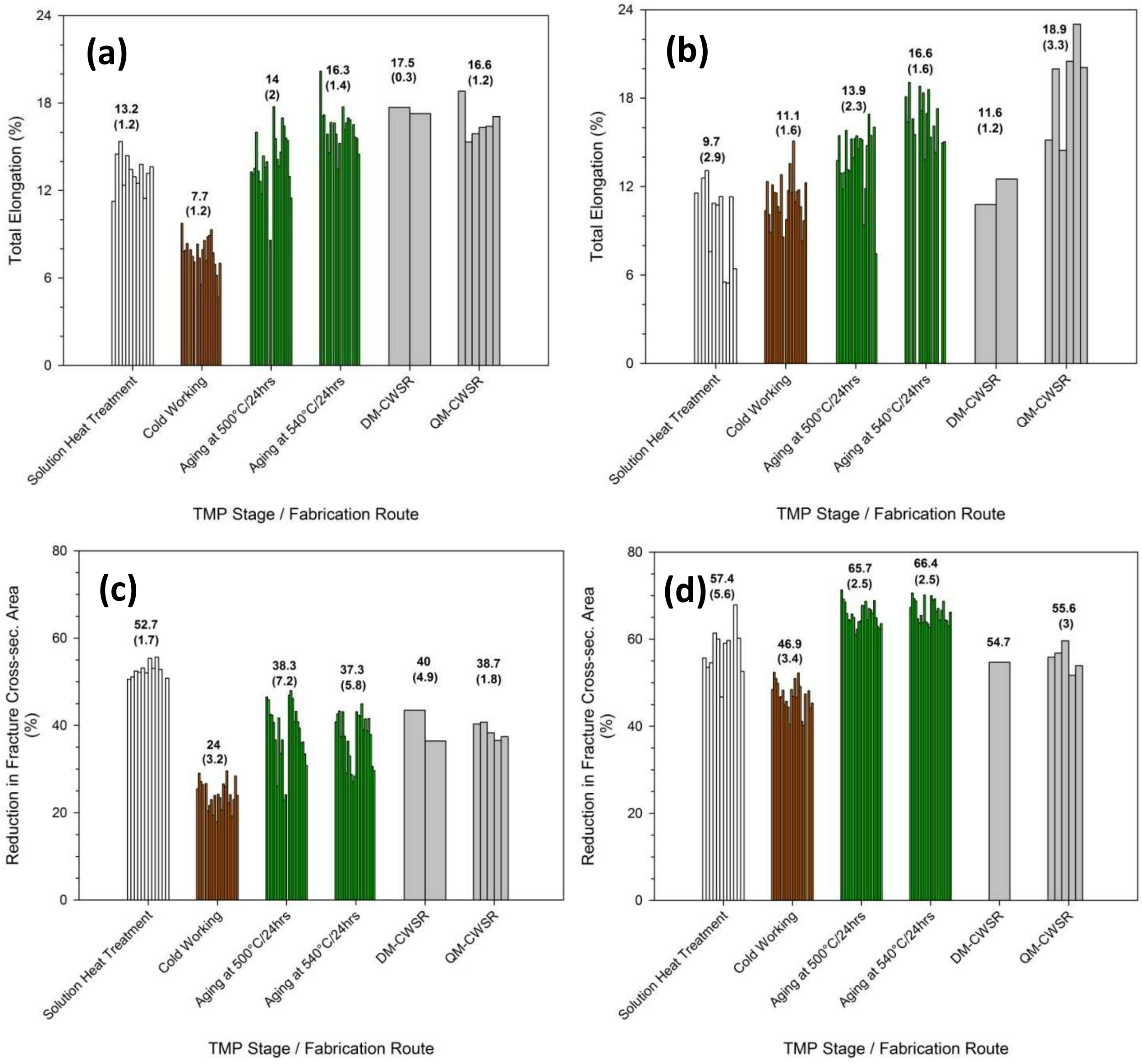

Figure 6.17: Evolution of ductility of Zr-2.5Nb alloy during three TMP stages; SHT, subsequently cold worked & aged and their comparison with CWSR pressure tube material. Plots (a) and (b) respectively show the total elongations before fracture of these two materials at RT and 300°C respectively and plots (c) and (d) respectively show the change in fracture cross-section areas of these materials at RT and 300°C respectively. In these plots, over each bar group, average of ductility parameter along with the corresponding standard deviation (within parentheses) is shown.

IV. Uniform Elongation

Aging at 500°C for 24 h had practically no influence on the uniform elongations of different cold worked-solution heat treated Zr-2.5Nb alloys. However, aging performed at higher soaking temperature, 540°C for 24 h for same duration resulted in appreciable increase in the uniform elongations of these cold worked materials at RT, Figure 6.18. In contrast, uniform elongations at 300°C were found to be practically insensitive to the aging at both 500 and 540°C soaking temperatures. The prior used SHT temperatures governed the extent of increase in uniform elongations of cold worked materials after aging treatment. The materials soaked at higher temperature, 890°C in contrast to 850°C during solution heat treatment stage had relatively less change in their uniform elongations after aging treatment. Another important observation is that after aging at either of the two soaking temperatures, uniform elongations of different cold worked-solution heat treated Zr-2.5Nb alloys considered in this study irrespective of their varying previous thermo-mechanical histories were almost similar.

Comparison of CWSR pressure tube material of 220MWe IPHWR and aged materials, Figure 6.19 showed lower uniform elongations of aged materials. The CWSR materials exhibited on average three and two times the uniform elongations of the 500°C aged materials at respectively RT and 300°C. In contrast, the materials aged at higher soaking temperature, 540°C showed ~ 32 to 40% lower uniform elongations as compared to that of the CWSR materials.

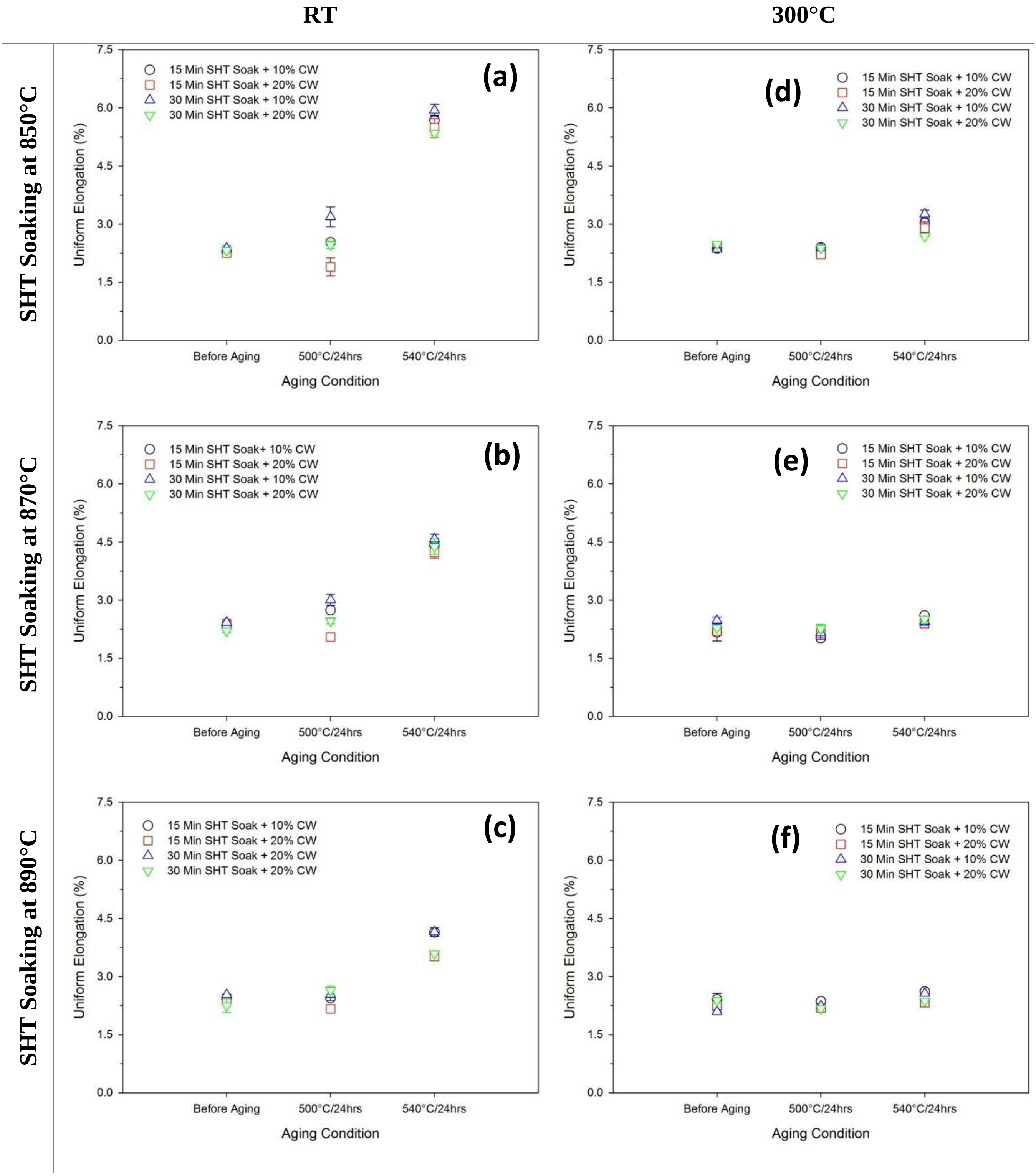

Figure 6.18: Uniform elongations of Zr-2.5Nb alloy under different cold worked-solution heat treated conditions before and after the aging treatments at 500 and 540°C for 24 h followed by furnace cooling.

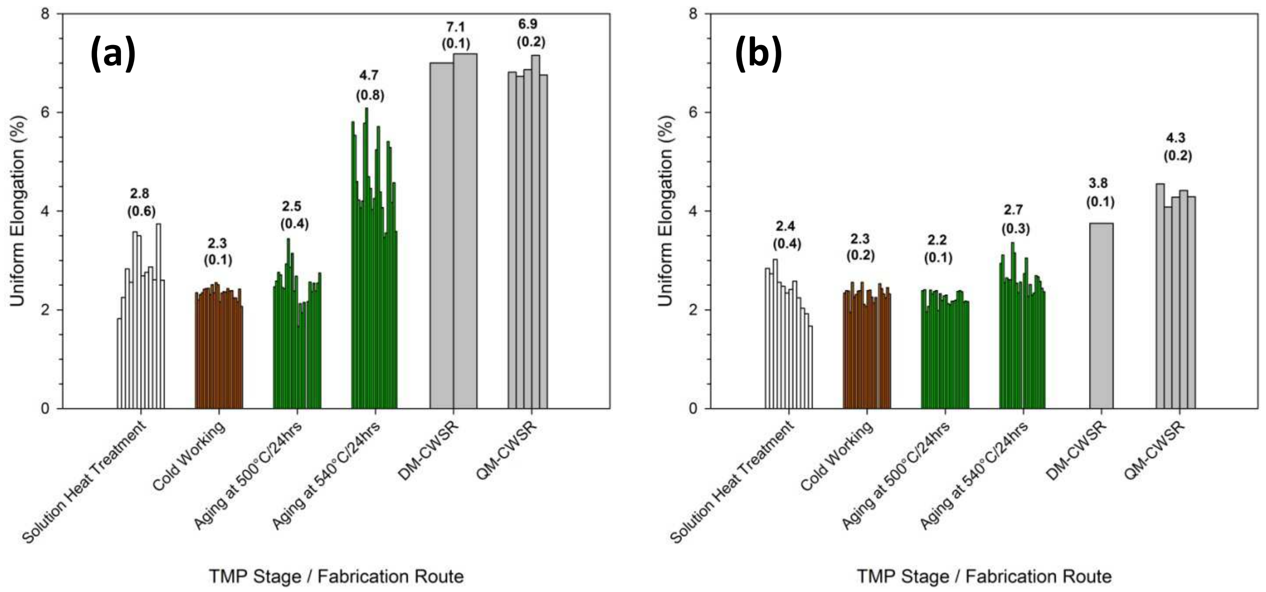

Figure 6.19: Evolution of uniform elongation of Zr-2.5Nb alloy during three TMP stages; SHT, subsequently cold worked & aged and their comparison with CWSR pressure tube material. Plots (a) and (b) respectively show the comparisons at RT and 300°C. In these plots, over each bar group, average of uniform elongation along with the corresponding standard deviation (within parentheses) is shown.

V. Strain Hardening Characteristics

Strain hardening characteristics of aged Zr-2.5Nb alloys were determined using Hollomon's empirical power law hardening relationship (Equation 4.3, Chapter 4) in terms of strain hardening exponent and strength coefficient parameters and are shown in Figures 6.20 and 6.21. Aging at 500°C for 24 h duration resulted in appreciable reduction of the strain hardening exponent of cold worked-solution heat treated Zr-2.5Nb alloy under ambient condition, as after aging, the hardening exponents of these materials became nearly half. However, aging carried out at the higher soaking temperature, 540°C for 24 h resulted in practically similar strain hardening exponents as that of the 500°C aged materials. At 300°C, the aging treatments had practically no influence on the hardening exponents of different cold worked-solution heat treated Zr-2.5Nb alloys. Nevertheless, with increase in temperature from RT to 300°C, the hardening exponents of these aged materials showed an appreciable rise, by almost two fold.

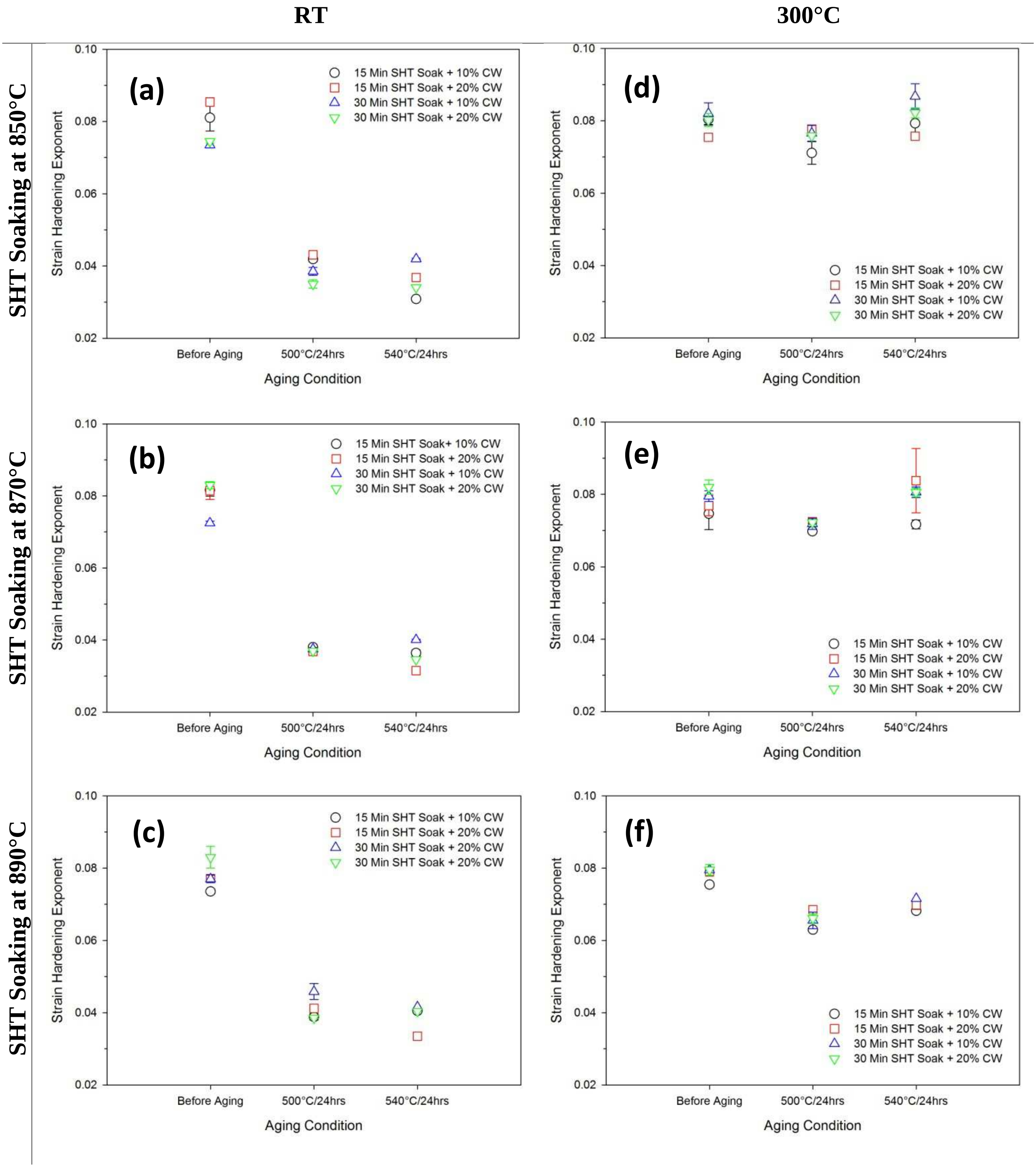

Figure 6.20: Hollomon's strain hardening exponents of Zr-2.5Nb alloy under different cold worked-solution heat treated conditions before and after the aging treatments at 500 and 540°C for 24 h followed by furnace cooling.

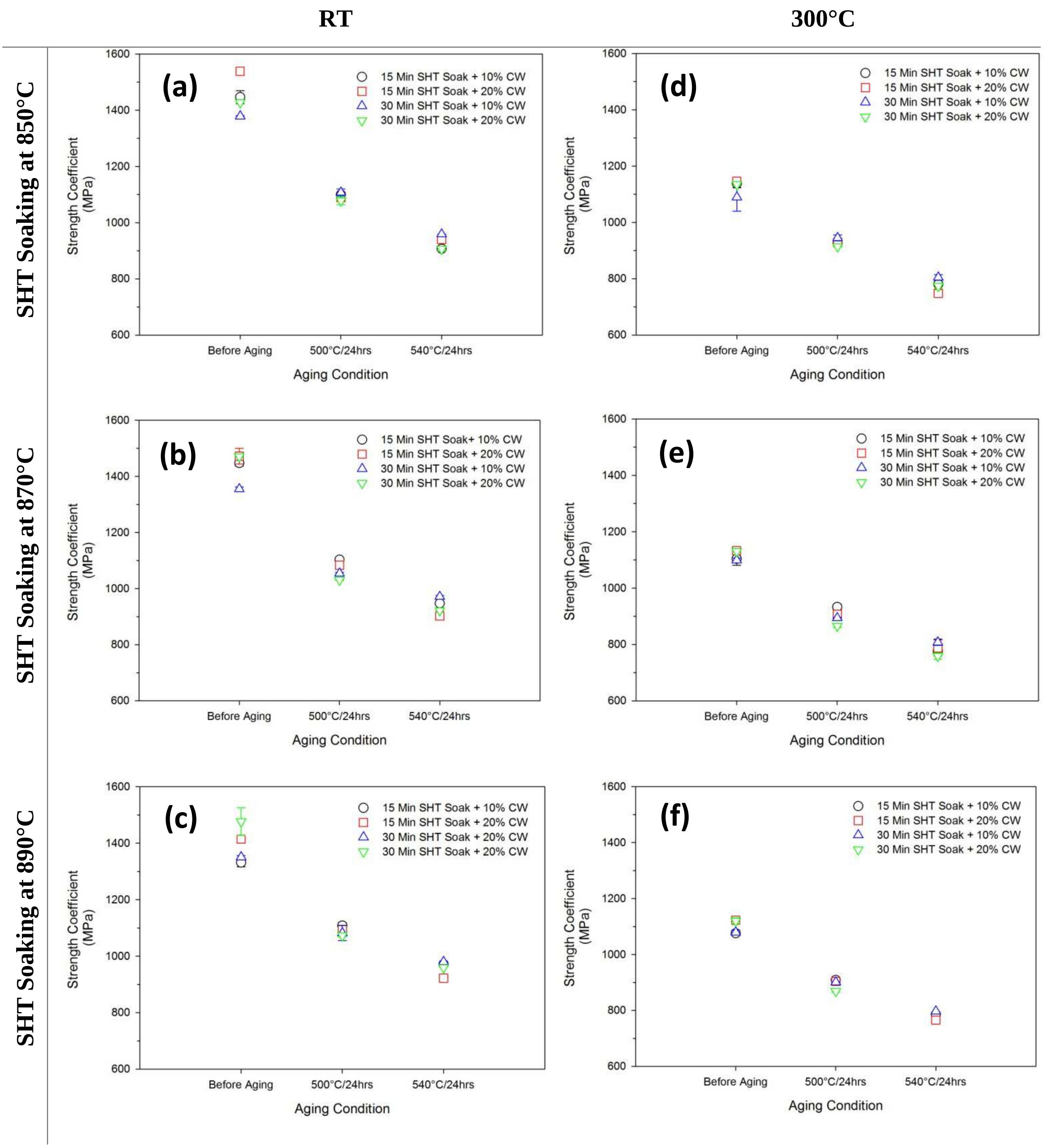

Figure 6.21: Strength coefficients of Zr-2.5Nb alloy under different cold worked-solution heat treated conditions before and after the aging treatments at 500 and 540°C for 24 h followed by furnace cooling. These strength coefficients were derived using the Hollomon’s empirical power hardening relationship, Equation 4.3, Chapter 4 [102].

The strength coefficients of different cold worked materials decreased by almost 30% after aging at 500°C. In contrast, aging at 540°C resulted for relatively higher, ~ 40% reduction in the strength coefficients of these materials, Figure 6.21.

Different cold worked materials considered in this study, irrespective of having varying thermo-mechanical histories, had nearly similar strain hardening characteristics both before and after the aging treatments.

The comparison of strain hardening behaviors of CWSR pressure tube material of 220MWe IPHWRs and WQA materials considered in this study is presented in Figure 6.22. In contrast to CWSR pressure tube materials, aged materials exhibited significantly lower work hardening characteristics, by showing on an average almost 70 and 40% lower strain hardening exponents at respective RT and 300°C, see Figure 6.22 (a) & (b). Relatively steeper flow curves exhibited by the aged materials as compared to the CWSR materials indicate such inferior work hardening feature of the former materials. Additionally, strength coefficient of CWSR materials was higher than that of aged materials, as shown Figure 6.22 (c) & (d).

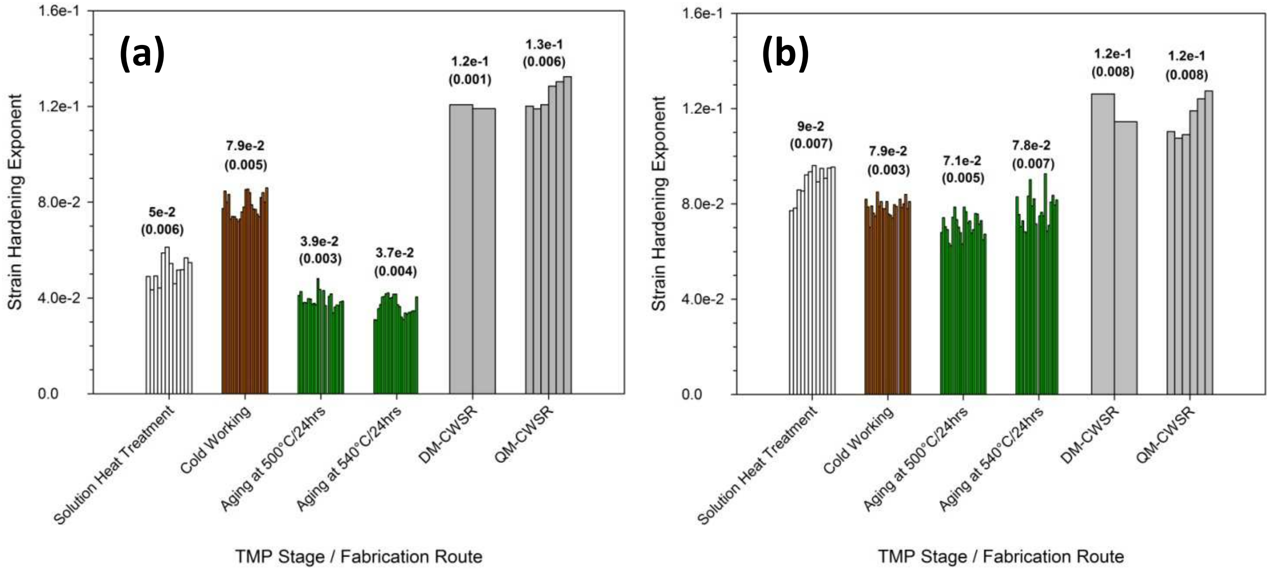

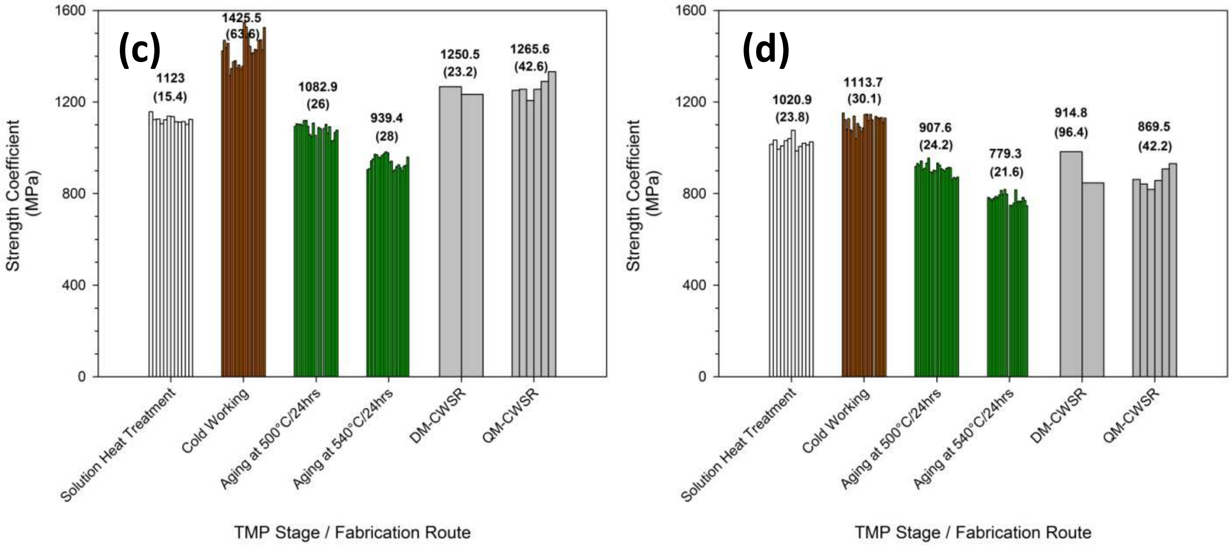

Figure 6.22: Evolution of the strain hardening characteristics of Zr-2.5Nb alloy during three TMP stages; SHT, subsequently cold worked & aged and their comparison with CWSR pressure tube material. Plots (a) and (b) show the strain hardening exponents of the two materials at RT and 300°C respectively. Plots (c) and (d) respectively show the strength coefficients of the two materials at RT and 300°C, respectively. These strain hardening parameters were derived from the Hollomon's empirical power hardening relationship, Equation 4.3, Chapter 4 [102]. In these plots, over each bar group, average of strain hardening parameters along with the corresponding standard deviation (within parentheses) is shown.

6.2.3 Fracture Toughness Parameters

I. Fracture Resistance, *J-R* curves

Figures 6.23-6.26 show the evolution of lower bound fracture resistance, *J-R* curves of various heat treated Zr-2.5Nb alloys having different thermo-mechanical histories. After aging, in general, the cold worked Zr-2.5Nb alloys exhibited relatively inferior *J-R* curves under ambient condition, signifying that aging treatment reduced the fracture toughness at RT (Figure 6.23 and 6.24). Aging treatments at 500 and 540°C did not make drastic difference in the *J-R* curves at RT nevertheless, in general, *J-R* curves of 540°C aged materials were observed to be on the higher side. In contrast, at 300°C, the aging treatment considerably improved fracture toughness of cold worked Zr-2.5Nb alloys; as the aged materials, compared to cold worked materials exhibited superior *J-R* curves

(Figures 6.25 and 6.26). At 300°C, the aged materials soaked at 500 and 540°C had notable difference in *J-R* curves however, analogous to RT, the aging treatment performed at 540°C improved fracture resistance.

Under ambient condition, *J-R* curves of the aged materials were found to be closer to that of DM-CWSR materials. However, at reactor operating temperature, 300°C, the fracture resistance improved significantly, as a result *J-R* curves of aged materials was closer to that of the QM-CWSR materials.

The thermo-mechanical histories of aged Zr-2.5Nb alloy considered in this study influenced the fracture resistance, especially at 300°C. The aged materials, previously soaked at lower soaking temperature, 850°C in contrast to 890°C during SHT stage, showed improved fracture resistance through exhibiting superior *J-R* curves. This SHT temperature dependency of fracture resistance of aged materials was especially observed for 20% cold worked materials. Though, SHT soaking duration (15 or 30 min) did not make drastic change on the fracture resistance, however, 30 min soaked materials exhibited marginally superior fracture resistance. Higher degree of cold work imparted on the solution heat treated materials provided notably better fracture resistance after the aging treatment, especially at 300°C; as the aged materials previously cold worked with 20% level, in contrast to 10% level showed superior *J-R* curves.

Another important observation was that at lower crack growth regime, *J* parameters of WQA materials had weak dependence on the TMP parameters. However, with increasing crack growth, such dependence became prominent.

Therefore, the optimum thermo-mechanical history of WQA Zr-2.5Nb alloy for obtaining the best fracture resistance is achieved by performing SHT at a lower soaking temperature (850°C) for 15-30 min duration followed by a higher degree of cold working (20%) and higher aging temperature (540°C).

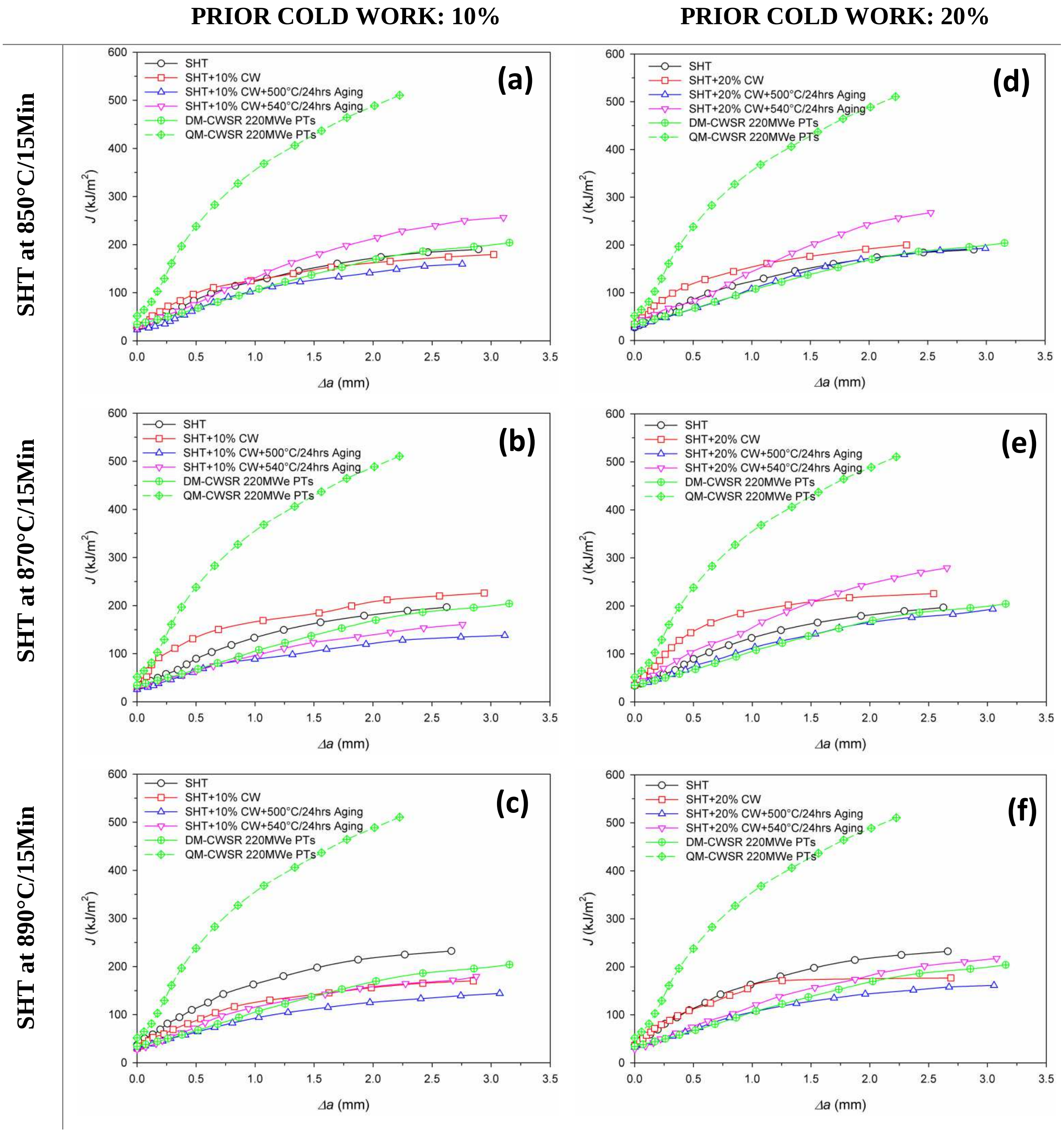

Figure 6.23: Evolution of the RT lower bound fracture resistance, *J-R* curves of Zr-2.5Nb alloy during three TMP stages; SHT, cold working & thermal aging, and their comparison with CWSR pressure tube material. Plots show the *J-R* curves of Zr-2.5Nb alloy previously soaked at 850, 870 and 890°C for 15 min during solution heat treatment stage. The *J-R* curves at RT of these heat treated materials were compared with that of Zr-2.5Nb alloy under CWSR conditions in which the pressure tubes of 220MWe IPHWRs are being used.

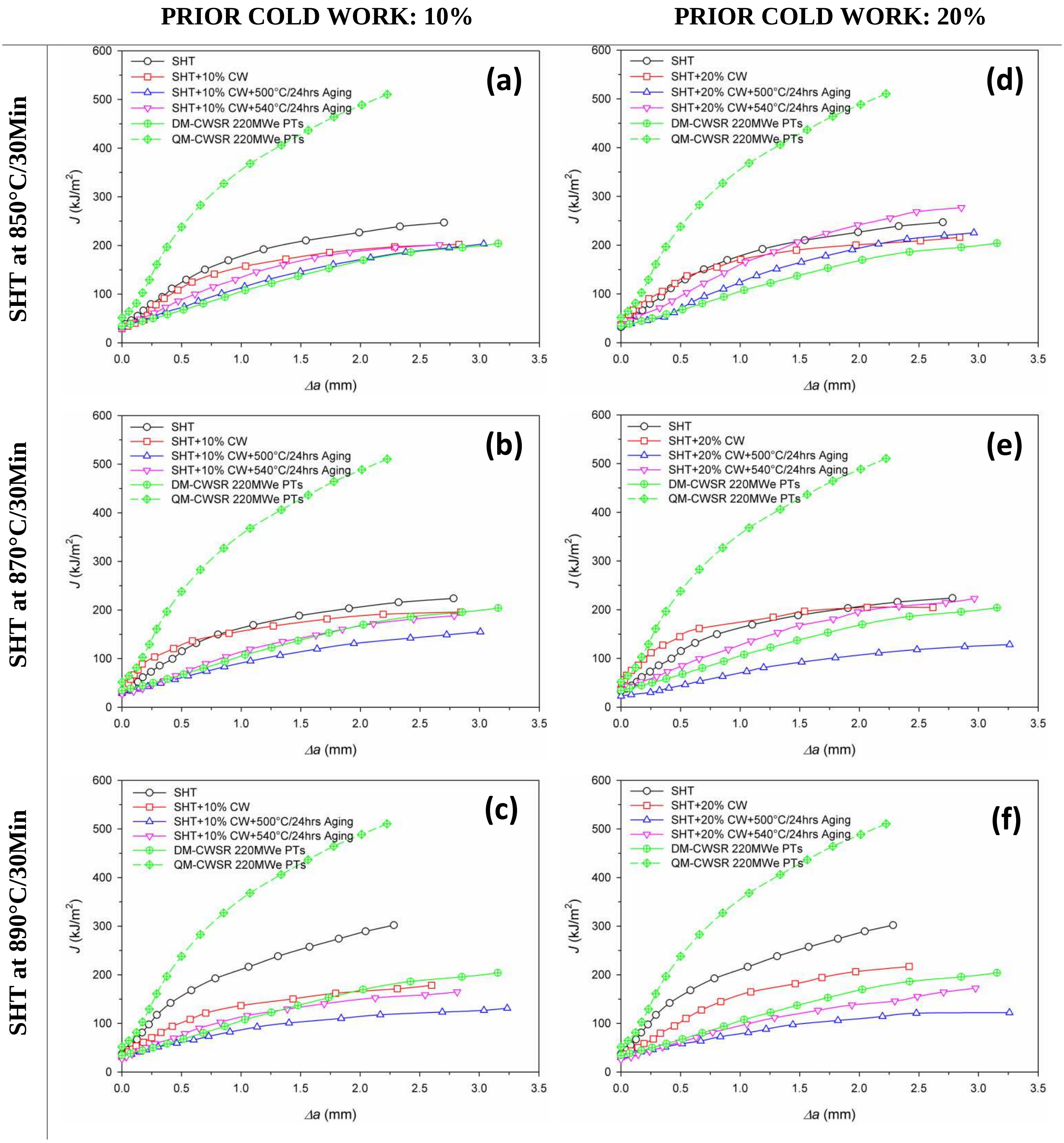

Figure 6.24: Evolution of the RT lower bound fracture resistance, *J-R* curves of Zr-2.5Nb alloy during three TMP stages; SHT, cold working & thermal aging, and their comparison with CWSR pressure tube material. Plots show the *J-R* curves of Zr-2.5Nb alloy previously soaked at 850, 870 and 890°C for 30 min during solution heat treatment stage. The *J-R* curves at RT of these heat treated materials were compared with that of Zr-2.5Nb alloy under CWSR conditions in which the pressure tubes of 220MWe IPHWRs are being used.

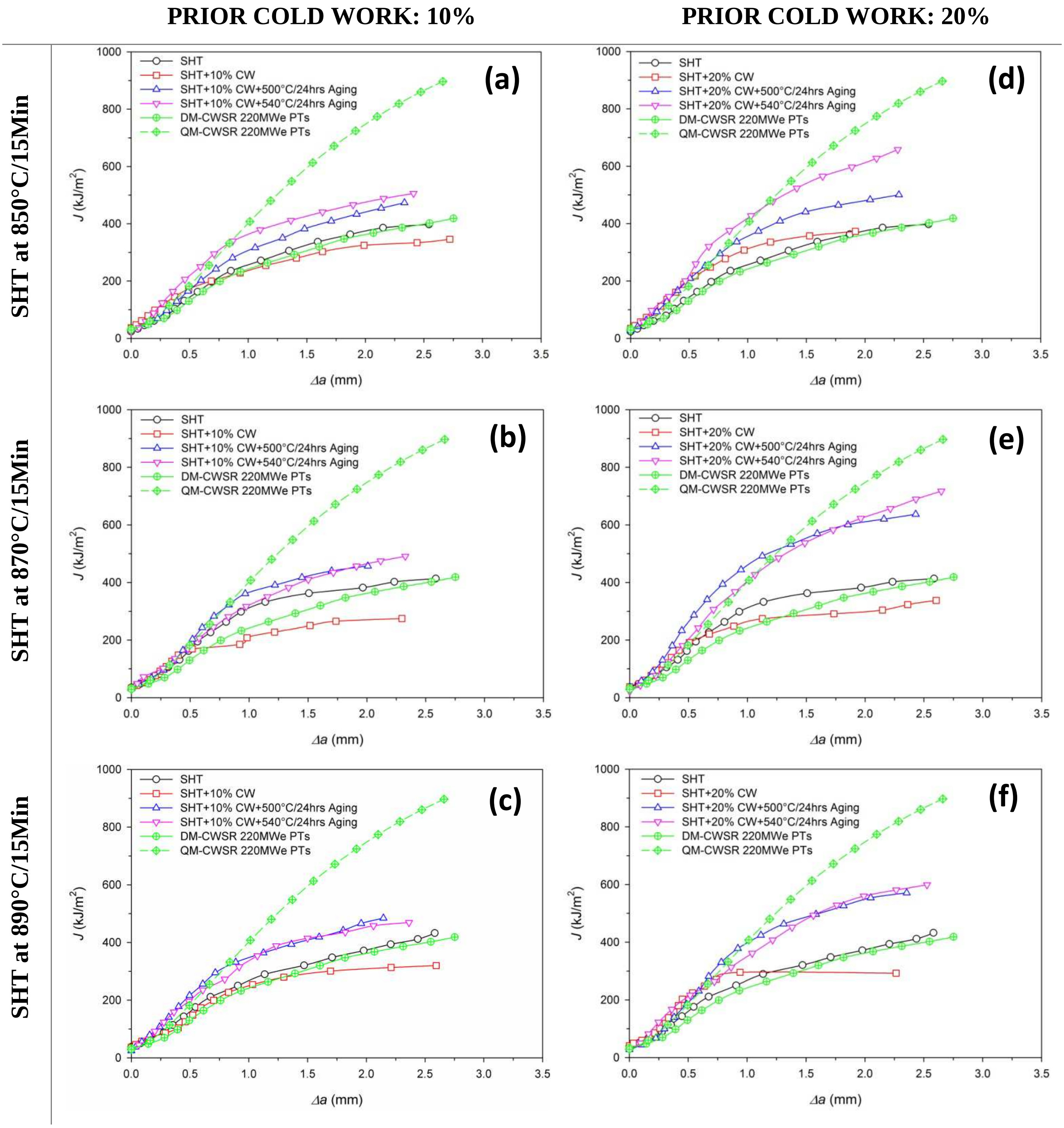

PRIOR COLD WORK: 10%

PRIOR COLD WORK: 20%

SHT at 850°C/15Min

SHT at 870°C/15Min

SHT at 890°C/15Min

Figure 6.25: Evolution of the lower bound fracture resistance, *J*-*R* curves of Zr-2.5Nb alloy at 300°C during three TMP stages; SHT, cold working & thermal aging, and their comparison with CWSR pressure tube material. Plots show the *J*-*R* curves of Zr-2.5Nb alloy previously soaked at 850, 870 and 890°C for 15 min during solution heat treatment stage. The *J*-*R* curves at 300°C of these heat treated materials were compared with that of Zr-2.5Nb alloy under CWSR conditions in which the pressure tubes of 220MWe IPHWRs are being used.

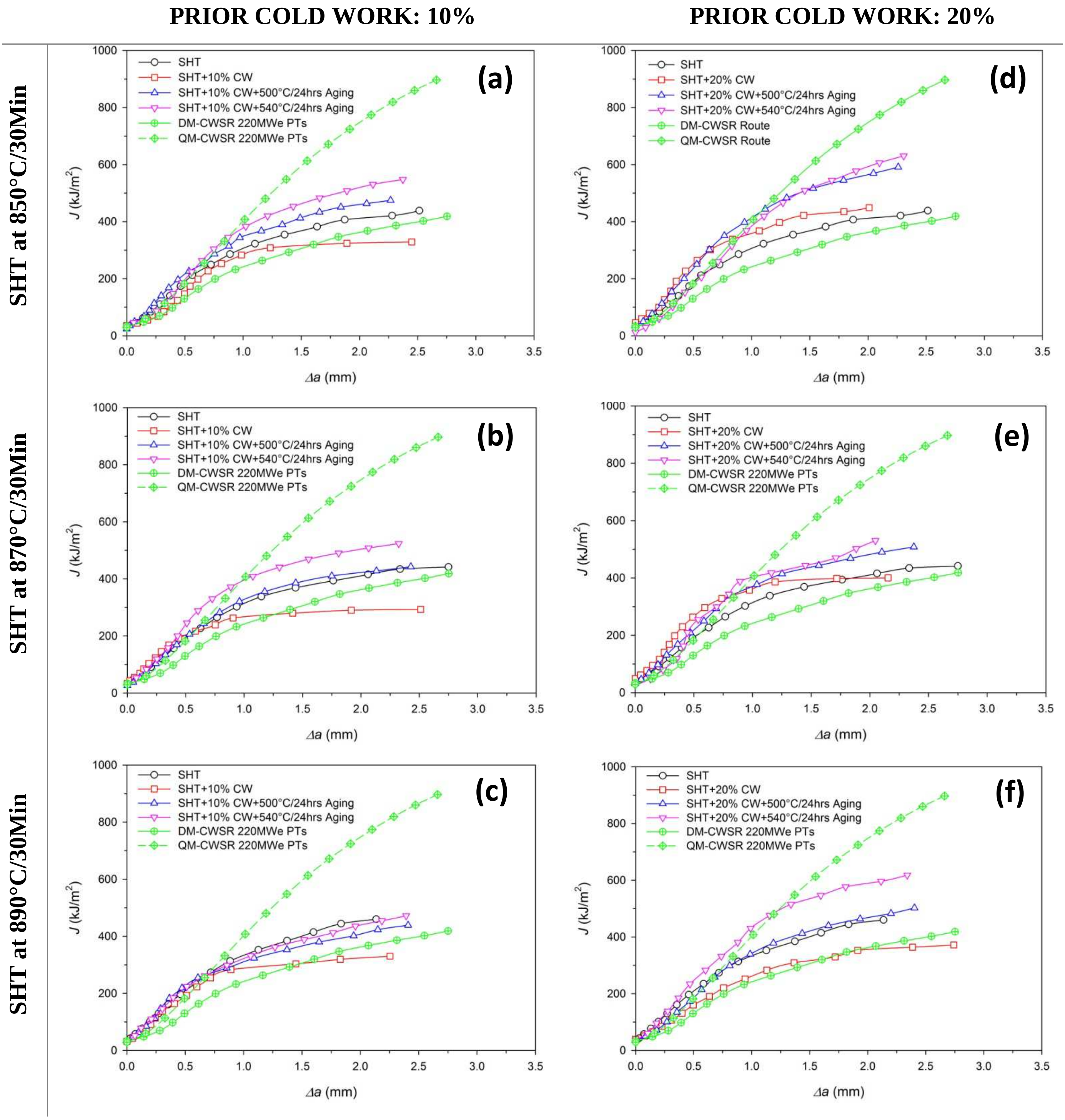

Figure 6.26: Evolution of the lower bound fracture resistance, *J-R* curves of Zr-2.5Nb alloy at 300°C during three TMP stages; SHT, cold working & thermal aging, and their comparison with CWSR pressure tube material. Plots show the *J-R* curves of Zr-2.5Nb alloy previously soaked at 850, 870 and 890°C for 30 min during solution heat treatment stage. The *J-R* curves at 300°C of these heat treated materials were compared with that of Zr-2.5Nb alloy under CWSR conditions in which the pressure tubes of 220MWe IPHWRs are being used.

II. Initiation Toughness (J_Q)

The influence of aging treatment on initiation fracture toughness of cold worked-solution heat treated Zr-2.5Nb alloy were opposite at RT and 300°C. Under ambient condition, after aging treatment, the initiation fracture toughness of cold worked Zr-2.5Nb alloys showed substantial drop by more than 50%. Aging performed at both 500 and 540°C soaking temperatures, though had very close influence on the initiation toughness, nevertheless materials aged at 540°C showed marginally better toughness. In contrast, at 300°C, aging treatments caused significant improvement in the initiation toughness of cold worked materials. At 300°C also, aging performed at higher temperature (540°C), in contrast to 500°C, resulted in relatively better initiation toughness. The initiation toughness of aged materials at 300°C were observed to be three to five times of the same at RT. Figure 6.27 shows the dissimilar trends of initiation toughness of various cold worked-solution heat treated Zr-2.5Nb alloys at RT and 300°C.

Under ambient condition, irrespective of having varying thermo-mechanical histories, the aged materials possessed more or less similar initiation toughness. However, at 300°C, though having higher data scatter, the aged materials previously cold worked at 20% in contrast to 10%, showed better initiation toughness.

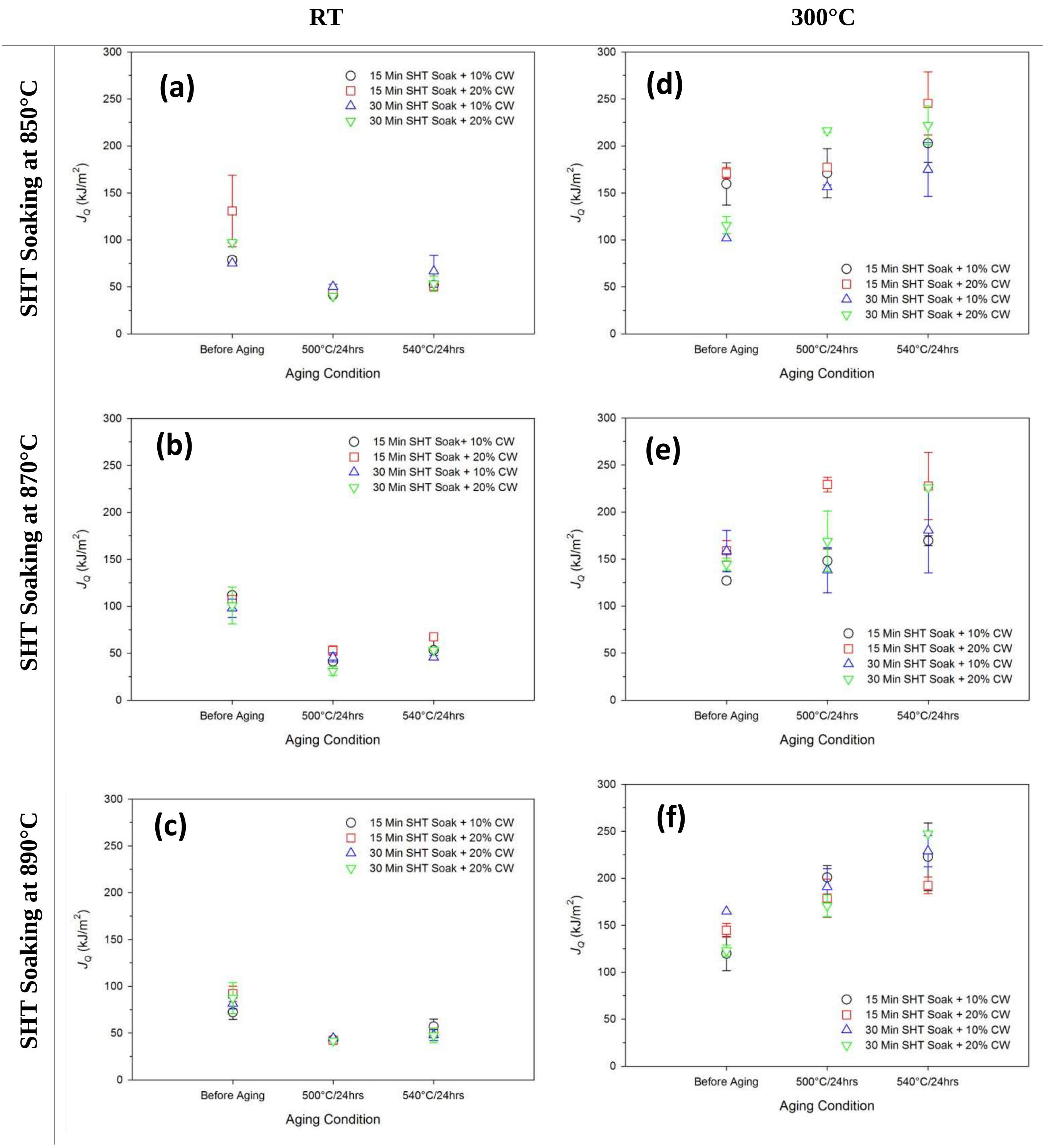

Figure 6.27: Initiation fracture toughness of Zr-2.5Nb alloy under different cold worked-solution heat treated conditions before and after the aging treatments at 500 and 540°C for 24 h followed by furnace cooling.

Figure 6.28 shows the comparison of initiation fracture toughness of Zr-2.5Nb alloy under WQA and CWSR conditions. Under ambient condition, the initiation toughness of WQA materials (aged at 540°C) were comparable, however marginally higher than those of DM-CWSR pressure tube materials of 220MWe IPHWRs (Figure 6.28 (a)), and were on an average ~ 75% lower than those of the QM-CWSR pressure tube materials. However, at 300°C, tremendous improvement in the toughness of aged materials resulted in nearly comparable initiation toughness of WQA (aged at 540°C) and QM-CWSR materials, as shown in Figure 6.28 (b).

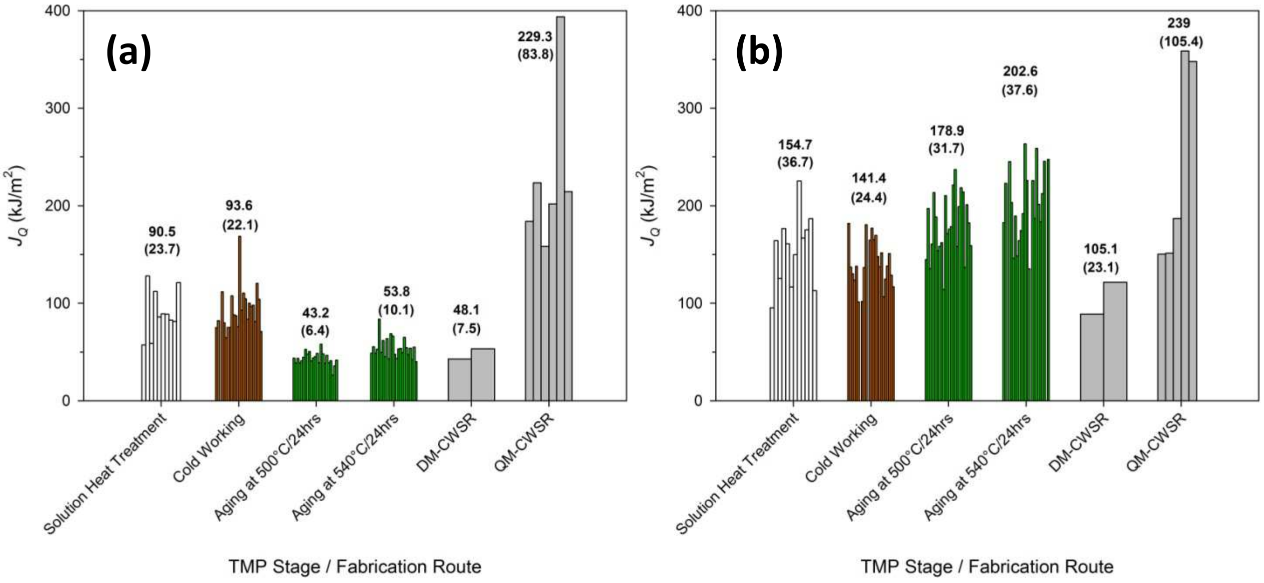

Figure 6.28: Evolution of initiation fracture toughness of Zr-2.5Nb alloy during three TMP stages; SHT, CW and vacuum aging. Toughness of these WQA materials was compared with that of the CWSR pressure tube materials of 220MWe IPHWRs. Plots (a) and (b) respectively show the comparisons at RT and 300°C. In these plots, over each bar group, average toughness value along with corresponding standard deviation (within parentheses) is shown.

II. Propagation toughness ($J_{F(max)}$ and *dJ/da* parameters)

The propagation fracture toughness of aged materials were determined in terms of $J_{F(max)}$ and *dJ/da* parameters. Under ambient condition, aging caused ~ 30% reduction in the $J_{F(max)}$ parameter of various cold worked-solution heat treated Zr-2.5Nb alloy, as shown in Figure 6.29.

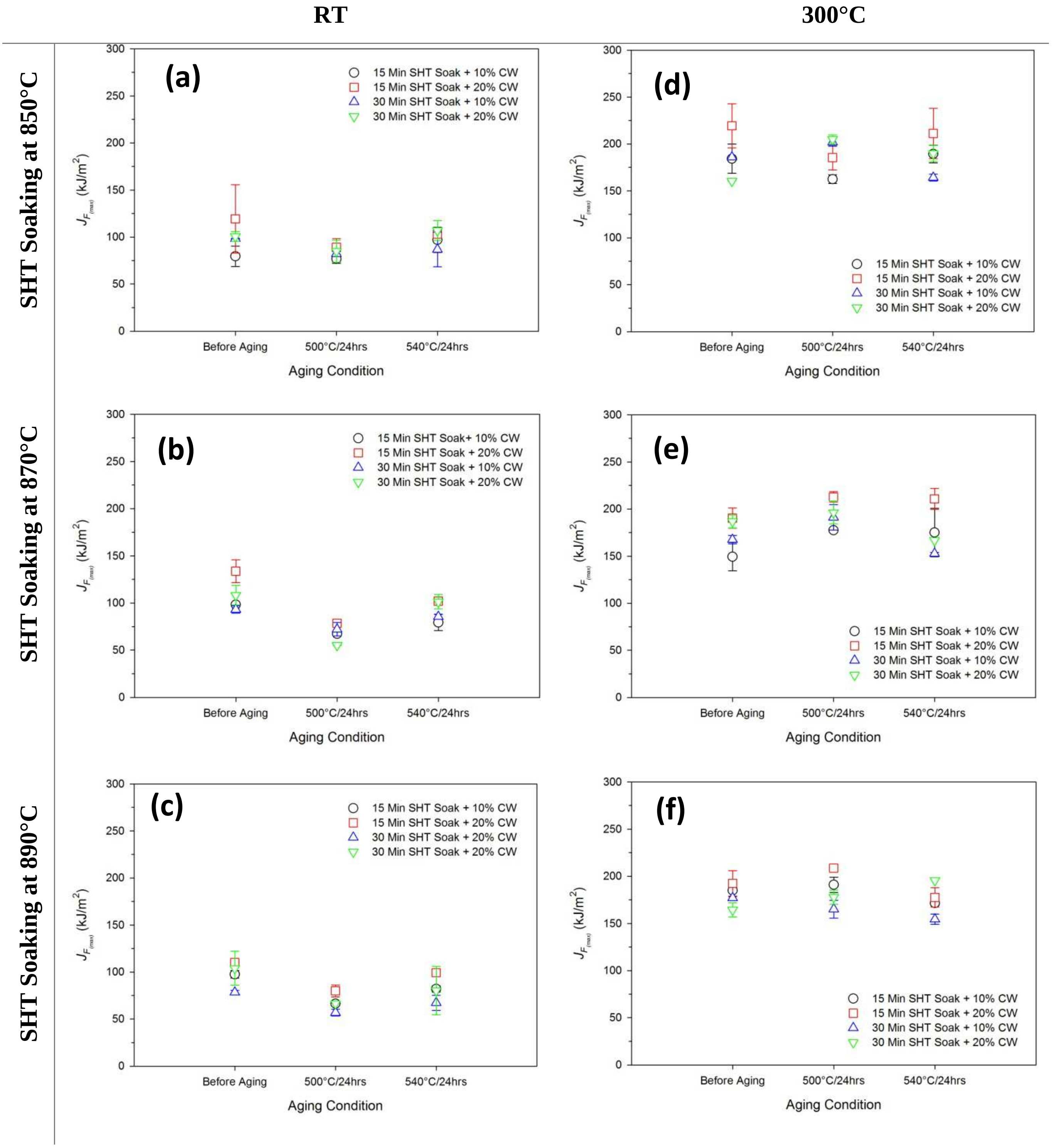

Figure 6.29: Propagation fracture toughness, $J_{F(max)}$ parameters of Zr-2.5Nb alloy under different cold worked-solution heat treated conditions before and after the aging treatments at 500 and 540°C for 24 hrs followed by furnace cooling.

As can be seen from Figure 6.29 that TMP parameters viz., SHT temperature (850-890°C), soaking duration (15-30 Min), degree of cold working (10-20%) and aging temperature (500-540°C) had weak influence on the $J_{F(max)}$ parameters of aged (i.e., WQA) Zr-2.5Nb alloy. Such insensitiveness of $J_{F(max)}$ parameters on TMP parameters could be seen as the consequence of corresponding least dependence of J parameters on TMP parameters at lower crack growth regime (as shown in Figures 6.23-6.26). Increasing test temperature from RT to 300°C resulted in almost twice $J_{F(max)}$, as compared to at RT.

In contrast to $J_{F(max)}$ parameter, the slope of resistance curve (*dJ/da* parameter), was considerably dependent on the TMP parameters; SHT temperature, degree of cold working and aging temperature, as shown in Figure 6.30, especially at 300°C. Increasing test temperature from RT to 300°C resulted in almost to four fold *dJ/da* parameters as compared to at RT.

Similar to initiation toughness, at RT, the $J_{F(max)}$ and *dJ/da* parameters of WQA materials were close to DM-CWSR materials, Figure 6.31 (a) and (c). However, at reactor operating temperature (300°C), these propagation toughness parameters of WQA materials were more or less close to the QM-CWSR materials, Figure 6.31 (b) and (d).

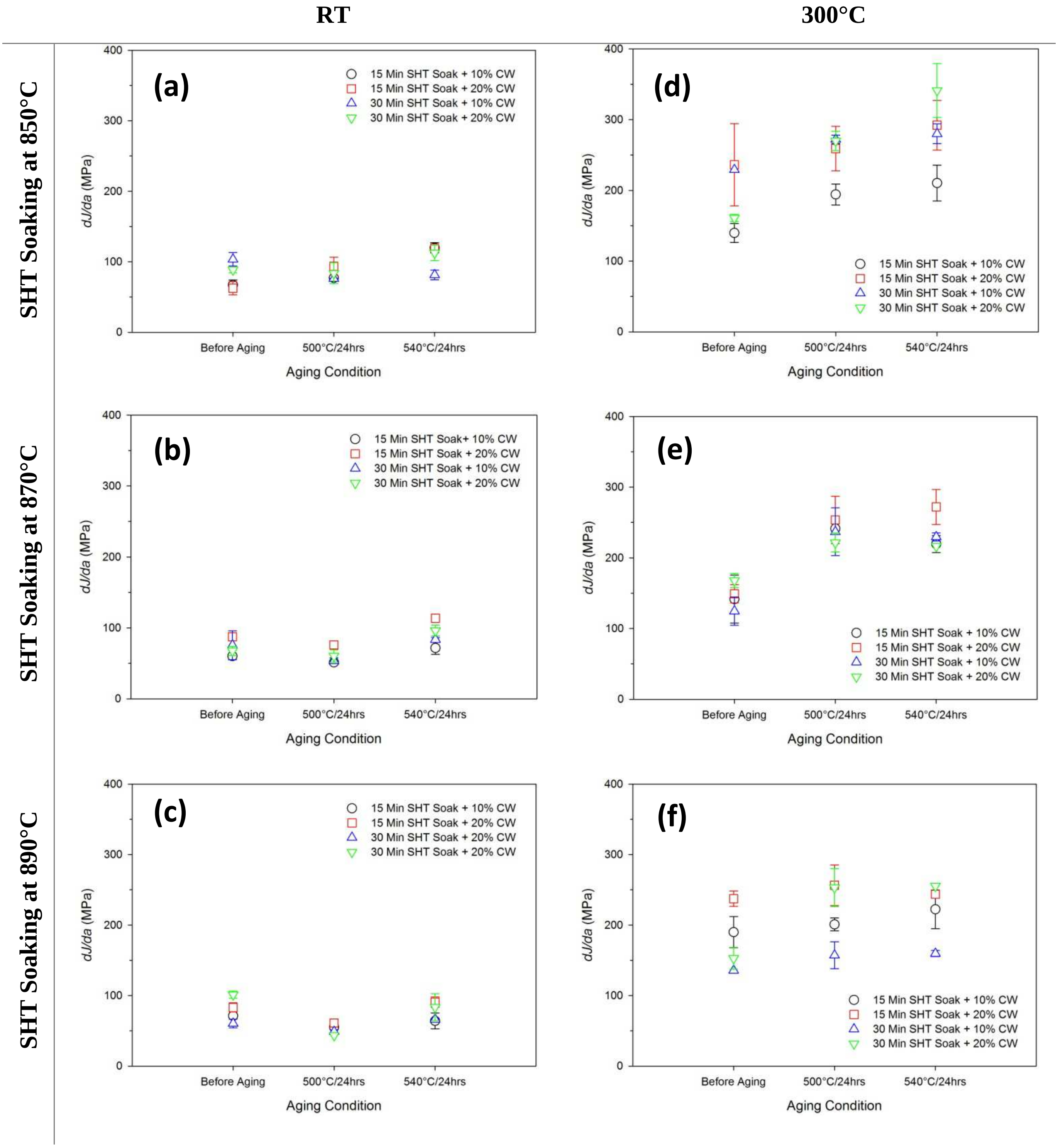

Figure 6.30: Propagation fracture toughness, *dJ/da* parameters of Zr-2.5Nb alloy under different cold worked-solution heat treated conditions before and after the aging treatments at 500 and 540°C for 24 h followed by furnace cooling.

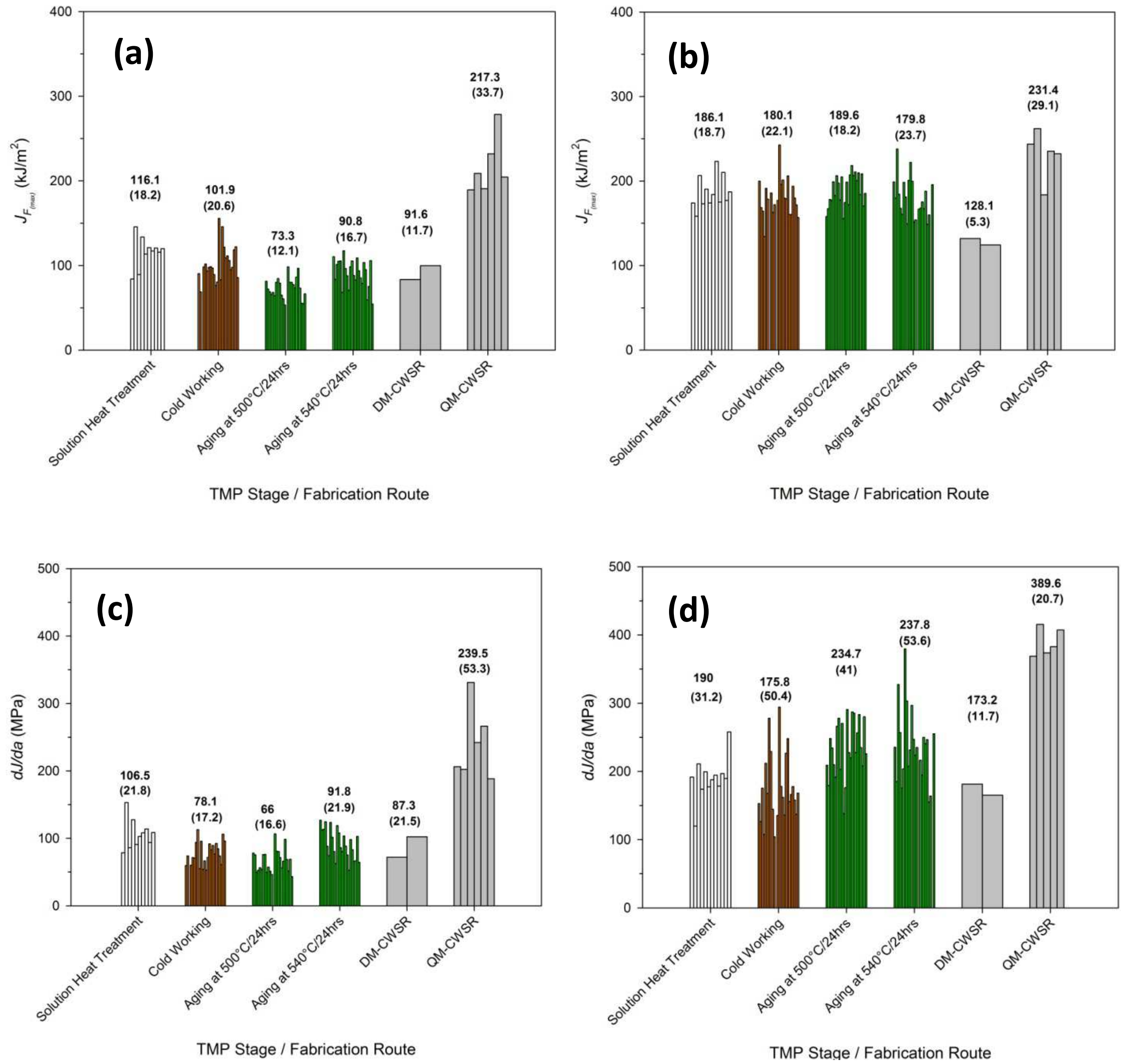

Figure 6.31: Evolution of propagation fracture toughness of Zr-2.5Nb alloy in the three thermo-mechanical processing stages, SHT, CW and vacuum aging. Toughness of these heat treated materials was compared with that of the CWSR pressure tube materials of 220MWe IPHWRs. Plots (a) and (b) respectively show the variation of $J_{F(max)}$ parameters at RT and 300°C and plots (c) and (d) respectively show the variation of *dJ/da* parameters at RT and 300°C . In these plots, over each bar group, average toughness value along with corresponding standard deviation (within parentheses) is shown.

IV. Critical Crack Length (*CCL*)

The critical crack length, *CCL* of WQA Zr-2.5Nb alloy was determined following an 'Iterative method'. Under this method, *CCL* parameter is calculated by determining the crack driving force (CDF) corresponding to a specific application (as defined by Equation 6.1) and equating CDF to the fracture resistance *J* parameter corresponding to maximum load (i.e., $J_{F(max)}$).

$$\text{CDF} = \frac{8a{\sigma_Y}^2}{\pi E} ln\left[sec\left(\frac{\pi M\sigma_h}{2\sigma_Y}\right)\right] \tag{6.1}$$

In Equation (6.1), σ_Y is the flow stress of pressure tube material, taken as the mean of 0.2% offset yield strength and ultimate tensile strength; E represents the elastic modulus; a represents the critical crack length; *M*, the 'Folias factor' is taken as $\sqrt{1+\frac{a^2}{rB}}$ where, *r* and *B* are respectively inner radius and wall thickness of the pressure tube.

The *CCL* of WQA materials were determined, considering its application for the pressure tubes of 220MWe IPHWR. For *CCL* determination, the hoop stress in operating pressure tube was calculated from Equation 6.2, and determined as 122.25 MPa.

$$\sigma_h = \frac{pd}{2B} \tag{6.2}$$

In Equation 6.2, σ_h represents hoop stress, determined based on the internal pressure (*p*) of 10.5 MPa, tube internal diameter (*d*) of 81.5 mm and wall thickness of 3.5 mm. In present calculation, the crack resistance $J_{F(max)}$ parameter derived from 3.17 mm thick specimen was assumed to be same as that derived from 3.5 mm thick specimen. In addition, Zr-2.5Nb alloy under CWSR and WQA conditions were assumed to have same elastic modulus.

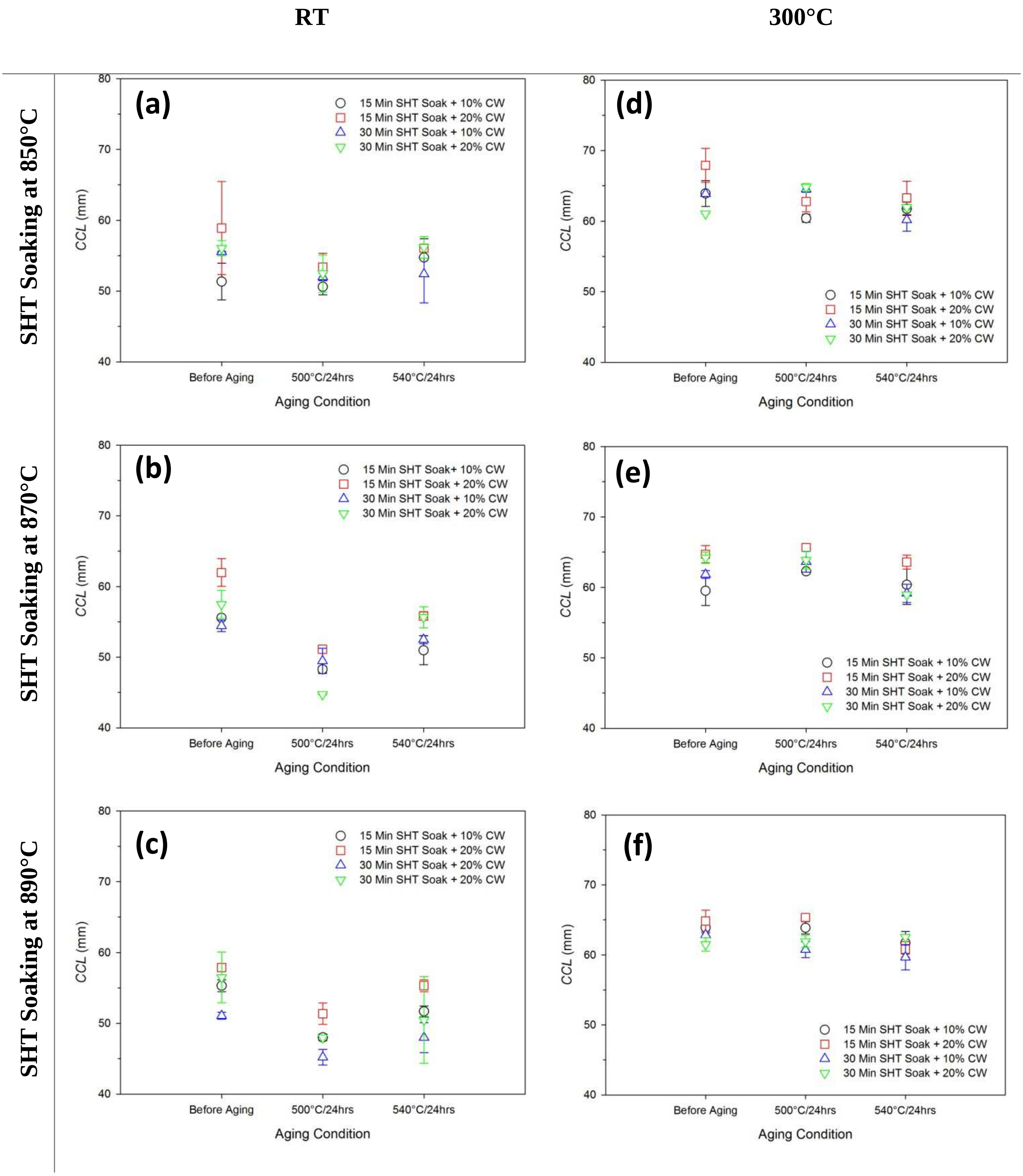

Figure 6.32: *CCL* parameters of Zr-2.5Nb alloy under different cold worked-solution heat treated conditions before and after the aging treatments at 500 and 540°C for 24 h followed by furnace cooling.

Being the function of $J_{F(max)}$ parameter, the trend of *CCL* was analogous to that of $J_{F(max)}$ parameter (Figure 6.32). Under ambient condition, *CCL* of the various cold worked-solution heat treated materials decreased after aging treatment. However, at 300°C, *CCL* of these materials were relatively less sensitive to the aging treatments. Similar to $J_{F(max)}$ parameters, *CCL* parameters of WQA Zr-2.5Nb alloy were weakly affected by the TMP parameters.

A comprehensive discussion on the influence of TMP parameters on fracture behavior of Zr-2.5Nb alloy is presented in 'Discussion' section. This includes suggestion for the optimized TMP parameters to achieve the best fracture behavior of as-fabricated WQA pressure tube material.

Figure 6.33 shows the comparison of *CCL* parameters of Zr-2.5Nb alloy under CWSR and WQA conditions. Under ambient condition, the WQA materials aged at 540°C exhibited nearly comparable *CCL* as that of the CWSR materials manufactured from double melted ingot. Under this condition, *CCLs* of WQA materials were appreciably lower (on an average 28%) than that of the quadruple melted CWSR materials. In contrast, at reactor operating temperature (300°C), WQA materials exhibited *CCL*, close to that of the CWSR materials manufactured from quadruple melted ingot.

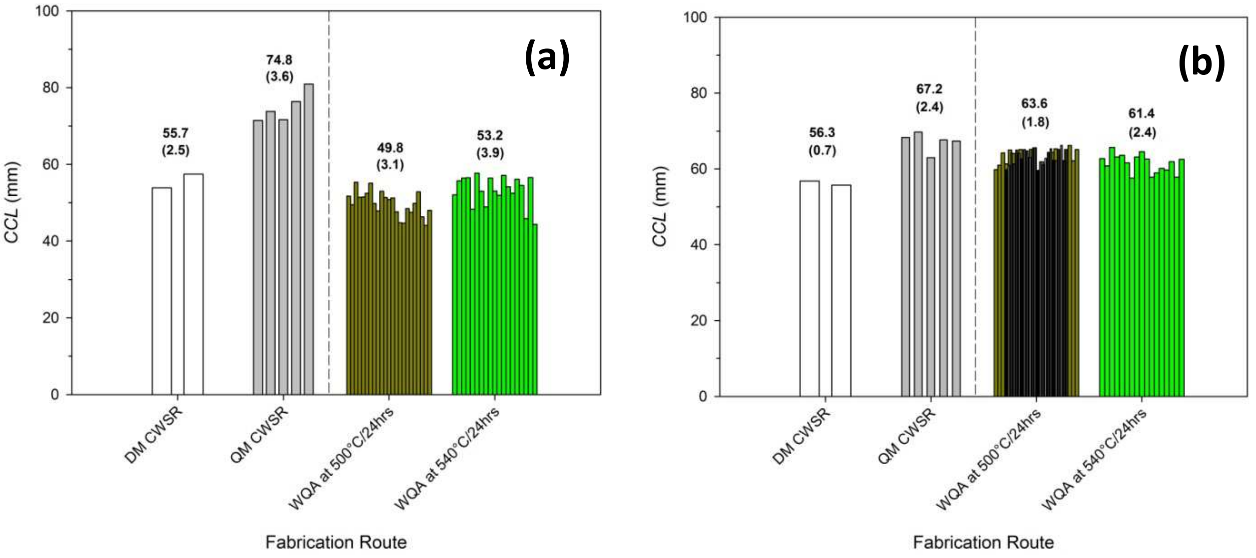

Figure 6.33: Comparison of *CCL* parameters of Zr-2.5Nb alloy under CWSR and WQA conditions at (a) RT and (b) 300°C. In these plots, over each bar group, average *CCL* parameter along with corresponding standard deviation (within parentheses) is shown.

Figure 6.34 shows another *CCL* evaluation approach, under which *CCL* of WQA Zr-2.5Nb alloy was determined using 'Tangent method' (commonly known as 'Graphical method'). Under this method, the *CCL* parameter is calculated by determining the crack driving force (CDF) corresponding to a specific application (as defined by Equation 6.1) and considering the tangential point of CDF and crack resistance curves. Figure 6.35 shows the influence of determination approaches on *CCL* parameters of one of the WQA materials. As can be seen from this figure that the tangent method, as compared to the iterative method provided 20-30% higher *CCL* parameter. Also, the slope of CDF and crack resistance curves increases with increase in temperature, which therefore results in higher *CCL* at 300°C, as compared to at RT.

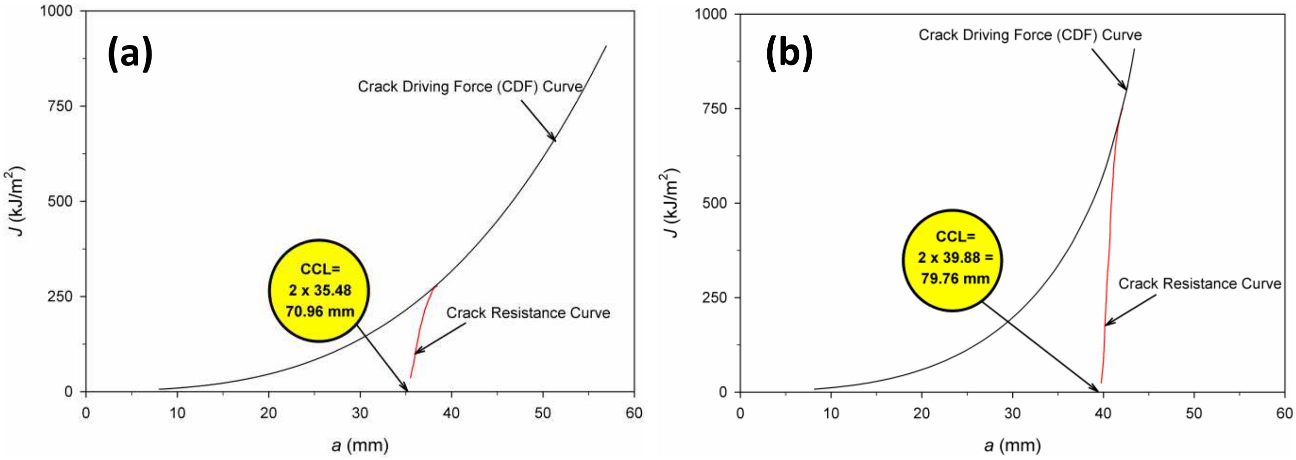

Figure 6.34: Evaluation of *CCL* parameters of Zr-2.5Nb alloy under WQA condition (850°C-15Min-WQ + 20% CW + 540°C) at (a) RT and (b) 300°C through the graphical method.

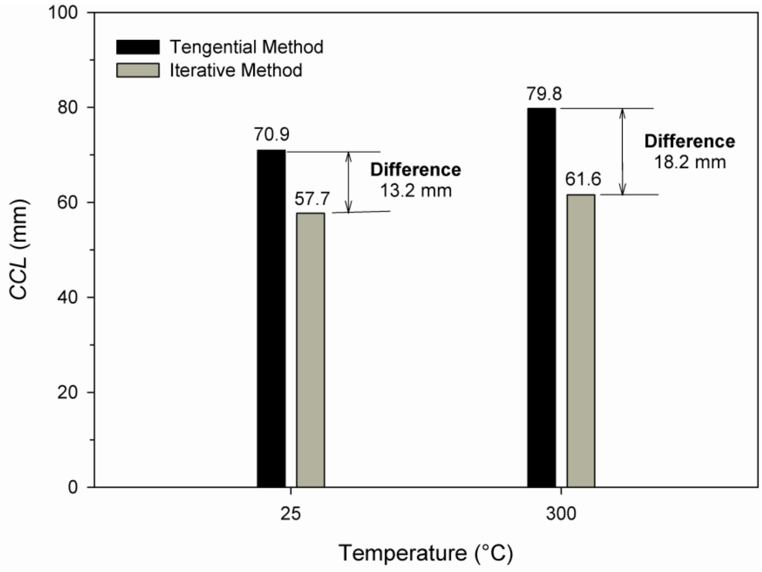

Figure 6.35: Influence of evaluation methodologies on the *CCL* parameters of WQA Zr-2.5Nb alloy.

6.3 Influence of Analysis Procedures on Fracture Toughness Parameters

6.3.1. Resistance Curve and Basic Test Methodologies

I. Fracture Resistance, *J-R* Curve

The fracture resistance, *J-R* curves of Zr-2.5Nb alloy before and after the aging treatment derived from the Resistance Curve (RC) and Basic Test (BT) methodologies have similar differences as have been seen in Chapter 4 for the solution heat treated materials. The RC methodology, as compared to BT showed conservative estimation of fracture resistance curves. For the lower crack growth regime, the *J* parameters derived from these two methodologies have marginal deviation. However, with increasing crack growth such deviation increased (Figure 6.36). Compared to ambient condition, at elevated temperature (300°C), the *J* parameters showed relatively weaker dependence on the methods of evaluation (as can be seen from Figure 6.36 (b)). Therefore, in summary, Zr-2.5Nb alloy under the three TMP conditions; SHT, CW and aged as considered in the present study has practically weak dependence on the RC and BT methodologies.

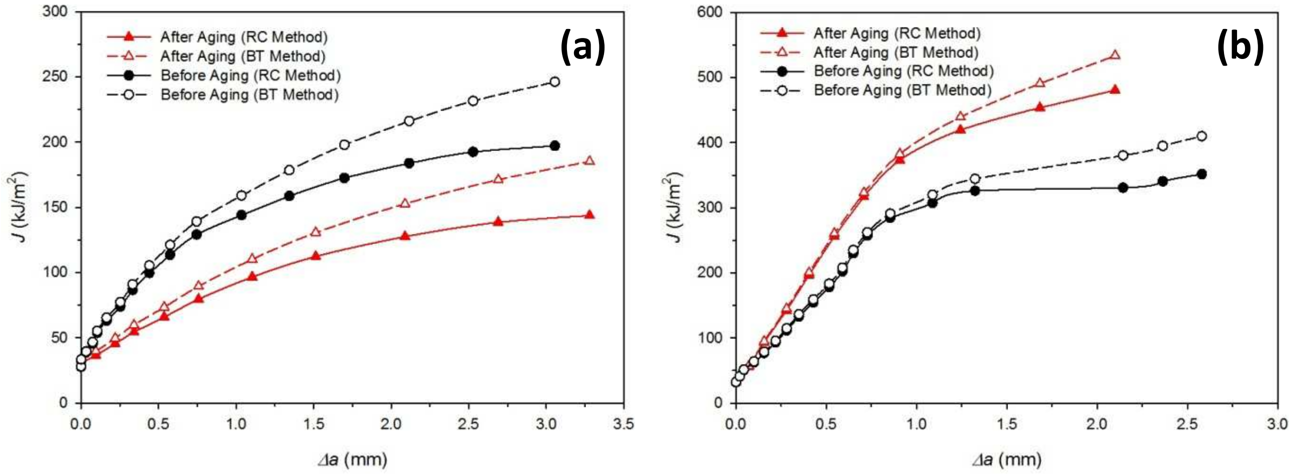

Figure 6.36: Influence of ASTM recommended RC and BT analysis methodologies on the fracture resistance curves before and after the aging treatment at (a) RT and (b) 300°C. The plots show the influence of analysis methodologies on the fracture resistance curves of one of the materials viz., solution heat treated from 850°C/30Min followed by 20%CW and aging at 540°C/24hrs. Similar influences were observed for the rest of materials.

II. Fracture Toughness Parameters

As discussed in Chapter 4 that the RC method in contrast to BT method results in conservative estimation of the fracture toughness. Similar to the solution heat treated materials, subsequently cold worked and aged materials showed insignificant difference in the fracture toughness parameters evaluated from these two methodologies. Figure 6.37 shows the influence of RC and BT methodologies on fracture toughness parameters of Zr-2.5Nb alloy before and after the aging treatment. As can be seen from these plots that TMP condition of Zr-2.5Nb alloy does not influence the difference in fracture toughness parameters. Initiation toughness and $J_{F(max)}$ parameters evaluated from these two methodologies exhibited marginal differences. As has been shown in Chapter 4 that these two toughness parameters are evaluated based on the initial portion of *J-R* curve, which has been shown to exhibit marginal dependence on the two evaluation methodologies. Therefore, such marginal differences in these toughness parameters can be understood as the consequence of the marginal difference in the RC and BT derived initial *J-R* data points at lower crack extension levels.

However, as can be seen from Figure 6.37 (c) that the slope of valid *J-R* region (*dJ/da*) showed slightly higher dependence on the two evaluation methodologies. With increase in crack extension, the deviation in the RC and BT derived *J-R* curves increased (as evident from Figure 6.36). Therefore, because of such increasing deviation, the *dJ/da* parameters showed such slightly higher dependence on the two evaluation methodologies.

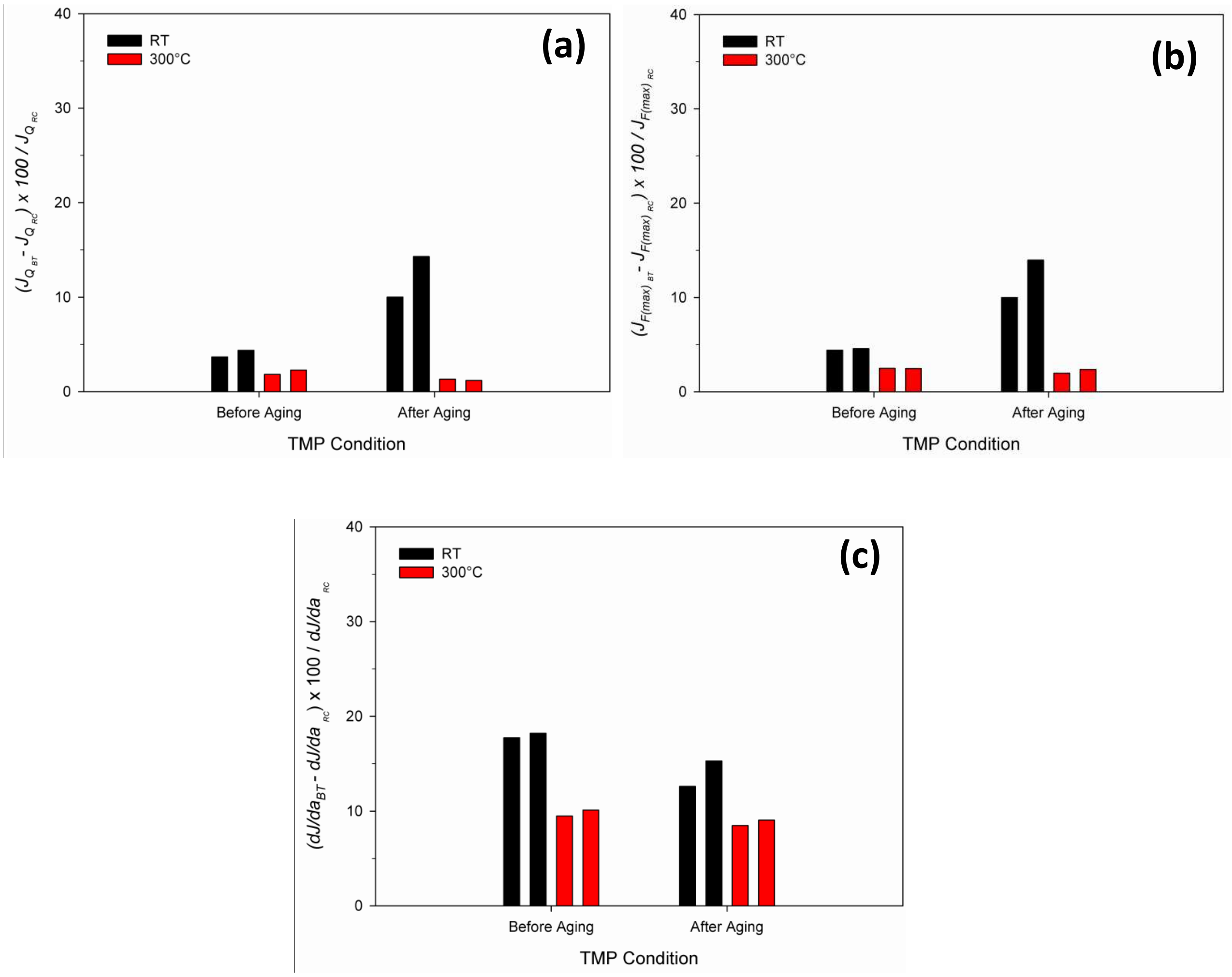

Figure 6.37: Influence of ASTM recommended RC and BT analysis methodologies on the fracture toughness parameters of Zr-2.5Nb alloy before and after the aging treatments. Plots (a), (b) and (c) respectively show the deviation in initiation toughness (J_Q), $J_{F(max)}$ and *dJ/da* parameters of one the of materials; solution heat treated from 850°C/30Min followed by 20%CW and aging at 540°C/24h.

6.3.2. ASTM and ISO Evaluation Approaches

I. Fracture Resistance, *J-R* Curve

Influence of the standard analysis approaches on fracture resistance *J-R* curves of Zr-2.5Nb alloy before and after aging treatment is illustrated in Figure 6.38. As can be seen from this figure and also discussed earlier in Chapter 4 that the ASTM standard in contrast to ISO, conservatively estimates the *J-R* curves. However, similar to solution heat treated condition, under subsequently cold worked and aged conditions, *J-R* curves of this alloy showed marginal dependency of these two standard approaches, especially at higher temperature (Figure 6.38 (b)).

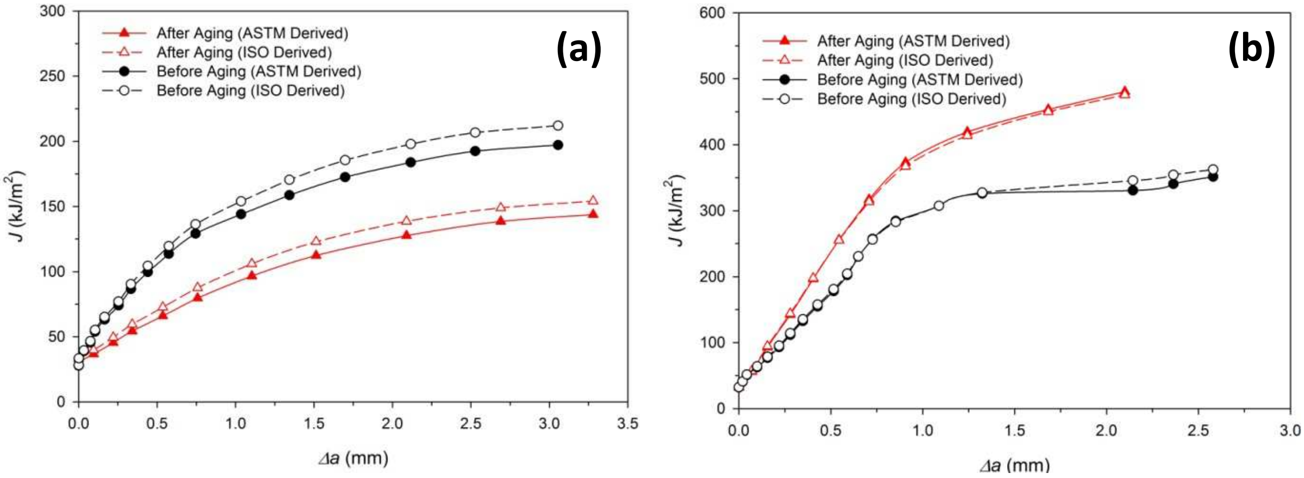

Figure 6.38: Influence of ASTM and ISO analysis approaches on the fracture resistance curves of Zr-2.5Nb alloy before and after the aging treatment at (a) RT and (b) 300°C. The plots show the influence of analysis methodologies on the fracture resistance curves of one of the materials; solution heat treated from 850°C/30Min followed by 20%CW and aging at 540°C/24h. Similar influences were observed for the rest of materials.

II. Fracture Toughness Parameters

i. Initiation Toughness

As discussed in Chapter 4 that the deviation in the initiation toughness parameters derived from ASTM and ISO standard approaches is mainly attributed to the difference in the slope of construction lines recommended by these standards. ISO standard in contrast to ASTM recommended higher slope of construction line, which consequently results in lower initiation toughness. Furthermore, such deviation becomes more prominent when the slope of *J-R* curve increases, which is expected to occur at elevated temperatures. Similar to solution heat treated condition, under cold worked and aged condition, deviation in the initiation toughness parameters derived from the two standards were lower under ambient condition (as shown in Figure 6.39 (a). Such weak dependence can be understood as the consequence of the lower slope of *J-R* curves of these three categories of materials under ambient condition.

In contrast, at elevated temperature (300°C), the slope of *J-R* curves increased substantially (as can be seen from Figure 6.38 (b)), which therefore results in getting appreciable deviations in the ASTM and ISO derived initiation toughness parameters of each of these three categories of materials.

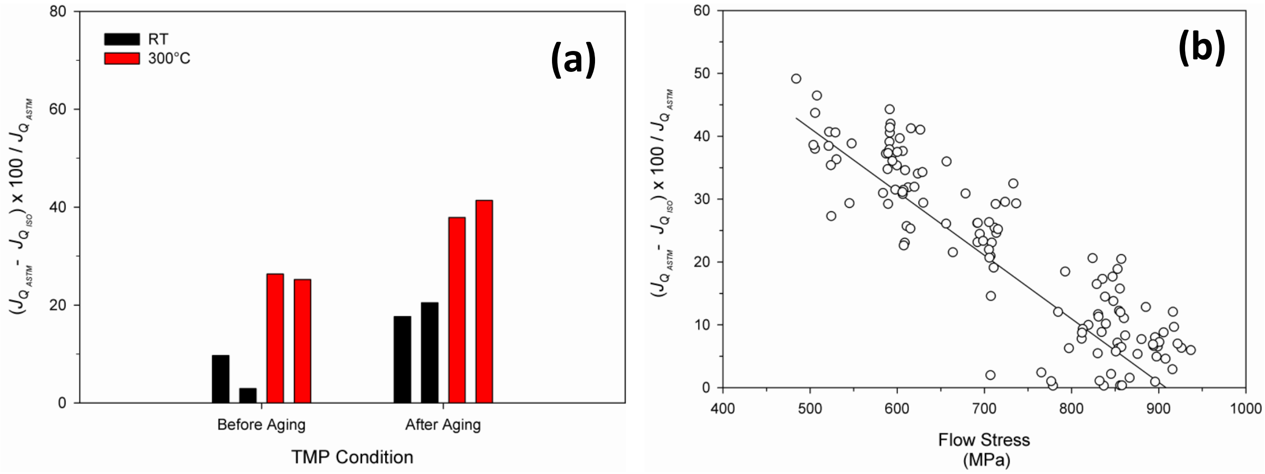

Figure 6.39: (a) Deviation in the ASTM and ISO standard derived initiation toughness parameters of Zr-2.5Nb alloy before and after the aging treatment. (b) Correlation of the deviation in ASTM and ISO derived initiation toughness parameters with material's flow stress.

At 300°C, after aging treatment, such deviation became more prominent as compared to under solution heat treated and cold worked conditions. This can be understood as influences of two phenomenon, which occurred simultaneously; first is the lower strength of aged materials (as illustrated earlier in Figure 6.14) and second is improvement in the fracture toughness leading in higher slope of *J-R* curve after aging treatment. These effects are graphically illustrated in Figure 6.40.

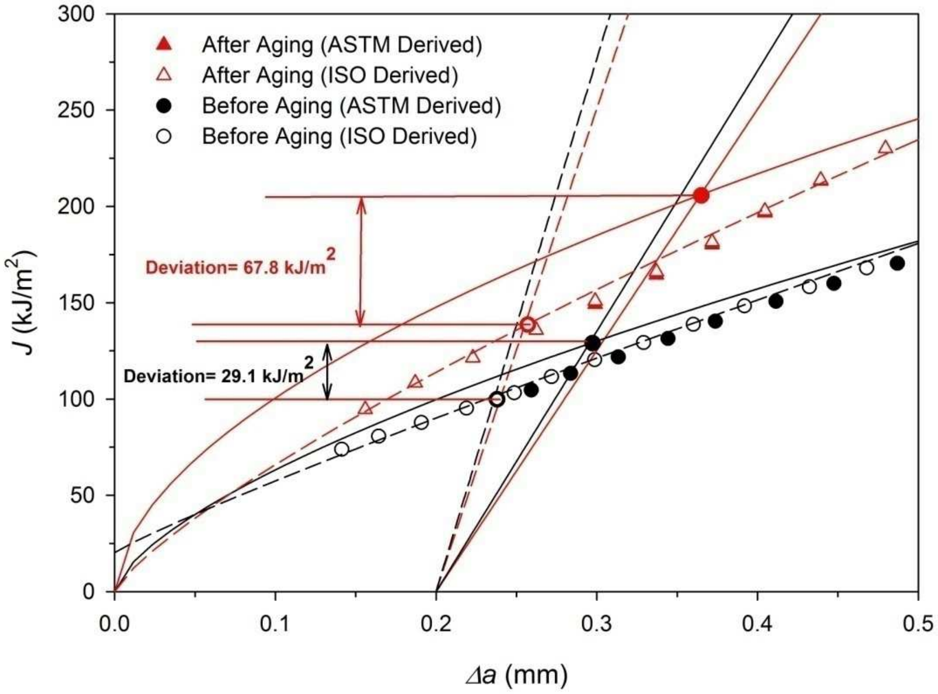

Figure 6.40: Magnified view of a *J-R* curve illustrating the prominence of deviation in ASTM and ISO derived initiation toughness parameter of aged Zr-2.5Nb alloy.

Figure 6.39 (b) shows the dependency of the deviation in initiation toughness parameters derived from ASTM and ISO standard on the flow stress. In this plot, the deviations in initiation toughness of Zr-2.5Nb alloy under all the three TMP conditions under both ambient condition and 300°C are plotted altogether as a function of the respective flow stress. The variation showed that such deviation decreases with increase in flow stress. For the materials having flow stress within 500-700 MPa range, initiation toughness parameter showed strong dependency on the two standard approaches. However, materials having flow stress beyond this range (specifically from 800-935MPa), this parameter is practically insensitive to the two standard approaches.

ii. $J_{F(max)}$ Parameter

The $J_{F(max)}$ parameters of aged materials, similar to solution heat treated and subsequently cold worked materials had weak dependence on the ASTM and ISO standard approaches, as corresponding deviations were < 20%, Figure 6.41 (a). This dependence was especially marginal under elevated temperature. Such lower deviations in the $J_{F(max)}$ parameters can be understood as the consequence of the marginal deviation in the *J-R* curves derived from the two standards (as shown in Figure 6.38). Figure 6.41 (b) shows the dependency of deviation in $J_{F(max)}$ parameters on the flow stress of Zr-2.5Nb alloy. Though, the $J_{F(max)}$ parameters derived from these two standard approaches are rarely different, the dependency suggests that the deviation in this parameter marginally increases with the material's flow stress. Therefore, this also implies that the critical crack length, which imposes the limit to stable crack propagation is weakly dependent to the ASTM and ISO evaluation approaches, as shown in Figure 6.41 (c).

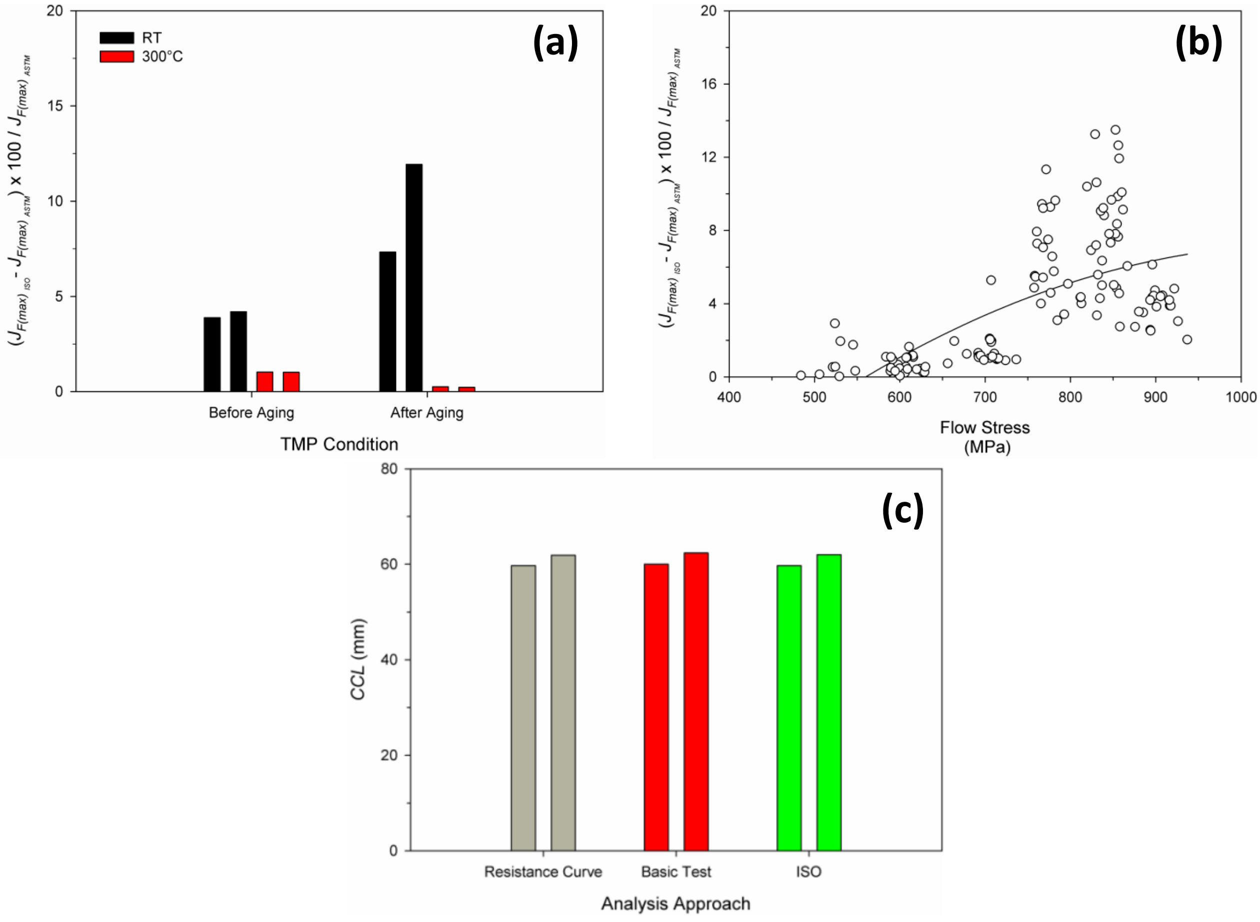

Figure 6.41: (a) Deviation in ASTM and ISO standard derived propagation toughness parameters ($J_{F(max)}$) of Zr-2.5Nb alloy before and after the aging treatment. (b) Correlation of the deviation in ASTM and ISO derived $J_{F(max)}$ parameters with material's flow stress, (c) Plot showing independence of *CCL* parameter on different analysis approaches.

iii. *dJ/da* Parameter

As compared to the initiation toughness and $J_{F(max)}$ parameters, the slope of valid *J-R* region, bounded by the exclusion lines (*dJ/da*) was strongly dependent on the ASTM and ISO standard approaches (see Figure 6.42 (a)). The deviations in ASTM and ISO derived *dJ/da* parameters, though exhibited considerable scatter, had weak dependence on the flow stress, Figure 6.42 (b).

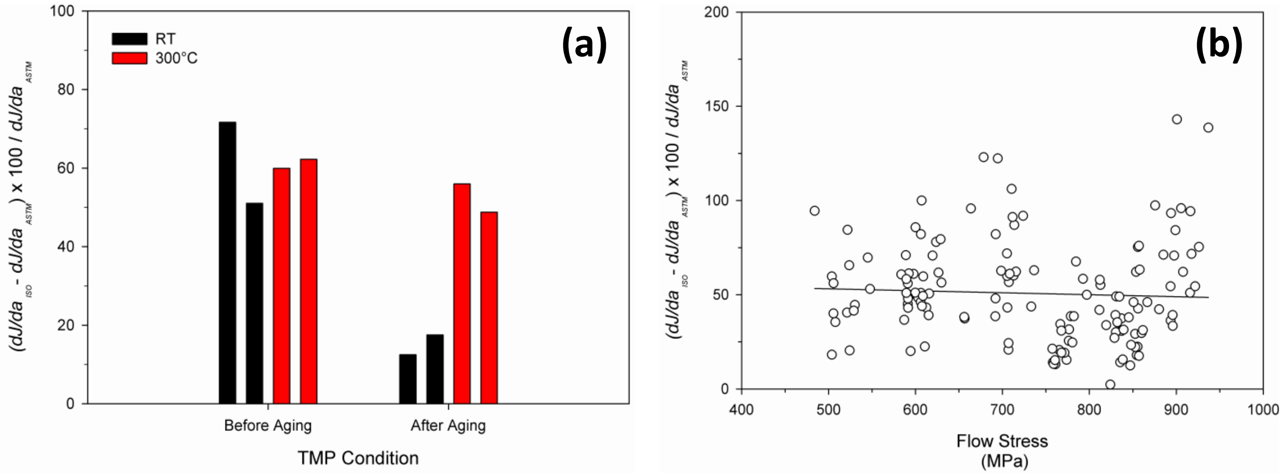

Figure 6.42: (a) Deviation in the ASTM and ISO standard derived propagation toughness parameters (*dJ/da*) of Zr-2.5Nb alloy before and after the aging treatment. (b) Correlation of the deviation in ASTM and ISO derived *dJ/da* parameters with material's flow stress.

6.4 Study of Fracture Surface

Figure 6.43 shows the evolution of fracture surface features of the broken C(T) specimens before and after aging treatments. Similar to cold worked condition, fracture surfaces of the aged materials comprised the inclined regions accompanied by an intermediate flat region. However, after aging treatment, proportion of such flat fractured region increased substantially.

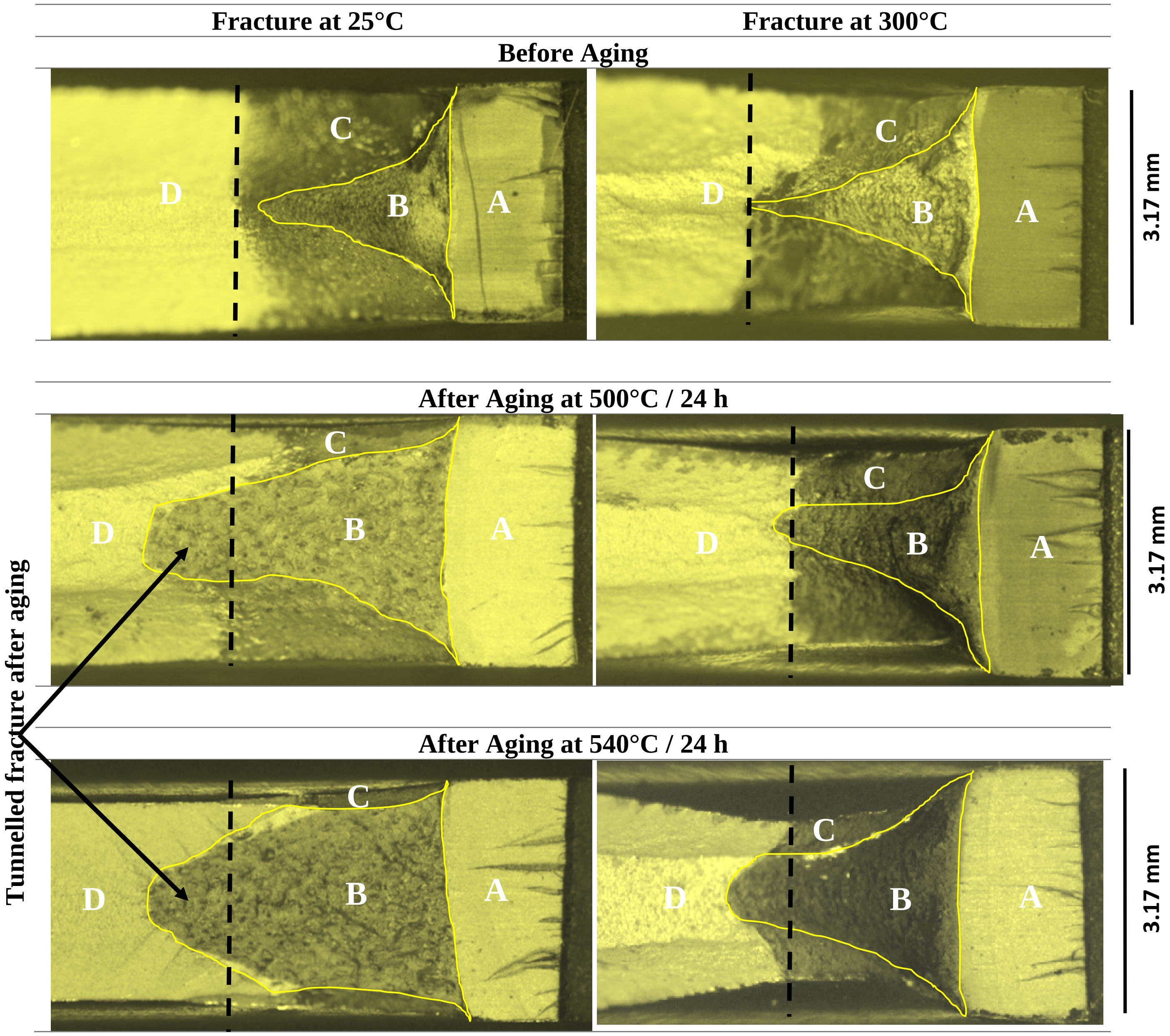

Figure 6.43: Evolution of fracture surfaces of the broken C(T) specimen in one of aged materials before and after the aging treatments. Fracture surface exhibits four remarkable regions: Pre-cracked region (A), Flat fracture region (B), Inclined fractured region (C) and Post cracked region (D). In these figures, regions enclosed by yellow lines show the flat fractured regions. Dashed lines in individual figures distinguish the 'Tunnelled' and 'non-tunnelled' fracture regions.

In addition, after aging, fracture surfaces of cold worked materials exhibited typical ‘tunnelling’ like feature, which is characterized by the higher crack growth at specimen's mid-section as compared to the side regions. With increase in aging temperature from 500 to 540°C, the fracture surfaces showed more dominant tunnelling characteristics.

Fracture surface areas of the broken C(T) specimens under different aging conditions were measured using 'Image-J' software. Figure 6.44 shows the comparison of proportionate flat surface areas of different aged materials. In contrast to the fracture surfaces of cold worked materials, where ~ 25% region was occupied by the flat surface, some of the aged materials exhibited as much as 90% flat region. With increase in aging temperature from 500 to 540°C, the flat region increased further.

Variables of SHT stage such as soaking temperature and soaking duration played an important role in controlling the central/mid section flat regions of aged materials. Materials, previously soaked at higher SHT temperature exhibited comparatively less flat region after aging treatment. In contrast, materials, previously soaked for 30 min duration during solution heat treatment stage showed sharp increase in the flat region after aging treatment and moreover with increase in aging temperature from 500 to 540°C. However, materials, which were previously soaked for 15 min duration during solution heat treatment stage exhibited relatively weaker change in the proportionate flat region after aging treatment as well as with increase in the aging temperature. Degree of prior cold working also played an important role in governing the flat fracture region of aged materials. Materials previously cold worked with a higher degree showed superior flat fracture after aging treatments, especially under ambient test condition.

Materials tested at 300°C, in contrast to RT showed relatively less change in the central flat fractured region after aging treatment. Additionally, at 300°C, flat fracture regions had weaker dependency on the aging temperatures.

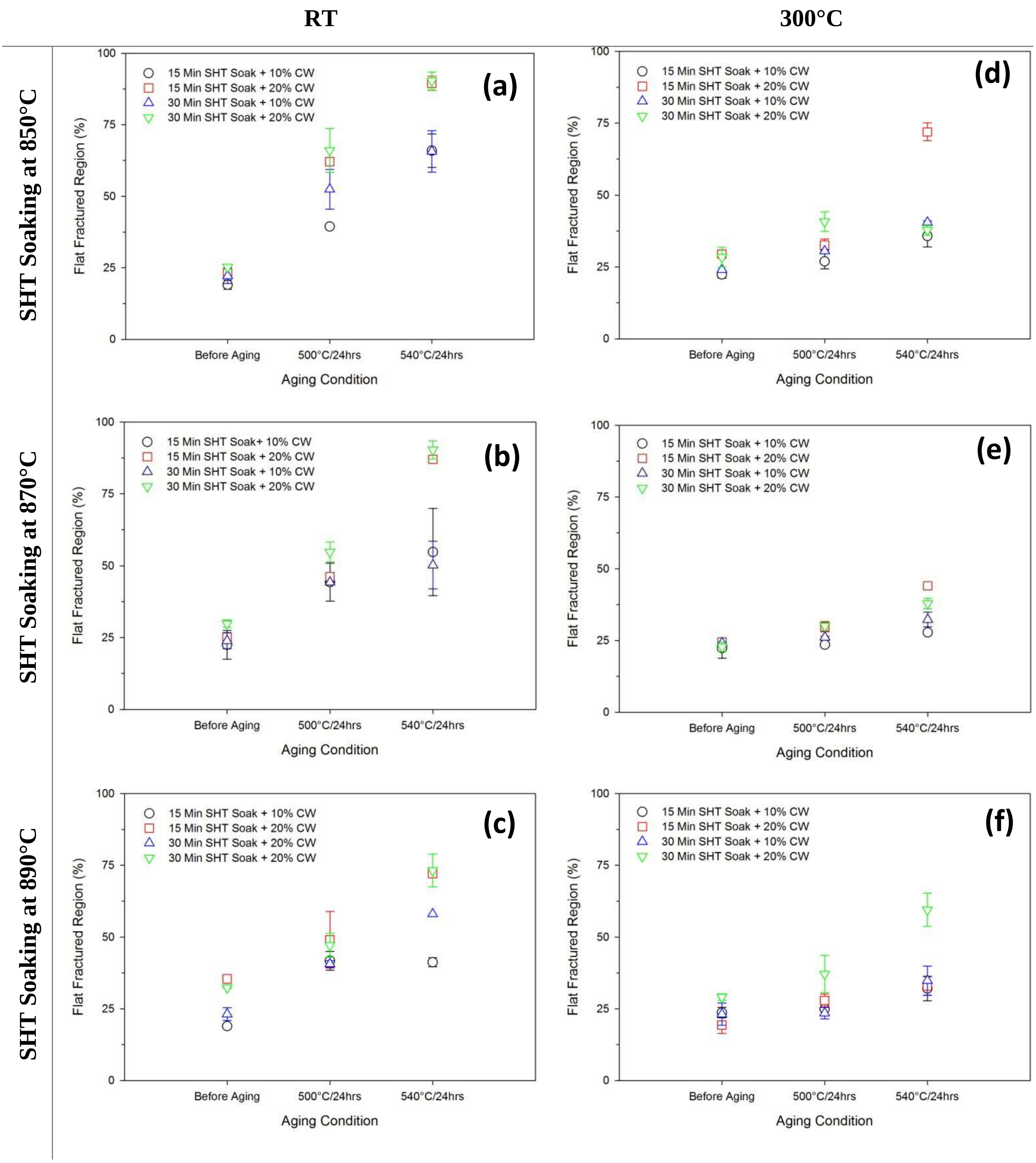

Figure 6.44: Proportionate flat fractured surface areas in the broken C(T) specimens of Zr-2.5Nb alloy under different cold worked-solution heat treated conditions before and after the aging treatments at 500 and 540°C for 24 h followed by furnace cooling.

6.4.1 SEM Fractography

I. Pre-cracked Surface

Fatigue pre-cracked surfaces of aged material, similar to solution heat treated and subsequently cold worked materials exhibited typical plateaus like features, over which the fatigue crack propagated. These plateaus, in general were oriented along the crack propagation direction. Figure 6.45 shows the evolution of the pre-cracked surface features before and after the aging treatments. After aging, relatively shallow plateaus were observed. Additionally, aging carried out at 540°C, in contrast to 500°C resulted in the formation of relatively shallower plateaus.

II. Fracture Surface

The fracture surface of aged materials, similar to solution heat treated and subsequently cold worked materials exhibited typical dimple structure characteristic of a ductile failure (Figures 6.46). However, the aging treatment resulted in the formation of relatively finer dimples as compared to the cold worked materials. The materials aged at 540°C, in contrast to 500°C for 24 h duration exhibited relatively coarser dimples, though the dimples under both of these aging conditions were smaller than that of the cold worked materials. In terms of morphology, most of the dimples formed under ambient condition had slightly oval shape, completely surrounded by the lip. In contrast, the dimples formed at 300°C, in general were coarser and deeper, having oval shape which was not completely surrounded by the lip. The major axes of these oval dimples indicate the crack propagation direction on the inclined fracture surface.

The flat fracture surface of aged specimens, as shown in Figure 6.47 comprised several parallel splits across the specimen thickness. The major axes of these cracks were orientated along the specimen’s fracture direction (i.e., along the specimen width). Similar axial splitting features have also been observed on the fracture surfaces of CWSR Zr-2.5Nb alloys fabricated from DM ingot, used for the earlier pressure tubes of IPHWRs. In the DM-CWSR materials, these splits are because of the impurities like, chlorine, phosphorous and carbon and their complexes, which form low energy facets, that open up under triaxial state of stress prevailing ahead of crack tip [44-45]. Furthermore, the DM-CWSR materials, as compared to QM-CWSR materials contain higher hydrogen concentration, because of which the hydride plates also help in joining these axial splits, as a result the axial split length increases with increase in hydrogen content [39,40]. During subsequent application of load, ligament between any two of such splits undergoes severe localized plastic deformation, as compared to the rest of matrix region, which correspondingly results in the early failure of the ligament region and therefore responsible for the inferior fracture toughness of these materials. Such interaction of the two parallel cracks present in the matrix during the application of load, resulting in the localized deformation of the ligament, has already been numerically verified in the literature [116]. In contrast to the DM-CWSR material, because of having lower impurity concentration, the fracture surface of QM-CWSR material does not show such low energy facet originated cracks, thereby accounting for the higher fracture toughness of the QM material as compared to the DM material. The hydrogen concentration examinations of current aged materials showed the higher concentration (avg. 17.5 wt. ppm), as compared to the SHT (4.7 wt. ppm) and CW (8 wt. ppm) materials. This, therefore emphasizes for the formation of hydride in the aged material, and hence, aiding the axial splitting.

III. Stretched Zone ahead of Pre-cracked Region

Stretched zones ahead of the pre-cracked region in WQA materials, showed good agreement with the observed influence of aging treatments on initiation toughness. Figure 6.48 shows the stretched zones formed in C(T) specimens before and after the aging treatments. As illustrated earlier in Figure 6.27 that aging treatment resulted in reducing the initiation toughness of cold worked-solution heat treated Zr-2.5Nb alloy under ambient condition. The WQA materials showed formation of very small stretched zone ahead of pre-cracked region (size: 12-16 µm). Such substantial reduction in SZW because of aging treatment also highlights the role of corresponding considerable reduction in strain hardening exponents on reducing the initiation toughness. However, at 300°C fracture condition, SZWs of cold worked Zr-2.5Nb alloy increased after aging treatments and also with increase in aging temperatures from 500 to 540°C. This therefore, indicates corresponding increase in initiation toughness of WQA Zr-2.5Nb alloy.

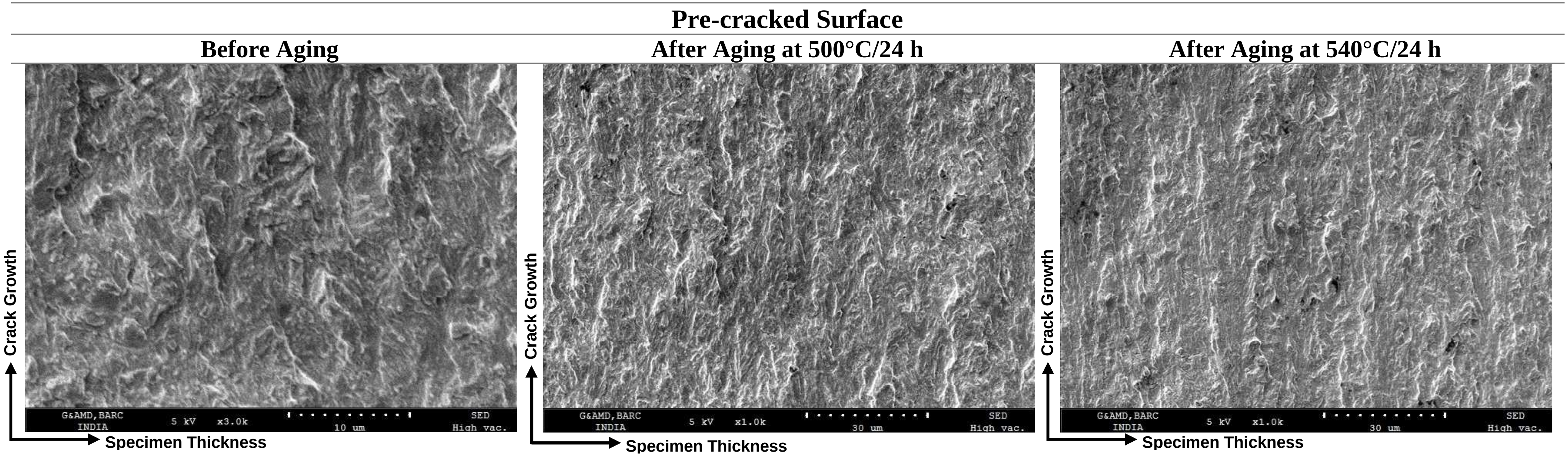
Pre-cracked Surface

Before Aging

After Aging at 500°C/24 h

After Aging at 540°C/24 h

Figure 6.45: SEM fractographic features of the fatigue pre-cracked region of broken C(T) specimens before and after the aging treatments at 500 and 540°C for 24 h. These materials were previously solution heat treated from 850°C/15Min followed by a 20% cold work.

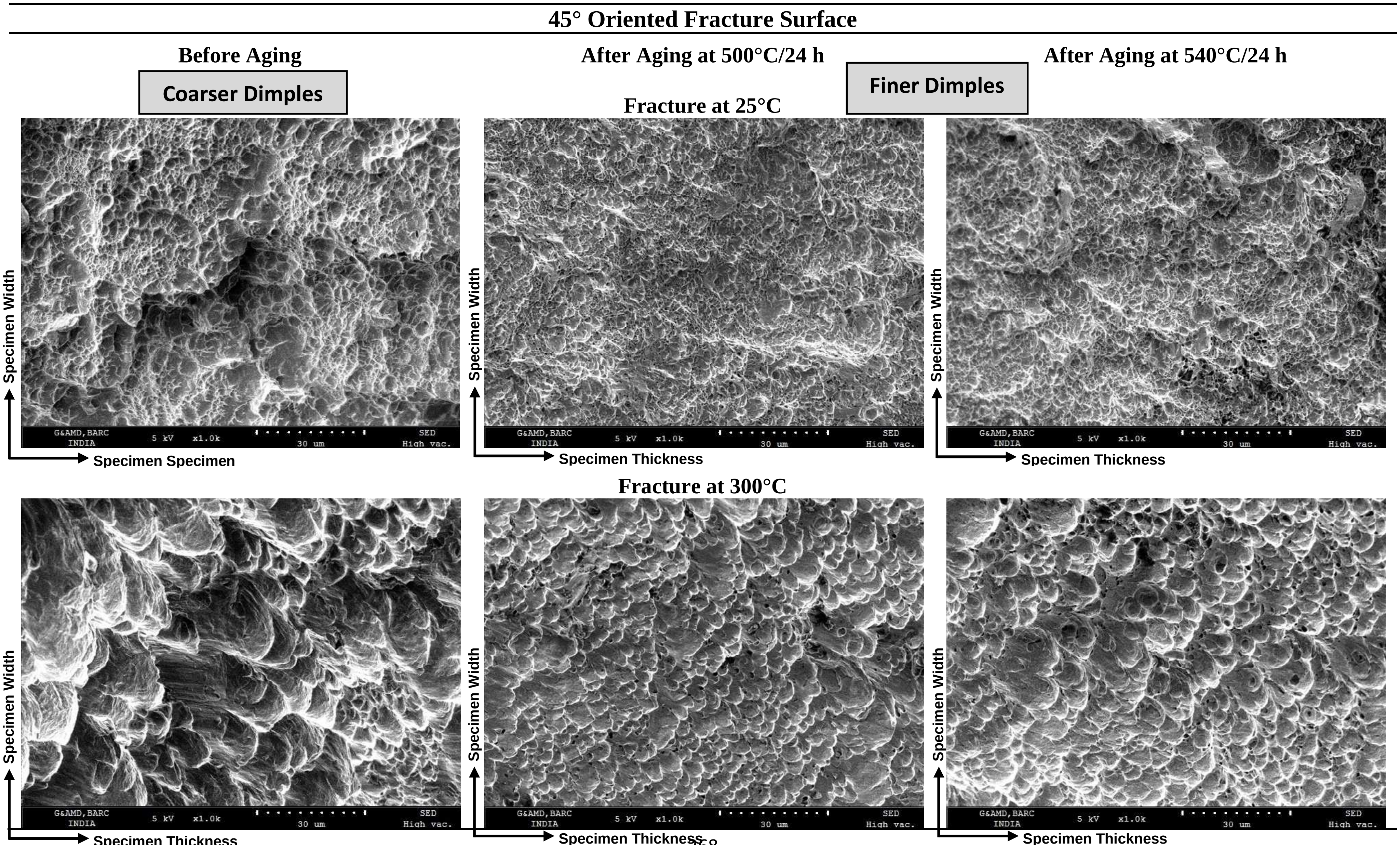

Figure 6.46: SEM fractographic features of the inclined fractured regions of broken C(T) specimens before and after the aging treatments at 500 and 540°C for 24 h. These materials were previously solution heat treated from 850°C/15Min followed by 20% cold work.

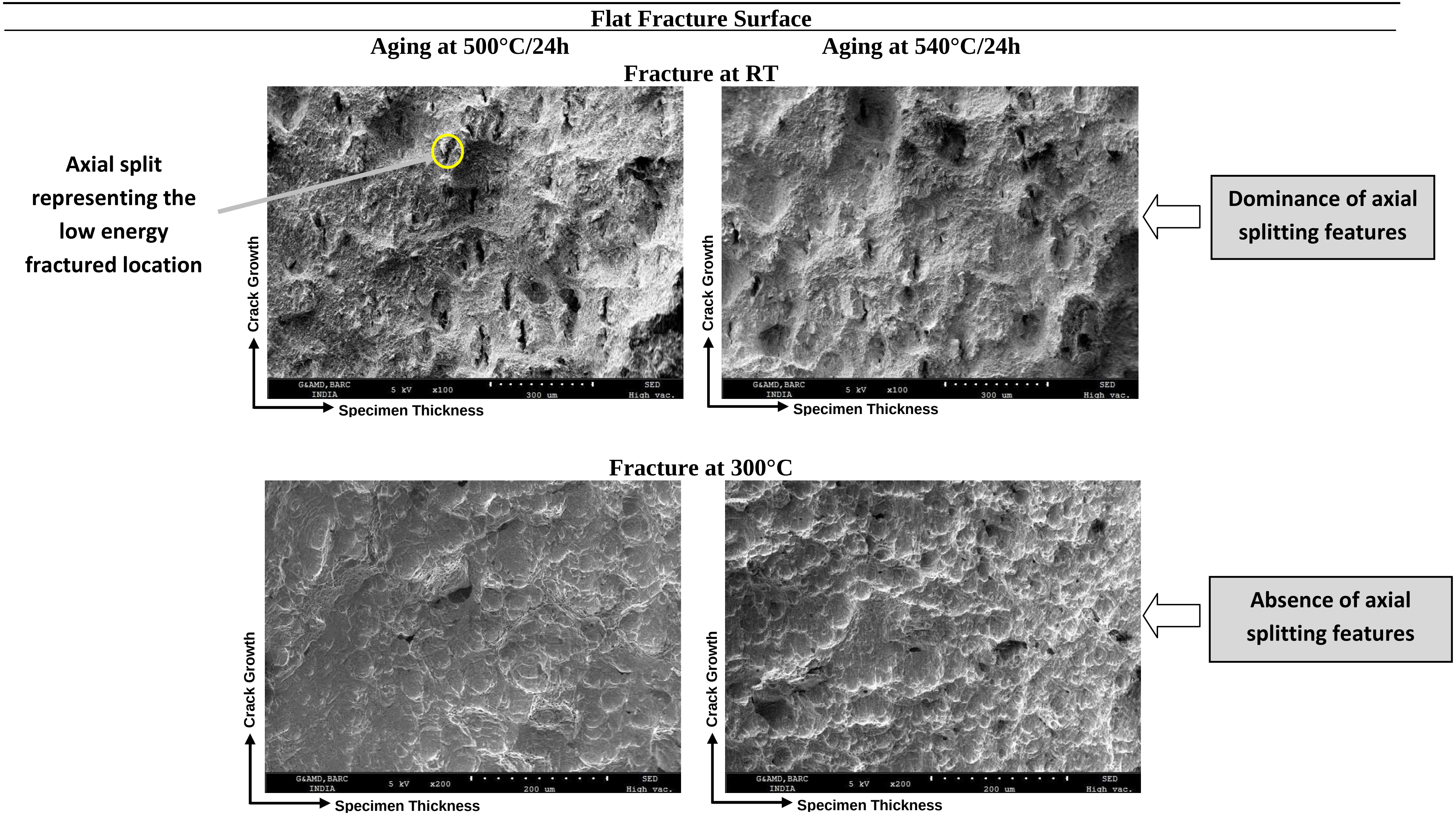

Figure 6.47: SEM fractographic features of the flat fractured regions under low magnification, illustrating presence of typical axial splitting features under ambient fracture, and absence at 300°C. These materials were previously solution heat treated from 850°C/15Min followed by 20% cold work.

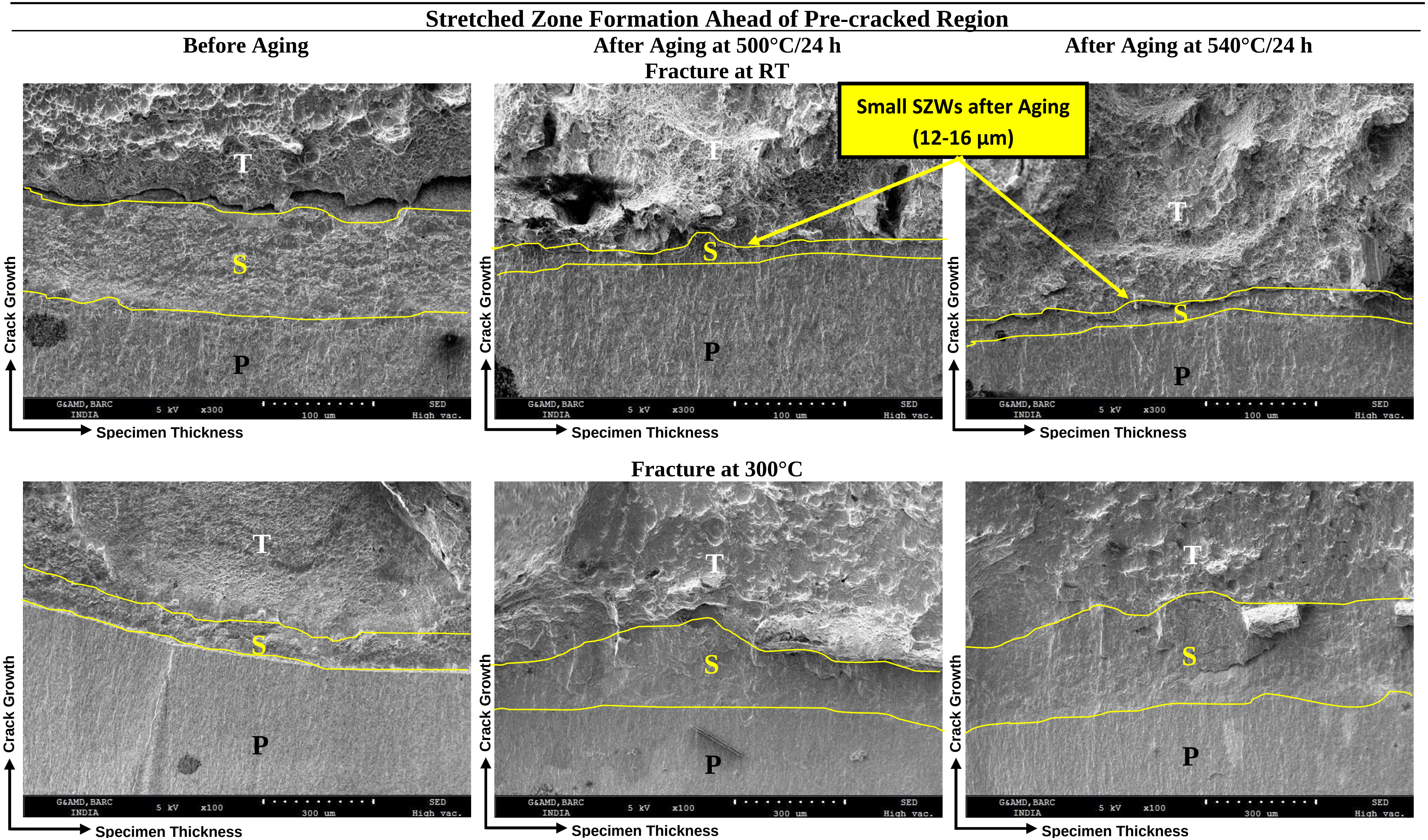

Stretched Zone Formation Ahead of Pre-cracked Region

Before Aging

After Aging at 500°C/24 h

After Aging at 540°C/24 h

Fracture at RT

Fracture at 300°C

Small SZWs after Aging (12-16 μm)

Figure 6.48: Stretched zone formation ahead of the pre-cracked regions in broken C(T) specimens before and after the aging treatments at 500 and 540°C for 24 h. In individual figures, the stretched zone (S) is bounded by yellow lines, which separate pre-cracked (P) region from tearing (T) region. These materials were previously solution heat treated from 850°C/15Min followed by 20% cold work.

The width of stretched zone ahead of pre-cracked region could be an indirect measure of initiation toughness. Considering this, in the present study, an attempt was made to correlate the SZW with initiation toughness of WQA Zr-2.5Nb alloy. For this, initiation toughness based on SZW (i.e., $J_{i\ (SZW)}$) was determined considering the intersecting point of power law fit *J*-*R* curve (after excluding data points lower than SZW) and a line parallel to *J* axis having an offset of SZW. Figure 6.49 illustrates correlation of SZW with $J_{i\ (SZW)}$ parameter for one of WQA Zr-2.5Nb alloy and its comparison with the standard initiation toughness parameter (J_Q). As can be seen from this figure that $J_{i\ (SZW)}$ parameter is considerably lower than J_Q parameter, derived from the standard 0.2 mm offset BL approach. One of the important suggestions from this correlation could be that higher SZW results in relatively lower proportionate difference in the two aforementioned initiation toughness parameters.

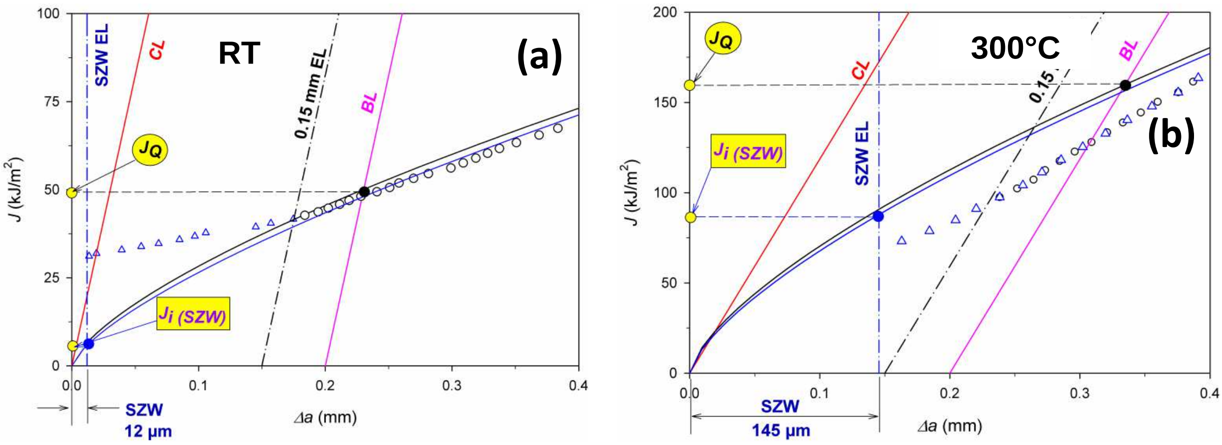

Figure 6.49: Correlation of SZW with initiation toughness ($J_{i\ (SZW)}$) and its comparison with the standard initiation toughness parameter (J_Q) for one of WQA materials at (a) RT and (b) 300°C.

6.5 Discussion

Structural integrity of pressure tube material is one of the important concerns for reactor's safety, and in turn, essentially a function of its fabrication route and associated TMP parameters. Present study is focused to assess the influence of TMP parameters of WQA fabrication route on the fracture behavior of Zr-2.5Nb alloy, so as to suggest a set of TMP parameter, which imparts the best fracture toughness.

This study suggests that variation of SHT temperature within 850-890°C domain, has marginal influence on the *CCL* parameters of WQA Zr-2.5Nb alloy. WQA materials previously soaked in this SHT temperature domain showed practically similar *CCL* parameters (Figure 6.50 (b) & (d) and Figure 6.51 (b) & (d)). This therefore emphasizes that the safety margin of WQA Zr-2.5Nb alloy pressure tubes against typical LBB situations is independent of prior selected SHT temperatures in the aforementioned window. However, SHT performed at relatively lower temperature ensured better propagation resistance of WQA Zr-2.5Nb alloy, by exhibiting higher fracture resistance slope (*dJ/da*), Figure 6.50 and 6.51. As discussed earlier that $J_{F(max)}$ parameter, which governs the *CCL* parameter, represents the low crack growth regime of *J-R* curve. In such small crack growth regime, *J* parameter had least dependence on SHT temperature (as can be seen from Figures 6.50 and 6.51). Therefore, insensitiveness of *CCL* parameters of WQA Zr-2.5Nb alloy on prior selected SHT temperatures can be understood as the consequence of weak SHT temperature dependence of *J* parameters in small crack growth regime. Selection of SHT soaking duration within 15-30 min domain has practically similar influence on fracture behavior of WQA Zr-2.5Nb alloy.

Therefore, as far as the safety margins of WQA pressure tubes against necessary LBB situations are concerned, even if SHT temperature would vary within 850-890°C domain during industrial processing, it will not affect the structural integrity of pressure tubes.

Nevertheless, selection of a lower SHT temperature could be desirable for ensuring better resistance for stable crack propagation.

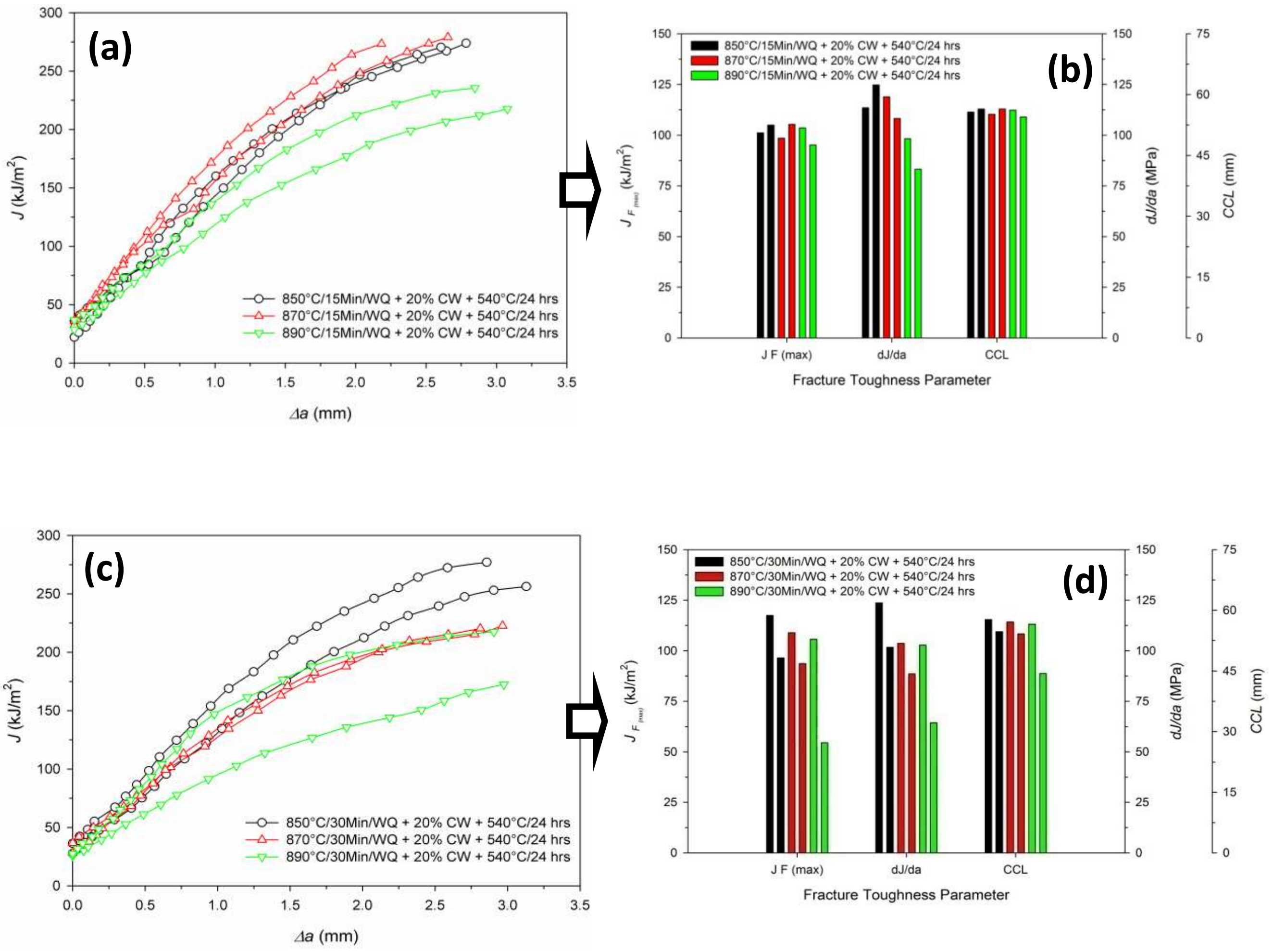

Figure 6.50: Influence of SHT parameters; soaking temperature and duration on fracture behavior of WQA Zr-2.5Nb alloy under ambient temperature. Plots (a) & (b) and (c) & (d) respectively illustrate the influences of materials, previously soaked for 15 and 30 min durations during SHT.

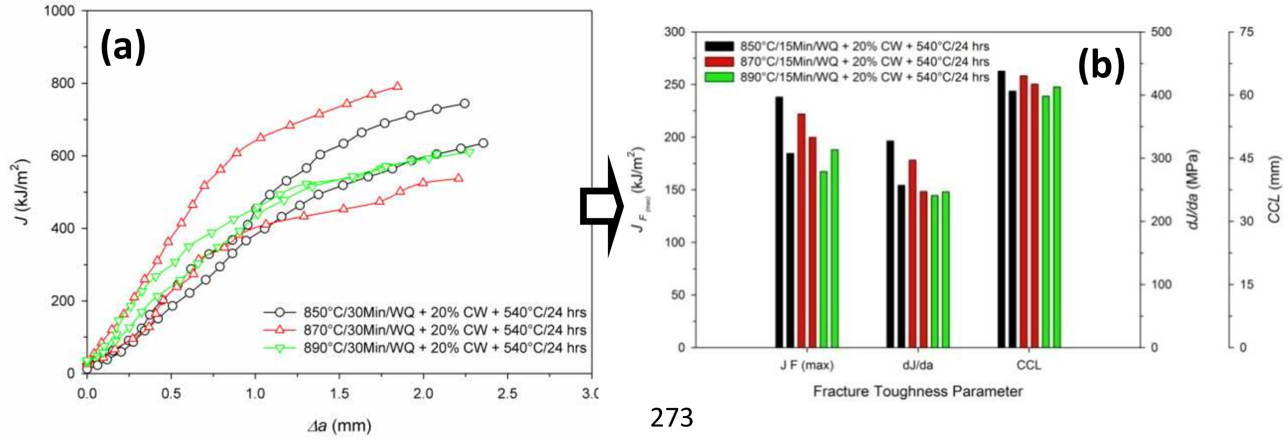

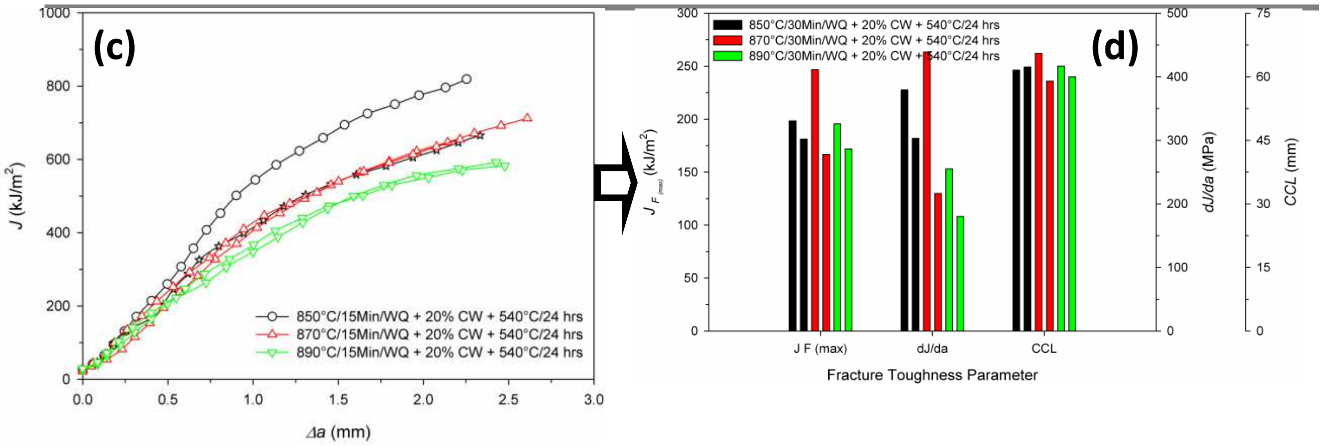

Figure 6.51: Influence of SHT parameters; soaking temperature and duration on fracture behavior of WQA Zr-2.5Nb alloy at 300°C. Plots (a) & (b) and (c) & (d) respectively illustrate the influences of materials, previously soaked for 15 and 30 min durations during SHT.

The improvement in fracture behavior (especially, propagation resistance) because of the use of lower SHT temperature suggested that after aging, simultaneous changes in microstructural features viz., higher primary α volume fraction, lower α’ grain size along with higher degree of Nb super-saturation in α' resulted in improvement of the fracture behavior of WQA Zr-2.5Nb alloy. This influence of the microstructural features associated with SHT on fracture behavior of WQA Zr-2.5Nb alloy is illustrated in Figure 6.52. As can be understood from this figure that the aforementioned changes in the microstructure features within 850-890°C SHT temperature domain resulted in considerable (~ 52%) increase in *dJ/da* parameter and insignificant (~10%) increase in *CCL* of WQA Zr-2.5Nb alloy.

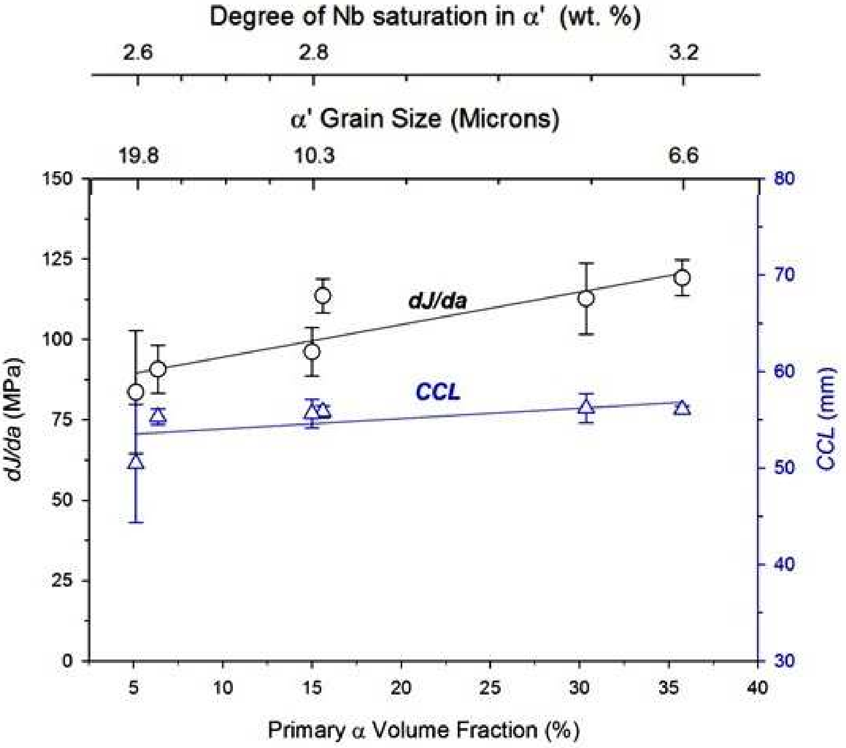

Figure 6.52: Influence of the microstructural features associated with SHT on propagation toughness and *CCL* parameters of WQA Zr-2.5Nb alloy.

This study suggests that prior degree of cold work plays an important role in governing the fracture behavior of WQA Zr-2.5Nb alloy, especially at 300°C (Figure 6.53). In this study, the imparted cold work was limited to 20% thickness reduction, mainly because a much higher cold working could induce significant embrittlement. The cold working treatment is supposed to increase crystal imperfections, especially dislocation density [105,107]. In addition, a higher degree of cold work ensures higher driving force for defect annihilation, which eventually means much faster defect annihilation during subsequent thermal aging treatment [107]. In this study, Zr-2.5Nb alloy previously cold worked with 20% in contrast to 10% have shown relatively lower flow stress after aging treatment. This observation, therefore indicates the influence of higher degree of cold working on greater defect annihilation during subsequent aging treatment. Present study suggests that a higher degree of prior cold working is desirable for ensuring superior fracture toughness after subsequent aging treatment. Though, similar to SHT parameters, degree of cold working also has marginal influence on *CCL* parameters of WQA Zr-2.5Nb alloy. Nevertheless, higher cold working seems to be desirable for ensuring superior crack propagation resistance, especially at 300°C. Such improvement in fracture behavior of WQA materials because of higher cold working can be understood as the consequence of two major aspects: greater defect annihilation and higher driving force for β precipitation. As mentioned earlier that higher degree of prior cold working is expected for greater defect annihilation, leading in much recovered microstructure after aging treatment. In addition, higher cold working is also supposed to increase the driving force for β precipitation during aging treatment, which thereby could cause higher β precipitate density. Therefore, the improved fracture behavior of higher cold worked materials after aging can be understood as the combined effect of greater defect annihilation along with higher β precipitate density.

Also, as can be seen from Figures 6.53 (a) and (c) that at small crack growth regime, *J* parameters had weak dependency on degree of cold working at both ambient and 300°C. Therefore, degree of prior cold working weakly affected the *CCL* parameters of WQA Zr-2.5Nb alloy.

In summary, prior degree of cold working primarily influenced the stable crack propagation resistance of WQA Zr-2.5Nb alloy, though it had weak influence on the limit for catastrophic failure.

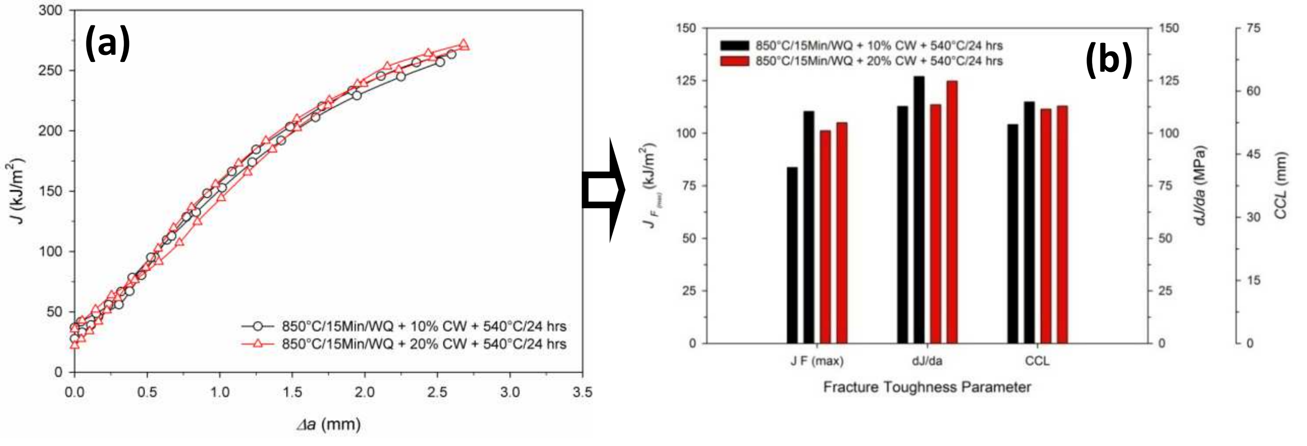

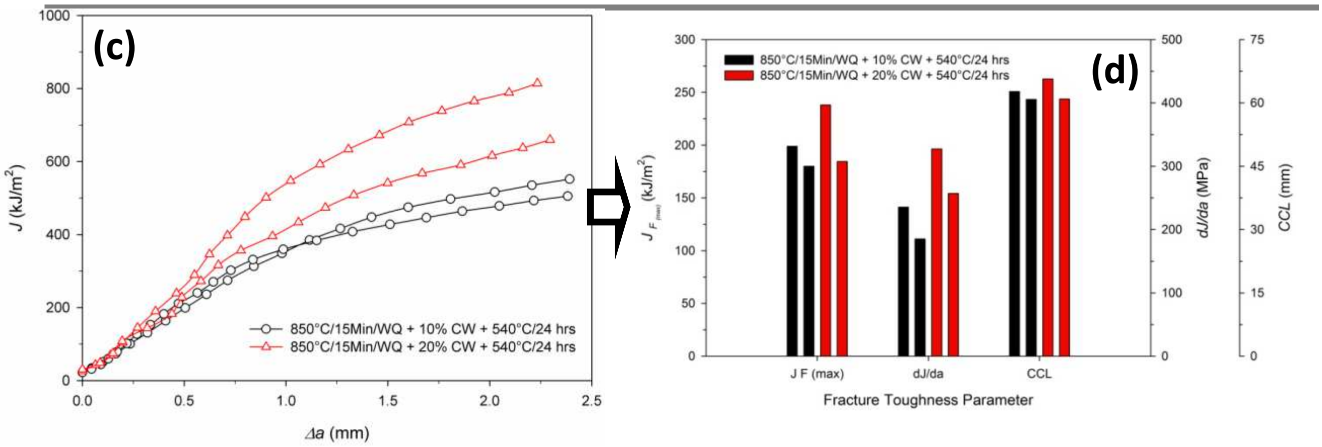

Figure 6.53: Influence of prior degree of cold working on fracture behavior of WQA Zr-2.5Nb alloy. Plots (a) & (b) and (c) & (d) respectively illustrate the influences at ambient and 300°C.

Present study suggests that selection of aging temperature has an important role in governing the chemistry of precipitation and its size. Aging at the higher temperature, 540°C, in contrast to 500°C resulted in the formation of the Nb lean and relatively coarser β-Zr precipitation, as compared to the finer β-Nb, which is significantly richer in Nb. Also, aging treatments resulted in the variation of size & distribution and volume fraction of β precipitates. In addition to precipitation, aging treatment is also supposed to reduce the imperfection density within material, which was introduced during previous cold working stage. Aging performed at higher temperature, 540°C in contrast to 500°C is liable to generate much more recovered structure, with less imperfection density. As can be seen from Figure 6.54 that within such small window of aging temperature (500-540°C), fracture toughness of Zr-2.5Nb alloy exhibited considerable changes. Aging at 540°C has caused significant improvement in the fracture toughness. Here again, aging temperature insignificantly influenced the *CCL* parameters, however strongly influenced the resistance for stable crack propagation of WQA Zr-2.5Nb alloy. This therefore, shows that during aging stage, precipitate chemistry, its size, distribution and volume fraction along with the extent of recovery play an important role in governing the fracture behavior of WQA Zr-2.5Nb alloy. Hence, improvement in propagation resistance because of the use of higher aging temperature, suggested the combined influence of higher β precipitate volume fraction, coarser precipitate size, Nb lean β phase precipitation, along with higher degree of recovery in improving the fracture behavior of WQA Zr-2.5Nb alloy. Figure 6.55 shows the influence of such microstructural features associated with aging stage on fracture behavior of WQA Zr-2.5Nb alloy. As can be understood from this figure that these simultaneous changes in microstructural features associated with increase in aging temperature from 500-540°C resulted in an average ~36% increase in *dJ/da* parameter, however marginal increase (by ~7%) increase in *CCL* of WQA Zr-2.5Nb alloy.

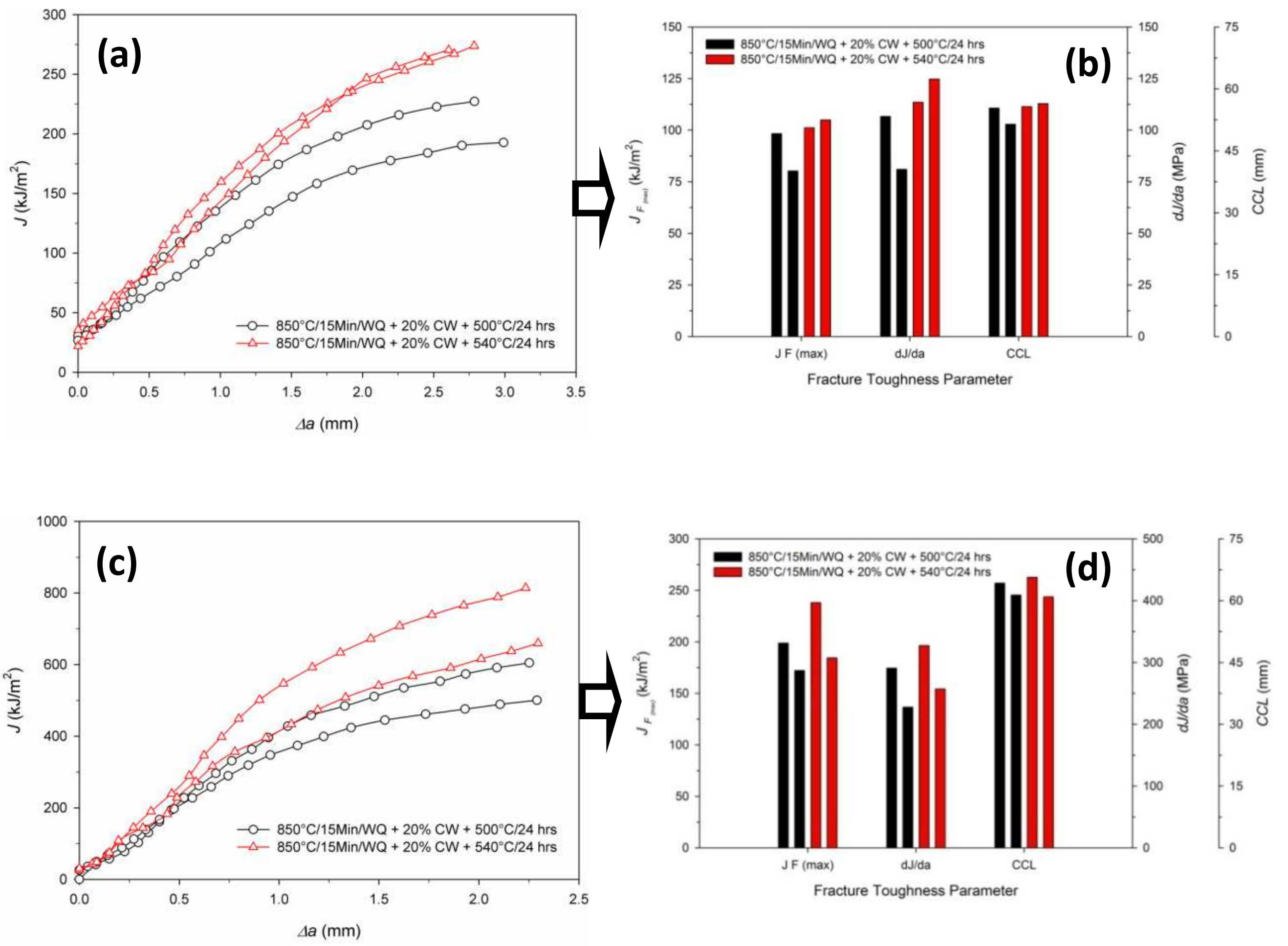

Figure 6.54: Influence of aging temperature on fracture behavior of WQA Zr-2.5Nb alloy. Plots (a) & (b) and (c) & (d) respectively illustrate the influences at ambient and 300°C.

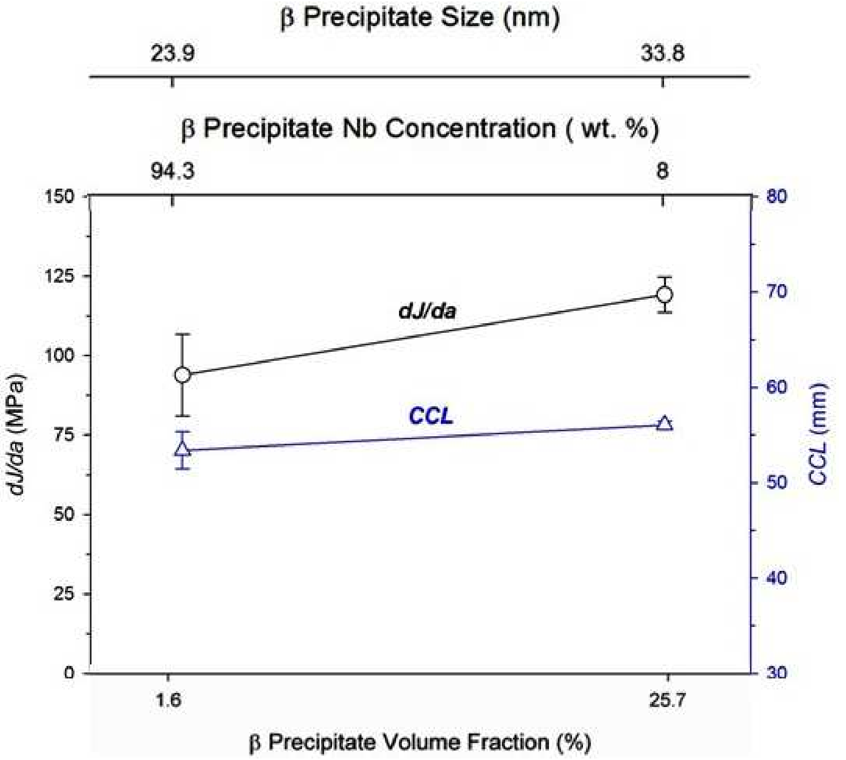

Figure 6.55: Influence of the major microstructural changes associated with increase in aging temperature on propagation toughness and *CCL* parameters of WQA Zr-2.5Nb alloy.

The present study proposes a master relationship between the microstructural features and stable crack propagation resistance of WQA Zr-2.5Nb alloy, in order to separate out the role of individual microstructural features on stable crack propagation resistance. This relationship is shown in Equation 6.3, which is a multi variable linear dependence of the microstructural features and *dJ/da* parameter of WQA Zr-2.5Nb alloy. As can be seen from this relationship that the coefficients of terms viz., Nb concentration of α’, β precipitate size and Nb concentration of β precipitates nearly approaches to zero. In contrast, coefficients of terms viz., primary α volume fraction and β precipitate volume fraction are very close and considerably higher. In addition, coefficient of the term α’ grain size, though comparably lower than the two parameters, still is notable. This relationship therefore suggests that out of several microstructural changes associated with SHT and aging treatments, only the changes in primary α and β precipitate volume fractions have played significant role in governing the fracture behavior of WQA Zr-2.5Nb alloy. Also, smaller α’ grain size is an important secondary microstructural feature, which improves the propagation resistance of WQA Zr-2.5Nb alloy.

$$\frac{dJ}{da} = 48.84 + 1.04\left(V_{Primary\ \alpha}\right) - 0.37\left(D_{\alpha'}\right) - 7.02 \times 10^{-8}\left(Nb_{\alpha'}\right) - 1.11\left(V_{\beta\ Precipitate}\right) - 4.51 \times 10^{-7}\left(D_{\beta\ Precipitate}\right) - 1.08 \times 10^{-10}\left(Nb_{\beta\ Precipitate}\right) \qquad (6.3)$$

In Equation 6.3, terms $V_{Primary\ \alpha}$ & $V_{\beta\ Precipitate}$ respectively represent the volume fractions (in %) of Primary α & β precipitates; $Nb_{\alpha'}$ & $Nb_{\beta\ Precipitate}$ respectively represent the Nb concentrations (in wt. %) of α’ & β precipitates; and $D_{\alpha'}$ & $D_{\beta\ Precipitate}$ respectively represent the grain sizes (in µm) of α’ & β precipitates.

In summary, this study showed that the *CCL* parameter of WQA Zr-2.5Nb alloy is weakly sensitive to even large variation in its TMP parameters. However, combination of TMP parameters viz., SHT at 850°C for 15-30 min, followed by 20% cold working and subsequent aging at 540°C for 24 h gives the best stable crack propagation resistance of WQA Zr-2.5Nb alloy.

Under ambient condition, the aging treatment has shown adverse effect on the fracture toughness of Zr-2.5Nb alloy. However, at reactor operating temperature, 300°C aging treatment improved the fracture toughness of Zr-2.5Nb alloy. The fractographic examinations of WQA materials were performed to study the fracture surfaces. Investigation showed that the WQA materials tested under ambient condition show several parallel axial split features on their fracture surfaces (as shown in Figure 6.47). Similar axial splitting features have also been observed on the fracture surfaces of the CWSR material fabricated from double melted ingot, see Figure 6.56. As described, the hydrogen concentration examinations of current aged materials showed the higher concentration (avg. 17.5 wt. ppm), as compared to the SHT (4.7 wt. ppm) and CW (8 wt. ppm) materials. This therefore emphasizes for the formation of hydride in the aged material, and hence, aiding for the axial splitting. These axial split features represent the low energy (brittle) fracture regimes, and therefore their presence at RT suggests the low fracture toughness of WQA material. However, fracture surfaces of WQA materials tested at 300°C does not show the formation of such low energy axially split features, which therefore contributes to the increasing toughness after aging treatment.

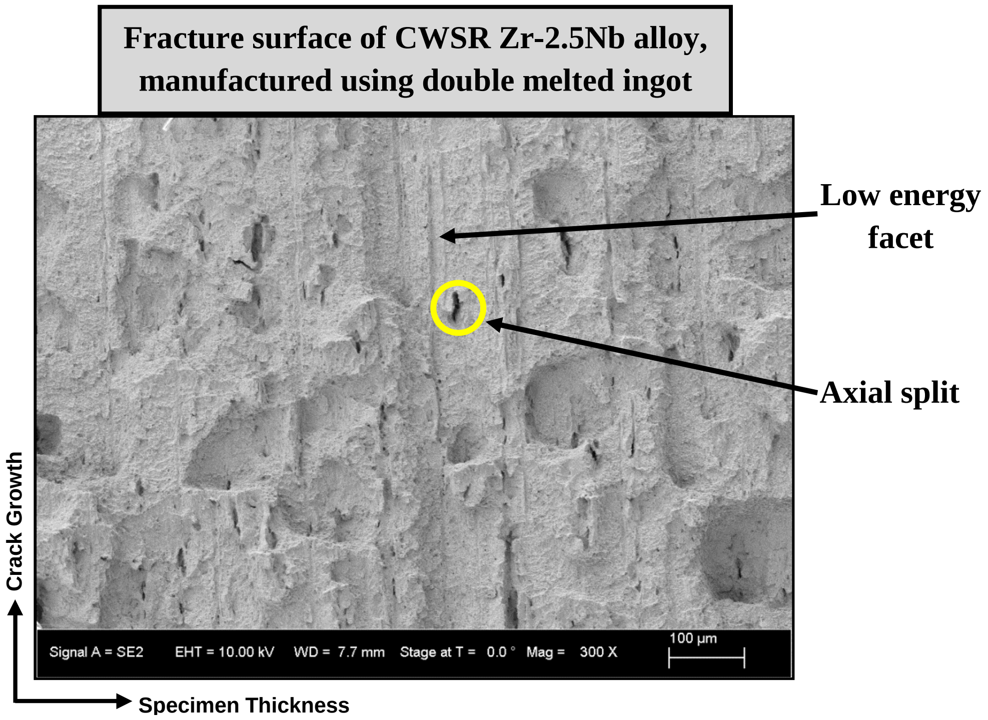

Figure 6.56: Fracture surface of Zr-2.5Nb alloy IPHWR 220MWe pressure tube fabricated from the DM-CWSR route, showing the presence of typical axial split regions originated from the brittle failure of the hydride plates and several low energy facets lying across the specimen thickness, directed towards the crack growth direction under ambient fracture condition.

As described earlier that aging treatments caused significant reduction in strain hardening exponents under ambient condition. The role of lower strain hardening of WQA materials will facilitate localized deformation resulting in reduction in fracture toughness, Figure 6.57. Therefore, such lower fracture toughness after aging could also be explained by the significantly lower strain hardening characteristics of WQA materials.

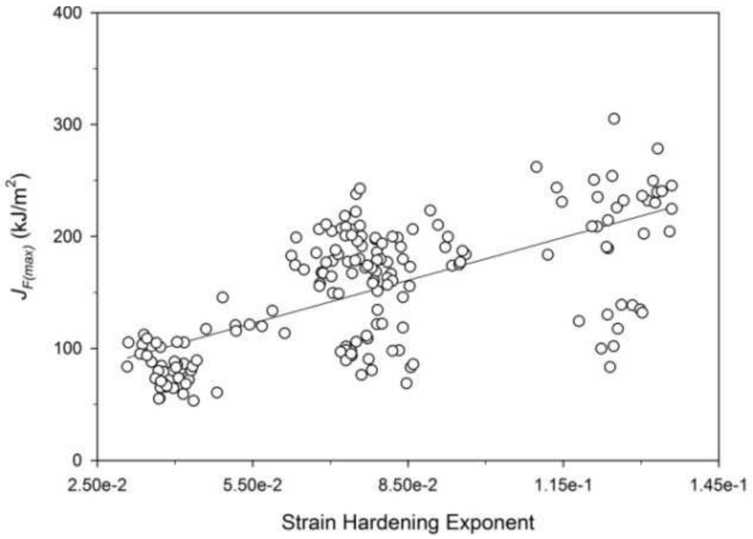

Figure 6.57: Correlation between the material’s strain hardening exponents and fracture toughness.

In WQA fabrication route of Zr-2.5Nb alloy pressure tubes for PHWRs (or, for future AHWR) applications (as introduced in Chapter 1, Figure 1.2), the vacuum aging treatment can be considered as the final mechanical behavior governing treatment, assuming that the subsequent autoclaving treatment has practically no role in further altering the mechanical properties of pressure tubes. The pressure tubes of 220MWe IPHWRs are currently being used under CWSR condition (fabrication route illustrated in Chapter 2, Figure 2.5). In this context, mechanical properties of Zr-2.5Nb alloy under the aforementioned preeminent WQA condition was compared with that under CWSR condition. For this, CWSR pressure tube materials fabricated using both the earlier used Double Melted (DM) and the recent Quadruple Melted (QM) ingots were considered.

Comparison suggests that the preeminent WQA material (as suggested from this study), is close to QM-CWSR materials in terms of flow stress (under higher plastic strains), Figure 6.58 (a). The WQA material, in contrast to QM-CWSR materials possesses relatively lower uniform elongation (at RT), which therefore indicates for relatively early void/neck formation in this material. In contrast to CWSR condition, Zr-2.5Nb alloy under WQA conditions had relatively flat flow curves, which therefore suggest the lower strain hardening characteristics of the WQA materials. Such difference in strain hardening characteristics of the two materials dominates especially under ambient condition; however at 300°C, difference becomes relatively small, Figure 6.58 (b).

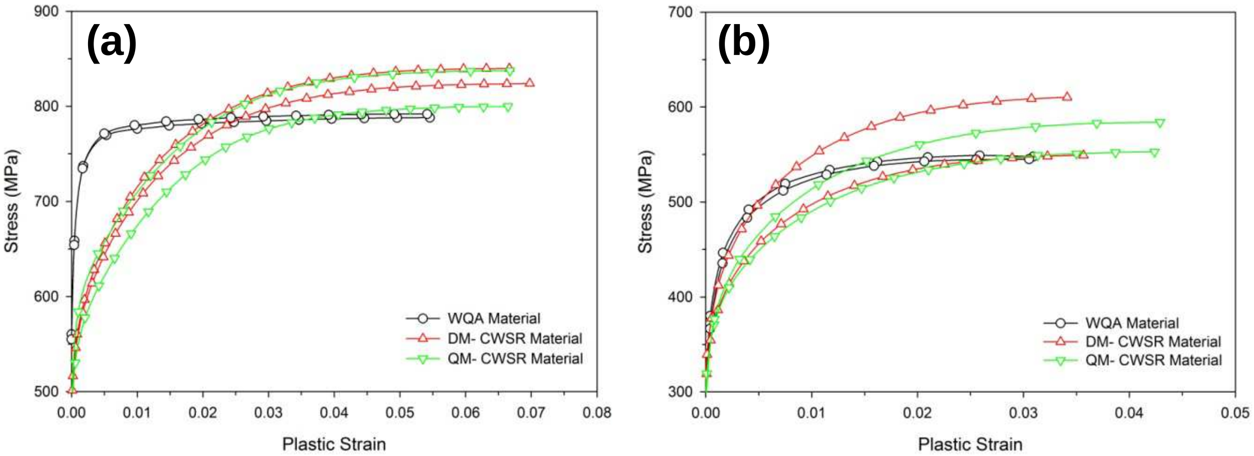

Figure 6.58: Comparison of flow behavior of Zr-2.5Nb alloy under the optimized WQA (850°C/15Min/WQ+20%CW+540°C/24h) and Indian CWSR (double melted, DM and quadruple melted, QM) conditions at (a) RT and (b) 300°C.

Under WQA condition, Zr-2.5Nb alloy exhibits higher tensile strength as compared to under CWSR condition. Under ambient condition, these two materials have considerable difference in their tensile strengths, Figure 6.59 (a); however at reactor operating temperature (300°C), both possess nearly analogous strengths, Figure 6.59 (b). The superior tensile strengths of WQA material could be understood as the contribution from its martensitic microstructure with finer substructure, as illustrated in Figures 6.2 and 6.3.

In terms of ductility, the preeminent WQA material is practically comparable with the QM-CWSR pressure tube material, Figure 6.59. The WQA material showed appreciably lower strain hardening as compared to both the conventional DM and recent QM-CWSR materials, as shown in Figure 6.59. The considerable strain hardening shown by CWSR materials could be explained in terms of its much fine grain microstructure [3]. In contrast, under WQA condition, Zr-2.5Nb alloy has much coarser grain structure, which comprises mostly (~ 62 %)

of α' phase having grain size of 15-20 µm, along with 35% α-Zr having grain size of ~ 3 µm and β precipitates with average size of ~ 25-35 nm. Because of the constraint imposed by neighbouring grains, deformation within a particular grain is usually inhomogeneous [107]. In addition, more slip systems usually activate near grain boundary region, as compared to the interior grain, which makes grain boundary region harder as compared to interior of grain region. A finer grain size aids in the homogenous grain deformation. In addition, because of fine grain size, more effects of grain boundaries are felt within the grain, which causes higher strain hardening [107].

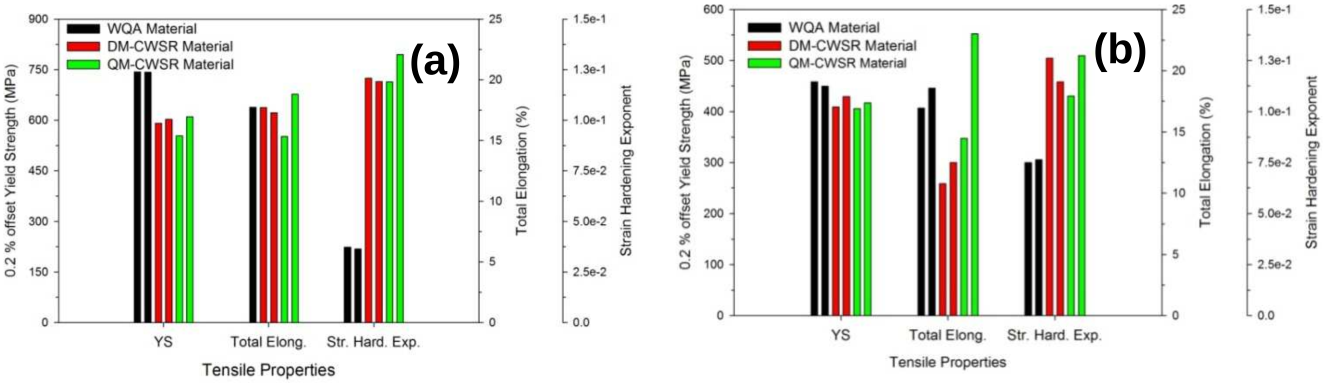

Figure 6.59: Comparison of tensile properties of Zr-2.5Nb alloy under optimized WQA (850°C/15Min/WQ+20%CW+540°C/24h) and Indian CWSR (double melted, DM and quadruple melted, QM) conditions at (a) RT and (b) 300°C.

A comparison of the fracture behavior of Zr-2.5Nb alloy under aforementioned preeminent WQA and CWSR conditions is presented in Figure 6.60. From Figure 6.60 (a) & (b), it can be understood that under ambient condition, WQA material has fracture resistance close to, but higher than that of the conventional DM-CWSR material. However, at reactor operating temperature, the fracture resistance of WQA material improved significantly and became practically comparable to that of the QM-CWSR material, Figure 6.60 (c) & (d).

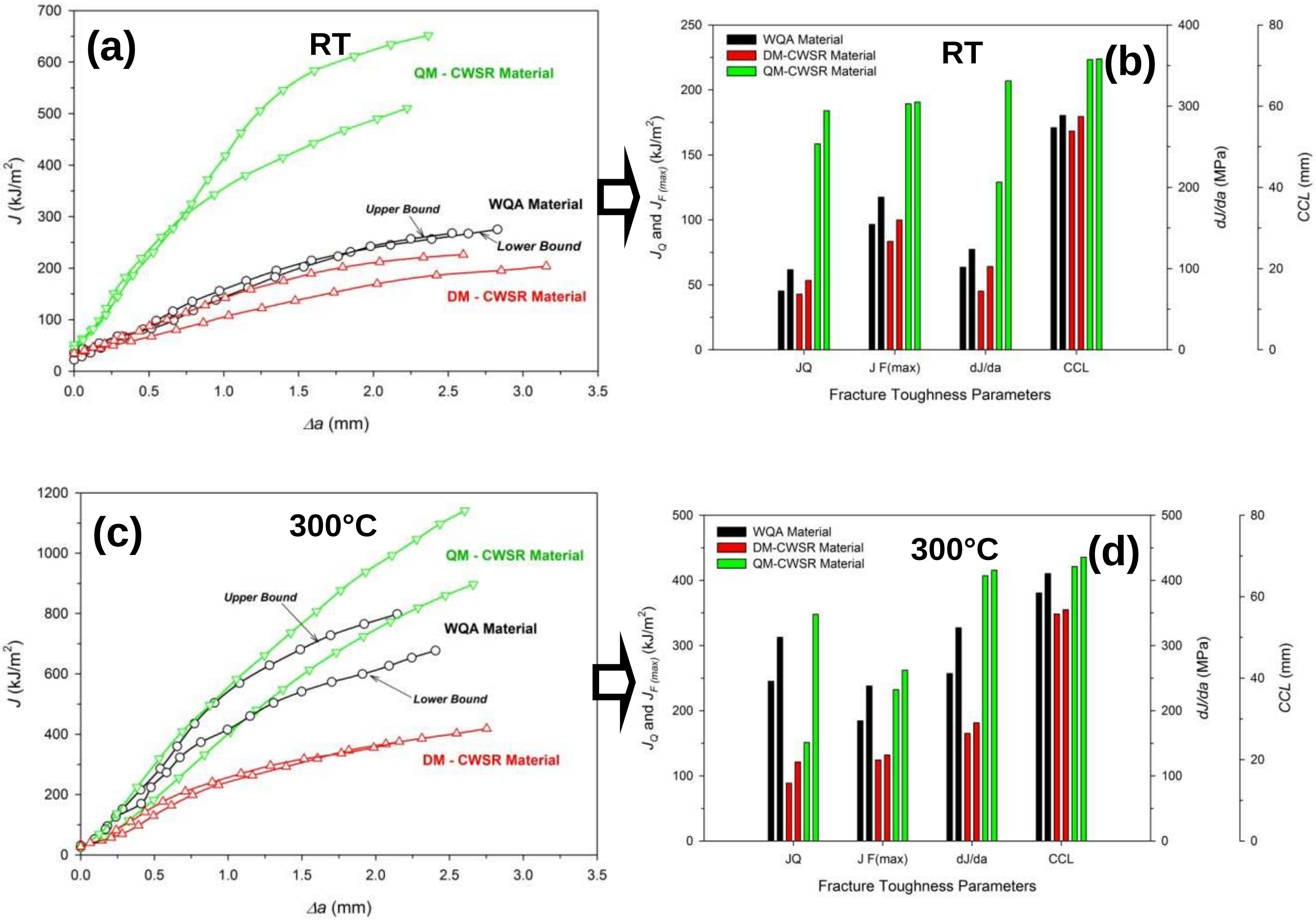

Figure 6.60: Comparison of the fracture behavior of Zr-2.5Nb alloy under optimized WQA (850°C/15Min/WQ+20%CW+540°C/24h) and Indian CWSR (double melted, DM and quadruple melted, QM) conditions at (a) & (b) RT and (c) & (d) 300°C.

After aging and also with increase in aging temperature, the fracture surfaces of cold worked-solution heat treated materials showed larger flat region. As discussed earlier that material's strength is one of the important factors that govern the state of stress ahead the crack tip such that with increasing strength, state of stress ahead the crack tip shifts towards the plane strain condition, which in general results in the flat fracture [105,106]. However, in the present case, material strength decreased after aging treatment and also with increasing aging temperature, which therefore in contrary to the observations, emphasized for relatively smaller flat region. Such controversial phenomenon put forward the role of strain hardening in localizing the deformation. The lower strain hardening of WQA materials under ambient condition (as described earlier in Figure 6.22 (a)) could resulted in localized deformation, which therefore contributed to larger flat fracture and also lower fracture toughness.

Fracture toughness examinations performed in the present study showed fracture surfaces comprising the mixture of flat and slanted regions. Fracture surfaces of Zr-2.5Nb alloy under solution heat treated and subsequent cold working conditions mostly occupied slanted region, with an intermediate narrow flat region. In contrast, under aged condition, and also with increasing aging temperature from 500 to 540°C, the fracture surfaces mostly occupied flat regions, with minor slanted regions. The fracture toughness parameters determined in terms of *J*-integral, represents the crack growth resistance in terms of required energy per unit area of crack extension [63]. Considering this, because of exhibiting slanted fracture region, the *J* parameters must be determined based on actual fracture surface areas, rather than the projected fracture areas. Therefore, in the present work, *J* parameters were first determined on the basis of projected fracture areas and subsequently corrected for the corresponding actual fracture surface areas. For accounting such area correction, the *J* parameters determined based on projected fracture areas, PA were multiplied by an ‘area correction factor’ (ACF), as defined by Equation 6.4.

$$\text{Area Correction Factor} = \frac{\text{Projected Fracture Area}}{\text{Fracture Surface Area}} \tag{6.4}$$

The fracture areas (i.e., actual fracture area, AA and projected area, PA) of Zr-2.5Nb alloy under three TMP stages (SHT, CW and aging) were measured using an image analysis technique through 'Image-J' software. Figure 6.61 shows the dependency of ACFs on the TMP stages. The ACFs under SHT and subsequent 10% & 20% CW conditions were close (ranged in 0.68-0.76 at RT and 0.78-0.79 at 300°C). This weak dependency of ACFs points towards insignificant alteration in the proportionate flat fracture regions of solution heat treated and cold worked materials. The comparison of flat fracture regions, as illustrated in

Figure 5.19 (Chapter 5) agrees with this theory, which showed insignificant alteration in the proportionate flat fracture regions under SHT and subsequent CW conditions. After subsequent aging treatment and also with increase in aging temperature, the ACFs showed significant rise. This can be understood as the consequence of significant increase in the occupied flat fracture region after aging treatment and also, with increase in aging temperature, especially under ambient condition, as illustrated in Figure 6.44. After aging treatment, especially performed at higher soaking temperature (540°C), most of the fracture surfaces covered a significant portion of flat region (>80%, also in some cases 99%), which results for corresponding high values of ACF.

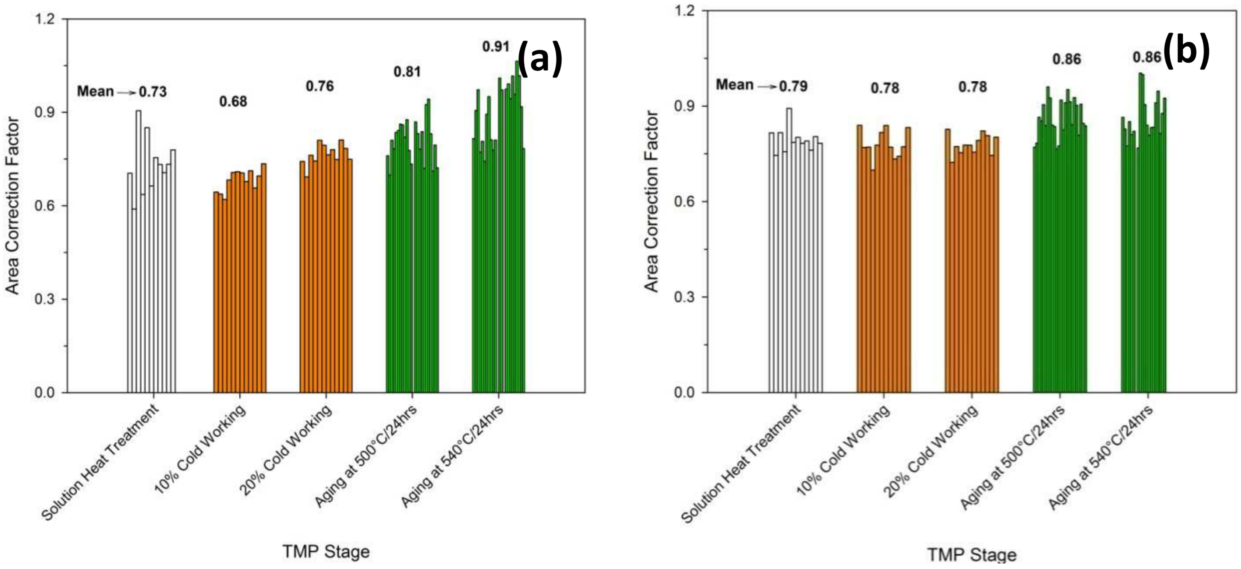

Figure 6.61: Dependency of area correction factors of Zr-2.5Nb alloy on different TMP stages at (a) RT and (b) 300°C.

After SHT and CW

Toughness $_{AA}$ < Toughness $_{PA}$ (differs considerably)

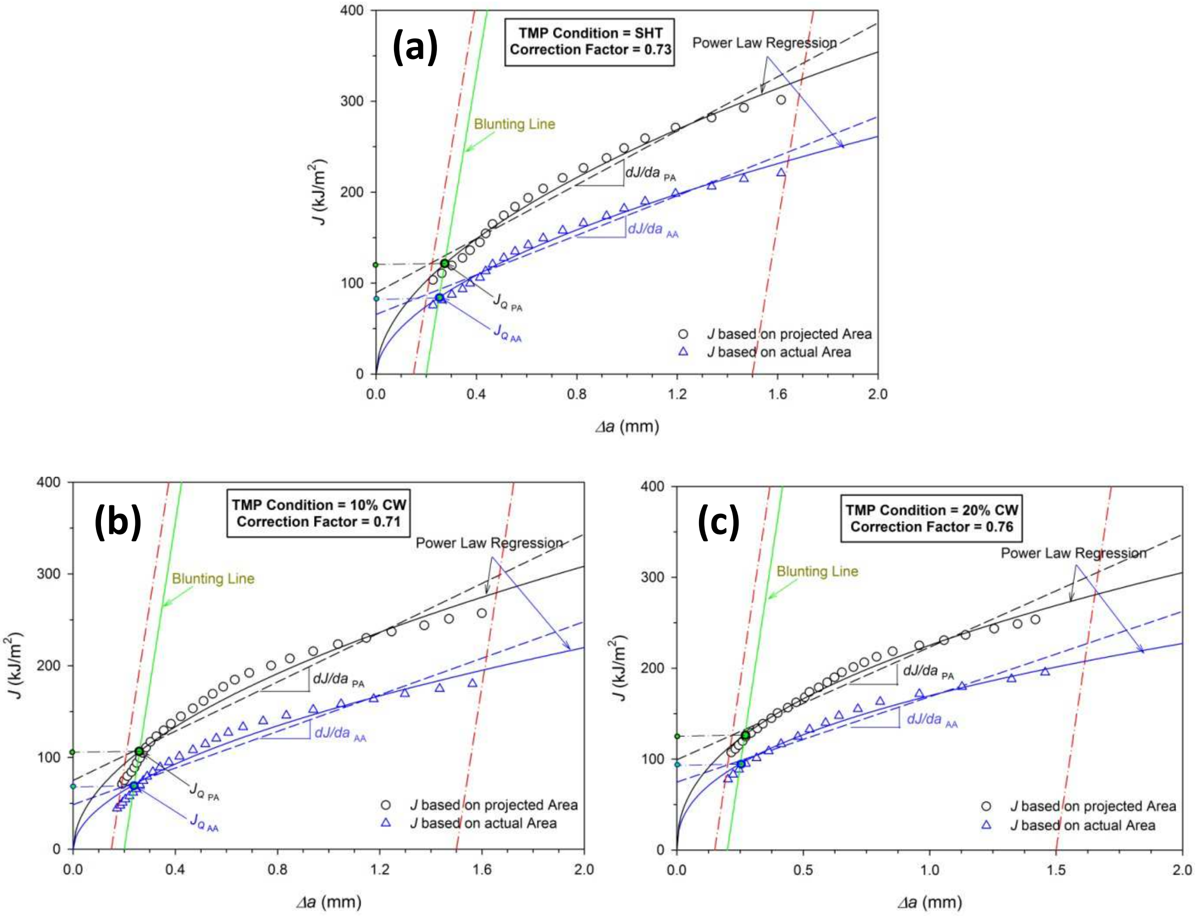

After Aging

Toughness $_{AA}$ ≈ Toughness $_{PA}$

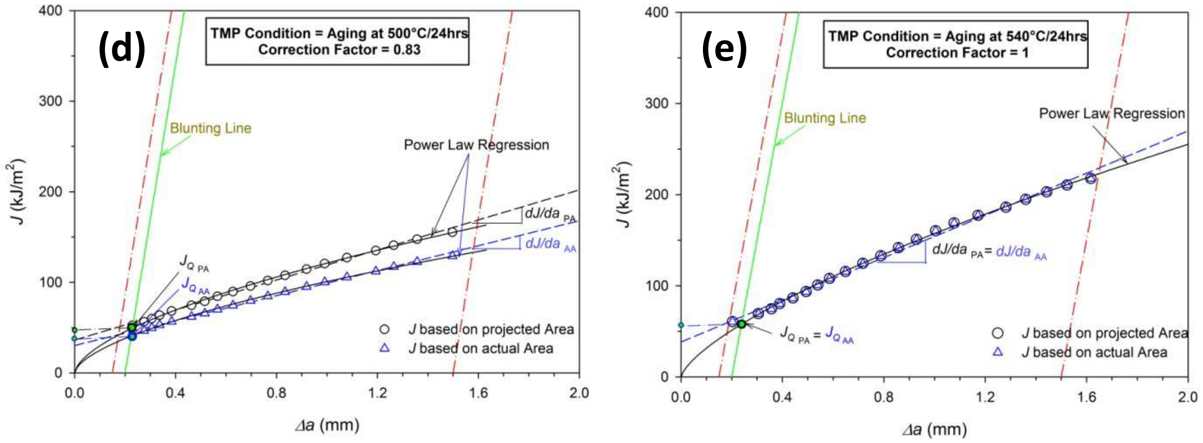

Figure 6.62: Influence of ACF multiplications on the *J-R* curve analysis of Zr-2.5Nb alloy under (a) SHT, subsequent (b) 10 & (c) 20 % CW and aged (d) at 500°C and (e) 540°C conditions.

The influence of ACF multiplication, so as to determine the corrected fracture toughness parameters is illustrated in Figure 6.62 for different TMP conditions. The effects on *J-R* curve analysis of Zr-2.5Nb alloy under different TMP conditions are shown over here. Multiplication of ACFs in *J* parameters (determined based on the projected fracture areas) caused reduction in both initiation (J_Q) and propagation toughness parameters ($J_{F(max)}$ and *dJ/da*). In contrast to SHT and CW conditions, higher value of ACF under aged condition resulted for marginal alterations in the aforementioned fracture toughness parameters.

Figure 6.63 specifically illustrates the influence of area corrections on the evaluated fracture toughness parameters under solution heat treated, subsequently cold worked and aged conditions. As can be seen from these plots that such correction mainly influenced the fracture toughness parameters of solution heat treated and subsequently cold worked materials. This can be understood as the consequence of smaller flat fracture regions shown by these materials (as discussed in Section 4.3 of Chapter 4 and Section 5.3 of Chapter 5). However, for the aged materials, specially soaked at 540°C, such effects of the area corrections were practically negligible. This is because of the relatively much larger flat fracture shown by these materials (as discussed earlier in Section 6.3). Another important observation is that as compared to *J* parameters (initiation toughness (J_Q) and propagation toughness ($J_{F(max)}$ and *dJ/da*)), the *CCL* parameters showed much weaker dependence on such area corrections.

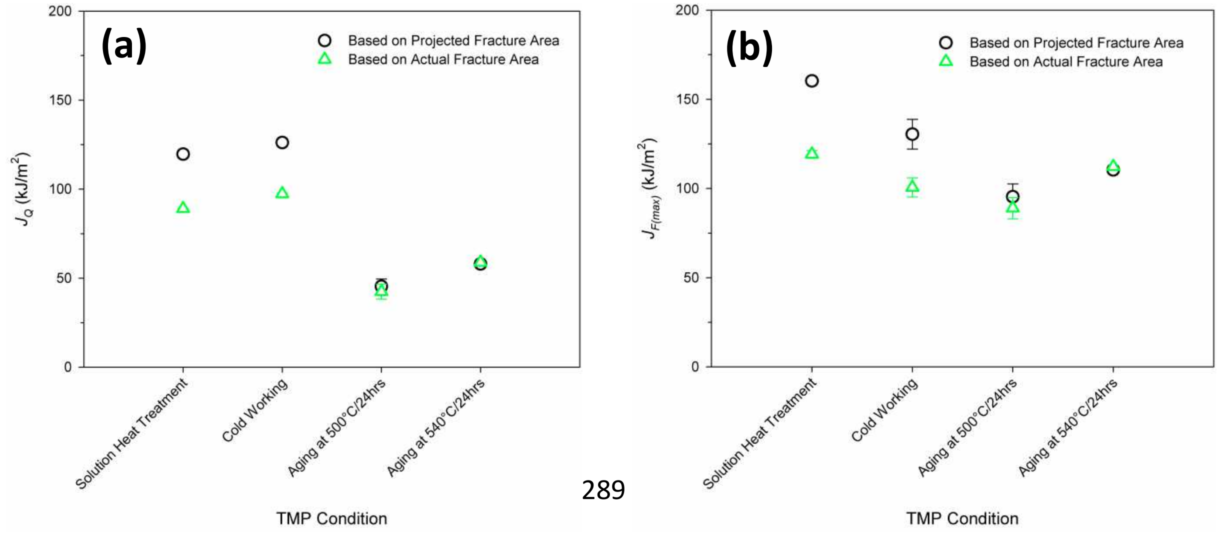

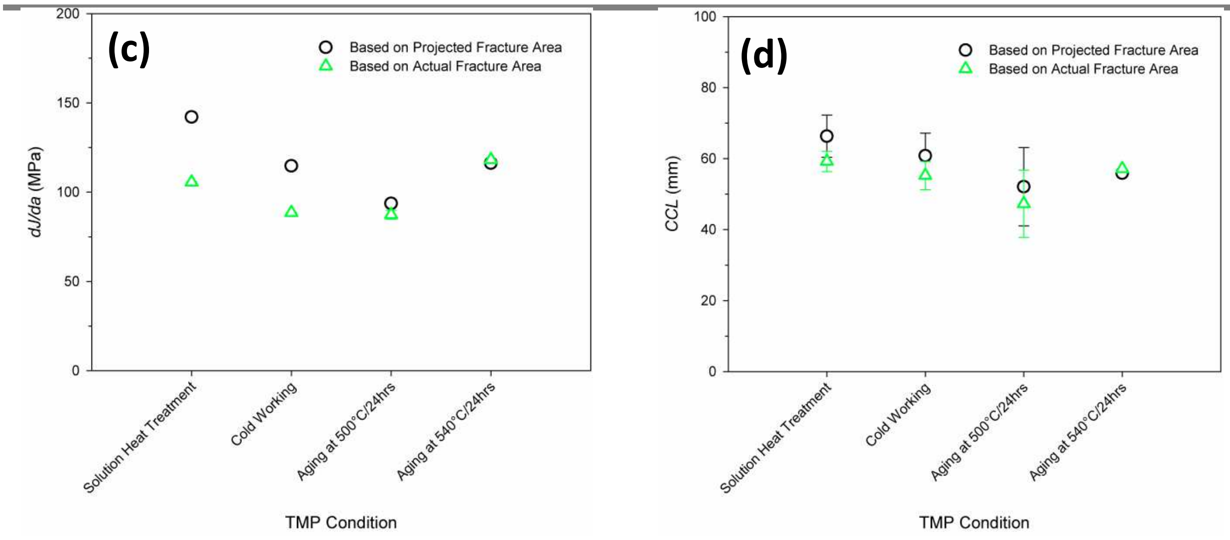

Figure 6.63: Influence of fracture area corrections on the fracture toughness parameters of Zr-2.5Nb alloy under solution heat treated, subsequently cold worked and aged conditions.

An important suggestion from this study is that the basal pole texture of current WQA material (850°C/30 min+20% CW+500°C/24h) has good agreement with that of the WQA material of RBMK 1500 fabricated using TMT-1 route [2] (described in Figure 2.12 (a), Chapter 2), Figure 6.64. Here, it is important to note that these two WQA materials have more or less comparable TMP fabrication histories. Furthermore, WQA material, even if aged at 540°C also exhibits comparable basal pole texture as that of the RBMK WQA material.

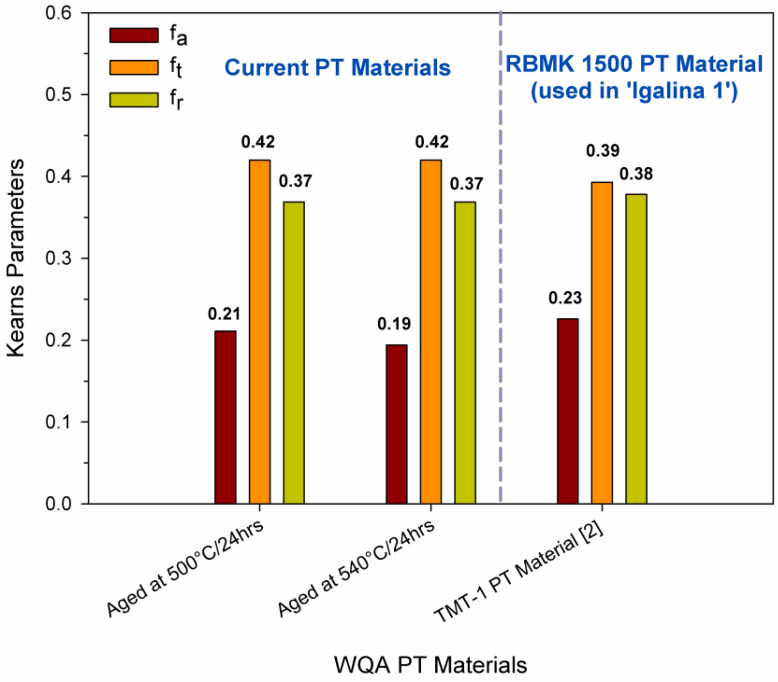

Figure 6.64: Comparison of the basal pole texture, Kearns parameters of current studied WQA and presently being used RBMK 1500 (Ignalina 1) WQA PT materials [2].

6.6 Summary

Present study on the influence of aging temperature on fracture behavior of cold worked-solution heat treated Zr-2.5Nb alloy is summarized as follows:

i. Aging treatments caused dissociation of metastable α' phase into α-Zr and β-Zr/β-Nb phases. Aged materials comprised typical array like β network at the lath boundaries of α'. Aging temperature played an important role in governing the chemistry of precipitation and its size. Aging at the higher temperature, 540°C, in contrast to 500°C resulted in the Nb lean and relatively coarser β-Zr precipitation, as compared to the finer β-Nb, which is significantly richer in Nb. Aging at 540°C, in contrast to 500°C resulted in relatively higher volume fraction of β precipitates. After aging treatment, the basal pole texture of cold worked-solution heat treated Zr-2.5Nb alloys became slightly more prominent along transverse direction with corresponding reduction along axial (previously rolling direction). Nevertheless, WQA materials, as compared to CWSR had relatively weaker texture. Furthermore, texture of currently studied WQA material (850°C-30Min-WQ + 20% CW + aged at 500/540°C/24 h) showed good agreement with that of the presently being used RBMK 1500 PT materials fabricated using TMT-1 route.

ii. Aging of cold worked-solution heat treated Zr-2.5Nb alloy resulted in appreciable reduction in tensile strength and strain hardening characteristics though considerable improvement in ductility. These effects further dominated with increase in aging temperature from 500 to 540°C. The aging had different influences on fracture toughness parameters at RT and 300°C. Under ambient condition, aging treatment resulted in reduction in fracture toughness of cold worked-solution heat treated Zr-2.5Nb alloy. However, at 300°C, the aged materials as compared to cold worked materials had relatively higher fracture toughness.

iii. Fractography examinations of WQA materials showed several axial splits under ambient fractured condition, which were oriented along crack growth direction. Presence of such low energy (brittle) fractured sites accounted for the observed lower fracture toughness of WQA Zr-2.5Nb alloy under ambient condition. In contrast, the fracture surfaces of WQA materials tested at 300°C did not show the formation of such low energy sites, which therefore contributes to enhancing the toughness after aging treatment.

iv. The aged materials, under ambient condition, exhibited much larger central flat fracture, associated with superior 'tunnelling' characteristic, despite having lower fracture toughness. Since, under ambient condition, aging caused significant reduction in the strain hardening exponents. The lower strain hardening of aged materials, therefore could also aid in facilitating localized deformation, resulting in reduction of fracture toughness after aging.

v. Stretched zones formation ahead of pre-cracked region in C(T) specimens of WQA materials showed good agreement with the observed influence of aging treatments on initiation toughness. After aging, the SZWs of cold worked solution heat treated materials, exhibited considerable reduction under ambient condition (to 12-16 μm) and improvement at 300°C (to > 145 μm). This therefore, correlated the influence of aging in reducing initiation toughness of cold worked-solution heat treated materials under ambient condition and improving the same at 300°C. Considering SZW as an indirect measure of the initiation toughness, this study suggested a correlation between SZW and initiation toughness for WQA material. The initiation toughness based on SZW, (i.e., $J_{i\,(SZW)}$ parameter) was observed to be considerably lower than the standard initiation toughness (J_Q parameter), derived from the 0.2 mm offset 'Blunting Line' approach.

vi. *CCL*, an important toughness parameter used for assessing the adherence to LBB criteria showed practically insensitiveness to different analysis approaches, such as; RC, BT and ISO. This, therefore suggested that the assessment of safety margins for necessary LBB condition of WQA pressure tubes is independent of fracture analysis approaches.

vii. In WQA fabrication route of Zr-2.5Nb alloy pressure tubes, the optimum parameters of its three TMP stages, forming an optimum material history to assure its best structural integrity in terms of fracture toughness are summarised as follows:

a. Variation of SHT temperature within 850-890°C range marginally influenced the *CCL* parameters of WQA Zr-2.5Nb alloy. However, SHT performed at relatively lower temperature ensured better stable crack propagation resistance of WQA Zr-2.5Nb alloy, by exhibiting higher fracture resistance slope (*dJ/da*). Such improvement in propagation resistance because of the use of lower SHT temperature suggested that after aging, microstructural features viz., higher primary α volume fraction, lower α’ grain size along with higher degree of Nb super-saturation in α' are beneficial for fracture behavior of WQA Zr-2.5Nb alloy. Selection of SHT soaking duration within 15-30 min domain had practically similar influence on the fracture behavior of WQA Zr-2.5Nb alloy.

b. The prior degree of cold working played an important role in governing the fracture behavior of WQA Zr-2.5Nb alloy, especially at elevated temperature. Though, similar to SHT parameters, degree of cold working also weakly influenced the *CCL* parameters of WQA Zr-2.5Nb alloy, thereby suggesting nearly insensitive limit of catastrophic failure. Nevertheless, a higher cold working appeared to be desirable for ensuring superior stable crack propagation resistance. This therefore, suggested the influence of higher cold working on greater extent of recovery during aging and higher number of β nucleation sites during aging, caused by increased dislocation density, resulting in finer and uniform distribution of β phase, leading to improvement in the fracture behavior of WQA Zr-2.5Nb alloy. The tensile property examinations, which showed lower strengths of 20% prior cold worked WQA materials, suggests such influence of higher degree of cold working on greater extent of recovery as well as higher β precipitate density during subsequent aging treatment.

c. Increasing aging temperature by ~ 10% (i.e., 500-540°C) caused considerable variation in β precipitate volume fraction, its size & distribution and composition, resulting in improvement in fracture toughness. Here again, the aging temperature marginally influenced the *CCL* parameters, however considerably influenced the stable crack propagation resistance of WQA Zr-2.5Nb alloy. This suggested the role of higher β precipitate volume fraction, coarser precipitate size, Nb lean precipitate, along with higher degree of recovery in improving the propagation resistance of WQA Zr-2.5Nb alloy.

In summary, *CCL* parameter of WQA Zr-2.5Nb alloy was observed to be weakly sensitive to even large variation in its TMP parameters. However, combination of TMP parameters viz., SHT at 850°C for 15-30 min, followed by 20% cold working and subsequent aging at 540°C for 24 h provided the best stable crack propagation resistance of WQA Zr-2.5Nb alloy.

viii. This study proposed a master relationship between the microstructural features and stable crack propagation resistance of WQA Zr-2.5Nb alloy (as shown below), to separate out the role of individual microstructural features on stable crack propagation resistance. The relationship suggested that out of several microstructural changes associated with SHT and aging treatments, only the changes in primary α & β precipitate volume fractions played significant role in governing the fracture behavior of WQA Zr-2.5Nb alloy. Also, smaller α’ grain size was observed to be an important secondary microstructural feature, which improved the propagation resistance of WQA Zr-2.5Nb alloy.

$$\boxed{\frac{dJ}{da} = 48.84 + 1.04\left(V_{Primary\ \alpha}\right) - 0.37(D_{\alpha'}) - 7.02 \times 10^{-8}(Nb_{\alpha'}) - 1.11(V_{\beta\ Precipitate}) - 4.51 \times 10^{-7}(D_{\beta\ Precipitate}) - 1.08 \times 10^{-10}(Nb_{\beta\ Precipitate})}$$

In this Equation, terms $V_{Primary\ \alpha}$ & $V_{\beta\ Precipitate}$ respectively represent the volume fractions (in %) of Primary α & β precipitates; $Nb_{\alpha'}$ & $Nb_{\beta\ Precipitate}$ respectively represent the Nb concentrations (in wt. %) of α’ & β precipitates; and $D_{\alpha'}$ & $D_{\beta\ Precipitate}$ respectively represent the grain sizes (in µm) of α’ & β precipitates.

An important highlight of this study was that the WQA material exhibited fracture toughness close to, though higher than double melted, DM-CWSR material at ambient and quadruple melted, QM-CWSR material at 300°C, despite having relatively coarser grain size and weaker texture. This is expected to ensure lower in-reactor dimensional changes due to reduced irradiation growth (because of possessing nearly random texture) and irradiation induced creep and hence improving the useful lives of the pressure tubes.

CHAPTER 7

CONCLUSIONS

This chapter concludes the three major studies performed in this work; influence of SHT parameters, subsequent degree of cold work and aging temperature on fracture behavior of Zr-2.5Nb alloy. It suggests the optimum TMP parameters associated with SHT, subsequent cold working and vacuum aging stages in WQA fabrication route of Zr-2.5Nb pressure tube from fracture behavior view point. These optimized TMP parameters can be useful during the fabrication of Zr-2.5Nb pressure tubes using WQA route, so as to achieve the favourable fracture behavior of as-fabricated material. The chapter ends with concluding the influence of selection of different analysis procedures on fracture toughness parameters of Zr-2.5Nb alloy under three TMP conditions.

7.1 Influence of Solution Heat Treatment Parameters on Fracture Behavior of Zr-2.5Nb Alloy

i. Solution heat treatment of Zr-2.5Nb alloy from 850-890°C temperature regime results in two phase (primary α and α’) microstructures. Variation in soaking temperature (850-890°C) and duration (15-30 min) during SHT cause variation in the microstructural features comprising phase volume fractions, grain sizes and composition. With increasing SHT temperature from 850-890°C, primary α volume fraction exhibits considerable reduction (from ~ 36 to 5%). Primary α grain size is weakly dependent on the SHT parameters; however, increase in SHT temperature and soaking duration cause substantial grain coarsening of prior β (i.e., α’). Increasing soaking temperature and duration also decreases the degree of Nb super saturation in α’. In addition, increasing soaking temperature and duration is also expected to increase the degree of oxygen depletion in α’.

ii. SHT, especially performed at higher soaking temperature for longer soaking duration, results in the randomization of basal pole texture with nearly one third distribution along the three principal directions viz., axial, circumferential and radial.

iii. Increasing soaking temperature from 850-890°C and duration from 15-30 min cause reduction in the tensile strength of solution heat treated Zr-2.5Nb alloy. Under ambient condition, the fracture toughness parameters of solution heat treated Zr-2.5Nb alloy are practically independent to the SHT parameters. Nevertheless, at 300°C, longer SHT soaking appears to show the improvement in fracture resistance. These observations suggest the combined effect of microstructural changes associated with increasing soaking temperature viz., decrease in primary α volume fraction, increase in grain size (especially of α’ phase), decrease in Nb super-saturation of α’ and increase in degree of oxygen depletion in α’; and those associated with increasing soaking duration viz., grain coarsening along with decrease in degree of Nb super-saturation of α’ and increase in degree of oxygen depletion in α’ on the tensile and fracture behavior.

iv. During SHT, soaking duration governs the sensitiveness of tensile properties on SHT temperatures, such as longer soaking results in the lower dependence of tensile properties on SHT temperature. This study shows that for longer soaking, the microstructural features viz., primary α volume fraction and degree of Nb super saturation in α’ have lower dependence on SHT temperatures. Such lower dependence of microstructural features on SHT temperatures could therefore explain the cause of obtaining lower dependence of tensile properties on SHT temperatures.

v. Zr-2.5Nb alloy under the six solution heat treated conditions, as considered in this study show typical dimple structure characteristics of a ductile failure, signifying the micro-void coalescence fracture mechanism. Fracture at elevated temperature (300°C), in contrast to RT results in the formation of relatively coarser dimples, having typical deformation markings on their surfaces. Under ambient fracture condition, the dimple has size variation from < ~ 1 µm to as big as ~ 6 µm. In contrast, during fracture at 300°C, the dimple has size variation from ~ 2 µm to as high as ~ 30 µm. Such coarser dimple formation during fracture at 300°C, correlates with the observed improvement in crack growth resistance of these solution heat treated materials at elevated temperature.

vi. The fractographic investigations of the broken C(T) specimens of Zr-2.5Nb alloy under different solution heat treated conditions show the stretched zone formation ahead of the pre-cracked tip. Under ambient condition, the SHT parameters have no drastic influence on the streched zone widths, SZWs; as the average SZWs varries between 45-67 µm. Nevertheless, at 300°C fractured condition, longer soaking results in the formation of relatively wider stretched zones. The SZWs, therefore show good agreement with the observed influence of SHT parameters on the fractrue behavior.

7.2 Influence of Degree of Cold Working on Fracture Behavior of Solution Heat Treated Zr-2.5Nb Alloy

i. Cold working through rolling results in the elongated grain microstructures of solution heat treated materials along rolling direction. Cold rolling treatment causes basal pole alignment along radial (i.e., compressive strain) direction with corresponding reduction along axial (i.e., rolling) direction. Nevertheless, upto 20% cold working, such changes in the basal pole texture of solution heat treated Zr-2.5Nb alloy are not significant.

ii. The tensile properties of solution heat treated Zr-2.5Nb alloy are strongly sensitive to the initial 10% cold working; however with subsequent additional 10% cold working these properties further exhibit lesser changes. Increase in cold working within 0-20% domain increases the tensile strengths and strain hardening characteristic, however, causes substantial reduction in the ductility of solution heat treated materials. Increase in dislocation multiplication factor, as caused by increase in degree of cold working, has good agreement with these observations.

iii. Increase in SHT temperature within 850-890°C, and soaking duration within 15-30 min domain cause considerable reduction in primary α volume fraction and increase in grain size (especially of prior β, i.e., α’) along with a slight decrease in degree of Nb super saturation of α’. These concurrent microstructural changes contributes to decrease in the tensile strength of solution heat treated materials. However, after cold working, such microstructural changes have relatively weak influence on the tensile strength. Ductility and strain hardening characteristic are practically insensitive to these microstructural changes.

iv. Cold working mainly influences the slope of fracture resistance curve, i.e., *dJ/da* parameter. Increasing degree of cold working causes reduction in the *dJ/da* parameters of solution heat treated materials (by 20-35%), suggesting corresponding reduction in the crack propagation resistance of these materials after cold working. Increasing temperature from RT to 300°C causes considerable improvement in *dJ/da* parameters (by > 70%). However, at 300°C, the *dJ/da* parameter exhibits considerable scatter as compared to that at RT.

v. After cold working, the solution heat treated materials, in general comprise relatively larger flat fractured region, especially under ambient test condition. This suggests the influence of cold working in shifting the state of stress towards plane strain condition.

vi. The fracture surfaces of cold worked materials, similar to SHT materials, comprise typical dimple structure characteristic of a ductile failure. However, contrary to SHT materials, the cold worked materials exhibit relatively shallow dimples, especially on the narrow central flat fractured region and the clusters of fine dimples, which correlate the reduction in fracture toughness because of cold working.

vii. The fracture toughness parameters of cold worked-solution heat treated Zr-2.5Nb alloy remain practically insensitive to the microstructural features viz., primary α volume fraction and degree of Nb super saturation in α', similar to before cold working.

viii. Increase in dislocation multiplication factor, as caused by increase in degree of cold working, have good agreement with the reduction in *dJ/da* parameter. In contrast, the $J_{F(max)}$ parameter is practically insensitive to these features, suggesting that the cold working weakly influences the *J* parameters under small crack growth regime.

7.3 Influence of Aging Temperature on Fracture Behavior of Cold Worked-Solution Heat Treated Zr-2.5Nb Alloy

i. Aging of the cold worked-solution heat treated Zr-2.5Nb alloy causes dissociation of metastable α’ phase into α-Zr and β-Zr/β-Nb phases. Aging treatments performed at 500 and 540°C for 24 h duration respectively results in the fine precipitation of β-Nb and β-Zr phases having respective mean sizes of 23.9 and 33.8 nm. Aging at 540°C, in contrast to 500°C results in relatively higher volume fraction of β precipitates. Morphology wise, these β precipitates exhibit a mixture of disc & rod shape and are mostly formed on the lath boundaries of martensite (α’ phase) in the form of arrays.

ii. Aging of cold worked-solution heat treated Zr-2.5Nb alloy causes slightly more prominent basal pole texture along transverse and radial directions with corresponding reduction along axial (i.e., previously rolling direction). Nevertheless, Zr-2.5Nb alloy under such WQA condition, as compared to CWSR condition comprises relatively much weaker basal pole texture. The Kearns parameters of WQA material (850°C-30Min-WQ + 20% CW + aged at 500/540°C/24 h) are mostly similar to that of the currently being used Russian’s RBMK 1500 PT materials, fabricated using TMT-1 route.

iii. Aging of cold worked-solution heat treated Zr-2.5Nb alloy results in appreciable reduction in tensile strength and strain hardening characteristics though, considerable improvement in ductility. These effects further dominated with increase in aging temperature from 500 to 540°C. The aging has different influences on fracture toughness parameters at RT and 300°C. Under ambient condition, aging treatment results in reduction in fracture toughness of cold worked-solution heat treated Zr-2.5Nb alloy. However, at 300°C, the aged materials as compared to cold worked materials had relatively higher fracture toughness.

iv. The major fractographic feature that distinguishes the fracture surfaces of aged materials with those of cold worked and solution heat treated materials is the presence of several parallel axially split regions under ambient fractured condition. Such axial splitting features represent the low energy (brittle) fractured locations, and therefore their presence emphasizes for the observed lower fracture toughness of aged Zr-2.5Nb alloys under ambient condition. In contrast, the fracture surfaces of WQA materials tested at 300°C did not show the formation of such low energy sites, which therefore contributes to enhancing the toughness after aging treatment.

v. The aged materials, under ambient condition, exhibit much larger central flat fracture, associated with superior 'tunnelling' characteristic, despite having lower fracture toughness. Under ambient condition, aging causes significant reduction in the strain hardening exponents. The lower strain hardening of aged materials, therefore could also aid in facilitating localized deformation, resulting in reduction of fracture toughness after aging.

vi. Stretched zones formation ahead of pre-cracked region in C(T) specimens of WQA materials show good agreement with the observed influence of aging treatments on initiation toughness. After aging, the SZWs of cold worked solution heat treated materials, exhibit considerable reduction under ambient condition (to 12-16 μm) and improvement at 300°C (to > 145 μm). This therefore, correlates the influence of aging in reducing initiation toughness of cold worked-solution heat treated materials under ambient condition and improving the same at 300°C. Considering SZW as an indirect measure of the initiation toughness, this study suggested a correlation between SZW and initiation toughness for WQA material. The initiation toughness based on SZW, (i.e., $J_{i\ (SZW)}$ parameter) is observed to be considerably lower than the standard initiation toughness (J_Q parameter), derived from the 0.2 mm offset ‘Blunting Line’ approach.

The role of TMP parameters associated with solution heat treatment, subsequent cold working and vacuum aging stages on fracture behavior of WQA Zr-2.5Nb alloy is summarized as under:

a. Influence of SHT Parameters

Variation of SHT temperature within 850-890°C range marginally influences the *CCL* parameters of WQA Zr-2.5Nb alloy. However, SHT performed at relatively lower temperature ensures better stable crack propagation resistance of WQA Zr-2.5Nb alloy, by exhibiting higher fracture resistance slope (*dJ/da*). Such improvement in propagation resistance because of the use of lower SHT temperature suggests that after aging, microstructural features viz., higher primary α volume fraction, lower α’ grain size along with higher degree of Nb super-saturation in α' are beneficial for fracture behavior of WQA Zr-2.5Nb alloy. Selection of SHT soaking duration within 15-30 min domain has practically similar influence on the fracture behavior of WQA Zr-2.5Nb alloy.

b. Influence of Degree of Cold Working

The prior degree of cold working plays an important role in governing the fracture behavior of WQA Zr-2.5Nb alloy, especially at elevated temperature. Though, similar to SHT parameters, degree of cold working also weakly influences the *CCL* parameters of

WQA Zr-2.5Nb alloy, thereby suggesting nearly insensitive limit of catastrophic failure. Nevertheless, a higher cold working appears to be desirable for ensuring superior stable crack propagation resistance. This therefore suggests the influence of higher cold working on greater extent of recovery during aging and higher number of β nucleation sites during aging, caused by increased dislocation density, resulting in finer distribution of β phase, leading to improvement in the fracture behavior of WQA Zr-2.5Nb alloy. The tensile property examinations, which showed lower strengths of 20% prior cold worked WQA materials, suggests such influence of higher degree of cold working on greater extent of recovery as well as higher β precipitate density during subsequent aging treatment.

c. *Influence of Aging Temperature*

Increasing aging temperature by ~ 10% (i.e., 500-540°C) causes considerable variation in β precipitate volume fraction, its size & distribution and composition, resulting in improvement in fracture toughness. Here again, the aging temperature marginally influences the *CCL* parameters, however considerably influences the stable crack propagation resistance of WQA Zr-2.5Nb alloy. This suggests the role of higher β precipitate volume fraction, coarser precipitate size, Nb lean precipitate, along with higher degree of recovery in improving the propagation resistance of WQA Zr-2.5Nb alloy.

In summary, *CCL* parameter of WQA Zr-2.5Nb alloy is weakly sensitive to even large variation in its TMP parameters. However, combination of TMP parameters viz., SHT at 850°C for 15-30 min, followed by 20% cold working and subsequent aging at 540°C for 24 h provides the best stable crack propagation resistance of WQA Zr-2.5Nb alloy.

vii. This study proposes a master relationship between the microstructural features and stable crack propagation resistance of WQA Zr-2.5Nb alloy (as shown below), to separate out the role of individual microstructural features on stable crack propagation resistance. The relationship suggests that out of several microstructural changes associated with SHT and aging treatments, only the changes in primary α & β precipitate volume fractions play significant role in governing the fracture behavior of WQA Zr-2.5Nb alloy. Also, smaller α' grain size is an important secondary microstructural feature, which improves the propagation resistance of WQA Zr-2.5Nb alloy.

$$\boxed{\begin{aligned}\frac{dJ}{da} = 48.84 + 1.04\left(V_{Primary\ \alpha}\right) - 0.37(D_{\alpha'}) - 7.02 \times 10^{-8}(Nb_{\alpha'}) - 1.11(V_{\beta\ Precipitate}) \\ - 4.51 \times 10^{-7}(D_{\beta\ Precipitate}) - 1.08 \times 10^{-10}(Nb_{\beta\ Precipitate})\end{aligned}}$$

In this Equation, terms $V_{Primary\ \alpha}$ & $V_{\beta\ Precipitate}$ respectively represent the volume fractions (in %) of Primary α & β precipitates; $Nb_{\alpha'}$ & $Nb_{\beta\ Precipitate}$ respectively represent the Nb concentrations (in wt. %) of α' & β precipitates; and $D_{\alpha'}$ & $D_{\beta\ Precipitate}$ respectively represent the grain sizes (in µm) of α' & β precipitates.

viii. An important highlight of this study is that the WQA material exhibits fracture toughness close to, though higher than double melted, DM-CWSR material at ambient and quadruple melted, QM-CWSR material at 300°C, despite having relatively coarser grain size and weaker texture. This is expected to ensure lower in-reactor dimensional changes due to reduced irradiation growth (because of possessing nearly random texture) and irradiation induced creep and hence improving the useful lives of the pressure tubes.

7.4 Influence of Analysis Procedures on Fracture Toughness Parameters

7.4.1 Resistance Curve and Basic Test Methodologies

i. Single specimen methodology of fracture toughness evaluation (Resistance Curve, RC method) as compared to multi specimen (Basic Test, BT method), ensures conservative estimation of toughness, as at a particular crack length it predicted relatively less *J* parameter. Deviation in the *J* parameter determined from two methods has dependence on the crack length, such that it increases with a/W ratio. The initiation toughness, J_Q and propagation toughness, $J_{F(max)}$ are weakly sensitive to these evaluation approaches, however, the resistance curve slope (dJ/da) shows substantial dependency on these approaches.

ii. In the BT method, ductile crack growth correction parameter 'α' (during second crack growth correction stage) influences the *J* parameter at a particular crack length and hence, the *J-R* curve. Increase in the magnitude of parameter α reduces the *J* parameter at a particular crack length and consequently reduces the deviation between the *J-R* curves derived from the RC and BT methodologies. To reduce the deviations and also to ensure its independence with crack length, an optimised range of 3-4 for the second crack growth correction parameter 'α' in BT method was suggested.

7.4.2 Influence of Test Standards

i. Under a given combination of geometry and loading condition (i.e., specimen dimensions and load & LLD values), both ASTM and ISO standards provide practically similar *J* values. This emphasizes that the DCG methodologies considered by these standards do not cause difference in the *J* parameters. Therefore, as far as determination of *J* parameter under a given scenario (i.e., geometrical dimensions and loading condition) is concerned, the two standards could be equally applicable.

ii. The post processing of *J-R* curve recommended by the two standards results in the difference in measured toughness parameters, and suggests the following:

a. Dissimilar BL slopes recommended by ASTM and ISO standards primarily cause difference in the initiation toughness parameters. Higher BL slope recommended by ISO standard correspondingly results in lower initiation toughness.

b. The structural integrity of internally pressurized components such as; pressure tubes, in terms of the limit against stable crack propagation for the catastrophic failure (governed by *CCL* parameter) is practically independent of the two standards. This is because, the $J_{F(max)}$ parameters, which govern the *CCL* parameters through an iterative assessment approach, were practically insensitive to the two standards. Since, the *J-R* curves derived from the two standards were nearly identical, even the graphical method of *CCL* determination will yield nearly identical *CCL* values. Therefore, to assess the safety margins for the necessary ‘Leak Before Break’ (LBB) condition of such components, so as to avoid their catastrophic failure during operation, the two standards should be equally applicable.

c. If the *J-R* curve slope is considered as a propagation toughness parameter and its determination is based on the consideration of valid data points, bounded by ELs, the ASTM standard might be a preferable choice because of utilizing the larger data range. It should be kept in mind that the valid data range for ISO standard is 10 % of the initial unbroken ligament of the sample and hence is dependent on sample width. The valid data range for the ASTM method is independent of samples width. For samples of width 30 mm and with unbroken ligament 50 % of sample width both the standards will have same valid data range and will yield identical fracture toughness parameters.

d. Deviation in ASTM and ISO derived toughness parameters is the function of material's flow stress, such that high strength materials, in general, shows least deviation.

SCOPE OF FUTURE WORK

Pressure tubes of Zr-2.5Nb alloy are being used in various metallurgical conditions in pressurized water reactors. During service their mechanical properties degrade due to hydrogen pick up and in-reactor dimensional changes. In-reactor performance of the pressure tubes is the function of their fracture toughness along with aqueous corrosion, irradiation growth and irradiation creep, which are controlled by composition of α and β phases, crystallographic texture and grain size. In the present study, influence of TMP parameters viz., SHT temperatures, SHT soaking duration, degree of cold work and aging temperatures on fracture behavior of Zr-2.5Nb alloy were studied, and a set of TMP parameters which provided the best crack fracture resistance of WQA material was suggested. The study showed that a lower SHT temperature (850°C) provides better stable crack propagation resistance of WQA Zr-2.5Nb alloy. However, this study also showed that a higher SHT temperature (890°C) results in nearly random basal pole texture of WQA Zr-2.5Nb alloy. Higher SHT temperature, because of causing texture randomization is expected to reduce the irradiation growth of WQA pressure tubes, which consequently lower the in-reactor dimensional changes of WQA pressure tubes. Furthermore, a higher SHT temperature also resulted in coarser microstructure, which could further be advantageous for the in-reactor creep point of view of WQA pressure tubes. Since, the scope of present work was limited to study the influence of TMP parameters on the fracture behaviour, other life limiting factor could not be studied. Hence, it is suggested that following works need to be carried out for the full exploitation of the potential of this alloy.

i. Studies of the in-pile and out of pile creep behavior of Zr-2.5Nb alloy under WQA condition and its comparison with that under CWSR condition.

ii. Study of the influence of hydrogen concentration on fracture toughness of WQA Zr-2.5Nb alloy.

iii. Studies on 'Delayed Hydride Cracking' (DHC) behavior of Zr-2.5Nb alloy under WQA condition and its comparison with that under CWSR condition.

iv. Examination of the aqueous corrosion resistance of Zr-2.5Nb alloy under WQA condition.

v. Study for the evaluation of influence of irradiation on the mechanical behavior of WQA Zr-2.5Nb alloy.

REFERENCES

[1] R.N. Singh, S. Mukherjee, R. Kishore, and B.P. Kashyap “Flow behaviour of a modified Zr–2.5 wt% Nb pressure tube alloy”, *Journal of Nuclear Materials*, **345** (2005) 146-161.

[2] C. Coleman, M. Griffiths, V. Grigoriev, V. Kiseliov, B. Rodchenkov and V. Markelov “Mechanical properties of Zr-2.5Nb pressure tubes made from electrolytic powder”, *ASTM STP* **1505** (2007) 699-723.

[3] D. Srivastava, G.K. Day, and S. Banerjee “Evolution of microstructure during fabrication of Zr-2.5 Wt pct Nb alloy pressure tubes”, *Metallurgical and Materials Transactions A,* **26A** (1995) 2707-2718.

[4] M. Koike and T. Asada “Irradiation creep and growth of pressure tubes in HWR Fugen”, *Journal of Nuclear Materials*, **159** (1988) 62-74.

[5] K. Takayam “Post-irradiation examination and evaluation of Zr-2.5%Nb pressure tube of FUGEN” Water channel reactor fuels and fuel channels: Design, performance, research and development, IAEA-TECDOC-**997** (1996).

[6] E.F. Ibrahim "In-reactor Creep of Zr-2.5Nb Tubes at 570 K" Zirconium in Nuclear Applications: *ASTM STP* **551** (1974) 249-262.

[7] A.V. Nikulina, N.G. Reshetnikov, P.V. Shebaldov, L.E. Ageenkova, V.S. Fomin, Yu. P. Shevnin, and S.A. Kochergin “Fabrication Technology of RBMK Zr-2.5Nb Pressure Tubes,” Ser. Materials Science and Novel Materials, **36 (2)**, (1990) 46-54.

[8] M.H. Koike, S. Onose, K. Nagamatsu and M. Kawajiri ‘Hydrogen pick-up and degradation of Heat-treated Zr-2.5Nb Pressure Tubes’, *JSME International Journal, Series B: Fluids and Thermal Engineering,* **36 (3)** (1993) 464-470.

[9] V. Grytsyna, A. Stukalov, T. Chernyayeva, V. Krasnorutskyy, D. Malykhin, V. Voyevodin and V. Bryk "Destruction of Crystallographic Texture in Zirconium Alloy Tubes" *Journal of ASTM International*, **2 (8)** (2005) 305-329.

[10] P.A. Ross-Ross and V. Fidleris, Proceeding of International Conference on Creep and Fatigue in Elevated Temperature Applications (1973) paper C216.73.

[11] R.N. Singh, A.K. Bind, J.B. Singh, J.K. Chakravartty, V. Thomas Paul, K. Madhusoodnan, Satyam Suwas, S. Saroja, A.K. Suri, and S. Banarjee "Development and Characterization of Microstructure and Mechanical Properties of Heat-Treated Zr–2.5Nb Alloy for AHWR Pressure Tubes" *Material Performance and Characterization*, **2** (2013) 120-133.

[12] R. Choubey and J.A. Jackman "Microsegregation of Oxygen in Zr-2.5Nb Alloy Materials" *Metallurgical and Materials Transactions A*, **27A** (1996) 431-440.

[13] R. Krishnan and M.K. Asundi "Zirconium alloys in nuclear technology" *Proc. Indian Acad. Sci (Engg Sci.)*, **4 (1)** (1981) 41-56.

[14] H.G. Rickover "The Decision to Use Zirconium in Nuclear Reactors" Zirconium Production and Technology, The Kroll Medal Papers 1975-2010, **TID 26740**, 9-20.

[15] Te-Lin Yau, "Corrosion of Zirconium", Corrosion Engineering Handbook, Second Edition-3 (1996).

[16] R.P. Syre "Zirconium activities in Europe: 1945-1984" Zirconium in the Nuclear Industry: Seventh International Symposium, *ASTM STP* **939** (1987) 35-46.

[17] H.S. Pomerance "Thermal Neutron Capture Cross Sections" *Physics Review*, **88** (1952) 412-413.

[18] H.S. Pomerance and J.I. Hoover "Thermal neutron absorption cross sections for separated isotopes" Oak Ridge, TN: Atomic Energy Commission, **MDDC-1650** (1948).

[19] D.O. Northwood "The development and applications of zirconium alloys" *Materials & Design*, **6 (2)** (1985) 58-70.

[20] “Assessment and management of ageing of major nuclear power plant components important to safety: CANDU pressure tubes” *IAEA, Vienna, IAEA-TECDOC*-**1037** (1998).

[21] “Delayed Hydride Cracking of Zirconium Alloy Fuel Cladding” IAEA-TECDOC-**1649** (2010).

[22] H.K. Khandelwal, K. Sharma, R. Chhibber "Mechanical Behavior of Nuclear Structural Materials-Application of Automated Ball Indentation Approach" LAP Lambert Academic Publishing (2013) ISBN-13: 9783659491733.

[23] V. Fidleris "Summary of experimental results on in-reactor creep and irradiation growth of zirconium alloys" *Atomic Energy Review* **13** (1975) 50-80.

[24] P.J. Richinson, H.W. Wong and P.J. Ellis "Fuel channel life limiting factors that dictate fuel channel maintenance requirements" CANDU Maintinence Conference, Toronto, Canada (1995) 305-309.

[25] A.R. Causey, V. Fidleris, S.R. MacEwen and C.W. Schulte "In reactor deformation of Zr-2.5Nb pressure tubes" Influence of Radiation on Mechanical Properties, Thirteen International Symposium (Part-II), *ASTM STP* **956** (1987) 54-68.

[26] Y. M. Cheong, U.S. Gong, K.N. Chao, S.S. Kim, Y.S. Kim “Formation and growth of hydride blisters in Zr-2.5Nb pressure tubes” *Journal of the Korean Nuclear Society*, **33 (2)**, 2001, 192-199.

[27] A.H. de Menibus, Q. Auzoux, O. Dieye, P. Berger, S. Bosonnet, E. Foy, V. Macdonald, J. Besson, and J. Cr´epin “Formation and Characterization of Hydride Blisters in Zircaloy-4 Cladding Tubes” *Journal of Nuclear Materials*, **449 (1-3)**, 2014, 132-147.

[28] C.E. Ells, E.F. Ibrahim and A.R. Causey "Predicted creep ductility of zirconium alloy pressure tubes in power reactors", presented at International Conference on Creep, (1986).

[29] R. Dutton and M.P. Puls "A theortical model for hydrogen induced sub critical crack growth" Conference on effect of hydrogen on behaviour of materials, American Institute of Mining, Metallurgical and Petroleum Engineers (1975) 516-525.

[30] M.P. Puls "Developments in Delayed Hydride Cracking in Zirconium Alloys"

[31] "Delayed hydride cracking in zirconium alloys in pressure tube nuclear reactors" *IAEA-TECDOC*-1410 (2004).

[32] A.F. Shalabi and D.A. Meneley "Initiation of delayed hydride cracking in zirconium-2.5 wt% niobium" *Journal of Nuclear Materials,* **173 (3)** (1990) 313-320.

[33] R.N. Singh, Niraj Kumar, R. Kishore, S. Roychaudhury, T.K. Sinha, and B.P. Kashyap "Delayed hydride cracking in Zr-2.5Nb pressure tube material" *Journal of Nuclear Materials* **304** (2002) 189-203.

[34] S. Sagat, C. Coleman, M. Griffiths and B. Wilkins "The Effect of Fluence and Irradiation Temperature on Delayed Hydride Cracking in Zr-2.5Nb" Zirconium in the Nuclear Industry: Tenth International Symposium, *ASTM STP* **1245** (1993) 35-61.

[35] R.N. Singh, P. Ståhle, J.K. Chakravartty and A.A. Shmakov "Threshold stress intensity factor for delayed hydride cracking in Zr-2.5%Nb pressure tube alloy" *Materials Science and Engineering: A* **523** (2009) 112-117.

[36] B.A. Cheadle and E.G. Price, "Operating performance of CANDU pressure tubes", presented at *IAEA Technical Committee Meeting on the Exchange of Operational Safety Experience of Heavy Water Reactors, Vienna*, **AECL-9939** (1989).

[37] B.A. Cheadle, C.E. Coleman, E.G. Price, V.K. Bajaj and W.R. Clendening "Advances in fuel channel technology for CANDU reactors" presented at *IAEA Technical Committee Meeting on Advances in Heavy Water Reactors, Toronto, Canada*, (1993).

[38] J.R. Theaker, R. Choubey, G.D. Moan, S.A. Aldridge, L. Davis, R.A. Graham and C.E. Coleman "Fabrication of Zr-2.5Nb pressure tubes to minimize the harmful effects of trace elements" *ASTM STP* **1245** (1994) 221-241.

[39] G.D. Moan, J.R. Theaker, P.H. Davis, I. Aitchison, C.E. Coleman, R.A. Graham and S.A. Aldridge "Improvements in the fracture toughness of CANDU Zr-2.5Nb Pressure Tubes", *International Nuclear Congress, Toronto, Canada,* (1993).

[40] E.G. Price, B.A. Cheadle, G.R. Evans and M.W. Hardie "Update of operating experience with cold-worked Zr-2.5%Nb pressure tubes in CANDU reactors" presented at *IAEA Technical Committee Meeting on Exchange of Operational Safety Experience of Pressurized Heavy Water Reactors, Cordoba, Argentina,* **COG-91-65** (1991).

[41] E.F. Ibrahim "Mechanical properties of cold drawn Zr-2.5Nb pressure tubes after up to 12 years in CANDU reactors" *Conference on Nuclear Reactor Core Applications, BNES, London,* **AECL-9480** (1987) 73-78.

[42] ASM Handbook "Alloy phase diagrams" **3**, (1992) 308.

[43] R.G. Fleck, E.G. Price and B.A. Cheadle “Pressure tube development for CANDU reactors” Zirconium in the Nuclear Industry: Sixth International Symposium, *ASTM STP* **824**, (1984) 88-105.

[44] C.E. Coleman, B.A. Cheadle, C.D. Cann, and J.R. Theaker "Development of Pressure Tubes with Service Life Greater Than 30 Years" Zirconium in the Nuclear Industry: Eleventh International Symposium, *ASTM STP* **1295** (1996) 884-898.

[45] J.R. Theaker, R. Choubey, G.D. Moan, S.A. Aldridge, L. Davis, R.A. Graham, and C.E. Coleman, "Fabrication of Zr-2.5Nb Pressure Tubes to Minimize the Harmful Effects of Trace Elements," Zirconium in the Nuclear Industry: Tenth International Symposium, *ASTM STP* **1245**, (1994) 221-242.

[46] A.K. Bind, R.N. Singh, H.K. Khandelwal, S. Sunil, J.K. Chakravartty “Fracture toughness evaluation of Zr-2.5Nb pressure Tubes manufactured employing double forging for PHWR700” *ASTM-Materials Performance and Characterization*, **3 (3)** (2014) 322-341.

[47] B.A. Cheadle "The Development of Zr-2.5Nb Pressure Tubes for CANDU Reactors" *Journal of ASTM International*, **7 (8)** (2010) 1-15.

[48] R. Choubey, S.A. Aldridge, J.R. Theaker, C.D. Cann, and C.E. Coleman "Effects of Extrusion-Billet Preheating on the Microstructure and Properties of Zr-2.5Nb Pressure Tube Materials" Zirconium in the Nuclear Industry: Eleventh International Symposium, *ASTM STP* **1295** (1996) 657-675.

[49] R.A. Holt and E.F. Ibrahim, "Factors affecting the anisotropy of irradiation creep and growth of zirconium alloys " *Acta Metallurgica* **27 (8)** (1979) 1319-1328.

[50] M.P. Puls, R.L. Tapping and Z.H. Walker "ACR-700 Advances in Materials" *Physics in Canada*, **60 (6)** (2004) 369-381.

[51] B.A. Cheadle, C.F. fills and W. Evans "The development of texture in zirconium alloy tubes" *Journal of Nuclear Materials*, **23** (1967) 199-208.

[52] B.A. Cheadle, "Fabrication of Zirconium Alloys into Components for Nuclear Reactors" Zirconium in the Nuclear Industry, *ASTM STP* **633** (1977) 457-485.

[53] M. Kiran Kumar, C. Vanitha, I. Samajdar, G.K. Dey, R. Tewari, D. Srivastava and S. Banerjee “Textural and microstructural developments during fabrication of Zr–2.5Nb pressure tubes” *Journal of Nuclear Materials* **335** (2004) 48-58.

[54] R.B. Adamson "Irradiation growth of zircaloy" Zirconium in the Nuclear Industry, *ASTM STP* **633** (1977) 326-343.

[55] M. Leger and R.G. Fleck "Irradiation Growth in Zr-2.5Nb" Zirconium in the Nuclear Industry: Sixth International Symposium, *ASTM STP* **824** (1984) 409-426.

[56] E.F. Ibrahim and B.A. Chedale "Development of Zirconium Alloys for Pressure Tubes in Candu Reactors" *Canadian Metallurgical Quarterly*, **24** (1985) 273-281.

[57] E.F. Ibrahim, "Deformation of cold-drawn tubes of Zr-2.5 wt% Nb after 7 years in-reactor" *Journal of Nuclear Materials*, **118** (1983) 260-268.

[58] V. Fidleris "The Creep Strength of Quenched and Aged Zr-2.5 wt% Nb Alloy" *Journal of Nuclear Materials*, **54 (2)** (1974) 199-211.

[59] L.G. Bell and T.S. Dicks "The Effect of Prior Beta Grain Size on the Ductility of Zirconium-2.5 Weight Per Cent Niobium Alloy" *Canadian Metallurgical Quarterly,* **4** (1965) 259-268.

[60] C.E.L. Hunt and P. Niessen "The continuous cooling transformation behaviour of Zirconium-Niobium-Oxygen alloys" *Journal of Nuclear Materials*, **38** (1971) 17-25.

[61] R. Choubey and J.A. Jackman, "Microsegregation of oxygen in Zr-2.5Nb alloy materials", *Metallurgical & Material Transactions: A*, **27A** (1996) 431-440.

[62] V.F. Urbanic and M. Griffiths: Zirconium in the Nuclear Industry: 12th International. Symposium, ASTM STP **1354**, 2000, 641-57.

[63] J.R. Rice "A Path Independent Integral and the Approximate Analysis of Strain Concentration by Notches and Cracks" *Journal of Applied Mechanics*, **35** (1968) 379-386.

[64] G.R. Irwin "Analysis of stresses and strains near the end of a crack traversing a plate". *Journal of Applied Mechanics,* **24** (1957) 361-364.

[65] M.L. Williams "On the stress distribution at the base of a stationary crack" *Journal of Applied Mechanics,* **24** (1957) 109-114.

[66] R.M. McMeeking and D.M. Parks "On criteria for J-dominance of crack-tip fields in large-scale yielding" Elastic-plastic fracture, *ASTM STP* **668** (1979) 175-194.

[67] F.A. McClintock “Plasticity aspect of fracture" *Fracture: an advanced treatise*, **3** *London: Academic press* (1971) 47-225.

[68] J.R. Rice, R.M. McMeeking, D.M. Parks and E.P. Sorensen “Recent finite element studies in plasticity and fracture mechanics” *Computer Methods in Applied Mechanics and Engineering*, **17/18** (1979) 411-442.

[69] ASTM E399-12 “Standard Test Method for Linear-Elastic Plane-Strain Fracture Toughness *KIc* of Metallic Materials” (2012).

[70] K. Wallin and A. Laukkanen “Improved Crack Growth Corrections for J-R Curve Testing” *Engineering Fracture Mechanics*, **71** (2004) 1601–1614.

[71] S.J. Garwood, J.N. Robinson and C.E. Turner “The measurement of crack growth resistance curves (R-curves) using the J integral” *International Journal of Fracture*, **11** (1975) 528-530.

[72] M.R. Etemad and C.E. Turner “An experimental investigation of slow stable crack growth using HY130 steel” *Journal of Strain Analysis*, **20** (1985) 201-208.

[73] H.A. Ernst, P.C. Paris and J.D. Landes “Estimations on J-integral and tearing modulus T from a single specimen test record” Fracture mechanics: thirteenth conference, *ASTM STP* **743** (1981) 476-502.

[74] J.A. Joyce and J.P. Gudas “Computer interactive J_{IC} testing of navy alloys” Elastic-plastic fracture, ASTM STP **668** (1979) 451-468.

[75] A. Neimitz “The jump-like crack growth model, the estimation of fracture energy and JR curve” *Engineering Fracture Mechanics*, **75** (2008) 236-252.

[76] M. Kroon, J. Faleskog and H. Oberg “A probabilistic model for cleavage fracture with a length scale – parameter estimation and predictions of growing crack experiments” *Engineering Fracture Mechanics*, **75** (2008) 2398-2417.

[77] X.K. Zhu and J.A. Joyce “Review of fracture toughness (G, K, J, CTOD, CTOA) testing and standardization” *Engineering Fracture Mechanics*, **85** (2012) 1-46.

[78] ASTM E 1820-11, “Standard Test Method for Measurement of Fracture Toughness” (2011).

[79] M. Daunys, R. Dundulisa, A. Grybenas and P. Krasauskasa “Hydrogen influence on mechanical and fracture mechanics characteristics of zirconium Zr–2.5Nb alloy at ambient and elevated temperatures” *Nuclear Engineering and Design*, **238** (2008), 2536-2545.

[80] P.H. Davies and C.P. Sterns “Fracture toughness testing of zircaloy pressure tube material with radial hydrides using direct-current potential drop” *ASTM STP* **905** (1986), 379-400.

[81] F.H. Huang “Fracture toughness evaluation for zircaloy-2 pressure tubes with the electric-potential method” *ASTM International Symposium on Small specimen test techniques applied to nuclear reactor vessel thermal annealing and plant life extension*, New Orlearns, LA, USA, 29-31 Jan 1992, 182-198.

[82] L.A. Simpson and C.K. Chow “Effect of metallurgical variable and temperature on the fracture toughness of zirconium alloys pressure tubes”, *ASTM STP* **939** (1987) 579-596.

[83] R.N. Singh, A.K. Bind, N.S. Srinivasan and P. Ståhle “Influence of Hydrogen Content on Fracture Toughness of CWSR Zr-2.5Nb Pressure Tube Alloy” *Journal of Nuclear Materials* **432** (2013) 87-93.

[84] T. Asada, H. Kimoto, N. Chiba and Y. Kasai “Fracture Toughness Evaluation of Heat-Treated Zr-2.5Nb Pressure Tubes”, *ASTM STP* **1132** (1991) 99-118.

[85] C.K. Chow, C.E. Coleman, R.R. Hosbons, P.H. Davies, M. Griffiths and R. Chouby “Fracture toughness of irradiated Zr-2.5Nb pressure tubes from CANDU reactors”, *ASTM STP* **1132** (1991) 246-275.

[86] R.R. Hosbons, P.H. Davies, M. Griffiths, S. Sagat and C.E. Coleman "Effect of long-term irradiation on the fracture properties of Zr-2.5Nb pressure tubes" *ASTM STP* **1354** (2000) 122-138.

[87] A.K. Bind, R.N. Singh, S. Sunil, H.K. Khandelwal "Comparison of *J*-parameters of Cold Worked and Stress Relieved Zr-2.5Nb Pressure Tube Alloy Determined using Load Normalization and Direct Current Potential Drop Technique" *Engineering Fracture Mechanics*, **105** (2013) 200-210.

[88] C.E. Coleman, J.R. Theaker and K.V. Kidd "Effect of fabrication variables on irradiation response of crack growth resistance of Zr-2.5Nb" *Journal of ASTM International*, **1 (7)** (2004).

[89] Y.S. Kim, Y.G. Matvienko and H.C. Jeong "Development of experimental procedure based on the load separation method to measure the fracture toughness of Zr-2.5Nb tubes" *Key Engineering Materials*, **345-346** (2007) 449-452.

[90] J.A. Joyce "Analysis of the E08.02 High Rate Round Robin" *Journal of Testing and Evaluation*, **29 (4)** (2001) 329-351.

[91] R. Herrera, and J.D. Landes "Direct J-R Curve Analysis: A Guide to the Methodology," *Fracture Mechanics: Twenty-First Symposium, ASTM STP* **1074** (1990) 24-43.

[92] J.D. Landes, Z. Zhou, K. Lee and R. Herrera "Normalization Method for Developing J-R Curves with the LMN Function" *Journal of Testing and Evaluation*, **19 (4)** (1991) 305-311.

[93] K. Lee "Elastic-Plastic Fracture Toughness Determination Under Some Difficult Conditions," Ph.D. Dissertation, The University of Tennessee, Knoxville (1995).

[94] J.D.G. Sumpter and C.E. Turner "Method for laboratory determination of J_C (contour integral for fracture analysis)" Cracks and fracture, *ASTM STP* **601** (1976) 3-18.

[95] C.E. Turner “Fracture toughness and specific energy: a reanalysis of results” *Materials Science and Engineering*, **11** (1973) 275-282.

[96] J.D.G. Sumpter “J_C determination for shallow notch welded bend specimens” *Fatigue & Fracture of Engineering Materials & Structures,* **10** (1987) 479-493.

[97] ISO 12135:2002(E) "Metallic materials-Unified method of test for the determination of quasistatic fracture toughness".

[98] ISO 12135:2002/Cor 1:2008 "Metallic materials-Unified method of test for the determination of quasistatic fracture toughness".

[99] V. Perovic, G.C. Weatherly and R.G. Fleck "Characterization of Dislocation Substructures in Zr-2.5 Nb Pressure Tube Alloys" *Canadian Metallurgical Quarterly*, **24** (1985) 253-257.

[100] J.J. Kearns, "Thermal Expansion and Preferred Orientation in Zircaloy" Report of Washinghouse Electric Corporation, Bettice Atomic Power Laboratory, Pittsburgh, P.A., **WAPD-TM-472** (1965).

[101] N. Saibaba, S. Jha, S. Tonpe, K. Vaibhaw, V. Deshmukh, S. Ramana Rao, K. Mani Krishna, S. Neogy, D. Srivastava, G.K. Dey, R. Kulkarni, B. Rath, E. Ramadasan and S. Anantharaman, “Microstructural studies of heat treated Zr-2.5Nb alloy for pressure tube applications” *Journal of ASTM International*, **8** (2011) 1-15.

[102] J.H. Hollomon "Tensile Deformation" *Transactions of the Metallurgical Society of AIME*, **162** (1945) 268-290.

[103] G.F. Pittinato, V. Kerlins, A. Phillips, M.A. Russo “SEM/TEM Fractography Handbook” Mc Donnell Douglas Astronautics Company, Huntington Beach, California, (1975) 31.

[104] C.D. Beachem, D.A. Meyn “Fracture by microscopic plastic deformation processes” Electron Fractography, *ASTM STP* **436** (1968) 59-88.

[105] R.W. Hertzberg “Deformation and Fracture Mechanics of Engineering Materials” Fifth Edition, 2012, John Wiley & Sons Publishing, United States.

[106] T.L. Anderson “Fracture Mechanics: Fundamentals and Applications” Third Edition, 2005.

[107] G.E. Dieter “Mechanical Metallurgy” Third Edition, 2013, McGraw Hill Education Publishing, United States.

[108] M.B. Bever, D.L. Holt and A.L. Titchener “The Stored Energy of Cold Work” *Progress in Materials Science*, **17** (1973) 5-177.

[109] M.B. Bever and L.B. Ticknor “The energy stored during the cold working of a gold-silver alloy” *Acta Metallurgica*, **1** (1953) 116-122.

[110] A.L. Etter, T. Baudin, M.H. Mathon, W. Swiatnicki and R. Penelle “Stored energy evolution in both phases of a duplex steel as a function of cold rolling reduction” *Scripta Materialia,* **54** (2006) 683-688.

[111] M. Verdier, I. Groma, L. Fladin, J. Landvai, Y. Brechet and P. Guyot “Dislocation densities and stored energy after cold rolling of Al-Mg alloys- using Resistivity and DSC” *Scripta Materialia,* **37 (4)**, 449-454.

[112] Shi-Hoon Choi and Young-Sool Jin “Evaluation of stored energy in cold-rolled steels from EBSD data” *Materials Science and Engineering-A,* **371** (2004) 149-159.

[113] A.L. Titchener and M.B. Bevert “The stored energy of cold work and its relation to work softening” *Acta Metallurgica*, **8** (1960) 338-342.

[114] A.A. Benzerga, Y. Bre´chet, A. Needleman and E. Van der Giessen “The stored energy of cold work: Predictions from discrete dislocation plasticity” *Acta Materialia,* **53** (2005) 4765-4779.

[115] A.L. Titchener “The stored energy of cold work in relation to the grain size and other variables” *Acta Metallurgica*, **9** (1961) 379-382 (Letters to the editor).

[116] I. Baker, L. Louis and D. Mandal “The Effect of Grain Size on the Stored Energy of Cold Work as a Function of Strain for Polycrystalline Nickel” *Scripta Materialia*, **32 (2)** (1995) 167-171.

[117] W. Oliferuk and M. Maj “Stress–strain curve and stored energy during uniaxial deformation of polycrystals” *European Journal of Mechanics A/Solids* **28** (2009) 266-272.

[118] B.T. Chang and J.C.M. Li “Stored Energy of Cold Work in Polystyrene” *Polymer Engineering and Science,* **28 (18)** (1988) 1198-1202.

[119] M. Ratwani and G.D. Gupta, "Interaction between parallel cracks in layered composites", Technical Report NASA TR-73-6, IFSM-73-37, Lehigh University, Bethlehem, P.A., USA (1973) 1-26.